2018

TRIPLE-HELICATE SELF-ASSEMBLY, DYNAMICS, AND ANION BINDING OF HALOGEN-BONDING m-ARYLENE-ETHYNYLENE OLIGOMERS

Casey John Massena

TRIPLE-HELICATE SELF-ASSEMBLY, DYNAMICS, AND ANION BINDING OF HALOGEN-BONDING *m*-ARYLENE-ETHYNYLENE OLIGOMERS

By

CASEY JOHN MASSENA

Bachelor of Arts, Westmont College, Santa Barbara, California, 2006

Dissertation

presented in partial fulfillment of the requirements
for the degree of

Doctor of Philosophy
in Organic and Supramolecular Chemistry

The University of Montana
Missoula, MT

November 2018

Approved by:

Scott Whittenburg, Dean of The Graduate School
Graduate School

Christopher P. Palmer, Ph.D., Chair
Department of Chemistry and Biochemistry

Orion B. Berryman, Ph.D., Adviser
Department of Chemistry and Biochemistry

Nigel D. Priestley
Department of Chemistry and Biochemistry

Earle R. Adams
Department of Chemistry and Biochemistry

Mark L. Grimes
Division of Biological Sciences

Massena, Casey, Ph.D., November 2018 Organic and Supramolecular Chemistry

TRIPLE-HELICATE SELF-ASSEMBLY, DYNAMICS, AND ANION BINDING OF HALOGEN-BONDING *m*-ARYLENE-ETHYNYLENE OLIGOMERS

Chairperson: Christopher P. Palmer

Adviser: Orion B. Berryman

The form and function of biopolymers depend on the precise folding and organization of vast arrays of chemical groups. Hence, the simple yet elegant helix is one of the most pervasive structural elements in nature. Moreover, given the ubiquity and importance of anions, anion-interfacing helical structures hold promise as useful, stimuli-responsive supramolecules. Like metals, anions can powerfully coordinate organic ligands and promote helical self-assembly. However, anion coordination is far less understood than that of metals. Halide ions are an especially challenging target due to their small size, low charge, and variable coordination number/geometry. This work presents a new strategy that leverages the linearity of halogen bonding to form high-fidelity, I^-- and Br^--encapsulating triple helicates in solution and the solid state. These triplexes proved kinetically stable, and their ligands exchanged slowly on the seconds timescale. In contrast, intrachannel anion exchange was rapid, on the millisecond-or-faster timescale. Taken together, these findings offer a tractable strategy to create anion-responsive and kinetically stable helical secondary structure.

Chapter 1 provides an introduction to anion helicates/foldamers and situates these supramolecules within their larger framework. This chapter will be augmented and submitted as a review article. Chapter 2 introduces preliminary work with a halogen-bonding *m*-arylene-ethynylene three-mer. Before synthesizing and studying the eventual nonameric target, the three-mer was screened for halide-ion and ReO_4^- affinity. Interestingly, this trimeric precursor formed stable complexes with ReO_4^- in solution and the solid state. This chapter includes work that was published in *Chemical Communications* (**2015**, 51, 1417–1420). Chapter 3 presents the design and synthesis of the helicate-forming, nonameric target. The first I^--encapsulating triple helicate was fully characterized using ^1H 1D and 2D NMR spectroscopy and single-crystal X-ray diffraction. This chapter includes work that was published in *Angewandte Chemie International Edition* (**2016**, 55, 12398–12402). Chapter 4 presents the first kinetic studies of an anion helicate. Additionally, the first Br^--encapsulating triple helicate was characterized in solution and the solid-state. This chapter includes work that was published in *Angewandte Chemie International Edition* (**2018**, *published online*). Chapter 5 touches on preliminary work and future directions for the project.

Acknowledgments

I thank my advisor, Orion Berryman, for mentoring me as an organic and supramolecular chemist. Together, we accomplished much. I also want to thank my inspirational grandfathers in chemistry, Darren Johnson and Julius Rebek, Jr. I gratefully acknowledge my lab mates (Nick Wageling, Asia Riel, Dan Decato, George Neuhaus, Eric John, Jiyu Sun, and others) and my committee (Chris Palmer, Nigel Priestley, Mark Grimes, and Earle Adams). I thank Ed Rosenberg who served on my committee before retirement. A big thanks also goes out to the Center for Biomolecular Structure and Dynamics, which introduced me to the work of inspiring biochemists (Bruce Bowler, Moses Leavens, Haotian Lei, and Dustin Becht), neurobiologists (Kasper Hansen, Jill Farnsworth, and Jenny Lind), and medicinal chemists (Philippe Diaz, Chuck Thompson, and Don and Andrea Stierle). A huge thanks goes out to all the people who have ever helped me with instrumentation, provided highly-appreciated research advice, or were a huge encouragement (Dan Decato, Earle Adams, Klara Briknarova, Kendal Ryter, Fanny Astruc-Diaz, Ian Chrisman, David Burkhart, Peter Gans, Michael Strain, Mark Cracolice, and Laurie Minns). I thank local business owners Tyler Smith and Steve Rowley for teaching me about the business and entrepreneurial side of chemistry. I also want to thank my family and friends (too many to name, but you know who you are) for their amazing support. And to Catie Wielgasz, my partner (along with our two cats, Adeline and Oliver), I give my thanks and love.

Table of Contents

List of Figures

List of Schemes

List of Tables

List of Abbreviations

$[BAr^{F}{}_{4}]^{-}$ – Tetrakis(3,5-bis(trifluoromethyl)phenyl)borate

^{13}C NMR – Carbon NMR

^{19}F NMR – Fluorine NMR

^{1}H NMR – Proton NMR

Acetone-d_6 – Deuterated acetone

Ag – Silver

at – Acquisition time in seconds

Br^{-} – Bromide

C – Carbon

C_6F_6 – Hexafluorobenzene

$CaCO_3$ – Calcium carbonate

$CaSO_4$ – Calcium sulfate

CD – Circular dichroism

CH_2Cl_2 – Dichloromethane (CD_2Cl_2 is the deuterated form)

CH_3CN – Acetonitrile (CD_3CN is the deuterated form)

CH_3I – Methyl iodide

CH_3OH – Methanol (CD_3OD is the deuterated form)

$CHCl_3$ – Chloroform ($CDCl_3$ is the deuterated form)

Cu – Copper

CuI – Copper (I) iodide

d1 – First delay period in seconds

DFT – Density functional theory

DIPEA – Diisopropylamine

DLS – Dynamic light scattering

DMAP – (*N*,*N*-dimethylamino)pyridine

DMF – Dimethylformamide (DMF-d_7 is the deuterated form)

DMSO – Dimethyl sulfoxide (DMSO-d_6 is the deuterated form)

DOSY – Diffusion-ordered spectroscopy

D_t – Diffusion coefficient

equiv – Equivalent(s)

ESI-HRMS – Electrospray ionization high-resolution mass spectrometry

Et_2O – Diethyl ether

Et_3N – Triethylamine

EtOAc – Ethyl acetate

EtOH – Ethanol

EWG – Electron withdrawing group

EXSY – Exchange spectroscopy

F^- – Fluoride

H_2O – Water

$H_2PO_4^-$ – Dihydrogen phosphate

HSO_4^- – Hydrogen sulfate

Hz – Hertz

I^- – Iodide

I – Iodine

I_2 – Molecular iodine

IPA – Isopropanol

ITC – Isothermal titration calorimetry

J – Coupling constant

K_2CO_3 – Potassium carbonate

K_a – Association constant (K_1 and K_2 are the first and second association constants, respectively, of a higher-order binding model as specified)

LA/LB – Lewis acid/base

LP – Lone pair

M – Left-handed helix

$MgSO_4$ – Magnesium sulfate

mixN/R – Mixing time in seconds

MTBE – Methyl-*tert*-butyl ether

N – Nitrogen

N_2 – Nitrogen gas

Na – Sodium (Na^+ is the cationic form)

$Na[BAr^F{}_4]$ – Sodium tetrakis(3,5-bis(trifluoromethyl)phenyl)borate

Na_2CO_3 – Sodium carbonate

$Na_2S_2O_3$ – Sodium thiosulfate

NaCl – Sodium chloride

NaI – Sodium iodide

NaOTf – Sodium triflate

n-BuLi – *n*-Butyllithium

ni – Number of increments

NMR – Nuclear magnetic resonance

NOE – Nuclear Overhauser effect

NOESY – Nuclear Overhauser effect spectroscopy

np – Number of points

nt – Number of transients

OEG – oligo(ethylene glycol)

–OH – Hydroxy group

Os – Osmium

OTf^- – Triflate

P – Right-handed helix

PF_6^- – Hexafluorophosphate

pH – Logarithmic scale of acidity

pK_a – Logarithmic acid dissociation constant

PO_4^{3-} – Phosphate

ppm – Parts per million

pw – Pulse width in microseconds

ReO_4^- – Perrhenate

R_f – Retention factor

r_H – Hydrodynamic radius

ROESY – Rotating frame Overhauser effect spectroscopy

RP-HPLC – Reversed-phase high-performance liquid chromatography

RT – Room temperature

Ru – Ruthenium

sfrq – Spectrometer frequency in MHz

S_NAr – Nucleophilic aromatic substitution

SO_4^{2-} – Sulfate

TBA – Tetra-*n*-butylammonium

TBABr – Tetra-*n*-butylammonium bromide

TBACl – Tetra-*n*-butylammonium chloride

TBAF – Tetra-*n*-butylammonium fluoride

TBAI – Tetra-*n*-butylammonium iodide

TBAOH – Tetra-*n*-butylammonium hydroxide

TcO_4^- – Pertechnetate

THF – Tetrahydrofuran (THF-d_8 is the deuterated form)

TLC – Thin-layer chromatography

TMA – Tetra-*n*-methylammonium

UV-Vis – Ultraviolet-visible

v/*v* – volume-volume ratio

vdW – van der Waals

$\Delta\delta$ – Change in NMR chemical shift

ΣvdW – Sum of the van der Waals

δ – Chemical shift

π – Pi electrons

σ – Standard deviation

Folding of molecular strands is the method nature has selected to position chemical groups in space with atomic precision over nanometric distances and endow biopolymers with such extraordinary functions as enzyme catalysis in proteins and genetic information storage in nucleic acids.[1]

—Ivan Huc

Supramolecular chemistry, which has been called a molecular information science, describes the spontaneous assembly of non-covalently linked molecular clusters of unique shape and composition.[2]

—Kenneth N. Raymond

I predict that the 20th century will come to be viewed as the period in which chemists acquired synthetic and technical mastery over small molecules, and the 21st century as the period in which that mastery was extended to heteropolymers. Mastery over foldamers should provide access to a new universe of molecules that profoundly influence chemistry and society.[3]

—Samuel H. Gellman

1 Introduction and Background

This brief introduction will present the state of the art of small-molecule anion helicates/foldamers that persist in solution. We will restrict our focus to ligands that complete one or more helical turn(s) around an anion or anion-delineated helical axis. Unfortunately, the most recent reviews on anion helicates/foldamers are not comprehensive,[4,5] and new developments have been reported only haphazardly since.[6–8] Therefore, a large portion of this introduction will serve to fill this gap. Guestless and neutral-guest foldamers as well as cation helicates/foldamers will also be broached. Additionally, a survey of *m*-arylene-ethynylene foldamers will be included. Ditopic (cation-anion),[9,10] helically-distorted macrocyclic,[4] polymeric,[11,12] and *o*-phenylene-ethynylene oligomers[13] will not be treated here, and I will refer the reader to the excellent review articles written on these topics. As they become relevant, salient principles of anion-coordination chemistry will be addressed. Lastly, halogen bonding will be discussed throughout the dissertation as needed.

1.1 Helices and Anions in Human Physiology and in the Purview of Supramolecular Chemistry

Quite literally, helices and anions give our bodies form and function—examples of which include light-energy conversions, cell signaling, transport, catalysis, information storage, specific binding, directed flow of electrons, energy capture, crystallization of inorganics, expression and repair of DNA, cochlear amplification, etc. But how does nature create and maintain its dizzying arrays of molecular machines? Out of all the myriad possible conformations and folded states, how do biomolecules assemble into

high-fidelity structures in as fast as microseconds?[14] It does so by efficiently synthesizing oligomers and polymers, which are programmed to fold into functional shapes. Folding is a function of maximizing favorable noncovalent and covalent interactions, minimizing unfavorable ones, and the entropic compensation concomitant with hydrophobic/solvophobic collapse.[15] The mechanisms underlying the hydrophobic/solvophobic effect are complex and not fully understood; however, these supremely important driving forces generally arise from: 1) the low affinity between lipophilic moieties and polar solvent as well as the high affinity between solvent molecules (enthalpic component) and 2) liberation of the rigid network of polar molecules that comprise the solvation shell around lipophilic moieties (entropic component). Hydrophobic collapse is of chief importance in protein folding, which explains why almost half of the amino acids bear lipophilic side chains. Strategically placed within a primary sequence, these nonpolar residues provide the initial thermodynamic driving force for self-assembly. Thereby, nonpolar and polar side chains are brought into close proximity (within molten globules), enabling more directional noncovalent interaction like hydrogen bonding to fine-tune the final folded state. Indeed, every nuance of a biomolecule's final folded state is encoded in the linear sequence of its monomers. Deciphering this molecular coding, which has been parameterized over 4.5 billion year of molecular evolution, is an ongoing goal for chemists and biologists alike. As a result, these biomolecules possess enough rigidity for high-affinity, specific binding while exhibiting sufficient flexibility to optimally accommodate guests within "active sites." Amazingly, the functional groups lining these microenvironments are often widely spaced along a polymeric backbone.[3] Hence and unfortunately for chemists, most natural

voids emerge at the level of tertiary or quaternary structure.[16] Moreover, macromolecular machinery is dynamically guest-responsive, a necessary attribute if is to be useful.

Increasingly, our understanding of the structure and dynamics of biomolecules imparts useful rules for designing life-saving therapies and nanocomponents. Towards functional mimicry of biomolecules, the oligomer/polymer strategy so deftly employed by nature may prove ideal for chemists too. Although many beautiful supramolecules with covalently preorganized active sites have been designed and synthesized for six decades[17]—macrocycles, cavitands, cucurbiturils, catenates, rotaxanes, etc.—it is unlikely they will give rise to the complex diversity seen in nature. These examples and others typically require long syntheses and low-yielding macrocyclizations. Additionally, the voids and curvatures afforded are often rigid and intractable. Indeed, as synthesis becomes increasingly automated, the strategies nature has selected will become progressively appealing to supramolecular chemists.

Supramolecular chemists have arisen from a small but distinguished line of synthetic chemists. Thus, a supramolecular chemist is inexorably a bottom-up tinkerer of molecules. She/he looks to nature for inspiration, but given the overwhelming sophistication of endogenous systems, what could a chemist possibly contribute? Truly, any attempt to recapitulate 4.5 billion years of molecular evolution would be a fool's errand. But chemists can and do create secondary and even tertiary structure that is both unnatural and unique. With good reason, the constraints of natural evolution have restricted the number of building blocks used in biological systems. For example, the human body can generate roughly two million different proteins but does so using only 21 amino acids. Only four RNA bases give rise to stunning molecular machines like

ribosomes. In contrast, the purview of the chemist is every possible combination of elements. In the words of Samuel Gellman, "Therefore, the realization of the potential of folding polymers may be limited more by the human imagination than by physical barriers."[3] Stated earlier, the three-dimensional structure and emergent functionality of supramolecules are encoded within their primary sequences. Thus, as abiotic functional groups are infused into the language of this code, new physicochemical properties have surfaced. *Herein, an entirely new class of helical secondary structure that interfaces with halide ions is introduced.* These helicate structures are switched on/off by adding/removing halide ions; moreover, the helical voids within these triplexes accommodate rapid halide-ion movement. Towards developing anion-responsive and functional supramolecules, anion helicates/foldamers have arisen as a truly unprecedented group of biomimetic oligomers that approach the complexity of nature while providing atomic-scale mechanistic insight related to the structure and dynamics of biological systems.

Helical secondary structure is the most basic form of biopolymeric organization and has been a primary topological focus for supramolecular chemists. This is unsurprising since it is the most expeditious way to introduce cyclicity, rigidity, and three-dimensional structure to a linear sequence of functional groups. In nature, examples of helical secondary structure are rife and include α- and β-helices in proteins, helical polysaccharides like α-amylose, and the diverse structures of DNA and RNA. Anions too are widespread in human physiology. This dissertation largely focuses on I^-, Br^-, and Cl^-, which all play critical roles. A few examples include the thyroid hormones, T_3 and T_4, which are synthesized by double iodination of thyroglobulin tyrosine residues in thyroid

follicles. These hormones are crucial for brain development and normal metabolism.[18] Br^- is an essential trace cofactor needed to form sulfilimine cross-links in collagen IV.[19] Interestingly, the formation of a methionine bromosulfonium encourages productive protein cross-linkages over sulfoxide formation. Lastly, there are copious examples of Cl^- in human physiology. The cystic fibrosis transmembrane conductance regulator, or CFTR, acts as an airway-epithelial passive Cl^- channel that is opened/closed by ATP-bound cytosolic nucleotide-binding domains.[20] Misfolded CFTRs result in compromised mucociliary clearance, leading to the morbidity associated with the disease. As a long-term goal, chemists envision developing channel-replacement therapeutics and other biologically useful molecular machines.[21] Lower-hanging fruits include antimicrobials,[22,23] protein-protein interaction inhibitors,[24–27] and anticancer agents.[28]

1.2 Guestless and Neutral-Guest Foldamers

First coined by Gellman in the mid-1990s,[29] "foldamers" are a class of synthetic oligomers that wrap themselves into well-ordered protein-like structures, which are stabilized by noncovalent interactions between non-adjacent monomers.[30] As is implied by their name, these oligomers dynamically fold/unfold in solution; therefore, molecules that are conformationally locked, such as helicenes, are not foldamers.[31] We will restrict our focus to helical foldamers. Analogous to α-helical structures, guestless helical foldamers lack large-enough central cavities for guest inclusion. Within this class of molecules are two main subclasses, amino-acid foldamers (or aliphatic foldamers) and aromatic-oligoamide foldamers. Amino-acid foldamers are *de novo*, regular-repeating, bioinspired structures that chemically resemble proteins. The linear sequences of these

molecular chains take into account the shapes of the functional groups, solvophobic effects, electrostatic complementarity, and hydrogen-bonding interactions.[32] Chemists who create these bioinspired oligomers are not limited to α-amino acids and frequently utilize β-, γ-, and δ-amino acids or combinations thereof—giving rise to unique structural properties.[3,32–34] For example, the backbone of a β-amino-acid foldamer is more conformationally flexible and in some cases more thermodynamically stable than that of an α-amino-acid counterpart.[1] This unique development has allowed chemists to expand the repertoire of secondary and tertiary structure.[35] More so than with any other category of foldamers, the rules underlying programmable secondary and even tertiary structure are well developed for the β-amino-acid foldamers.[32] For instance, the stereochemical patterning approach has yielded excellent agreement between predicted and realized structures.[29]

Diverging from natural peptides but still utilizing amide linkages (due to their ease of synthesis and hydrogen-bonding capability),[36] the other large subclass of guestless helical foldamers consists of aromatic oligoamides. These synthetic foldamers appropriate *m*- or *p*-amide-linked aromatic rings—typically benzenes, pyridines, and/or quinolines[37]—whose rigidity limits the space of accessible conformations.[38] Introverted or extroverted hydrogen-bond acceptors (pyridine/quinoline-nitrogen lone pairs, methoxy or ether groups, carbonyl oxygens, phenoxide salts, or even halogens[37,39]) often decorate the arenes to: 1) establish strong intramolecular three-centered, amide hydrogen bonding to restrict Ar–CONHAr- and Ar–NHCOAr-bond rotation and 2) favor either *syn* or *anti* coplanar aryl- and amide-group conformations.[16,36] Additionally, sterically bulky side chains too large to occupy the helical cavity can be appended to the backbone to

encourage correct folding. These electrostatic, steric, and solvophobic interactions also provide preorganizational rigidity to the oligomeric skeleton, offsetting the entropic cost of folding.[1] As a result, aromatic-oligoamide foldamers adopt predictable helical curvatures. Tuning the ratio and placement of *m*- or *p*-amide linkages allows for the tailoring of foldameric dimensions as well as inlay tapering. As a consequence, this class of abiotic foldamers can be adapted for guest-inclusion, which can provide further host-conformational stability.

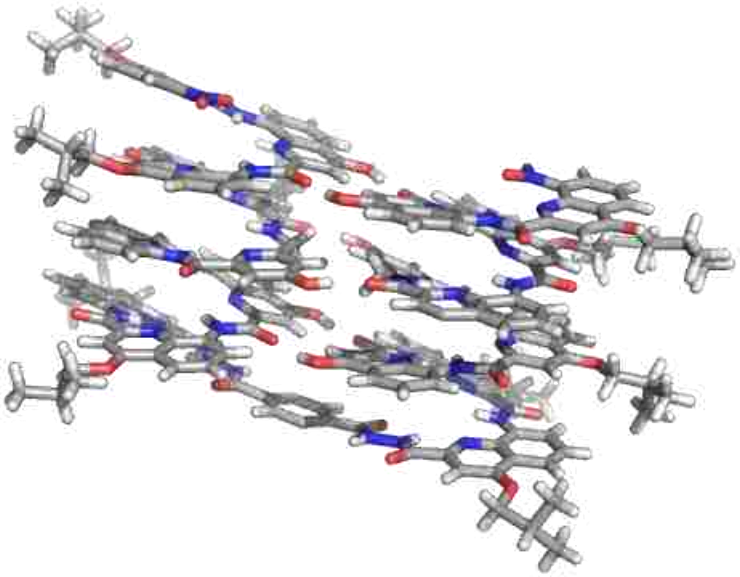

Figure 1.1 X-ray crystal structure of a synthetic aromatic-oligoamide two-helix bundle developed by Ivan Huc et al.

While amino-acid foldamers have dominated the scene, aromatic oligoamides are probably the second-biggest player.[15] Furthermore, this class of unnatural oligomers is noteworthy for its thermodynamic and kinetic stability. It should also be noted that some hybrid foldamers incorporating both aliphatic- and aromatic-amide monomers have been

developed, giving rise to unprecedented secondary structure like knots and non-canonical helices.[1,37] Lastly, there are notable examples of aromatic-oligoamide multi-strand foldamers[31,37] and even helix bundles,[40] (Figure 1.1) highlighting the programmability and stability of these guestless foldamers.

As alluded to earlier, some backbone curvatures afford helical voids. One of the few examples of a natural pore-containing oligopeptide is the antibiotic gramicidin, which folds into a β-helix (4-Å pore). Nature abhors a vacuum or at least more than 45 % of one according to Julius Rebek, Jr.[38] Thus, these voids are usually occupied by solvent or complementary guests. Examples of neutral guest molecules include diols, amino-alcohols, saccharides, organic acids, rod-like molecules like decanediol, etc. Chiral guests give rise to chiroptical properties that can be monitored using CD spectroscopy. Both hydrogen-bonding and solvophobic interactions drive encapsulation, and in contrast to some of the more rigid supramolecular hosts mentioned earlier, foldameric containers are adaptable (induced fit).[41]

1.3 Cation Helicates/Foldamers

We will now move on to a category more analogous to the supramolecules presented in this dissertation: cation helicates/foldamers. Within the realm of metallosupramolecular chemistry, ligand-metal interactions are governed by coordinative bonds between donor ligands (which are electron rich) and acceptor metals. These two-center, 2-electron interactions are highly covalent in nature (often referred to as coordinate-covalent or dative bonds). However, depending on the metal-ion system employed, these interactions can be labile. Preferred coordination geometries/numbers

(first described by Alfred Werner) of the metal ions as well as ligand design are important considerations for the metallosupramolecular chemist.[42]

What is a helicate? The word "helicate" is a combination of the Greek word *helix* and the suffix *-ate*, which is used to describe ligand-metal complexes. Jean-Marie Lehn coined the term in 1987 to evoke a helical di- or oligonuclear metallosupramolecule with one or more oligomeric donor ligands. These ligands enwrap a common helical axis (which may be curved) defined by a series of metal ions.[43] A very early example even before the term was coined was Kenneth Raymond's dinuclear iron hydroxy-pyridinoate triplex, which acted as a synthetic siderophore.[44] The first structurally-characterized double-strand helicate was Lehn's oligobipyridine trinuclear Cu(I) complex, described as an "inorganic double helix, reminiscent of the double-helical structure of nucleic acids."[45]

In essence, these Werner-type complexes are mediated by coordinative ligand-metal bonds, and the donor moieties are connected by spacers. Bidentate chelating ligands (like Lehn's bipyridines) interacting with metals that prefer a tetrahedral or octahedral coordination geometry result in complexes with a helical twist. Additionally, the strand number is often embedded in the coordination preference of the metals. For example, double-strand helicates can be synthesized using metals that prefer a tetrahedral, octahedral, or nondirectional coordination geometry. Triple-strand helicates are created using octahedral-coordination metals or lanthanides. Cation helicates also benefit from the tunability of dative-bond strength between the ligands and metals. As examples, d^6 low-spin Ru(II) and Os(II) metals afford strongly covalent and inert bonds, while Na(I) provides labile electrostatic interactions. In addition to the intrinsic properties of metals, attractive or repulsive interactions between ligand moieties can influence

regiochemistry. Moreover, the length and geometry of the spacer unit are extremely influential. Short and/or rigid spacers promote helicate formation vs. single-strand complexation.[46] In the case of a ditopic ligand with alkyl linkers, an even number of linker carbons typically gives rise to chiral helicates, whereas an odd number non-chiral mesocates.[42] Although they often self-assemble from achiral components, helicates (and foldamers) inherently possess chirality: plus (*P*) or minus (*M*).[47]

Helicate topology has been richly developed over the years and includes linear complexes using oligonitrogen and -oxygen donor ligands; circular helicates and molecular knots; and helicates comprised of sulfur, carbon, and phosphorus donor ligands. Moreover, there is large library of hybrid-type helicates: complexes with ligands that incorporate mixtures of nitrogen and oxygen donor groups; self-sorting hetero-strand helicates; and heterotopic helicates with more than one species of metal. Lastly, helicates have been synthesized to possess up to six strands.[48]

As a segue to the next section, Ag(I)- and Cu(I)-mediated *m*-arylene-ethynylene helicates have been reported.[49] Another example developed by Jeffrey Moore et al. will be described below.

1.4 *m*-Arylene-Ethynylene Foldamers

Oligomers that possess more than ~six *meta*-connected arylene-ethynylene repeat units (Figure 1.2) fold into well-ordered helical containers. This class of supramolecules depends on nonspecific, solvophobic interactions to fold. In particular, the periodic ethylene segments necessitate long-range π-π stacking between non-adjacent backbone units. Therefore, *m*-arylene-ethynylenes usually require polar solvents to drive their self-

assembly.[15] These interactions are additive and lead to robust structures that exhibit flexibility and dynamics induced by external stimuli (solvent, binding, light, etc.). Chemical modification of the primary sequences of *m*-arylene-ethynylenes allows for the tailoring of helix dimensions.[13] Only a handful of scientists have created *m*-arylene-ethynylene foldamers: Moore, Masahiko Inouye, and Stefan Hecht. Much of the work they have accomplished will be covered in this section.

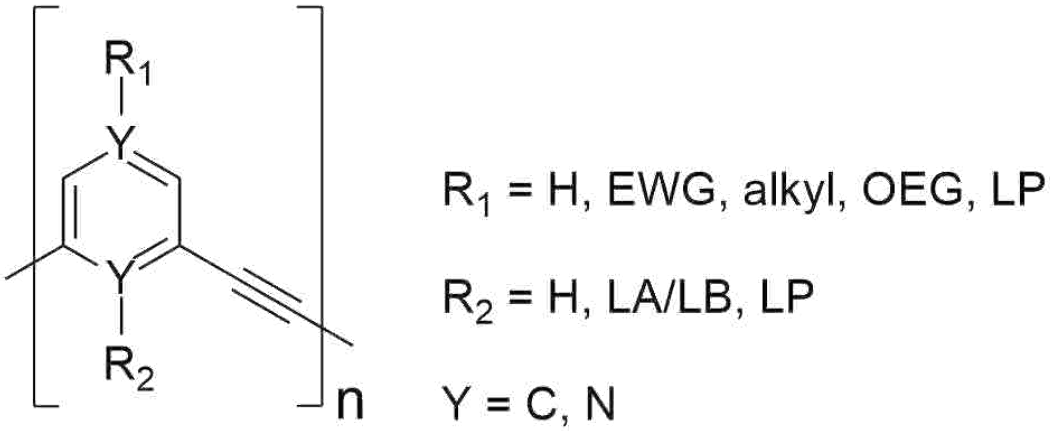

Figure 1.2 Typical *m*-arylene-ethynylene repeat sequence. EWG = electron withdrawing group; OEG = oligo(ethylene glycol); LA/LB = Lewis acidic/basic moeity; LP = lone pair.

The solvophobic collapse and folding of an *m*-arylene-ethynylene was first reported by Nelson and Moore in 1997 in *Science*.[50] Increasing the chain length from two repeat units to 18, the authors noted a sigmoidal increase in the folded population relative to random coils in CH_3CN. However, in $CHCl_3$, no increase in the folded population was detected, demonstrating that solvophobic interactions drove helical self-assembly. In another study, a two-state equilibrium model was used to elucidate the energetics of a random-coil vs. folded state, which linearly depended on solvent composition in the case

of the shorter oligomers (% $CHCl_3$ in CH_3CN). As evidenced by the distinct sigmoidal curves afforded by the longer chains upon increasing solvent polarity, the coil-to-helix transitions were demonstrated to be highly cooperative and on par with α-helix self-assembly in water.[51]

In a follow-up paper, Moore et al. attached six introverted cyano ligating groups to alternating rings of an *m*-arylene-ethylene 12-mer. (Note: throughout this dissertation, an *n*-mer consists of *n* covalently-bound aromatic units that comprise an oligomer.) Upon folding, two tridentate binding sites converged upon two intracavity Ag(I) ions. THF was selected as a solvent for UV-Vis binding studies since the 12-mer displayed random-coil behavior sans cations. In the presence of Ag(I), the oligomer underwent a coil-to-helix transition and encapsulated two cations with a K_1 and K_2 of roughly 2×10^4 and $\sim 10^7$ M^{-1}, respectively (1:2 host-guest binding model). The stronger second association indicated cooperative guest binding. Subsequently, the cyano groups were removed so that the tubular cavity could accommodate chiral hydrocarbon guests. The diameter of the hydrogen-only helical cavity was calculated to be 8.7 Å. In these studies, polar solvents were used so that the foldamer could pre-assemble prior to guest inclusion.[52] Unsurprisingly, in the absence of guest, no CD signal was observed. Upon addition of an enantiomerically pure compound like (–)-α-pinene, a strong Cotton effect was observed. CD spectroscopy was used to fit the 1:1 association data, and a binding constant of 6,830 M^{-1} in 40 % *v*/*v* H_2O-CH_3CN was obtained for the foldamer-(–)-α-pinene complex. Solvophobically driven, the binding constant increased and scaled linearly with increasing H_2O concentration. The molecular volume of α-pinene relative to the helical cavity was 55 %, in full agreement with Rebek's ideal guest-to-void volume.

Next, Moore et al. surmised that a rod-like, chiral guest would fit well within the hydrophobic cavity of their foldamer. *cis*-(2*S*,5*S*)-2,5-Dimethyl-*N*,*N*′-diphenylpiperazine was selected based on molecular modeling and its ease of synthesis.[53] This guest was screened against an oligomeric series (10-mer through 24-mer) using CD spectroscopy in 40 % H_2O-CH_3CN. The authors discovered that the 1:1 association had a chain-length dependence that leveled off at 20 *m*-arylene-ethynylene repeat units ($K_a > 10^{4.5}$ for the icosamer). These data suggested that nondirectional, solvophobic interactions were at play. Developing this system further, the researchers targeted the same rod-like guest with triarylmethyl caps.[54] The dumbbell-shaped derivative was screened against the same oligomeric series, and a pronounced selectivity for the 20- and 22-mer was seen. The much lower binding affinity observed in the case of the 24-mer arose from poor size complementarity. Interestingly, the 20-mer-dumbbell complex was appreciably more stable ($K_a = 10^6$ M^{-1} in 40 % H_2O-CH_3CN, 1:1 binding model) than that of the 20-mer-rod complex. Through molecular modeling, the authors observed stabilizing aromatic-aromatic interactions between the foldamer and triarylmethyl caps. To get a sense of the mechanism of binding, Moore et al. conducted kinetic studies using CD spectroscopy. When adding the rod-like guest to pre-formed 20-mer, the reaction reached equilibrium within the 60-second mixing time. In contrast, it took roughly 30 minutes for dumbbell-guest inclusion to reach steady state. The authors surmised that a direct threading mechanism explained the fast kinetics of the former reaction, whereas slow unfolding of the 20-mer was required to accommodate the dumbbell-like guest.

For a single-strand helical foldamer, Moore et al. used the following equation to capture the coil-helix equilibrium:

$$K_{eq} = \sigma s^{n-n_0} \quad (1.1)$$

For this equation, *s* represents the enthalpic gain from monomer-monomer interactions and σ the entropic cost of restricting the free rotation of monomers when forming the first helical turn. *n* is the chain length of the oligomer and n_0 the number of monomers required for one helical turn.[55] For *m*-arylene-ethynylenes, the thermodynamic stability of the folded state arises from π-π stacking, vdW interactions, and solvophobic effects (from folding and guest inclusion). To provide further stability, the authors incorporated a β-turn unit, which consisted of two adjacent, extroverted functional groups: an amide hydrogen-bond donor and an ester-carbonyl acceptor. The inclusion of this bioinspired β-turn unit helped absorb the cost of helix nucleation, a strategy used in nature to nucleate tertiary structure.[56] It was discovered that one such β-turn unit lowered the energy of folding (Δ*G*) by 1.2 kcal/mol.

Incorporating imine bonds within the *m*-arylene-ethynylene backbone, it was demonstrated that helical folding encouraged segment ligation in favor of conformational order.[57] Furthermore, dumbbell-like guest inclusion favored specific ligation sequences even when multiple oligomers of varied length and imine-site number were mixed in solution.[58]

Through exterior hexaethylene-glycol functionalization, Moore et al. augmented the water solubility of their *m*-arylene-ethynylenes, enabling further investigations of their hydrophobically driven host-guest interactions.[59] (–)-α-pinene was again selected as

a suitable guest so that binding constants could be obtained with CD spectroscopy. In all previous studies and with a suitable guest, foldamers with triethylene glycol side chains activated a CD response with as little as 10 % H_2O. In contrast, the 12-mer hexaethylene-glycol derivative required at least 50 % H_2O to promote guest inclusion. Clearly the larger side chains influenced guest binding (perhaps competitively threading the helical cavity). Interestingly, the CD-induced signal leveled off at 90 % H_2O-CH_3CN. Plotting affinity vs. % H_2O in CH_3CN, the authors discovered a nonlinear trend with a sharp increase between 70 and 80 % H_2O. The maximum binding constant was 1.4×10^6 M^{-1} in 90 % *v*/*v* H_2O-CH_3CN (1:1 binding model). Surprisingly, in 100 % H_2O, the binding constant depreciated by an order of magnitude, evidencing perhaps a constriction of the binding cavity. The kinetics of binding were also investigated using CD spectroscopy. In 70 % H_2O-CH_3CN, complexation reached equilibrium quickly within the mixing time. In 80, 90, and 100 % H_2O, the complexation half-lives (pseudo-first-order) were seconds-, minutes-, and hours-long, respectively. These data suggest slow unfolding of wrong-handed foldamers prior to guest inclusion. A higher percentage of H_2O would likely stabilize the folded state, stymieing unfolding.

Transitioning into supramolecular catalysis, Moore et al. synthesized an *m*-arylene-ethynylene three-mer with a central DMAP core unit.[60] When the backbone adopted the *cisoid* conformation, the pyridine lone pairs could point interiorly. This three-mer was incrementally grown by two arene units up to the 17-mer.[61] The series was reacted with CH_3I in both CH_3CN and $CHCl_3$. Rates of methylation were accelerated in CH_3CN and with increasing chain length. These results evidenced the rate-enhancing effect of hydrophobic guest inclusion within a helical active site. These same foldamers

were also used to quantify the stabilizing effect (ΔG) of a methyl-pyridinium cation-π interaction in CH_3CN (roughly 1.8 kcal/mol).[62] This pyridine could also be protonated, and the pK_a range could be modulated (5–14) by varying the exterior side chain functionality.[63] Additionally, changing the central arene—to a phenylene, pyridinylene, pyrazinylene, 4-nitropyridinylene, etc.—was shown to have little effect on foldamer stability.[64] Lastly, the research group swapped the pyridine core for isomeric amide sequences to test their effect on piperazinium-dihydrochloride encapsulation.[65]

Expanding the substrate scope of their supramolecular catalyst, methyl sulfonates with varying linear or branched alkyl chains were used to establish the substrate specificity of *m*-arylene-ethynylene DMAP active sites. Molecular sieving became highly evident, and a 1600-fold rate increase was observed when the longer 17-mer was reacted with 3-pentyl methanesulfonate.[66] Unsurprisingly, when the DMAP unit was placed more terminally in the primary sequence, sieving efficiency dropped.[67]

In addition to the synthesis of polymers, Inouye et al. have actively created and studied *m*-arylene-ethynylene helical foldamers. To incorporate hydrogen-bond acceptor groups for saccharide encapsulating, the authors functionalized the interiors of their binding cavities with pyridine nitrogens. A series of oligomers were synthesized up to a 24-mer. *n*-Octylated β-D-glucopyranoside was encapsulated by the 24-mer with an association constant of 1.2×10^3 M^{-1} (1:1 binding model) in CH_2Cl_2 as determined by CD spectroscopy.[68] Unlike Moore's binding studies, which utilized pre-folded helices in polar media, Inouye's oligomers demonstrated guest-induced folding. In another study, Inouye's group conjugated helix-templating saccharides (α- and β-glucopyranoside, galactoside, and mannose) directly to their *m*-arylene-ethynylene backbones (three-, six-,

10-, and 14-mer).[69] Although the linker length between the foldamer and template did not affect helix formation, the overall span of the *m*-arylene-ethynylene had a pronounced effect. The 10- and 14-mer exhibited strong CD signals, indicating chiral helical self-assembly in CH_2Cl_2. The signs of the CD signals depended on the structures of the appended saccharides.

Next, Inouye et al. synthesized three-, five-, seven-, nine-, and 11-mers with alternating hydrogen-bond acceptors/donors (pyridines-pyridones). These ligands sans guest were found to self-associate in $CHCl_3$. The ligands were designed to inwardly direct pyridine-N and pyridone-NH groups when helically folded. Impressively, the pyridine-pyridone ligands self-assembled into helical dimers via intracavity pyridine–N···HN–pyridone intermolecular hydrogen bonding. However, the pyridones could tautomerize to pyridinols. Consequently, the pyridine-pyridinol ligand formed sheet-like structures. When β-D-glucopyranoside was added to the 11-mer, an induced CD signal was observed in CH_2Cl_2. Only a single ligand in the pyridine-pyridone form could bind β-D-glucopyranoside. The apparent 1:1 association constant was 3.2×10^3 M^{-1}. This guest-switchable conformational change from a self-associating duplex to a 1:1-host-guest complex was a unique discovery.[70]

In order to develop better helical hosts for saccharides, Inouye et al. created pyridine-phenol *m*-arylene-ethynylene six- and 12-mers. By design, stable and introverted pyridine–N and phenol–OH groups formed push-pull hydrogen-bond donating/accepting interactions with glycosides. Measuring hexose affinity in 1,2-dichlorethane, association constants approached ~10^8 M^{-1} (1:1 binding model). Solvation

of native saccharides (typically insoluble in nonpolar media) from the solid phase was also demonstrated with particular efficiency in the case of D-mannose.[71]

In 2018, an all-phenol-based oligomer was prepared by the same group.[72] Based on an X-ray crystal structure (Figure 1.3), intramolecular O–H···O hydrogen bonding within the helical void helps to preorganize the foldamer.

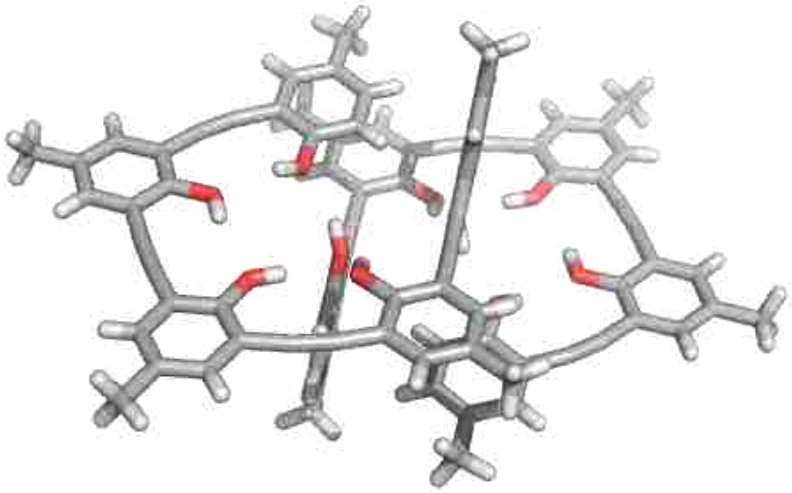

Figure 1.3 X-ray crystal structure of a phenol-based *m*-arylene-ethynylene five-mer developed by Inouye et al. An interesting dimer formed in the solid state, stabilized by π-π stacking and intermolecular hydrogen bonding.

Inward bending of the ethynylene substituents occurs on account of the strong intramolecular hydrogen bonding. The addition of chiral-amine guests induced a CD signal in CH_2Cl_2. In a recent study, Inouye et al. also synthesized a 13-mer with alternating, inwardly-directed pyridine–N and phenol–OH groups. In addition, exterior oligo(ethylene glycol) groups were appended to enhance water solubility.[73] The host's

affinity for D-glucosamine hydrochloride was measured with CD spectroscopy in pure water, and the association constant was 2×10^3 M^{-1} (1:1 binding model).

Hecht et al. have also worked with *m*-arylene-ethynylenes. These researchers developed the first-ever light-switchable foldamer.[74] Two hexameric backbone sequences were adjoined to a photo-responsive azobenzene core. Irradiation of the "turn-off" foldamer in 60 % H_2O-CH_3CN resulted in denaturation of the helix. The thermal reversion from *cis* to *trans* occurred over the course of hours at RT, which regenerated the original helix. Attempts to create a "turn-on" foldamer were unsuccessful.[75]

1.5 Anion Foldamers and Anion Helicates

"Anion-coordination chemistry," first christened by Lehn in 1978, is a relatively young field of research when compared to transition-metal coordination chemistry. As such, no orbital theories have been thoroughly established. Instead, geometrical patterns of binding and coordination number can largely be explained by the noncovalent interactions between donor-ligand moieties, anion topology (spherical, linear, trigonal planar, or tetrahedral), and dimensionality and design of the host receptor. In general, anion topology relative to that of cations is more diverse. Overall, it has been observed that multivalent tetrahedral anions prefer high coordination numbers (up to 12), whereas there is no clear preference with regard to coordination number or geometry in the case of halide ions. Indeed, halide ions routinely adopt monodentate, tetrahedral, square-planar, and other binding arrangements up to nine-coordinate. As a general rule, halide-ion binding geometry is dictated by ligand charge repulsion and host receptor constraints.[76] In the case of anion helicates/foldamers, the geometric constraints concomitant with helix

formation (such as pitch, pore size, etc.) are influential as well. Overall, the significant challenges associated with anion coordination arise from the inherent properties of anions: their diverse topologies, pH dependence, and high free energies of solvation as compared to similarly-sized cations.[7] Additionally, electrostatic interactions between anions and ligands are largely noncovalent. Overcoming the significant entropic cost of complexing one or more ligands and anions through the use of noncovalent interactions alone is extremely difficult.

Two representative examples of anion helicates that form only in the solid state will be discussed. The first X-ray crystal structure of an anion helicate was reported by Paul Kruger and Noreen Martin et al. in 2001.[77] This double-strand diammonium-bis-pyridinium helicate bound two Cl^-s in a pincer-like fashion (linear bidentate, Figure 1.4).

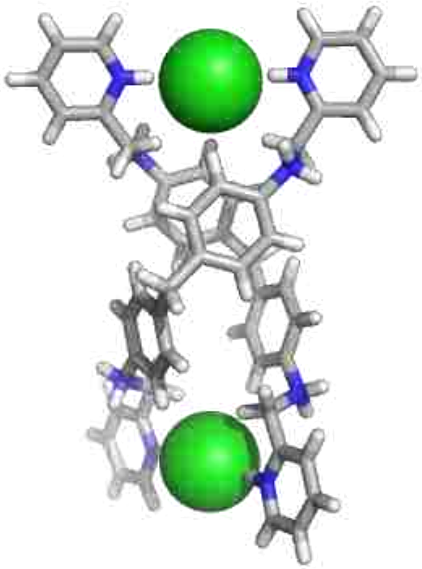

Figure 1.4 X-ray crystal structure of Kruger and Martin's Cl^- double helicate, which was characterized in the solid state.

The rigidity of the diphenylmethane spacer helped encourage higher-order helication. The same ligand was utilized by Kureshy and Subramanian et al. to form the first Br^- double helicate. The X-ray crystal structure was very similar to that of its Cl^- counterpart. Moreover, the Br^- helicate successfully catalyzed a solvent-free, three-component aminoalkylation reaction.[78]

Before continuing, we must distinguish anion helicates from anion foldamers. Following Lehn's original definition of a helicate, we will call any multinuclear, single- or multi-strand helical anion complex as an anion helicate. The ligands enwrap a helical axis as defined by the anions. These multinuclear complexes are generally more difficult to create than anion foldamers (which are mononuclear) due to intracavity anion-anion repulsion. An anion foldamer is a single- or multi-strand helical complex that encapsulates a single anion. In contrast to single-strand foldamers, there are only a few examples of multi-strand anion foldamers that have been characterized in solution.

One of the main contributors to the field of anion foldamers is Kyu-Sung Jeong. The first reported example of an anion foldamer showcased an oligoindole-ethynylene backbone, which adopted a helical conformation in solution via indole–NH hydrogen-bonding to Cl^-.[79] Upon adding Cl^- to a four-, six-, and eight-mer in CD_3CN, downfield shifting of the indole–NH signals was witnessed, characteristic of hydrogen bonding. Upfield shifting of several aromatic–CH signals on only the six- and eight-mer (which were long enough to helically fold) evidenced ring-shielding effects from aromatic stacking. In addition, NOE correlations between protons that were brought into close proximity due to helical folding were seen. These NOEs disappeared in the absence of Cl^-, establishing the anion-switchability of the helical self-assembly. Cl^- affinity for the

eight-mer (1:1 binding model) was appreciable ($K_a > 10^7$ M^{-1} in CH_3CN; 2.3×10^4 M^{-1} in 10 % *v*/*v* H_2O-CH_3CN), as determined by UV-Vis titration experiments. The latter association constant is impressively high considering the competitive media used, underscoring the viability of using molecular folding to create binding sites that are secluded from bulk solvent.

Without a means to bias the population, helical oligomers are typically racemic in solution (an equal ratio of *P* and *M* enantiomers). To influence the relative populations, chemists can use chiral guests or append chiral groups to their helical backbones. Utilizing the latter approach, Jeong et al. appended (1*S*)- or (1*R*)-phenylethylamido groups to the termini of their oligoindole-ethynylene foldamer.[80] Prior to adding anions, almost no CD signal was detected in CH_2Cl_2. However, upon adding Cl^- to the (1*S*)-phenylethylamido-functionalized oligomer, strong and positive CD signals corresponding to the absorption wavelengths of benzoate and biindole functional groups were seen. This spectroscopic response intensified with increasing Cl^- concentration. Repeating the experiment with the (1*R*)-phenylethylamido derivative resulted in an identical CD response but with the opposite Cotton effect.

Conveniently, these oligoindole-ethynylenes proved strongly fluorescent in the absence of anion. Adding Cl^- to foldamers of sufficient length (six-, eight-, and 10-mers) in 20 % *v*/*v* CH_3OH-$CHCl_3$ led to large hypochromic and bathochromic shifts of the emission bands, likely arising from intramolecular excimer formation in the aromatic arrays.[81] For the shorter four-mer, the emission band was unperturbed by the addition of Cl^-. Aside from possessing strong Cl^- affinity (as established earlier), the 10-mer also

bound F^- quite strongly in 20 % *v*/*v* CH_3OH-CH_2Cl_2 (K_a = 1.2 × 10^6 M^{-1}, 1:1 binding model).

Mentioned earlier, synthetic foldamers can possess internal cavities capable of sequestering anionic guests from bulk solution, even in pure water. To enhance the water solubility of their foldamers, Jeong et al. functionalized an oligoindolocarbazole-ethynylene backbone with sodium carboxylates.[82] In D_2O, the three-indolocarbazole adopted a collapsed form, as indicated by the upfield shifts (0.4–1.0 ppm) of the terminal-benzoate protons relative to that of the mono-indolocarbazole. These data suggested that the longer oligomer adopted a partially folded conformation in water sans guest. Upon adding NaCl, further upfield shifting of several terminal-benzoate protons evidenced increased folding. This folded conformation was corroborated by a ^{1}H 2D ROESY experiment. The association constant of the Cl^- adduct in D_2O was 65 M^{-1} (1:1 binding model). This binding constant is impressive given the enormous penalty associated with dehydrating chloride (~81 kcal/mol). The work of Jeong et al. helps establish the power of foldamer-based anion recognition in pure water.

The same three-indolocarbazole foldamer was fitted with two terminal alkynyl dimethylcarbinol protecting groups to provide additional hydrogen-bond donors.[83] Upon adding SO_4^{2-} to the receptor in 1:1:8 *v*/*v*/*v* CD_3OD-CD_2Cl_2-CD_3CN, characteristic upfield shifts of terminal arene protons were seen by ^{1}H NMR spectroscopy. ^{1}H 2D NOESY NMR confirmed helical stacking of these arenes. As determined by fluorescence spectroscopy in 10 % *v*/*v* CH_3OH-CH_3CN, the foldamer was found to be selective for SO_4^{2-} (K_a = 640,000 M^{-1}, 1:1 binding model) by two orders of magnitude above the next-best guest, Cl^-. In the solid state, SO_4^{2-} is held within the helical cavity of the foldamer

by eight hydrogen bonds (six indolocarbazole–NH and two dimethylcarbinol–OH, Figure 1.5).

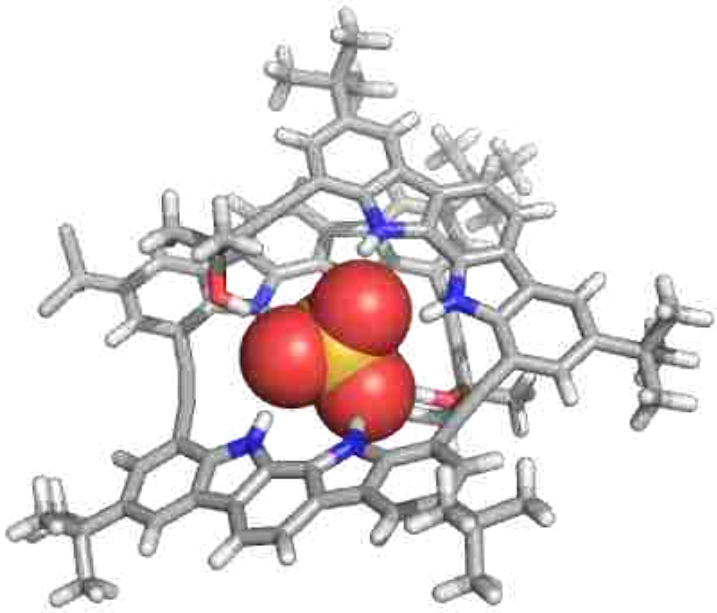

Figure 1.5 X-ray crystal structure of an ethynylene-linked three-indolocarbazole foldamer encapsulating SO_4^{2-} synthesized by Jeong et al.

In addition to hydrogen-bonding interactions, π-π stacking helps to stabilize the helical conformation—a common motif for helicates/foldamers. SO_4^{2-} selectivity was attributed to the dimethylcarbinol hydrogen-bond donors, which could not reach Cl^-. By inserting butadiynyl spacers between the indolocarbazoles, the expanded three-indolocarbazole foldamer exhibited inferior SO_4^{2-} binding. However, superior $H_2PO_4^-$ binding was observed (K_a = 261,000 M^{-1} vs. 3600 M^{-1} for the ethynylene-spacer derivative, 1:1 binding model, 10 % *v*/*v* CH_3OH-CH_3CN).[84]

Appending terminal amides to an indolocarbazole two-mer spaced by butadiynyl linkers, intramolecular hydrogen bonding between the indolocarbazole–NHs and the amide oxygens was realized.[85] Attachment of (*S*)-arylethylamido groups to the oligomer termini led to the preferential formation of left-handed (*M*) isomers, as measured by CD spectroscopy in CH_2Cl_2, CH_3CN, acetone, and DMSO. As the solvent polarity increased, the CD-signal intensity decreased (especially in DMSO). Polar media effectively disrupted intramolecular hydrogen bonding and folding sans guest. Attachment of (*R*)-arylethylamido groups resulted in the same CD features with opposite Cotton effects. Interestingly, when the left-handed isomer was mixed with SO_4^{2-} (~one equivalent) in CH_2Cl_2, a total switch of helical sense was witnessed. However, when SO_4^{2-} was added to the guestless right-handed foldamer, its helical sense did not change.

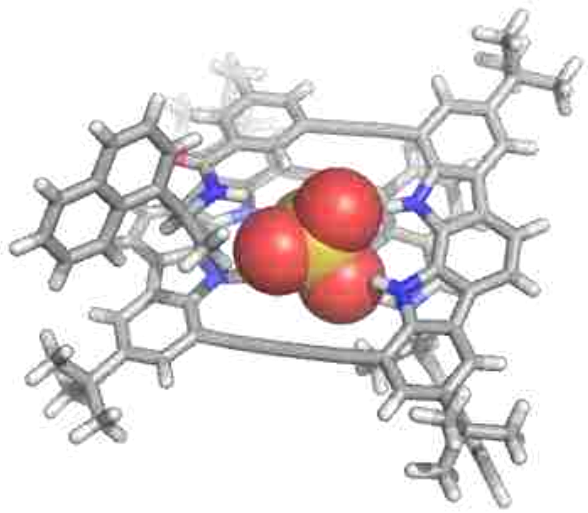

Figure 1.6 X-ray crystal structure of a two-indolocarbazole oligomer spaced by butadiynyl linkers and capped with (*S*)-arylethylamido groups (synthesized by Jeong et al). The ligand forms a right-handed helix around SO_4^{2-}.

In the X-ray crystal structure of the adduct (Figure 1.6), SO_4^{2-} is held by four indolocarbazole–NHs and two amide–NHs in an overall pseudo-square-planar coordination geometry (if each donor unit is considered as a monodentate coordination vector). These studies introduce a powerful means to realize anion-switchable chirality.

Using the ethynylene-linked three-indolocarbazole with two terminal dimethylcarbinol protecting groups, Jeong et al. next targeted chiral organic anions to induce one-handed folding.[86] In CH_2Cl_2, the guestless oligomer was CD silent, and the addition of SO_4^{2-} did not produce a CD signal. However, with addition of (*R*)-10-camphorsulfonate, strong CD signals with a positive Cotton effect (attributed to the exciton coupling of indolocarbazole chromophores) were observed. Complete inversion of the CD spectrum resulted when (*S*)-10-camphorsulfonate was added to the same oligomer. Thus, by adding either the (*R*) or (*S*) organic anion, biased formation of the corresponding diastereomeric helical complex could be achieved.

Switching to a diphenylurea-based ligand, Jeong et al. synthesized a series of ethynylene-spaced oligomers (one to five diphenylurea units). Two terminal dimethylcarbinol protecting groups provided additional hydrogen bonding.[87] Association constants measured in organic solvents for smaller guests like Cl^- increased with increasing chain length, plateauing with the three-diphenylurea. However, no plateauing was observed for SO_4^{2-}. These results illustrate the difficulty in targeting anions, as they encompass a large range of attributes (size, topology, charge, chirality, pK_a etc.). Despite these challenges, chiral induction was accomplished by adding adenosine 3',5'-cyclic monophosphate to the oligomer, which induced a CD signal. Through protonation of the chiral guest with trifluoracetic acid, anion binding became negligible, and the CD signal

was turned off. Adding a base, 1,4-diazabicyclo[2.2.2]octane, to solution resulted in almost complete recovery of the CD signal. This cycle could be repeated many times with nearly the same result.

The folding and chiroptical properties of a three-indolocarbazole-ethynylene oligomer bearing terminal amide-linked (*S*)-arylethylamido groups were investigated.[88] In nonpolar solvents, strong negative Cotton effects in the CD spectra were evident, whereas in polar solvents (acetone, CH_3CN, and DMSO) these signals were abolished. Similar polar-solvent-induced disruptions of folding sans guest were seen with the butadiynyl-linked three-indolocarbazole. Interestingly, adding anions of appropriate size (Cl^-, Br^-, or acetate in the present study) resulted in inversions of the CD spectra in CH_2Cl_2.

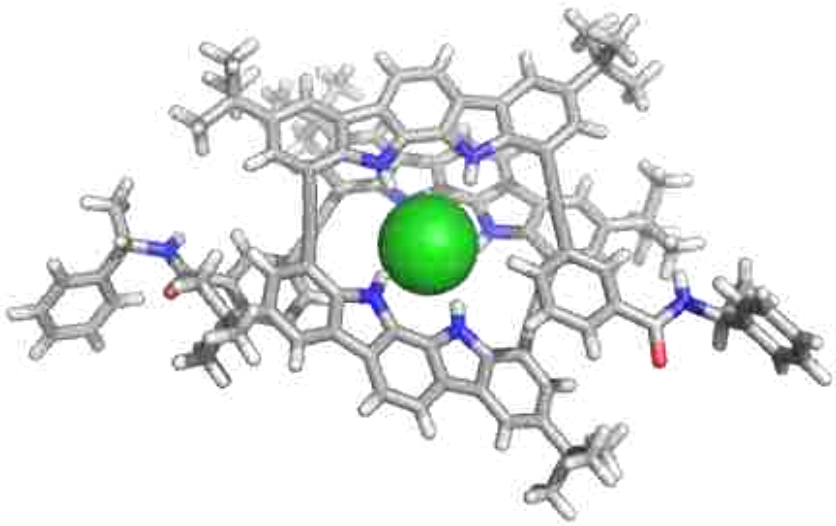

Figure 1.7 X-ray crystal structure, obtained by Jeong et al., of a left-handed three-indolocarbazole-ethynylene foldamer (with two terminal amide-linked (*S*)-arylethylamido groups) chelating Cl^-.

Based on an X-ray crystal structure of the Cl^- complex, helical folding was determined to be left-handed (Figure 1.7). All six indolocarbazole–NHs hydrogen bond a single, intracavity Cl^-. These results suggest that both the helicity and chirality of this class of foldamers is highly solvent- and guest-responsive.

Interspersing pyridine units between indolocarbazole moieties, Jeong et al. created new foldamers with strongly fluorescent turn-on properties in the presence of SO_4^{2-}, F^-, and other anions.[89] The pyridine lone pairs pointed interiorly and served as hydrogen-bond acceptors upon helical folding. An X-ray crystal structure (not shown) highlights the penchant of these foldamers to bind water molecules within their helical cavities. Thus, the oligomer could adopt a helical conformation in wet nonpolar solvents ($CHCl_3$, CH_2Cl_2, and toluene) but reverted to a random coil in polar solvents (acetone and DMSO). In the former solvents, the foldamer was essentially nonfluorescent due to the stacking of its indolocarbazoles and pyridines. However, in the denatured state, the ligand became strongly fluorescent, evidencing the disruption of π-π stacking in competitive media. Additionally, both acetone and DMSO were too large to fit within the helical cavity, further encouraging a random-coil conformation. Anions also disrupted helix formation, which promoted strong turn-on fluorescence. In water-saturated CH_2Cl_2, SO_4^{2-} and F^- produced the highest-intensity fluorescence. It was surmised that anion and pyridine-lone-pair repulsion was largely responsible for anion-induced unfolding. In support of this hypothesis, protonation of the introverted pyridines with perchloric acid led to the formation of a helical SO_4^{2-} adduct in wet CH_2Cl_2.

One of the early pioneers of anion foldamers, Stephen Craig, developed the first phenylene-1,2,3-triazole-based ligand (Figure 1.8).[90]

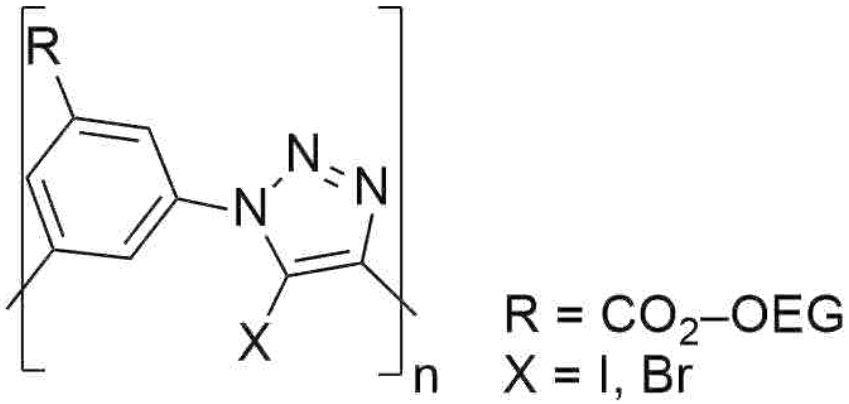

Figure 1.8 Representative phenylene-1,2,3,-triazole foldameric backbone. Hydrogen-bond donors *ortho* to the "R" substituent may be appended to offer intramolecular rigidification.

Cu(I)-catalyzed Huisgen 1,3-dipolar cycloadditions of azides to alkynes (click chemistry) afforded 1,4-diaryl-1,2,3-triazole-containing nine-mers (the minimum number for a helical turn) with acceptable yields. ^{1}H 2D NOESY experiments confirmed helical folding of the nine-mer around Cl^- in acetone-d_6. Subsequent ^{1}H NMR titration experiments measured strong binding in solution ($K_a = 1.7 \times 10^4$ M^{-1}, 1:1 binding model). Downfield shifting of the introverted phenylene and triazole protons evinced CH hydrogen bonding within the helical cavity. The same foldamer bound Br^- with slightly lower affinity, but the binding constant dropped two orders of magnitude in the case of I^-.

Craig et al. proposed a conceptual binding model in which an anion's solvation sphere is replaced by the functional groups of a binding pocket.[91] Furthermore, they argued that the flexibility of a foldamer can facilitate more optimal hydrogen bonding

within this site than that afforded by a rigid macrocycle. Notwithstanding, macrocyclic phenylene-1,2,3-triazoles studied by Amar Flood and others typically bound halide ions more tightly than their foldameric counterparts. Why? In addition to prepaid entropy, the authors hypothesized that the high-energy unbound state of a macrocycle (due to repulsive triazole dipoles) amounted to 5–6 kcal/mol. In contrast, an unbound foldamer can relax into a more stable "anti" arrangement of dipoles. Presumably, pre-assembled foldamers embody every productive quality described above: prepaid entropy and optimal electrostatic interactions via induced fit.

Another notable contributor to research on anion foldamers is Hua Jiang. His group synthesized cationic phenylene-1,2,3-triazole oligomers with water-soluble side chains (quaternary ammonium salts).[92] Like *m*-arylene-ethynylene foldamers, these phenylene-1,2,3-triazoles existed as random coils in nonpolar solvents like CH_3OH but adopted helical conformations in water (even without a guest). This behavior was confirmed by the marked ^1H NMR upshifts of aromatic protons with increasing D_2O content. When the solvent reached 80 % D_2O-CD_3CN, broadening of the resonances was also noticed, which evidenced aggregation. UV-Vis spectroscopic experiments at lower concentrations of ligand revealed a hypochromic response with increasing H_2O content, which was indicative of π-π stacking. When plotting the degree of foldedness vs. % H_2O, cooperative, sigmoidal relationships were observed for the longer oligomers, whereas a more linear trend was evident for the shorter chains. The chiral derivative—with a terminally-appended (*S*)-arylethylamido group—exhibited CD responses with increasing H_2O content. DLS and CD spectroscopy allowed for the characterization of higher-order helical columns that formed in aqueous media. In 75 % H_2O-CH_3OH, Cl^- and to a lesser

degree F^- induced hypochromic changes in the UV-Vis spectra, suggesting enhancement of the folded state. Additionally, the binding of anions retarded higher-order aggregation, possibly due to anion-anion repulsion.

Jiang et al. also developed a light-switchable phenyl-1,2,3-triazole foldamer, whose affinity for anions could essentially be modulated through reversible photoisomerization of the ligand.[93] To this end, two phenyl-1,2,3-triazole units were attached to an azobenzene core. The *trans* azo linker encouraged an overall extended helical conformation (corroborated by ^{1}H NOESY NMR in acetone-d_6). The *cis* azo linker was activated by UV irradiation (365 nm), resulting in a constricted, scissor-like conformation of the ligand. By storing the *cis* ligand in the dark for 10 days, the *trans* conformation could be restored. Interestingly, the *cis* ligand bound anions more strongly than the *trans* (fourfold greater affinity in the case of Cl^-, $K_{a,cis}$ = 290 M^{-1} in acetone-d_6, 1:1 binding model).

Turning to acid-base chemistry, Jiang et al. designed a phenylene-1,2,3-triazole with a central resorcinol group to serve as a switch regulator.[94] To preorganize the ligand, extroverted acyl-amino groups were appended to the oligomeric backbone. Deprotonation of the resorcinol–OHs (pK_a = 9.44) led to the rearrangement of the hydrogen-bonding network along the backbone of the oligomer. Specifically, triazole intramolecular hydrogen bonding to the central resorcinolate deactivated these two hydrogen-bond donors, inducing an open "W" conformation of the ligand. Thus, the authors could induce the "W" conformation with two ligand equivalents of basic 1,8-diazabicyclo[5.4.0]undec-7-ene and restore the helical conformation with picric acid. First, the helical foldamer was studied in solution. In the presence of Cl^- in 3:47 *v*/*v* DMSO-d_6-$CDCl_3$, intracavity

protons downshifted, whereas exterior aryl protons barely shifted. Terminal aryl protons, however, shifted upfield on account of ring-current effects. This anion-induced folding was confirmed by ^{1}H NOESY NMR spectroscopy, and a 1:1 association constant of 8.1×10^4 M^{-1} was determined for the Cl^- adduct. In stark contrast, Cl^- affinity for the deprotonated, "W" oligomer was 260-fold lower (K_a = 308 M^{-1}, 1:1 binding model). Interconversion of the isomers proved facile even in the presence of anion.

By incorporating two pyridinium units, Jiang et al. introduced charge-assisted CH hydrogen-bond donors to their foldamer.[95] This strategy allowed the authors to achieve appreciable halide-ion affinity in competitive media. ^{1}H NMR titrations of their nine-mer with Cl^-, Br^-, and I^- in 3:47 *v*/*v* D_2O-pyridine-d_5 afforded impressive and comparable binding constants (K_as = ~10^4 M^{-1}, 1:1 binding model).

A 15-mer phenylene-1,2,3-triazole with three interspersed ethynylene spacers was tested by Jiang et al. for halide-ion (Cl^-, Br^-, and I^-) and oxoanion (nitrate, $H_2PO_4^-$, HSO_4^-, and acetate) affinity.[96] In 1:9 *v*/*v* DMSO-THF, the association constants were within an order of magnitude (K_a = ~10^6 M^{-1}, 1:1 binding model) as determined by UV-Vis spectroscopic titrations. Based on DFT-minimized Cl^- and SO_4^{2-} complexes, the flexibility of the ethynylene spacers most likely accounted for the low selectivity of the receptor.

Two terminal 1,8-naphthalimides were appended to a phenylene-1,2,3-triazole five-mer. Jiang et al. added these functional groups to assist with π-π stacking and serve as a spectroscopic handle.[97] ^{1}H NMR titrations in THF-d_8 suggested the initial formation of a 2:1 host-guest complex based on the pattern of chemical shifting of several phenylene protons (upfield until 0.5 equiv of Cl^- were added then downfield). This is one

of the few examples of a 2:1 host-guest helical foldamer. The duplex could only be assembled using NMR concentrations of ligand (~0.5 mM); moreover, the double foldamer was somewhat unstable (K_2 < 100 M^{-1}). UV-Vis and/or fluorescence titration experiments in THF afforded more accurate binding constants, and the data were fitted to a 1:1 binding model (K_a = ~10^6 M^{-1} for Cl^-, Br^-, and I^-). Interestingly, the helical receptor exhibited low anion selectivity. In support of anion-induced folding, an excimer emission arising from stacked naphthalimides centered at 480 nm was observed. Using NMR concentrations of ligand, ^{1}H 2D NOESY spectroscopy also confirmed compact helical folding upon adding anions.

Together, Jeong and Jiang et al. have worked towards establishing structure-activity relationships by varying the hydrogen-bond donor, binding-cavity geometry, chain length, and degree of preorganization. In a recent investigation, Jiang and coworkers explored the impact of the terminal functional groups.[98] To this end, phenylene-1,2,3-triazole five-mers terminated by methyl-ester and amide-linked *N*-butyl, *N*-benzyl, and *N*-pyrenylmethyl groups were synthesized. Due to aggregation of the foldamers in pure $CDCl_3$, a mixed solvent system of 3:17 *v*/*v* DMSO-d_6-$CDCl_3$ was selected. No significant Cl^-, Br^-, or I^- binding was detected by ^{1}H NMR spectroscopy in the case of the methyl-ester derivative. The *N*-butyl derivative, which possessed two amide hydrogen-bond donors, chelated the halide ions measurably (K_a = 90, 153, and 142 M^{-1}, respectively; 1:1 binding model). The *N*-benzyl groups negatively impacted halide-ion affinity due to steric clashing. However, the *N*-pyrenylmethyl groups slightly enhanced association on account of favorable π-π stacking. These studies nicely illustrate

the many factors that influence structure-activity relationships between oligomer primary sequence and anion binding.

With expanded helical cavities, Xin Zhao and Zhan-Ting Li have developed aromatic-oligoamide foldamers that enwrap organic anions. To accommodate large guests like benzene,1,3,5-tricarboxylate, Zhao and Z.-T. Li et al. designed aromatic oligoamides with alternating benzene and naphthalene units (Figure 1.9).[99]

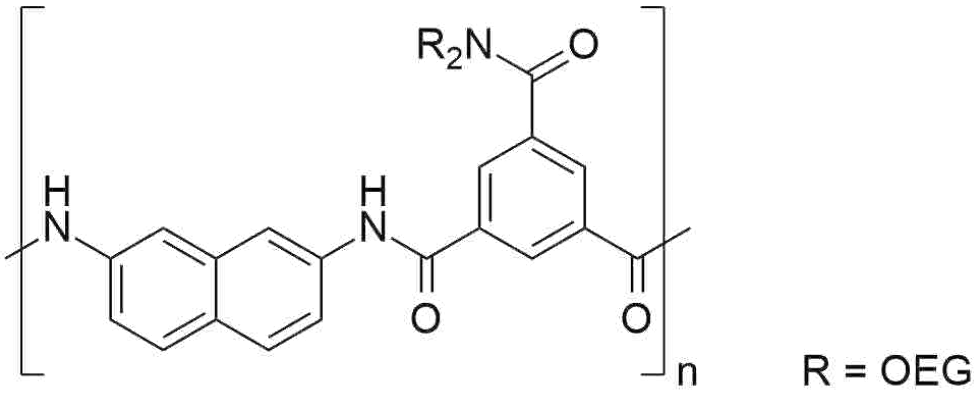

Figure 1.9 Oligomers with alternating benzene and naphthalene units created by Zhao and Z.-T. Li et al.

Interestingly, the free seven-mer and complex exchanged slowly on the NMR timescale in DMSO-d_6. When more than one equivalents of guest were added, free host signals could no longer be detected, which was suggestive of tight binding. On the basis of the marked downfield shifting of numerous amide–NH and CH protons, it was deduced that strong intermolecular hydrogen bonding occurred in solution. In contrast to those of the five-mer, the majority of the seven-mer terminal naphthalene protons experienced upshifts, consistent with helical folding. The nine-mer exhibited similar behavior in

solution. Additionally, ^{1}H 2D NOESY spectroscopy confirmed the helical folding of both oligomers around their guest as evidenced by intra- and intermolecular NOEs. The nine-mer bound benzene-1,3,5-tricaboxylate strongly in DMSO ($K_a = 5.5 \times 10^6$ M^{-1}, 1:1 binding model), as determined by UV-Vis spectroscopy. The seven-mer, in contrast, performed inferiorly in terms of guest binding by an order of magnitude.

Zhao and Z.-T. Li et al. next created *m*-substituted-benzamides—a three-, five-, and seven-mer—to bind mono-, di-, and tricarboxylate anions.[100] In DMSO-d_6, downfield shifting of the amide–NH protons on the five- and seven-mer upon adding benzene-1,3,5-tricarboxylate was noticed, which was consistent with strong hydrogen bonding in solution. 2D NOESY NMR experiments evinced both intra- and intermolecular through-space interactions for the complexes involving both ligands, confirming helical folding around benzene-1,3,5-tricarboxylate. However, the association constants were fairly low ($K_a = \sim 10^2$ M^{-1} for both complexes, 1:1 binding model), which suggested poor host-guest complementarity. Screening the seven-mer against mono-, di-, and tri- benzene carboxylates with varying substitution patterns did not afford higher affinities. Noteworthy, however, was the chiral induction afforded by L- and D-glutamate, as confirmed by CD spectroscopy in $CHCl_3$.

Next we turn to the work of Flood and coworkers, which has contributed much to our understanding of phenylene-1,2,3-triazole foldamers. In an effort to create bioinspired supramolecules whose active/inactive conformations are reversible and stimuli-responsive, Flood et al. synthesized a chiral phenylene-1,2,3-triazole nine-mer terminated by two azobenzene groups to enable *cis*/*trans* photoisomerization.[101] Placing the azobenzenes at the termini of the foldamer rather than the center was a novel

approach. In the more thermodynamically favorable *trans* form, the azobenzene units are coplanar with the rest of the oligomeric backbone. By design, the *cis* form disrupts coplanarity, π-π stacking, and helical folding. Photoisomerization of the two azobenzenes introduces three possible isomers: *trans-trans*, *trans-cis*, and *cis-cis*. When exposed to visible light in CH_3CN, the photostationary-states were roughly 67:30:3 % (*trans-trans*, *trans-cis*, and *cis-cis*, respectively), as determined by RP-HPLC. In contrast, when the oligomers were exposed to UV light (365 nm), the ratios changed to 0:33:66 %. In the dark, the oligomers (predominately in the *trans-trans* form) bound Cl^- with an association constant of 3,000 M^{-1} (based on UV-Vis titrations). After exposure to 365-nm UV light, the binding constant dropped appreciably to 380 M^{-1}. Exposure to 436-nm UV light restored the predominately all-*trans* isomer and its original Cl^- affinity. In parallel, conductivity experiments with equimolar concentrations of the foldamer and Cl^- (1 mM) were conducted. The free Cl^- concentration was estimated to be 0.23 mM in the presence of the predominately all-trans photostationary state. Upon exposure to 365-nm UV light, the free Cl^- concentration increased to 0.56 mM. Moreover, a concomitant increase in conductivity was observed (128 to 135 μS cm^{-1}). Exposing the solution to 465-nm UV light resulted in a conductivity decrease to almost the original level. This process could be repeated multiple times, illustrating the ability of foldamers to control Cl^- concentrations in bulk solution. In another study, the same nine-mer sans azobenzene terminal groups bound Cl^- less strongly than its macrocyclic counterpart in $CDCl_3$.[102]

To improve the overall difference in Cl^- binding upon irradiation, Flood et al. incorporated a β-sheet-like hydrogen-bonding array to interlock the folded helical backbone.[103] UV-Vis titrations in 50 % *v*/*v* CH_3CN-THF revealed that the 13-mer without

the array exhibited only a 17-fold difference in binding upon UV irradiation. Incorporating the peptide-like array to the oligomeric backbone resulted in an impressive 84-fold difference.

Extending their backbone to a 15-mer with six intramolecular hydrogen-bonding amide groups, Flood et al. probed the effect of bulk H_2O concentration on Cl^- affinity.[104] Based on broadened ^1H NMR signals and CD features in the absence of Cl^-, the authors deduced that the foldamer was at least partially preorganized in pure CH_3CN. Interestingly, the addition of Cl^- produced another rare example of a double-strand anion foldamer, which was in equilibrium with a 1:1 host-guest complex and free host. Quantitative UV-Vis titrations were conducted to measure Cl^- affinity in pure CH_3CN, 25 % *v*/*v* CH_3CN-H_2O, and 50 % *v*/*v* CH_3CN-H_2O (the limit of the 15-mer's solubility). Unsurprisingly, the overall Cl^- affinity of the 15-mer dropped by a factor of 13 when the H_2O concentration was increased from 0 to 25 %. However, at 50 %, the overall association doubled as compared to that in 25 % *v*/*v* CH_3CN-H_2O. In addition, the double foldamer formed preferentially in solution with increasing H_2O composition. In 100 % CH_3CN, the duplex was outcompeted by the single foldamer when > 0.5 equiv of Cl^- were titrated. These data demonstrate the influence of the hydrophobic effect, which enhanced Cl^- affinity and promoted duplex self-assembly. van't Hoff and ITC analyses revealed that in 50 % H_2O Cl^- binding was enthalpically dominated. Nevertheless, duplex formation came at no entropic cost, which suggests π-π stacking served to offset this penalty. Overall, the high Cl^- affinity that the foldamer exhibited in 50 % *v*/*v* CH_3CN-H_2O ($K_1 = 2.3 \times 10^5$ M^{-1}, $K_2 = 3.8 \times 10^7$ M^{-1}; 2:1 host-guest binding model) was an impressive feat. Unfortunately, only the single foldamer could be crystallized (Figure

1.10). Within the helical cavity, Cl^- is held by all six 1,2,3-triazole–CH hydrogen-bond donors in a distorted octahedral coordination geometry. Weaker phenylene–CH hydrogen bonds are also evident. Additionally, a Na^+ is chelated by the oxygens of two acyclic oligoether groups located outside of the helical cavity (not shown).

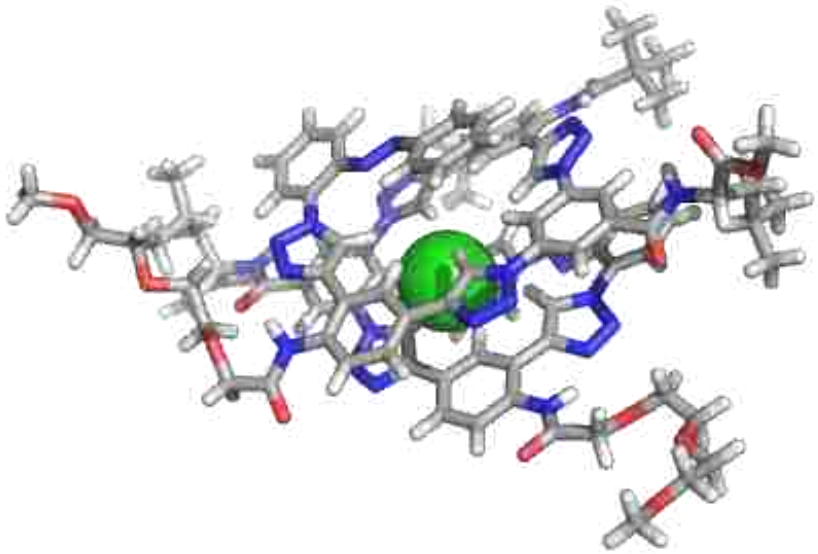

Figure 1.10 X-ray crystal structure of a phenylene-1,2,3-triazole foldamer with an intracavity Cl^- developed by Flood et al. (some functional groups removed for clarity).

Analogous to oligopyridines used to chelate transition metals, Biao Wu et al. have developed oligourea receptors to target anions. In an early example, an *o*-phenylene-bridged four-urea oligomer was fashioned to bind SO_4^{2-} in competitive media.[105] An X-ray crystal structure of the *p*-nitrophenyl-capped oligomer binding SO_4^{2-} was obtained. Eight hydrogen bonds in a pseudo-square-planar coordination geometry (when each urea is considered as a monodentate coordination vector; Figure 1.11). Binding studies in 0, 10, and 25 % H_2O-DMSO (assessed by UV-Vis spectroscopy) revealed that the naphthyl-

capped oligomer exhibited superior water-resistant SO_4^{2-} binding over its *p*-nitrophenyl derivative. The Log K_a (1:1 binding model) for the naphthyl derivative in 25 % H_2O-DMSO was 4.87.

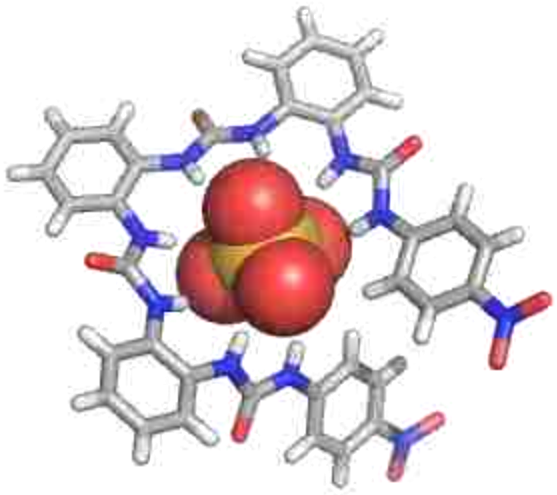

Figure 1.11 X-ray crystal structure of an *o*-phenylene-bridged oligourea chelating SO_4^{2-} developed by Wu and coworkers.

Hiromitsu Maeda and Jiang et al. have versatilely developed both anion foldamers and anion helicates. Maeda et al. introduced a tractable strategy for chiral induction using chiral countercations.[106] These π-conjugated salts (binaphthylammonium Cl^- and Br^-) induced the chiral folding of boron-difluoride complexes of 1,3-dipyrrolyl-1,3-propanedione oligomers (Figure 1.12). In the presence of the (*R*,*R*) countercation, the four-pyrrole oligomer in CH_2Cl_2 generated Cotton effects associated with the excitonic interaction between the two receptor arms connected by the *m*-phenylene linker. Time-dependent DFT suggested that the *M*-type diastereomeric ion-pair formed preferentially. The foldameric complex was also characterized using ^1H NMR spectroscopy. With 1.5

equiv of (*R*,*R*)-binaphthylammonium Cl^- at –50 °C, two sets of resonances corresponding to slow-exchanging *M* and *P* helices (50:32 ratio, respectively) could be seen. In one of the few kinetic studies of an anion foldamer, EXSY NMR was utilized to determine a rate constant of 3.8 s^{-1} for the *M*-to-*P* conversion.

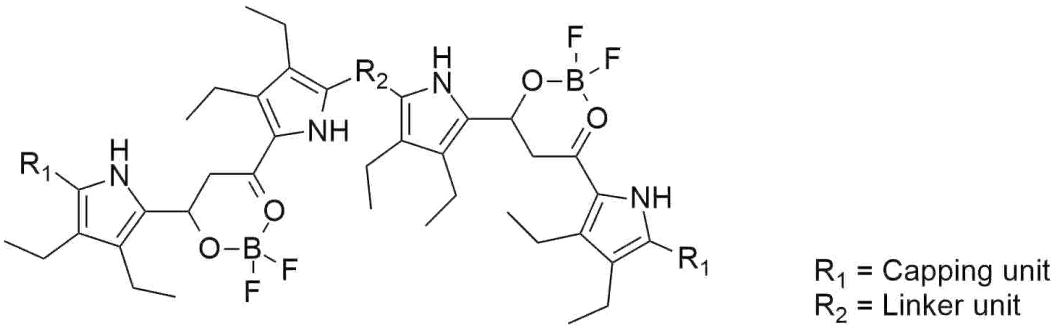

Figure 1.12 Boron-difluoride complexes of 1,3-dipyrrolyl-1,3-propanedione oligomers developed by Maeda et al.

The same dipyrrolyldiketone ligands with either an *m*-terphenyl and *o*-terphenyl linker were synthesized to target L-amino-acid anions.[107] Both foldamers formed helical complexes with Cl^- or acetate at low temperatures, as confirmed by ^1H NMR and ROESY NMR spectroscopy. Additionally, both foldamers with addition of anionic L-phenylalanine produced enhanced Cotton effects in CH_2Cl_2 at 20 °C, indicative of chiral induction. Anionic D-phenylalanine rendered the opposite CD patterns. With two of the few foldamers designed to target chiral anions, Maeda et al. demonstrate the potent chiroptical properties of these synthetic systems.

Yongjun Li, Yuliang Li, and Yulan Zhu developed an amide-linked phenylene-1,2,3-triazole oligomer with a terminal photoactive pyrene unit (Figure 1.13).[108] This

ligand in the presence of less than half an equivalent of SO_4^{2-} in 0.5 % DMSO-d_6-acetone-d_6 at –30 °C formed a duplex, which was characterized by a ^{1}H 2D NOESY NMR spectroscopy. The NOEs were consistent with a double anion foldamer, as were the characteristic shifts of key aromatic signals (upfield-then-downfield with an inflection at 0.5 equiv of SO_4^{2-}). > 0.5 equiv of guest favored 1:1 host-guest speciation.

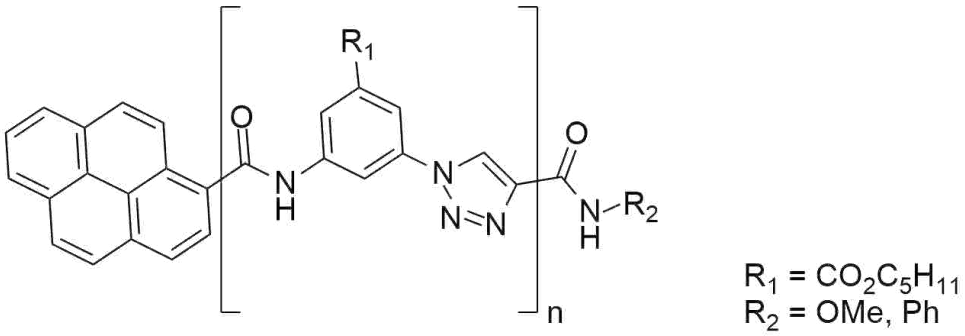

Figure 1.13 Amide-linked phenylene-1,2,3-triazole backbone constructed by Yongjun Li, Yuliang Li, and Zhu et al.

In a follow-up study, Zhu and Yongjun Li et al. created new amide-linked phenylene-1,2,3-triazole derivatives.[109] To one terminus of a three-triazole ligand a photoactive pyrene was appended. Less than half an equivalent of SO_4^{2-} induced 2:1 host-guest complexation in CD_2Cl_2. Several aromatic signals initially moved upfield in response to intermolecular π-π stacking but subsequently moved to their original positions when > 0.5 equiv of guest were present. This characteristic pattern in shifting was consistent with the formation of a double anion foldamer. When a terminal, amide-linked *N*-phenyl group was appended to the ligand, three amide–NHs, three triazole–CHs, and two phenylene–CHs could converge on a single SO_4^{2-} anion in CD_2Cl_2. Accordingly,

all eight of these protons shifted downfield upon addition of SO_4^{2-}. However, the majority of the terminal, *N*-phenyl and pyrene protons shifted upfield, which evidenced π-π stacking. This helical binding conformation was confirmed by ^{1}H 2D NOESY NMR spectroscopy. Moreover, the association constant for the SO_4^{2-} adduct was determined by ^{1}H NMR titrations (K_a = 1,300 M^{-1}, 1:1 binding model).

Bipyridyl-bisurea and 1,10-phenanthroline-bisurea foldamers were synthesized by Darren Johnson and Michael Haley et al. to chelate anions in 10 % *v*/*v* DMSO-d_6-$CDCl_3$.[110] ^{1}H NMR titrations were carried out with Cl^-, Br^-, I^-, and $H_2PO_4^-$ by fitting the changes in urea–NH chemical shifts to a 1:1 binding model. The 1,10-phenanthroline-bisurea demonstrated a modest selectivity for Cl^- (K_a = 2.6 ×10^2 M^{-1}) over the larger halide ions (K_a = 6.0 × 10^1 M^{-1} for Br^-). However, the truncated control molecule bearing only one urea unit bound halide ions weakly and indiscriminately (K_a = ~10^1 M^{-1} for all three).

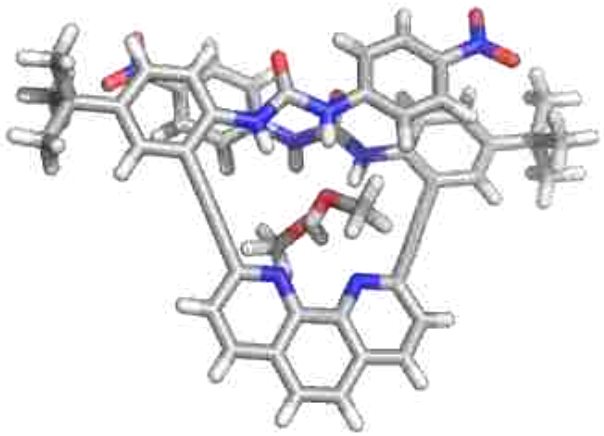

Figure 1.14 X-ray crystal structure of a 1,10-phenanthroline-bisurea oligomer fashioned by Johnson and Haley et al.

The 1,10-phenanthroline-bisurea ligand formed stable complexes with $H_2PO_4^-$ (K_a = 4.6 $\times 10^4$ M^{-1}) in 10 % DMSO-$CHCl_3$, as determined by UV-Vis titrations. $H_2PO_4^-$ affinity for the bipyridyl-bisurea ligand was higher (K_a = 7.8 $\times 10^4$ M^{-1}) due to the superior flexibility of the host backbone.[111] In an X-ray crystal structure, two CH_3OH molecules reside within the foldameric binding pocket (Figure 1.14). Interestingly, each methanol–OH hydrogen bonds a single phenanthroline–N, while each urea unit hydrogen bonds a separate methanolic oxygen.

Helical chirality and selective anion binding are two strategies utilized by nature to achieve enantioselective chemical transformations. However, the efficient transfer of chirality from a helical organocatalyst has been rarely seen. To this end, Olga Garcia Mancheño et al. synthesized a four-1,2,3-triazole nine-mer, which included a *trans*-1,2-diaminocyclohexyl core unit to preorganize the helical scaffold and bias one-handed folding.[112] The (*R*,*R*) and (*S*,*S*) catalysts accelerated enantioselective dearomatization of quinolines (96:4 and 4:96 e.r., respectively) via C2-selective nucleophilic addition of silyl ketene acetals. Mechanistically, the Cl^- complexation of a preformed *N*-acylquinolinium salt helped bring the catalyst and substrate in close proximity, whereby substrate interaction with the *M* or *P* helical backbone resulted in efficient chiral transfer.

The previously discussed anion foldamers utilized hydrogen bonding to chelate anions within their helical cavities. In contrast, halogen bonding[113–127] has been utilized only sparingly to create anion helicates/foldamers. The first solution-phase example of a helical foldamer that included a halogen-bond donor was developed by Antonio Caballero and Pedro Molina.[128] Two iodo-1,2,3-triazolium halogen-bond donors were connected by a naphthalene-2,7-diol core. To serve as a spectroscopic handle and

encourage π-π stacking, the oligomer was capped with photoactive, terminal pyrene units. Subsequently, fluorescence titrations with hydrogen pyrophosphate and $H_2PO_4^-$ afforded impressive binding constants in acetone (K_as $\geq 10^6$ M^{-1}, 1:1 binding model). As compared to the proteo-control molecule, the halogen-bonding oligomer bound $H_2PO_4^-$ an order of magnitude more strongly. Moreover, in 9:1 *v*/*v* CD_3CN- CD_3OD, the halogen-bonding oligomer bound hydrogen pyrophosphate five-fold better than the proteo-control molecule, as determined by ^1H NMR titrations. Moreover, this convenient "turn-on" fluorescence chemosensors was selective for hydrogen pyrophosphate.

The second example of a solution-phase helical foldamer was created by Paul Beer et al. Phenylene-iodo-1,2,3-triazole foldamers were synthesized with four convergent halogen-bond donors.

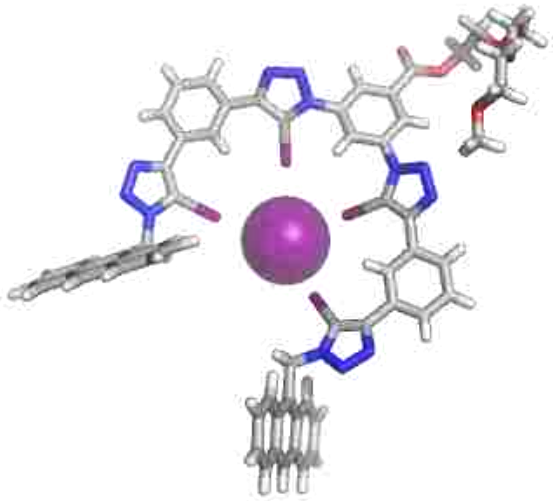

Figure 1.15 X-ray crystal structure of a phenylene-iodo-1,2,3-triazole foldamer with a bound I^- created by Beer et al.

The anthracene-capped ligand complexed I^- noticeably in 1:1 *v*/*v* $CDCl_3$-acetone-d_6 (K_a = 2,712 M^{-1}, 1:1 binding model) as ascertained by ^1H NMR titration experiments. An X-ray crystal structure of the complex was obtained (Figure 1.15), and due to the size of the iodine atoms, the four halogen-bond donors convergently point away from the backbone plane to bind its guest. Interestingly, the anthracene terminal groups are not π-stacked. Concomitantly, no excimer emission was seen during fluorescence spectroscopic titrations.[129]

Anion helicates encapsulate multiple guests within their helical cavities, necessitating strong, multidentate hydrogen or halogen bonds to overcome the severe electrostatic repulsion between the anions. To create multi-strand anion helicates, the chemist must surmount the additional challenges associated with interstrand interactions and the entropic cost of complexing multiple anions and ligands.

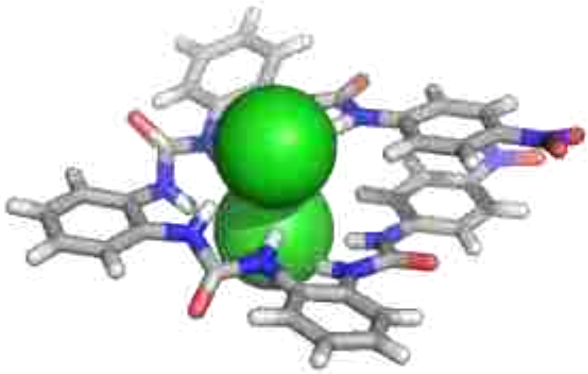

Figure 1.16 X-ray crystal structure of an *o*-phenylene-bridged four-urea helicate holding two Cl^-s developed by Wu et al.

Before reviewing these latter supramolecules, we will begin with solution-phase single-strand anion helicates. Wu et al. synthesized a series of *o*-phenylene-bridged oligoureas with increasing chain length (from a three- to a six-urea), capped with *p*-nitrophenyl groups.[130] Four new dinuclear anion helicates and one isomer were characterized in the solid state. In an X-ray crystal structure of the four-urea oligomer, Cl^-s sit above and below the helical planes (Figure 1.16). Each Cl^- is held by urea–NH hydrogen bonds with an overall bent coordination geometry (when each urea is considered as a monodentate coordination vector). Due to rotation about the phenylene–urea bonds, the urea donors point in an up-down-up-down pattern, so that the first and third ureas chelate one Cl^-, while the second and fourth chelate the other Cl^-. Taken together, the binding cavity is arranged in a square-like configuration. Impressively, the Cl^--Cl^- distance is only 3.6 Å, which must be stabilized by hydrogen-bonding interactions to overcome the severe electrostatic repulsion. In the case of the five-urea oligomer, the Cl^--Cl^- distance widens (3.8 Å) in response to the slightly larger helical cavity. The six-urea ligand houses two Cl^-s that are 3.9 Å apart. The first two urea donors bind the first Cl^- in plane with the helical turn. The third, fourth, and fifth ureas chelate the second Cl^-. Interestingly, the sixth urea flips to align itself with the helical axis and hydrogen bonds the second urea oxygen. Its terminal *p*-nitrophenyl is orthogonally rotated from the helical-turn plane. In the X-ray crystal structure of the six-urea isomer, the Cl^--Cl^- distance grows to 4.0 Å (Figure 1.17).

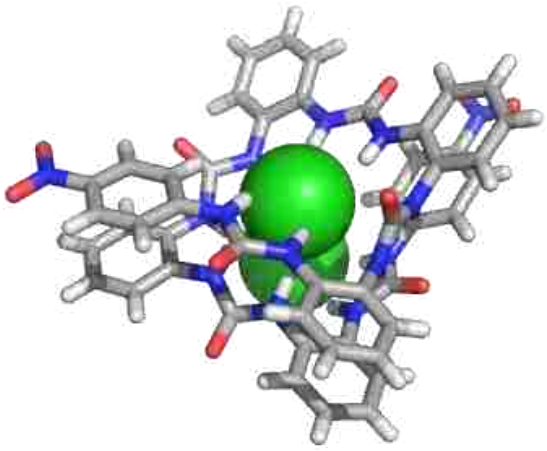

Figure 1.17 X-ray crystal structure of an *o*-phenylene-bridged six-urea helicate encapsulating two Cl^-s synthesized by Wu et al.

The second urea points along the helical axis and hydrogen bonds the sixth urea oxygen. DFT calculations revealed that the six-urea isomers have similar energies (within 2.0 kcal mol^{-1}). Possibly, a urea moiety in each structure aligns itself with the helical axis in order to increase helical pitch, thus, relieving Cl^--Cl^- repulsion. The helicates were also studied in solution. Qualitative ^1H NMR titrations were performed in $CDCl_3$, and the patterns in chemical shifting upon adding Cl^- were consistent with helical folding. Additionally, 2D NOESY NMR spectroscopy confirmed structural congruence between the solution-phase and solid-state data. Lastly, UV-Vis titrations in 0.5 % *v*/*v* DMSO-$CHCl_3$ revealed two-step changes in the difference spectra, which provided evidence for 1:2 host-guest binding.

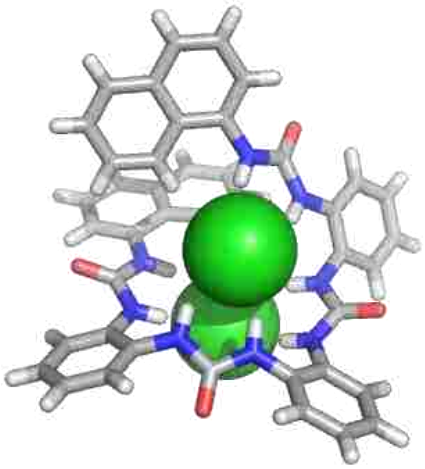

Figure 1.18 X-ray crystal structure of a 1-naphthyl-terminated four-urea helicate with *o*-phenylene bridges developed by Wu et al.

Wu et al. synthesized a similar series of *o*-phenylene-bridged oligoureas (four-, five-, and six-urea) but with fluorescent 1-naphthyl or 1-anthracenyl terminal groups.[131] Six new Cl^- complexes were elucidated with single-crystal X-ray diffraction. Almost all ligands racemically bound two Cl^-s in a helical conformation. However, the 1-naphthyl five-urea derivative, which included two TBA cations in the units cell, was completely *M* resolved. The 1-naphthyl four-urea cocrystallized with two Cl^-s in much the same way as the *p*-nitrophenyl derivative. Interestingly, the naphthyl units are not π-stacked, but a naphthyl–CH hydrogen bonds the first urea oxygen (Figure 1.18). Each Cl^- is bound by urea–NH hydrogen bonds from alternating units. The Cl^--Cl^- distance of 3.9 Å suggests that sterically bulky groups help encourage cavity expansion. The even bulkier 1-anthracenyl groups appended to the four-urea allow for a greater expansion (Cl^--Cl^- distance is 4.0 Å, not shown).

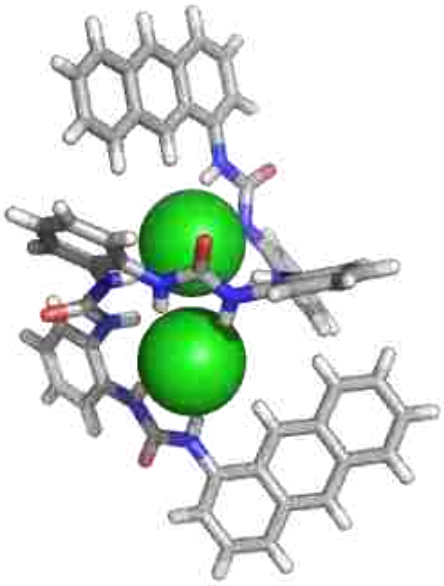

Figure 1.19 X-ray crystal structure of a 1-anthracenyl-capped five-urea helicate synthesized by Wu et al.

Additionally, 1-anthranceyl protons form CH hydrogen bonds with each Cl^-, stabilizing this expanded conformation. In the case of the 1-anthracenyl-capped five-urea, both 1-anthracenyl-urea units nearly align themselves with the helical axis, which allows these groups to hydrogen bond (Figure 1.19). The helicates were also studied in solution. Cl^- affinity in DMSO-d_6 was ascertained with ^{1}H NMR titrations (K_a = ~10^2 M^{-1} for all ligands, 1:1 binding model as determined by Job plots—a method used to determine the binding stoichiometry of a host-guest system). However, 1:2 complexes were characterized with ESI-HRMS when infusing $CHCl_3$ solutions, suggesting that the helicates self-assembled in less competitive media. Correspondingly, a 1:2 complex was inferred through ^{1}H NMR spectroscopy in $CDCl_3$.

Jiang et al. constructed a series of anion-switchable amide-linked phenylene-1,2,3-triazoles designed to fold into helical conformations around halide ions. Upon

titrating Cl^-/Br^- to a six-mer in pyridine-d_5, triazole–CH and amide–NH protons shifted downfield as expected, indicative of intermolecular hydrogen bonding. Moreover, association constants for Cl^- and Br^- were calculated (540 and 83 M^{-1}, respectively; 1:1 binding model). Supported by 2D NOESY NMR spectroscopy, a one-turn helical complex was deduced. In comparison, the 12-mer was expected to fold around its guests in two turns. Upon titrating Cl^-, the amide–NH protons initially upshifted when less than 1.6 equiv of guest were present. When > 1.6 equiv of guest were present, these resonances shifted downfield. From this pattern in chemical shifting, the authors surmised a 1:2 host-guest stoichiometry. Accordingly, the binding isotherms fit well to a 1:2 host-guest model, affording noteworthy association constants ($K_1 = 4.9 \times 10^2$ and $K_2 =$ 13 M^{-1}) in competitive media. The weaker second association suggested the process was not cooperative, consistent with the electrostatic repulsion between intracavity guests. Two Br^-s were also accommodated by the 12-mer with lower affinity. Interestingly, quantitative 2D NOESY NMR evinced a deformation of the host to increase its helical pitch upon adding excess Cl^-, presumably to relieve electrostatic repulsion. The 18-mer was designed to form three helical turns around halide ions. 1:4 *v*/*v* DMSO-d_6-pyridine-d_5 was utilized to prevent aggregation of these longer oligomers. In this more competitive solvent system, the 18-mer bound Cl^- two-fold more strongly than the 12-mer; additionally, the second association was almost 32-fold stronger. These data strongly suggest that the longer oligomer better alleviated the charge repulsion between bound guests. Notably, these dinuclear single-strand helicates were the first to be characterized in solution.

Frequently, biopolymers form ditopic complexes that result in various "turn-on" functional states. Synthetic analogues are scarce, which motivated Jiang et al. to create a foldamer that encapsulated Cl^- and β-D-glucopyranoside simultaneously.[132] To accomplish this task, the researchers synthesized benzoylbenzohydrazide five-mers capped with either dimethoxyphenyl or pyrene units. To help preorganize the ligands, hydrazide–NH···oxygen hydrogen bonds were incorporated along the backbone. Additionally, multiple hydrogen-bond donors/acceptors could point inwardly to complement both anions and saccharides. When studying the dimethoxyphenyl derivative in $CDCl_3$ by ^1H NMR spectroscopy, the hydrazide–NH protons initially shifted upfield with less than five equivalents of Cl^- then experience a chemical shift inversion. This pattern in chemical shifting was consistent with a 1:2 host-guest stoichiometry, corroborated by Job plots. Additionally, ^1H 2D NOESY NMR spectroscopy confirmed helical folding of the ligand around Cl^-. Providing further evidence, adding Cl^- to the pyrene-capped ligand generated a broad excimer emission (centered at ~480 nm) due to the association of an excited-state dimer. Cl^- and β-D-glucopyranoside affinities were initially determined separately with ^1H NMR titrations. Cl^- complexation afforded by both oligomers was modest ($K_a = 10^1$–10^2 M^{-1}, 1:1 binding model) in $CDCl_3$. β-D-glucopyranoside affinity for both ligands was comparable ($K_a = 10^2$ M^{-1}, 1:1 binding model). Moreover, addition of the saccharide to the pyrene-capped oligomer caused homologous changes in the emission spectra, indicating a folded host-guest complex. To deduce the synergistic effect of adding both guests to the dimethoxyphenyl-capped derivative simultaneously, CD spectroscopy was utilized. A strong CD signal was created

only in the presence of both guests (20 equiv each). Addition of either guest without the other resulted in a weak or nonexistent CD signal.

Maeda and coworkers have versatilely created both single- and multi-strand anion foldamers as well as helicates. As before, boron-difluoride complexes of 1,3-dipyrrolyl-1,3-propanediones were synthesized. In the present study a seven-, nine-, and 15-mer were created.[133] Impressively, seven-mer-1:1, 15-mer-1:2, and nine-mer-2:2 host-guest complexes were characterized in the solid state. The stunning double helicate possesses a Cl^- channel lined with eight pyrrole–NH hydrogen-bond donors (not shown). Each of the two Cl^-s are bound in a distorted tetrahedral coordination geometry. However, only 1:1 host-guest species were observed when studying the seven- and nine-mers in solution. In contrast, the 15-mer with two equivalents of Cl^- in CD_2Cl_2 at –50 °C formed a 1:2 complex in agreement with its X-ray structure (Figure 1.20). This was the second example of a solution-persistent single-strand dinuclear helicate. In the solid state, each of the two Cl^-s is bound by four pyrrole–NH hydrogen bonds in a pseudo-square-planar coordination geometry, and the intracavity Cl^--Cl^- distance is 4.6 Å. Additionally, 1,3-propanedione α-hydrogen-CH hydrogen bonding is seen. The formation of this Cl^- helicate in solution was confirmed by the downfield shifted signals consistent with the X-ray crystal structure. In addition, COSY and ROESY NMR experiments supported the formation of the helicate. To ascertain Cl^-, Br^-, and I^- affinity. UV-Vis titrations were conducted in in CH_2Cl_2. In the case of the 15-mer, Cl^- binding was extremely strong (K_1 = 1.2 ×10^8 and K_2 = 3200 M^{-1}, 1:2 host-guest binding model) and uncooperative. Finally, UV-Vis stopped-flow spectroscopy was utilized to assess the kinetics of 1:1-foldamer

self-assembly. At this concentration, the kinetics of 1:2-helicate self-assembly could not be assessed. Interestingly, folding rates slowed with increasing chain length.

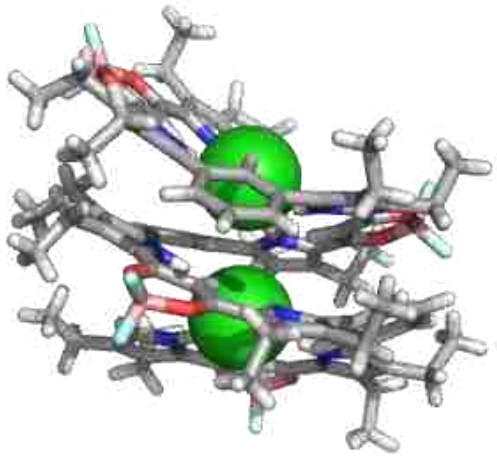

Figure 1.20 X-ray crystal structure of a single-strand 15-mer Cl^- helicate composed of boron-difluoride complexes of 1,3-dipyrrolyl-1,3-propanedione oligomers synthesized by Maeda et al.

We will finish this introduction with a comprehensive treatment of higher-order anion helicates. The first helical anion complex of any kind was a double helicate discovered by Javier de Mendoza et al in 1996.[134] Utilizing enantiomerically pure bicyclic guanidiniums spaced by dimethyl-sulfide linkers, the authors created double helicates that encapsulated SO_4^{2-} in solution (Figure 1.21). When SO_4^{2-} was added to the two-mer (and other derivatives) in $CDCl_3$, strong downfield shifts of the guanidinium–NH protons were observed by ^1H NMR spectroscopy. A 2D ROESY experiment confirmed intermolecular ROEs, consistent with double-helicate formation. As bicyclic guanidiniums themselves possess stereocenters, (*R*,*R*) or (*S*,*S*), the resultant helicates were one-handed. CD-spectroscopic studies in CH_3CN revealed that the enantiomers

gave rise to mirror-image spectra. The higher ellipticities in the presence of SO_4^{2-} evidenced anion-induced helicity.

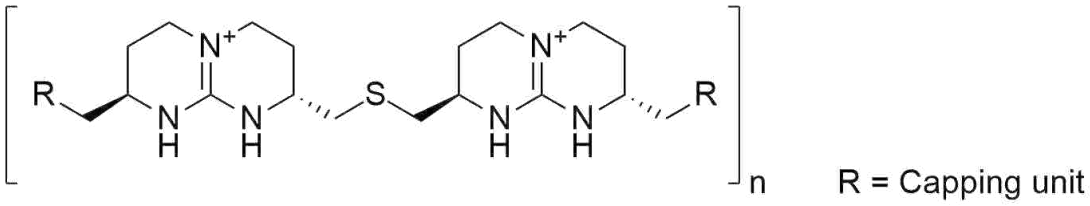

Figure 1.21 A representative bicyclic guanidinium oligomer (two-mer) composed by de Mendoza et al.

We will now return to the exemplary work of Wu et al. who have greatly contributed to the field of multi-strand anion helicates as well as our understanding of anion coordination in general. Their first report of a multi-strand anion helicate in 2011 was also the first example of a triple anion helicate.[135] Again, Wu and coworkers utilized *o*-phenylene-bridged biurea oligomers but targeted larger anions in the present work. Inspired by the odd-even rule of M_2L_3 helicates developed by Albrecht et al.,[136,137] an ethylene spacer (even number of carbons) was utilized to link two biurea subunits. A beautiful X-ray crystal structure was obtained in which three bis(biurea) ligands enwrap two intracavity PO_4^{3-}s (Figure 1.22). Each PO_4^{3-} is held by six ureas (through 12 urea–NH hydrogen bonds) originating from three separate ligands. Each edge of a PO_4^{3-} tetrahedron is bound by one urea with an overall pseudo-octahedral coordination geometry (if each urea is considered as a monodentate coordination vector). Hence, the biurea is analogous to a bipyridine moiety.

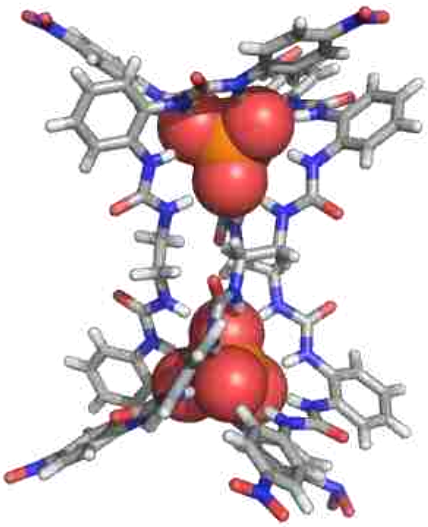

Figure 1.22 X-ray crystal structure of an *o*-phenylene-bridged bis(biurea) triple helicate developed by Wu et al.

At its termini, the triple helicate is stabilized by nearly-orthogonal CH···π interactions. At the midpoint of the triplex, the ethylene linkers taper so that the structure resembles an hourglass. The triple helicate was studied in solution using ^{1}H NMR spectroscopy in 5 % *v*/*v* D_2O-DMSO-d_6. Upon titrating more than 0.66 equiv of PO_4^{3-}, the ligand resonances were well-resolved and consistent with the solid-state structure. Moreover, marked downfield chemical shifts of the urea–NH protons indicated strong hydrogen bonding in solution. In contrast, terminal *p*-nitrophenyl protons were strongly upfield shifted due to ring-current shielding effects. 2D NOESY and DOSY NMR experiments also corroborated the proposed structure. Interestingly, upon titrating SO_4^{2-}, the ^{1}H NMR spectroscopic changes were more consistent with a 1:1 complex, likely due to the lower charge density SO_4^{2-}.

In a follow-up paper, Wu et al. explored the effect of spacer length/rigidity in forming helicates, mono-bridged structures, or mesocates[137] Using the same *o*-phenylene-bridged biureas linked by a *p*-xylylene spacer, an elongated PO_4^{3-} triple helicate was synthesized. Unfortunately, only a preliminary X-ray crystal structure of the complex was obtained. Using the same functional groups linked by a phenylene spacer, Wu et al. created yet another PO_4^{3-} triple helicate.[138] Impressively, this helicate reversibly converted to an A_4L_6 tetrahedral cage as a function of peripheral templation and solvent.

In an effort to create a highly selective choline binding site within the linker region of the PO_4^{3-} triple helicate, Wu et al. utilized the same *o*-phenylene-bridged biureas linked by a 4,4'-methylenebis(phenyl) spacer.[139] The resulting aromatic box was electron-rich, a suitable binding site for complementary cations. In a magnificent X-ray crystal structure, three intertwining ligands are held together by two terminal PO_4^{3-}s. As before, each PO_4^{3-} is bound by six ureas in a pseudo-octahedral coordination geometry (Figure 1.23). Interestingly, unlike the first PO_4^{3-} triple helicate, the new complex lacks molecular C^3 symmetry. Remarkably, within the aromatic box, a TMA countercation is encapsulated—stabilized by multiple cation-π interactions afforded by six aromatic rings (average N···centroid distance is 4.5 Å) as well as intracavity ion-pairing. The triple helicate could also bind biologically relevant cations like choline. Upon mixing one equivalent of choline with ligand, chemical upshifts of the choline protons in 1.5 % D_2O-acetone-d_6 indicated guest encapsulation within the aromatic box.

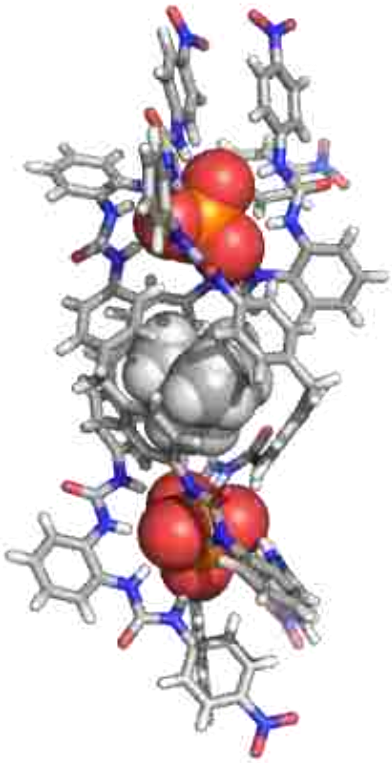

Figure 1.23 X-ray crystal structure of a 4,4'methylenebis(phenyl)-linked *o*-phenylene-bridged bis(biurea) triple helicate created by Wu et al.

This binding arrangement was confirmed by ^{1}H 2D NOESY and DOSY NMR as well as HRMS experiments. Acetylcholine also proved to be a suitable guest for the triple helicate but was bound 20-fold less strongly. Through fluorescence displacement titrations (using a 4-(4′-dimethylamino)styryl-1-methylpyridinium probe), a selectivity value of 15 was obtained (chlorine:acetylcholine). Mechanistically, choline selectivity emerged from a dual-site binding motif: trimethylammonium headgroup encapsulation as well as hydroxyl-tail hydrogen bonding (presumably to a urea oxygen). In the next study, it was discovered that the hydroxyl tail likely hydrogen bonded a PO_4^{3-} oxygen.

Next, Wu et al. studied seven chiral quaternary ammonium cations, which were used to induce one-handed triple-helicate complexation.[140] The same triple helicate used previously to bind choline was repurposed for the present studies. Crystallization of the ligand with racemic α-methylcholine resulted in equal populations of *M*- and *P*-helicates. Enantioselective encapsulation of the (*R*)- or (*S*)-enantiomer by an *M*- or *P*-helicate, respectively, was observed in the solid state.

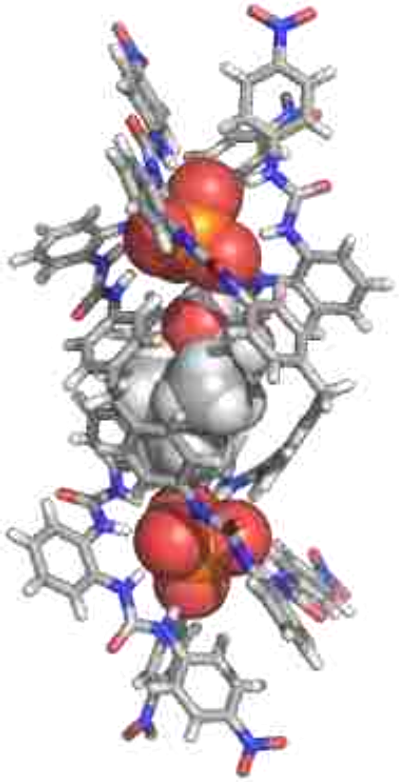

Figure 1.24 X-ray crystal structure of a 4,4'methylenebis(phenyl)-linked *o*-phenylene-bridged bis(biurea) triple helicate encapsulating a chiral guest created by Wu et al.

As expected, the trimethylammonium headgroup is held within the aromatic box by numerous cation-π interactions. Additionally, the hydroxyl group is located within the helicate and hydrogen bonds a PO_4^{3-} oxygen (Figure 1.24). As evidenced by the upfield shifts of their trimethylammonium headgroup protons, all seven of the targeted guests were encapsulated by the PO_4^{3-} triple helicate in solution (CD_3CN). Monitored by CD spectroscopy, the addition of chiral, non-racemic guests to the triple helicate resulted in enhanced populations of *M* or *P* helices. CD spectroscopic titrations also afforded binding constants in CH_3CN. Notably, both α- and β-methylcholine were bound by the helicate with association constants in the ~10^6 M^{-1} range (1:1 binding model). Taken together, this ditopic triple helicate, which employs hydrogen bonding, solvophobic interactions, ion pairing, and cation-π interactions, is a unique and exciting supramolecular receptor that stands at the forefront of the field. The first examples of multi-strand halide-ion helicates were developed by Maeda and coworkers.[141] Solution-persistent 2:2 (host-guest) Cl^- and Br^- double helicates were assembled using boron-difluoride 1,3-dipyrrolyl-1,3-propanediones linked by phenylene-diethynylene spacers. The eight- and 10-mer in $CDCl_3$ at –50 °C formed double helicates upon adding ~one equivalent of Cl^-. The slow-exchanging species (free ligand, 1:2, and 2:2) were distinguishable by ^1H NMR spectroscopy. Addition of excess Cl^- destabilized the double helicate in favor of the 1:2 complexes. Impressively, the 10-mer Cl^- double helicate also formed at RT. Additionally, double-helicate self-assembly was corroborated by DOSY NMR spectroscopy. Double helicates were also formed around Br^- under similar conditions. Given their small size, low charge, and variable coordination preference,

halide ions are extremely challenging targets. Thus, Maeda et al. are truly pioneers of halide-ion-templated helicate self-assembly.

1.6 Summary and Bridge to Chapter 2

In a relatively short period of time, supramolecular chemists have defined new chemical space through the incorporation of abiotic functional groups in secondary structure. Towards this goal, anion-switchable single-/multi-strand helices have been realized. Moreover, as many anions undergo acid-base chemistry at physiologically relevant pH, anion helicates/foldamers can be developed into pH-responsive nanocomponents. By incorporating photoisomerizable azo groups, these supramolecules become light responsive. Additionally, various stimuli have been explored to powerfully induce helical chirality. Thus, dynamic and potentially useful building blocks that possess stimuli-responsive properties have been established. Furthermore, anion helicates/foldamers are tractable hosts. Mimicking nature, chemists have created diverse solvent-secluded active sites capable of adjusting their dimensions in response to guests—often in aqueous or competitive media. Through helical self-assembly around a target guest, these increasingly sophisticated and modular supramolecules can bring into contact photoactive functional groups, which emit fluorescence. Taken together, the creativity and ingenuity of supramolecular chemists have worked towards Gellman's vision: "Mastery over foldamers should provide access to a new universe of molecules that profoundly influence chemistry and society."[3]

Prior to the work presented herein, there had not been any reports of a multi-strand I^- helicate nor of a triple-strand Br^- helicate. This is unsurprising given the

challenges associated with coordinating multiple ligands around a small anion with a low charge. To develop a robust halide-ion triple helicate that self-assembles even at elevated temperatures, halogen-bonding *m*-arylene-ethynylene oligomers were synthesized. Prior to the work presented here, introverted halogen-bond donors had never been attached to an *m*-arylene-ethynylene backbone. As the synthesis of the eventual nine-mer target was expected to be challenging, a three-mer was first constructed, and preliminary anion binding studies were carried out in solution and the solid state. In a separate investigation by Asia Riel et al., a closely related three-mer bound Cl^-, Br^-, and I^- modestly in 2:3 *v*/*v* $CDCl_3$-CH_3NO_2 (K_1 = 2630, 4690, 4380 M^{-1}, respectively; 1:2 host-guest binding model).[142] Noteworthy was the preference of the receptor for the larger halide ions. Impressively, the oligomer also chelated a large and charge-diffuse oxoanion, ReO_4^-, in solution and the solid state. The following chapter is an exploration of the this phenomenon.

2 Solution and Solid-Phase Halogen and CH Hydrogen Bonding to ReO_4^-

2.1 Abstract and Artwork

^{1}H NMR spectroscopic and X-ray crystallographic investigations of a 1,3-bis(4-ethynyl-3-iodopyridinium)benzene scaffold with ReO_4^- reveal strong halogen bonding in solution, and bidentate association in the solid state. A nearly isostructural host molecule demonstrates significant CH hydrogen bonding to ReO_4^- in the same phases.

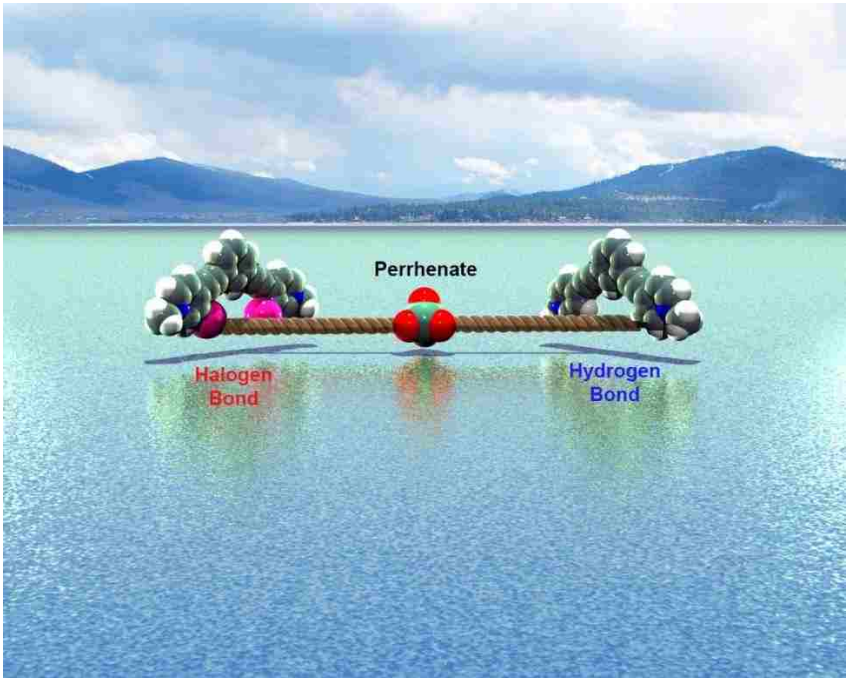

Figure 2.1 Cover artwork for *Chemical Communications* publication. Exploiting halogen and CH hydrogen bonding to target the medically and environmentally important ReO_4^- anion is an exciting strategy. The intricate balance between halogen and hydrogen bonding in both the solid state and in solution is represented by two crystal structures competing for the ReO_4^- anion.

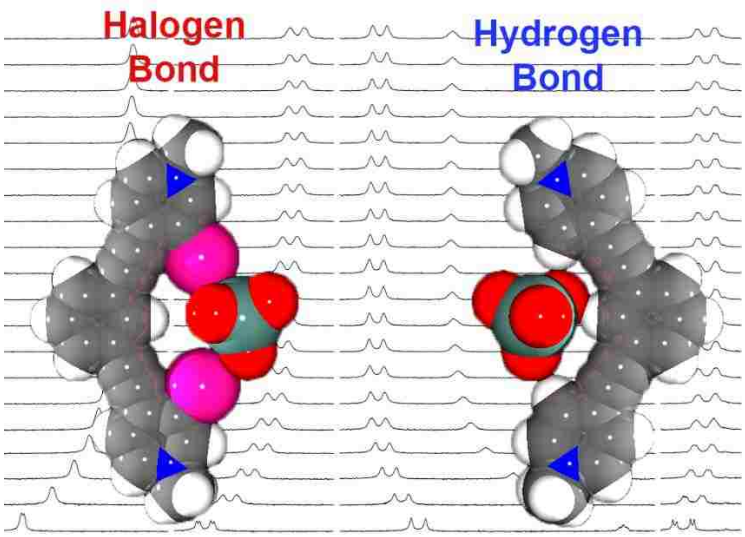

Figure 2.2 Table of contents artwork for *Chemical Communications* publication.

2.2 Introduction

This chapter includes work that was published in *Chemical Communications* (**2015**, 51, 1417–1420) and was co-authored by Asia M. S. Riel, George F. Neuhaus, Daniel A. Decato, and Dr. Orion B. Berryman. Riel conducted the anion metatheses, optimized the lithium-halogen exchange reaction, synthesized the control three-mer, grew X-ray-quality crystals, helped interpret the data, prepared the Supplementary Information for the publication, and created the cover artwork. Neuhaus conducted the ^{13}C NMR titration. Decato collected and refined the X-ray crystallographic data. Dr. Berryman worked out the lithium-halogen exchange reaction, helped with data interpretation, and edited all documents before publication. Massena, the first author, developed all of the synthetic steps (except the ones mentioned above), conducted the ^{1}H NMR spectroscopic titrations, interpreted the data, and wrote the manuscript.

With similar structural and electronic characteristics, ReO_4^- is a tractable surrogate for the medically ubiquitous and environmentally pernicious oxoanion, TcO_4^-. The metastable form of technetium and its long half-life decay product (2.15×10^5 years), ^{99}Tc, are standards for radiolabeling and in situ radiotherapy. The medically useful ^{99m}TC has an ideal half-life of six hours and a γ-ray emission energy of 141 keV. However, considering the high mobility of $^{99}TcO_4^-$, its stability and increasing production as a by-product of uranium-235 fission, the need for synthetic receptors to function as strong and selective chelating agents, liquid-liquid extractants, and ion-exchange stationary phases is pressing.

ReO_4^- and TcO_4^- are challenging targets due to their low hydration energies and diffuse charge densities.[143] To combat these difficulties, a number of hydrogen-bonding scaffolds and hosts have been developed. Elegant hydrogen-bonding examples include aza-cryptands with pH-tunable cavities,[144] and charge neutral pyrrole-based macrocycles.[145] In contrast, bidentate halogen-bonding and unconventional CH hydrogen-bonding receptors for ReO_4^- or TcO_4^- have not been reported. Receptors that utilize concerted NH and CH hydrogen bonding have been reported, but ours is the first to use CH hydrogen bonding alone.[146] Halogen bonding[113–127] in particular offers an exciting competitive/cooperative alternative with the benefit of hard-soft acid-base complementarity. Herein, we report the first two receptors that exhibit strong halogen bonding and CH hydrogen bonding to ReO_4^- in solution and the first bidentate and tridentate structures of each in the solid state.

2.3 Results and Discussion

2.3.1 Design and Synthesis of Anion Receptors

We have developed two bidentate receptor molecules based on a diethynylene benzene core (**1** and **2**, Scheme 2.1). **1** is designed to direct two halogen-bond donors towards one anionic guest in a planar conjugated conformation. Nevertheless, facile rotation of alkynyl-aromatic C–C bonds provides interconversion between mono- and bidentate receptor conformations.

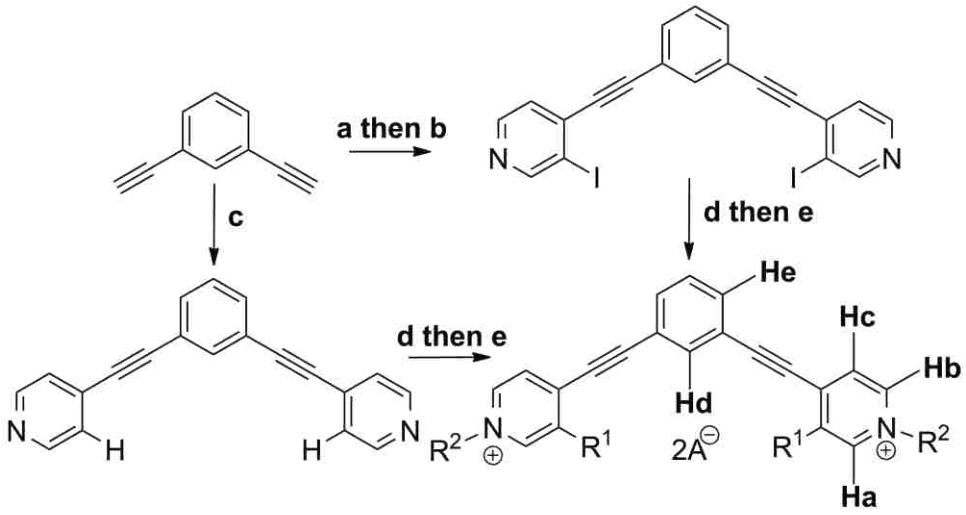

Scheme 2.1 (a) 3-Bromo-4-iodopyridine, CuI, $PdCl_2(PPh_3)_2$, DMF, DIPEA, RT, 24 h, 88 %; (b) *n*-BuLi, THF, –78 °C, I_2, 24 h, 41 %; (c) prepared according to a previously reported literature procedure,[147] 22 %; (d) octyl OTf^- or methyl OTf^-, DCM, RT, 24 h, 98 %; (e) vapor diffusion of Et_2O into a DCM solution of TBACl, 55–75 %; $Na[BAr^F_4]$, DCM, RT, 30 min, 59–75 %.

Molecule **2**—which lacks halogen-bond donors—was prepared to quantify CH hydrogen bonding to ReO_4^- and serve as a comparison. Both receptor scaffolds were synthesized by the Sonogashira[148] cross-couplings of 1,3-diethynyl benzene with either 3-bromo-4-iodopyridine or 4-bromopyridine hydrochloride. The halogen-bond-donor iodines of **1** were installed by lithium halogen exchange followed by quenching with I_2. Alkylation of the pyridines with octyl OTf^- activated the halogen-bond and hydrogen-bond donors of **1** and **2**, respectively, and enhanced solubility in organic solvents. To minimize competitive intermolecular interactions, OTf^- counteranions were exchanged by metathesis for non-coordinating $[BAr^F{}_4]^-$ anions. Methyl derivatives **1b** and **2b** were synthesized in a similar manner for single-crystal X-ray diffraction studies.

2.3.2 Solid-State Investigation of ReO_4^- Binding

The crystal structure of $\mathbf{1b}^{2+}\bullet 2ReO_4^-$ represents the first example of bidentate halogen bonding to ReO_4^- in the solid state. There are only two known examples of solid-state halogen bonding to ReO_4^-. One is a serendipitous monodentate halogen bond between $CHCl_3$ and ReO_4^-.[149] The other is a trifurcated monodentate halogen bond to three 1,4-diiodotetrafluorobenzene molecules.[150] Yellow single crystals of $\mathbf{1b}^{2+}\bullet 2ReO_4^-$ suitable for X-ray diffraction were grown by diffusing CH_2Cl_2 into a DMF-CH_3OH solution of receptor **1b** and TBA ReO_4^-. $\mathbf{1b}^{2+}\bullet 2ReO_4^-$ crystallized in space group $P2_1/c$, forming bidentate halogen bonds to separate oxygens of a ReO_4^- anion (Figure 2.3, top). The CI···O^- distances, 2.97 and 3.06 Å, correspond to 84 and 86 % of the ΣvdW radii and corroborate strong halogen bonding interactions.

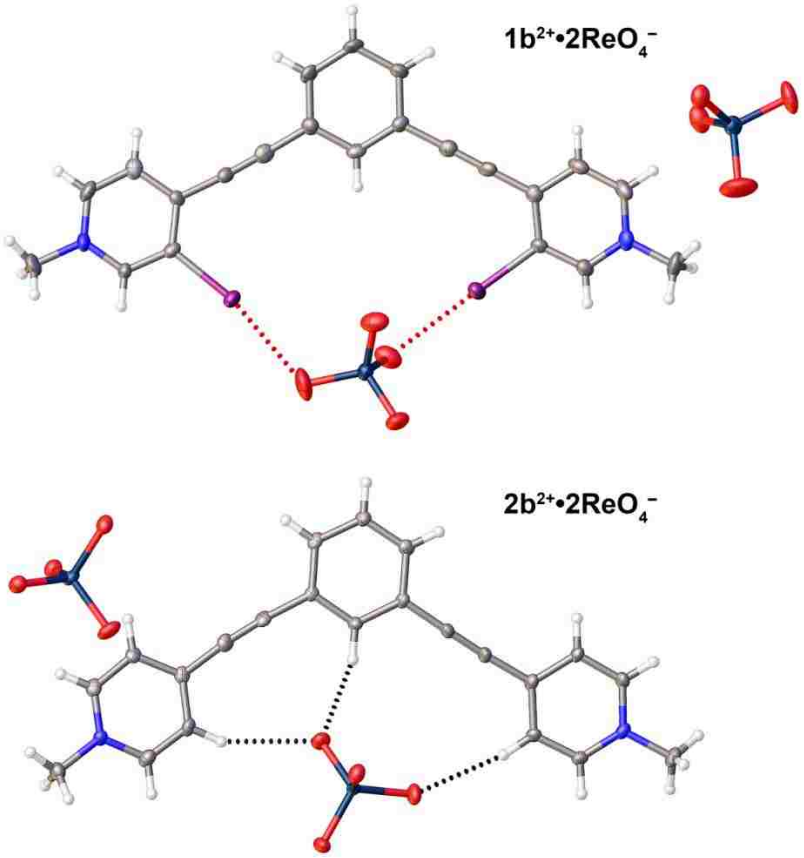

Figure 2.3 X-ray crystal structure of **1b**$^{2+}$•2ReO_4^- (top) highlighting bidentate halogen bonding to ReO_4^- in the solid state (red). X-ray crystal structure of **2b**$^{2+}$•2ReO_4^- (bottom) illustrating tridentate CH hydrogen bonding to ReO_4^- (black).

To accommodate the size of ReO_4^-, both pyridinium rings rotate 11 ° from coplanarity. As a result, the observed CI···O$^-$ bond angles of 175 and 168 ° also confirm strong halogen bonding interactions. Examination of the crystal packing reveals CH hydrogen bonding and electrostatic contacts between ReO_4^- and five additional molecules of **1b** (see Section 2.4.3). The second ReO_4^- participates in seven CH hydrogen bonding interactions and two weak σ contacts (one weak σ and one anion-π interaction) with electron-deficient pyridinium rings. Interestingly, the anion-π oxygen-centroid distance is

3.22 Å with an oxygen-centroid-nitrogen angle of 89 °. A head-to-tail π-stacked dimer (3.4 Å) is also observed; however, no solution dimer is observed in the current solvent system. This arrangement produces columns of **1b** with each ReO_4^- on alternating sides of the receptor. See Figures 2.56–2.57 for crystal packing data.

In contrast, the X-ray crystal structure of $\mathbf{2b}^{2+}\bullet 2ReO_4^-$ illustrates unique CH hydrogen bonding to ReO_4^-. Colorless single crystals of $\mathbf{2b}^{2+}\bullet 2ReO_4^-$ were obtained by diffusing Et_2O into a CH_3OH solution of receptor **2b** and TBA ReO_4^-. $\mathbf{2b}^{2+}\bullet 2ReO_4^-$ crystallized in space group $P2_1/n$. Notably, tridentate CH hydrogen bonding to ReO_4^- occurs using two Hc hydrogens and Hd (Scheme 2.1) with C–H···O$^-$ distances of 2.64, 2.71 and 2.31 Å (Figure 2.3, bottom). Four additional intermolecular CH hydrogen bonds to ReO_4^- are also evident. One interaction is bidentate (Hc and He), and the C–H···O$^-$ distances of 2.53 and 2.55 Å correspond to weak HB interactions. Two weak σ interactions occur over the same electron-deficient pyridinium ring (*ortho* and *meta* carbons; O–C distances are 3.18 and 2.92 Å, respectively) and involve separate oxygens of a ReO_4^- anion. The second ReO_4^- is involved in nine CH hydrogen bonds and two weak σ interactions. To enable tridentate binding to ReO_4^-, both pyridinium rings adjust 9 ° from coplanarity and one ethynylene spacer deviates 8 ° from linearity. An off-centered head-to-tail π-stacked dimer (3.3 Å) is also noted (see Section 2.4.3). Together, the crystal structures of $\mathbf{1b}^{2+}\bullet 2ReO_4^-$ and $\mathbf{2b}^{2+}\bullet 2ReO_4^-$ illustrate the importance of bidentate/tridentate halogen- and hydrogen-bond coordination to ReO_4^- in the solid state. See Figures 2.58–2.59 for crystal packing data.

2.3.3 Summary of X-Ray Crystallographic Data

Crystal data for **1b** $C_{22}H_{16}I_2N_2O_8Re_2$, M = 1062.57, monoclinic, $P2_1/c$, a = 6.9841(5), b = 34.338(3), c = 11.4497(9), β = 99.704(2), V = 2706.6(4), Z = 4, T = 150 K, μ(MoKα) = 11.265 mm^{-1}, ρ_{calcd} = 2.608 g ml^{-1}, $2\theta_{max}$ = 52.74 °, 65752 reflections collected, 5485 unique (R_{int} = 0.0505, R_{sigma} = 0.0250) R_1 = 0.0477 ($I > 2\sigma(I)$) and wR_2 = 0.1108 (all data). CCDC 1028026 contains the supplementary crystallographic data.

Crystal Data for **2b** $C_{22}H_{18}N_2O_8Re_2$, M = 810.78, monoclinic, $P2_1/n$, a = 15.5756(10), b = 7.6106(5) c = 19.6042(13), β = 100.084(2), V = 2288.0(3) , Z = 4, T = 100.0 K, μ(MoKα) = 10.623 mm^{-1}, ρ_{calcd} = 2.354 g ml^{-1}, $2\theta_{max}$ = 56.56 °, 40497 reflections collected, 5583 unique (R_{int} = 0.0706, R_{sigma} = 0.0467), R_1 = 0.0286 ($I > 2\sigma(I)$), wR_2 = 0.0604 (all data). CCDC 1028025 contains the supplementary crystallographic data. These data can be obtained free of charge from The Cambridge Crystallographic Data Centre via www.ccdc.cam.ac.uk/data_request/cif.

2.3.4 Solution-Phase Thermodynamics and Structural Considerations

^{1}H NMR spectroscopic titrations of **1a** and **2a** were conducted to probe their corresponding halogen bonding and CH hydrogen bonding capabilities in solution. Both **1a**, **2a** and TBA ReO_4^- were independently soluble in $CDCl_3$; however, precipitation of host-guest complexes necessitated a 3:2 *v*/*v* $CDCl_3$-acetone-d_6 mixed solvent.

Stock solutions of **1a** and **2a** —1.56(1) and 1.55(1) mM, respectively—were prepared in 3.84 mL of 3:2 *v*/*v* $CDCl_3$-acetone-d_6. 0.50-mL aliquots from each stock

solution were syringed into three separate NMR tubes with screw caps and septa. The stock solution of **1a** was then used to make three guest solutions corresponding to the experiment number—13.9(3), 13.6(3), 13.6(3) mM, respectively. Likewise, the stock solution of **2a** was used to make three guest solutions—all 13.3(3) mM. After obtaining free-host spectra of **1a** and **2a**, aliquots of corresponding guest solution (containing **1a** or **2a** and TBA ReO_4^-) were added to their respective NMR tubes. Spectra were obtained after each addition (20 times). A constant host concentration was maintained while the concentration of TBA ReO_4^- gradually increased throughout the titration.

Titrating TBA ReO_4^- produced noteworthy pyridinium (Ha, Hb, and Hc) and phenyl (Hd) proton shifts for both **1a** and **2a** (Figures 2.4–2.13). Hydrogens He and the sole phenyl core triplet were not followed due to limited shifting and/or residual solvent peak ($CHCl_3$) obstruction. The significant upfield shifting of Ha and Hb ($\Delta\delta$ = -0.099 and -0.082 ppm, respectively; Figures 2.5–2.8) on **1a** was indicative of strong halogen bonding in solution. The dominant halogen-bonding conformation as suggested by the X-ray crystal structure of $\mathbf{1b}^{2+}\bullet 2ReO_4^-$ is distinctly bidentate (Figure 2.3, top). Additionally, facile rotation of alkynyl-aromatic C–C bonds enables a second halogen-bonding mode. Constructive bidentate halogen-hydrogen bonding involving a single halogen and Hc/Hd is consistent with the downfield shifting of these hydrogens ($\Delta\delta$ = 0.038 and 0.154 ppm). An ancillary Hc and Hd binding mode may have also contributed to solution stability (see the crystal structure of $\mathbf{2b}^{2+}\bullet 2ReO_4^-$; Figure 2.3, bottom).Taken together, the greater upfield (Ha and Hb) and greater downfield (Hc and Hd) shifting of **1a** was explained by strong bidentate halogen bonding in solution as well as halogen-hydrogen-bond synergy.

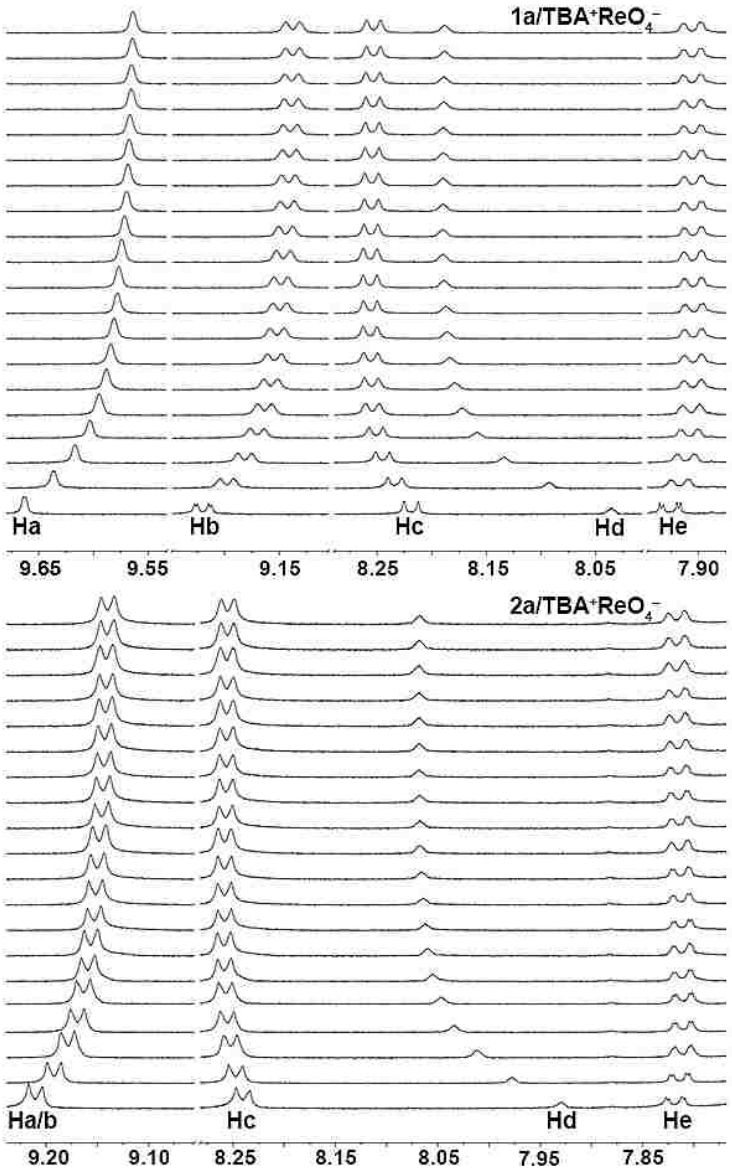

Figure 2.4 Partial ^{1}H NMR spectra of **1a** (top, 0–4.78 equiv) and **2a** (bottom, 0–4.62 equiv) upon titrating TBA ReO_4^- (equivalents from bottom to top).

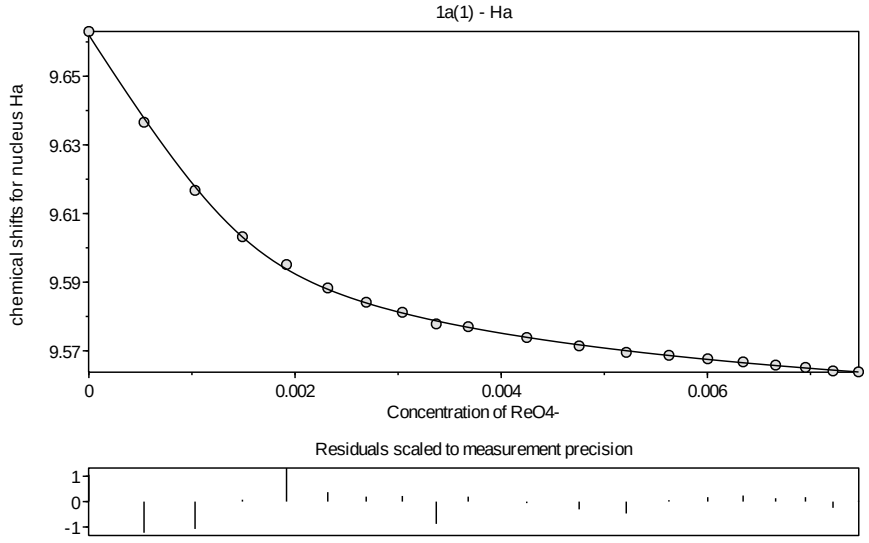

Figure 2.5 Representative binding isotherm following proton Ha on **1a** with increasing ReO_4^- concentration (replicate 1).

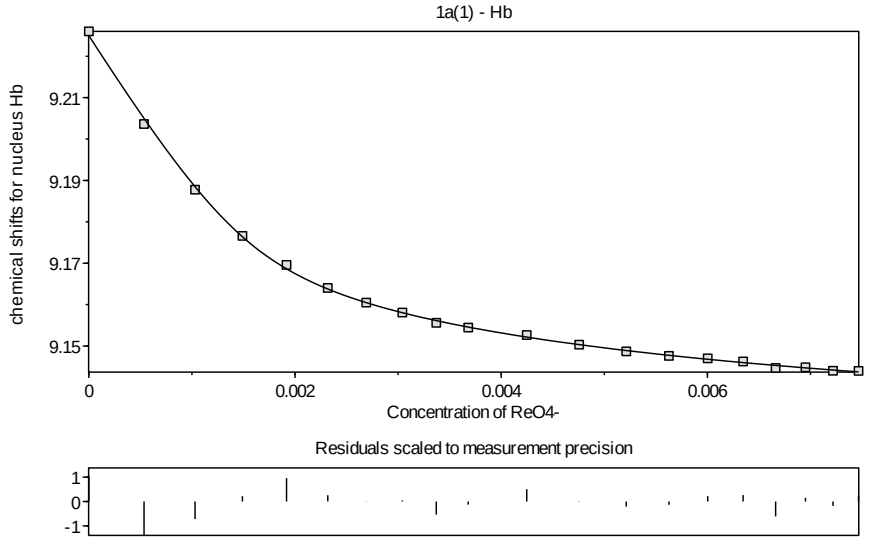

Figure 2.6 Representative binding isotherm following proton Hb on **1a** with increasing ReO_4^- concentration (replicate 1).

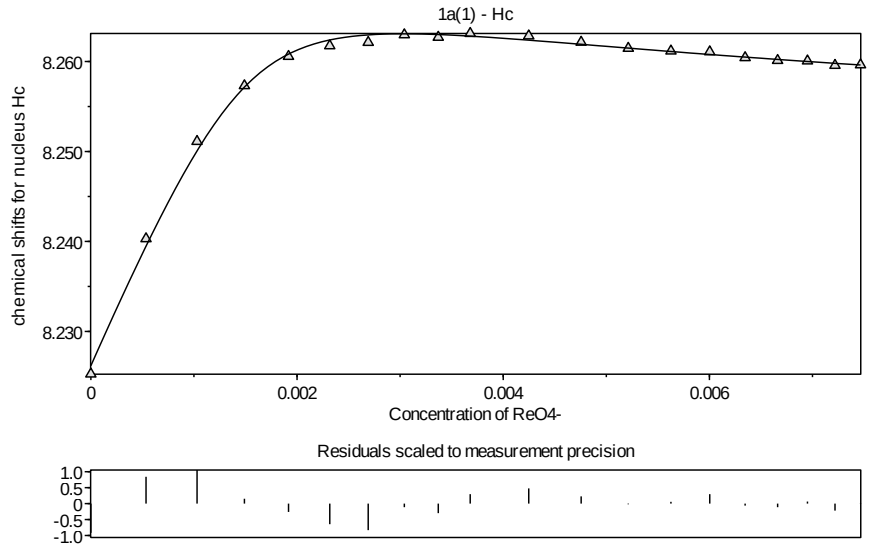

Figure 2.7 Representative binding isotherm following proton Hc on **1a** with increasing ReO_4^- concentration (replicate 1).

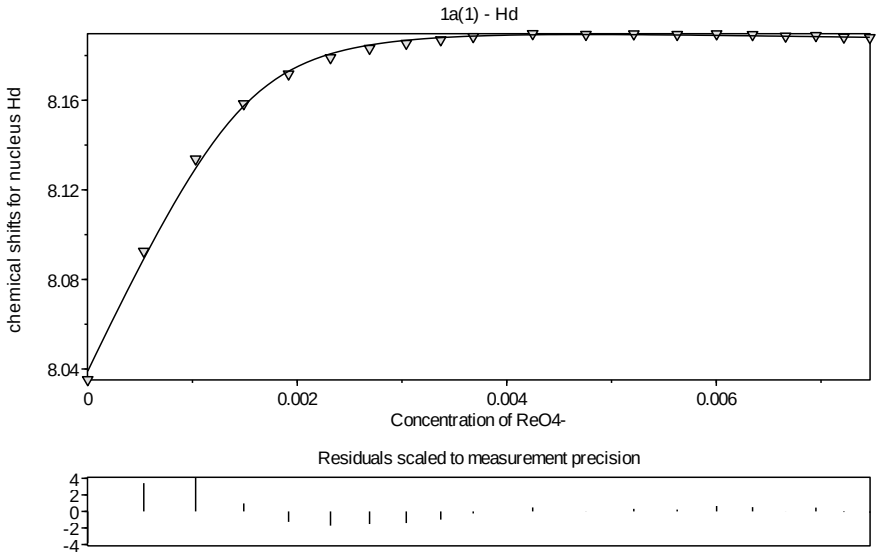

Figure 2.8 Representative binding isotherm following proton Hd on **1a** with increasing ReO_4^- concentration (replicate 1).

Further evidence of halogen bonding in solution was seen in the downfield ^{13}C NMR shifting of the CX carbons of **1a** ($\Delta\delta$ = 0.150 ppm, Figures 2.9–2.10) upon titrating TBA ReO_4^-. A solution of **1a**—4.89(9) mM—was dissolved in 3:2 *v*/*v* $CDCl_3$-acetone-d_6. ^{13}C NMR spectra were obtained prior to and directly after addition of TBA ReO_4^-, which resulted in a final guest concentration of 8.7(1) mM. The observed ^{13}C NMR downshifts are consistent with previous reports of the phenomenon.[151]

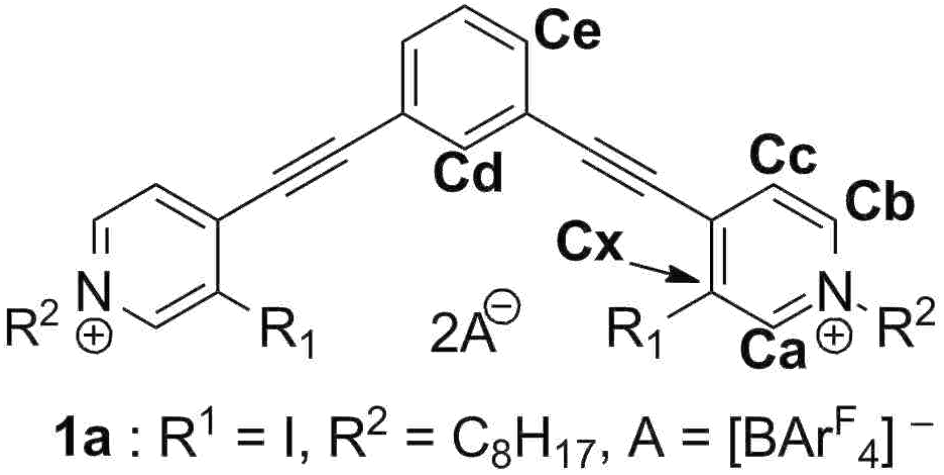

Figure 2.9 Carbon assignments on **1a** as determined by ^1H 2D ROESY and ^1H-^{13}C HMBC NMR experiments (not shown).

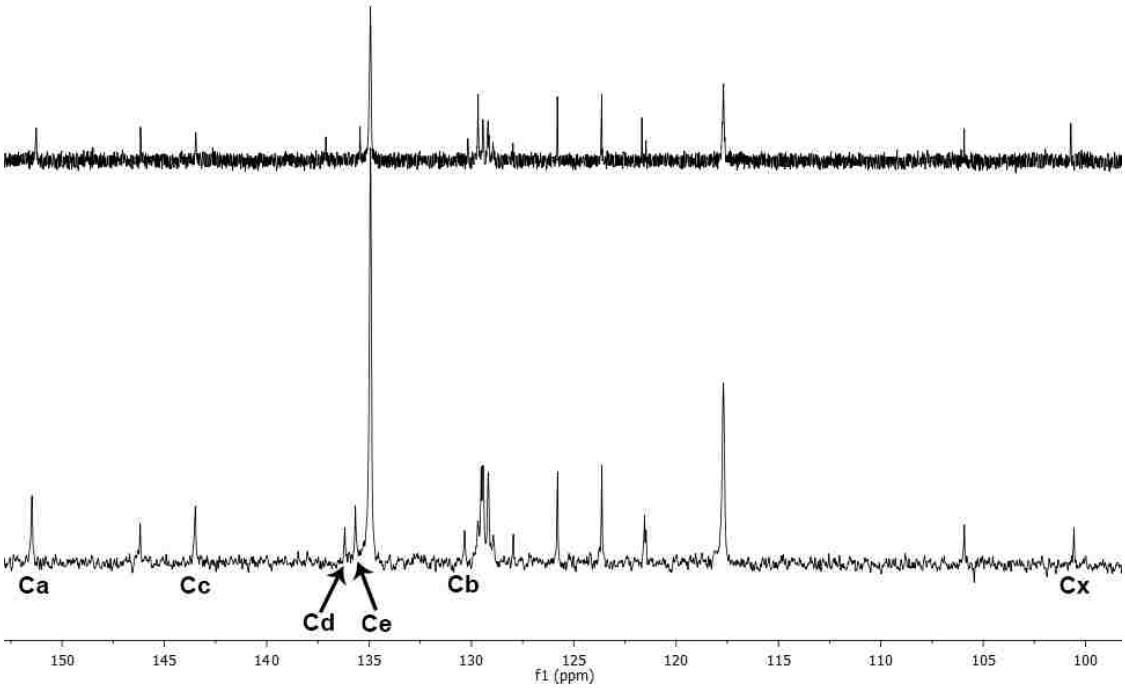

Figure 2.10 Partial ^{13}C NMR spectra of **1a** (bottom) and **1a** with 1.79 equiv of TBA ReO_4^- (top).

For **2a**, CH hydrogen bonding and electrostatic contacts were the prevailing interactions in solution. Specifically, a tridentate binding site involving two Hc hydrogens and Hd proved the most active as evidenced by the X-ray crystal structure of $\mathbf{2b}^{2+}\bullet 2ReO_4^-$ and the downfield progression of these hydrogens ($\Delta\delta$ = 0.019 and 0.139 ppm, respectively; Figures 2.11–2.13). Upfield shifting of **2a**'s Ha/b ($\Delta\delta$ = -0.071 ppm) was indicative of anion-hydrogen-bond augmentation of ring electron density.

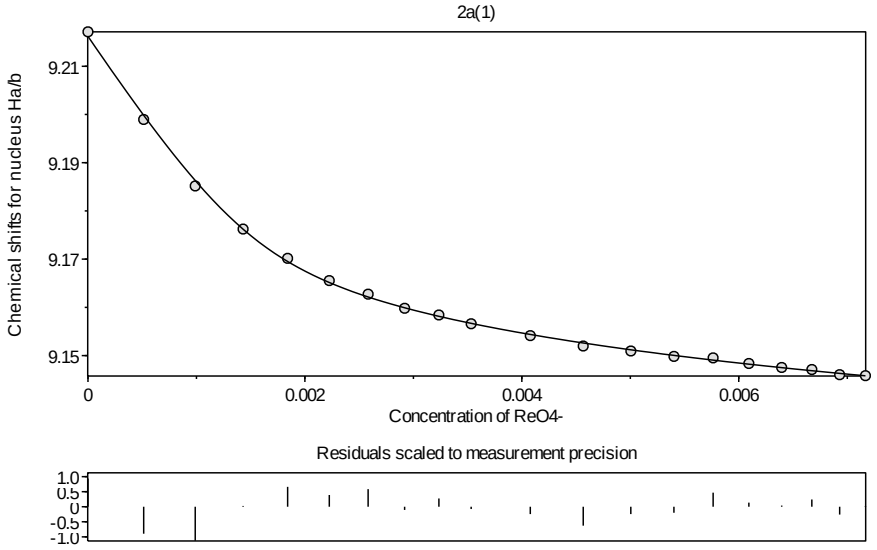

Figure 2.11 Representative binding isotherm following proton Ha/b on **2a** with increasing ReO_4^- concentration (replicate 1).

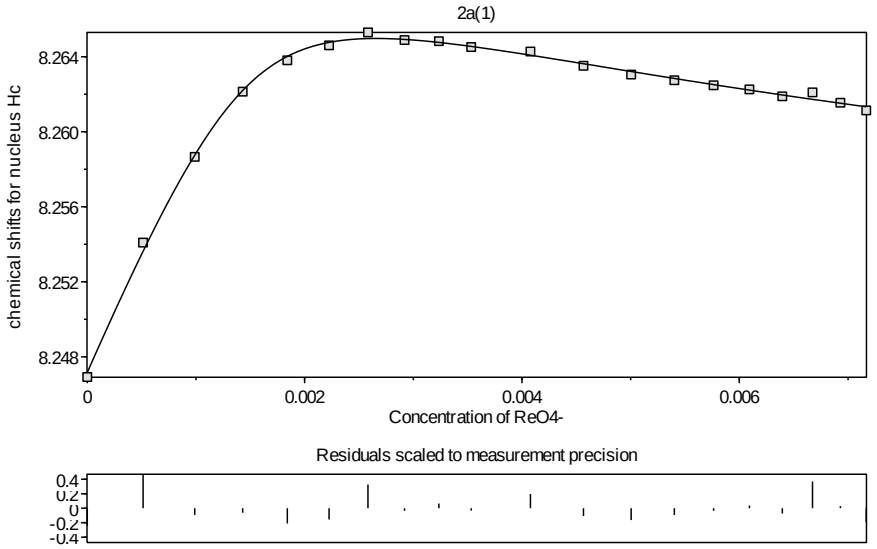

Figure 2.12 Representative binding isotherm following proton Hc on **2a** with increasing ReO_4^- concentration (replicate 1).

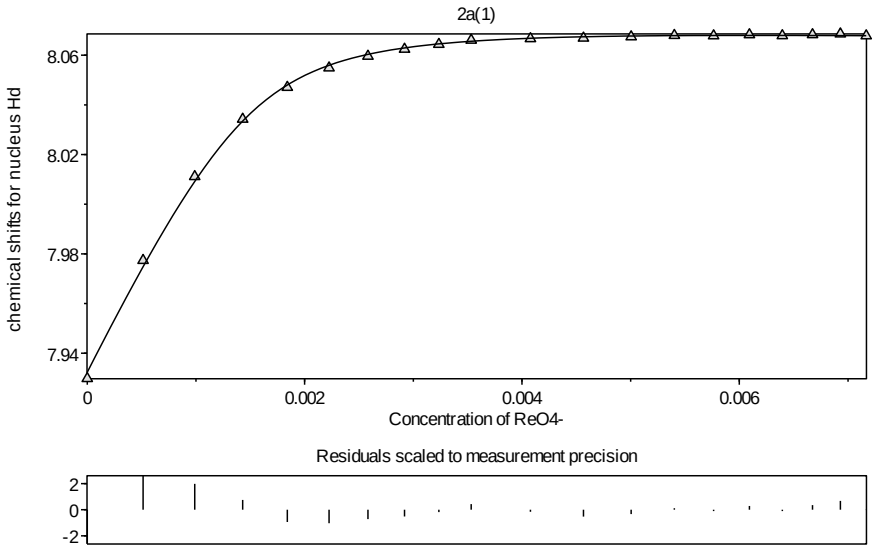

Figure 2.13 Representative binding isotherm following proton Hd on **2a** with increasing ReO_4^- concentration (replicate 1).

HypNMR 2008[152] was used to fit changes in chemical shift to a stepwise association model:

$$H + G \rightleftharpoons HG, K_1 = \frac{[HG]}{[H][G]} \quad (2.1)$$

$$HG + G \rightleftharpoons HG_2, K_2 = \frac{[HG_2]}{[HG][G]} \quad (2.2)$$

Iterative and simultaneous refinement of multiple isotherms provided association constants for both **1a** and **2a** with ReO_4^-. Reported log K_1s with σs are the means of triplicate data sets (experimental error is estimated at 10 %). All titrations were conducted at 290 K. Full details of the titration experiments including σs and model determination

can be found in Section 2.4.2. For receptor **1a**, a log K_1 of 3.95(4) represents the first quantification of halogen bonding to ReO_4^- in solution, highlighting the effectiveness of halogen bonding to target this challenging oxoanion. Alternatively, **2a** exhibits CH hydrogen bonding and electrostatic interactions with ReO_4^-, which resulted in a log K_1 of 3.87(2). A *t*-test for two means suggests that the difference in the log K_1 values is statistically significant (one-tail *P* value = 0.022; two-tail *P* value = 0.045). Analysis of the binding modes of both receptors helps contextualize these data. The tridentate CH hydrogen-bonding site of **2a** is active regardless of conformational changes. By comparison, **1a** can oscillate between bidentate, monodentate, and inactive halogen-bonding modes. Given these differences, the superior association to ReO_4^- of **1a** establishes the effectiveness of halogen bonding to target charge diffuse anions. Lastly, both **1a** and **2a** display modest K_2 values on the order of 10^2 M^{-1} (see Section 2.4.2) that likely resulted from a combination of weak mono- and bidentate hydrogen bonding and weak σ interactions.

2.4 Experimental

2.4.1 Synthesis and Characterization Data

All materials were obtained from Sigma-Aldrich, Acros, TCI-America, and Strem Chemicals and used without further purification. ^{1}H NMR, ^{13}C NMR, and ^{19}F NMR spectra were recorded on Varian Direct Drive 500 MHz and Bruker Avance 400 MHz spectrometers. Chemical shifts are expressed as ppm. For the ^{19}F NMR spectra C_6F_6 (δ = –164.9 ppm) was used as an internal standard. Signal splitting patterns are indicated as s,

singlet; d, doublet; t, triplet; m, multiplet; b, broad. *J*s are given in Hz. Melting points were determined with a Mel-temp. Compounds were analyzed via HPLC-ESI-MS to obtain accurate mass data. HPLC was performed with a reverse-phase HPLC column. An Agilent PLRP-S PSDVB column with 3.0 [MU]m particles and dimensions of 50 mm length and 1.0 mm diameter (P/N PL1312-1300) was used with an Agilent 1290 HPLC system. The column was maintained at 40 °C with a flow rate of 0.6 mL/min. Chromatography was as follows: the solvent consisted of CH_3OH with 0.1% *v*/*v* formic acid for channel A. Channel B was a 1:1 *v*/*v* mixture of IPA and acetone. Following column equilibration at 20 % B, the sample was injected via autosampler, and the column was flushed for 1.0 min to waste. From 1.0 min to the end of the run, the column eluent was directed to the MS source. From 1.0 min to 4.0 min, the gradient was linearly ramped from 20 % to 95 % B. From 4.8 to 5.0 min, the solvent mixture was held at 20 % B. A Bruker micrOTOF mass spectrometer with ESI source was used. The resolution was approximately 10,000 and accuracy 1 ppm. Source parameters were the following: drying gas 7.0 L/min, drying gas heat at 180 °C, nebulizer 3 bar, capillary voltage 4500 V, capillary exit 100 V. Spectra were collected in negative or positive modes as appropriate from 50 to 1700 *m*/*z* at a rate of 2 Hz. Theoretical spectra were generated in Bruker Data Analysis to compare against experimental spectra.

General procedure for methylation: in an oven-dried round bottom flask, **2** or **5** (1.0 equiv) was dissolved in dry DCM. In a separate round bottom, methyl OTf^- (4.1 equiv) was dissolved in dry DCM. Both round bottoms were sparged with dry N_2 gas for 15 min. The methyl OTf^- solution was then added dropwise to the solution of **2** or **5**. The

solution was stirred for 16 h under inert atmosphere. Removal of the DCM by roto-evaporation left a solid that was triturated with hexanes followed by filtration.

General procedure for octylation: in an oven-dried round bottom flask, **2** or **5** (1.0 equiv) was dissolved in dry DCM. Octyl OTf^- (4.5 equiv, prepared according to a previously reported literature procedure[153]) was dissolved in dry DCM. Both round bottoms were sparged with dry N_2 gas for 15 min. The octyl OTf^- solution was then added dropwise to the solution of **2** or **5**. The solution was stirred for 16 h under inert atmosphere. Removal of the DCM by roto-evaporation left a solid/oil that was triturated with hexanes followed by filtration.

General procedure for anion metathesis: in a one-dram scintillation vial, **3** or **6** (1.0 equiv) and TBACl (2.2 equiv) were dissolved in DCM. Vapor diffusion of Et_2O afforded a precipitate that was isolated by filtration. To remove excess TBACl, the precipitate was washed with acetone, which left a powder/oil.

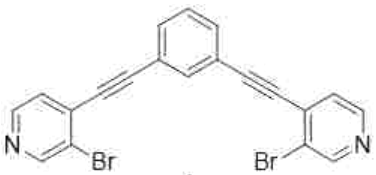

1

1,3-bis(4-ethynyl-3-bromopyridinyl)benzene (**1**)

To an oven-dried 25-mL round bottom flask was added DIPEA (2.46 mL, 14.1 mmol), 1,3-diethynylbenzene (0.693 mL, 5.22 mmol), and 15 mL of DMF. To another dry 25-mL round bottom flask was added 10 mL of DMF. Both 25-mL round bottom flasks were sparged for 20 min with dry N_2 gas. An oven-dried Schlenk flask was charged with 3-bromo-4-iodopyridine (4.00 g, 14.1 mmol) then vacuumed and backfilled

with dry N_2 gas three times. $PdCl_2(PPh_3)_2$ (0.219 g, 0.313 mmol) was added then vacuumed and backfilled with dry N_2 three times. CuI (0.099 g, 0.522 mmol) was added then vacuumed and backfilled with dry N_2 three times. The acetylene solution was transferred by cannula to the Schlenk flask. Excess DMF was used to wash the acetylene round bottom flask, which was then transferred to the Schlenk flask. The orange solution stirred for 20 h, and subsequent removal of DMF by roto-evaporation left an orange solid that was purified by column chromatography (2:1 *v*/*v* hexanes-EtOAc) to afford **1** (2.00 g, 4.56 mmol, 88 %) as a cream-colored solid. Mp: 111–112 °C. ^{1}H NMR (400 MHz, acetone-d_6; 25 °C) δ 8.84 (s, 2H), 8.60 (d, J = 4.9 Hz, 2H), 7.89 (s, 1H), 7.78 (d, J = 7.7 Hz, 2H), 7.65–7.59 (m, 3H). ^{13}C NMR (100.6 MHz, acetone-d_6; 25 °C) δ 152.76, 149.47, 135.78, 134.10, 133.10, 130.69, 127.89, 123.56, 123.47, 97.52, 87.31. HRMS (CI pos) *m/z*: 438.903 (M^{2+}+2, 100 %), 436.905 (M^{2+}+2, 51.4), 440.901 (M^{2+}+2, 48.6); $C_{20}H_{10}Br_2N_2^{2+}$+2 (438.93).

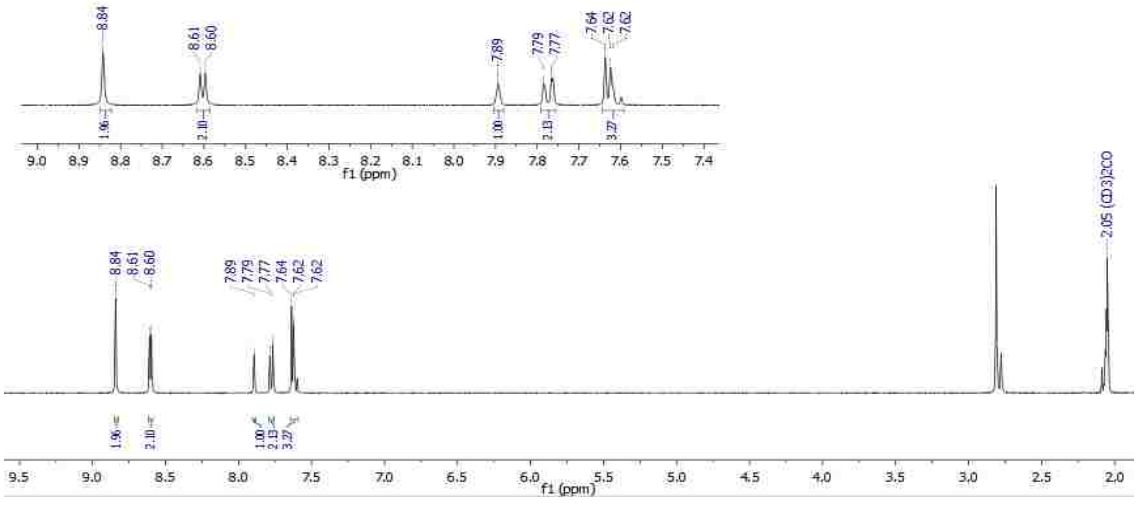

Figure 2.14 ^{1}H NMR spectrum of **1**.

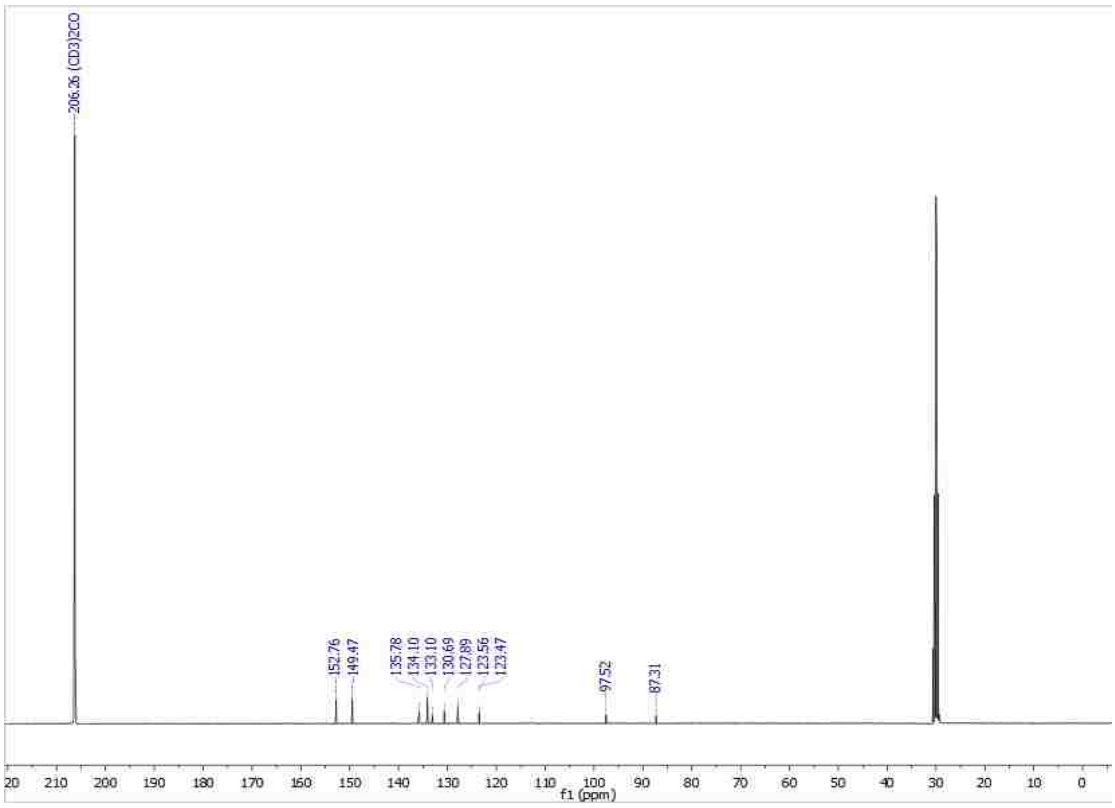

Figure 2.15 ^{13}C NMR spectrum of **1**.

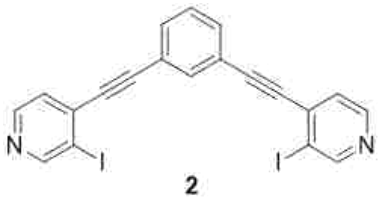

2

1,3-bis(4-ethynyl-3-iodopyridinyl)benzene (**2**)

This procedure was adapted from a previously reported literature procedure.[154] An oven-dried round bottom flask (50-mL) was charged with **1** (0.200 g, 0.457 mmol), which was subsequently dissolved in 20 mL of THF, cooled to –67 °C, and sparged with dry N_2 gas for 20 min. *n*-BuLi (2.3 M in hexanes, 0.50 mL, 1.15 mmol) was added dropwise to the light yellow solution of **1**. The deep green mixture was stirred for 30 min

at –67 °C and was monitored by TLC. I_2 (0.571 g, 2.25 mmol) in 5 mL of THF was added dropwise, keeping the temperature below –65 °C. The red solution was allowed to gradually warm to RT and stirred for 18 h. The red solution was washed with saturated $Na_2S_2O_3$ and subjected to a Et_2O extraction. The organic layers were combined and dried with $MgSO_4$. Removal of Et_2O by roto-evaporation left an orange solid that was purified via column chromatography (7:3 hexanes-EtOAc) to yield a beige solid (0.250 g, 0.469 mmol, 41 %). Mp: 147–149 °C. ^{1}H NMR (400 MHz, acetone-d_6; 25 °C) δ 9.03 (s, 2H), 8.60 (d, J = 4.9 Hz, 2H), 7.92 (s, 1H), 7.78 (d, J = 8.8 Hz, 2H), 7.67–7.56 (m, 3H). ^{13}C NMR (100.6 MHz, acetone-d_6; 25 °C) δ 158.00, 149.74, 137.24, 135.46, 133.80, 130.58, 127.32, 123.48, 99.73, 96.30, 90.79. HRMS (CI pos) *m/z*: 532.901 (M^{2+}+2, 100 %), 533.904 (M^{2+}+2, 22.4), 534.907 (M^{2+}+2, 2.3); $C_{20}H_{10}I_2N_2^{2+}$+2 (532.90).

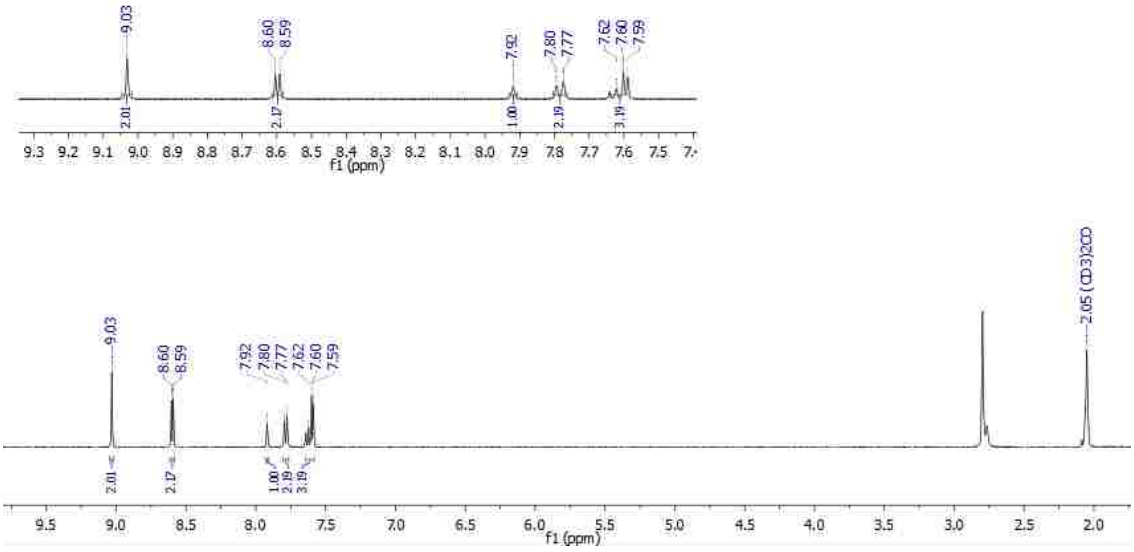

Figure 2.16 ^{1}H NMR spectrum of **2**.

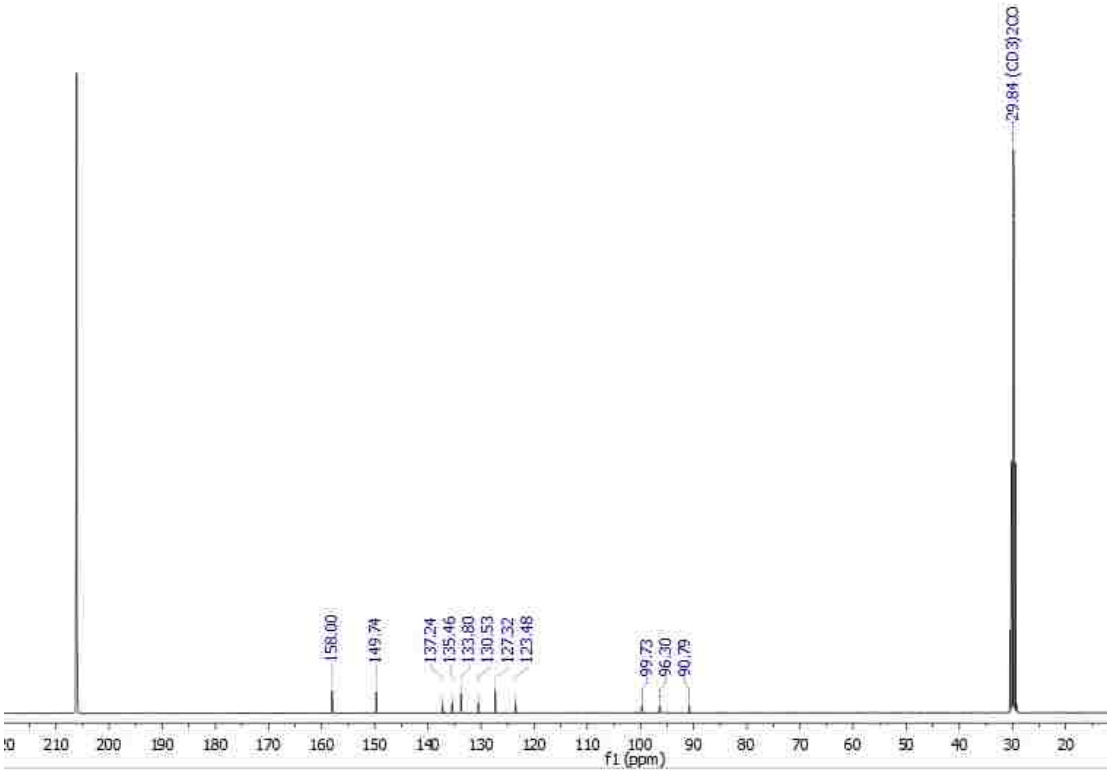

Figure 2.17 ^{13}C NMR spectrum of **2**.

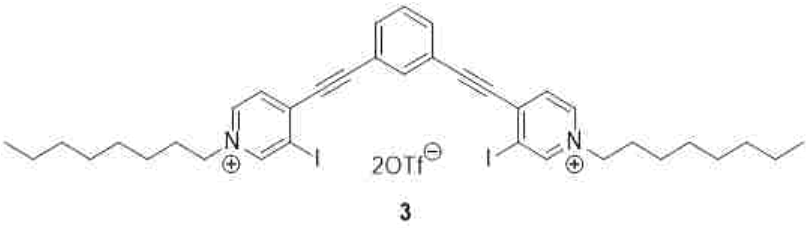

3

1,3-bis(4-ethynyl-N-octyl-3-iodopyridinium)benzene ditriflate (**3**)

2 (0.189 g, 3.55 mmol) was reacted with octyl OTf^- (0.616 mL, 3.94 mmol) according to the General Procedure for Octylation. The product was a beige solid (0.318 g, 0.301 mmol, 85 %). Mp: 113–115 °C. ^{1}H NMR (500 MHz, CD_2Cl_2; 25 °C) δ 9.05 (s, 1H), 8.91 (d, *J* = 5.9 Hz, 2H), 8.08 (d, *J* = 6.4 Hz, 2H), 8.03 (s, 1H), 7.83 (d, *J* = 7.3 Hz, 2H), 7.57 (t, *J* = 7.9 Hz, 1H), 4.58 (t, *J* = 1.6 Hz, 4H), 1.38 (b, 8H), 1.28 (b, 16H), 0.88

(b, 6H). ^{13}C NMR (100.6 MHz, CD_2Cl_2; 25 °C) δ 150.80, 146.56, 143.96, 137.40, 135.91, 130.39, 130.38, 129.96, 121.79, 106.62, 100.54, 90.21, 62.91, 32.21, 32.02, 29.52, 29.45, 26.61, 23.15, 14.39. ^{19}F NMR (376.3 MHz, CD_3CN; 25 °C) δ –76.89. HRMS (CI pos) *m/z*: 379.079 (M^{+2}, 100 %), 379.581 (M^{+2}, 39.7), 380.082 (M^{+2}, 7.6); $C_{38}H_{44}I_2N_2^{2+}$ (379.08).

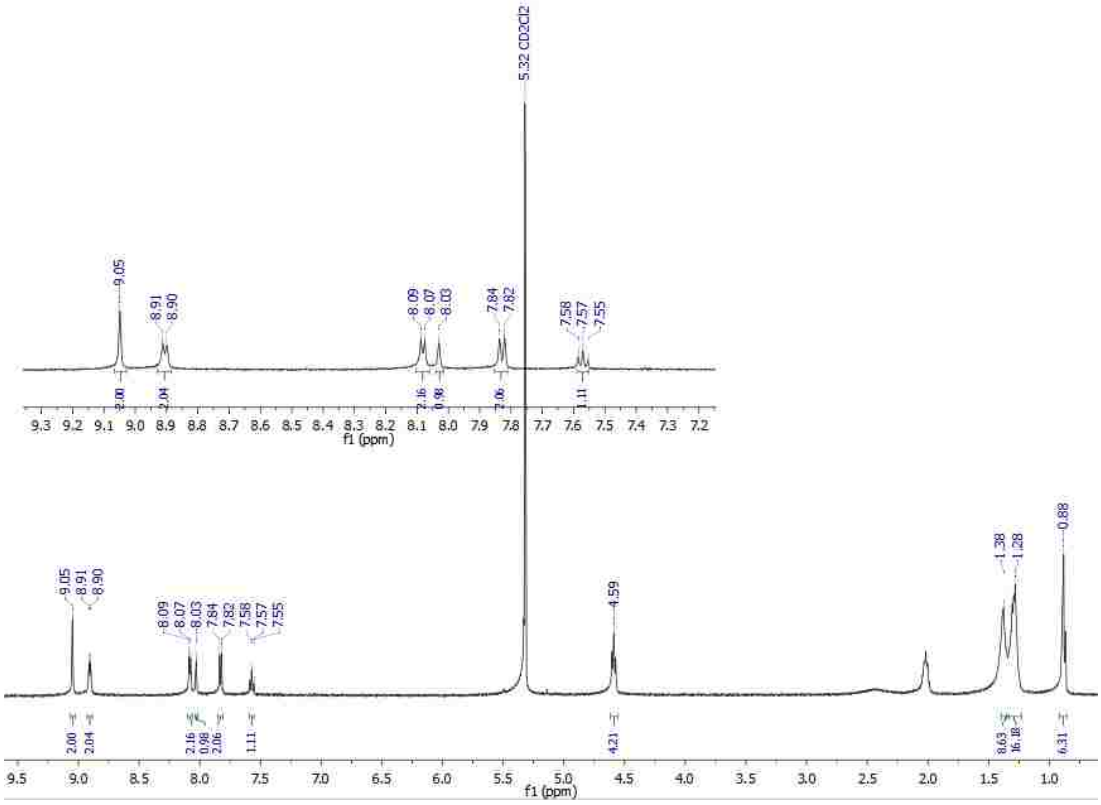

Figure 2.18 ^{1}H NMR spectrum of **3**.

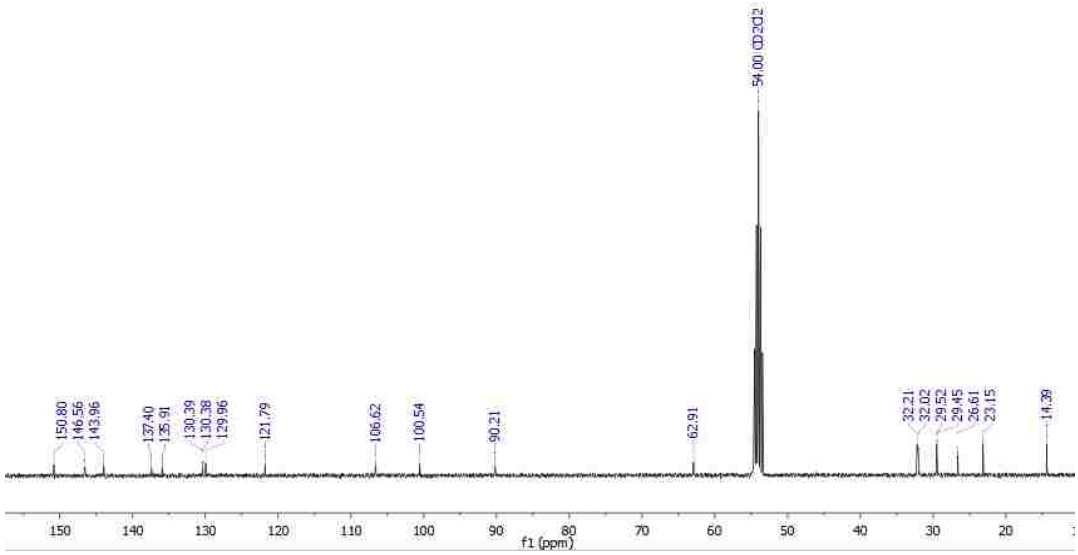

Figure 2.19 ^{13}C NMR spectrum of **3**.

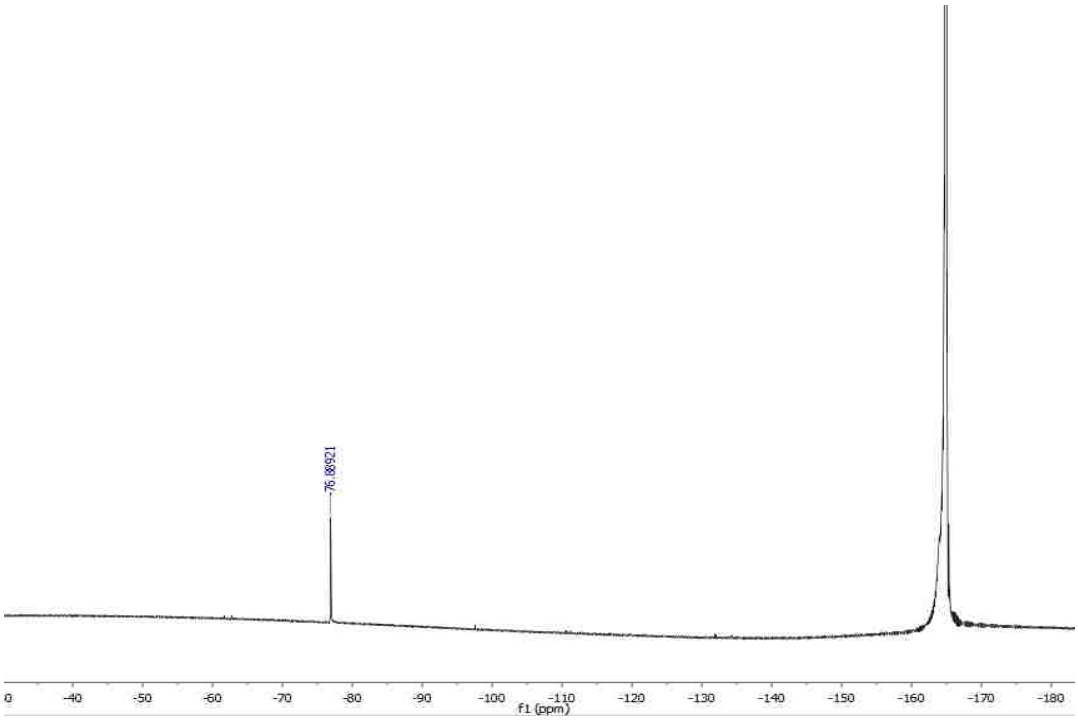

Figure 2.20 ^{19}F NMR spectrum of **3**.

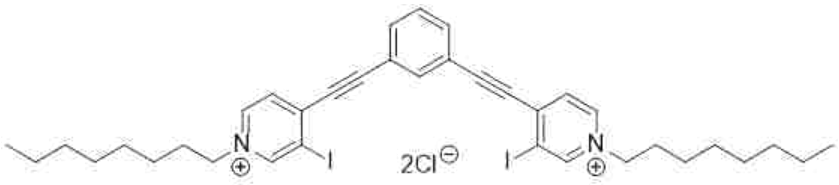

4

1,3-bis(4-ethynyl-N-octyl-3-iodopyridinium)benzene dichloride (**4**)

3 (0.156 g, 0.147 mmol) and TBACl (0.0975 g, 0.351 mmol) were reacted according to the General Procedure for Anion Metathesis. The product was isolated as a yellow powder (0.060 g, 0.0791 mmol, 55 %). Mp: 182–184 °C. ^{1}H NMR (400 MHz, CD_3CN; 25 °C) δ 9.07 (s, 2H), 8.56 (d, *J* = 6.4 Hz, 2H), 8.24 (s, 1H), 7.95 (d, *J* = 6.4 Hz, 2H), 7.88 (d, *J* = 9.4 Hz, 2H), 7.67 (t, *J* = 16.0 Hz, 1H), 4.39 (t, *J* = 15.2 Hz, 4H), 1.34 (b, 8H), 1.29 (b, 16H), 0.89 (b, 6H). ^{13}C NMR (100.6 MHz, CD_3CN; 25 °C) δ 151.38, 145.86, 143.33, 138.32, 135.67, 131.19, 129.40, 122.58, 108.23, 104.77, 90.88, 62.34, 32.38, 31.70, 29.66, 29.52, 26.53, 23.29, 14.33.

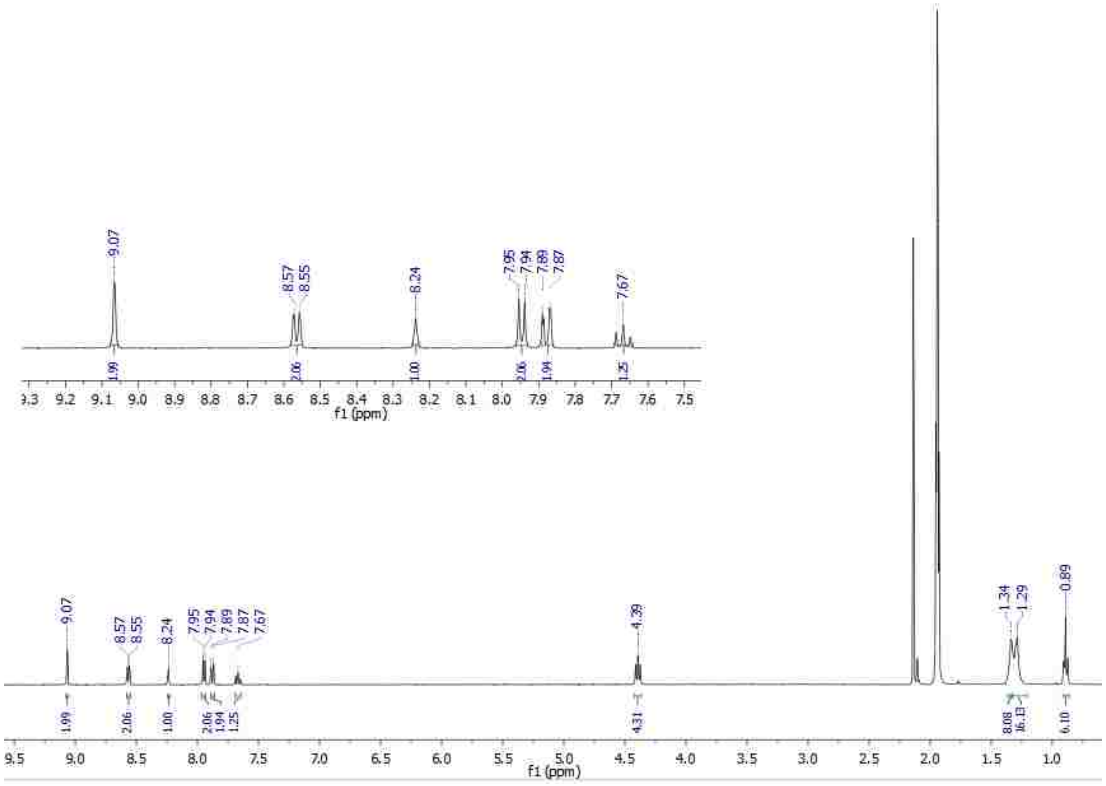

Figure 2.21 ^{1}H NMR spectrum of **4**.

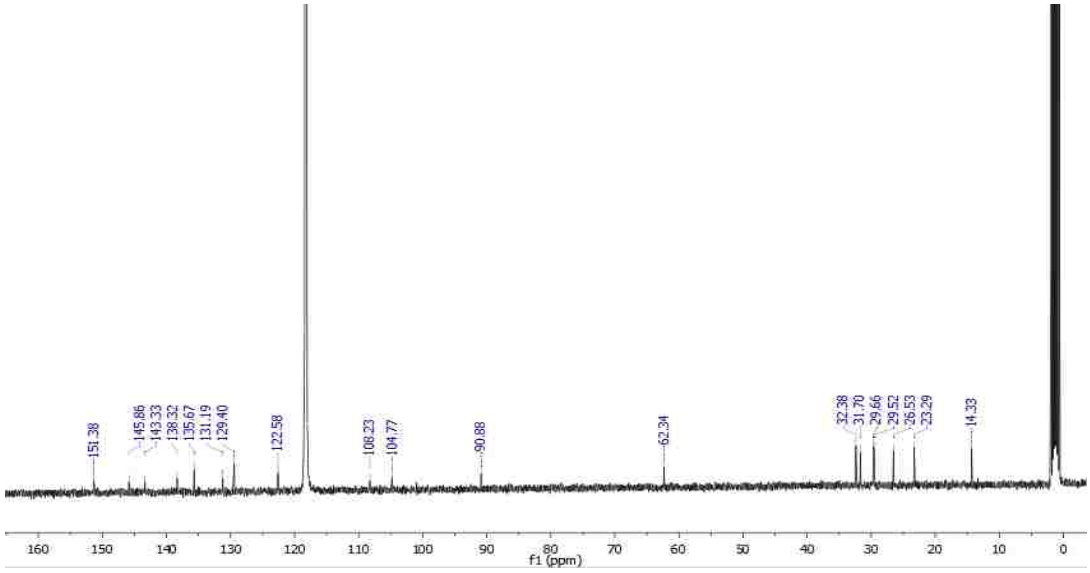

Figure 2.22 ^{13}C NMR spectrum of **4**.

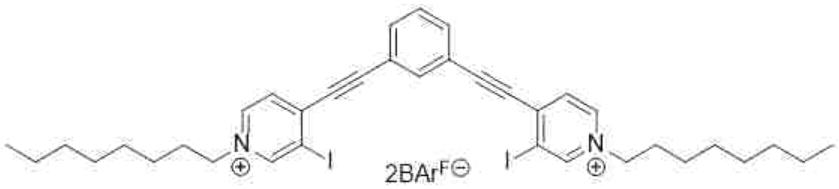

1a

1,3-bis(4-ethynyl-N-octyl-3-iodopyridinium)benzene bis(tetrakis(3,5-bis-(trifluoromethyl)phenyl)borate (**1a**)

This procedure was adapted from a previously reported literature procedure.[155] A 25-mL round bottom flask was charged with **4** (0.050 g, 0.0603 mmol), which was subsequently suspended in 8 mL of DCM. Na[BAr^{F}_{4}] (0.107 g, 0.121 mmol), prepared according to a previously reported literature procedure,[156] was added to the solution of **4** and stirred for 15 min at RT. NaCl precipitated from solution. The mixture was filtered through Celite, and the filtrate was concentrated under reduced pressure. Purification via HPLC afforded a dark-yellow oil (0.0223 g, 0.0089 mmol, 79 %). ^{1}H NMR (400 MHz, CD_3CN; 25 °C) δ 9.08 (s, 2H), 8.62 (d, *J* = 6.3 Hz, 2H), 8.06 (s, 1H), 8.00 (d, *J* = 6.4 Hz, 2H), 7.92 (d, *J* = 7.8 Hz, 2H), 7.69 (b, 17H), 7.66 (b, 8H), 4.42 (t, *J* = 15.2 Hz, 4H), 1.34 (b, 8H), 1.29 (b, 16H), 0.89 (m, 6H). ^{13}C NMR (100.6 MHz, CD_3CN; 25 °C) δ 162.56 (q, *J* = 50.3 Hz), 151.85, 146.45, 144.05, 136.81, 136.11, 135.64, 131.17, 130.16, 129.80, 129.89 (qq, *J* = 34.2 Hz), 125.51 (q, *J* = 271.6 Hz), 122.29, 105.56, 100.83, 90.08, 62.64, 32.40, 31.73, 29.67, 26.53, 23.31, 14.32. ^{19}F NMR (376.3 MHz, CD_3CN; 25 °C) δ –63.67. HRMS (CI pos) *m/z*: 379.075 (M^{+2}, 100 %), 379.581 (M^{+2}, 39.7), 380.082 (M^{+2}, 7.6); $C_{36}H_{44}I_2N_2^{2+}$ (379.08).

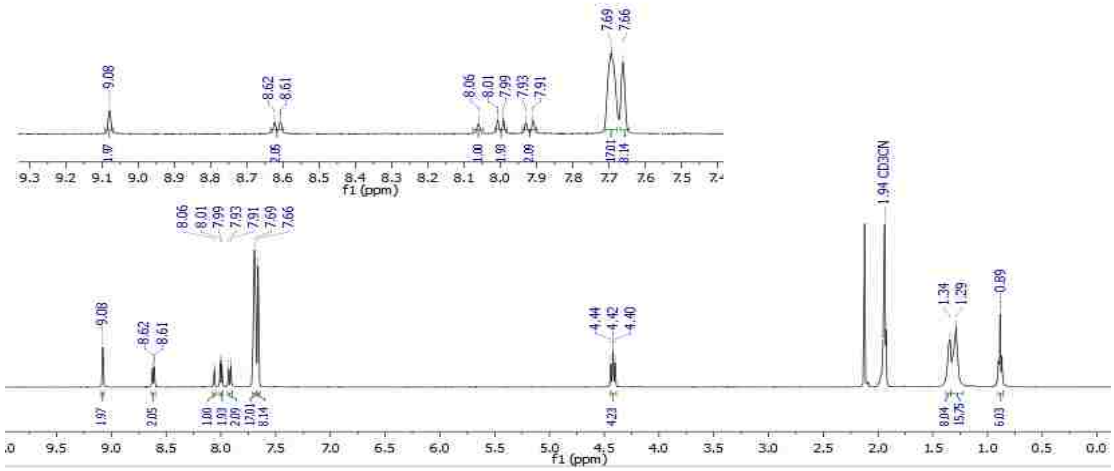

Figure 2.23 [1]H NMR spectrum of **1a**.

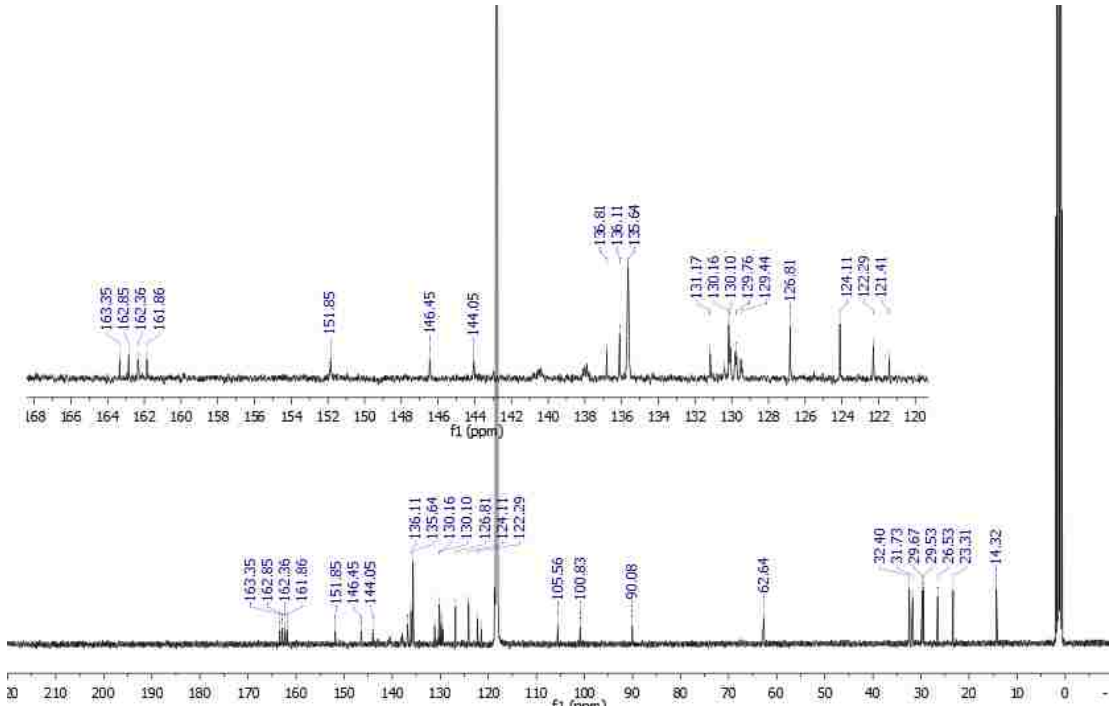

Figure 2.24 [13]C NMR spectrum of **1a**.

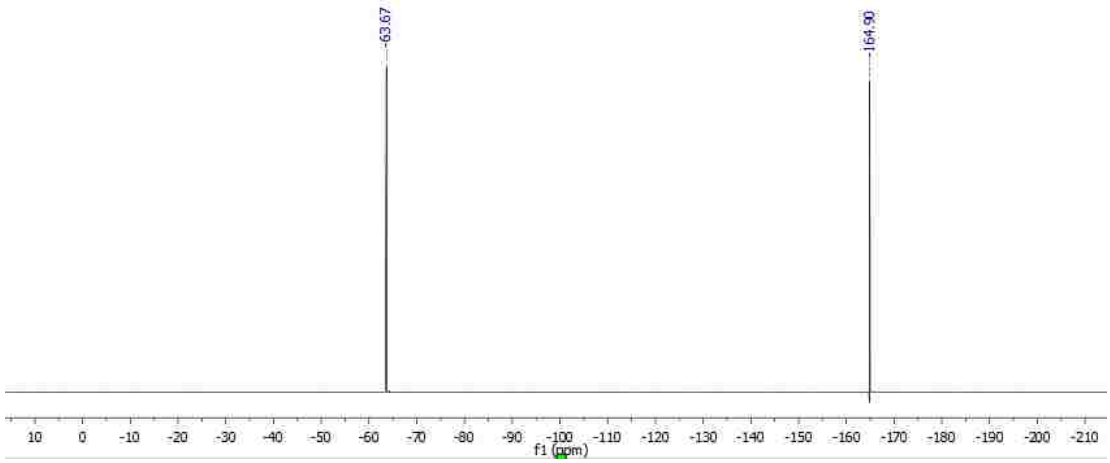

Figure 2.25 ^{19}F NMR spectrum of **1a**.

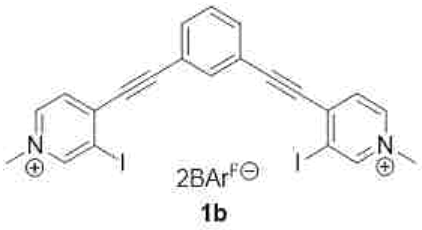

1b

1,3-bis(4-ethynyl-N-methyl-3-iodopyridinium)benzene bis(tetrakis(3,5-bis-(trifluoromethyl)phenyl)borate (**1b**)

First, **2** was alkylated according to the General Procedure for Methylation. The product (0.06 g, 0.072 mmol) and Na[BAr$^{F}_{4}$] (0.165 g, 0.181 mmol) were dissolved in 5 mL of DCM. The reaction was stirred for 30 min. A mixture of toluene and hexanes (10 mL, 2:1 *v*/*v*) precipitated the NaOTf, which was filtered off. The filtrate was concentrated under reduced pressure and purified via HPLC to afford an off-white solid (0.105 g, 0.0459 mmol, 66 %). ^{1}H NMR (400 MHz, CD_3CN; 25 °C) δ 9.05 (s, 2H), 8.57 (d, *J* = 6.3 Hz, 2H), 8.06 (s, 1H), 7.99 (d, *J* = 6.4 Hz, 2H), 7.92 (d, *J* = 7.8 Hz, 2H), 7.69 (b, 17H), 7.66 (b, 8H), 4.22 (s, 6H). ^{13}C NMR (100.6 MHz, CD_3CN; 25 °C) δ 162.58 (q, *J* = 49.3

Hz), 152.88, 146.23, 144.95, 136.76, 136.05, 135.63, 131.15, 129.88 (qq, J = 26.2 Hz), 122.26, 105.50, 100.16, 89.97, 48.83. ^{19}F NMR (376.3 MHz, CD_3CN; 25 °C) δ –60.82. HRMS (CI pos) *m/z*: 280.970 (M^{+2}, 100 %), 281.471 (M^{+2}, 24.5), 281.973 (M^{+2}, 2.7); $C_{22}H_{16}I_2N_2^{2+}$ (280.97).

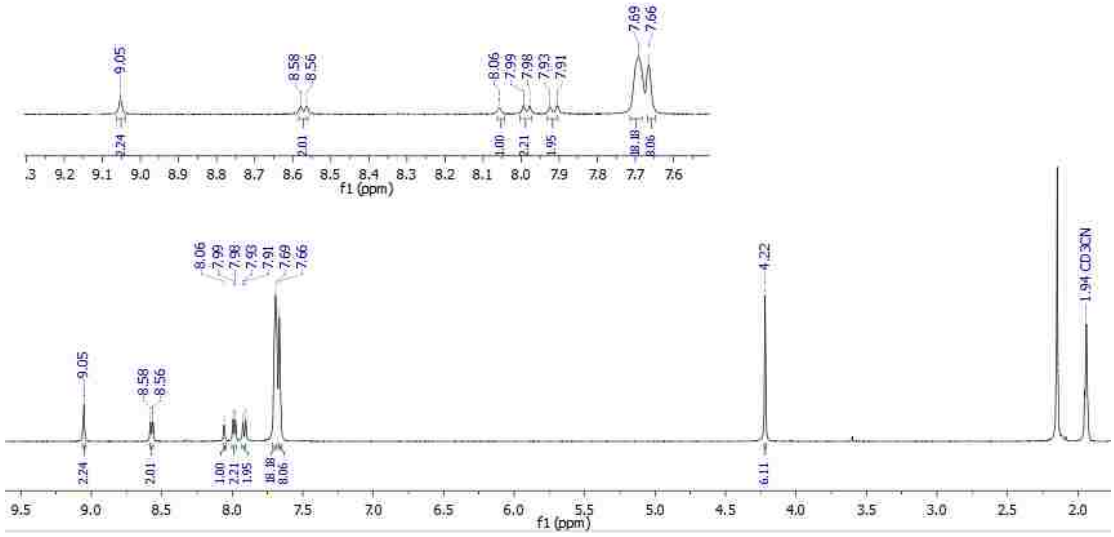

Figure 2.26 ^{1}H NMR spectrum of **1b**.

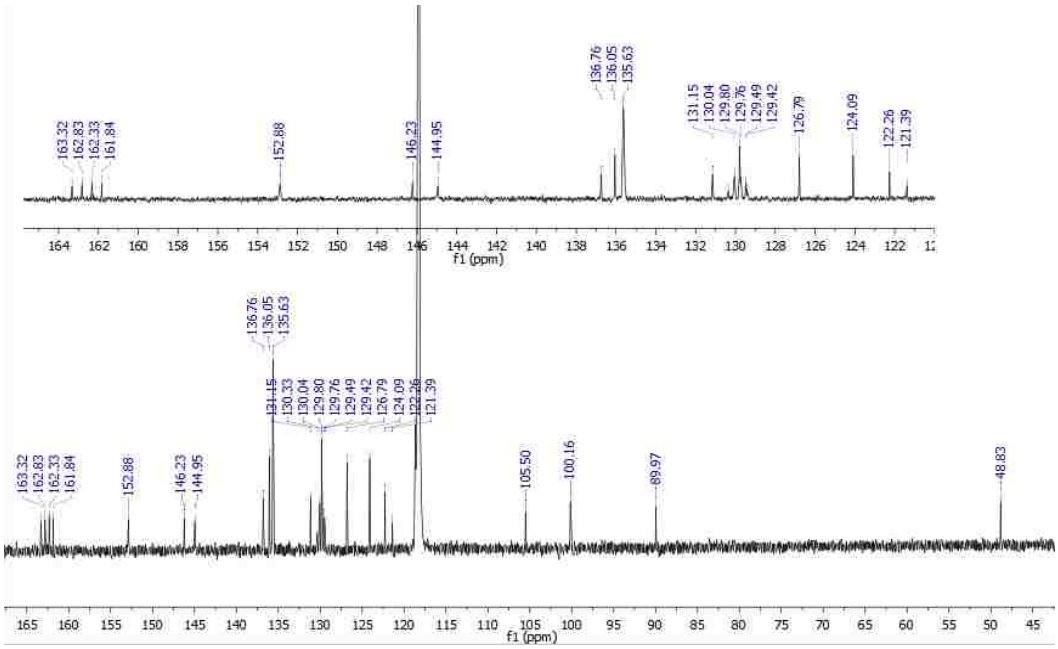

Figure 2.27 ^{13}C NMR spectrum of **1b**.

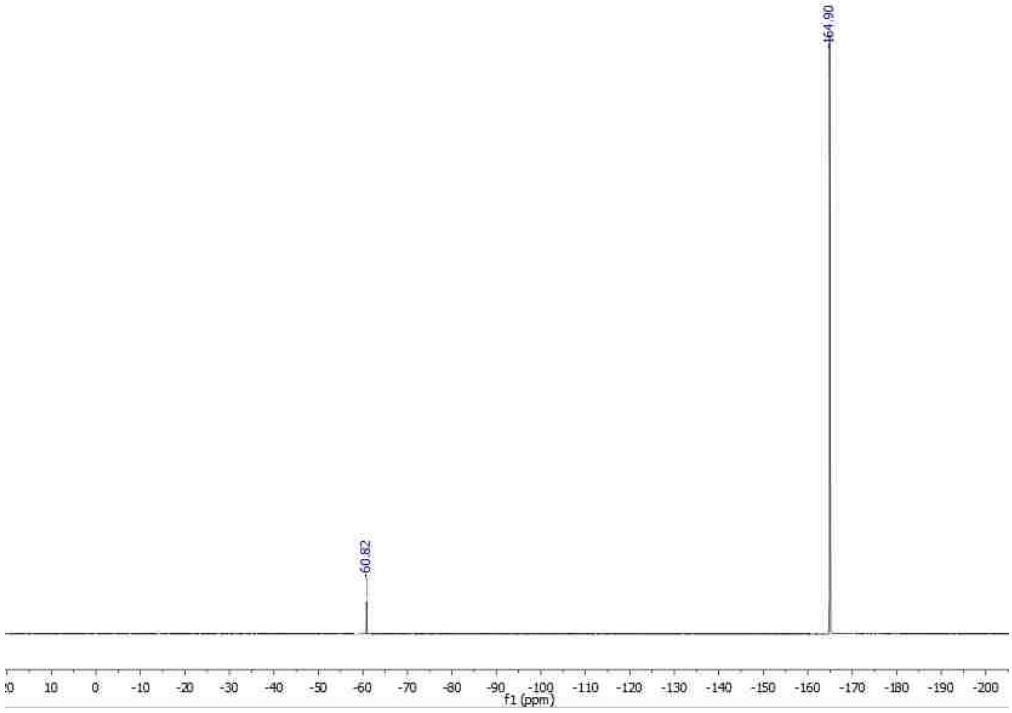

Figure 2.28 ^{19}F NMR spectrum of **1b**.

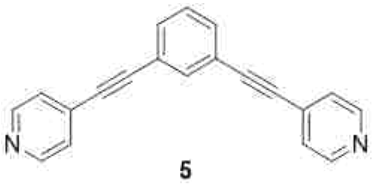

5

1,3-bis(4-ethynylpyridinyl)benzene (**5**)

This compound was prepared according to a previously reported literature procedure,[147] affording a white solid (0.124 g, 0.597 mmol, 22 %). ^{1}H NMR (500 MHz, $CDCl_3$; 25 °C) δ 8.63 (b, 4H), 7.76 (s, 1H), 7.57 (d, *J* = 7.7 Hz, 2H), 7.41 (t, *J* = 7.6 Hz, 1H), 7.39 (d, *J* = 5.4 Hz, 4H).

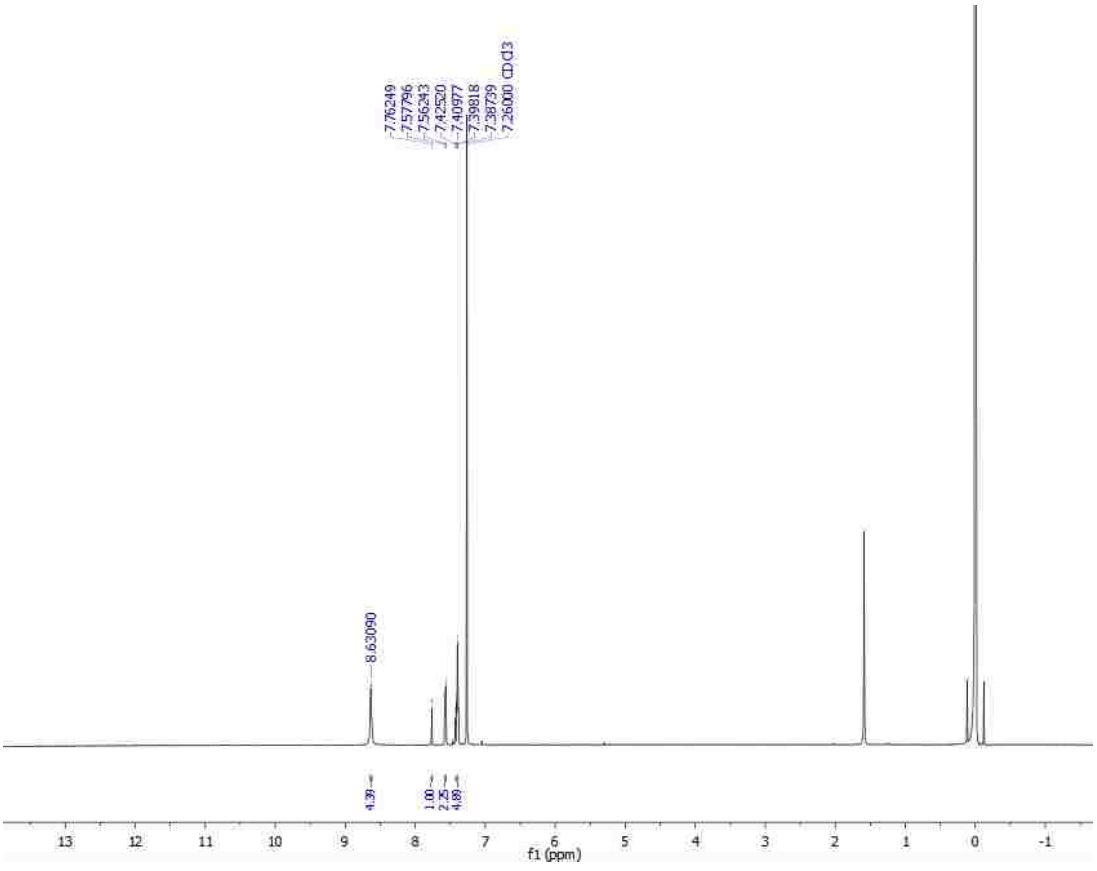

Figure 2.29 ^{1}H NMR spectrum of **5**.

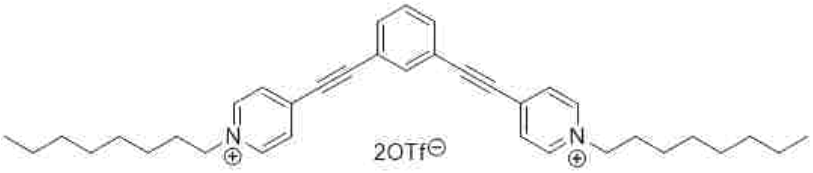

6

1,3-bis(4-ethynyl-N-octylpyridinium)benzene ditriflate (**6**)

5 (0.124 g, 0.597 mmol) was reacted with octyl OTf^{-} (0.631 mL, 3.99 mmol) according to the General Procedure for Octylation. The product was isolated as a sticky light-brown solid (0.349 g, 0.434 mmol, 97.7 %). Mp: 96–98 °C. ^{1}H NMR (400 MHz, CD_3CN; 25 °C) δ 8.68 (d, *J* = 6.9 Hz, 4H), 8.06 (d, *J* = 6.8 Hz, 4H), 8.00 (s, 1H), 7.85 (d, *J* = 7.8 Hz, 2H), 7.64 (t, *J* = 16.0 Hz, 1H), 4.49 (t, *J* = 15.2 Hz, 4H), 1.35 (b, 8H), 1.29 (b, 16H), 0.89 (s, 6H). ^{13}C NMR (100.6 MHz, CD_3CN; 25 °C) δ 145.39, 140.77, 136.72, 135.67, 130.92, 130.82, 122.38, 102.08, 86.58, 62.70, 32.39, 31.78, 29.67, 29.55, 26.54, 23.30, 14.33. ^{19}F NMR (376.3 MHz, CD_3CN; 25 °C) δ –76.85. HRMS (CI pos) *m/z*: 253.183 (M^{+2}, 100 %), 253.683 (M^{+2}, 39.5), 254.186 (M^{+2}, 7.7); $C_{36}H_{46}N_2^{2+}$ (253.18).

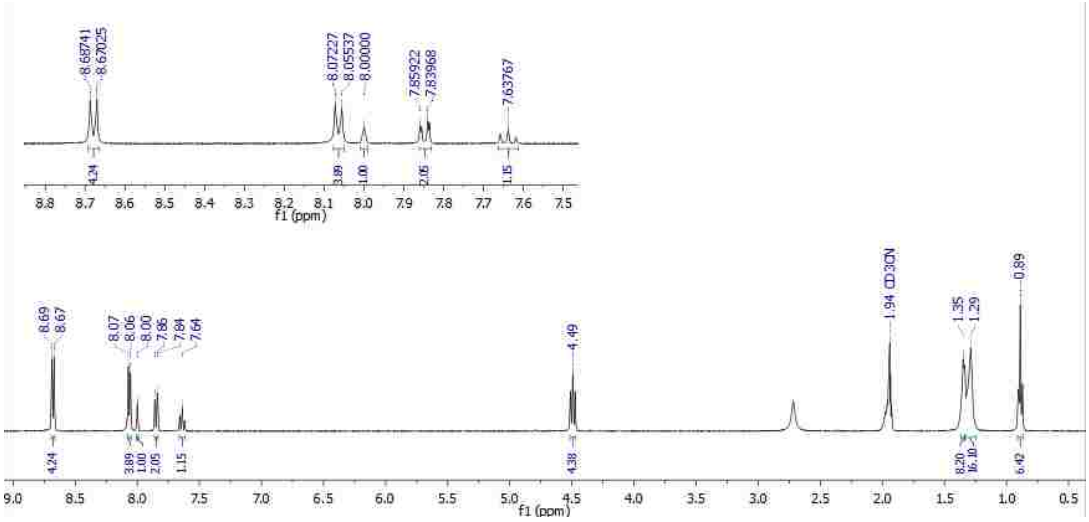

Figure 2.30 ^{1}H NMR spectrum of **6**.

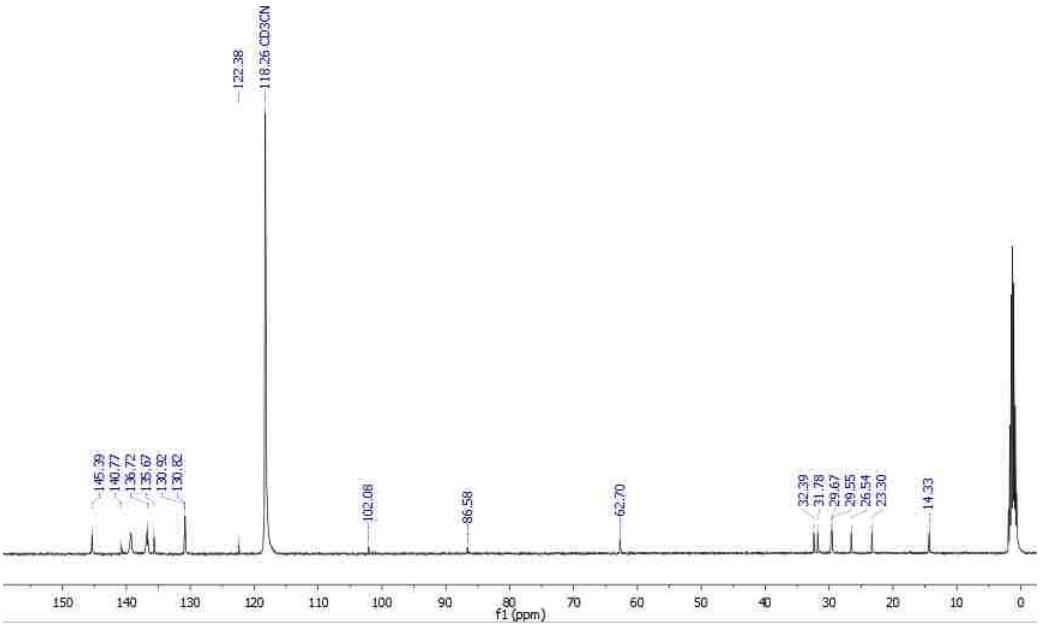

Figure 2.31 ^{13}C NMR spectrum of **6**.

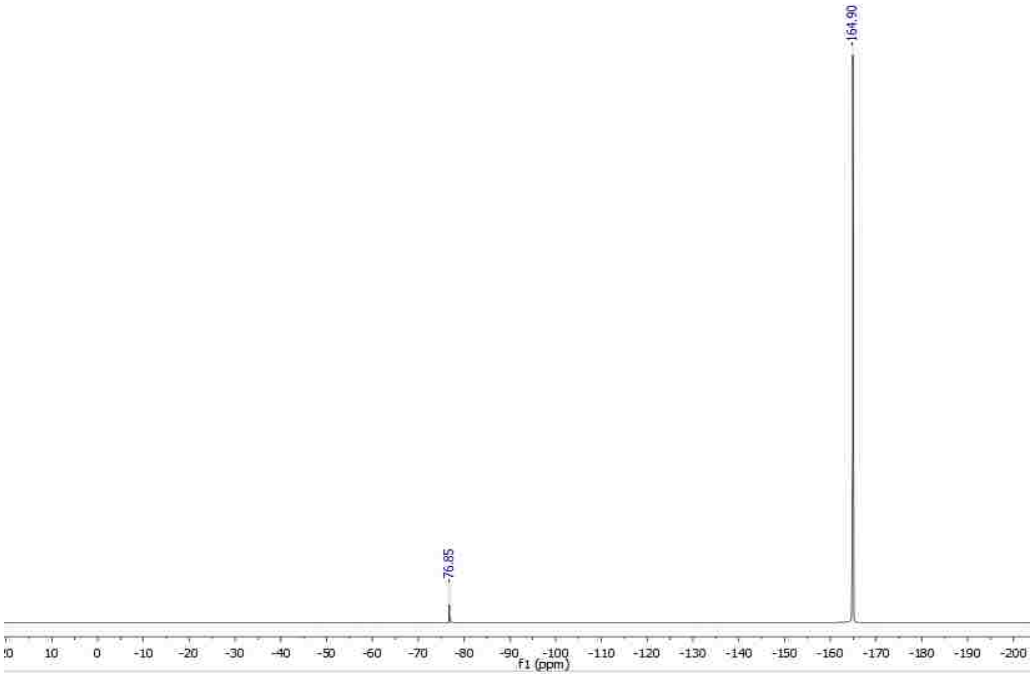

Figure 2.32 ^{19}F NMR spectrum of **6**.

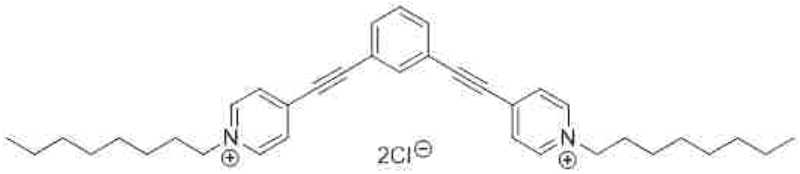

7

1,3-bis(4-ethynyl-N-octylpyridinium)benzene dichloride (**7**)

6 (0.010 g, 0.0124 mmol) and TBACl (0.0093 g, 0.0335 mmol) were reacted according to the General Procedure for Anion Metathesis. The product was isolated as a golden-yellow oil (0.0047 g, 0.00927 mmol, 74.7 %). ^{1}H NMR (400 MHz, CD_3CN; 25 °C) δ 8.98 (d, *J* = 6.8 Hz, 4H), 8.09 (d, *J* = 6.7 Hz, 4H), 8.00 (s, 1H), 7.84 (d, *J* = 7.8 Hz, 2H), 7.63 (t, *J* = 15.6 Hz, 1H), 4.62 (t, *J* = 14.8 Hz, 4H), 1.34 (b, 8H), 1.28 (b, 16H), 0.89 (b, 6H). ^{13}C NMR (100.6 MHz, CD_3CN; 25 °C) δ 145.70, 140.57, 136.94, 135.62, 130.90, 130.75, 122.41, 101.86, 86.64, 62.41, 32.41, 31.97, 29.71, 29.60, 26.56, 23.30, 14.34.

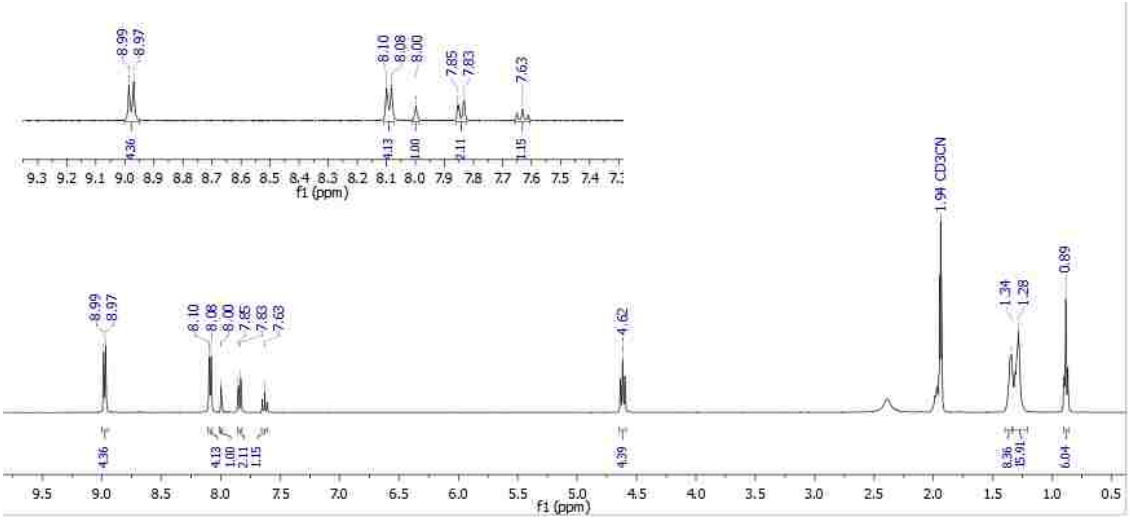

Figure 2.33 ^{1}H NMR spectrum of **7**.

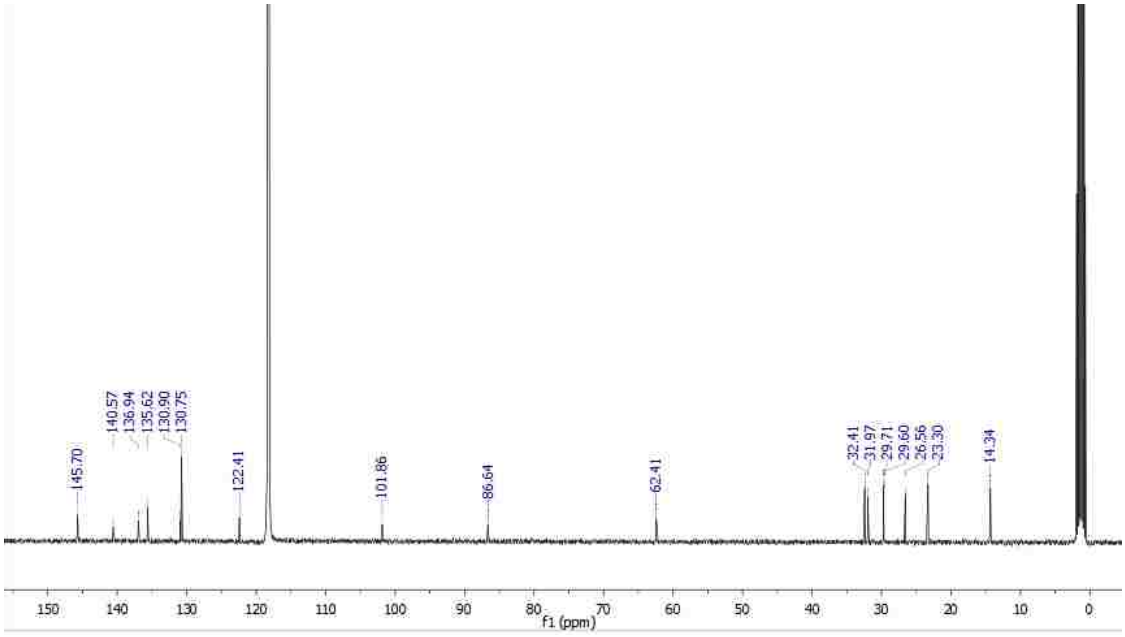

Figure 2.34 ^{13}C NMR spectrum of **7**.

2a

1,3-bis(4-ethynyl-N-octylpyridinium)benzene bis(tetrakis(3,5-bis-(trifluoromethyl)phenyl)borate (**2a**)

This procedure was adapted from a previously reported literature procedure.[155] A 25-mL round bottom flask was charged with **7** (0.004 g, 0.00813 mmol), which was subsequently suspended in 3 mL of DCM. Na[BAr$^{F}_{4}$] (0.0144 g, 0.0163 mmol), prepared according to a previously reported literature procedure,[156] was added to the solution of **7** and stirred for 15 min at RT. NaCl precipitated from solution. The mixture was filtered through Celite, and the filtrate was concentrated under reduced pressure. Purification via HPLC afforded a yellow oil (0.0106 g, 0.00475 mmol, 58 %). ^{1}H NMR (400 MHz,

CD_3CN; 25 °C) δ 8.63 (d, *J* = 6.7 Hz, 4H), 8.04 (d, *J* = 6.6 Hz, 4H), 7.97 (s, 1H), 7.84 (d, *J* = 7.8 Hz, 2H), 7.69 (b, 16H), 7.66 (b, 8H), 7.63 (t, *J*= 5.6 Hz, 1H), 4.48 (t, *J* = 15.2 Hz, 1H), 1.35 (b, 8H), 1.28 (b, 16H), 0.88 (m, 6H). ^{13}C NMR (100.6 MHz, CD_3CN; 25 °C) δ 162.61 (q, *J* = 50.3 Hz), 145.34, 140.82, 136.81, 135.65, 130.94, 130.83, 129.94 (qq, *J* = 28.2 Hz), 125.53 (q, *J* = 271.6 Hz), 102.12, 86.52, 62.72, 32.39, 31.81, 29.68, 29.55, 26.54, 23.30, 14.31. ^{19}F NMR (376.3 MHz, CD_3CN; 25 °C) δ –63.67. HRMS (CI pos) *m/z*: 253.183 (M^{+2}, 100 %), 253.684 (M^{+2}, 39.5), 254.186 (M^{+2}, 7.7); $C_{36}H_{46}N_2^{2+}$ (253.18).

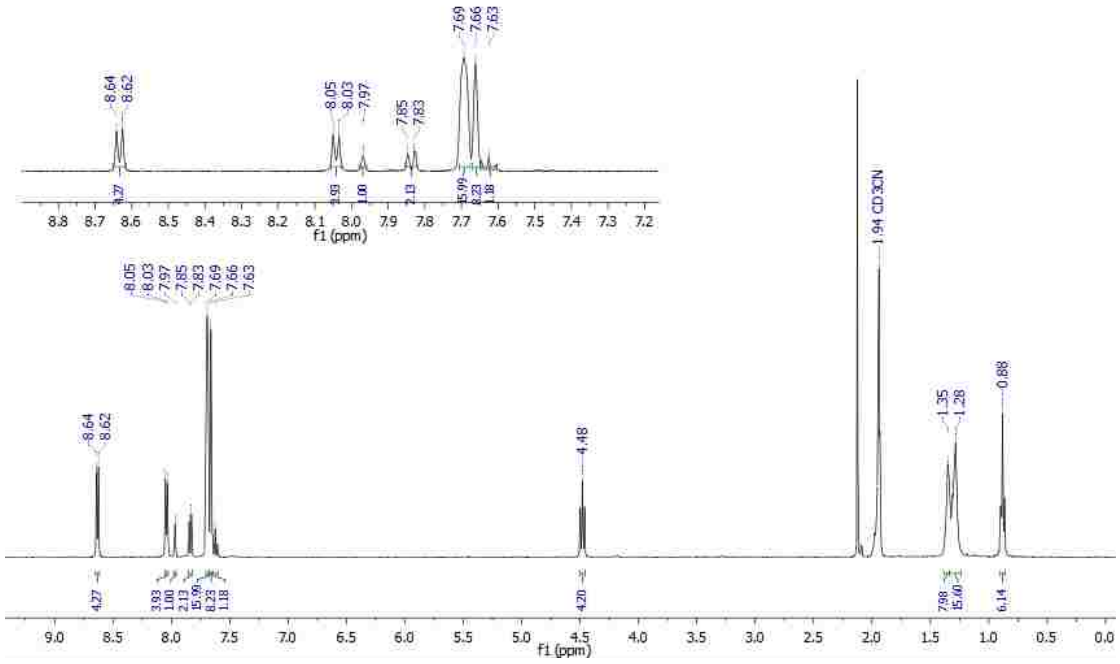

Figure 2.35 ^1H NMR spectrum of **2a**.

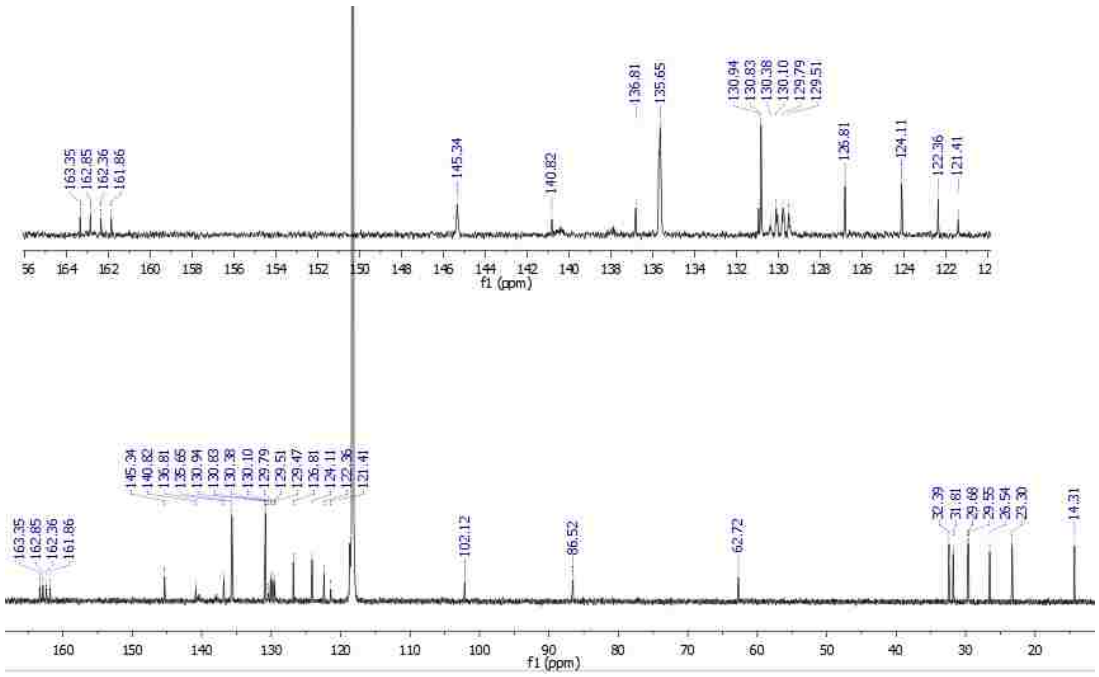

Figure 2.36 ^{13}C NMR spectrum of **2a**.

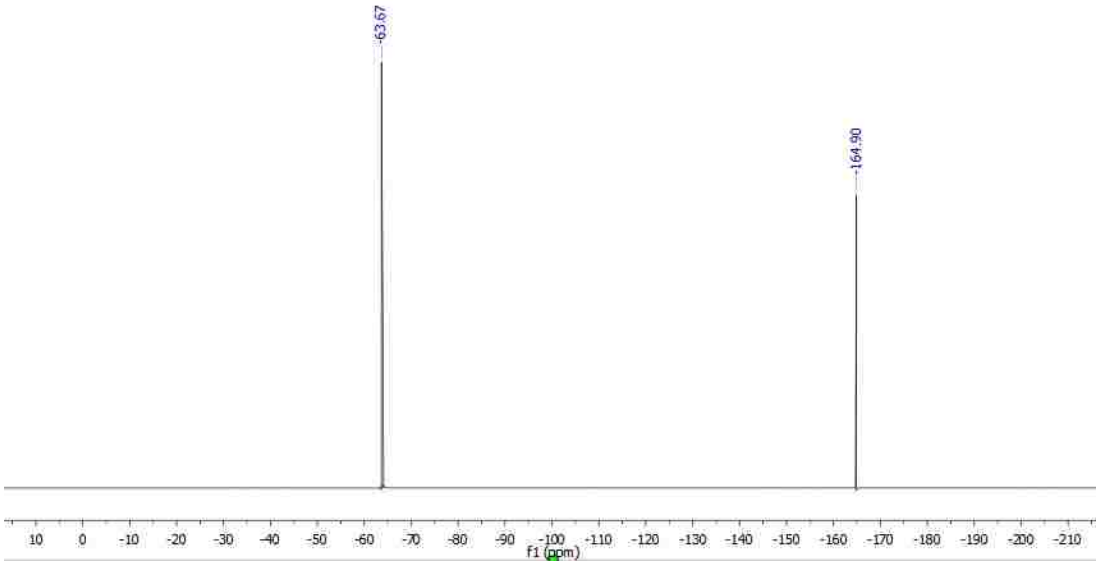

Figure 2.37 ^{19}F NMR spectrum of **2a**.

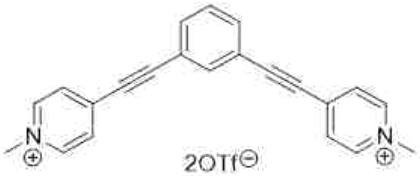

2b

1,3-bis(4-ethynyl-N-methylpyridinium)benzene ditriflate (**2b**)

5 (0.020 g, 0.096 mmol) and methyl OTf^{-} (0.043 mL, 0.394 mmol) were reacted according to the General Procedure for Methylation. The product was isolated as a white solid (0.033 g, 0.054 mmol, 56 %). ^{1}H NMR (400 MHz, CD_3CN; 25 °C) δ 8.62 (d, *J* = 6.6 Hz, 2H), 8.04 (d, *J* = 6.6 Hz, 2H), 7.99 (s, 1H), 7.84 (d, *J* = 7.8 Hz, 2H), 7.64 (t, *J* = 15.6 Hz, 1H), 4.28 (s, 6H). ^{13}C NMR (100.6 MHz, CD_3CN; 25 °C) δ 146.28, 140.50, 136.88, 135.59, 130.88, 130.44, 123.66, 122.34, 120.48, 101.92, 86.46, 49.14. ^{19}F NMR (376.3 MHz, CD_3CN; 25 °C) δ –76.84. HRMS (CI pos) *m/z*: 155.071 (M^{+2}, 100 %), 155.573 (M^{+2}, 24), 156.079 (M^{+2}, 2.9); $C_{22}H_{18}N_2^{2+}$ (155.07).

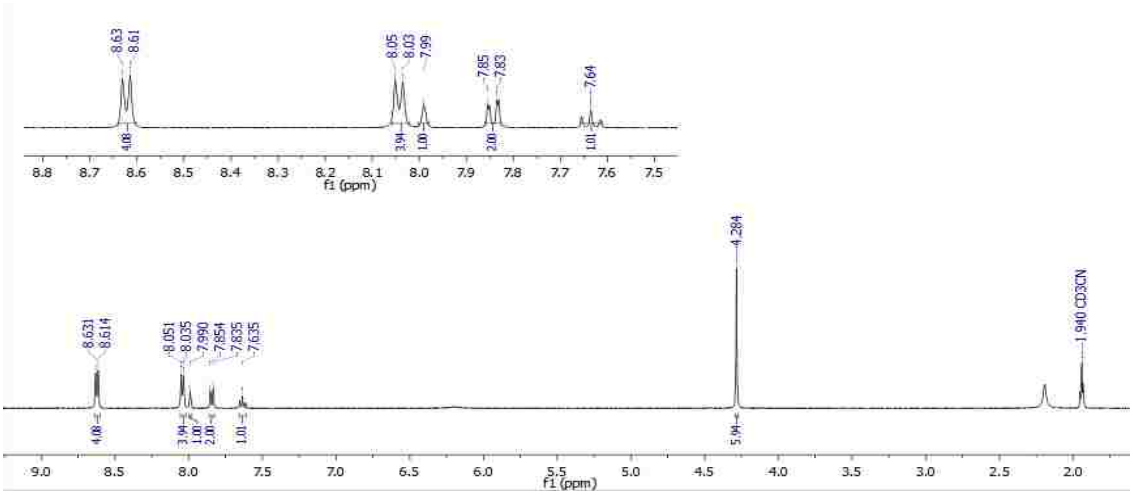

Figure 2.38 ^{1}H NMR spectrum of **2b**.

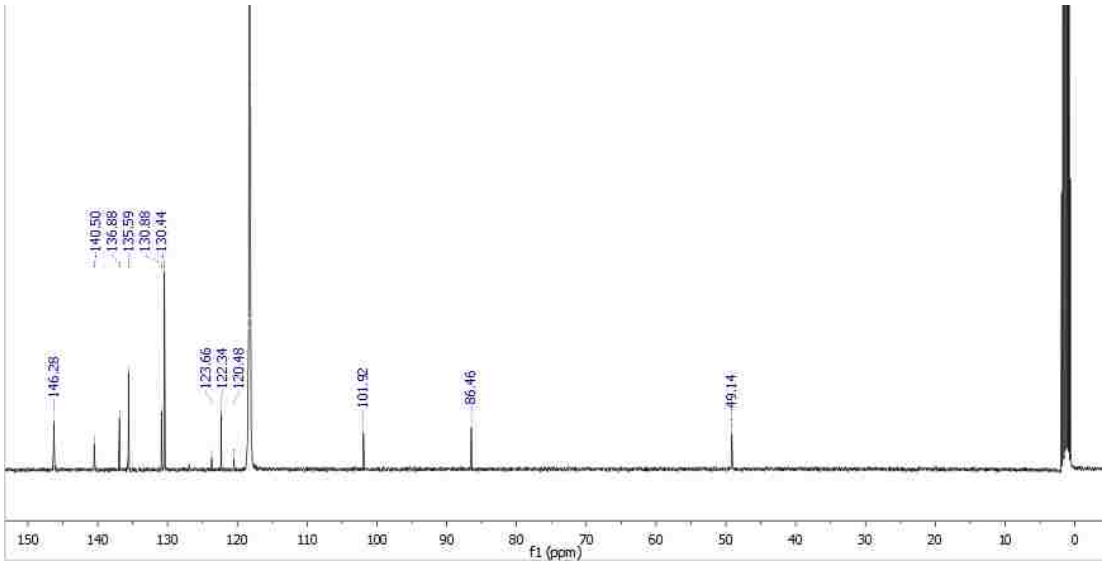

Figure 2.39 ^{13}C NMR spectrum of **2b**.

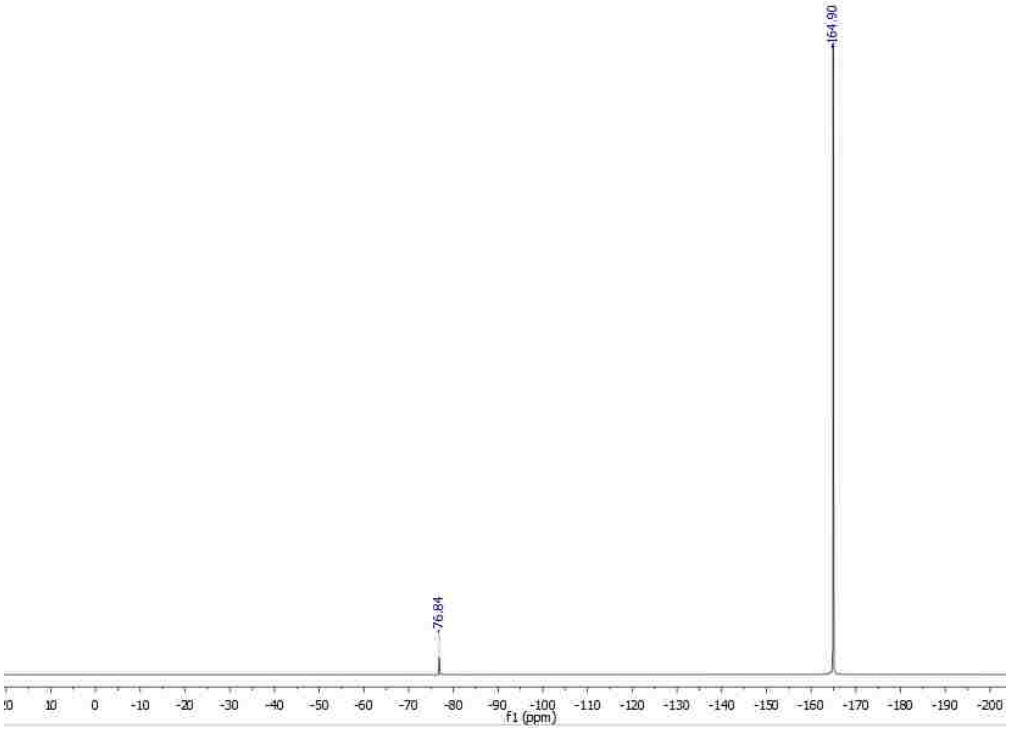

Figure 2.40 ^{19}F NMR spectrum of **2b**.

2.4.2 ^{1}H NMR Titration Data

All experiments were performed on a Varian Drive Direct 500 MHz NMR Spectrometer. Acetone-d_6 was stirred in Drierite ($CaSO_4$) under N_2 for 2 h, distilled, and used immediately after distillation. $CDCl_3$ was eluted through a column of activated alumina and dried over 3 Å molecular sieves. TBA ReO_4^- was dried under vacuum and stored in a desiccator.

Intuitions of stoichiometric displacement led to a stepwise anion exchange model. A simple 1:1 model, dimerization, and higher-order binding were ruled out due to the emergence of an obvious pattern in residuals, unrealistically assigned chemical shifts, poor convergence, and/or larger σs. HypNMR 2008 was used to refine the isothermal fits of multiple signals simultaneously (**1a**: Ha, Hb, Hc, and Hd; **2a**: Ha/b, Hc, and Hd). Mole fractions of species in solution (e.g. free host or host-guest complex) contributed to changes in the observed chemical shifts. These perturbations were monitored with increasing guest concentration. Subsequently, nonlinear regression analysis determined the unobserved chemical shifts of each contributing species, as well as binding constants with the following equation:

$$\delta = \sum \frac{x_i C_i}{T_x} \delta_i \qquad (2.3)$$

where δ is the observed chemical shift, x_i is the stoichiometric coefficient of the species, C_i is the equilibrium concentration of the species, T_x is the total concentration of a given

reagent (e.g. total host or total ReO_4^-), and δ_i is the unobserved chemical shift of each species.

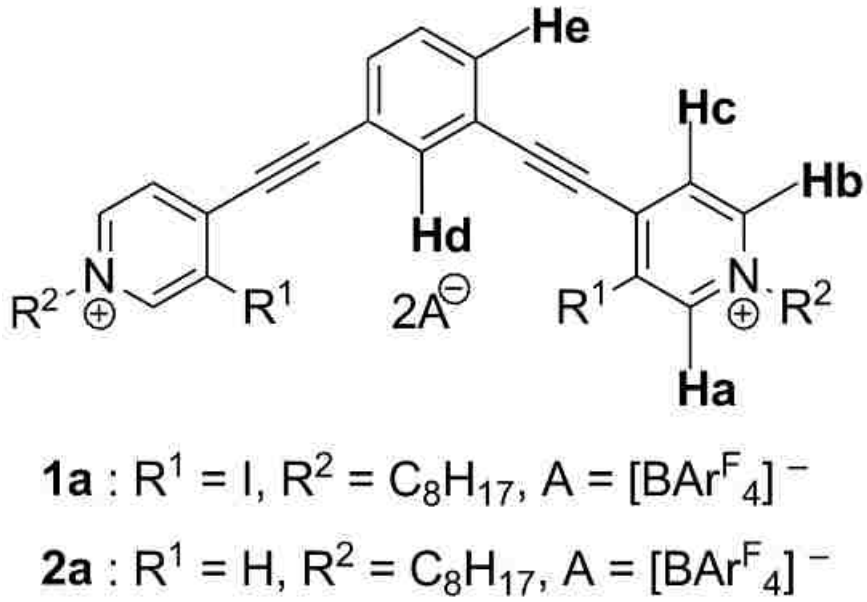

Figure 2.41 Proton assignments of **1a**/**2a** determined by ^{1}H 2D ROESY NMR (not shown).

1a and TBA ReO_4^- (Replicate 1)

1a (Exp.1)

Species	Log beta	ReO_4^-	**1a**	
1	3.9732	1	1	refine
2	6.2728	2	1	refine

Species concentrations/mol dm^{-3}

Point	T(ReO_4^-)	T(**1a**)	F(ReO_4^-)	F(**1a**)	species 1	species 2
1	0.00E+00	1.56E-03	4.77E-91	1.56E-03	7.00E-90	6.65E-18
2	5.35E-04	1.56E-03	4.72E-05	1.08E-03	4.79E-04	4.50E-06
3	1.03E-03	1.56E-03	1.32E-04	6.86E-04	8.53E-04	2.25E-05
4	1.49E-03	1.56E-03	2.80E-04	4.13E-04	1.09E-03	6.08E-05
5	1.92E-03	1.56E-03	4.95E-04	2.56E-04	1.19E-03	1.17E-04
6	2.32E-03	1.56E-03	7.48E-04	1.72E-04	1.21E-03	1.80E-04
7	2.69E-03	1.56E-03	1.01E-03	1.25E-04	1.19E-03	2.41E-04
8	3.04E-03	1.56E-03	1.28E-03	9.70E-05	1.17E-03	2.98E-04
9	3.37E-03	1.56E-03	1.54E-03	7.84E-05	1.13E-03	3.48E-04

10	3.68E-03	1.56E-03	1.79E-03	6.55E-05	1.10E-03	3.93E-04
11	4.25E-03	1.56E-03	2.27E-03	4.89E-05	1.04E-03	4.70E-04
12	4.76E-03	1.56E-03	2.70E-03	3.90E-05	9.90E-04	5.33E-04
13	5.21E-03	1.56E-03	3.10E-03	3.24E-05	9.45E-04	5.84E-04
14	5.63E-03	1.56E-03	3.47E-03	2.78E-05	9.07E-04	6.27E-04
15	6.00E-03	1.56E-03	3.80E-03	2.44E-05	8.74E-04	6.63E-04
16	6.35E-03	1.56E-03	4.11E-03	2.19E-05	8.46E-04	6.94E-04
17	6.66E-03	1.56E-03	4.40E-03	1.99E-05	8.21E-04	7.20E-04
18	6.95E-03	1.56E-03	4.66E-03	1.82E-05	8.00E-04	7.44E-04
19	7.22E-03	1.56E-03	4.91E-03	1.69E-05	7.81E-04	7.64E-04
20	7.47E-03	1.56E-03	5.14E-03	1.58E-05	7.64E-04	7.82E-04

Measured chemical shifts

Point	Ha	Hb	Hc	Hd
1	9.66E+00	9.23E+00	8.23E+00	8.04E+00
2	9.64E+00	9.20E+00	8.24E+00	8.09E+00
3	9.62E+00	9.19E+00	8.25E+00	8.13E+00
4	9.60E+00	9.18E+00	8.26E+00	8.16E+00
5	9.60E+00	9.17E+00	8.26E+00	8.17E+00
6	9.59E+00	9.16E+00	8.26E+00	8.18E+00
7	9.58E+00	9.16E+00	8.26E+00	8.18E+00
8	9.58E+00	9.16E+00	8.26E+00	8.19E+00
9	9.58E+00	9.16E+00	8.26E+00	8.19E+00
10	9.58E+00	9.15E+00	8.26E+00	8.19E+00
11	9.57E+00	9.15E+00	8.26E+00	8.19E+00
12	9.57E+00	9.15E+00	8.26E+00	8.19E+00
13	9.57E+00	9.15E+00	8.26E+00	8.19E+00
14	9.57E+00	9.15E+00	8.26E+00	8.19E+00
15	9.57E+00	9.15E+00	8.26E+00	8.19E+00
16	9.57E+00	9.15E+00	8.26E+00	8.19E+00
17	9.57E+00	9.14E+00	8.26E+00	8.19E+00
18	9.57E+00	9.14E+00	8.26E+00	8.19E+00
19	9.56E+00	9.14E+00	8.26E+00	8.19E+00
20	9.56E+00	9.14E+00	8.26E+00	8.19E+00

Calculated chemical shifts

Point	Ha	Hb	Hc	Hd
1	9.66E+00	9.23E+00	8.23E+00	8.04E+00
2	9.64E+00	9.21E+00	8.24E+00	8.09E+00
3	9.62E+00	9.19E+00	8.25E+00	8.13E+00
4	9.60E+00	9.18E+00	8.26E+00	8.16E+00
5	9.59E+00	9.17E+00	8.26E+00	8.17E+00

6	9.59E+00	9.16E+00	8.26E+00	8.18E+00
7	9.58E+00	9.16E+00	8.26E+00	8.18E+00
8	9.58E+00	9.16E+00	8.26E+00	8.19E+00
9	9.58E+00	9.16E+00	8.26E+00	8.19E+00
10	9.58E+00	9.15E+00	8.26E+00	8.19E+00
11	9.57E+00	9.15E+00	8.26E+00	8.19E+00
12	9.57E+00	9.15E+00	8.26E+00	8.19E+00
13	9.57E+00	9.15E+00	8.26E+00	8.19E+00
14	9.57E+00	9.15E+00	8.26E+00	8.19E+00
15	9.57E+00	9.15E+00	8.26E+00	8.19E+00
16	9.57E+00	9.15E+00	8.26E+00	8.19E+00
17	9.57E+00	9.15E+00	8.26E+00	8.19E+00
18	9.57E+00	9.14E+00	8.26E+00	8.19E+00
19	9.56E+00	9.14E+00	8.26E+00	8.19E+00
20	9.56E+00	9.14E+00	8.26E+00	8.19E+00

Chemical shifts for each nucleus

species	Ha	Hb	Hc	Hd
1a	9.66E+00	9.23E+00	8.23E+00	8.04E+00
(ReO_4^-)(**1a**)	9.58E+00	9.16E+00	8.27E+00	8.20E+00
(ReO_4^-)$_2$(**1a**)	9.54E+00	9.13E+00	8.25E+00	8.18E+00

Converged in 6 iterations with sigma = 1.050141

	value	standard deviation	Comments
1 log beta((ReO_4^-)(**1a**))	3.9732	0.066	3.97(7)
2 log beta((ReO_4^-)$_2$(**1a**))	6.2727	0.1884	6.3(2)

Correlation coefficients between stability constants. Numbering as above

2 0.804
1

For the binding isotherms of **1a** of replicate 1, see Section 2.3.4.

1a and TBA ReO_4^- (Replicate 2)

1a (Exp.2)

Species	Log beta	ReO_4^-	**1a**	
1	3.9054	1	1	refine
2	6.1335	2	1	refine

Species concentrations/mol dm^{-3}

Point	T(ReO_4^-)	T(**1a**)	F(ReO_4^-)	F(**1a**)	species 1	species 2
1	0.00E+00	1.56E-03	5.12E-91	1.56E-03	6.43E-90	5.57E-178
2	5.24E-04	1.56E-03	5.26E-05	1.09E-03	4.63E-04	4.12E-06
3	1.01E-03	1.56E-03	1.43E-04	7.16E-04	8.26E-04	2.00E-05
4	1.46E-03	1.56E-03	2.94E-04	4.48E-04	1.06E-03	5.27E-05
5	1.88E-03	1.56E-03	5.06E-04	2.88E-04	1.17E-03	1.00E-04
6	2.27E-03	1.56E-03	7.54E-04	1.99E-04	1.21E-03	1.54E-04
7	2.64E-03	1.56E-03	1.02E-03	1.48E-04	1.21E-03	2.07E-04
8	2.98E-03	1.56E-03	1.28E-03	1.16E-04	1.19E-03	2.57E-04
9	3.30E-03	1.56E-03	1.53E-03	9.44E-05	1.17E-03	3.02E-04
10	3.61E-03	1.56E-03	1.78E-03	7.95E-05	1.14E-03	3.43E-04
11	4.16E-03	1.56E-03	2.25E-03	6.02E-05	1.09E-03	4.13E-04
12	4.66E-03	1.56E-03	2.68E-03	4.84E-05	1.04E-03	4.71E-04
13	5.11E-03	1.56E-03	3.07E-03	4.06E-05	1.00E-03	5.20E-04
14	5.51E-03	1.56E-03	3.43E-03	3.50E-05	9.66E-04	5.60E-04
15	5.88E-03	1.56E-03	3.76E-03	3.10E-05	9.36E-04	5.95E-04
16	6.22E-03	1.56E-03	4.06E-03	2.78E-05	9.09E-04	6.24E-04
17	6.53E-03	1.56E-03	4.34E-03	2.54E-05	8.86E-04	6.50E-04
18	6.81E-03	1.56E-03	4.60E-03	2.34E-05	8.65E-04	6.73E-04
19	7.07E-03	1.56E-03	4.84E-03	2.17E-05	8.47E-04	6.93E-04
20	7.32E-03	1.56E-03	5.06E-03	2.04E-05	8.30E-04	7.11E-04

Measured chemical shifts

Point	Ha	Hb	Hc	Hd
1	9.66E+00	9.23E+00	8.23E+00	8.04E+00
2	9.64E+00	9.21E+00	8.24E+00	8.09E+00
3	9.62E+00	9.19E+00	8.25E+00	8.13E+00
4	9.61E+00	9.18E+00	8.26E+00	8.16E+00
5	9.60E+00	9.17E+00	8.26E+00	8.17E+00
6	9.59E+00	9.17E+00	8.26E+00	8.18E+00
7	9.59E+00	9.16E+00	8.26E+00	8.18E+00
8	9.58E+00	9.16E+00	8.26E+00	8.18E+00
9	9.58E+00	9.16E+00	8.26E+00	8.19E+00
10	9.58E+00	9.16E+00	8.26E+00	8.19E+00
11	9.58E+00	9.15E+00	8.26E+00	8.19E+00
12	9.57E+00	9.15E+00	8.26E+00	8.19E+00

13	9.57E+00	9.15E+00	8.26E+00	8.19E+00
14	9.57E+00	9.15E+00	8.26E+00	8.19E+00
15	9.57E+00	9.15E+00	8.26E+00	8.19E+00
16	9.57E+00	9.15E+00	8.26E+00	8.19E+00
17	9.57E+00	9.15E+00	8.26E+00	8.19E+00
18	9.57E+00	9.15E+00	8.26E+00	8.19E+00
19	9.57E+00	9.15E+00	8.26E+00	8.19E+00
20	9.57E+00	9.14E+00	8.26E+00	8.19E+00

Calculated chemical shifts

Point	Ha	Hb	Hc	Hd
1	9.66E+00	9.23E+00	8.23E+00	8.04E+00
2	9.64E+00	9.21E+00	8.24E+00	8.09E+00
3	9.62E+00	9.19E+00	8.25E+00	8.13E+00
4	9.61E+00	9.18E+00	8.26E+00	8.15E+00
5	9.60E+00	9.17E+00	8.26E+00	8.17E+00
6	9.59E+00	9.17E+00	8.26E+00	8.18E+00
7	9.59E+00	9.16E+00	8.26E+00	8.18E+00
8	9.58E+00	9.16E+00	8.26E+00	8.19E+00
9	9.58E+00	9.16E+00	8.26E+00	8.19E+00
10	9.58E+00	9.16E+00	8.26E+00	8.19E+00
11	9.58E+00	9.15E+00	8.26E+00	8.19E+00
12	9.57E+00	9.15E+00	8.26E+00	8.19E+00
13	9.57E+00	9.15E+00	8.26E+00	8.19E+00
14	9.57E+00	9.15E+00	8.26E+00	8.19E+00
15	9.57E+00	9.15E+00	8.26E+00	8.19E+00
16	9.57E+00	9.15E+00	8.26E+00	8.19E+00
17	9.57E+00	9.15E+00	8.26E+00	8.19E+00
18	9.57E+00	9.15E+00	8.26E+00	8.19E+00
19	9.57E+00	9.15E+00	8.26E+00	8.19E+00
20	9.56E+00	9.14E+00	8.26E+00	8.19E+00

Chemical shifts for each nucleus

species	Ha	Hb	Hc	Hd
1a	9.66E+00	9.23E+00	8.23E+00	8.04E+00
(ReO_4^-)(**1a**)	9.58E+00	9.16E+00	8.27E+00	8.20E+00
(ReO_4^-)$_2$(**1a**)	9.54E+00	9.12E+00	8.25E+00	8.18E+00

Converged in 8 iterations with sigma = 0.900117

	value	standard deviation	Comments
1 log beta((ReO_4^-)(**1a**))	3.9054	0.0569	3.91(6)
2 log beta((ReO_4^-)$_2$(**1a**))	6.1335	0.1764	6.1(2)

Correlation coefficients between stability constants. Numbering as above

2 0.7997
1

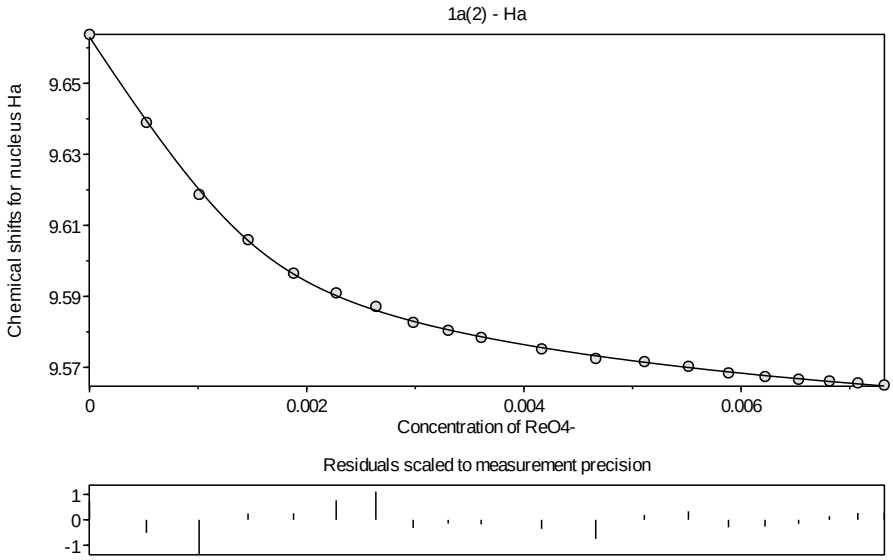

Figure 2.42 Binding isotherm following proton Ha on **1a** with increasing ReO_4^- concentration (replicate 2).

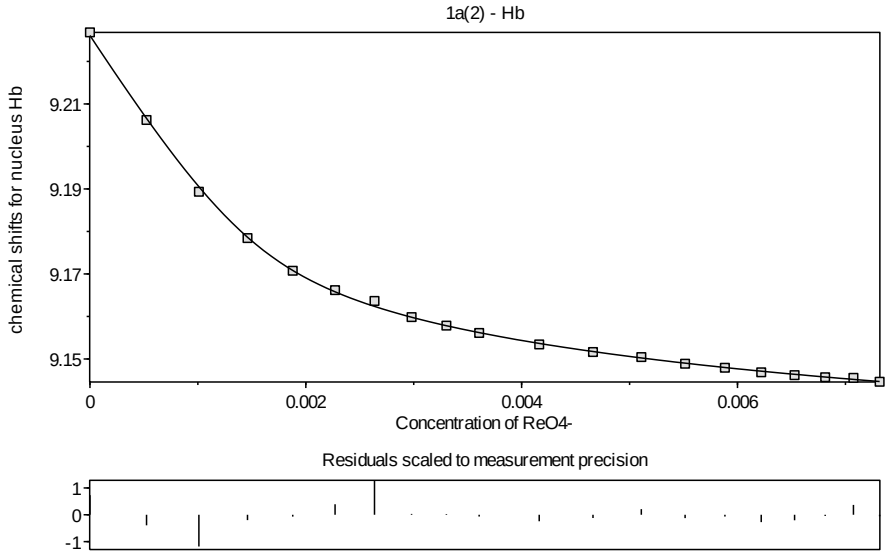

Figure 2.43 Binding isotherm following proton Hb on **1a** with increasing ReO_4^- concentration (replicate 2).

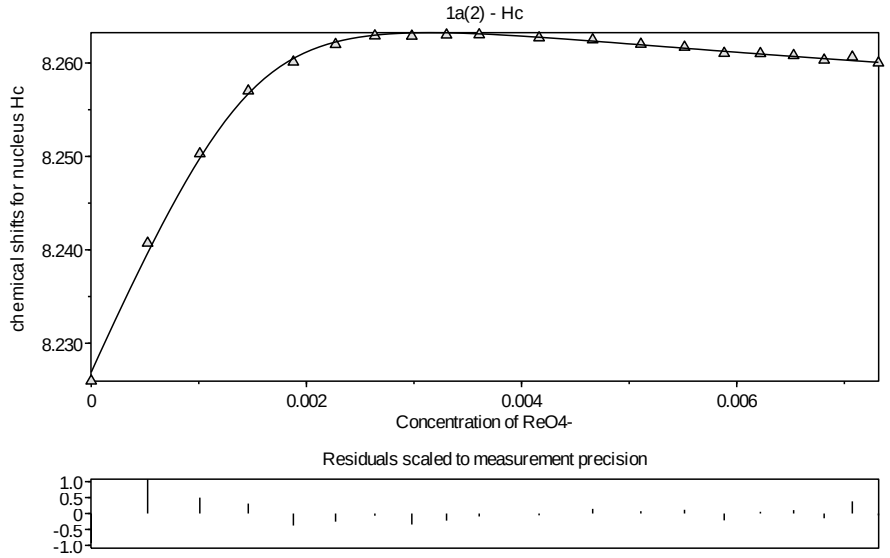

Figure 2.44 Binding isotherm following proton Hc on **1a** with increasing ReO_4^- concentration (replicate 2).

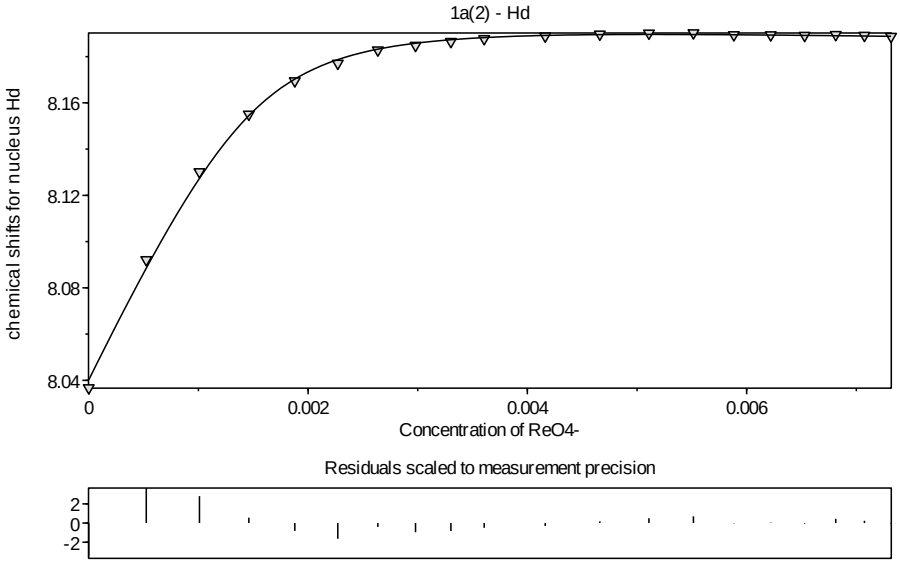

Figure 2.45 Binding isotherm following proton Hd on **1a** with increasing ReO_4^- concentration (replicate 2).

1a and TBA ReO_4^- (Replicate 3)

1a (Exp.3)

Species	Log beta	ReO_4^-	**1a**	
1	3.9794	1	1	refine
2	6.1451	2	1	refine

Species concentrations/mol dm^{-3}

Point	T(ReO_4^-)	T(**1a**)	F(ReO_4^-)	F(**1a**)	species 1	species 2
1	0.00E+00	1.56E-03	4.74E-91	1.56E-03	7.05E-90	4.89E-178
2	5.24E-04	1.56E-03	4.56E-05	1.09E-03	4.72E-04	3.15E-06
3	1.01E-03	1.56E-03	1.28E-04	6.96E-04	8.49E-04	1.59E-05
4	1.46E-03	1.56E-03	2.74E-04	4.20E-04	1.10E-03	4.41E-05
5	1.88E-03	1.56E-03	4.90E-04	2.60E-04	1.21E-03	8.72E-05
6	2.27E-03	1.56E-03	7.48E-04	1.75E-04	1.25E-03	1.37E-04
7	2.64E-03	1.56E-03	1.02E-03	1.28E-04	1.25E-03	1.86E-04
8	2.98E-03	1.56E-03	1.29E-03	1.00E-04	1.23E-03	2.32E-04
9	3.30E-03	1.56E-03	1.55E-03	8.16E-05	1.21E-03	2.74E-04
10	3.61E-03	1.56E-03	1.80E-03	6.87E-05	1.18E-03	3.12E-04
11	4.16E-03	1.56E-03	2.28E-03	5.21E-05	1.13E-03	3.77E-04
12	4.66E-03	1.56E-03	2.71E-03	4.21E-05	1.09E-03	4.32E-04
13	5.11E-03	1.56E-03	3.11E-03	3.54E-05	1.05E-03	4.77E-04
14	5.51E-03	1.56E-03	3.47E-03	3.07E-05	1.02E-03	5.16E-04

15	5.88E-03	1.56E-03	3.80E-03	2.72E-05	9.86E-04	5.49E-04
16	6.22E-03	1.56E-03	4.11E-03	2.45E-05	9.60E-04	5.77E-04
17	6.53E-03	1.56E-03	4.39E-03	2.24E-05	9.37E-04	6.02E-04
18	6.81E-03	1.56E-03	4.65E-03	2.07E-05	9.17E-04	6.24E-04
19	7.07E-03	1.56E-03	4.89E-03	1.93E-05	8.99E-04	6.43E-04
20	7.32E-03	1.56E-03	5.11E-03	1.81E-05	8.83E-04	6.61E-04

Measured chemical shifts

Point	Ha	Hb	Hc	Hd
1	9.66E+00	9.23E+00	8.23E+00	8.04E+00
2	9.64E+00	9.20E+00	8.24E+00	8.09E+00
3	9.62E+00	9.19E+00	8.25E+00	8.13E+00
4	9.61E+00	9.18E+00	8.26E+00	8.16E+00
5	9.60E+00	9.17E+00	8.26E+00	8.17E+00
6	9.59E+00	9.17E+00	8.26E+00	8.18E+00
7	9.59E+00	9.16E+00	8.26E+00	8.18E+00
8	9.58E+00	9.16E+00	8.26E+00	8.19E+00
9	9.58E+00	9.16E+00	8.26E+00	8.19E+00
10	9.58E+00	9.16E+00	8.26E+00	8.19E+00
11	9.58E+00	9.15E+00	8.26E+00	8.19E+00
12	9.57E+00	9.15E+00	8.26E+00	8.19E+00
13	9.57E+00	9.15E+00	8.26E+00	8.19E+00
14	9.57E+00	9.15E+00	8.26E+00	8.19E+00
15	9.57E+00	9.15E+00	8.26E+00	8.19E+00
16	9.57E+00	9.15E+00	8.26E+00	8.19E+00
17	9.57E+00	9.15E+00	8.26E+00	8.19E+00
18	9.57E+00	9.15E+00	8.26E+00	8.19E+00
19	9.57E+00	9.14E+00	8.26E+00	8.19E+00
20	9.56E+00	9.14E+00	8.26E+00	8.19E+00

Calculated chemical shifts

Point	Ha	Hb	Hc	Hd
1	9.66E+00	9.23E+00	8.23E+00	8.04E+00
2	9.64E+00	9.21E+00	8.24E+00	8.09E+00
3	9.62E+00	9.19E+00	8.25E+00	8.13E+00
4	9.61E+00	9.18E+00	8.26E+00	8.16E+00
5	9.60E+00	9.17E+00	8.26E+00	8.17E+00
6	9.59E+00	9.17E+00	8.26E+00	8.18E+00
7	9.59E+00	9.16E+00	8.26E+00	8.18E+00
8	9.58E+00	9.16E+00	8.26E+00	8.19E+00
9	9.58E+00	9.16E+00	8.26E+00	8.19E+00
10	9.58E+00	9.16E+00	8.26E+00	8.19E+00
11	9.58E+00	9.15E+00	8.26E+00	8.19E+00

12	9.57E+00	9.15E+00	8.26E+00	8.19E+00
13	9.57E+00	9.15E+00	8.26E+00	8.19E+00
14	9.57E+00	9.15E+00	8.26E+00	8.19E+00
15	9.57E+00	9.15E+00	8.26E+00	8.19E+00
16	9.57E+00	9.15E+00	8.26E+00	8.19E+00
17	9.57E+00	9.15E+00	8.26E+00	8.19E+00
18	9.57E+00	9.15E+00	8.26E+00	8.19E+00
19	9.57E+00	9.15E+00	8.26E+00	8.19E+00
20	9.56E+00	9.14E+00	8.26E+00	8.19E+00

Chemical shifts for each nucleus

species	Ha	Hb	Hc	Hd
1a	9.66E+00	9.23E+00	8.23E+00	8.04E+00
(ReO_4^-)(**1a**)	9.59E+00	9.16E+00	8.27E+00	8.20E+00
(ReO_4^-)$_2$(**1a**)	9.53E+00	9.12E+00	8.25E+00	8.18E+00

Converged in 7 iterations with sigma = 0.986089

	value	standard deviation	Comments
1 log beta((ReO^{4-})(**1a**))	3.9794	0.0607	3.98(6)
2 log beta((ReO^{4-})$_2$(**1a**))	6.1451	0.1901	6.1(2)

Correlation coefficients between stability constants. Numbering as above

2 0.7796
1

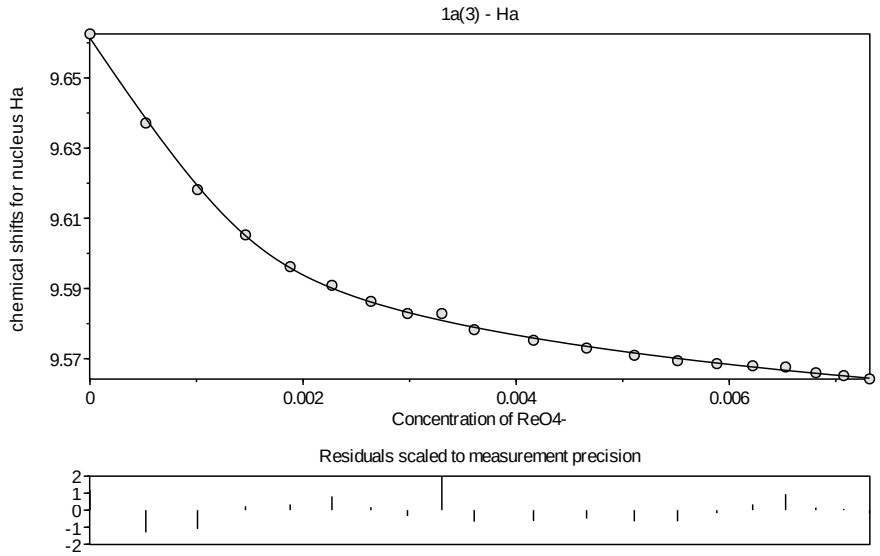

Figure 2.46 Binding isotherm following proton Ha on **1a** with increasing ReO_4^- concentration (replicate 3).

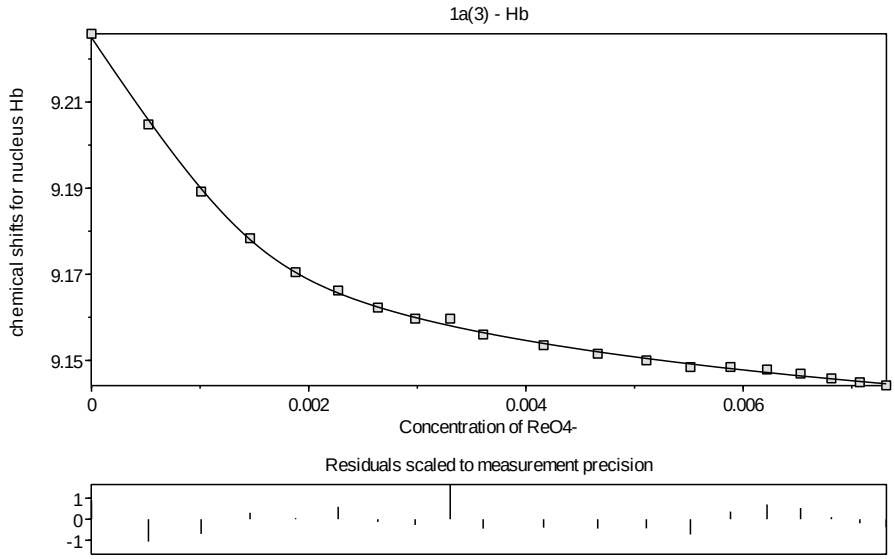

Figure 2.47 Binding isotherm following proton Hb on **1a** with increasing ReO_4^- concentration (replicate 3).

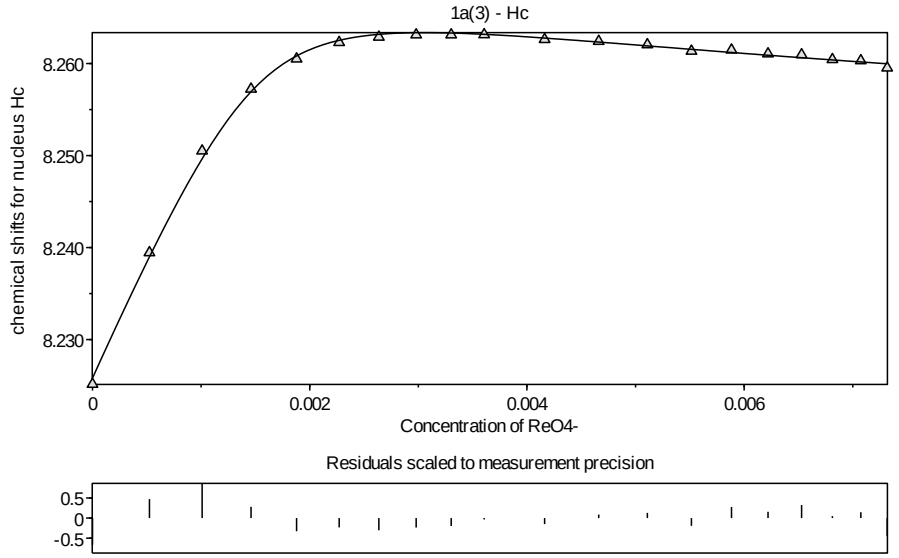

Figure 2.48 Binding isotherm following proton Hc on **1a** with increasing ReO_4^- concentration (replicate 3).

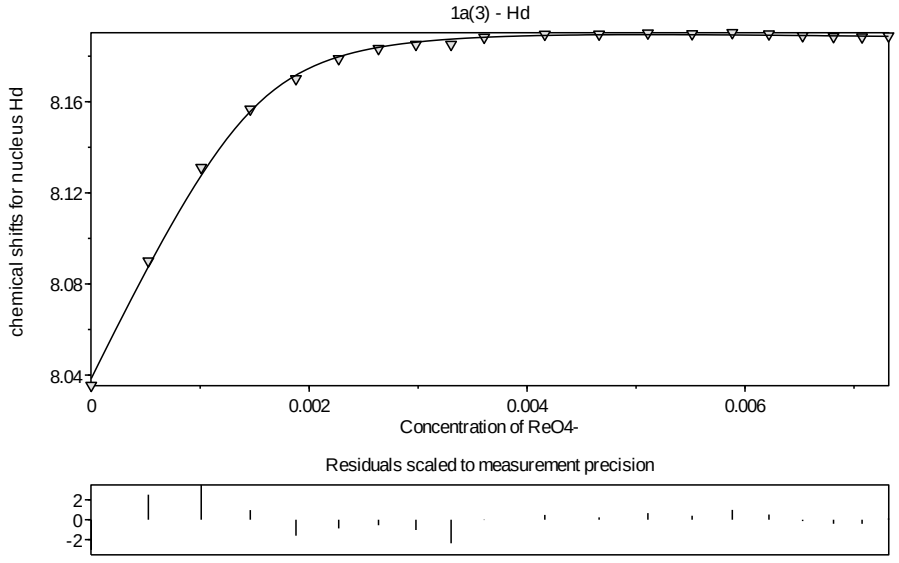

Figure 2.49 Binding isotherm following proton Hd on **1a** with increasing ReO_4^- concentration (replicate 3).

2a and TBA ReO_4^- (Replicate 1)

2a (Exp.1)

Species	Log beta	ReO_4^-	**2a**	
1	3.8876	1	1	refine
2	6.0026	2	1	refine

Species concentrations/mol dm^{-3}

Point	T(ReO_4^-)	T(**2a**)	F(ReO_4^-)	F(**2a**)	species 1	species 2
1	0.00E+00	1.55E-03	5.21E-91	1.55E-03	6.24E-90	4.24E-178
2	5.13E-04	1.55E-03	5.36E-05	1.09E-03	4.53E-04	3.17E-06
3	9.89E-04	1.55E-03	1.45E-04	7.24E-04	8.12E-04	1.54E-05
4	1.43E-03	1.55E-03	2.97E-04	4.59E-04	1.05E-03	4.07E-05
5	1.84E-03	1.55E-03	5.10E-04	2.98E-04	1.17E-03	7.81E-05
6	2.22E-03	1.55E-03	7.60E-04	2.08E-04	1.22E-03	1.21E-04
7	2.58E-03	1.55E-03	1.02E-03	1.56E-04	1.23E-03	1.64E-04
8	2.92E-03	1.55E-03	1.29E-03	1.23E-04	1.22E-03	2.05E-04
9	3.24E-03	1.55E-03	1.54E-03	1.01E-04	1.21E-03	2.43E-04
10	3.53E-03	1.55E-03	1.79E-03	8.60E-05	1.19E-03	2.77E-04
11	4.08E-03	1.55E-03	2.26E-03	6.59E-05	1.15E-03	3.37E-04
12	4.57E-03	1.55E-03	2.68E-03	5.36E-05	1.11E-03	3.88E-04
13	5.00E-03	1.55E-03	3.07E-03	4.54E-05	1.08E-03	4.30E-04
14	5.40E-03	1.55E-03	3.42E-03	3.96E-05	1.05E-03	4.66E-04
15	5.76E-03	1.55E-03	3.75E-03	3.52E-05	1.02E-03	4.98E-04
16	6.09E-03	1.55E-03	4.05E-03	3.18E-05	9.95E-04	5.25E-04
17	6.40E-03	1.55E-03	4.32E-03	2.92E-05	9.74E-04	5.49E-04
18	6.67E-03	1.55E-03	4.58E-03	2.70E-05	9.55E-04	5.70E-04
19	6.93E-03	1.55E-03	4.82E-03	2.52E-05	9.38E-04	5.88E-04
20	7.17E-03	1.55E-03	5.03E-03	2.37E-05	9.23E-04	6.05E-04

Measured chemical shifts

Point	Ha/b	Hc	Hd
1	9.22E+00	8.25E+00	7.93E+00
2	9.20E+00	8.25E+00	7.98E+00
3	9.19E+00	8.26E+00	8.01E+00
4	9.18E+00	8.26E+00	8.03E+00
5	9.17E+00	8.26E+00	8.05E+00
6	9.17E+00	8.26E+00	8.05E+00
7	9.16E+00	8.27E+00	8.06E+00
8	9.16E+00	8.26E+00	8.06E+00
9	9.16E+00	8.26E+00	8.06E+00
10	9.16E+00	8.26E+00	8.07E+00
11	9.15E+00	8.26E+00	8.07E+00
12	9.15E+00	8.26E+00	8.07E+00

13	9.15E+00	8.26E+00	8.07E+00
14	9.15E+00	8.26E+00	8.07E+00
15	9.15E+00	8.26E+00	8.07E+00
16	9.15E+00	8.26E+00	8.07E+00
17	9.15E+00	8.26E+00	8.07E+00
18	9.15E+00	8.26E+00	8.07E+00
19	9.15E+00	8.26E+00	8.07E+00
20	9.15E+00	8.26E+00	8.07E+00

Calculated chemical shifts

Point	Ha/b	Hc	Hd
1	9.22E+00	8.25E+00	7.93E+00
2	9.20E+00	8.25E+00	7.97E+00
3	9.19E+00	8.26E+00	8.01E+00
4	9.18E+00	8.26E+00	8.03E+00
5	9.17E+00	8.26E+00	8.05E+00
6	9.17E+00	8.26E+00	8.06E+00
7	9.16E+00	8.27E+00	8.06E+00
8	9.16E+00	8.26E+00	8.06E+00
9	9.16E+00	8.26E+00	8.06E+00
10	9.16E+00	8.26E+00	8.07E+00
11	9.15E+00	8.26E+00	8.07E+00
12	9.15E+00	8.26E+00	8.07E+00
13	9.15E+00	8.26E+00	8.07E+00
14	9.15E+00	8.26E+00	8.07E+00
15	9.15E+00	8.26E+00	8.07E+00
16	9.15E+00	8.26E+00	8.07E+00
17	9.15E+00	8.26E+00	8.07E+00
18	9.15E+00	8.26E+00	8.07E+00
19	9.15E+00	8.26E+00	8.07E+00
20	9.15E+00	8.26E+00	8.07E+00

Chemical shifts for each nucleus

species	Ha/b	Hc	Hd
2a	9.22E+00	8.25E+00	7.93E+00
(ReO_4^-)(**2a**)	9.16E+00	8.27E+00	8.08E+00
(ReO_4^-)$_2$(**2a**)	9.12E+00	8.25E+00	8.06E+00

Converged in 1 iterations with sigma = 0.749908

	value	standard deviation	Comments
1 log beta((ReO_4^-)(**2a**))	3.8876	0.0582	3.89(6)
2 log beta((ReO_4^-)$_2$(**2a**))	6.0026	0.2519	6.0(3)

Correlation coefficients between stability constants. Numbering as above

2 0.7668
1

For the binding isotherms of **2a** of replicate 1, see Section 2.3.4.

2a and TBA ReO_4^- (Replicate 2)

2a (Exp.2)

Species	Log beta	ReO_4^-	**2a**	
1	3.854	1	1	refine
2	6.0594	2	1	refine

Species concentrations/mol dm-3

Point	T(ReO_4^-)	T(**2a**)	F(ReO_4^-)	F(**2a**)	species 1	species 2
1	0.00E+00	1.55E-03	5.45E-91	1.55E-03	6.04E-90	5.28E-178
2	5.13E-04	1.55E-03	5.70E-05	1.10E-03	4.48E-04	4.10E-06
3	9.89E-04	1.55E-03	1.52E-04	7.34E-04	7.98E-04	1.95E-05
4	1.43E-03	1.55E-03	3.03E-04	4.74E-04	1.03E-03	4.99E-05
5	1.84E-03	1.55E-03	5.10E-04	3.14E-04	1.14E-03	9.36E-05
6	2.22E-03	1.55E-03	7.51E-04	2.21E-04	1.19E-03	1.43E-04
7	2.58E-03	1.55E-03	1.01E-03	1.66E-04	1.19E-03	1.92E-04
8	2.92E-03	1.55E-03	1.26E-03	1.31E-04	1.18E-03	2.39E-04
9	3.24E-03	1.55E-03	1.51E-03	1.08E-04	1.16E-03	2.82E-04
10	3.53E-03	1.55E-03	1.75E-03	9.11E-05	1.14E-03	3.20E-04
11	4.08E-03	1.55E-03	2.21E-03	6.94E-05	1.09E-03	3.88E-04
12	4.57E-03	1.55E-03	2.63E-03	5.60E-05	1.05E-03	4.43E-04
13	5.00E-03	1.55E-03	3.01E-03	4.72E-05	1.01E-03	4.90E-04
14	5.40E-03	1.55E-03	3.36E-03	4.08E-05	9.81E-04	5.29E-04
15	5.76E-03	1.55E-03	3.68E-03	3.62E-05	9.52E-04	5.63E-04
16	6.09E-03	1.55E-03	3.98E-03	3.26E-05	9.27E-04	5.92E-04
17	6.40E-03	1.55E-03	4.26E-03	2.97E-05	9.04E-04	6.18E-04
18	6.67E-03	1.55E-03	4.51E-03	2.74E-05	8.84E-04	6.40E-04
19	6.93E-03	1.55E-03	4.74E-03	2.56E-05	8.66E-04	6.60E-04
20	7.17E-03	1.55E-03	4.96E-03	2.40E-05	8.50E-04	6.77E-04

Measured chemical shifts

Point	Ha/b	Hc	Hd
1	9.22E+00	8.25E+00	7.93E+00
2	9.20E+00	8.25E+00	7.98E+00
3	9.19E+00	8.26E+00	8.01E+00
4	9.18E+00	8.26E+00	8.03E+00
5	9.17E+00	8.26E+00	8.05E+00
6	9.17E+00	8.27E+00	8.05E+00
7	9.16E+00	8.27E+00	8.06E+00
8	9.16E+00	8.27E+00	8.06E+00
9	9.16E+00	8.27E+00	8.06E+00
10	9.16E+00	8.26E+00	8.07E+00
11	9.16E+00	8.26E+00	8.07E+00
12	9.15E+00	8.26E+00	8.07E+00
13	9.15E+00	8.26E+00	8.07E+00
14	9.15E+00	8.26E+00	8.07E+00
15	9.15E+00	8.26E+00	8.07E+00
16	9.15E+00	8.26E+00	8.07E+00
17	9.15E+00	8.26E+00	8.07E+00
18	9.15E+00	8.26E+00	8.07E+00
19	9.15E+00	8.26E+00	8.07E+00
20	9.15E+00	8.26E+00	8.07E+00

Calculated chemical shifts

Point	Ha/b	Hc	Hd
1	9.22E+00	8.25E+00	7.93E+00
2	9.20E+00	8.25E+00	7.97E+00
3	9.19E+00	8.26E+00	8.01E+00
4	9.18E+00	8.26E+00	8.03E+00
5	9.17E+00	8.26E+00	8.05E+00
6	9.17E+00	8.27E+00	8.06E+00
7	9.16E+00	8.27E+00	8.06E+00
8	9.16E+00	8.27E+00	8.06E+00
9	9.16E+00	8.27E+00	8.06E+00
10	9.16E+00	8.27E+00	8.07E+00
11	9.16E+00	8.26E+00	8.07E+00
12	9.15E+00	8.26E+00	8.07E+00
13	9.15E+00	8.26E+00	8.07E+00
14	9.15E+00	8.26E+00	8.07E+00
15	9.15E+00	8.26E+00	8.07E+00
16	9.15E+00	8.26E+00	8.07E+00
17	9.15E+00	8.26E+00	8.07E+00
18	9.15E+00	8.26E+00	8.07E+00

19	9.15E+00	8.26E+00	8.07E+00
20	9.15E+00	8.26E+00	8.07E+00

Chemical shifts for each nucleus

species	Ha/b	Hc	Hd
2a	9.22E+00	8.25E+00	7.93E+00
(ReO_4^-)(**2a**)	9.16E+00	8.27E+00	8.08E+00
(ReO_4^-)$_2$(**2a**)	9.13E+00	8.25E+00	8.06E+00

Converged in 11 iterations with sigma = 0.852949

	value	standard deviation	Comments
1 log beta((ReO_4^-)(**2a**))	3.854	0.0667	3.85(7)
2 log beta((ReO_4^-)$_2$(**2a**))	6.0594	0.2604	6.1(3)

Correlation coefficients between stability constants. Numbering as above

2 0.7736
1

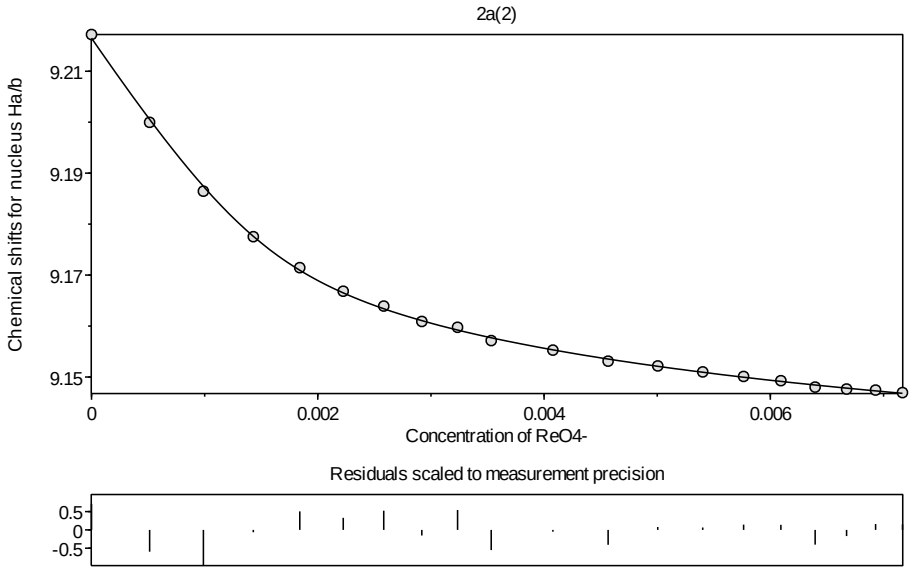

Figure 2.50 Binding isotherm following proton Ha/b on **2a** with increasing ReO_4^- concentration (replicate 2).

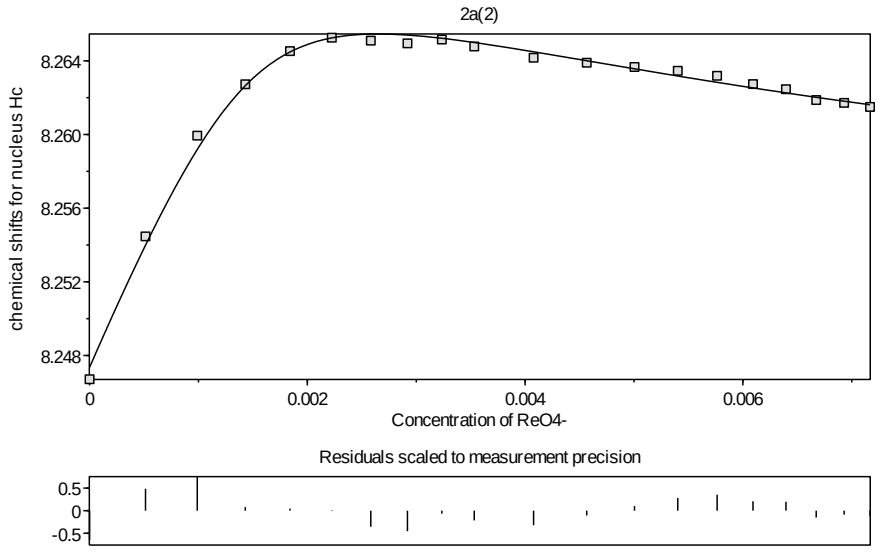

Figure 2.51 Binding isotherm following proton Hc on **2a** with increasing ReO_4^- concentration (replicate 2).

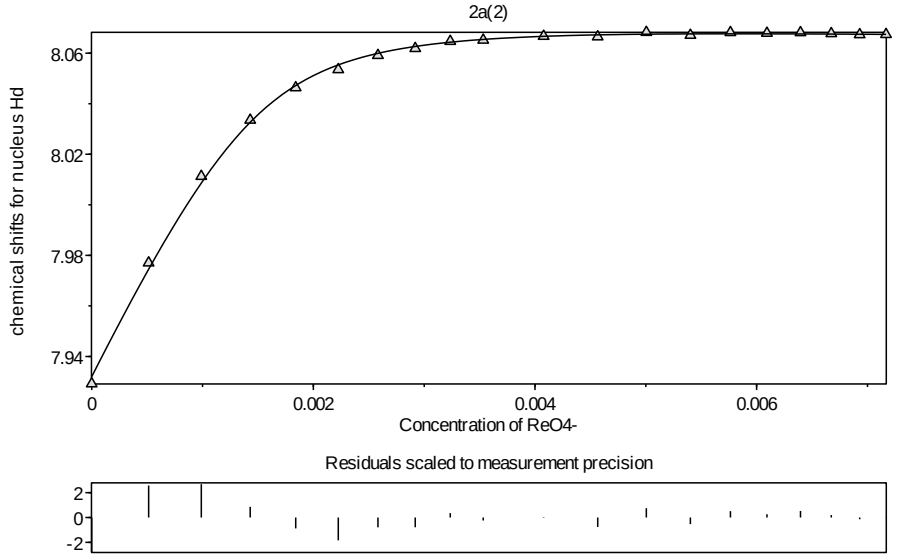

Figure 2.52 Binding isotherm following proton Hd on **2a** with increasing ReO_4^- concentration (replicate 2).

2a and TBA ReO_4^- (Replicate 3)

2a (Exp. 3)

Species	Log beta	ReO_4^-	**2a**	
1	3.8638	1	1	refine
2	6.0193	2	1	refine

Species concentrations/mol dm^{-3}

Point	T(ReO_4^-)	T(**2a**)	F(ReO_4^-)	F(**2a**)	species 1	species 2
1	0.00E+00	1.55E-03	5.37E-91	1.55E-03	6.09E-90	4.68E-178
2	5.13E-04	1.55E-03	5.61E-05	1.10E-03	4.50E-04	3.61E-06
3	9.89E-04	1.55E-03	1.50E-04	7.31E-04	8.04E-04	1.73E-05
4	1.43E-03	1.55E-03	3.03E-04	4.69E-04	1.04E-03	4.49E-05
5	1.84E-03	1.55E-03	5.13E-04	3.09E-04	1.16E-03	8.50E-05
6	2.22E-03	1.55E-03	7.59E-04	2.17E-04	1.20E-03	1.31E-04
7	2.58E-03	1.55E-03	1.02E-03	1.63E-04	1.21E-03	1.77E-04
8	2.92E-03	1.55E-03	1.28E-03	1.29E-04	1.20E-03	2.20E-04
9	3.24E-03	1.55E-03	1.53E-03	1.06E-04	1.19E-03	2.60E-04
10	3.53E-03	1.55E-03	1.78E-03	8.98E-05	1.17E-03	2.96E-04
11	4.08E-03	1.55E-03	2.24E-03	6.87E-05	1.12E-03	3.59E-04
12	4.57E-03	1.55E-03	2.66E-03	5.58E-05	1.08E-03	4.12E-04
13	5.00E-03	1.55E-03	3.04E-03	4.71E-05	1.05E-03	4.56E-04
14	5.40E-03	1.55E-03	3.40E-03	4.09E-05	1.02E-03	4.94E-04
15	5.76E-03	1.55E-03	3.72E-03	3.63E-05	9.89E-04	5.26E-04
16	6.09E-03	1.55E-03	4.02E-03	3.28E-05	9.64E-04	5.54E-04
17	6.40E-03	1.55E-03	4.29E-03	3.00E-05	9.42E-04	5.79E-04
18	6.67E-03	1.55E-03	4.55E-03	2.78E-05	9.23E-04	6.01E-04
19	6.93E-03	1.55E-03	4.78E-03	2.59E-05	9.06E-04	6.20E-04
20	7.17E-03	1.55E-03	5.00E-03	2.43E-05	8.90E-04	6.37E-04

Measured chemical shifts

Point	Ha/b	Hc	Hd
1	9.22E+00	8.25E+00	7.93E+00
2	9.20E+00	8.25E+00	7.98E+00
3	9.19E+00	8.26E+00	8.01E+00
4	9.18E+00	8.26E+00	8.03E+00
5	9.17E+00	8.26E+00	8.05E+00
6	9.17E+00	8.27E+00	8.05E+00
7	9.16E+00	8.27E+00	8.06E+00
8	9.16E+00	8.27E+00	8.06E+00
9	9.16E+00	8.27E+00	8.06E+00
10	9.16E+00	8.26E+00	8.06E+00
11	9.16E+00	8.26E+00	8.07E+00
12	9.15E+00	8.26E+00	8.07E+00
13	9.15E+00	8.26E+00	8.07E+00

14	9.15E+00	8.26E+00	8.07E+00
15	9.15E+00	8.26E+00	8.07E+00
16	9.15E+00	8.26E+00	8.07E+00
17	9.15E+00	8.26E+00	8.07E+00
18	9.15E+00	8.26E+00	8.07E+00
19	9.15E+00	8.26E+00	8.07E+00
20	9.15E+00	8.26E+00	8.07E+00

Calculated chemical shifts

Point	Ha/b	Hc	Hd
1	9.22E+00	8.25E+00	7.93E+00
2	9.20E+00	8.25E+00	7.97E+00
3	9.19E+00	8.26E+00	8.01E+00
4	9.18E+00	8.26E+00	8.03E+00
5	9.17E+00	8.26E+00	8.05E+00
6	9.17E+00	8.26E+00	8.06E+00
7	9.16E+00	8.27E+00	8.06E+00
8	9.16E+00	8.27E+00	8.06E+00
9	9.16E+00	8.27E+00	8.06E+00
10	9.16E+00	8.26E+00	8.07E+00
11	9.16E+00	8.26E+00	8.07E+00
12	9.15E+00	8.26E+00	8.07E+00
13	9.15E+00	8.26E+00	8.07E+00
14	9.15E+00	8.26E+00	8.07E+00
15	9.15E+00	8.26E+00	8.07E+00
16	9.15E+00	8.26E+00	8.07E+00
17	9.15E+00	8.26E+00	8.07E+00
18	9.15E+00	8.26E+00	8.07E+00
19	9.15E+00	8.26E+00	8.07E+00
20	9.15E+00	8.26E+00	8.07E+00

Chemical shifts for each nucleus

species	Ha/b	Hc	Hd
2a	9.22E+00	8.25E+00	7.93E+00
(ReO_4^-)(**2a**)	9.16E+00	8.27E+00	8.08E+00
(ReO_4^-)$_2$(**2a**)	9.12E+00	8.25E+00	8.06E+00

Converged in 11 iterations with sigma = 0.815066

	value	standard deviation	Comments
1 log beta((ReO_4^-)(**2a**))	3.8638	0.0632	3.86(6)
2 log beta((ReO_4^-)$_2$(**2a**))	6.0193	0.2612	6.0(3)

Correlation coefficients between stability constants. Numbering as above

2 0.7716
1

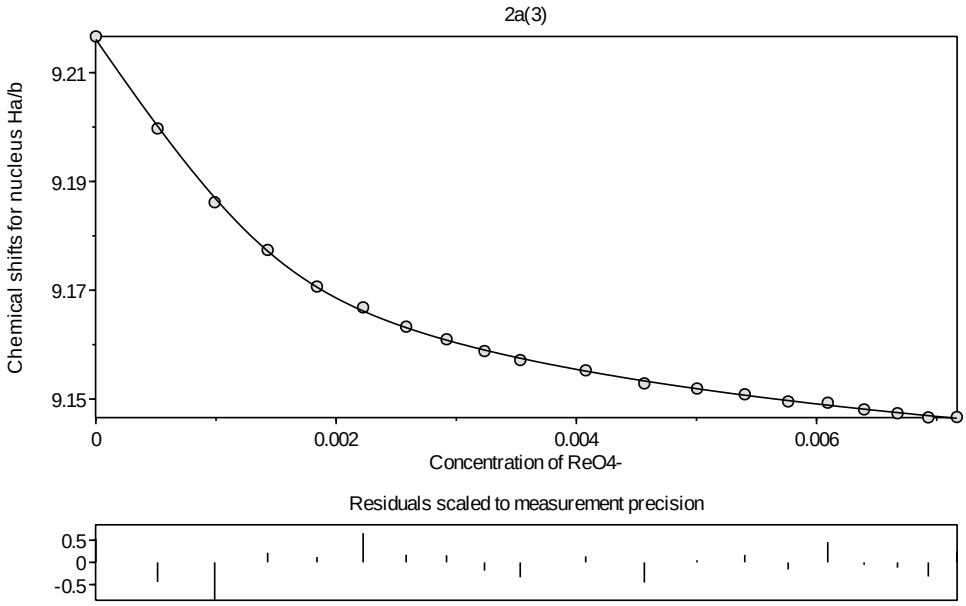

Figure 2.53 Binding isotherm following proton Ha/b on **2a** with increasing ReO_4^- concentration (replicate 3).

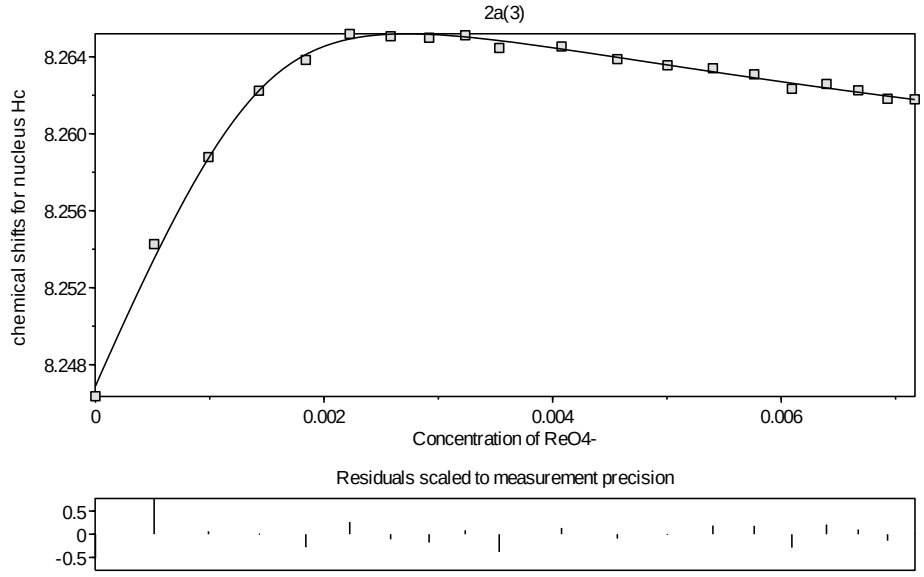

Figure 2.54 Binding isotherm following proton Hc on **2a** with increasing ReO_4^- concentration (replicate 3).

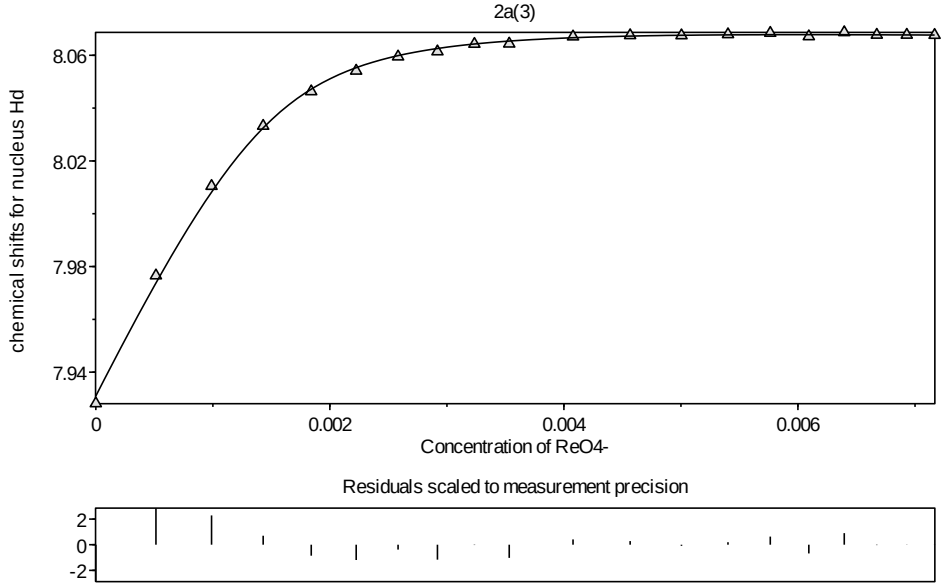

Figure 2.55 Binding isotherm following proton Hd on **2a** with increasing ReO_4^- concentration (replicate 3).

2.4.3 X-Ray Crystallographic Data

Receptors **1b** and **2b** (0.001 g each) were dissolved in 1 mL of CH_3OH in 10 × 75 mm test tubes. TBA ReO_4^- (0.0005g) was added to the test tubes. For **1b**, DMF (0.5 mL) was added for solubility. The test tubes were placed in a scintillation vials filled with Et_2O. After two days, yellow (**1b**$^{2+}$•2ReO_4^-) or colorless (**2b**$^{2+}$•2ReO_4^-) crystals were harvested for single-crystal X-ray diffraction studies. Refer to .cif files for exact structural details.

X-ray diffraction data for **1b** were collected at 150 K and for **2b** at 100 K. Data were collected on a Bruker D8 Venture using MoKα-radiation (λ = 0.71073 Å). Data have been corrected for absorption using the SADABS[157] area detector absorption correction program. Using Olex2, the structure was solved with the ShelXT structure solution program using Direct Methods and refined with the ShelXL refinement package using least squares minimization. All non-hydrogen atoms were refined with anisotropic thermal parameters. Hydrogen atoms were refined in calculated positions in a ridged group model with isotropic thermal parameters U(H) = 1.2Ueq (C) for all C(H) groups and U(H)=1.5Ueq (C) for all C(H,H,H) groups. Calculations and refinement of structures were carried out using APEX2, SHELXTL,[158] and Olex2 software.

After refinement, both **1b** and **2b** continued to display a number of residual Q peaks greater than 1.0 e Å^{-3}—all of which were observed less than 1 Å from the large atoms (I or Re) regardless of the absorption correction applied. These Q peaks should be regarded as artifacts from these heavy atoms.

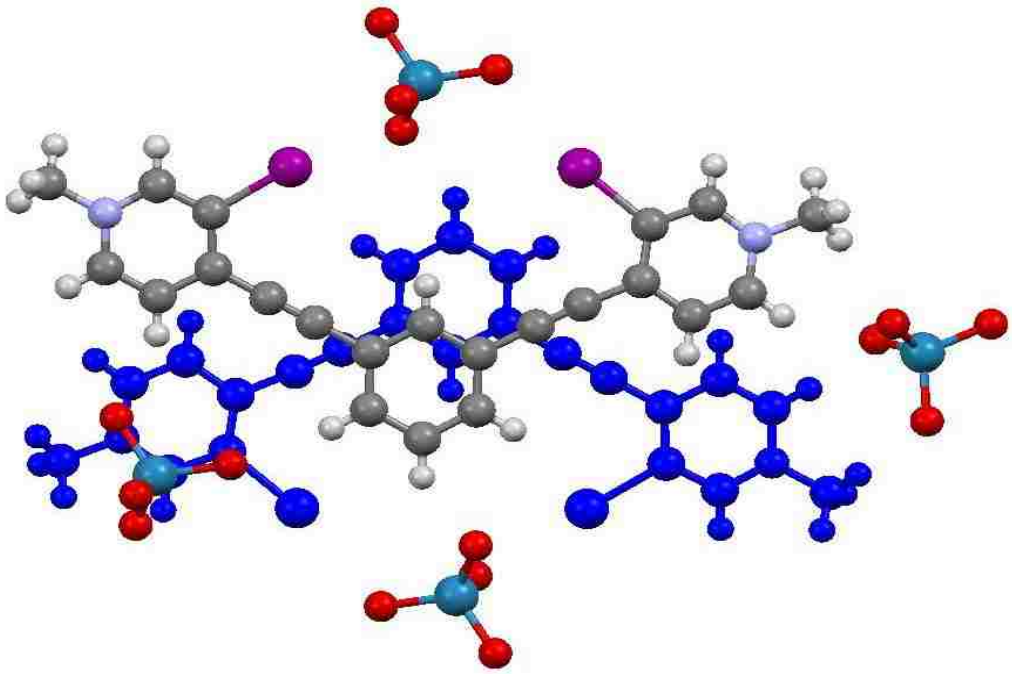

Figure 2.56 Crystal packing of $\mathbf{1b}^{2+}\bullet 2ReO_4^-$.

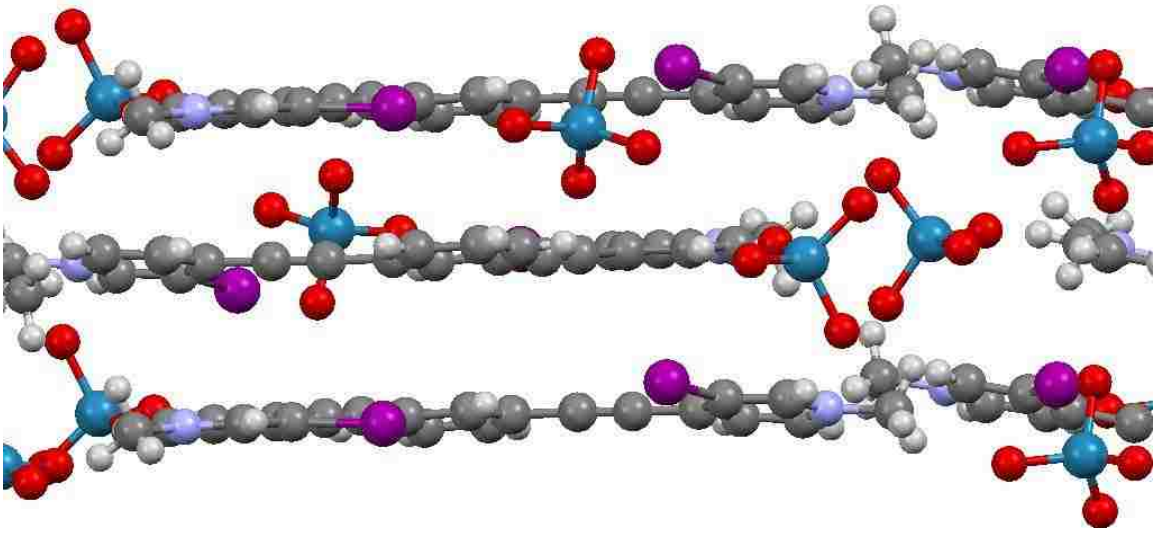

Figure 2.57 Crystal packing of $\mathbf{1b}^{2+}\bullet 2ReO_4^-$.

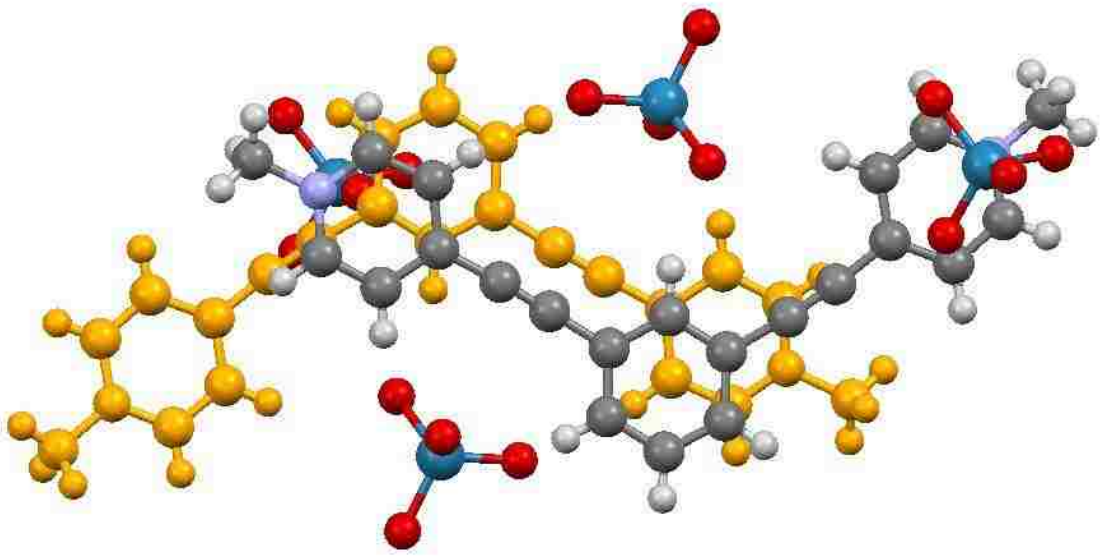

Figure 2.58 Crystal packing of $\mathbf{2b}^{2+}\bullet 2ReO_4^-$.

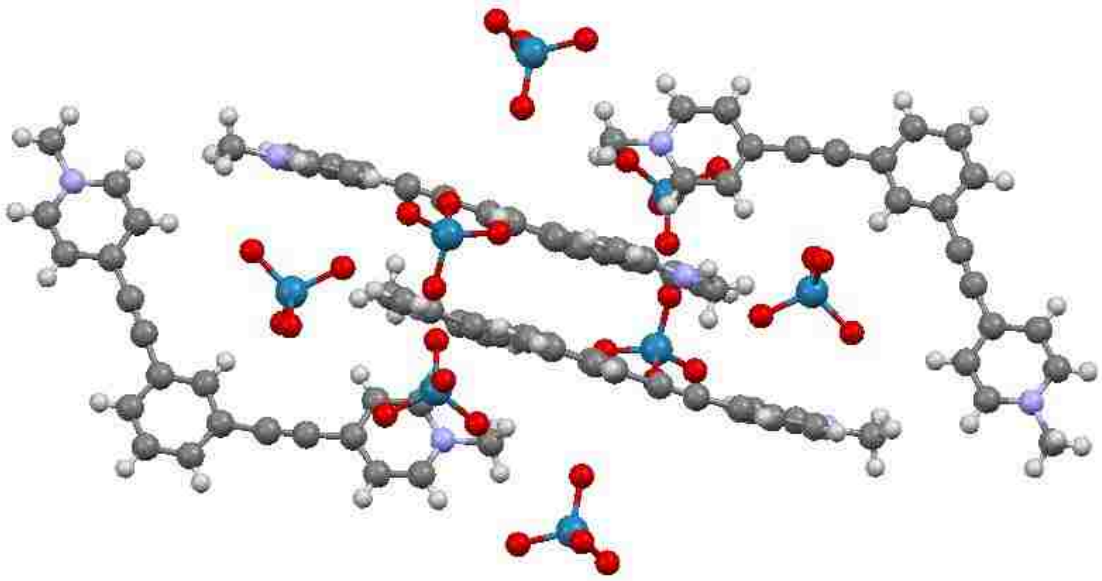

Figure 2.59 Crystal packing of $\mathbf{2b}^{2+}\bullet 2ReO_4^-$.

2.5 Conclusion and Bridge to Chapter 3

The earliest quantification of halogen bonding and CH hydrogen bonding to ReO_4^- in solution and their corresponding bidentate/tridentate complexation in the solid state have been reported. The enhanced association of **1a** to ReO_4^- when compared directly to a nearly isostructural and potent CH-hydrogen-bonding molecule validates the place of halogen bonding alongside hydrogen bonding in an ongoing effort to design rational and selective receptors for ReO_4^- and TcO_4^-. Future work with **1a** and **2a** will include liquid-liquid extraction of ReO_4^- from aqueous phase and exploration of halogen bonding and CH hydrogen bonding with other anionic guests.

The *m*-arylene-ethynylene three-mer provided invaluable insights. The binding cavity of the receptor decidedly favored larger anions. But perhaps the most instructive information was a lesson in entropy. Facile rotation about the alkynyl-aromatic C–C bonds increased the entropic penalty associated with a bidentate conformation. Later, Riel et al. demonstrated that rigidification of the bidentate conformation through hydrogen bonding increased halide-ion affinity by an order of magnitude.[142]

Another strategy to bias a high-affinity conformation is through molecular folding. As we have seen with other *m*-arylene-ethynylene oligomers, helical folding is stabilized by solvophobic forces, π-π stacking, and host-guest interactions. This dissertation introduces a new host-guest interaction, halogen bonding. In the next chapter, the design and synthesis of the first halogen-bonding *m*-arylene-ethynylene oligomer will be presented. Furthermore, the self-assembly of the first I^--encapsulating multi-strand anion helicate will be characterized in solution and the solid state.

3 A Halogen-Bond-Induced Triple Helicate Encapsulates I^-

3.1 Abstract and Artwork

The self-assembly of higher-order anion helicates in solution remains an elusive goal. Herein, we present the first triple helicate to encapsulate I^- in organic and aqueous media as well as the solid state. The triple helicate self-assembles from three tricationic *m*-arylene-ethynylene strands and resembles a tubular anion channel lined with nine halogen bond donors. Eight strong CI···I^- halogen bonds and numerous buried π-surfaces endow the triplex with remarkable stability, even at elevated temperatures. We suggest that the natural rise of a single-strand helix renders its linear halogen-bond donors non-convergent. Thus, the stringent linearity of halogen bonding is a powerful tool for the synthesis of multi-strand anion helicates.

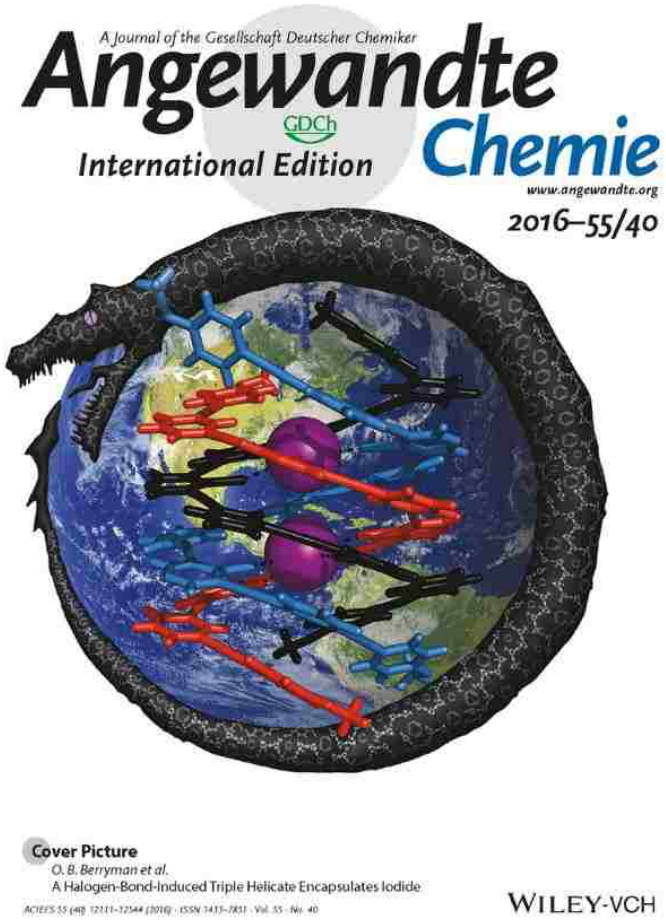

Figure 3.1 Cover artwork for *Angewandte Chemie International Edition* publication. Like Jörmungandr—the World Serpent of Norse mythology that encircled Midgard—*m*-arylene-ethynylene oligomers envelop their guests with halogen bonds. Massena et al. present the first halogen-bond-induced triple helicate to encapsulate I^- in solution and the solid state. Strong and linear halogen bonds promote this intricate and robust self-assembly. Garron Hale (Univ. of Oregon) is gratefully acknowledged for assisting with preparation of the cover artwork.

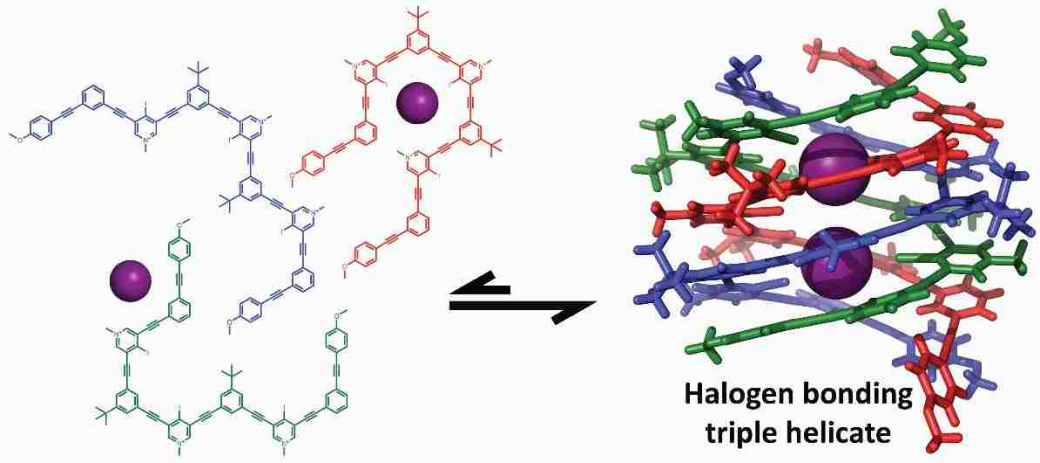

Figure 3.2 Table of contents artwork for *Angewandte Chemie International Edition* publication.

3.2 Introduction

This chapter includes work that was published in *Angewandte Chemie International Edition* (**2016**, 55, 12398–12402) and was co-authored by Dr. Nicholas B. Wageling, Daniel A. Decato, Enrique Martin Rodríguez, Ari M. Rose, and Dr. Orion B. Berryman. Dr. Wageling characterized most of the novel compounds and wrote much of the synthesis and characterization sections of the Supporting Information for the publication. Decato collected and refined the X-ray crystallographic data. Martin Rodríguez helped with the synthesis of some of the precursor molecules and obtained the melting points of novel compounds. Rose conducted the DFT calculations. Dr. Berryman helped with data interpretation and edited all publication materials. Massena, the first author, conceived of the project, designed the oligomers, synthesized all of the compounds, grew X-ray quality crystals, characterized all of the supramolecular complexes in solution, interpreted the data, wrote the manuscript, wrote the Supporting

Information (except the sections stated above) for the publication, and created the cover artwork.

The helical folding of a molecule confers extraordinary higher-order structure and function. Examples are rife in nature, ranging from the structural role of collagen to the safeguarding of genetic information in polynucleotides. By implementing this privileged molecular pattern, cation- and neutral-guest-induced helicates/foldamers (see Sections 1.2–1.4) have led to myriad applications, including biomolecular and chiral recognition, supramolecular catalysis, and materials. In contrast, the progression of anion helicates, especially those involving multiple strands, has lagged. This delay is understandable given the complexities of guest-induced helical folding, which are magnified by the high solvation energies and variable coordination geometries of anions. To date, a small but growing number of single-strand anion helicates/foldamers have been synthesized and investigated. However, only a handful of hydrogen-bonding solution-phase duplexes have been developed. Wu et al. have produced the only other anion triplexes, which enfolded two PO_4^{3-}s within bis(biurea) ligands (see Section 1.5 for a review of anion helicates/foldamers). Herein, we describe an alternative approach to assemble higher-order anion helicates. Exploiting the stringent linearity of halogen bonding, the first triple helicate to bind I^- in solution and in the solid state is presented. This cylindrical structure self-assembles from three *m*-arylene-ethynylene strands that encircle two I^- anions with halogen bonds. The helix demonstrates remarkable stability at high temperatures and in aqueous and organic solvents. The linearity of halogen bonding facilitates multi-strand complexation and offers a tractable approach to self-assemble large tubular containers with high affinity for complementary anions.

During the last two decades, halogen-bonding molecular hosts have evolved with increasing sophistication, while crystallographic, gas-phase, and biomolecular investigations have continued to refine our understanding of this emerging noncovalent interaction.[113–127] A halogen bond is an attractive interaction between an electrophilic region of a halogen atom and a nucleophilic region of an atomic or molecular entity.[159] Although analogous to hydrogen bonding with regard to strength, the halogen bond is far more directional (the angle R–X···Y tends to be close to 180 °, where X is a halogen, R a covalently bound group, and Y the halogen-bond acceptor).

3.3 Results and Discussion

3.3.1 Design and Synthesis of Nonameric *m*-Arylene-Ethynylene Oligomers

Recently, we synthesized a bidentate halogen-bonding receptor (**1**) that demonstrated notable affinity for ReO_4^- in solution and the solid state (Scheme 3.1). Receptor **1** employed two convergent 3-iodopyridinium halogen-bond donors that extended from a 1,3-diethynylbenzene core. Expanding on this design, we envisioned an oligomer with three 4-iodopyridinium halogen-bond donors spaced by two 1-*tert*-butyl-3,5-diethynylbenzene groups and capped with two 4-methoxytolan groups. Design principles were drawn from Moore's seminal work with *m*-phenylene-ethynylene foldamers (see Section 1.4) and Flood's elegant Cl^--encapsulating double foldamer[104] to encourage the favorable π-π stacking of alternating electron-deficient and electron-rich aromatic rings. Our departure from previous work is the strategic placement of inwardly directed halogen-bond donors.

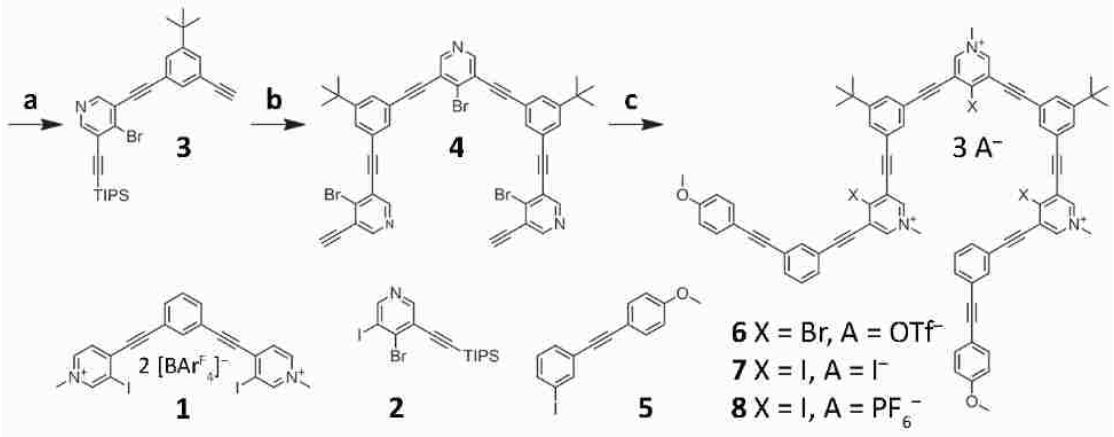

Scheme 3.1 Synthesis of the bromo- and iodopyridinium nine-mers. Reagents and conditions: (a) **2**, 1-*tert*-butyl-3,5-diethynylbenzene, $PdCl_2(PPh_3)_2$, CuI, Et_3N, DMF, RT, 12 h, 21 %; (b) 4-bromo-3,5-diiodopyridine, $PdCl_2(PPh_3)_2$, CuI, Et_3N, DMF, 50 °C, 12 h, 75 %; then TBAF, THF, 0 °C to RT, 10 min, quantitative; (c) **5**, $PdCl_2(PPh_3)_2$, CuI, Et_3N, DMF, 50 °C, 24 h, 61 %; then methyl OTf^-, DCM, RT, 12 h, 93 % (6); then NaI, 1:3 *v*/*v* DMF-CH_3CN, RT, 12 h, 90 % (7); then $AgPF_6$, 1:1 *v*/*v* DMF-EtOAc, 30 min, RT, 80 % (8).

Synthesis of the *m*-arylene-ethynylene oligomers began with the Sonogashira mono-cross-coupling of known 4-bromo-3,5-diiodopyridine and commercially available (triisopropylsilyl)acetylene to create the monoacetylenated halopyridine **2** (Scheme 3.1). Mono-cross-coupling **2** with known 1-*tert*-butyl-3,5-diethynylbenzene afforded the *m*-arylene-ethynylene dimer **3**. Cross-coupling two equivalents of **3** to 4-bromo-3,5-diiodopyridine followed by removing both triisopropylsilyl protecting groups yielded *m*-arylene-ethynylene pentamer **4**. Synthesis of the 4-methoxytolan cap, **5**, was conducted by mono-cross-coupling of commercially available 4-ethynylanisole and 1,3-diiodobenzene. Cross-coupling two equivalents of **5** to **4** and subsequent alkylation of the bromopyridines with methyl OTf^- resulted in the tricationic bromopyridinium nine-mer

6. Exchange of the halogens (bromine for iodine) and counteranions (OTf^- for I^-) was achieved by stirring **6** with excess NaI, providing the iodopyridinium target, **7** (for further synthetic details, see Section 3.4.1).

3.3.2 Solid-State Characterization

Yellow plates of **7** suitable for X-ray diffraction were grown by the vapor diffusion of MTBE into a 1:2 *v*/*v* DMF-CH_3CN solution of **6** and excess TBAI. Triple helicate **7** crystallized in space group *C*2/*c*, adopting both *M*- and *P*-helical conformations. Each complex is composed of three intertwined tricationic nine-mer strands offset along a common screw axis as defined by the two intrachannel I^-s (Figure 3.3a). Each I^- is bound tightly by four strong and linear halogen bonds within the helical channel (average halogen-bond C$I\cdots I^-$ distance is 3.4 Å, 83 % of ΣvdW radii; average C$I\cdots I^-$ angle is 171 °; intrachannel $I^-\cdots I^-$ distance is 5.1 Å). Consequently, pseudo-square-planar coordination is achieved (Figure 3.3c). The halogen bonds are complemented by numerous aromatic and ethynylene π-π interactions (44 buried aromatic surfaces, Figure 3.3b; average ring-ring distance is ca. 3.7 Å). Additionally, seven I^-s held to the exterior of the helicate by ion-pairing interactions help balance the nine positive charges associated with the cationic strands (Figure 3.37). Each triplex exhibits an approximate height and width of 13 and 19 Å, respectively, and a pitch of 10 Å. Finally, a 2.7 Å pore adorned with halogen-bond donors highlights the unique microenvironment found within the triple helicate (Figures 3.3a–b). The only molecular axis of symmetry (C_2) for the triplex aligns with the CI bond of the non-bonding

iodopyridinium (Figures 3.3a,c, yellow sticks; for further crystallographic details, see Section 3.4.2).

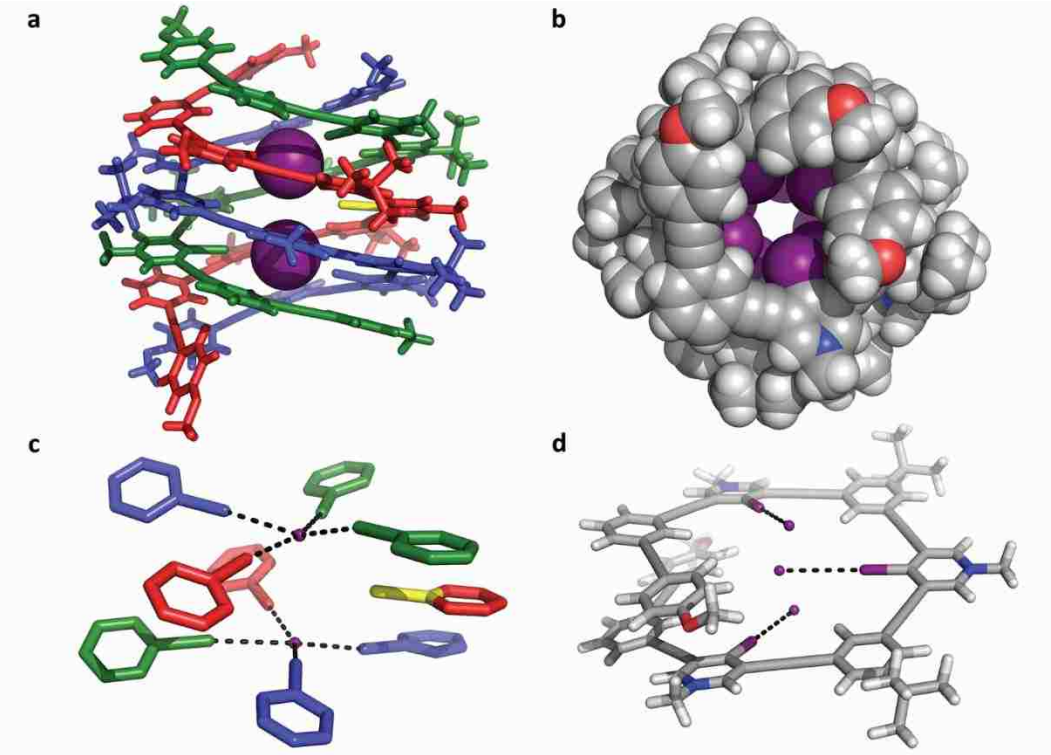

Figure 3.3 Solid-state representations of triple helicate **7** and DFT-minimized nine-mer. (a) Solid-state structure of the triple helicate binding two intrachannel I^-s; (b) crystal structure of the triplex looking down its anion channel (I^-s removed for clarity); (c) pseudo-square-planar coordination geometry of the halogen-bond donors (scaffolding removed; black dashes denote halogen bonds); (d) DFT-minimized nine-mer (**7**; black dashes and I^-s added to emphasize the non-convergence of the halogen-bond donors). (a–c) External I^- atoms removed for clarity; (a) and (c) yellow CX stick demarcates the non-bonding halogen-bond donor and axis of molecular C_2 symmetry (not all colors are representative of atom identity).

3.3.3 Summary of X-Ray Crystallographic Data

Crystallographic Data for **7** $C_{80}H_{61}I_6N_3O_2$, M_r=1857.71, monoclinic, space group *C2/c* (no. 15), *a*=54.1200(19), *b*=36.8537(14), *c*=35.419(2), β=128.1810(10), *V*=55530(5), *Z*=24, *T*=100 K, μ($Cu_{K\alpha}$)=16.102 mm^{-1}, D_{calcd}=1.333 g mL^{-1}, $2\theta_{max}$=101.124, 291827 reflections collected, 29038 unique (R_{int}=0.0668, R_{sigma}=0.0322), R_1=0.0837 ($I>2\sigma(I)$), *wR*2=0.2858 (all data). See Section 3.4.2 for crystallographic details. CCDC 1476727 contains the supplementary crystallographic data for this paper.

3.3.4 DFT Analysis of a Single Strand

To explore the implications of helical rise and halogen-bond linearity, we calculated the conformation of a single strand of **7** using DFT. The added black dashes and I^-s in Figure 3.3d emphasize the poor preorganization of a single strand. I^- was placed in this non-convergent binding pocket, and the energies of both tridentate and bidentate halogen bonding were calculated. Regardless of guest placement, non-bonding or repulsive interactions were inevitable (for computational details, see Section 3.4.3). These calculations suggest that the strict linearity of halogen bonding disfavors 1:1 binding.

3.3.5 Solution-Phase Characterization

The elucidation of triple helicate **7** in solution began with ^{1}H NMR spectroscopic titrations. Compared to the relatively simple ^{1}H NMR spectrum of **6** in DMF-d_7, the

spectrum of triplex **7** suggests a thermodynamically stable aggregate (Figure 3.4a). In contrast, even an excess of TBABr failed to complicate the spectrum of **6** (Figure 3.5).

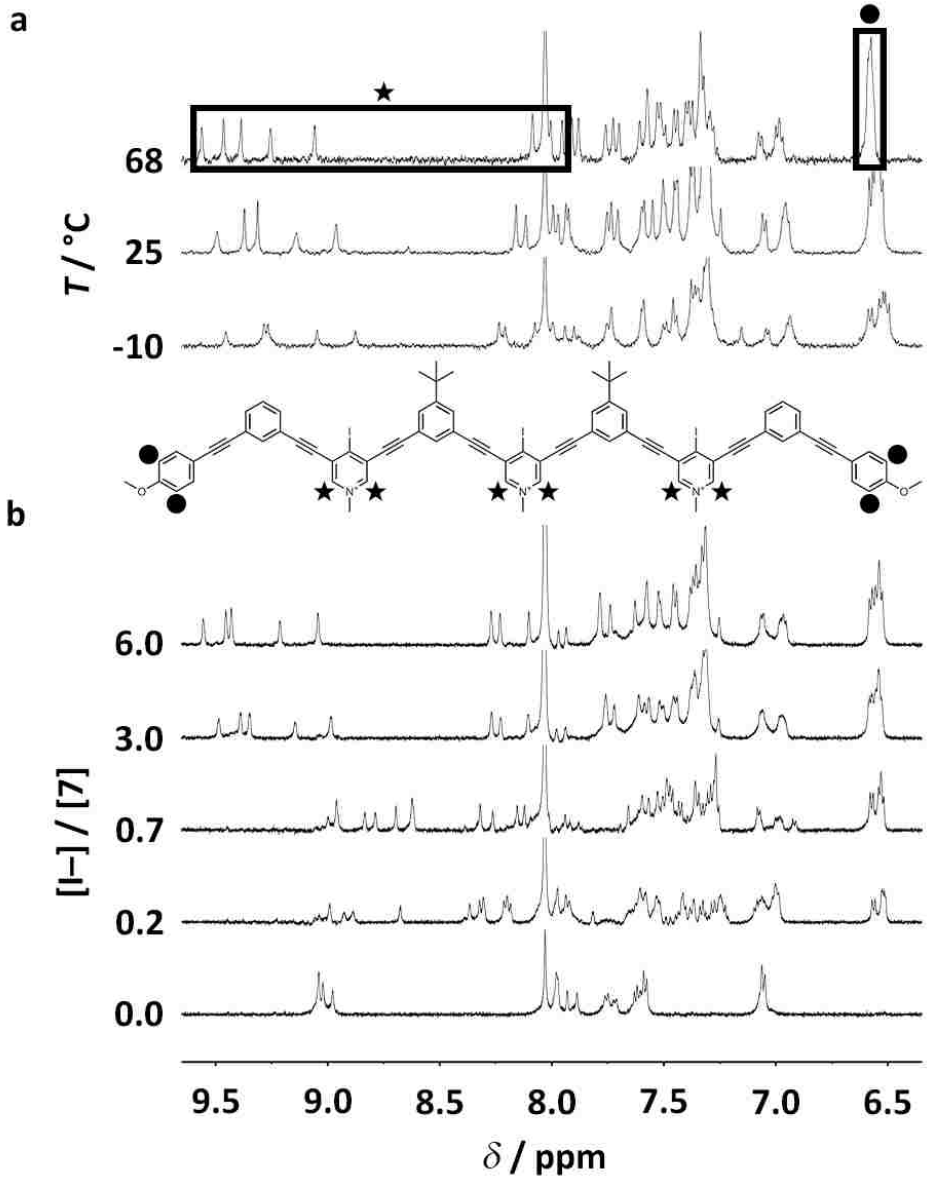

Figure 3.4 Partial ^{1}H NMR variable temperature and titration spectra of **7**. (a) Triple helicate **7** subjected to variable temperature (500 MHz, 1:4 *v*/*v* DMF-d_7-CD_3CN); (b) ^{1}H NMR titration of **8** with TBAI (600 MHz, 1:3 *v*/*v* DMF-d_7-CD_3CN, 298 K).

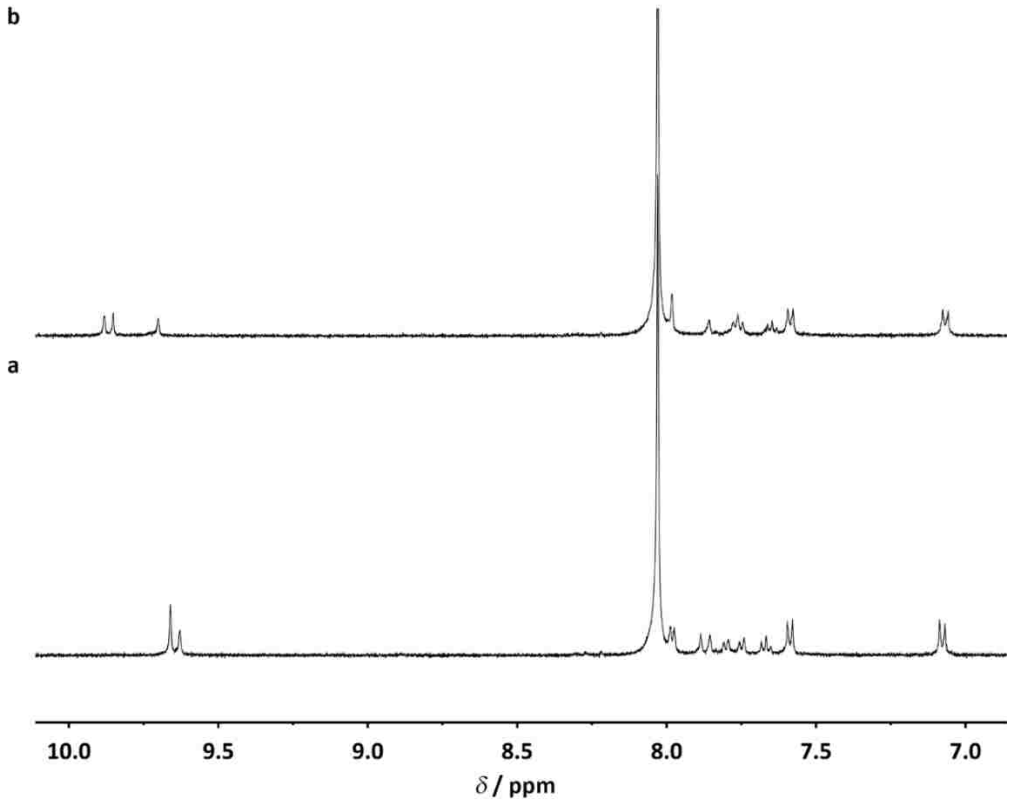

Figure 3.5 ^{1}H NMR spectroscopic titration experiment. (a) ^{1}H NMR spectrum of **6**; (b) ^{1}H NMR spectrum of **6** with excess TBABr. Conditions for (a–b): 500 MHz, DMF-d_7, 298 K.

Given the superior halogen-bonding ability of iodines, these data provided evidence that **7** persisted as a halogen-bond-induced aggregate. Furthermore, adding $AgPF_6$—which precipitated AgI leaving non-coordinating PF_6^- anions—to a solution of **7** resulted in the formation of the random-coil nine-mer, **8** (Figure 3.6). Isolation of the PF_6^- salt, **8**, (Scheme 3.1) permitted the reverse titration, holding the concentration of **8** constant while titrating TBAI. Surprisingly, even 0.2 equiv of guest induced significant complex formation that slowly exchanged with single strands of **7** on the NMR timescale (Figure 3.4b). The aggregate's pyridinium and anisole signals were markedly shifted upfield (up

to –0.79 and –0.54 ppm, respectively; for proton assignments, see Figure 3.44), suggesting significant π-π stacking in solution. With three equivalents of TBAI, the resulting ^{1}H NMR spectrum was analogous to that of **7**, indicating strong halogen bonding in solution (Figure 3.4b).

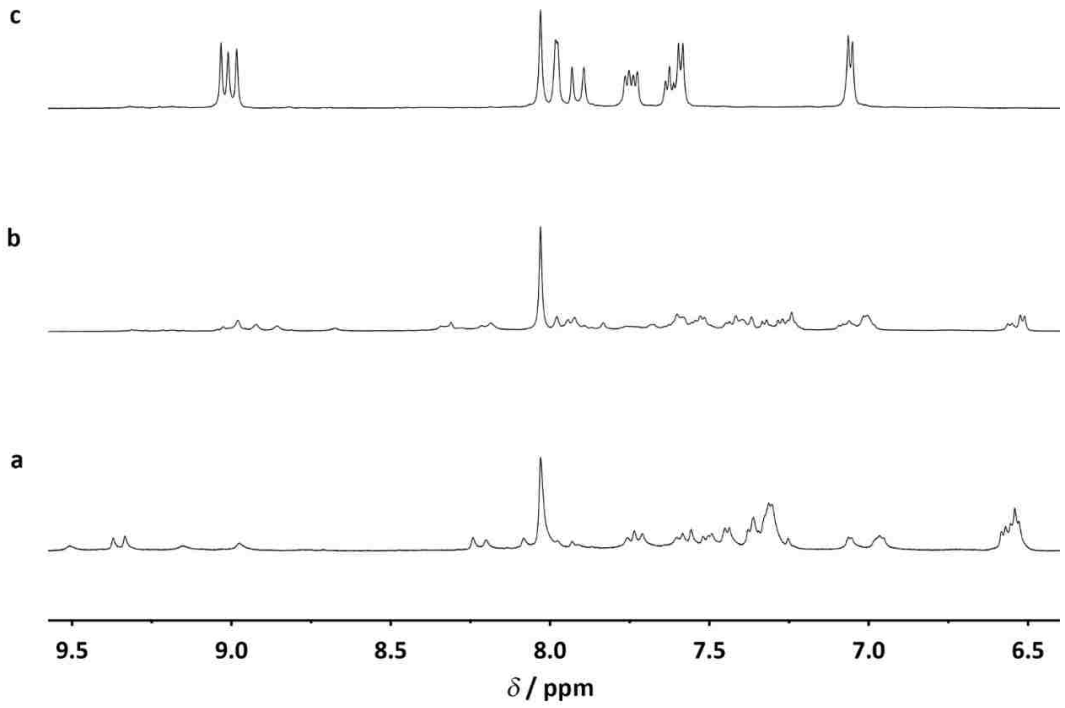

Figure 3.6 ^{1}H NMR spectroscopic titration of **7** with $AgPF_6$. (a) ^{1}H NMR spectrum of **7**; (b) ^{1}H NMR spectrum of **7** with roughly 1.5 equiv of $AgPF_6$; (c) ^{1}H NMR spectrum of **7** with excess $AgPF_6$. Conditions for (a–c): 600 MHz, 1:3 *v*/*v* DMF-d_7-CD_3CN, 298 K.

The 2D NOESY spectrum of triplex **7** provided further evidence of higher-order helication in solution. Strong in-phase cross peaks corresponding to pyridinium methyl and *tert*-butyl signals were consistent with the solid-state structure but impossible for a single strand (over 7 Å apart; Figure 3.7). Likewise, medium in-phase cross peaks

between *tert*-butyl and pyridinium protons as well as *tert*-butylbenzene and pyridinium methyl protons agreed with the X-ray crystal structure but could not originate from a single strand (over 5 and 6 Å apart, respectively).

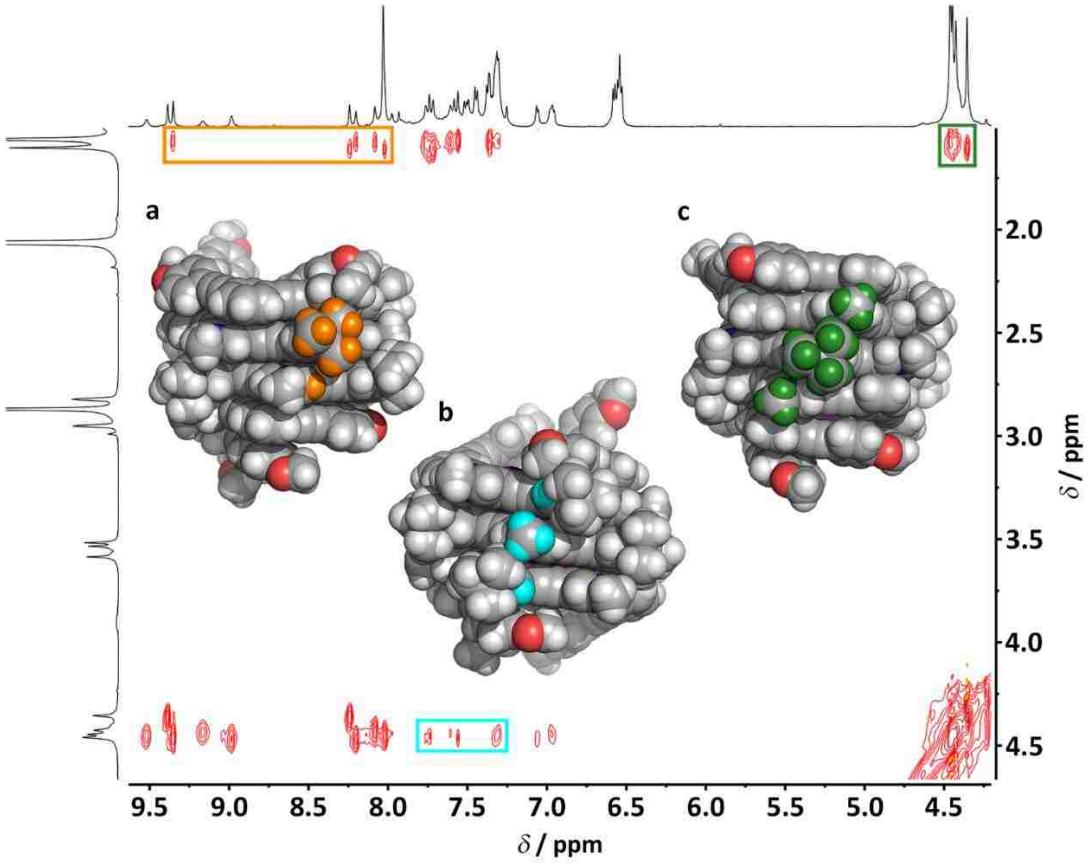

Figure 3.7 ^{1}H 2D NOESY NMR spectrum of triple helicate **7**. (a) *tert*-Butyl and pyridinium cross peaks; (b) *tert*-butylbenzene and pyridinium methyl cross peaks; (c) pyridinium methyl and *tert*-butyl cross peaks. Conditions for (a–c): 600 MHz, 1:3 *v*/*v* DMF-d_7-CD_3CN, 298 K, 400-ms mixing time (not all colors are representative of atom identity).

In stark contrast, the 2D NOESY spectrum of **8** manifested none of these features. Instead, only opposite-phase cross peaks between aromatic protons and same-ring substituents were evident, consistent with random-coil behavior in solution (Figure 3.8).

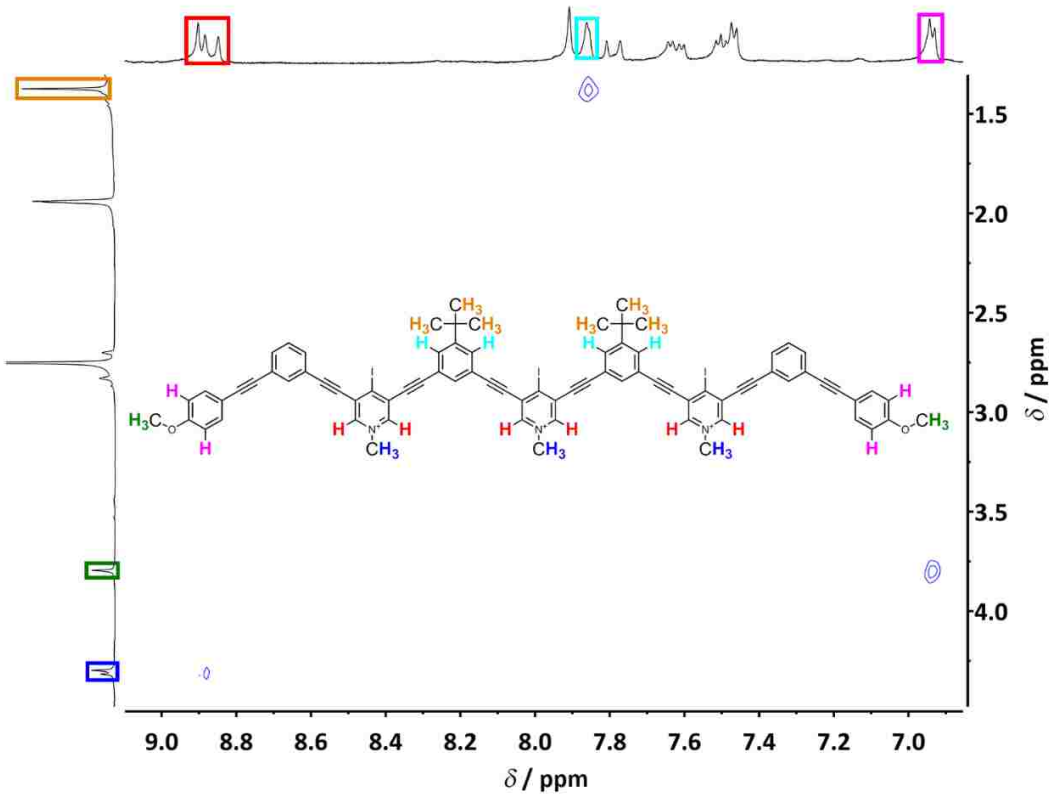

Figure 3.8 ^{1}H 2D NOESY NMR spectrum of **8** (600 MHz, 1:3 *v*/*v* DMF-d_7-CD_3CN, 298 K, 400-ms mixing time).

Further comparisons between the ^{1}H NMR spectrum of **7** and its solid-state structure confirmed triple helicate fidelity in solution. The numbers and intensities of ^{1}H NMR signals corresponding to the solid-state triplex were readily predictable due to its molecular C_2 symmetry (Figure 3.9).

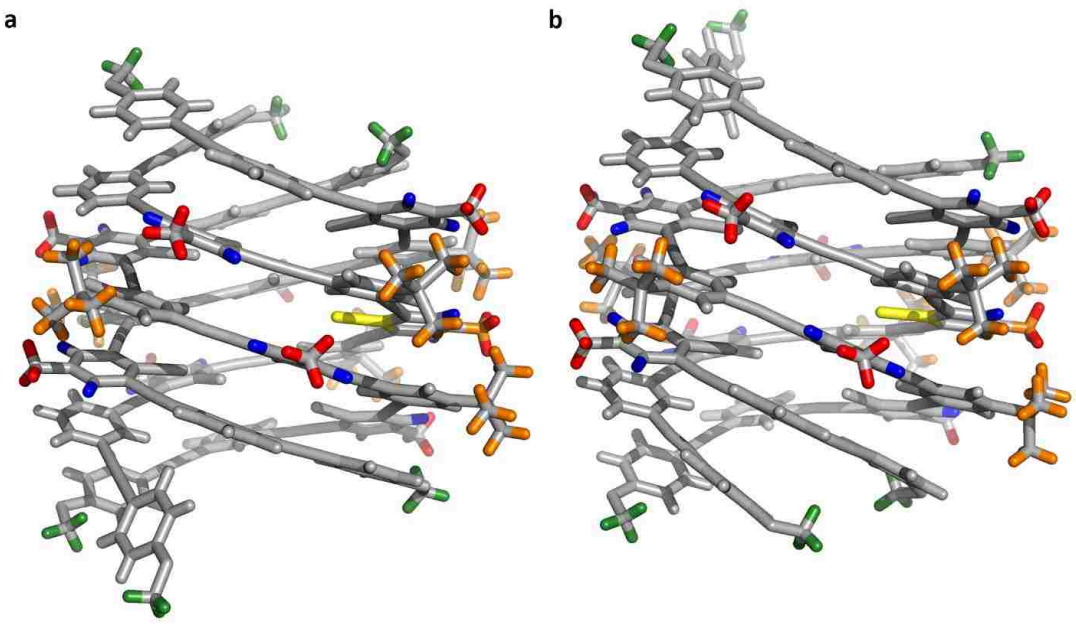

Figure 3.9 (a) Solid-state representation of triple helicate **7** in the starting position; (b) the same structure after a C_2 operation. (a–b) Yellow sticks represent the CX bond of the non-bonding iodopyridinium, which aligns with the complex's axis of molecular C_2 symmetry (not all colors are representative of atom identity).

The spectrum of the triplex should exhibit three *tert*-butyl signals of equal intensity, three methoxy-methyl signals of equal intensities, four equal-intensity pyridinium-methyl signals and one of half intensity, and nine equal-intensity pyridinium signals. The ^{1}H NMR spectrum of **7** is in full agreement with these predictions (Figure 3.10), indicating solution and solid-state structural congruence. Higher or lower order helicates would produce more or fewer ^{1}H NMR signals, and variations in molecular symmetry would result in altered ratios between peak counts and relative intensities.

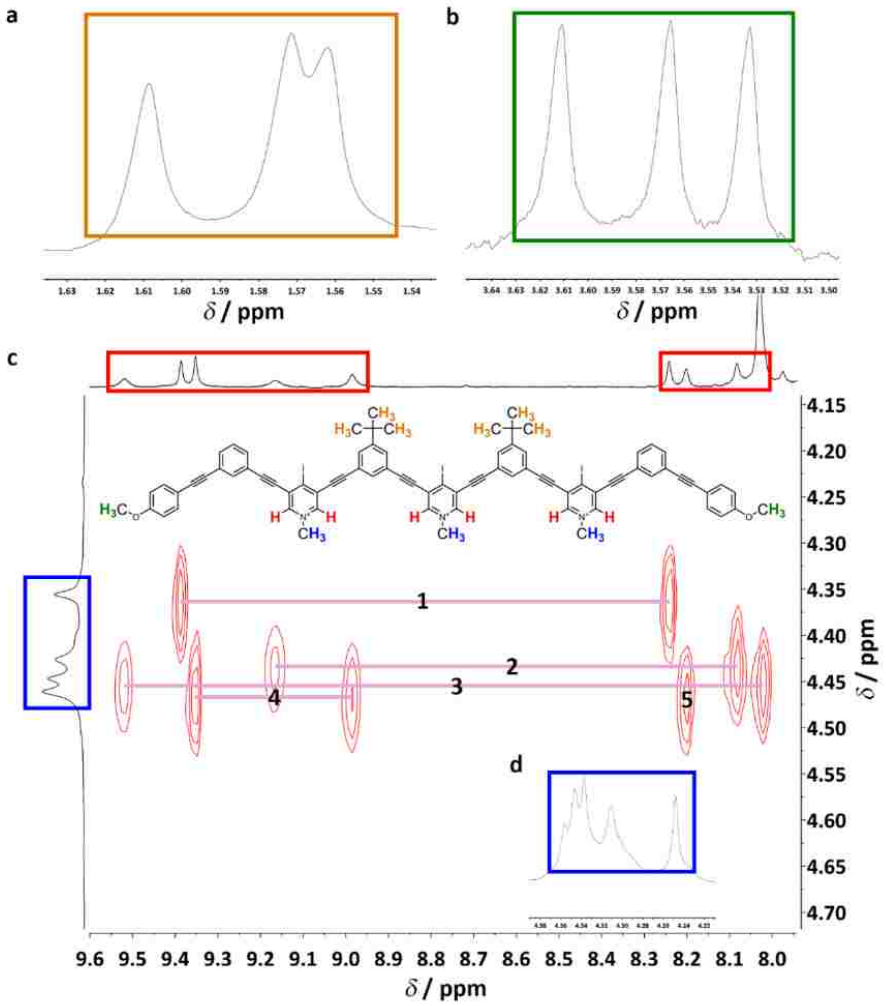

Figure 3.10 ^{1}H NMR and 2D NOESY spectroscopic analysis of the numbers and relative intensities of key resonances of **7**. (a) ^{1}H NMR spectrum of three *tert*-butyl peaks of equal intensity; (b) ^{1}H NMR spectrum of three methoxy-methyl peaks of equal intensity; (c) nine pyridinium protons along the F2 axis are present with their NOEs (one is obscured by the DMF residual solvent peak); ^{1}H NMR spectrum of three resolved pyridinium-methyl peaks of equal intensity (corresponding to the horizontal mauve lines 1–3) and one peak of × 1.5 intensity (4–5); NOEs between pyridinium-methyl and pyridinium resonances elucidate the overlapped components of this peak; pyridinium-methyl peaks corresponding to 1–4 each correlate with one relatively upfield pyridinium peak and one downfield (600 MHz, 298 K, 400-ms mixing time); (d) a better-resolved ^{1}H NMR spectrum displaying four equal pyridinium methyl signals and one of half intensity (400 MHz, 298 K). Conditions for (a–b): 500 MHz, 1:4 *v*/*v* DMF-d_7-CD_3CN, 336 K. Conditions for (c–d): 1:3 *v*/*v* DMF-d_7-CD_3CN.

2D DOSY NMR data were collected to further characterize triple helicate **7** in solution. The ^{1}H NMR resonances of **7** and **8** correlated with discrete D_t lines, verifying that both species were distinct and monodisperse (see Section 3.4.4, Figures 3.47–3.48). Additionally, the r_Hs of **7**, **8**, and an internal standard (CH_2Cl_2) were compared. Not surprisingly, the r_H of **8** was 1.3-times larger than that of the triple helicate. Given the dynamics of **8** in solution, a r_H inclusive of uncoiled conformations is sensible. In contrast, the π-stacked and coiled conformation of **7** would likely result in a smaller r_H. The triple helicate's estimated r_H of 8 Å agrees with the crystallographic dimensions of the complex (for details pertaining to DOSY refinement and analysis, see Section 3.4.4).

Given that most anion multiplexes require either highly charged anions or low temperatures to form in solution, it was remarkable that the helicate proved stable up to 68 °C (the limit of the probe; Figure 3.4a). Surmising that halogen bonds are critical for triple helicate stability, we probed them directly with UV-Vis titrations. The UV-Vis spectra of **8** suggested significant conformational changes upon adding TBAI (Figure 3.49). Gradual depression of the λ = 312 nm π-π* band was observed, consistent with the hypochromic effect of π-stacked *m*-phenylene-ethynylene oligomers.[50] Overall, the absorbance decreased by 22 % after titrating two equivalents of guest. In later studies, it was discovered that at low concentrations of ligand (< 0.5 mM) the triplex became a minor species. Therefore, the observed hypochromicity likely arose from the formation of lower-order folded aggregates. At higher concentrations of **8**, titrating TBAI produced a dark yellow solution associated with the appearance and growth of an absorption band at 400 nm (Figure 3.50). The absorption band is consistent with halogen-bond charge

transfer in solution.[160] Alongside the demonstrated anion switchability of the triplex, these data implicate halogen bonding as a vital component of helicate formation.

To ascertain triple helicate stability in aqueous phase, **7** was subjected to ^{1}H NMR and 2D NOESY spectroscopy in 1:1 *v*/*v* D_2O-DMF-d_7 (the limit of solubility). Aside from differences in chemical shifts, the spectroscopic features of **7** were fully consistent with those identified in organic solvents (Figures 3.11–3.13).

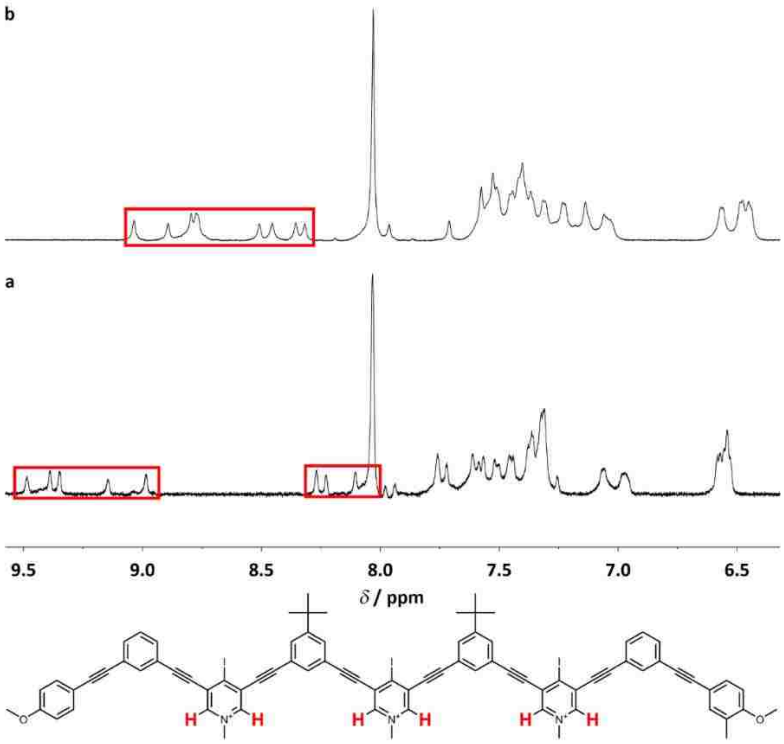

Figure 3.11 Pyridinium resonances of triple helicate **7** in organic and aqueous media. (a) Triplex **7** in organic solvents (three equivalents of I^-; 1:3 *v*/*v* DMF-d_7-CD_3CN); (b) triplex **7** in an aqueous environment (three equivalents of I^-; 1:1 *v*/*v* D_2O-DMF-d_7). The five downfield pyridinium resonances (two are overlapped) are shifted upfield relative to the corresponding peaks in (a) (up to 0.45 ppm). Conditions for (a–b): 600 MHz, 298 K.

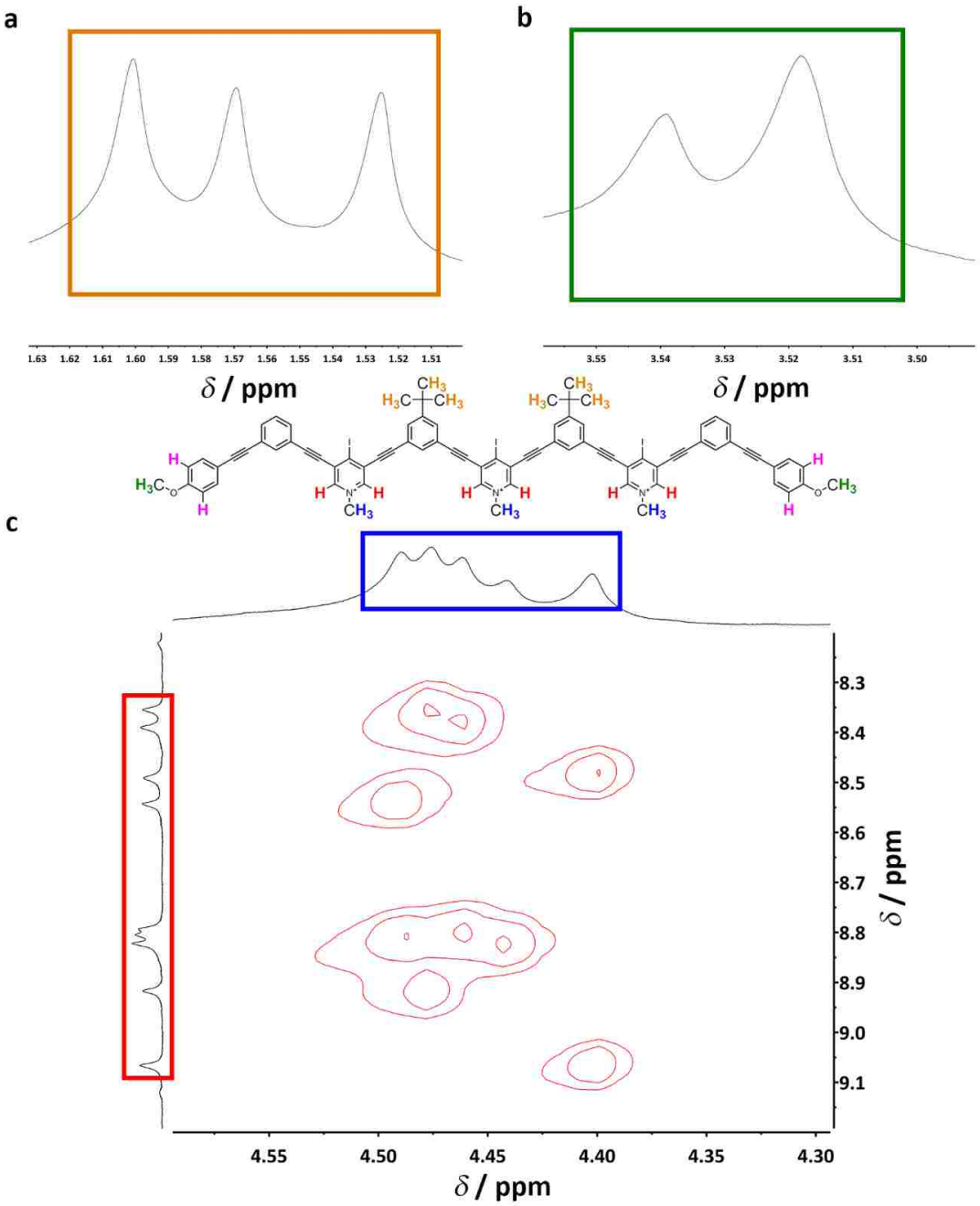

Figure 3.12 ^{1}H NMR and 2D NOESY spectroscopic analysis of the numbers and relative intensities of key resonances of **7**. (a) ^{1}H NMR spectrum of three *tert*-butyl peaks of equal intensity; (b) ^{1}H NMR spectrum of two methoxy-methyl peaks; one is twice the intensity of the other and is likely two overlapping peaks; (c) ^{1}H NMR spectrum of four pyridinium-methyl peaks of equal intensity and one of half intensity; nine pyridinium protons are clearly seen with their NOEs. Conditions for (a–c): 600 MHz, 1:1 *v*/*v* D_2O-DMF-d_7, 298 K.

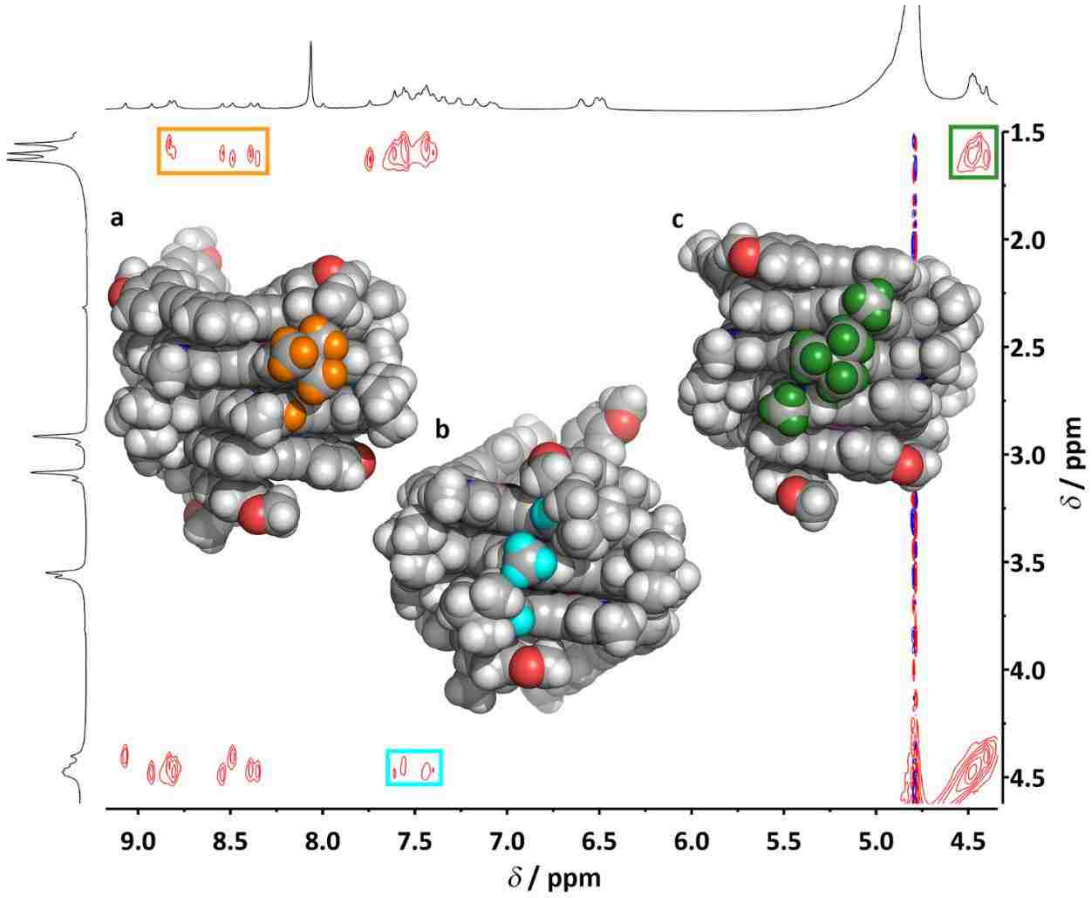

Figure 3.13 ^{1}H 2D NOESY NMR spectrum of triple helicate **7** in an aqueous environment. (a) *tert*-Butyl and pyridinium cross peaks; (b) *tert*-butyl and pyridinium-methyl cross peaks; (c) pyridinium-methyl and *tert*-butyl cross peaks. Conditions for (a–c): 600 MHz, 1:1 *v*/*v* D_2O-DMF-d_7, 298 K, 400-ms mixing time; not all colors are representative of atom identity.

Remarkably, after 20 days in solution, **7** exhibited minimal decomposition notwithstanding the chemical instability of 4-iodopyridiniums (Figure 3.14). In contrast, residual H_2O hydrolyzed **8** in a matter of hours. The compact and helical conformation of **7** protects the otherwise chemically sensitive 4-iodopyridinium halogen-bond donors. This helix conferred chemical stability is not without precedent.[46]

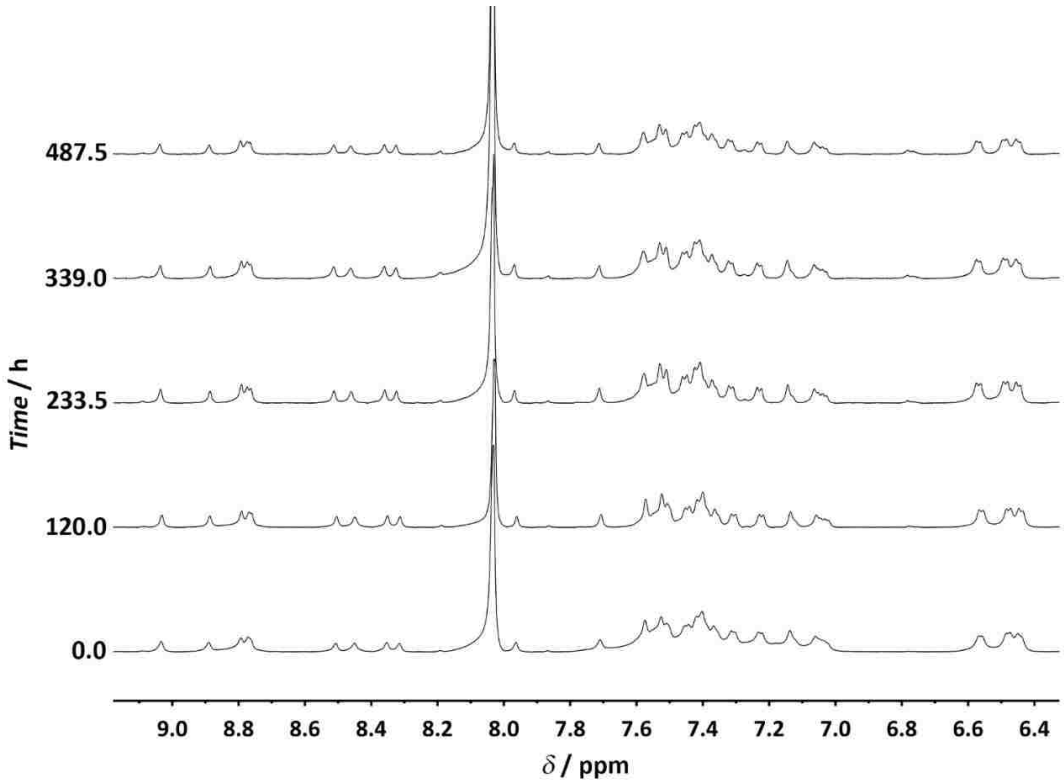

Figure 3.14 ^{1}H NMR spectra of triple helicate **7** in an aqueous environment. After 487.5 h (approximately 20 days), **7** showed only minimal signs of decomposition (600 MHz, 1:1 *v*/*v* D_2O-DMF-d_7, 298 K).

3.4 Experimental

3.4.1 Synthesis and Characterization Data

All reagents were obtained from commercial sources and were used without further purification unless otherwise noted. Column chromatography was performed using normal-phase silica gel (230–400 mesh, SiliaFlash® P60, SiliCycle). TLC was performed using normal-phase silica gel glass-backed plates (0.25 mm, F-254, SiliCycle)

and observed under UV light. Activated Fischer Grade 514 molecular sieves were used when anhydrous solvents were required. For the synthesis of compounds **2**, **3**, **5**, **12**, **18**, and **19**, modified Sonogashira procedures were utilized. Standard Schlenk line and air-free techniques were employed for these reactions. Preparatory HPLC separations were conducted with a Teledyne Isco CombiFlash RF+. A Teledyne Isco RediSep RF Gold Reversed-phase C18 column was utilized to carry out these separations. High-resolution masses for new compounds were obtained using an Agilent 6520 Accurate-Mass Q-TOF LC/MS. Due to their instability, compounds **6** and **8** were directly injected into a Bruker amaZon SL Ion Trap ESI-MS. X-ray crystallographic data were measured on a Bruker D8 Venture (for crystallographic collection and refinement details, see Section 3.4.2). The Gaussian 09 suite was used to minimize the folded conformation of a single nonamer of **7** (for computational details, see Section 3.4.3). NMR spectra were recorded on a VNMRS Varian 500 MHz, Bruker Avance 400 MHz, or Agilent DD2 400 MHz spectrometer. Chemical shifts are reported in ppm from high to low frequency using the residual solvent peak as the internal reference ($CHCl_3$ = 7.26 ppm, DMF = 8.03 ppm). All ^1H resonances are reported to the nearest 0.01 ppm. The multiplicity of the signals is designated as: s = singlet, d = doublet, t = triplet, m = multiplet, or some combination thereof. *J*s are reported in to the nearest 0.01 Hz. ^{13}C resonances are reported to the nearest 0.01 ppm and are labeled relative to the center resonance of the residual solvent as the internal reference ($CDCl_3$ = 77.16 ppm, DMF-d_7 = 163.15 ppm). For the ^{19}F NMR spectra, C_6F_6 (δ = –164.9 ppm) was used as an internal standard. NOESY and DOSY NMR experiments were conducted to aid in structure determination of the triple helicate in solution. All 2D NOESY NMR data, select ^1H NMR spectra for the characterization of

compounds, and select ^{1}H NMR titration spectra were collected using a VNMRS Varian 600 MHz spectrometer. DOSY experiments were performed on a Bruker Avance III HD 600 MHz with a Prodigy BBO CryoProbe spectrometer. UV-Vis titration data were measured on an Agilent 8453 spectrophotometer. To setup ^{1}H and ^{13}C NMR samples of compound **6**, a Vigor Gas Separation Technologies Co., Ltd. Glovebox with a gas purification system (SG1200/750TS-F) was used.

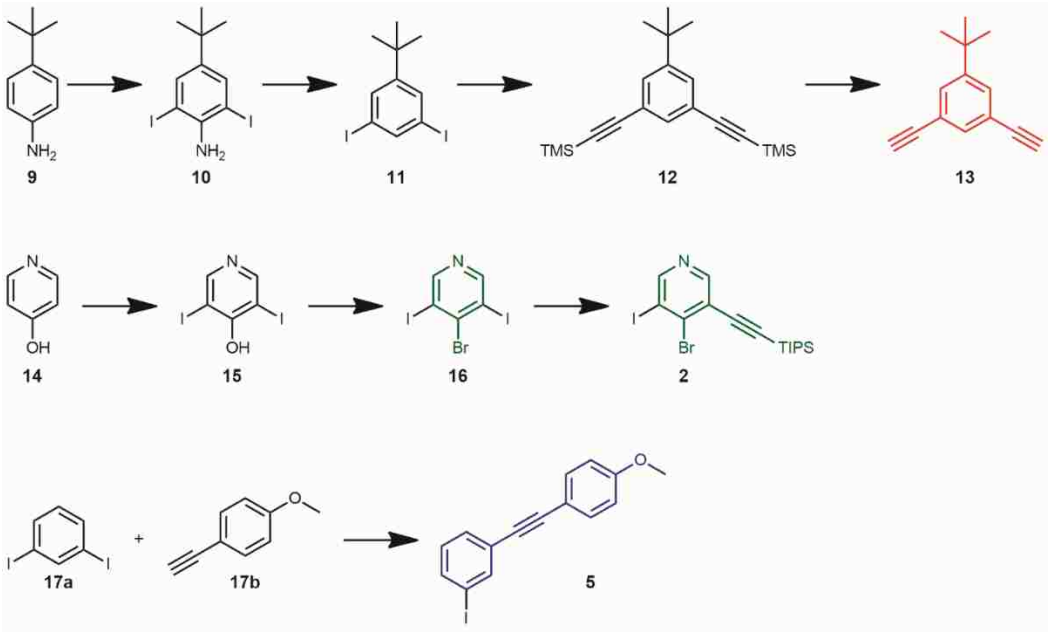

Scheme 3.2 Synthesis of monomeric and dimeric synthons.

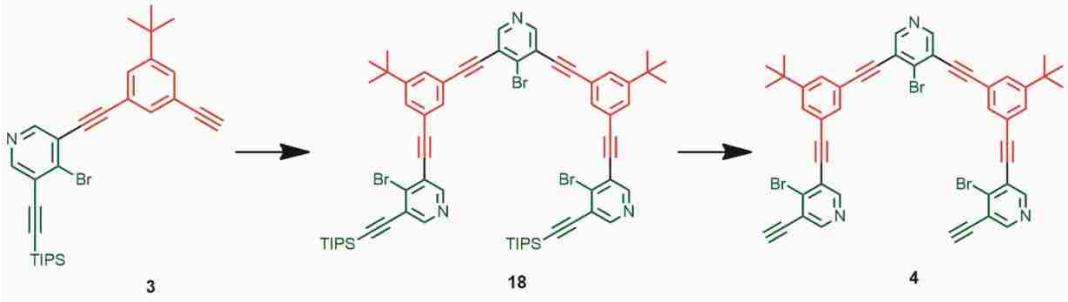

Scheme 3.3 Synthesis of dimeric and pentameric compounds.

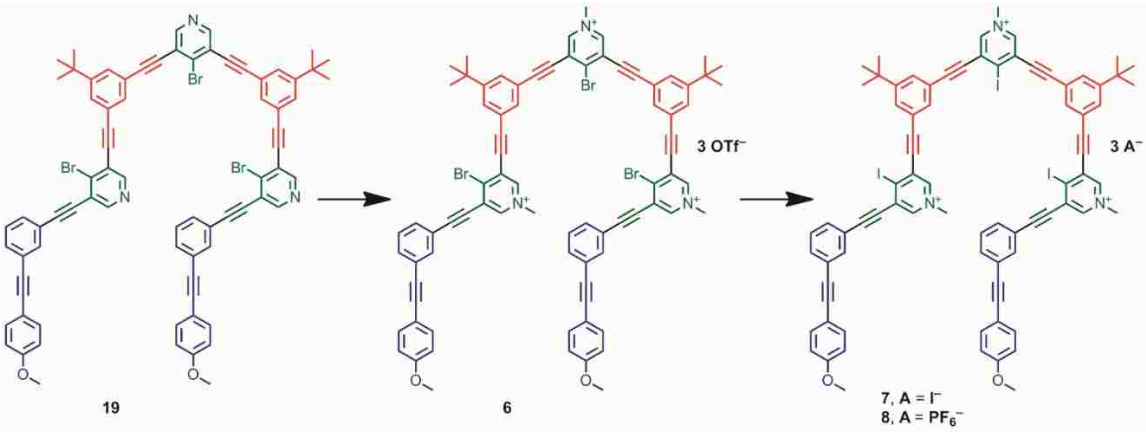

Scheme 3.4 Synthesis of neutral and alkylated nine-mers.

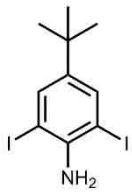

4-(tert-butyl)-2,5-diiodoaniline (**10**)

A round bottom flask (2000-mL) was charged with 4-(*tert*-butyl)aniline (21.9 mL, 0.138 mol, 1.0 equiv), benzyl triethylammonium dichloroiodate (100.0 g, 0.287 mol, 2.0 equiv), $CaCO_3$ (55.46 g, 0.554 mol, 4.0 equiv), CH_3OH (513 mL), and DCM (1020 mL). The reaction was stirred at reflux for 12 h, open to the air. The reaction mixture was

cooled to RT, filtered, and concentrated under reduced pressure. The residue was redissolved in DCM (250 mL), and the solution was washed with $Na_2S_2O_3$ (20 % *w*/*v*, 150 mL), DI H_2O (150 mL), and brine (150 mL). The DCM solution was then dried with anhydrous $MgSO_4$, filtered, and concentrated under reduced pressure. The product was purified by flash column chromatography (dry load, SiO_2, 1 % EtOAc-hexanes, R_f = 0.3) to give a maroon oil (26.05 g, 47 %). ^{1}H NMR (400 MHz, $CDCl_3$) δ 7.61 (s, 2H), 4.46 (s, 2H), 1.24 (s, 9H). ^{13}C NMR (101 MHz, $CDCl_3$) δ 144.77, 143.88, 136.66, 81.84, 33.86, 31.46. Spectroscopic data are in accordance with published material.[161]

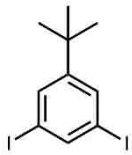

1-(tert-butyl)-3,5-diiodobenzene (**11**)

A round bottom flask (2000-mL) was charged with **10** (36.70 g, 91.51 mmol, 1.0 equiv) and glacial AcOH (1000 mL). A second round bottom flask (1000-mL) was charged with copper(I) oxide (37.44 g, 261.64 mmol, 2.86 equiv) and EtOH (600 mL). A third round bottom flask (2000-mL) was purged with N_2 and charged with H_2SO_4 (52 mL). The flask containing H_2SO_4 was brought to 0 °C, and sodium nitrite (28.70 g, 415.97 mmol, 4.5 equiv) was added slowly, generating a slate blue, cloudy solution. The solution of **10** and AcOH was slowly added to the H_2SO_4 and sodium nitrite mixture while still at 0 °C and under N_2, resulting in a yellow precipitate. The combined solutions were allowed to stir for 30 min under N_2. The combined solutions were removed from the ice bath, and the copper(I) oxide in EtOH was slowly added to them under N_2. N_2 gas bubbles evolved from the cloudy maroon solution. After the addition, the solution was

slowly heated to 50 °C, returned to RT, and then allowed to sit for 24 h. The solution was concentrated under reduced pressure and redissolved in DCM (500 mL). Na_2CO_3 was added to the solution until the gas evolution ceased. The Na_2CO_3 was filtered off, and the solution was washed with DI H_2O (250 mL) and brine (150mL). The maroon organic layer was dried with brine and anhydrous $MgSO_4$ and concentrated under reduced pressure. The product was separated from the maroon residue by flash column chromatography (dry load, SiO_2, hexanes, R_f = 0.5, top spot) to give a white powder (21.96 g, 62 %). ^{1}H NMR (400 MHz, $CDCl_3$) δ 7.86 (t, *J* = 1.49 Hz, 1H), 7.65 (d, *J* = 1.48 Hz, 2H), 1.27 (s, 9H). ^{13}C NMR (101 MHz, $CDCl_3$) δ 155.63, 142.30, 134.19, 95.10, 34.96, 31.16. This procedure is similar to those employed recently.[162] Spectroscopic data are in accordance with published material.[163]

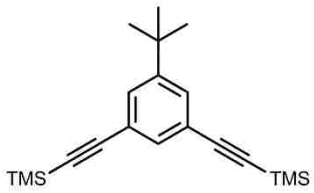

3,5-bis(trimethylsilylethynyl)-(tert-butyl)benzene (**12**)

An oven dried Schlenk flask (500 mL) was charged with $PdCl_2(PPh_3)_2$ (0.660 g, 0.94mmol, 0.05 equiv) and CuI (0.358 g, 1.88 mmol, 0.1 equiv). The Schlenk flask was then evacuated/backfilled with N_2 three times. To this flask was added an N_2-sparged solution of **11** (7.253 g, 18.8 mmol, 1.0 equiv), Et_3N (72 mL, 520 mmol, 27.7 equiv), ethynyltrimethylsilane (6.64 mL, 47 mmol, 2.5 equiv), and anhydrous THF (200 mL) via cannula. The reaction was allowed to stir under N_2 overnight at 40 °C. The reaction was cloudy and yellow/orange in coloration then eventually turned black. The solution was

removed from heat. Hexanes (150 mL) was added to the mixture until a white precipitate formed. The solution was filtered, and the filtrate was concentrated under reduced pressure to give a cloudy yellow/orange oil. The product was purified by flash column chromatography (SiO_2, 0 % → 10 % EtOAc-hexanes, R_f = 0.38) to give a clear yellow oil (5.29 g, 86 %). ^{1}H NMR (400 MHz, $CDCl_3$) δ 7.42 (s, 3H), 1.29 (s, 9H), 0.24 (s, 18H). ^{13}C NMR (101 MHz, $CDCl_3$) δ 151.44, 132.91, 129.28, 123.08, 104.87, 94.18, 34.79, 31.22, 0.12. Spectroscopic data are in accordance with published material.[164]

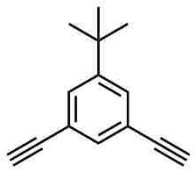

1-(tert-butyl)-3,5-diethynylbenzene (**13**)

A round bottom flask (500-mL) was charged with **12** (5.29 g, 16.2 mmol, 1.0 equiv), K_2CO_3 (4.48 g, 32.4 mmol, 2.0 equiv), CH_3OH (160 mL), and THF (20 mL). The solution was allowed to stir under N_2 for 2 h. The product was purified by flash column chromatography (SiO_2, hexanes, R_f = 0.6) to give a yellow oil (2.641 g, 89 %). ^{1}H NMR (400 MHz, $CDCl_3$) δ 7.50 (d, J = 1.48 Hz, 2H), 7.45 (t, J = 1.47 Hz, 1H), 3.06 (s, 2H), 1.30 (s, 9H). ^{13}C NMR (101 MHz, $CDCl_3$) δ 151.72, 132.88, 129.87, 122.20, 83.32, 77.41, 34.75, 31.14. Spectroscopic data are in accordance with published material.[165]

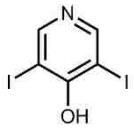

3,5-diiodopyridin-4-ol (**15**)

A round bottom flask (2000-mL) was charged with 4-hydroxypyridine (18.00 g, 0.189 mol, 1.0 equiv), NaOH (47.69 g, 1.19 mol, 6.3 equiv), sodium acetate (144.4 g, 1.76 mol, 9.3 equiv), and DI H_2O (600 mL). The solution was brought to reflux while stirring (using an overhead stirrer), and I_2 (168 g, 0.662 mol, 3.5 equiv) was added in portions. To this stirring solution was added aqueous AcOH (50 % *v*/*v*, 25 mL) causing a beige precipitate to form. This was followed by the addition of an aqueous NaOH solution (50 % *w*/*v*, 25 mL), which caused the precipitate to disappear, leaving a clear yellow solution. This acidification/basification process was repeated twice with the same changes in solution. After the final addition of the NaOH, aqueous AcOH (50% *v*/*v*, 25 mL) was added until elemental iodine precipitated from solution. A beige precipitate also formed. The reaction was allowed to cool to RT and was filtered. The beige solid was washed with boiling DI H_2O and was dried on vacuum (~1 Torr) overnight to give pure product (52.45 g, 80 %). ^{1}H NMR (400 MHz, $(CD_3)_2SO$) δ 11.96 (s, 1H), 8.28 (s, 2H). ^{13}C NMR (101 MHz, $(CD_3)_2SO$) δ 170.43, 143.19, 86.58. Spectroscopic data are in accordance with published material.[166]

4-bromo-3,5-diiodopyridine (**16**)

A flame-dried, 3-neck round bottom flask (2000-mL) was charged with **15** (51.45 g, 0.148 mol, 1.0 equiv) and neat PBr_3 (~75 mL, "enough to cover the solids"). The mixture was allowed to stir at reflux under N_2 for 4.5 h. The reaction was then allowed to cool to RT and was placed in an ice-water bath. The reaction mixture was quenched with an aqueous NaOH (50 % *w*/*v*) solution until gas formation ceased **(WARNING: the gas formation was violent, pungent, and corrosive. Be sure to vent it to the top of the hood. Aqueous NaOH should be added in small portions and with great care.)** A gas inlet adapter was added to one neck (left), and compressed air was used to vent the forming gases out the top of the condenser (center), while a stopper was in the last neck (right). The solution was allowed to stir for 30 min to ensure that the quenching was complete. Subsequently, the solution was brought to pH 9. A liquid-liquid extraction was completed with DCM (2 × 150 mL). The solids that formed between layers gradually dissolved in the DCM layer. The combined organics were dried with brine (150 mL) and concentrated under reduced pressure to give a peach colored solid. The product was purified using flash column chromatography (SiO_2, dry load, DCM, R_f = 0.45) to give white needles (26.22 g, 43 %). ^{1}H NMR (400 MHz, $CDCl_3$) δ 8.81 (s, 2H). ^{13}C NMR (101 MHz, $CDCl_3$) δ 156.63, 145.76, 100.68. Spectroscopic data are in accordance with published material.[166]

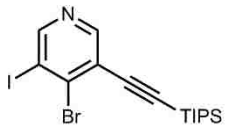

4-bromo-3-iodo-5-((triisopropylsilyl)ethynyl)pyridine (**2**)

An oven-dried Schlenk flask (200-mL) was charged with **16** (8.63 g, 21.1 mmol, 1.0 equiv), $PdCl_2(PPh_3)_2$ (0.887 g, 1.26 mmol, 0.06 equiv), and CuI (0.401 g, 2.11 mmol, 0.1 equiv). The reaction flask was evacuated/backfilled with N_2 three times. An N_2-sparged solution of ethynyltriisopropylsilane (5.0 mL, 22.3 mmol, 1.05 equiv), Et_3N (15 mL, 108 mmol, 5.1 equiv), and anhydrous DMF (150 mL) was transferred to the Schlenk flask via cannula, and the reaction was allowed to stir in a 55 °C oil bath under N_2 for 12 h. The yellow solution was concentrated under reduced pressure, and the crude solid was purified by column chromatography (SiO_2, 5% EtOAc-hexanes, R_f = 0.38) to give a white powder (3.05 g, 31 %). Mp = 60–64 °C. ^{1}H NMR (400 MHz, $CDCl_3$) δ 8.79 (s, 1H), 8.52 (s, 1H), 1.19–1.13 (m, 21H). ^{13}C NMR (101 MHz, $CDCl_3$) δ 156.20, 151.98, 142.10, 124.42, 102.09, 101.20, 101.12, 18.75, 11.34. HRMS ($C_{16}H_{24}BrINSi$ = $[M+H]^+$): calculated = 463.9906; found = 463.9918.

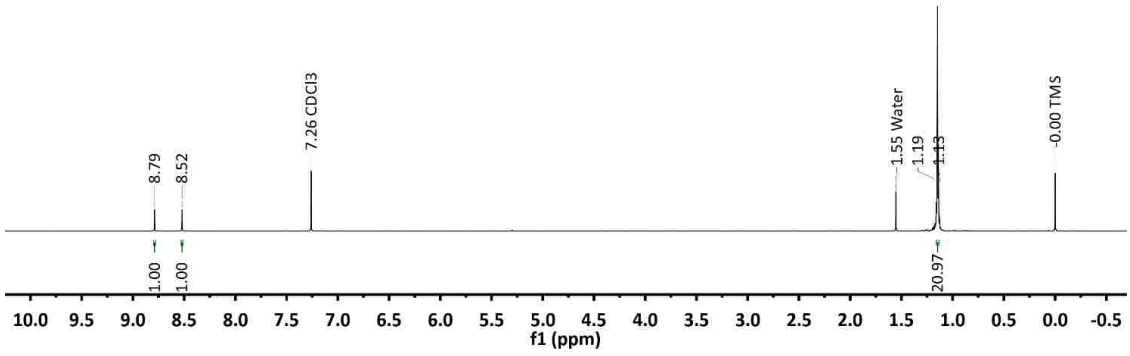

Figure 3.15 ^{1}H NMR spectrum of **2** (400 MHz, $CDCl_3$, 298 K).

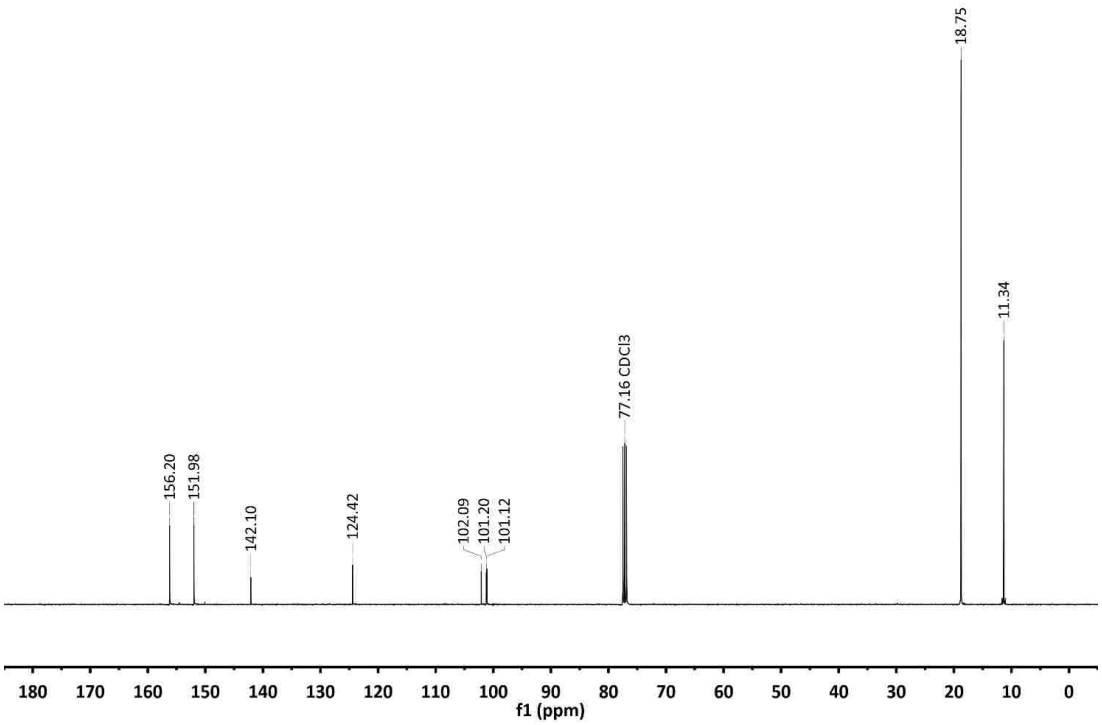

Figure 3.16 ^{13}C NMR spectrum of **2** (101 MHz, $CDCl_3$, 298 K).

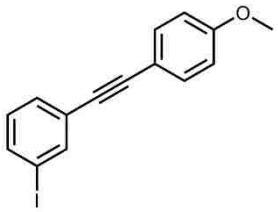

1-iodo-3-((4-methoxyphenyl)ethynyl)benzene (**5**)

An oven-dried Schlenk flask (200-mL) was purged with N_2, and charged with 1,3-diiodobenzene (4.00 g, 12.1 mmol, 1.0 equiv), $PdCl_2(PPh_3)_2$ (0.426 g, 0.606 mmol, 0.05 equiv), and CuI (0.231 g, 1.21 mmol, 0.1 equiv). The Schlenk flask was evacuated/backfilled with N_2 three times. An N_2-sparged solution of 1-ethynyl-4-methoxybenzene (1.57 mL, 12.1 mmol, 1.0 equiv), Et_3N (26 mL, 187 mmol, 15 equiv), and anhydrous THF (64 mL) was transferred to the Schlenk flask via cannula. The

solution was allowed to stir under N_2 in a 50 °C oil bath for 12 h. The solution was allowed to come to RT and was concentrated under reduced pressure. The crude material was purified by flash column chromatography (SiO_2, dry load, 10 % EtOAc-hexanes, R_f = 0.39) to give a white powder (1.935 g, 48 %). Mp = 99–101 °C. ^{1}H NMR (400 MHz, $CDCl_3$) δ 7.87 (t, *J* = 1.6 Hz, 1H), 7.64 (ddd, *J* = 7.96, 1.82, 1.05 Hz, 1H), 7.47–7.44 (m, 3H), 7.06 (t, *J* = 7.85 Hz, 1H), 6.88 (dt, *J* = 8.76, 2.80, 2.04 Hz, 2H), 3.83 (s, 3H). ^{13}C NMR (101 MHz, $CDCl_3$) δ 160.01, 140.12, 137.01, 133.27, 130.65, 129.94, 125.86, 114.98, 114.20, 93.83, 90.94, 86.55, 55.47. HRMS ($C_{15}H_{12}IO$ = $[M+H]^+$): calculated = 334.9933; found = 334.9936.

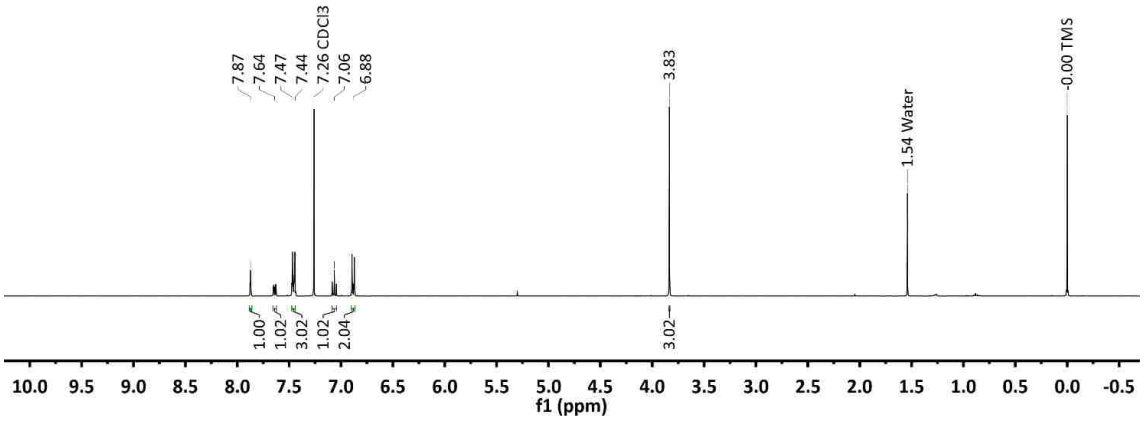

Figure 3.17 ^{1}H NMR spectrum of **5** (400 MHz, $CDCl_3$, 298 K).

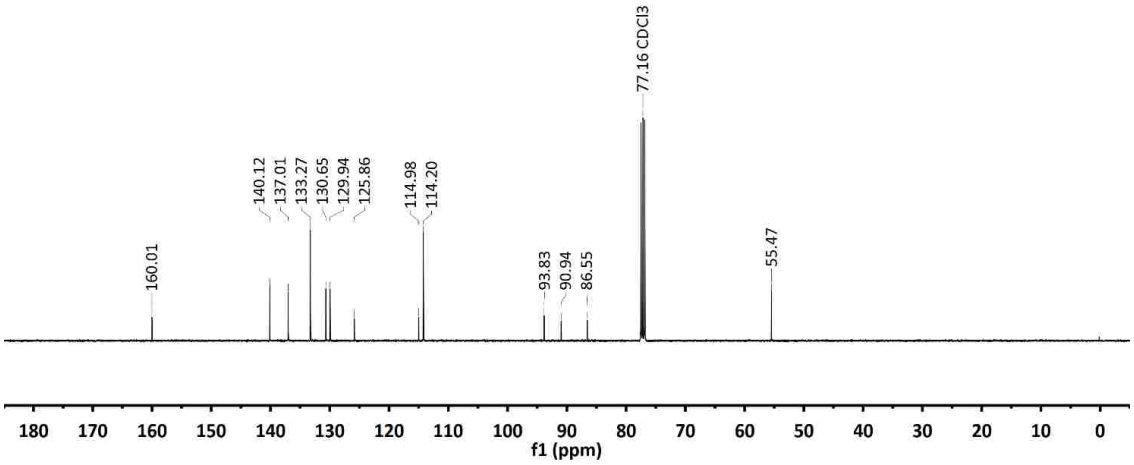

Figure 3.18 ^{13}C NMR spectrum of **5** (101 MHz, $CDCl_3$, 298 K).

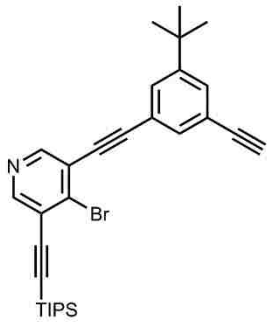

4-bromo-3-((3-(tert-butyl)-5-ethynylphenyl)ethynyl)-5-((triisopropylsilyl)ethynyl)pyridine (**3**)

An oven-dried Schlenk flask (500-mL) was charged with $PdCl_2(PPh_3)_2$ (0.231 g, 0.329 mmol, 0.5 equiv) and CuI (0.125 g, 0.657 mmol, 0.1 equiv) and was evacuated/backfilled with N_2 three times. A sonicated N_2-sparged solution of **13** (3.590 g, 19.7 mmol, 3.0 equiv), Et_3N (115 mL, 131 mmol, 20 equiv), and anhydrous DMF (200 mL) was transferred to the Schlenk flask via cannula. An N_2-sparged solution of **2** (3.052 g, 6.57 mmol, 1.0 equiv) and anhydrous DMF (100 mL) was loaded into a gas-tight syringe and added to the Schlenk flask over 10 h at RT. The reaction was allowed to stir

under N_2 for 12 h total. The solution was concentrated under reduced pressure, and the crude product was purified by flash column chromatography (SiO_2, 5 % EtOAc-hexanes, R_f = 0.31) to give a yellow oil (0.710 g, 21 %). We reason that the yield could be increased to ~33 % if the reaction were monitored by TLC and a 1:1 ratio of starting materials were used. Even at RT, some product was consumed by a second cross-coupling at the bromine functionalities (with excess **13** and via self-dimerization). ^{1}H NMR (400 MHz, $CDCl_3$) δ 8.57 (s, 1H), 8.53 (s, 1H), 7.57 (t, J = 1.74 Hz, 1H), 7.54 (d, J = 1.72 Hz, 2H), 3.09 (s, 1H), 1.34 (s, 9H), 1.19–1.13 (m, 21H). ^{13}C NMR (101 MHz, $CDCl_3$) δ 152.01, 151.82, 151.12, 138.04, 132.64, 130.34, 129.42, 123.52, 123.13, 122.43, 122.28, 101.45, 101.04, 96.68, 84.96, 83.22, 77.61, 34.89, 31.21, 18.79, 11.37. HRMS ($C_{30}H_{37}BrNSi$ = $[M+H]^+$): calculated = 518.1879; found = 518.1861.

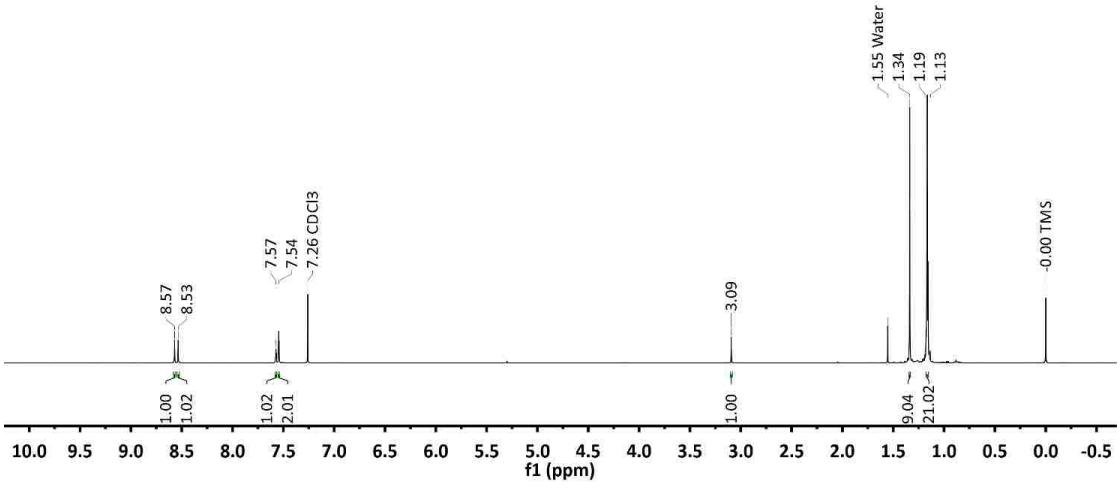

Figure 3.19 ^{1}H NMR spectrum of **3** (400 MHz, $CDCl_3$, 298 K).

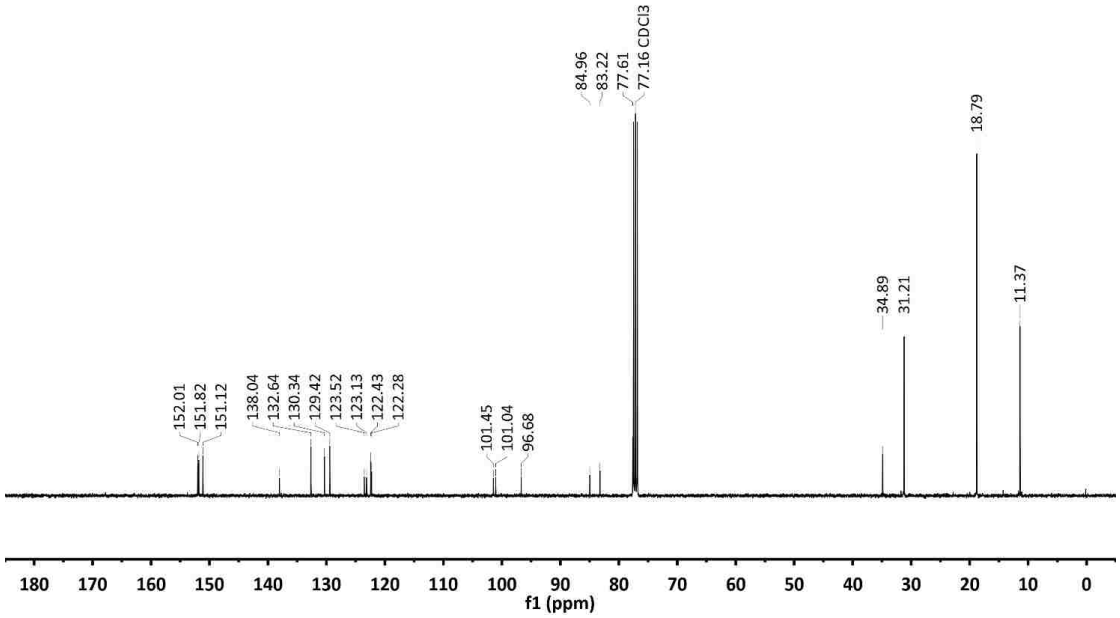

Figure 3.20 ^{13}C NMR spectrum of **3** (101 MHz, $CDCl_3$, 298 K).

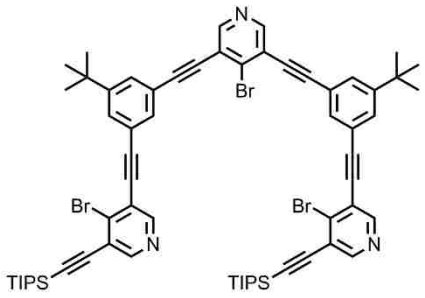

5,5'-((((4-bromopyridine-3,5-diyl)bis(ethyne-2,1-diyl))bis(3-(tert-butyl)-5,1-phenylene))bis(ethyne-2,1-diyl))bis(4-bromo-3-((triisopropylsilyl)ethynyl)pyridine) (**18**)

An oven-dried Schlenk flask (100-mL) was charged with **16** (0.281 g, 0.685 mmol, 1.0 equiv), $PdCl_2(PPh_3)_2$ (0.0481g, 0.0685 mmol, 0.1 equiv), and CuI (0.0261 g, 0.137 mmol, 0.2 equiv). The Schlenk flask was evacuated/backfilled with N_2 three times. An N_2-sparged solution of **3** (0.710 g, 1.37 mmol, 2.0 equiv), Et_3N (0.955 mL, 6.85 mmol, 10 equiv) and anhydrous DMF (31 mL) was transferred to the Schlenk flask via

cannula. The reaction was allowed to stir under N_2 in a 50 °C oil bath for 12 h. The solution was concentrated under reduced pressure and the crude product was purified by flash column chromatography (SiO_2, 7.5 % → 25 % EtOAc-hexanes, R_f = 0.1 with 7.5 % EtOAc-hexanes) to give a yellow oil (0.375 g, 75 %). ^{1}H NMR (400 MHz, $CDCl_3$) δ 8.63 (s, 2H), 8.59 (s, 2H), 8.55 (s, 2H), 7.66 (t, *J* = 1.49 Hz, 2H), 7.65–7.63 (m, 4H), 1.38 (s, 18), 1.19–1.13 (m, 42H). ^{13}C NMR (101 MHz, $CDCl_3$) δ 152.26, 151.88, 151.39, 151.15, 138.04, 137.71, 132.32, 129.94, 129.89, 123.53, 123.22, 123.06, 122.55, 122.45, 101.43, 101.09, 96.74, 96.52, 85.22, 85.09, 34.99, 31.24, 18.78, 11.37. HRMS ($C_{65}H_{73}Br_3N_3Si_2$ = $[M+H]^+$): calculated = 1188.2893; found = 1188.2926.

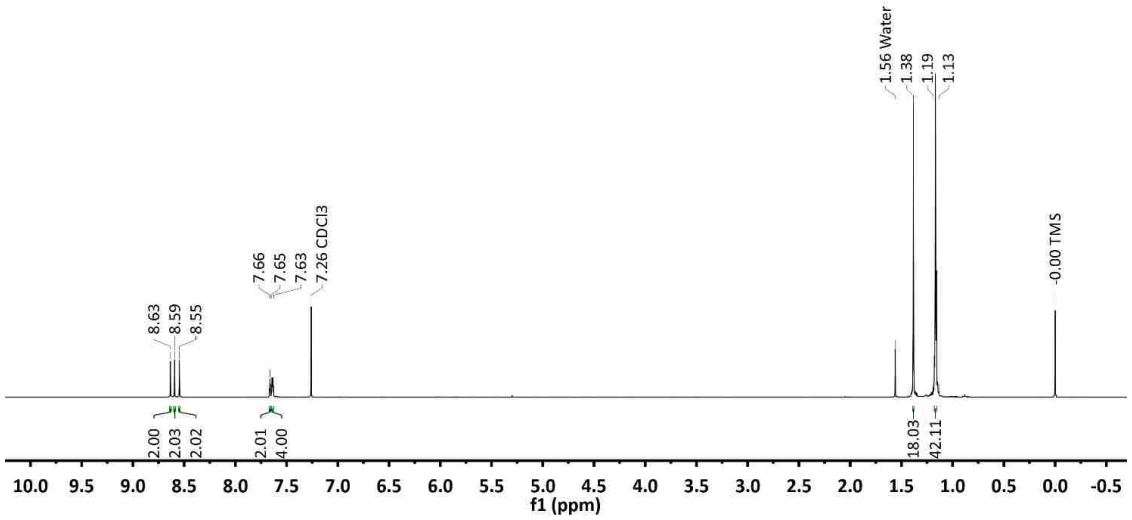

Figure 3.21 ^{1}H NMR spectrum of **18** (400 MHz, $CDCl_3$, 298 K).

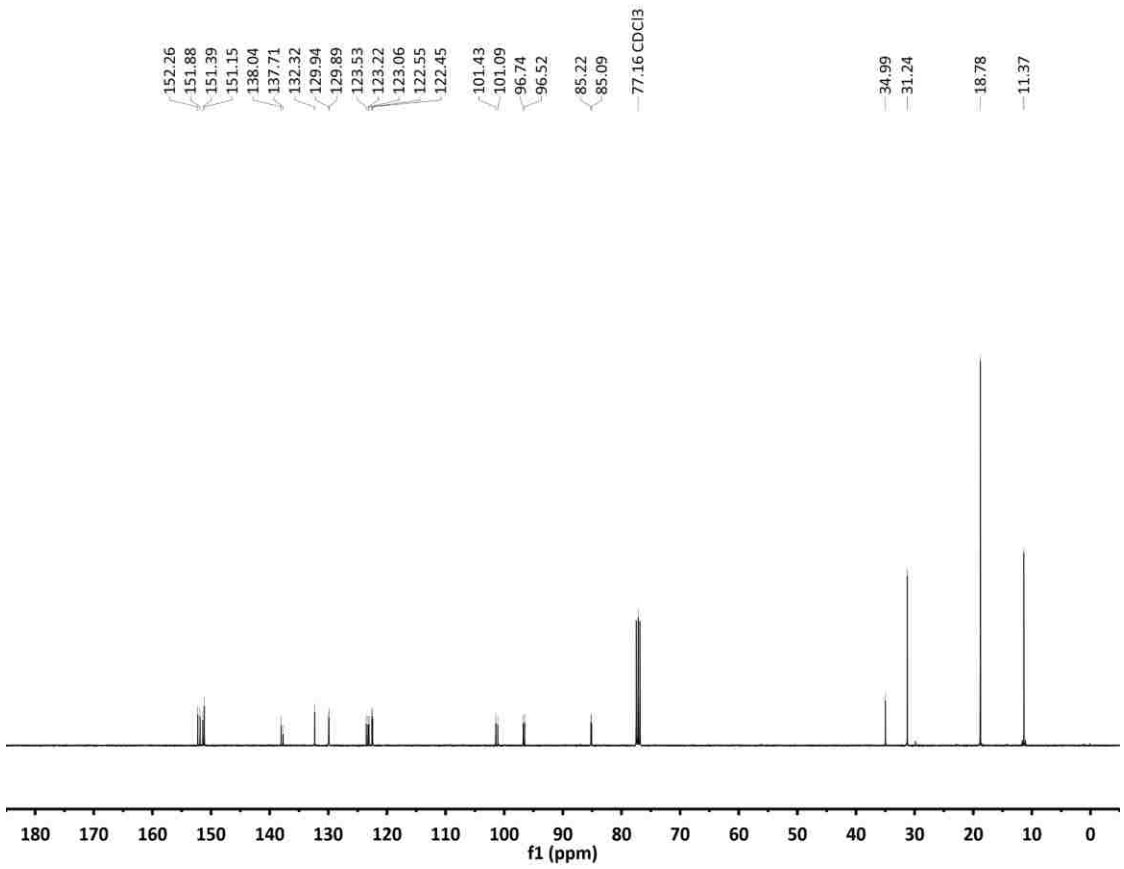

Figure 3.22 ^{13}C NMR spectrum of **18** (101 MHz, $CDCl_3$, 298 K).

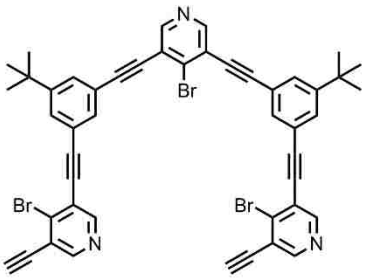

5,5'-((((4-bromopyridine-3,5-diyl)bis(ethyne-2,1-diyl))bis(3-(tert-butyl)-5,1-phenylene))bis(ethyne-2,1-diyl))bis(4-bromo-3-ethynylpyridine) (**4**)

A solution of **18** (2.192 g, 1.84 mmol, 1.0 equiv) was dissolved in anhydrous THF (92 mL) and sparged with N_2 in an oven-dried Schlenk flask (200-mL). The pale-yellow solution was cooled to 0 °C. TBAF (1.0 M in THF, 5.52 mL, 5.52 mmol, 3.0 equiv) was

added dropwise over one min. The red solution was removed from the ice bath after the addition of the TBAF and was allowed to stir for 10 min. The copper-colored solution was diluted with DI H_2O (200 mL), which caused the solution to become white and cloudy. The aqueous layer was subjected to an extraction with DCM (3 × 250 mL). The combined organics were dried with brine and anhydrous $MgSO_4$. The solution was concentrated under reduced pressure to give an off-white powder (1.60 g, quantitative). No further purification was necessary. TLC conditions: 5 % acetone-DCM, R_f = 0.37. Mp = 215 °C with decomposition. ^{1}H NMR (500 MHz, $CDCl_3$) δ 8.64 (s, 2H), 8.63 (s, 2H), 8.57 (s, 2H), 7.67 (t, *J* = 1.4 Hz, 2H), 7.64 (dt, *J* = 6.65, 1.70 Hz, 4H), 3.55 (s, 2H), 1.38 (s, 18H). ^{13}C NMR (126 MHz, $CDCl_3$) δ 152.36, 152.10, 151.88, 151.40, 138.04, 137.75, 132.36, 130.00, 129.95, 123.28, 123.26, 122.53, 122.45, 122.37, 96.86, 96.76, 85.40, 85.15, 84.97, 78.96, 35.02, 31.25. HRMS ($C_{47}H_{33}Br_3N_3$ = $[M+H]^+$): calculated = 876.0225; found = 876.0264.

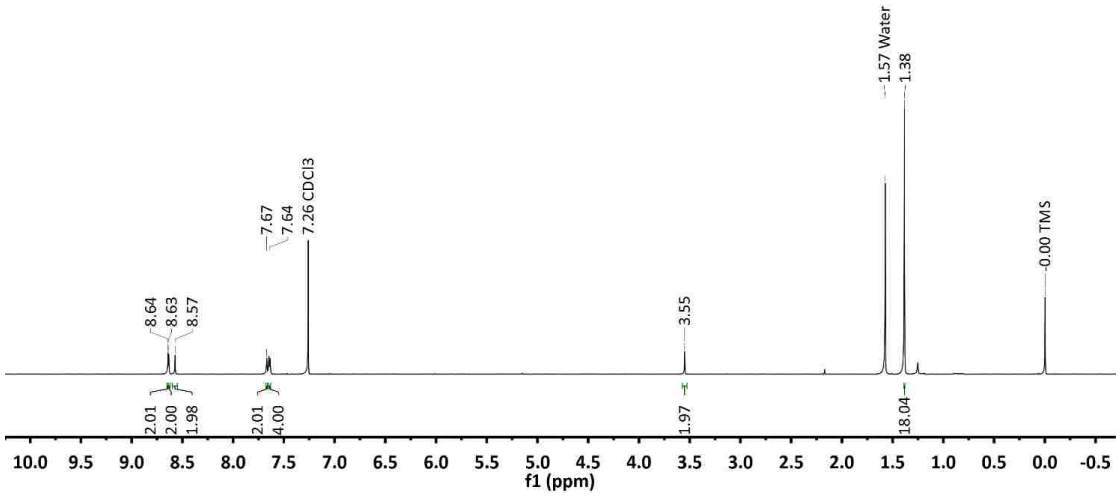

Figure 3.23 ^{1}H NMR spectrum of **4** (500 MHz, $CDCl_3$, 298 K).

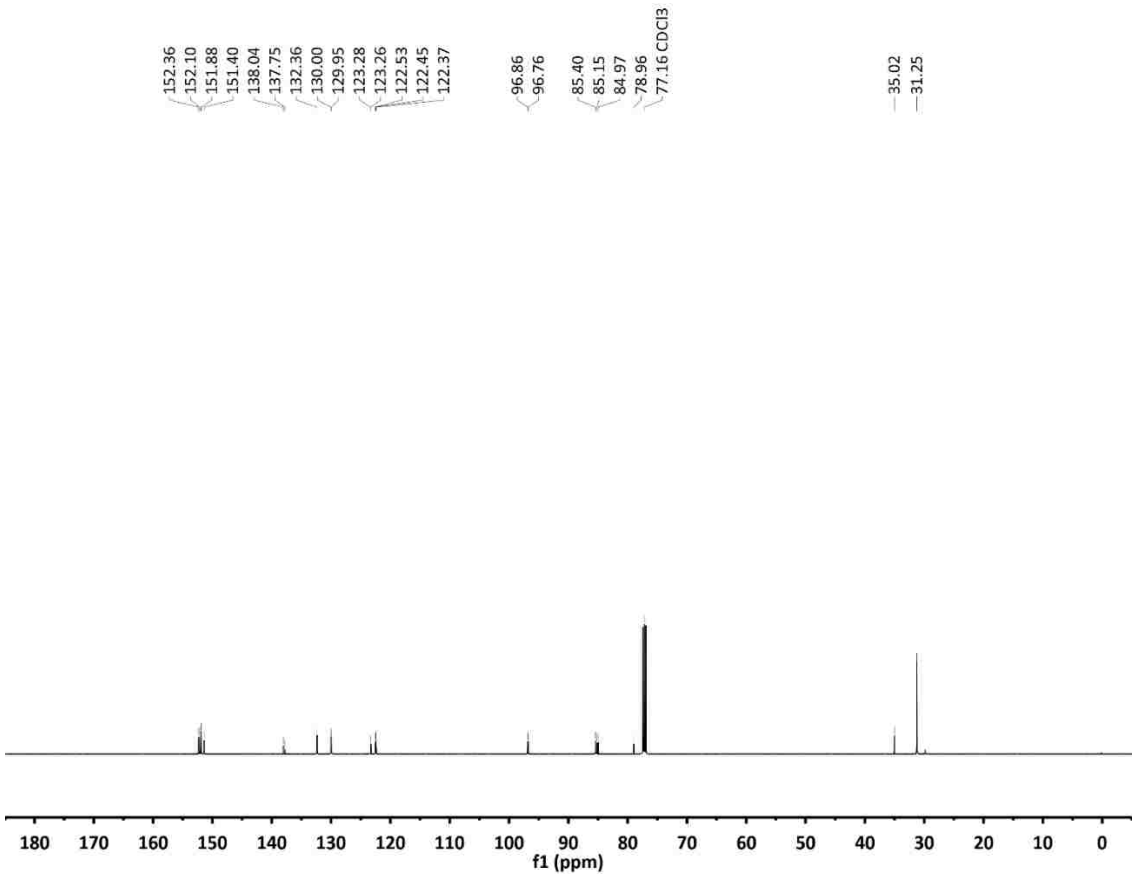

Figure 3.24 ^{13}C NMR spectrum of **4** (126 MHz, $CDCl_3$, 298 K).

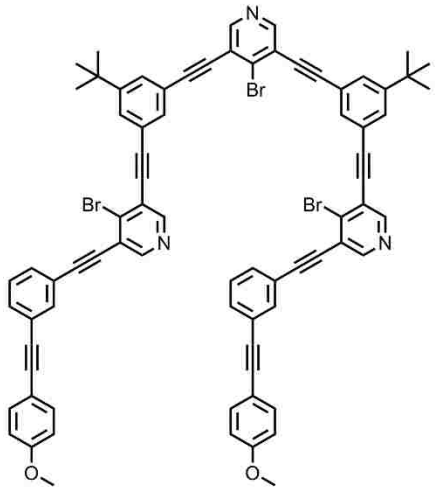

5,5'-((((4-bromopyridine-3,5-diyl)bis(ethyne-2,1-diyl))bis(3-(tert-butyl)-5,1-phenylene))bis(ethyne-2,1-diyl))bis(4-bromo-3-((3-((4-methoxyphenyl)ethynyl)phenyl)ethynyl)pyridine) (**19**)

An oven-dried Schlenk flask (100-mL) was charged with **4** (0.141 g, 0.161 mmol, 0.45 equiv), $PdCl_2(PPh_3)_2$ (0.0149g, 0.0212 mmol, 0.06 equiv), and CuI (0.0067 g, 0.0351 mmol, 0.1 equiv). The Schlenk flask was evacuated/backfilled with N_2 three times. An N_2-sparged solution of **5** (0.118 g, 0.353 mmol, 1.0 equiv), Et_3N (1.0 mL, 7.06 mmol, 20 equiv), and THF (29 mL) was transferred to the Schlenk flask via cannula. The reaction was allowed to stir under N_2 in a 50 °C oil bath for 24 h. The solution was concentrated under reduced pressure, and the residue was purified by flash column chromatography (SiO_2, 35 % EtOAc-hexanes → 7.5% CH_3OH-EtOAc, R_f = 0.27 with 35 % EtOAc-hexanes) to give a white solid (0.124 g, 61 %). All efforts to remove traces of hydrocarbon grease from **19** were unsuccessful. Multiple flash chromatographic and reversed-phase preparatory HPLC separations were attempted. With either method, traces of hydrocarbon grease invariably coeluted with **19** due to its high retention and lipophilicity. Hexanes extractions only resulted in hexanes contamination.

Recrystallizations also failed. However this contamination was removed in the subsequent step. Mp = 146–150 °C. ^{1}H NMR (400 MHz, $CDCl_3$) δ 8.64 (s, 2H), 8.63 (s, 2H), 8.61 (s, 2H), 7.76 (t, *J* = 1.24 Hz, 2H), 7.69 (t, *J* = 1.44 Hz, 2H), 7.65 (d, *J* = 1.44 Hz, 4H), 7.56–7.52 (m, 4H), 7.48 (dt, *J* = 8.88, 2.08 Hz, 4H), 7.37 (t, *J* = 7.92 Hz, 2H), 6.89 (dt, *J* = 8.88, 2.04 Hz, 4H), 3.84 (s, 6H), 1.39 (s, 18H). ^{13}C NMR (101 MHz, $CDCl_3$) δ 160.00, 152.30, 151.42, 151.36, 137.75, 134.76, 133.30, 132.36, 132.30, 131.26, 129.97, 128.75, 124.41, 123.34–123.19, 122.52, 122.50, 122.48, 115.07, 114.21, 96.76, 96.69, 96.66, 90.62, 87.14, 85.31, 85.16, 85.13, 55.47, 35.02, 31.26. HRMS ($C_{77}H_{53}Br_3N_3O_2$ = $[M+H]^+$): calculated = 1288.1688; found = 1288.1714.

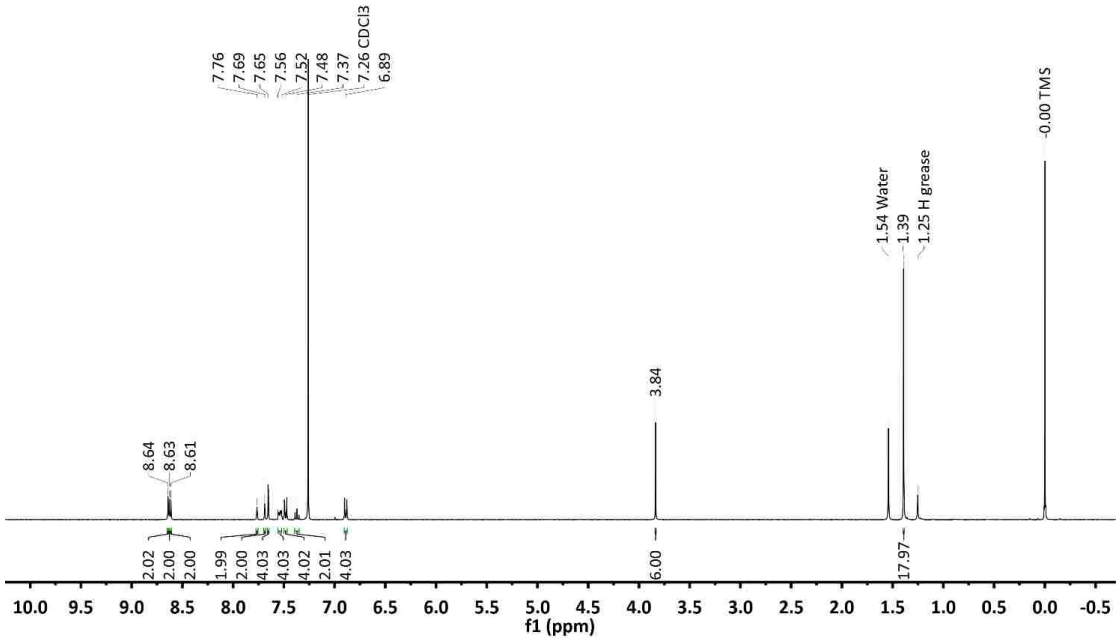

Figure 3.25 ^{1}H NMR spectrum of **19** (400 MHz, $CDCl_3$, 298 K).

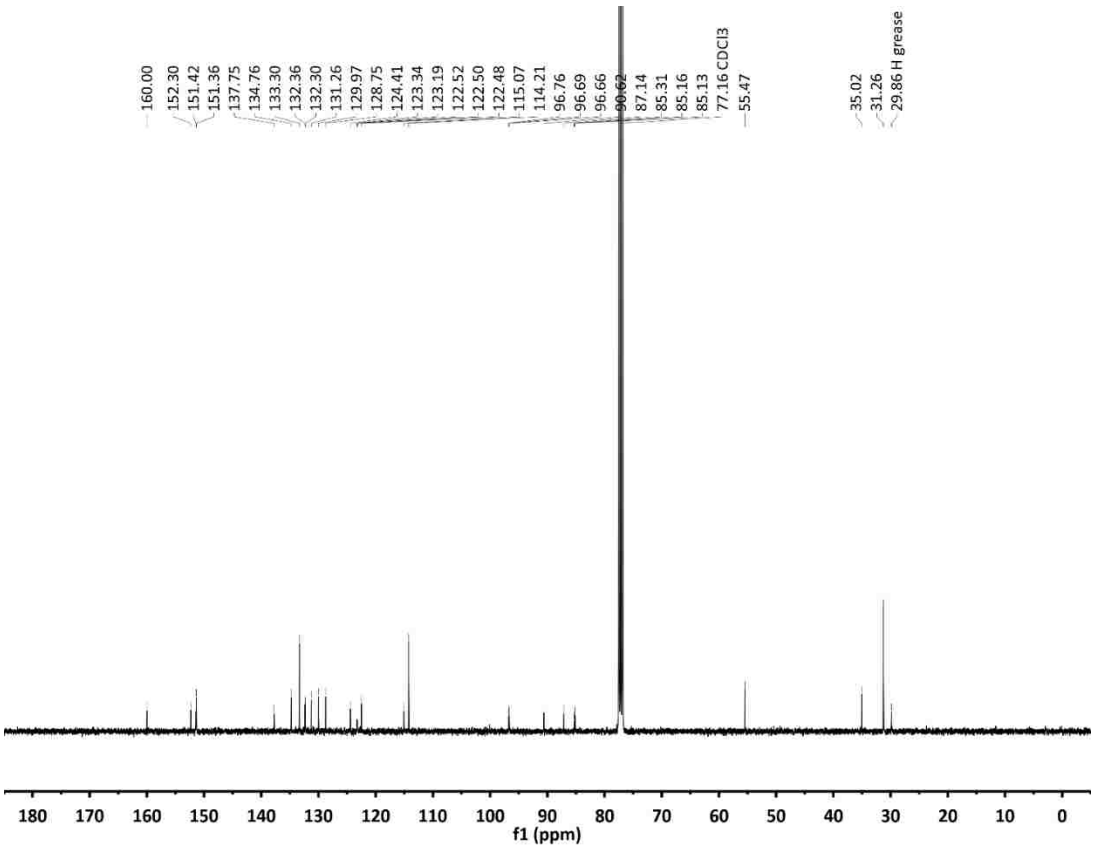

Figure 3.26 ^{13}C NMR spectrum of **19** (101 MHz, $CDCl_3$, 298 K).

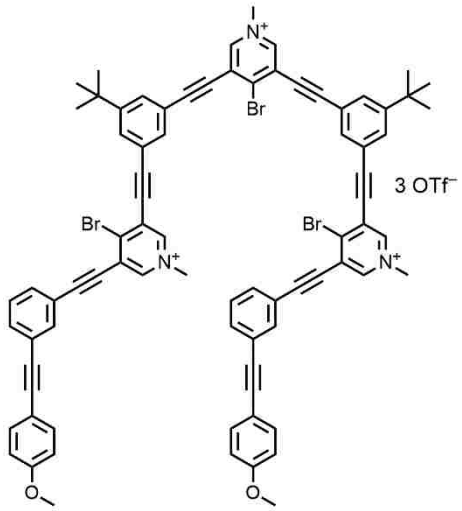

5,5'-((((4-bromo-1-methylpyridine-1-ium-3,5-diyl)bis(ethyne-2,1-diyl))bis(3-(tert-butyl)-5,1-phenylene))bis(ethyne-2,1-diyl))bis(4-bromo-3-((3-((4-methoxyphenyl)ethynyl)phenyl)ethynyl)-1-methylpyridin-1-ium) trifluoromethanesulfonate (**6**)

An oven-dried round bottom flask was charged with **19** (0.300 g, 0.232 mmol, 1.0 equiv) and anhydrous DCM (60 mL). The headspace was purged with N_2, and methyl OTf^- (0.105 mL, 0.930 mmol, 4.0 equiv) was added via syringe. The reaction was allowed to stir under N_2 at RT for 12 h. The solution was filtered, and the solid was rinsed with anhydrous DCM to give a pale-yellow powder (0.387 g, 93 %). Due to the instability of **6** in solution, ^{1}H NMR samples were prepared in an N_2-filled glovebox (for glovebox details, see Section 3.4). ^{13}C NMR spectroscopic data could not be collected on account of peak broadening at high concentration (37 mM), consistent with nonspecific aggregation (see Figures 3.28–3.29). Furthermore, the instability of **6** precluded ^{13}C spectroscopic data collection at lower concentration. Mp = 210 °C with decomposition. ^{1}H NMR (400 MHz, 1:4 *v*/*v* DMF-d_7-CD_3CN) δ 9.19 (s, 2H), 9.17 (s, 2H), 9.15 (s, 2H), 7.98 (d, *J* = 1.53 Hz, 4H), 7.92 (t, *J* = 1.48 Hz, 2H), 7.90 (t, *J* = 1.4 Hz, 2H), 7.79–7.73

(m, 4H), 7.65–7.59 (m, 6H), 7.07 (d, J = 8.92 Hz, 4H), 4.48 (s, 3H), 4.47 (s, 6H), 3.92 (s, 6H), 1.50 (s, 18H). ^{19}F NMR (376 MHz, 1:4 v/v DMF-d_7-CD_3CN) δ –79.69. ESI-MS ($C_{80}H_{61}Br_3N_3O_2$ = $[M]^{3+}$): 444.10; ($C_{81}H_{61}Br_3F_3N_3O_5S$ = $[M+OTf^-]^{2+}$): 740.62.

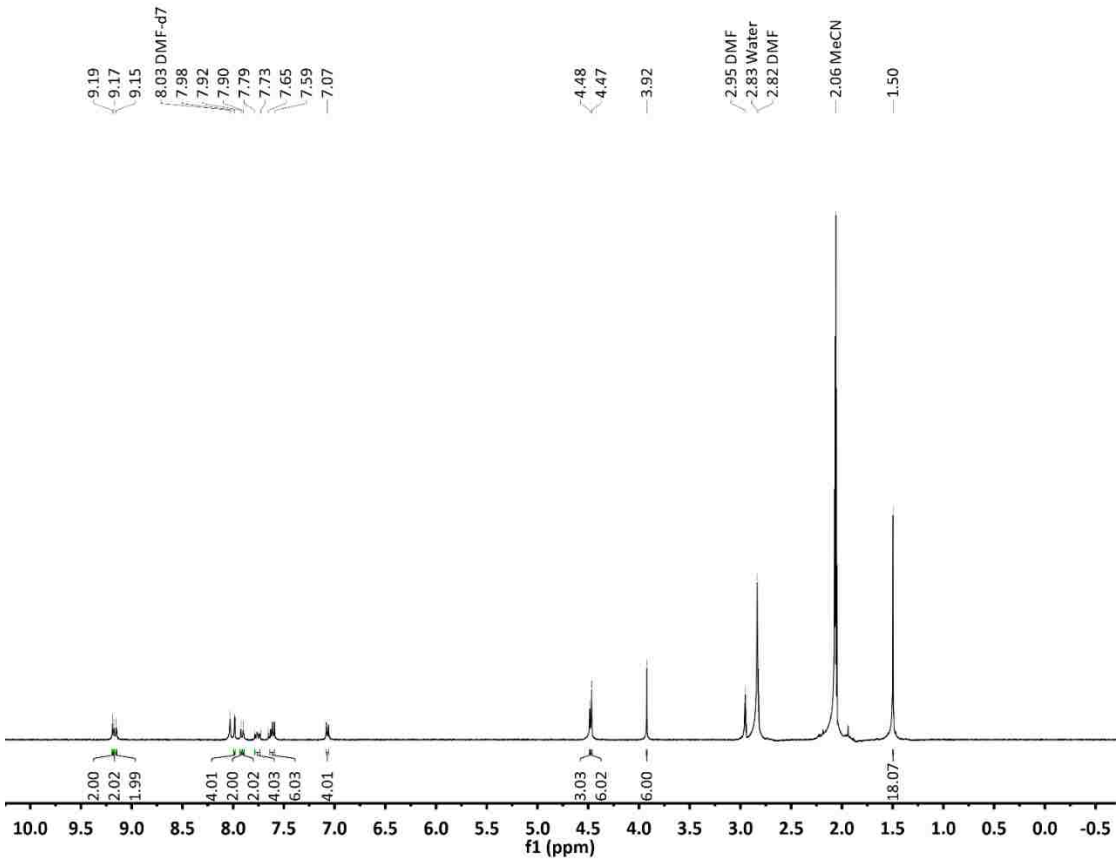

Figure 3.27 ^{1}H NMR spectrum of **6** (600 MHz, 1:4 v/v DMF-d_7-CD_3CN, 298 K).

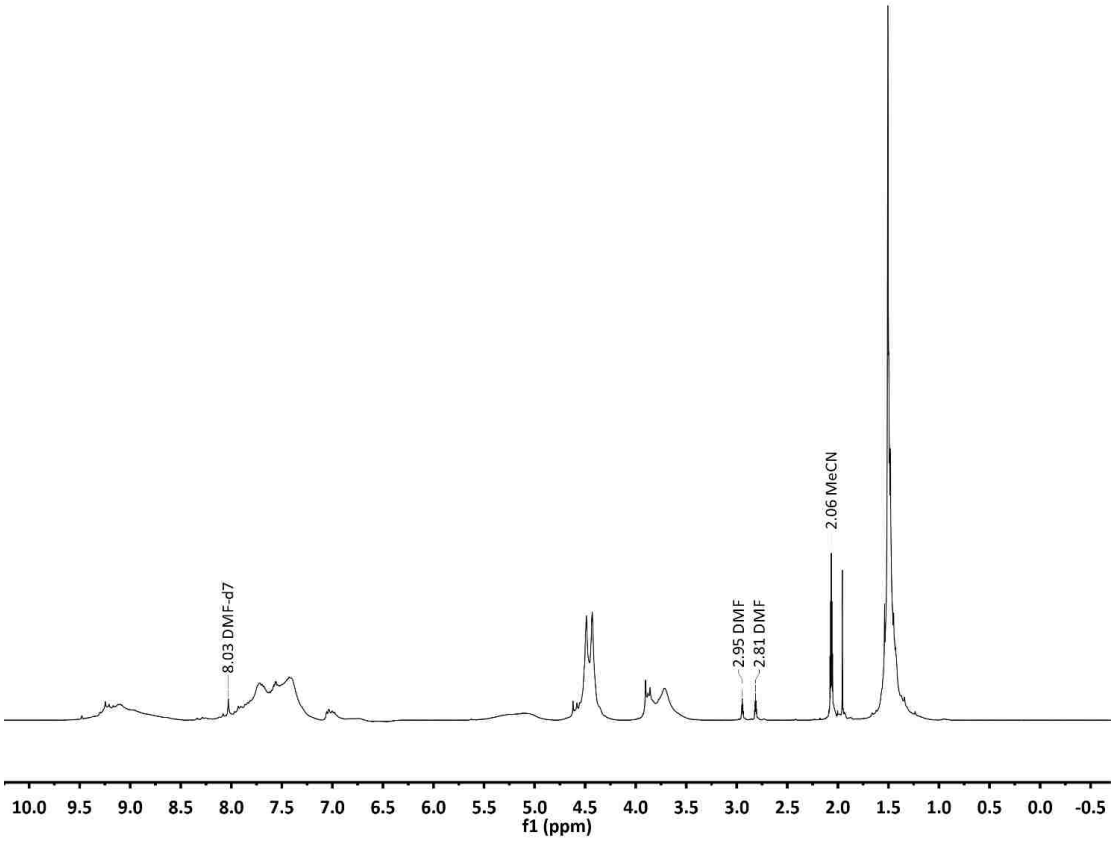

Figure 3.28 ^{1}H NMR spectrum of **6** at high concentration (37 mM, 400 MHz, 1:4 *v*/*v* DMF-d_7-CD_3CN, 298 K).

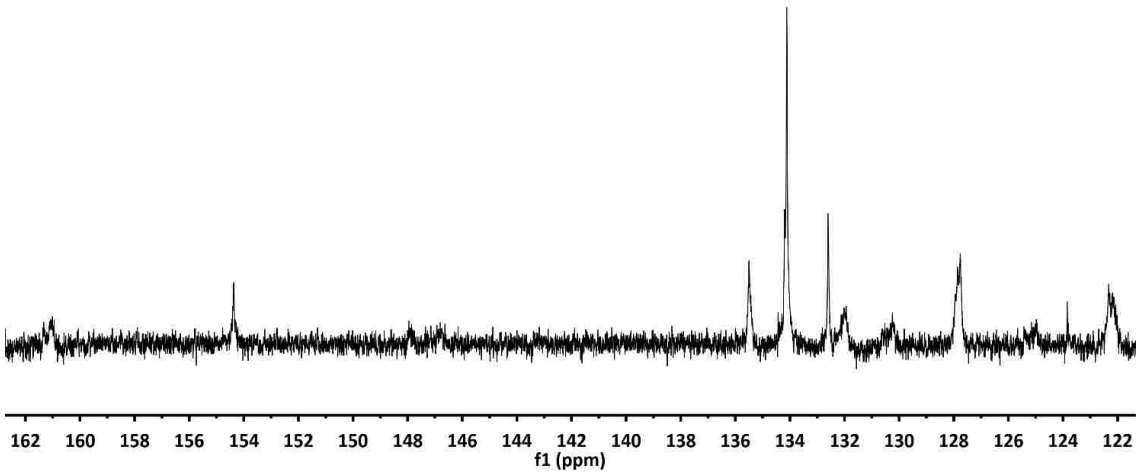

Figure 3.29 Portion of ^{13}C NMR spectrum of **6** at high concentration (37 mM, 101 MHz, 1:4 *v*/*v* DMF-d_7-CD_3CN, 298 K).

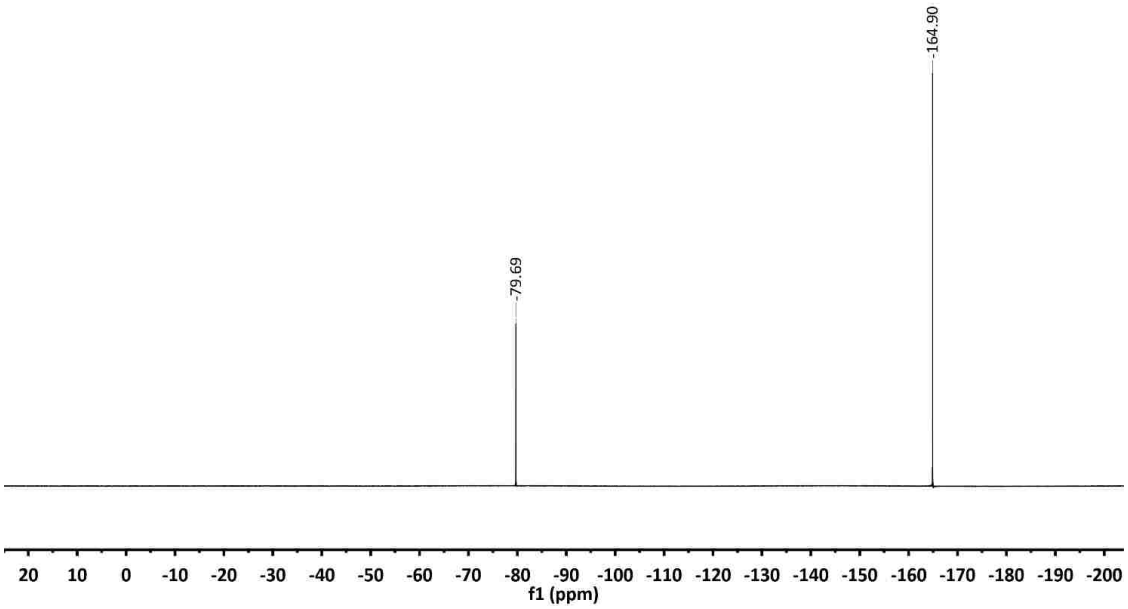

Figure 3.30 ^{19}F NMR spectrum of **6** (376 MHz, 1:4 *v*/*v* DMF-d_7-CD_3CN, 298 K).

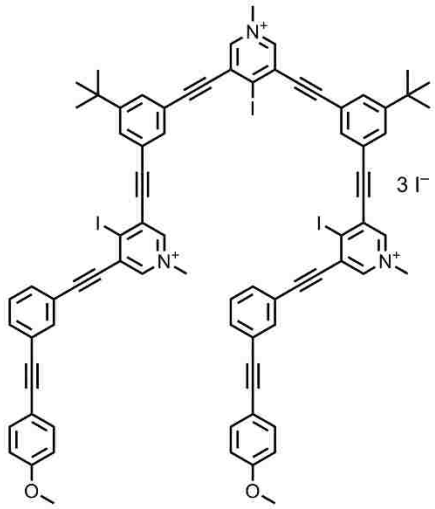

5,5'-((((4-iodo-1-methylpyridine-1-ium-3,5-diyl)bis(ethyne-2,1-diyl))bis(3-(tert-butyl)-5,1-phenylene))bis(ethyne-2,1-diyl))bis(4-iodo-3-((3-((4-methoxyphenyl)ethynyl)phenyl)ethynyl)-1-methylpyridin-1-ium) iodide (**7**)

A round bottom flask (100 mL) was charged with **6** (0.0530 g, 0.0297 mmol, 1.0 equiv), NaI (0.134 g, 0.892 mmol, 30.0 equiv), DMF (12.5 mL), and CH_3CN (37.5 mL). The solution was allowed to stir for 12 h under N_2. The solution was concentrated under reduced pressure. The residue was suspended in DI H_2O (50 mL) with the help of sonication and was filtered. The solid was triturated with DI H_2O (50 mL) and Et_2O (50 mL) and allowed to dry on vacuum to give a yellow solid (0.050 g, 90 %). A ^{1}H NMR spectrum was collected at RT, but the best peak resolution was seen at 341 K. Therefore, the latter was integrated. Mp = 192 °C with decomposition. ^{1}H NMR (400 MHz, 1:3 *v*/*v* DMF-d_7-CD_3CN) δ 9.55 (s), 9.44 (s), 9.41 (s), 9.21 (s), 9.02 (s), 8.23 (s), 8.19 (s), 8.08 (s), 8.02 (s), 7.97 (s), 7.92 (s), 7.75 (t, *J* = 1.48 Hz), 7.71 (s), 7.58 (t, *J* = 1.56 Hz), 7.56 (t, *J* = 1.80 Hz), 7.53 (s), 7.51 (t, *J* = 1.60 Hz), 7.50 (t, *J* = 1.40 Hz), 7.46–7.43 (m), 7.39–7.24 (m), 7.05 (dt, *J* = 3.88, 1.32 Hz), 6.99–6.94 (m), 6.59–6.52 (m), 4.48–4.41 (m), 4.36 (s), 3.59 (s), 3.54 (s), 3.52 (s), 1.60 (s), 1.56 (d, *J* = 2.56 Hz). ^{1}H NMR (500 MHz, 1:4 *v*/*v*

DMF-d_7-CD_3CN, 341 K) δ 9.56 (s, 2H), 9.46 (s, 2H), 9.39 (s, 2H), 9.26 (s, 2H), 9.06 (s, 2H), 8.09 (s, 2H), 8.00 (s, 2H), 7.95 (s, 2H), 7.91 (s, 2H), 7.88 (s, 2H), 7.76 (s, 2H), 7.73 (s, 2H), 7.70 (s, 2H), 7.61 (s, 2H), 7.57 (s, 4H), 7.54–7.49 (m, 6H), 7.45 (d, *J* = 7.73 Hz, 4H), 7.41–7.26 (m, 24H), 7.07 (d, *J* = 6.2 Hz, 2H), 6.98 (t, *J* = 7.65 Hz, 4H) , 6.57 (s, 12H), 4.48 (s, 3H), 4.43 (s, 12H), 4.40 (s, 6H), 4.34 (s, 6H), 3.61 (s, 6H), 3.57 (s, 6H), 3.53 (s, 6H), 1.61 (s, 18H), 1.57 (d, *J* = 4.8 H, 36H). ^{13}C NMR (101 MHz, 1:3 *v*/*v* DMF-d_7-CD_3CN) δ 160.83, 160.79, 160.57, 154.42, 153.98, 153.55, 153.44, 145.62–145.36, 143.72–143.45, 134.35, 134.25, 134.22, 133.51–129.59, 124.39, 124.33, 124.05, 123.60, 123.57, 123.11, 123.03–122.31, 115.61–115.26, 115.04, 100.89–100.39, 100.06, 99.84, 99.65, 99.45, 99.22, 99.17, 99.09, 98.83, 92.57, 92.42, 91.92, 90.29–89.18, 88.70, 88.47, 88.15, 87.98, 87.78, 87.57, 87.30, 56.40–56.22, 55.91, 55.81, 55.79, 49.41–48.50, 32.52, 32.29, 32.04, 31.52. HRMS ($C_{80}H_{61}I_4N_3O_2$ = $[M+I^-]^{2+}$): calculated = 801.5466; found = 801.5433.

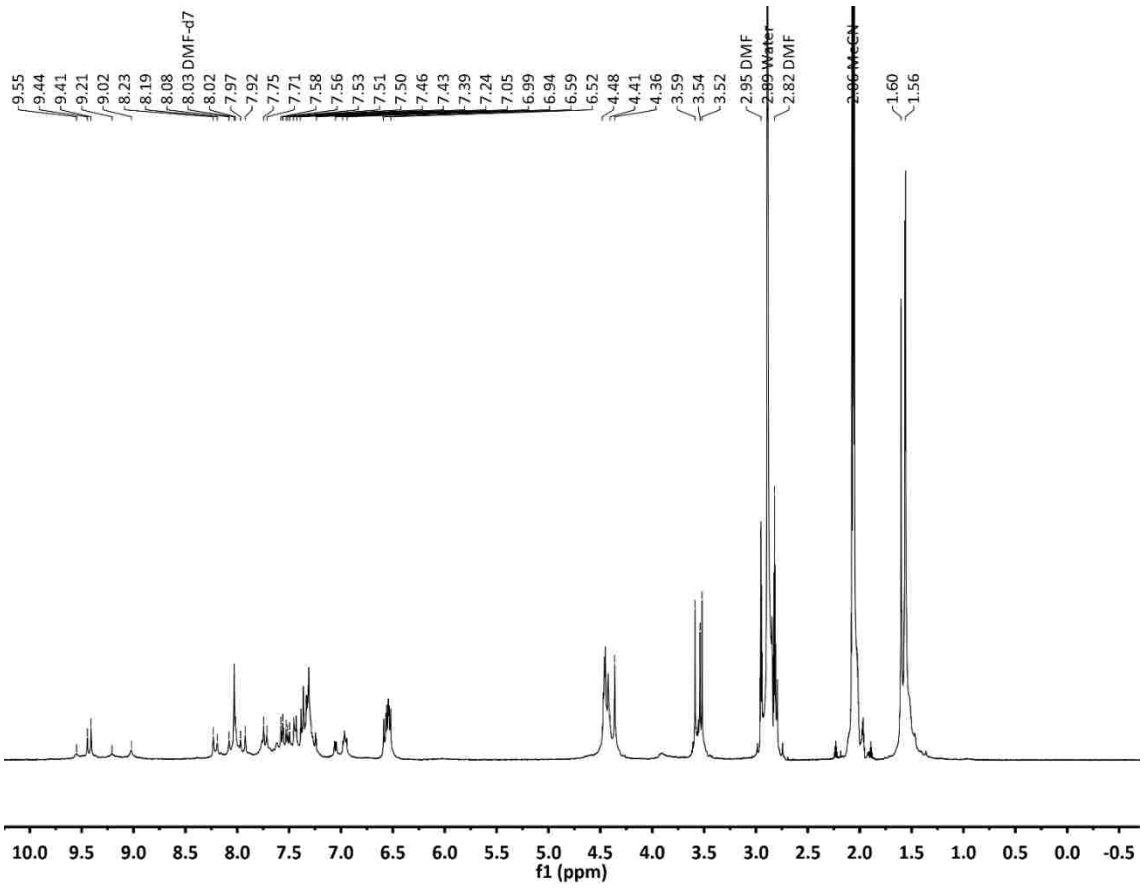

Figure 3.31 ^{1}H NMR spectrum of **7** (400 MHz, 1:3 *v*/*v* DMF-d_7-CD_3CN, 298 K).

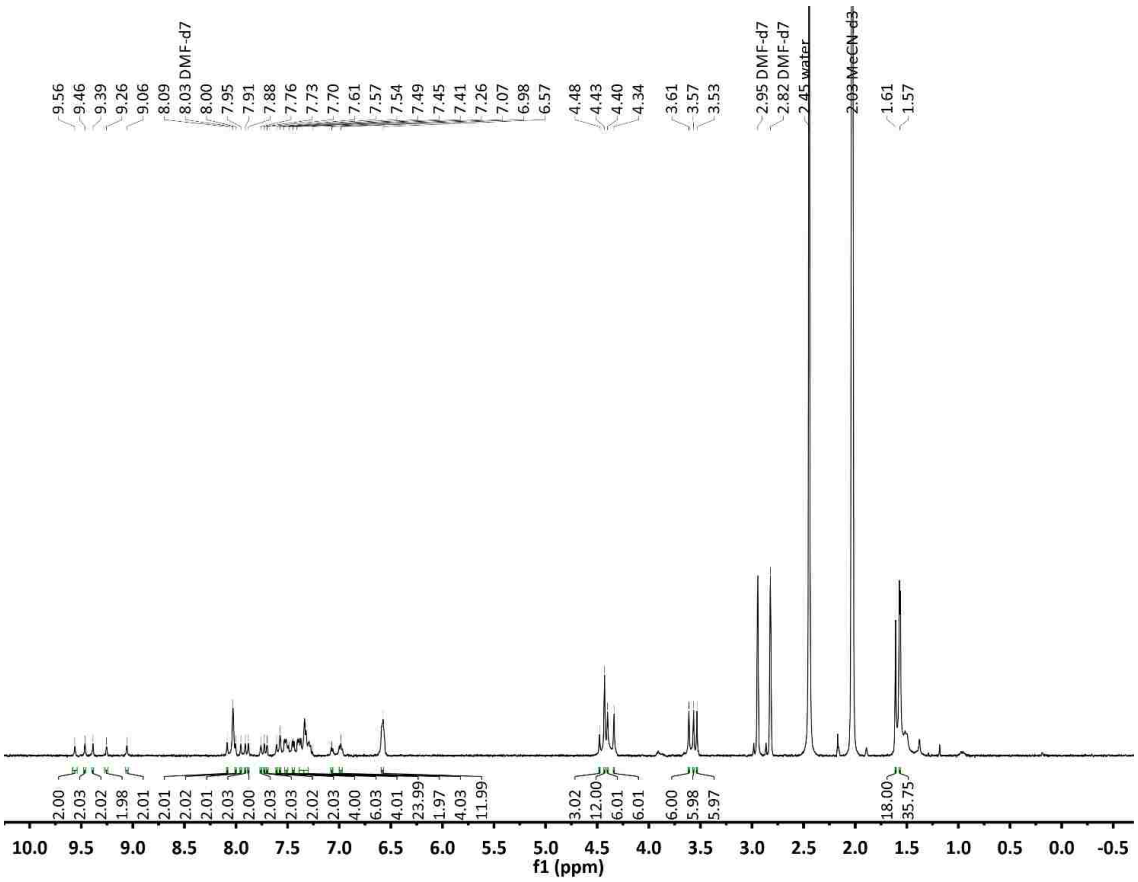

Figure 3.32 ^{1}H NMR spectrum of **7** (500 MHz, 1:4 *v*/*v* DMF-d_7-CD_3CN, 341 K).

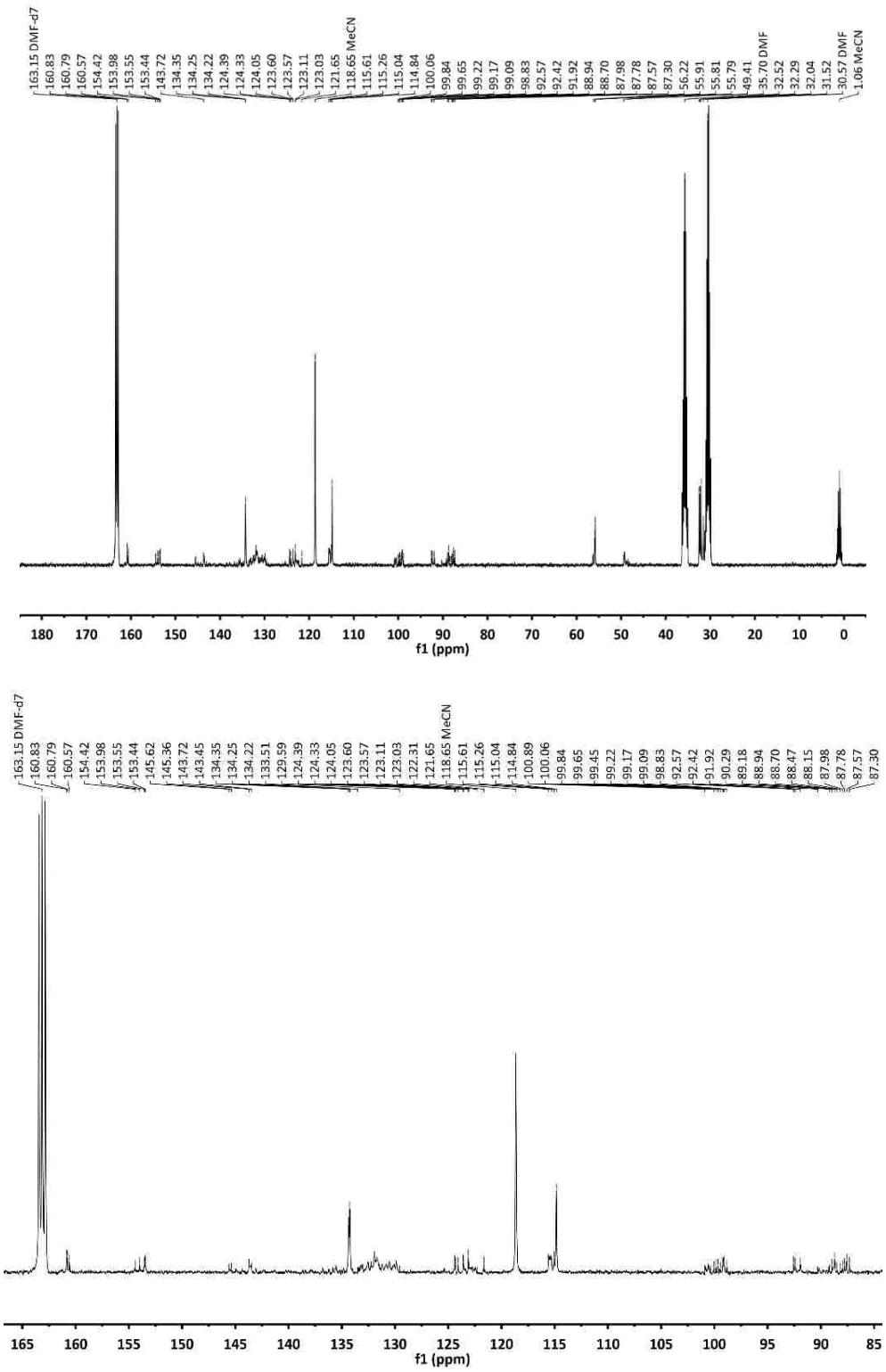

Figure 3.33 ^{13}C NMR spectrum of **7** (top) with downfield portion of spectrum (bottom; 101 MHz, 1:3 *v*/*v* DMF-d_7-CD_3CN, 298 K).

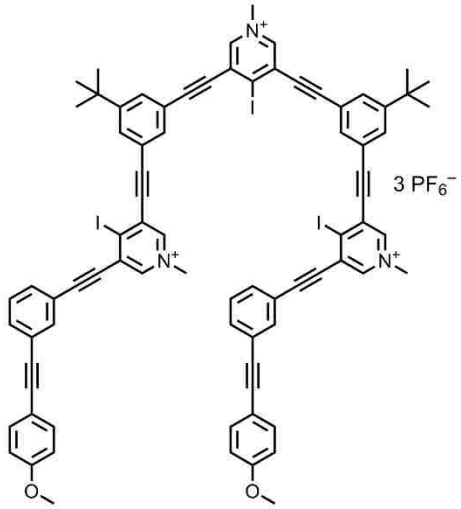

5,5'-((((4-iodo-1-methylpyridine-1-ium-3,5-diyl)bis(ethyne-2,1-diyl))bis(3-(tert-butyl)-5,1-phenylene))bis(ethyne-2,1-diyl))bis(4-iodo-3-((3-((4-methoxyphenyl)ethynyl)phenyl)ethynyl)-1-methylpyridin-1-ium) hexafluorophosphate(V) (**8**)

A flame-dried round bottom flask (25 mL) was charged with **7** (0.0150 g, 0.0081 mmol, 1.0 equiv), $AgPF_6$ (0.0082 g, 0.0323 mmol), and an anhydrous mixture of 1:1 *v*/*v* DMF-EtOAc (5 mL). The solution was allowed to stir under N_2 for 30 min. The cloudy mixture was passed through a syringe filter (0.2 μm). The filtrate was concentrated under reduced pressure, and the residue was recrystallized by the vapor diffusion of dry Et_2O into a 1:1 *v*/*v* DMF-CH_3CN solution of **8**. The resulting beige powder was dried under vacuum to give the product (0.0152 g, 80 %). Residual hexanes could not be removed from **8** even after drying in vacuo and recrystallizations. ^{13}C NMR spectroscopic data could not be collected for the same reasons described for compound **6**. Mp = 112 °C with decomposition. ^1H NMR (600 MHz, 1:3 *v*/*v* DMF-d_7-CD_3CN) δ 9.03 (s, 2H), 9.01 (s, 2H) 8.98 (s, 2H), 7.98 (d, *J* = 3.42 Hz, 4H), 7.93 (s, 2H), 7.89 (s, 2H), 7.76 (d, *J* = 7.62 Hz, 2H), 7.73 (d, *J* = 7.86 Hz, 2H), 7.62 (t, *J* = 7.92 Hz, 2H), 7.59 (d, *J* = 8.28 Hz, 4H), 7.06

(d, J = 8.28 Hz, 4H), 4.44 (s, 3H), 4.42 (s, 6H), 3.92 (s, 6H), 1.50 (s, 18H). ^{19}F NMR (376 MHz, 1:3 *v*/*v* DMF-d_7-CD_3CN) δ –72.17, –74.05. ESI-MS ($C_{80}H_{61}I_3N_3O_2$ = $[M]^{3+}$): 492.34; ($C_{80}H_{61}F_6I_3N_3O_2P$ = $[M+PF_6^-]^{2+}$): 810.45.

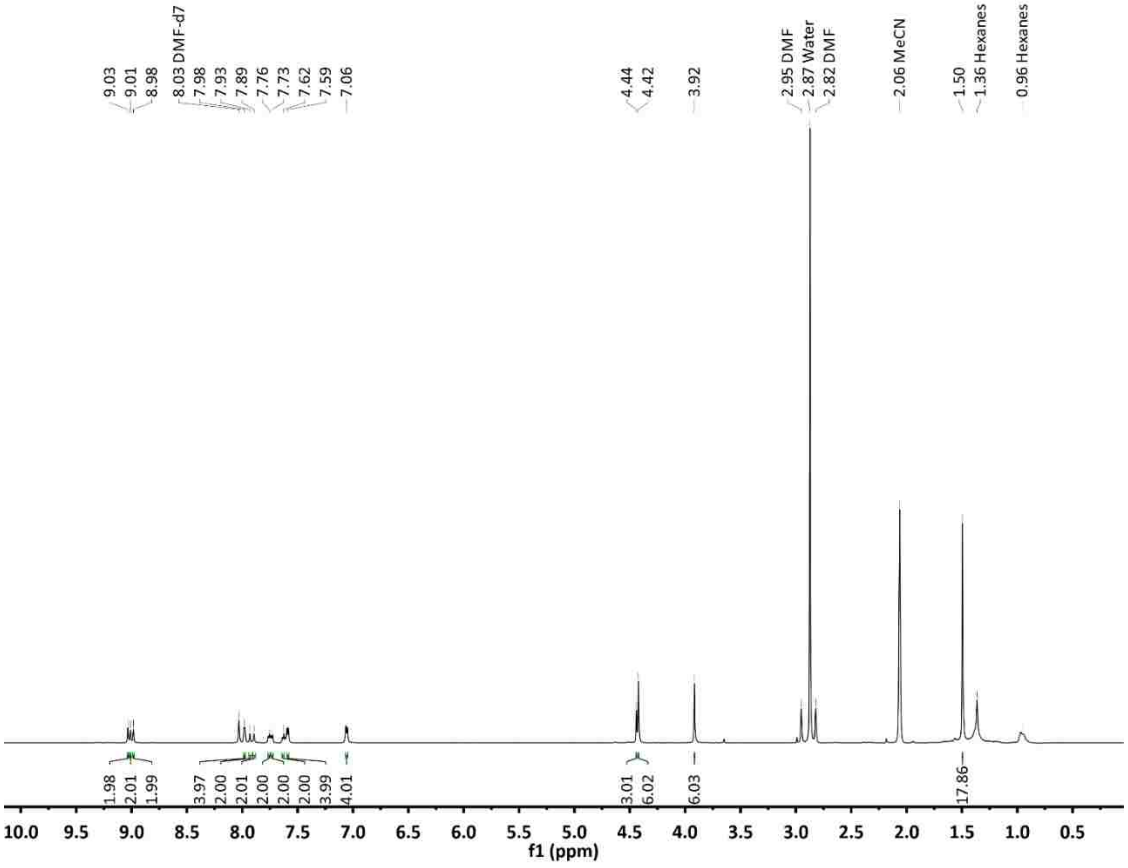

Figure 3.34 ^{1}H NMR spectrum of **8** (400 MHz, 1:3 *v*/*v* DMF-d_7-CD_3CN, 298 K).

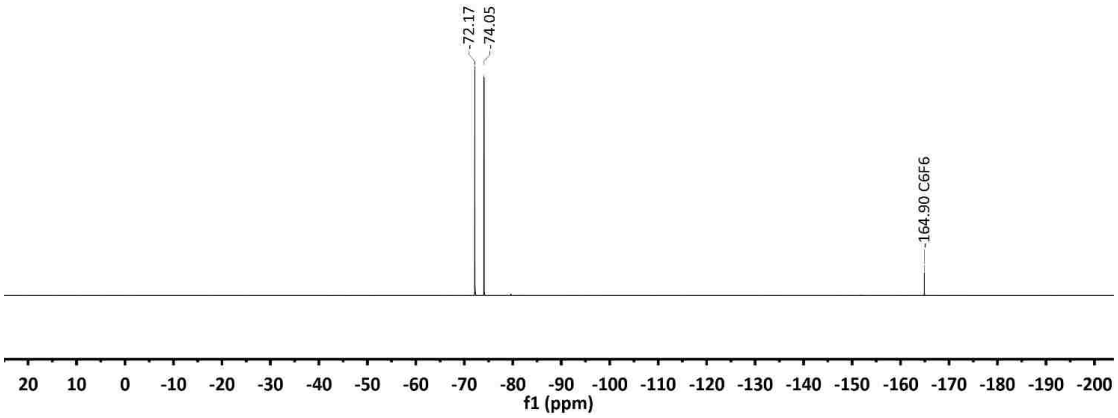

Figure 3.35 ^{19}F NMR spectrum of **8** (376 MHz, 1:3 *v*/*v* DMF-d_7-CD_3CN, 298 K).

3.4.2 X-Ray Crystallographic Data

Single-crystal X-ray diffraction data for **7** were collected at 100 K on a Bruker D8 Venture using CuKα (λ = 1.54178) radiation. Data have been corrected for absorption using SADABS area detector absorption correction program. Using Olex2,[157] the structure was solved with the ShelXT[158] structure solution program using Direct Methods and refined with the ShelXL refinement package using least squares minimization. Hydrogen atoms were placed in calculated positions using a ridged group model and refined with isotropic thermal parameters. The majority of non-hydrogen atoms were refined with anisotropic thermal displacement parameters (see below discussion for further details). The structure was found to contain indistinguishable solvent molecules within the lattice voids. Attempts at modeling this solvent were not able to produce a suitable model. The SQUEEZE[167] routine within PLATON was utilized to account for the residual, diffuse electron density, and the model was refined against these data. A

total of 4425 electrons per unit cell were corrected for. All calculations and refinements were carried out using APEX2, SHELXTL, Olex2, and PLATON.

The initial solution had a significant resemblance to the predicted nonamer. After initial refinement the main chains were fully established and identification of the anisole rings and *tert*-butyl groups from the difference map were possible. The anisole rings required geometric restraints as refinement lacking these restraints led to chemically unreasonable rings. The use of displacement parameter restraints (RIGU, SIUM, ISOR) were employed as the locations of the anisole rings lend themselves to multiple positions or thermal motion, as illustrated by elongated ellipsoid shapes. The anisole methoxy groups required bond length and angle restraints (1,3-distances) (DFIX 1.37(2) for O-C(sp^2) and O-C(sp^3) 1.42(2) and DANG 2.39(4)). Additionally a few of these methoxy groups were refined isotropically, as the anisotropic displacement parameters were unreasonable even with the use of displacement restraints. A number of the *tert*-butyl groups were also refined isotropically. The difference map and the anisotropic displacement parameters indicate possible positional disorder of the *tert*-butyl carbons. Attempts at modeling the disorder over a number of positions were unsuccessful. Given these results it was decided to model a few of the more troublesome tert-butyl groups isotropically. Distance and angle restraints have also been placed on *tert*-butyl groups (DFIX 1.54(2) and DANG 2.68(4)). Upon initial refinement, the location of seven of the nine I^- atoms were located from the difference map. The other I^- atoms were subsequently identified, one of which was modeled as having disorder over two positions with site occupancy factors refined using a free variable. Use of displacement parameter

restraints, RIGU and SIMU, for the main chain (not including the anisole rings, *tert*-butyl groups, and the iodine atoms) were applied.

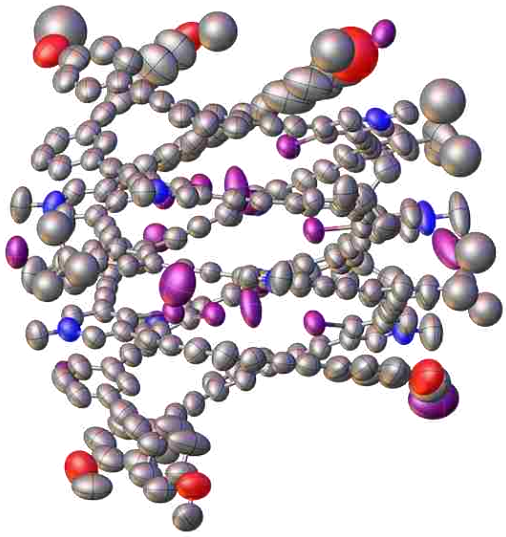

Figure 3.36 Thermal ellipsoidal representation of triple helicate **7** (at 50 % probability; hydrogen atoms omitted for clarity).

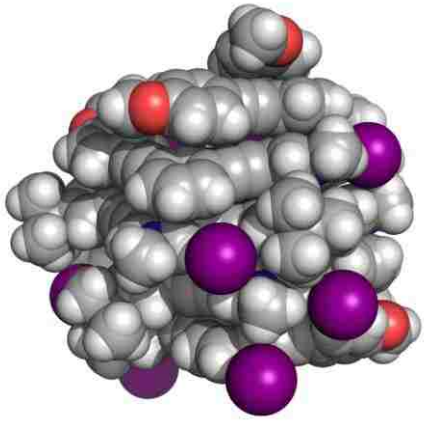

Figure 3.37 Solid-state space-filling representation of the extrachannel space of **7**.

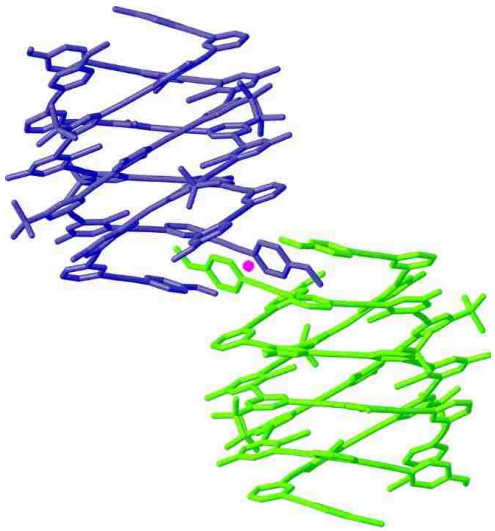

Figure 3.38 Solid-state stick representation of enantiomers of **7**. An intriguing inversion center (pink sphere) is sandwiched by two extra-channel anisole rings.

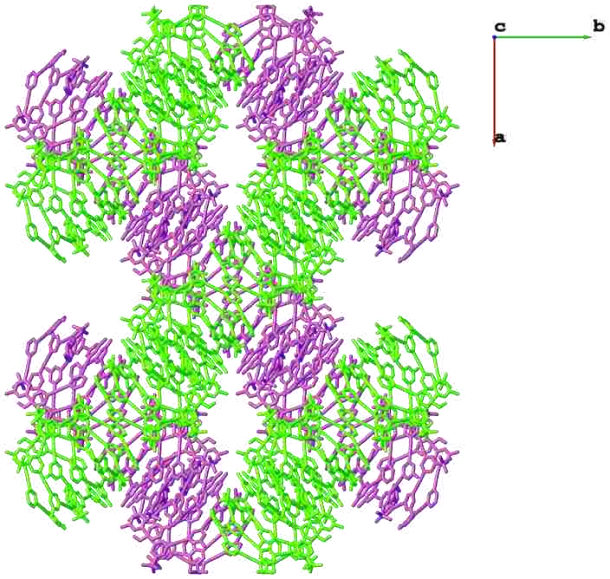

Figure 3.39 Crystal packing of **7** viewed down the crystallographic *c* axis. Triplex dimers proliferate end-on-end. A set of parallel columns (purple) stacks orthogonally to the other set (green).

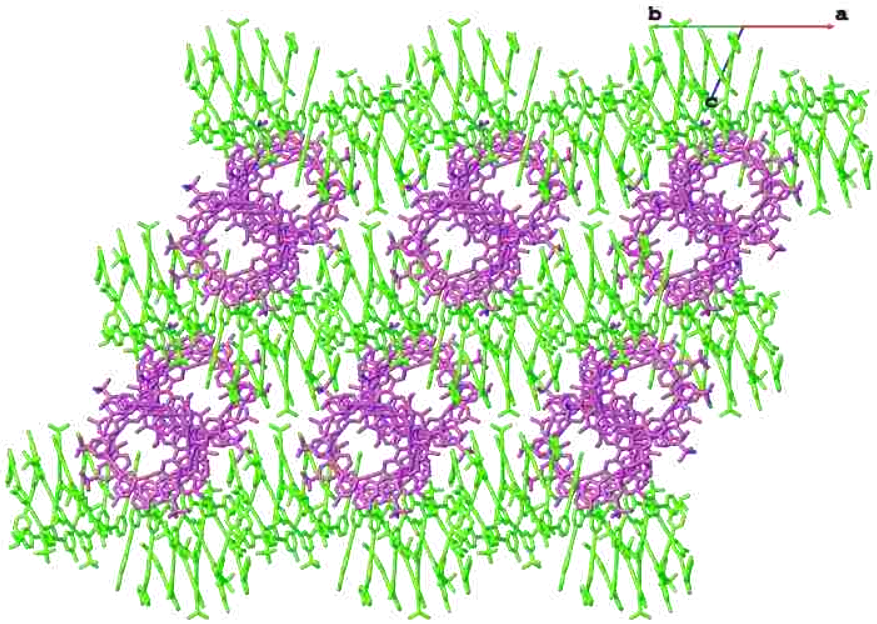

Figure 3.40 Crystal packing of **7** viewed along the [110] direction. Triplex dimers (green) proliferate end-on-end. Orthogonally stacked dimers (purple) are seen down their anion channels.

3.4.3 DFT Calculations Data

All DFT calculations were performed using the Gaussian 09 suite. We performed a geometry optimization on the scaffold of **7** without I^- at the B98 level, using the LANL2DZ basis set for all atoms with effective core potential(ECP) for iodine. Single-point energy calculations were carried out with I^- in two binding arrangements. In the first experiment, we calculated the energy (ΔG) of tridentate binding and in the second the energy of bidentate binding. These calculations were also at the B98 level, using the 6-31+G(d,p) basis set for non-halogen atoms C, O, N, H, and LANL2DZ with ECP for iodine and the I^- anion augmented with diffuse functions of p-symmetry and polarization functions of d-symmetry downloaded from the EMSL Basis Set Exchange.[168] This

method takes into account the large polarizability of the covalently bonded iodines on the receptor and accurately models the "σ-hole". We began the conformational search from an MM2-minimized folded position. Due to long run times, an exhaustive conformational search was not conducted.

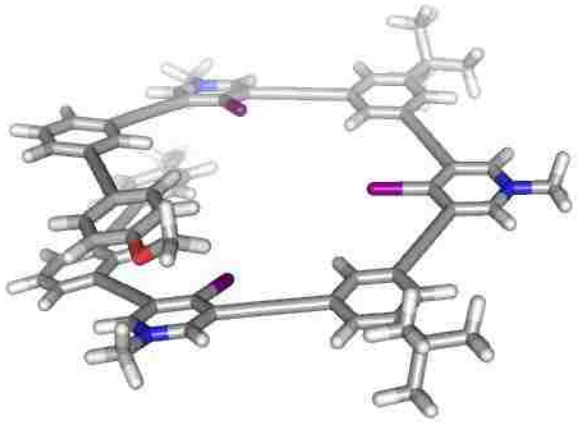

Figure 3.41 DFT-minimized single strand of **7** sans I^-.

SCF Done: E(RB98) = -3430.97540643 A.U. after 1 cycles
Convg = 0.2805D-08 -V/T = 2.0137
Center Atomic Forces (Hartrees/Bohr)

#	#	X	Y	Z
1	53	0.002231598	-0.000513591	-0.001695230
2	53	0.000574764	0.001018462	0.002422171
3	53	-0.002755753	-0.000651001	-0.000424034
4	6	0.003551069	0.002688850	0.000913389
5	6	-0.002891622	0.001236914	0.003690681
6	6	-0.003449003	-0.002243652	-0.000790780
7	6	0.000392625	-0.000292203	-0.000710834
8	6	-0.000516788	-0.000992563	-0.001258051
9	1	-0.001089783	-0.001705827	-0.002243033
10	6	-0.000946375	-0.000347659	-0.000014014
11	6	-0.001293536	0.000436684	0.001544661
12	1	-0.001662456	0.000789678	0.002226635
13	6	0.000834506	0.001305689	0.001668341
14	1	0.001042274	0.001706468	0.002225410

15	6	0.001998422	0.000539407	-0.000145961
16	1	0.002678445	0.000901423	-0.000065255
17	6	-0.000748329	-0.000432332	-0.000430776
18	6	-0.000354099	-0.000737012	-0.001741051
19	1	-0.000684182	-0.001421862	-0.002385681
20	6	0.003281445	-0.001457506	-0.001315806
21	6	0.001390973	0.000782616	0.000025171
22	1	0.002585017	0.001257901	0.000409527
23	6	0.000264879	0.000638866	0.000785872
24	6	-0.001052125	0.000001165	0.001278126
25	1	-0.001927763	0.000001178	0.002187748
26	6	-0.004986429	-0.001589950	0.000301582
27	6	-0.003194573	-0.000057936	0.002574530
28	6	0.000191901	-0.000025633	-0.000017057
29	1	0.000604760	-0.000200266	0.002714823
30	1	-0.001055982	0.002659965	-0.000390010
31	1	-0.002337055	-0.001902814	-0.000352411
32	6	0.000549266	0.000011014	-0.000718181
33	6	0.001567728	0.000711350	0.000305338
34	1	0.002542309	0.001284564	0.000587733
35	6	0.000101522	0.000061186	0.001019898
36	6	-0.000868717	-0.000063403	0.001107889
37	1	-0.001769826	-0.000194130	0.002153258
38	6	0.000066000	-0.000191242	-0.000131293
39	6	0.014196873	-0.005103961	-0.001460636
40	6	-0.000071978	-0.000500873	-0.001526773
41	1	-0.000244741	-0.000762075	-0.002415710
42	6	0.000441703	0.000627747	0.001773396
43	1	0.000336882	0.001063927	0.002589882
44	7	-0.001605880	0.000227800	0.001512069
45	6	-0.001609782	-0.000455510	-0.000737689
46	1	-0.002804830	-0.000610956	-0.000859471
47	6	0.000079780	-0.000255934	-0.000470879
48	6	0.001854579	-0.000332027	-0.001319607
49	6	0.000688896	-0.000013335	-0.000080786
50	6	0.000455928	0.000814638	0.002061351
51	6	0.000498070	0.000290654	0.000250077
52	6	0.001224080	0.000210004	-0.001186522
53	1	0.001873969	0.000284769	-0.002220456
54	7	-0.000381146	-0.000887109	-0.001159071
55	6	-0.001583086	-0.000801692	-0.000057941
56	1	-0.002490015	-0.001402029	-0.000494248
57	6	-0.000251064	0.000043954	0.000563092
58	6	-0.002984019	-0.000756475	0.003103417
59	6	0.002721210	0.000653536	-0.002930903
60	6	0.012507234	-0.005585446	-0.001516623

61	6	0.000026617	0.000963394	0.001534315
62	1	0.000110299	0.001465384	0.002598019
63	6	-0.000657169	0.000100564	0.000622735
64	6	-0.001475054	-0.001063011	-0.000628052
65	1	-0.002298837	-0.001592613	-0.000686468
66	6	-0.000236570	-0.001011623	-0.001591414
67	1	-0.000053636	-0.001530362	-0.002487655
68	6	0.001259977	-0.000335534	-0.001117558
69	8	0.004146743	-0.002051822	-0.004127166
70	6	0.001262572	0.001132978	0.000716864
71	1	0.002445195	0.001440836	0.000669443
72	6	-0.000495745	0.000022207	0.000295922
73	6	-0.002097497	-0.000667218	-0.000265309
74	6	-0.000468074	-0.000271268	-0.000566932
75	6	0.001210366	-0.000527009	-0.001533854
76	1	0.002025354	-0.000596097	-0.001916200
77	7	0.001906173	0.000852735	0.000491903
78	6	0.000326751	0.000777207	0.001373103
79	1	0.000938177	0.001382436	0.002491576
80	6	-0.004498761	-0.001351789	-0.001359005
81	6	0.003167851	0.000032630	-0.002558591
82	6	0.001281784	0.000434284	-0.000051970
83	6	0.008789560	-0.005313595	-0.011442466
84	6	-0.000347192	-0.001455922	-0.002129045
85	1	-0.001430490	-0.001692382	-0.001990596
86	6	-0.001911518	-0.000799208	-0.000220986
87	6	-0.000917940	0.000803118	0.001616272
88	1	-0.001406048	0.001140154	0.002395872
89	6	0.000715825	0.001227159	0.001264874
90	1	0.001283180	0.001771609	0.002037446
91	6	0.004670380	0.001387437	0.001808306
92	8	0.001679162	-0.004083864	-0.003996075
93	6	-0.000276237	-0.000529828	-0.001557958
94	1	-0.000356913	-0.000854941	-0.002708716
95	6	-0.000860128	-0.000301183	-0.000264077
96	6	-0.001544257	-0.000023469	0.001173313
97	1	-0.002200075	-0.000014823	0.001813191
98	6	0.000320201	0.000644289	0.002029040
99	1	0.000386428	0.000836164	0.002738343
100	6	0.001691594	0.000554797	0.000544637
101	1	0.002595059	0.000842001	0.000917203
102	6	0.000756662	0.000027525	-0.000488982
103	6	0.002553415	-0.001145389	-0.003573262
104	6	0.004846259	0.001262064	-0.000489571
105	6	-0.000208915	0.000281305	-0.000095792
106	1	0.000504411	0.001469503	0.002460939

107	1	0.001926636	-0.002611166	0.000267380
108	1	0.001159438	0.001641325	-0.002190746
109	6	-0.000674705	-0.000699834	-0.004288766
110	6	0.000664997	0.000890655	0.003840767
111	6	0.000906013	0.002089657	0.003767648
112	6	-0.000962714	-0.002382649	-0.004000553
113	6	0.005290268	0.000164688	-0.001443328
114	1	-0.000576419	-0.003030832	0.000239283
115	1	-0.002358307	0.001614410	-0.002775889
116	1	-0.003122612	0.000009421	0.000065346
117	6	-0.001923138	0.003847546	0.002775872
118	6	-0.002125158	0.001005351	0.000638874
119	6	-0.000187756	-0.000089942	0.000010355
120	6	0.000270567	0.000092494	-0.000283241
121	6	-0.000772224	-0.000035630	0.000726382
122	1	0.002329190	0.000042810	-0.002533858
123	1	-0.000663254	-0.003323118	0.000512046
124	1	-0.002753919	0.001309829	-0.001448273
125	1	0.001265547	0.001883904	0.002484302
126	1	0.002366113	0.000324720	-0.002508238
127	1	-0.002740584	0.001713165	-0.001167925
128	1	0.001474311	0.001536430	0.002756016
129	1	-0.000385648	-0.003273576	0.000912907
130	1	0.002301100	0.000043267	-0.002438919
131	6	-0.003473107	0.000780464	0.000165361
132	6	-0.007080307	0.001986745	0.000680153
133	6	-0.003837623	0.000614205	0.000230798
134	1	0.000087907	0.000606012	0.003288634
135	1	0.002547111	-0.001323098	-0.001358851
136	1	-0.003103968	-0.002540965	0.000287841
137	1	-0.000077151	0.002783175	-0.001846649
138	1	-0.000265894	0.001089005	0.002951227
139	1	-0.004100110	-0.000170594	-0.000117554
140	1	-0.000034545	0.002440349	-0.002386777
141	1	-0.003120900	-0.001793500	-0.001665952
142	1	0.002392224	-0.001959886	0.000255077
143	1	-0.006477279	0.003608074	0.008222531
144	1	-0.000041934	-0.002478169	0.002160198
145	1	-0.002104600	-0.000061133	-0.002478069
146	1	0.003086462	0.001092013	-0.000791461
147	1	-0.002959181	0.009586803	0.000224506
148	1	-0.002207628	0.001024778	0.006192030
149	1	-0.012813928	-0.001448436	-0.000405397

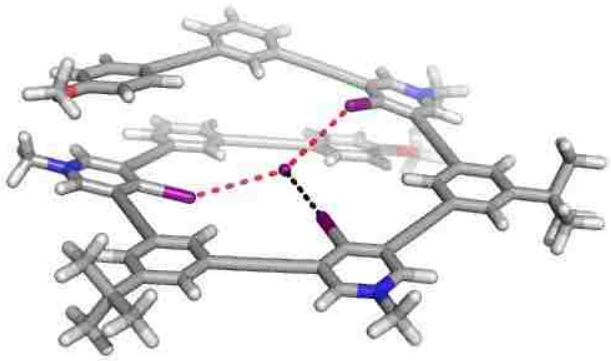

Figure 3.42 Single-point energy calculation of a single strand of **7** with I^-. The DFT-minimized conformation of a single strand of **7** was used in this calculation. Black dashes represent an energetically favorable halogen bond. Red dashes represent a non-bonding/repulsive interaction. The C$I\cdots I^-$ angles are 179 (black dashes), 141, and 146 ° (red dashes).

SCF Done: E(RB98) = -3443.27471508 A.U. after 50 cycles
Convg = 0.4787D-08 -V/T = 2.0179

I	-3.3793	-0.2712	1.7721
I	0.5474	4.2413	-0.0793
I	3.1079	-1.3837	-1.5052
C	4.3441	5.3114	-0.5362
C	2.597	-5.3765	-1.5734
C	3.3415	6.0255	-0.4549
C	1.4303	-6.1838	-1.8082
C	0.1432	-5.5812	-1.8829
H	0.0412	-4.5019	-1.7612
C	-1.0091	-6.3772	-2.1224
C	-0.8543	-7.7888	-2.2856
H	-1.7361	-8.4024	-2.4763
C	0.423	-8.3855	-2.2105
H	0.5254	-9.4634	-2.3434
C	1.567	-7.5955	-1.9721
H	2.5553	-8.0547	-1.9206
C	5.5081	4.4686	-0.616
C	6.8133	5.0482	-0.6564
H	6.8998	6.1338	-0.6313
C	7.9777	4.2452	-0.727
C	7.8024	2.8346	-0.7556
H	8.6736	2.1801	-0.8134

C	6.5104	2.2372	-0.7183
C	5.3541	3.0592	-0.6492
H	4.3601	2.6115	-0.6232
C	-3.4578	-5.3206	-2.3104
C	0.9606	-5.4186	2.4942
C	-9.2964	-2.3324	0.3675
H	-9.5132	-3.2459	0.9349
H	-9.3203	-2.5382	-0.7142
H	-10.0323	-1.5637	0.6347
C	-4.125	5.8994	0.3388
C	-4.3497	4.5054	0.4708
H	-3.512	3.8073	0.4648
C	-5.6805	4.0284	0.6054
C	-6.7662	4.9493	0.6112
H	-7.7784	4.5566	0.7179
C	-6.5612	6.3507	0.4855
C	-7.7822	7.3119	0.5016
C	-5.2275	6.8076	0.3487
H	-5.0227	7.8722	0.246
C	-6.9504	-2.7526	1.0504
H	-7.2305	-3.8031	1.0613
N	-7.9193	-1.8449	0.7338
C	-7.6439	-0.5071	0.669
H	-8.4587	0.16	0.3969
C	-6.3448	-0.0078	0.9429
C	-5.3166	-0.9446	1.2981
C	-5.6204	-2.3483	1.3407
C	0.8512	6.318	-0.1964
C	2.1766	6.8467	-0.3608
C	2.3313	8.2572	-0.4343
H	3.3133	8.7075	-0.5591
N	1.2555	9.0958	-0.3523
C	-0.0146	8.6103	-0.1962
H	-0.8235	9.3357	-0.1384
C	-0.2686	7.2174	-0.113
C	-2.7799	6.388	0.1867
C	-1.6162	6.7728	0.048
C	-9.8095	-4.0072	-3.4749
C	4.5572	-5.7364	2.4813
H	4.2662	-6.7806	2.3541
C	3.5431	-4.7396	2.6198
C	3.9437	-3.3895	2.8366
H	3.1793	-2.622	2.9708
C	5.3086	-3.033	2.8948
H	5.5877	-1.994	3.0763
C	6.2991	-4.035	2.7317

O	7.6777	-3.7695	2.7107
C	5.9198	-5.3886	2.535
H	6.6996	-6.1498	2.4722
C	4.7892	-3.9383	-1.1267
C	4.8444	-2.504	-1.1092
C	6.0919	-1.846	-0.8393
C	7.2374	-2.6464	-0.6055
H	8.2063	-2.2018	-0.3914
N	7.1697	-4.0118	-0.638
C	5.9925	-4.6545	-0.8834
H	6.0036	-5.7415	-0.8853
C	-4.6521	-3.35	1.6403
C	2.1491	-5.0977	2.5539
C	-4.8003	-4.8161	-2.4437
C	-5.0863	-3.4261	-2.2814
C	-6.3998	-2.9411	-2.4167
H	-6.6203	-1.8741	-2.3409
C	-7.4615	-3.8364	-2.7143
C	-7.1971	-5.2187	-2.8941
H	-7.9965	-5.9173	-3.1433
C	-5.876	-5.6968	-2.7585
H	-5.6717	-6.7591	-2.9025
C	-3.8104	-4.2237	1.8676
O	-8.7389	-3.2641	-2.7857
C	-1.4361	-4.8331	2.1956
H	-1.1602	-3.7843	2.0771
C	-2.8037	-5.2187	2.1172
C	-3.1662	-6.5893	2.2779
H	-4.2151	-6.8836	2.2217
C	-2.1636	-7.5533	2.5136
H	-2.4392	-8.6005	2.6449
C	-0.8057	-7.1728	2.5856
H	-0.0344	-7.9218	2.771
C	-0.4263	-5.805	2.4253
C	3.6002	-4.6855	-1.3741
C	-2.3198	-5.7857	-2.2119
C	8.4141	-4.8014	-0.3326
H	8.2202	-5.8642	-0.5178
H	8.668	-4.6444	0.726
H	9.2266	-4.4627	-0.9891
C	-5.9243	2.6139	0.7304
C	-6.1194	1.402	0.842
C	6.2343	-0.4217	-0.7921
C	6.3709	0.8029	-0.7545
C	1.4513	10.5872	-0.4283
H	1.1352	11.0429	0.5196

H	0.8589	10.9927	-1.2611
H	2.4992	10.8134	-0.616
C	8.1791	-2.6298	3.4763
C	9.4059	4.8466	-0.7887
C	9.3964	6.406	-0.7462
C	10.1091	4.3927	-2.116
C	10.2245	4.3238	0.4437
H	10.4342	6.7747	-0.7834
H	8.9437	6.7921	0.1844
H	8.8632	6.8394	-1.6108
H	10.1909	3.2947	-2.1875
H	11.131	4.8055	-2.1544
H	9.5596	4.7545	-3.0019
H	10.3145	3.2239	0.4445
H	9.7552	4.632	1.3938
H	11.2452	4.7403	0.4149
C	-8.5614	7.1589	1.8537
C	-8.7664	6.9443	-0.693
C	-7.3824	8.8092	0.3283
H	-8.9274	6.1296	2.0087
H	-7.9092	7.4229	2.7038
H	-9.4368	7.8294	1.8724
H	-8.2597	7.0496	-1.6678
H	-9.1437	5.9107	-0.6112
H	-9.6397	7.6178	-0.6864
H	-6.8716	8.9937	-0.6335
H	-8.2833	9.4434	0.3477
H	-6.7274	9.1448	1.1518
H	-4.2855	-2.7405	-2.0863
H	7.7745	-2.6496	4.5012
H	7.9265	-1.6721	2.9879
H	9.2684	-2.7568	3.5049
H	-9.497	-4.3374	-4.49
H	-10.1554	-4.8865	-2.8978
H	-10.662	-3.3029	-3.5902
I	0.0723	0.639	0.0673

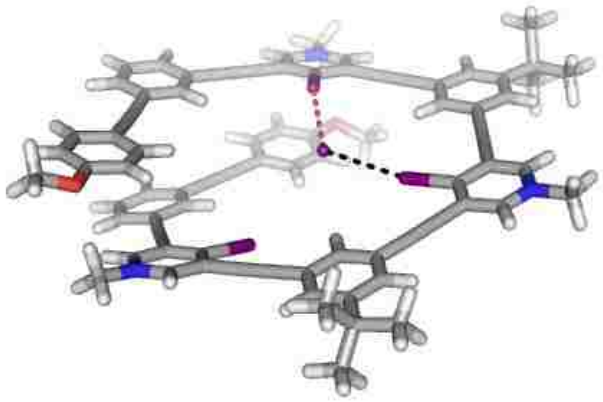

Figure 3.43 Single-point energy calculation of a single strand of **7** with I^-. The DFT-minimized conformation of a single strand of **7** was used in this calculation. Black dashes represent an energetically favorable halogen bond. Red dashes represent a suboptimal interaction. The I···I^- distance between the non-bonding halogen-bond donor and I^- is 4.6 Å (113 % of ΣvdW radii). The CI···I^- angles are 168 (black dashes) and 152 ° (red dashes). The I···I^- distances were set to 3.5 and 3.6 Å to closely match a crystal structure of **1** with I^- (Scheme 3.1). When the CI···I^- angles were set to 160 °, the calculation failed to converge.

SCF Done: E(RB98) = -3443.27304780 A.U. after 31 cycles
Convg = 0.6310D-08 -V/T = 2.0179

I	-3.3793	-0.2712	1.7721
I	0.5474	4.2413	-0.0793
I	3.1079	-1.3837	-1.5052
C	4.3441	5.3114	-0.5362
C	2.597	-5.3765	-1.5734
C	3.3415	6.0255	-0.4549
C	1.4303	-6.1838	-1.8082
C	0.1432	-5.5812	-1.8829
H	0.0412	-4.5019	-1.7612
C	-1.0091	-6.3772	-2.1224
C	-0.8543	-7.7888	-2.2856
H	-1.7361	-8.4024	-2.4763
C	0.423	-8.3855	-2.2105
H	0.5254	-9.4634	-2.3434
C	1.567	-7.5955	-1.9721

H	2.5553	-8.0547	-1.9206
C	5.5081	4.4686	-0.616
C	6.8133	5.0482	-0.6564
H	6.8998	6.1338	-0.6313
C	7.9777	4.2452	-0.727
C	7.8024	2.8346	-0.7556
H	8.6736	2.1801	-0.8134
C	6.5104	2.2372	-0.7183
C	5.3541	3.0592	-0.6492
H	4.3601	2.6115	-0.6232
C	-3.4578	-5.3206	-2.3104
C	0.9606	-5.4186	2.4942
C	-9.2964	-2.3324	0.3675
H	-9.5132	-3.2459	0.9349
H	-9.3203	-2.5382	-0.7142
H	-10.0323	-1.5637	0.6347
C	-4.125	5.8994	0.3388
C	-4.3497	4.5054	0.4708
H	-3.512	3.8073	0.4648
C	-5.6805	4.0284	0.6054
C	-6.7662	4.9493	0.6112
H	-7.7784	4.5566	0.7179
C	-6.5612	6.3507	0.4855
C	-7.7822	7.3119	0.5016
C	-5.2275	6.8076	0.3487
H	-5.0227	7.8722	0.246
C	-6.9504	-2.7526	1.0504
H	-7.2305	-3.8031	1.0613
N	-7.9193	-1.8449	0.7338
C	-7.6439	-0.5071	0.669
H	-8.4587	0.16	0.3969
C	-6.3448	-0.0078	0.9429
C	-5.3166	-0.9446	1.2981
C	-5.6204	-2.3483	1.3407
C	0.8512	6.318	-0.1964
C	2.1766	6.8467	-0.3608
C	2.3313	8.2572	-0.4343
H	3.3133	8.7075	-0.5591
N	1.2555	9.0958	-0.3523
C	-0.0146	8.6103	-0.1962
H	-0.8235	9.3357	-0.1384
C	-0.2686	7.2174	-0.113
C	-2.7799	6.388	0.1867
C	-1.6162	6.7728	0.048
C	-9.8095	-4.0072	-3.4749
C	4.5572	-5.7364	2.4813

H	4.2662	-6.7806	2.3541
C	3.5431	-4.7396	2.6198
C	3.9437	-3.3895	2.8366
H	3.1793	-2.622	2.9708
C	5.3086	-3.033	2.8948
H	5.5877	-1.994	3.0763
C	6.2991	-4.035	2.7317
O	7.6777	-3.7695	2.7107
C	5.9198	-5.3886	2.535
H	6.6996	-6.1498	2.4722
C	4.7892	-3.9383	-1.1267
C	4.8444	-2.504	-1.1092
C	6.0919	-1.846	-0.8393
C	7.2374	-2.6464	-0.6055
H	8.2063	-2.2018	-0.3914
N	7.1697	-4.0118	-0.638
C	5.9925	-4.6545	-0.8834
H	6.0036	-5.7415	-0.8853
C	-4.6521	-3.35	1.6403
C	2.1491	-5.0977	2.5539
C	-4.8003	-4.8161	-2.4437
C	-5.0863	-3.4261	-2.2814
C	-6.3998	-2.9411	-2.4167
H	-6.6203	-1.8741	-2.3409
C	-7.4615	-3.8364	-2.7143
C	-7.1971	-5.2187	-2.8941
H	-7.9965	-5.9173	-3.1433
C	-5.876	-5.6968	-2.7585
H	-5.6717	-6.7591	-2.9025
C	-3.8104	-4.2237	1.8676
O	-8.7389	-3.2641	-2.7857
C	-1.4361	-4.8331	2.1956
H	-1.1602	-3.7843	2.0771
C	-2.8037	-5.2187	2.1172
C	-3.1662	-6.5893	2.2779
H	-4.2151	-6.8836	2.2217
C	-2.1636	-7.5533	2.5136
H	-2.4392	-8.6005	2.6449
C	-0.8057	-7.1728	2.5856
H	-0.0344	-7.9218	2.771
C	-0.4263	-5.805	2.4253
C	3.6002	-4.6855	-1.3741
C	-2.3198	-5.7857	-2.2119
C	8.4141	-4.8014	-0.3326
H	8.2202	-5.8642	-0.5178
H	8.668	-4.6444	0.726

H	9.2266	-4.4627	-0.9891
C	-5.9243	2.6139	0.7304
C	-6.1194	1.402	0.842
C	6.2343	-0.4217	-0.7921
C	6.3709	0.8029	-0.7545
C	1.4513	10.5872	-0.4283
H	1.1352	11.0429	0.5196
H	0.8589	10.9927	-1.2611
H	2.4992	10.8134	-0.616
C	8.1791	-2.6298	3.4763
C	9.4059	4.8466	-0.7887
C	9.3964	6.406	-0.7462
C	10.1091	4.3927	-2.116
C	10.2245	4.3238	0.4437
H	10.4342	6.7747	-0.7834
H	8.9437	6.7921	0.1844
H	8.8632	6.8394	-1.6108
H	10.1909	3.2947	-2.1875
H	11.131	4.8055	-2.1544
H	9.5596	4.7545	-3.0019
H	10.3145	3.2239	0.4445
H	9.7552	4.632	1.3938
H	11.2452	4.7403	0.4149
C	-8.5614	7.1589	1.8537
C	-8.7664	6.9443	-0.693
C	-7.3824	8.8092	0.3283
H	-8.9274	6.1296	2.0087
H	-7.9092	7.4229	2.7038
H	-9.4368	7.8294	1.8724
H	-8.2597	7.0496	-1.6678
H	-9.1437	5.9107	-0.6112
H	-9.6397	7.6178	-0.6864
H	-6.8716	8.9937	-0.6335
H	-8.2833	9.4434	0.3477
H	-6.7274	9.1448	1.1518
H	-4.2855	-2.7405	-2.0863
H	7.7745	-2.6496	4.5012
H	7.9265	-1.6721	2.9879
H	9.2684	-2.7568	3.5049
H	-9.497	-4.3374	-4.49
H	-10.1554	-4.8865	-2.8978
H	-10.662	-3.3029	-3.5902
I	0.4466	0.7509	-0.5232

3.4.4 Solution-Phase Data

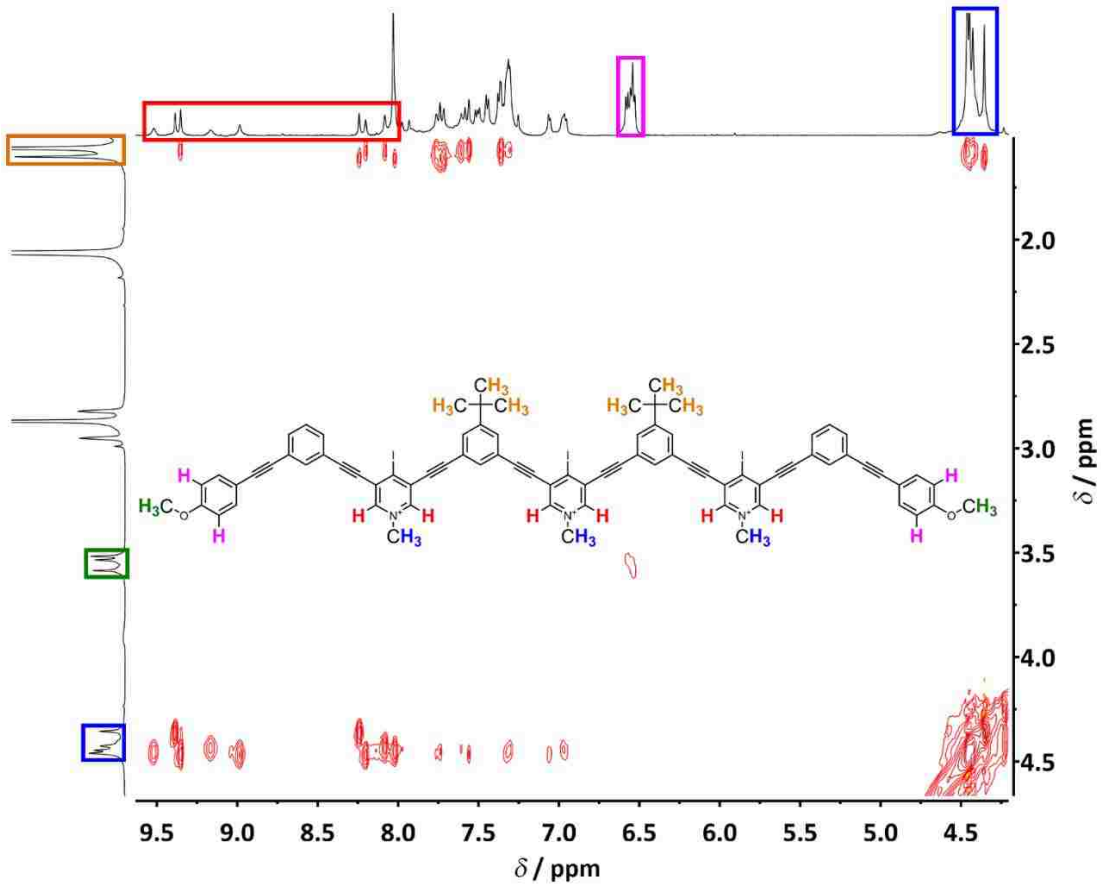

Figure 3.44 Proton assignments of **7** deduced from chemical shifts and NOEs (600 MHz, 1:3 *v*/*v* DMF-d_7-CD_3CN, 298 K).

Analysis of the electronics, symmetries, and steric environments of the nine pyridinium aromatics provided a more nuanced comparison between the solution and crystallographic data. The non-bonding pyridinium ring—whose own axis of C_2 symmetry defines that of the entire triplex—contributes a single ^{1}H NMR signal (see Figure 3.45, orange). The two terminally exposed pyridinium rings (a symmetrical pair) contribute two signals (see Figure 3.45, cyan and red). The final six signals are produced

by the six remaining and buried pyridiniums, which constitute three symmetrical pairs (see Figure 3.45, black, magenta, green, brown, blue, and yellow; see Table 3.1 for a summary). Of the nine pyridinium signals, five are shifted downfield and four upfield in organic solvents (see Figure 3.44). We hypothesize that the five downfield pyridinium protons are deshielded on account of HBing with extrachannel I^-s. Adding TBAI to **7** shifted these five pyridinium resonances downfield (up to 0.55 ppm, see Figure 3.4b), while the chemical shifts of all other signals were unaffected. The downfield migration of the five pyridinium protons was largely suppressed in an aqueous environment (see Figure 3.11).

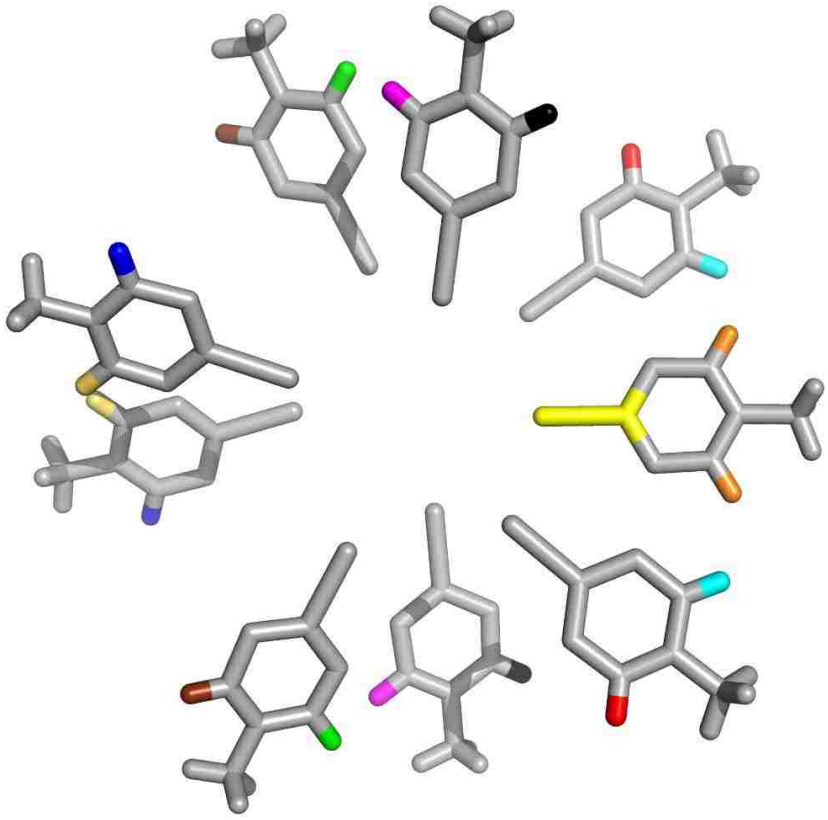

Figure 3.45 Top view of the X-ray crystallographic configuration of pyridinium XB donors (scaffolding removed for clarity). The yellow stick aligns with the complex's axis of molecular C_2 symmetry. The pyridiniums with the cyan and red protons are terminal aromatic rings. The orange, black, magenta, green, brown, blue, and yellow protons belong to the pyridiniums buried within the cylindrical wall of the complex.

Table 3.1 The origins of each pyridinium proton due to the complex's molecular C_2 symmetry (500 MHz, 1:3 *v*/*v* DMF-d_7-CD_3CN, 341 K; for color code, see Figure 3.45).

Color code	**Pyridinium location**	**Protons (#)**	**^{1}H NMR Signals based on symmetry (#)**
Orange	Buried (non-bonding)	2	1
Cyan	Terminal	2	1
Red	Terminal	2	1
Black	Buried	2	1
Magenta	Buried	2	1
Green	Buried	2	1
Brown	Buried	2	1
Blue	Buried	2	1
Yellow	Buried	2	1

In addition, NOEs between the upfield pyridinium and *tert*-butyl protons suggest steric shielding (see Figures 3.7). These distinctive ^{1}H NMR spectroscopic and crystallographic features find unity in a common supramolecular structure (see Table 3.2 for a summary).

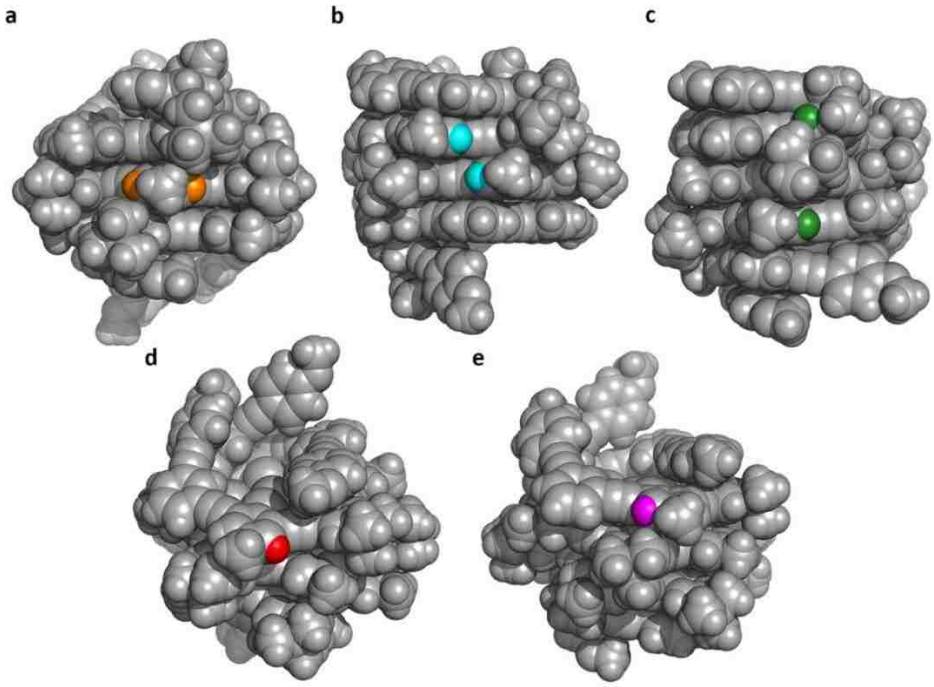

Figure 3.46 Crystallographic and steric environments of the pyridinium protons of **7**. (a) Protons belonging to the non-bonding pyridinium donor; both are sterically shielded by *tert*-butyl groups; (b) examples of pyridinium protons that are buried within the cylindrical wall of the complex; these protons are buried but not sterically shielded by *tert*-butyl groups; (c) examples of buried pyridinium protons that are also sterically shielded by *tert*-butyl groups; (d) an example of a pyridinium proton that is terminally exposed but not in close proximity to a *tert*-butyl group; (e) example of a pyridinium proton that is terminally exposed and also in close proximity to a *tert*-butyl group.

Table 3.2 A summary of the solution and crystallographic environments of the pyridinium protons of **7** (500 MHz, 1:4 *v*/*v* DMF-d_7-CD_3CN, 336 K).

Type	**Figure 3.46 color code**	**^{1}H NMR Signals (#)**	**Triple helicate protons (#)**	**Relative shift**	**Crystallographic environment**
Non-bonding	Orange (a)	1	2	Upfield	Shielded
Terminal shielded	Magenta (e)	1	2	Downfield	Shielded; terminally exposed
Terminal exposed	Red (d)	1	2	Downfield	Terminally exposed
Buried shielded	Green (c)	3	6	Upfield	Shielded
Buried exposed	Cyan (b)	3	6	Downfield	Exposed

Through 1H 2D EXSY NMR, it was discovered later that the pyridinium resonances of the non-bonding halogen-bond donor are in fact in the downfield region of the spectrum. Whereas the hypothesis that steric shielding afforded by the *tert*-butyl group was causative of upfield shifting is not completely misguided, a better overall explanation is provided by whether the proton in question can participate in bidentate hydrogen bonding vs. monodentate (see Section 4.3.6).

To calculate the r_Hs of **7**, **8**, and an internal standard (DCM), the Einstein-Stokes equation was used:

$$D_t = \frac{kT}{6\pi\eta r_H} \tag{3.1}$$

where D_t is the diffusion coefficient of the analyte, k the Boltzmann constant, T the temperature, η the solvent viscosity, and r_H the hydrodynamic radius of the analyte. The reported D_t values are an average of all peaks corresponding a given species. Ratios of r_H values were used to compare the relative sizes of **8** and **7**, as well as **7** and the internal standard (DCM r_{solv} = 2.49 Å). The latter ratio was used to establish a rough estimate of the radius of the triple helicate (8.2 Å). The heightwise crystallographic radius of the triplex was determined by averaging 20 evenly spaced measurements taken parallel to the screw axis of **7** (6.4 Å).The widthwise crystallographic radius of the triplex was estimated by calculating the length of the line drawn orthogonally from the screw axis of **7** to the methyl carbon of the non-bonding pyridinium (9.5 Å).

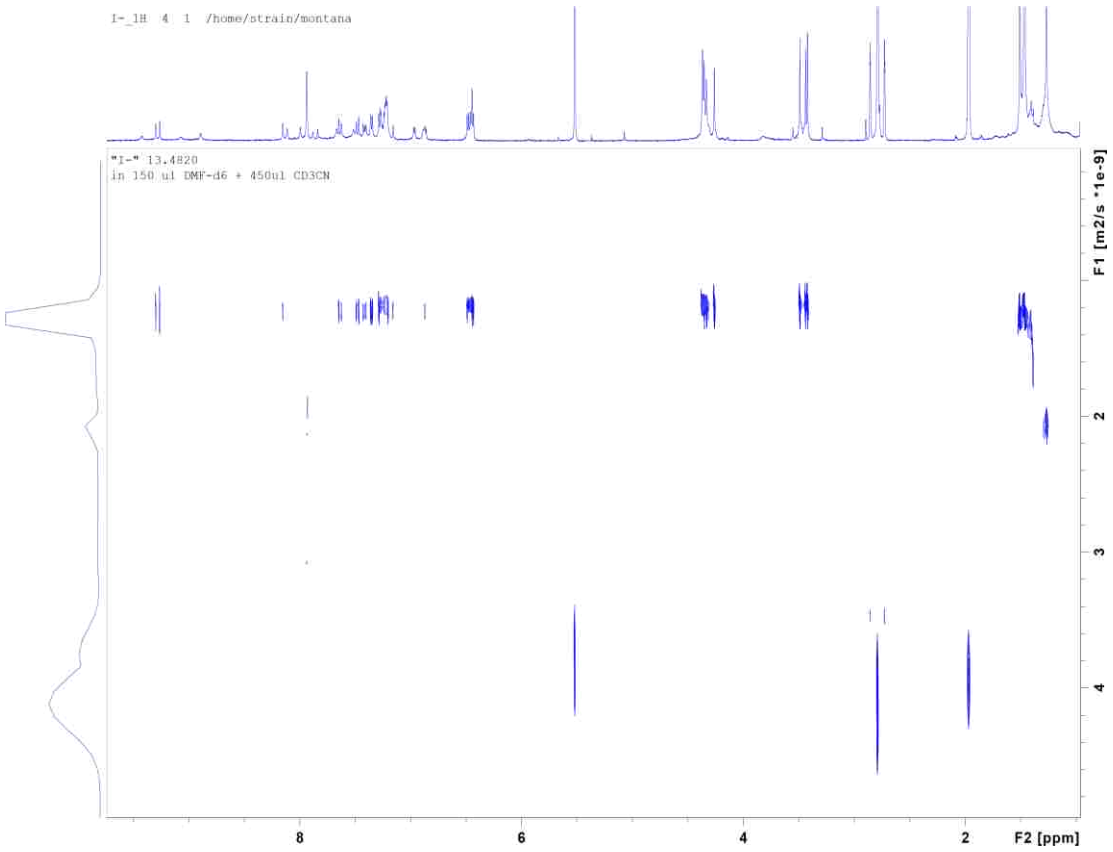

Figure 3.47 2D DOSY NMR spectrum of triple helicate **7**. The average D_t is 1.12×10^{-9} m^2 s^{-1} (600 MHz, 1:3 *v*/*v* DMF-d_7-CD_3CN, 298 K).

SIMFIT RESULTS
Dataset : /home/strain/montana/I-_1H/4/pdata/1/ct1t2.txt
AREA fit : Diffusion : Variable Gradient :
I=I[0]*exp(-D*SQR(2*PI*gamma*Gi*LD)*(BD-LD/3)*1e4)
40 points for Integral 1, Integral Region from 9.330 to 9.230 ppm
Converged after 63 iterations!
Results Comp. 1
I[0] = 3.220e-02
Diff Con. = 1.125e-09 m2/s
Gamma = 4.258e+03 Hz/G
Little Delta = 3.400m
Big Delta = 49.900m
RSS = 2.305e-05
SD = 7.591e-04

Point	Gradient	Expt	Calc	Difference
1	0.000e+00	2.994e-02	3.220e-02	2.259e-03
2	0.000e+00	2.930e-02	3.220e-02	2.901e-03
3	5.803e+00	2.900e-02	2.764e-02	-1.360e-03
4	6.297e+00	2.804e-02	2.690e-02	-1.144e-03
5	6.790e+00	2.695e-02	2.612e-02	-8.313e-04
6	7.284e+00	2.634e-02	2.531e-02	-1.030e-03
7	7.778e+00	2.522e-02	2.447e-02	-7.513e-04
8	8.272e+00	2.429e-02	2.361e-02	-6.849e-04
9	8.766e+00	2.328e-02	2.272e-02	-5.565e-04
10	9.260e+00	2.200e-02	2.182e-02	-1.756e-04
11	9.753e+00	2.159e-02	2.091e-02	-6.813e-04
12	1.025e+01	2.035e-02	2.000e-02	-3.515e-04
13	1.074e+01	1.928e-02	1.908e-02	-2.003e-04
14	1.123e+01	1.825e-02	1.816e-02	-9.406e-05
15	1.173e+01	1.742e-02	1.725e-02	-1.732e-04
16	1.222e+01	1.620e-02	1.635e-02	1.495e-04
17	1.272e+01	1.567e-02	1.546e-02	-2.105e-04
18	1.321e+01	1.499e-02	1.459e-02	-4.064e-04
19	1.370e+01	1.391e-02	1.373e-02	-1.771e-04
20	1.420e+01	1.286e-02	1.290e-02	3.995e-05
21	1.469e+01	1.210e-02	1.209e-02	-3.353e-06
22	1.519e+01	1.094e-02	1.131e-02	3.710e-04
23	1.568e+01	1.028e-02	1.055e-02	2.762e-04
24	1.617e+01	9.304e-03	9.827e-03	5.232e-04
25	1.667e+01	8.821e-03	9.129e-03	3.082e-04
26	1.716e+01	7.883e-03	8.463e-03	5.794e-04
27	1.766e+01	7.525e-03	7.827e-03	3.021e-04
28	1.815e+01	6.762e-03	7.224e-03	4.618e-04
29	1.864e+01	6.399e-03	6.652e-03	2.526e-04
30	1.914e+01	6.017e-03	6.112e-03	9.533e-05
31	1.963e+01	5.359e-03	5.604e-03	2.452e-04
32	2.012e+01	4.480e-03	5.126e-03	6.466e-04
33	2.062e+01	4.345e-03	4.679e-03	3.340e-04
34	2.111e+01	4.129e-03	4.261e-03	1.316e-04
35	2.161e+01	3.641e-03	3.872e-03	2.314e-04
36	2.210e+01	3.139e-03	3.511e-03	3.716e-04
37	2.259e+01	2.854e-03	3.177e-03	3.231e-04
38	2.309e+01	2.662e-03	2.868e-03	2.053e-04
39	2.358e+01	2.384e-03	2.583e-03	1.984e-04
40	2.408e+01	2.129e-03	2.321e-03	1.921e-04

40 points for Integral 2, Integral Region from 8.183 to 8.082 ppm
Converged after 54 iterations!
Results Comp. 1

I[0] = 3.219e-02
Diff Con. = 1.179e-09 m2/s
Gamma = 4.258e+03 Hz/G
Little Delta = 3.400m
Big Delta = 49.900m
RSS = 2.356e-05
SD = 7.675e-04

Point	Gradient	Expt	Calc	Difference
1	0.000e+00	2.996e-02	3.219e-02	2.224e-03
2	0.000e+00	2.930e-02	3.219e-02	2.884e-03
3	5.803e+00	2.872e-02	2.742e-02	-1.297e-03
4	6.297e+00	2.726e-02	2.666e-02	-6.050e-04
5	6.790e+00	2.713e-02	2.585e-02	-1.279e-03
6	7.284e+00	2.618e-02	2.501e-02	-1.167e-03
7	7.778e+00	2.459e-02	2.414e-02	-4.494e-04
8	8.272e+00	2.366e-02	2.325e-02	-4.127e-04
9	8.766e+00	2.307e-02	2.233e-02	-7.366e-04
10	9.260e+00	2.200e-02	2.141e-02	-5.939e-04
11	9.753e+00	2.128e-02	2.047e-02	-8.082e-04
12	1.025e+01	1.991e-02	1.953e-02	-3.715e-04
13	1.074e+01	1.892e-02	1.860e-02	-3.280e-04
14	1.123e+01	1.757e-02	1.766e-02	8.962e-05
15	1.173e+01	1.700e-02	1.673e-02	-2.674e-04
16	1.222e+01	1.594e-02	1.582e-02	-1.215e-04
17	1.272e+01	1.479e-02	1.492e-02	1.244e-04
18	1.321e+01	1.427e-02	1.404e-02	-2.323e-04
19	1.370e+01	1.324e-02	1.318e-02	-6.315e-05
20	1.420e+01	1.228e-02	1.234e-02	6.282e-05
21	1.469e+01	1.148e-02	1.153e-02	5.420e-05
22	1.519e+01	1.057e-02	1.075e-02	1.745e-04
23	1.568e+01	9.893e-03	9.997e-03	1.035e-04
24	1.617e+01	8.659e-03	9.277e-03	6.187e-04
25	1.667e+01	8.323e-03	8.588e-03	2.652e-04
26	1.716e+01	7.639e-03	7.932e-03	2.929e-04
27	1.766e+01	7.048e-03	7.309e-03	2.608e-04
28	1.815e+01	6.520e-03	6.720e-03	2.000e-04
29	1.864e+01	5.641e-03	6.163e-03	5.219e-04
30	1.914e+01	5.317e-03	5.640e-03	3.225e-04
31	1.963e+01	4.647e-03	5.150e-03	5.025e-04
32	2.012e+01	4.477e-03	4.690e-03	2.131e-04
33	2.062e+01	4.162e-03	4.262e-03	9.976e-05
34	2.111e+01	3.236e-03	3.864e-03	6.279e-04
35	2.161e+01	2.779e-03	3.495e-03	7.166e-04
36	2.210e+01	2.847e-03	3.154e-03	3.067e-04
37	2.259e+01	2.650e-03	2.840e-03	1.898e-04

38	2.309e+01	2.170e-03	2.551e-03	3.811e-04
39	2.358e+01	1.831e-03	2.286e-03	4.557e-04
40	2.408e+01	1.658e-03	2.044e-03	3.857e-04

40 points for Integral 4, Integral Region from 7.706 to 7.571 ppm
Converged after 54 iterations!
Results Comp. 1
I[0] = 7.521e-02
Diff Con. = 1.157e-09 m2/s
Gamma = 4.258e+03 Hz/G
Little Delta = 3.400m
Big Delta = 49.900m
RSS = 1.216e-04
SD = 1.743e-03

Point	Gradient	Expt	Calc	Difference
1	0.000e+00	7.017e-02	7.521e-02	5.039e-03
2	0.000e+00	6.838e-02	7.521e-02	6.828e-03
3	5.803e+00	6.675e-02	6.427e-02	-2.479e-03
4	6.297e+00	6.475e-02	6.250e-02	-2.256e-03
5	6.790e+00	6.249e-02	6.064e-02	-1.847e-03
6	7.284e+00	6.101e-02	5.871e-02	-2.304e-03
7	7.778e+00	5.794e-02	5.670e-02	-1.235e-03
8	8.272e+00	5.605e-02	5.464e-02	-1.406e-03
9	8.766e+00	5.437e-02	5.254e-02	-1.830e-03
10	9.260e+00	5.191e-02	5.040e-02	-1.512e-03
11	9.753e+00	4.972e-02	4.824e-02	-1.481e-03
12	1.025e+01	4.702e-02	4.607e-02	-9.564e-04
13	1.074e+01	4.481e-02	4.389e-02	-9.205e-04
14	1.123e+01	4.256e-02	4.172e-02	-8.426e-04
15	1.173e+01	4.028e-02	3.957e-02	-7.162e-04
16	1.222e+01	3.767e-02	3.744e-02	-2.289e-04
17	1.272e+01	3.575e-02	3.535e-02	-3.985e-04
18	1.321e+01	3.352e-02	3.330e-02	-2.152e-04
19	1.370e+01	3.139e-02	3.130e-02	-9.044e-05
20	1.420e+01	2.934e-02	2.935e-02	1.068e-05
21	1.469e+01	2.693e-02	2.746e-02	5.270e-04
22	1.519e+01	2.476e-02	2.563e-02	8.699e-04
23	1.568e+01	2.351e-02	2.387e-02	3.566e-04
24	1.617e+01	2.140e-02	2.218e-02	7.825e-04
25	1.667e+01	1.925e-02	2.056e-02	1.307e-03
26	1.716e+01	1.796e-02	1.902e-02	1.058e-03
27	1.766e+01	1.649e-02	1.755e-02	1.059e-03
28	1.815e+01	1.548e-02	1.616e-02	6.776e-04
29	1.864e+01	1.398e-02	1.485e-02	8.652e-04
30	1.914e+01	1.297e-02	1.361e-02	6.361e-04

31	1.963e+01	1.190e-02	1.245e-02	5.495e-04
32	2.012e+01	1.055e-02	1.136e-02	8.081e-04
33	2.062e+01	9.846e-03	1.034e-02	4.912e-04
34	2.111e+01	8.543e-03	9.389e-03	8.453e-04
35	2.161e+01	7.786e-03	8.508e-03	7.218e-04
36	2.210e+01	7.224e-03	7.692e-03	4.678e-04
37	2.259e+01	5.763e-03	6.940e-03	1.177e-03
38	2.309e+01	5.110e-03	6.246e-03	1.136e-03
39	2.358e+01	4.665e-03	5.609e-03	9.438e-04
40	2.408e+01	3.813e-03	5.025e-03	1.212e-03

40 points for Integral 5, Integral Region from 7.546 to 7.320 ppm
Converged after 54 iterations!
Results Comp. 1
I[0] = 1.759e-01
Diff Con. = 1.136e-09 m2/s
Gamma = 4.258e+03 Hz/G
Little Delta = 3.400m
Big Delta = 49.900m
RSS = 5.896e-04
SD = 3.839e-03

Point	Gradient	Expt	Calc	Difference
1	0.000e+00	1.643e-01	1.759e-01	1.152e-02
2	0.000e+00	1.609e-01	1.759e-01	1.501e-02
3	5.803e+00	1.564e-01	1.507e-01	-5.732e-03
4	6.297e+00	1.521e-01	1.466e-01	-5.481e-03
5	6.790e+00	1.475e-01	1.424e-01	-5.140e-03
6	7.284e+00	1.426e-01	1.379e-01	-4.675e-03
7	7.778e+00	1.370e-01	1.333e-01	-3.675e-03
8	8.272e+00	1.324e-01	1.285e-01	-3.880e-03
9	8.766e+00	1.269e-01	1.237e-01	-3.274e-03
10	9.260e+00	1.215e-01	1.187e-01	-2.800e-03
11	9.753e+00	1.163e-01	1.137e-01	-2.605e-03
12	1.025e+01	1.107e-01	1.087e-01	-2.048e-03
13	1.074e+01	1.055e-01	1.036e-01	-1.860e-03
14	1.123e+01	1.005e-01	9.860e-02	-1.861e-03
15	1.173e+01	9.422e-02	9.361e-02	-6.156e-04
16	1.222e+01	8.882e-02	8.867e-02	-1.500e-04
17	1.272e+01	8.345e-02	8.380e-02	3.441e-04
18	1.321e+01	7.929e-02	7.903e-02	-2.627e-04
19	1.370e+01	7.403e-02	7.435e-02	3.263e-04
20	1.420e+01	6.993e-02	6.980e-02	-1.272e-04
21	1.469e+01	6.420e-02	6.538e-02	1.180e-03
22	1.519e+01	6.051e-02	6.110e-02	5.970e-04
23	1.568e+01	5.607e-02	5.698e-02	9.079e-04

24	1.617e+01	5.180e-02	5.302e-02	1.226e-03
25	1.667e+01	4.722e-02	4.922e-02	2.001e-03
26	1.716e+01	4.268e-02	4.559e-02	2.912e-03
27	1.766e+01	4.007e-02	4.213e-02	2.067e-03
28	1.815e+01	3.673e-02	3.885e-02	2.119e-03
29	1.864e+01	3.415e-02	3.575e-02	1.594e-03
30	1.914e+01	3.155e-02	3.282e-02	1.267e-03
31	1.963e+01	2.854e-02	3.006e-02	1.519e-03
32	2.012e+01	2.541e-02	2.748e-02	2.065e-03
33	2.062e+01	2.411e-02	2.505e-02	9.436e-04
34	2.111e+01	2.080e-02	2.279e-02	1.993e-03
35	2.161e+01	1.903e-02	2.069e-02	1.662e-03
36	2.210e+01	1.783e-02	1.874e-02	9.125e-04
37	2.259e+01	1.512e-02	1.694e-02	1.820e-03
38	2.309e+01	1.358e-02	1.528e-02	1.698e-03
39	2.358e+01	1.207e-02	1.374e-02	1.674e-03
40	2.408e+01	1.130e-02	1.234e-02	1.038e-03

40 points for Integral 6, Integral Region from 7.320 to 7.136 ppm
Converged after 51 iterations!
Results Comp. 1
I[0] = 2.356e-01
Diff Con. = 1.117e-09 m2/s
Gamma = 4.258e+03 Hz/G
Little Delta = 3.400m
Big Delta = 49.900m
RSS = 1.006e-03
SD = 5.014e-03

Point	Gradient	Expt	Calc	Difference
1	0.000e+00	2.207e-01	2.356e-01	1.487e-02
2	0.000e+00	2.156e-01	2.356e-01	1.999e-02
3	5.803e+00	2.096e-01	2.024e-01	-7.205e-03
4	6.297e+00	2.041e-01	1.970e-01	-7.052e-03
5	6.790e+00	1.979e-01	1.914e-01	-6.488e-03
6	7.284e+00	1.919e-01	1.855e-01	-6.414e-03
7	7.778e+00	1.847e-01	1.794e-01	-5.313e-03
8	8.272e+00	1.777e-01	1.731e-01	-4.652e-03
9	8.766e+00	1.712e-01	1.666e-01	-4.557e-03
10	9.260e+00	1.635e-01	1.601e-01	-3.383e-03
11	9.753e+00	1.568e-01	1.535e-01	-3.353e-03
12	1.025e+01	1.498e-01	1.468e-01	-3.006e-03
13	1.074e+01	1.421e-01	1.401e-01	-2.019e-03
14	1.123e+01	1.354e-01	1.334e-01	-2.012e-03
15	1.173e+01	1.276e-01	1.268e-01	-8.626e-04
16	1.222e+01	1.211e-01	1.202e-01	-9.533e-04

17	1.272e+01	1.139e-01	1.137e-01	-1.735e-04
18	1.321e+01	1.077e-01	1.073e-01	-3.823e-04
19	1.370e+01	1.010e-01	1.011e-01	4.176e-05
20	1.420e+01	9.448e-02	9.500e-02	5.181e-04
21	1.469e+01	8.759e-02	8.908e-02	1.494e-03
22	1.519e+01	8.247e-02	8.335e-02	8.763e-04
23	1.568e+01	7.698e-02	7.782e-02	8.364e-04
24	1.617e+01	6.998e-02	7.250e-02	2.517e-03
25	1.667e+01	6.445e-02	6.739e-02	2.940e-03
26	1.716e+01	5.997e-02	6.250e-02	2.537e-03
27	1.766e+01	5.570e-02	5.784e-02	2.139e-03
28	1.815e+01	5.100e-02	5.341e-02	2.415e-03
29	1.864e+01	4.673e-02	4.921e-02	2.487e-03
30	1.914e+01	4.292e-02	4.524e-02	2.326e-03
31	1.963e+01	3.949e-02	4.151e-02	2.024e-03
32	2.012e+01	3.546e-02	3.800e-02	2.534e-03
33	2.062e+01	3.287e-02	3.470e-02	1.833e-03
34	2.111e+01	2.940e-02	3.162e-02	2.226e-03
35	2.161e+01	2.697e-02	2.876e-02	1.783e-03
36	2.210e+01	2.406e-02	2.609e-02	2.034e-03
37	2.259e+01	2.197e-02	2.363e-02	1.659e-03
38	2.309e+01	1.916e-02	2.134e-02	2.186e-03
39	2.358e+01	1.744e-02	1.924e-02	1.798e-03
40	2.408e+01	1.548e-02	1.730e-02	1.823e-03

40 points for Integral 7, Integral Region from 6.550 to 6.382 ppm
Converged after 54 iterations!
Results Comp. 1
I[0] = 1.267e-01
Diff Con. = 1.117e-09 m2/s
Gamma = 4.258e+03 Hz/G
Little Delta = 3.400m
Big Delta = 49.900m
RSS = 3.000e-04
SD = 2.738e-03

Point	Gradient	Expt	Calc	Difference
1	0.000e+00	1.185e-01	1.267e-01	8.203e-03
2	0.000e+00	1.160e-01	1.267e-01	1.080e-02
3	5.803e+00	1.125e-01	1.089e-01	-3.561e-03
4	6.297e+00	1.100e-01	1.060e-01	-3.938e-03
5	6.790e+00	1.064e-01	1.030e-01	-3.406e-03
6	7.284e+00	1.031e-01	9.980e-02	-3.256e-03
7	7.778e+00	9.948e-02	9.651e-02	-2.965e-03
8	8.272e+00	9.579e-02	9.313e-02	-2.666e-03
9	8.766e+00	9.271e-02	8.966e-02	-3.047e-03

10	9.260e+00	8.810e-02	8.614e-02	-1.964e-03
11	9.753e+00	8.459e-02	8.258e-02	-2.017e-03
12	1.025e+01	8.067e-02	7.898e-02	-1.687e-03
13	1.074e+01	7.662e-02	7.538e-02	-1.246e-03
14	1.123e+01	7.244e-02	7.178e-02	-6.635e-04
15	1.173e+01	6.902e-02	6.820e-02	-8.163e-04
16	1.222e+01	6.465e-02	6.466e-02	1.787e-05
17	1.272e+01	6.157e-02	6.117e-02	-3.946e-04
18	1.321e+01	5.769e-02	5.775e-02	5.939e-05
19	1.370e+01	5.433e-02	5.439e-02	6.292e-05
20	1.420e+01	5.106e-02	5.112e-02	5.646e-05
21	1.469e+01	4.710e-02	4.794e-02	8.393e-04
22	1.519e+01	4.456e-02	4.485e-02	2.938e-04
23	1.568e+01	4.114e-02	4.187e-02	7.372e-04
24	1.617e+01	3.774e-02	3.902e-02	1.279e-03
25	1.667e+01	3.459e-02	3.627e-02	1.679e-03
26	1.716e+01	3.224e-02	3.364e-02	1.395e-03
27	1.766e+01	2.958e-02	3.113e-02	1.553e-03
28	1.815e+01	2.737e-02	2.874e-02	1.376e-03
29	1.864e+01	2.475e-02	2.648e-02	1.731e-03
30	1.914e+01	2.344e-02	2.435e-02	9.121e-04
31	1.963e+01	2.135e-02	2.234e-02	9.910e-04
32	2.012e+01	1.904e-02	2.045e-02	1.411e-03
33	2.062e+01	1.771e-02	1.868e-02	9.648e-04
34	2.111e+01	1.585e-02	1.702e-02	1.175e-03
35	2.161e+01	1.457e-02	1.548e-02	9.085e-04
36	2.210e+01	1.293e-02	1.404e-02	1.113e-03
37	2.259e+01	1.199e-02	1.272e-02	7.273e-04
38	2.309e+01	1.047e-02	1.149e-02	1.019e-03
39	2.358e+01	9.343e-03	1.035e-02	1.010e-03
40	2.408e+01	8.259e-03	9.312e-03	1.053e-03

40 points for Integral 9, Integral Region from 4.431 to 4.288 ppm
Converged after 44 iterations!
Results Comp. 1
I[0] = 2.767e-01
Diff Con. = 1.101e-09 m2/s
Gamma = 4.258e+03 Hz/G
Little Delta = 3.400m
Big Delta = 49.900m
RSS = 1.283e-03
SD = 5.664e-03

Point	Gradient	Expt	Calc	Difference
1	0.000e+00	2.598e-01	2.767e-01	1.682e-02
2	0.000e+00	2.540e-01	2.767e-01	2.267e-02

3	5.803e+00	2.474e-01	2.382e-01	-9.145e-03
4	6.297e+00	2.406e-01	2.320e-01	-8.632e-03
5	6.790e+00	2.331e-01	2.254e-01	-7.735e-03
6	7.284e+00	2.253e-01	2.186e-01	-6.786e-03
7	7.778e+00	2.174e-01	2.114e-01	-5.904e-03
8	8.272e+00	2.097e-01	2.041e-01	-5.619e-03
9	8.766e+00	2.017e-01	1.966e-01	-5.060e-03
10	9.260e+00	1.929e-01	1.890e-01	-3.854e-03
11	9.753e+00	1.847e-01	1.813e-01	-3.361e-03
12	1.025e+01	1.761e-01	1.735e-01	-2.601e-03
13	1.074e+01	1.678e-01	1.657e-01	-2.078e-03
14	1.123e+01	1.594e-01	1.579e-01	-1.544e-03
15	1.173e+01	1.512e-01	1.501e-01	-1.040e-03
16	1.222e+01	1.426e-01	1.424e-01	-1.885e-04
17	1.272e+01	1.349e-01	1.349e-01	-8.164e-05
18	1.321e+01	1.271e-01	1.274e-01	2.739e-04
19	1.370e+01	1.197e-01	1.201e-01	4.443e-04
20	1.420e+01	1.119e-01	1.130e-01	1.073e-03
21	1.469e+01	1.049e-01	1.060e-01	1.077e-03
22	1.519e+01	9.789e-02	9.929e-02	1.408e-03
23	1.568e+01	9.169e-02	9.279e-02	1.101e-03
24	1.617e+01	8.454e-02	8.653e-02	1.993e-03
25	1.667e+01	7.795e-02	8.052e-02	2.566e-03
26	1.716e+01	7.213e-02	7.475e-02	2.625e-03
27	1.766e+01	6.723e-02	6.925e-02	2.021e-03
28	1.815e+01	6.134e-02	6.402e-02	2.678e-03
29	1.864e+01	5.682e-02	5.905e-02	2.232e-03
30	1.914e+01	5.136e-02	5.435e-02	2.996e-03
31	1.963e+01	4.736e-02	4.993e-02	2.569e-03
32	2.012e+01	4.310e-02	4.576e-02	2.651e-03
33	2.062e+01	3.978e-02	4.184e-02	2.066e-03
34	2.111e+01	3.613e-02	3.818e-02	2.053e-03
35	2.161e+01	3.273e-02	3.476e-02	2.030e-03
36	2.210e+01	3.017e-02	3.158e-02	1.415e-03
37	2.259e+01	2.684e-02	2.864e-02	1.794e-03
38	2.309e+01	2.383e-02	2.590e-02	2.071e-03
39	2.358e+01	2.157e-02	2.338e-02	1.815e-03
40	2.408e+01	1.961e-02	2.106e-02	1.448e-03

40 points for Integral 10, Integral Region from 4.288 to 4.205 ppm
Converged after 58 iterations!
Results Comp. 1

I[0] = 7.831e-02
Diff Con. = 1.098e-09 m2/s
Gamma = 4.258e+03 Hz/G

Little Delta = 3.400m
Big Delta = 49.900m
RSS = 1.022e-04
SD = 1.598e-03

Point	Gradient	Expt	Calc	Difference
1	0.000e+00	7.346e-02	7.831e-02	4.850e-03
2	0.000e+00	7.206e-02	7.831e-02	6.251e-03
3	5.803e+00	6.983e-02	6.745e-02	-2.376e-03
4	6.297e+00	6.810e-02	6.569e-02	-2.412e-03
5	6.790e+00	6.627e-02	6.384e-02	-2.428e-03
6	7.284e+00	6.390e-02	6.190e-02	-2.003e-03
7	7.778e+00	6.173e-02	5.989e-02	-1.837e-03
8	8.272e+00	5.949e-02	5.783e-02	-1.666e-03
9	8.766e+00	5.707e-02	5.571e-02	-1.359e-03
10	9.260e+00	5.455e-02	5.355e-02	-9.943e-04
11	9.753e+00	5.244e-02	5.137e-02	-1.065e-03
12	1.025e+01	4.971e-02	4.917e-02	-5.348e-04
13	1.074e+01	4.743e-02	4.696e-02	-4.687e-04
14	1.123e+01	4.518e-02	4.476e-02	-4.212e-04
15	1.173e+01	4.284e-02	4.256e-02	-2.761e-04
16	1.222e+01	4.029e-02	4.039e-02	1.017e-04
17	1.272e+01	3.836e-02	3.824e-02	-1.126e-04
18	1.321e+01	3.585e-02	3.614e-02	2.832e-04
19	1.370e+01	3.390e-02	3.407e-02	1.719e-04
20	1.420e+01	3.173e-02	3.205e-02	3.170e-04
21	1.469e+01	2.994e-02	3.009e-02	1.488e-04
22	1.519e+01	2.800e-02	2.818e-02	1.817e-04
23	1.568e+01	2.604e-02	2.634e-02	3.033e-04
24	1.617e+01	2.347e-02	2.457e-02	1.098e-03
25	1.667e+01	2.221e-02	2.286e-02	6.569e-04
26	1.716e+01	2.064e-02	2.123e-02	5.911e-04
27	1.766e+01	1.914e-02	1.967e-02	5.387e-04
28	1.815e+01	1.759e-02	1.819e-02	6.002e-04
29	1.864e+01	1.595e-02	1.678e-02	8.308e-04
30	1.914e+01	1.467e-02	1.545e-02	7.845e-04
31	1.963e+01	1.374e-02	1.420e-02	4.559e-04
32	2.012e+01	1.229e-02	1.301e-02	7.266e-04
33	2.062e+01	1.096e-02	1.190e-02	9.381e-04
34	2.111e+01	1.010e-02	1.086e-02	7.584e-04
35	2.161e+01	9.678e-03	9.893e-03	2.150e-04
36	2.210e+01	8.532e-03	8.991e-03	4.581e-04
37	2.259e+01	7.810e-03	8.154e-03	3.438e-04
38	2.309e+01	7.013e-03	7.378e-03	3.655e-04
39	2.358e+01	6.196e-03	6.662e-03	4.656e-04
40	2.408e+01	5.664e-03	6.002e-03	3.376e-04

40 points for Integral 11, Integral Region from 3.526 to 3.459 ppm
Converged after 47 iterations!
Results Comp. 1
I[0] = 9.545e-02
Diff Con. = 1.099e-09 m2/s
Gamma = 4.258e+03 Hz/G
Little Delta = 3.400m
Big Delta = 49.900m
RSS = 1.559e-04
SD = 1.974e-03

Point	Gradient	Expt	Calc	Difference
1	0.000e+00	8.951e-02	9.545e-02	5.937e-03
2	0.000e+00	8.765e-02	9.545e-02	7.804e-03
3	5.803e+00	8.549e-02	8.221e-02	-3.277e-03
4	6.297e+00	8.316e-02	8.006e-02	-3.096e-03
5	6.790e+00	8.010e-02	7.780e-02	-2.298e-03
6	7.284e+00	7.810e-02	7.544e-02	-2.660e-03
7	7.778e+00	7.511e-02	7.300e-02	-2.115e-03
8	8.272e+00	7.236e-02	7.047e-02	-1.886e-03
9	8.766e+00	6.950e-02	6.789e-02	-1.606e-03
10	9.260e+00	6.659e-02	6.526e-02	-1.324e-03
11	9.753e+00	6.382e-02	6.261e-02	-1.214e-03
12	1.025e+01	6.085e-02	5.993e-02	-9.219e-04
13	1.074e+01	5.787e-02	5.723e-02	-6.380e-04
14	1.123e+01	5.530e-02	5.454e-02	-7.593e-04
15	1.173e+01	5.221e-02	5.187e-02	-3.461e-04
16	1.222e+01	4.919e-02	4.922e-02	2.536e-05
17	1.272e+01	4.684e-02	4.660e-02	-2.401e-04
18	1.321e+01	4.395e-02	4.403e-02	8.134e-05
19	1.370e+01	4.129e-02	4.151e-02	2.230e-04
20	1.420e+01	3.847e-02	3.905e-02	5.853e-04
21	1.469e+01	3.617e-02	3.666e-02	4.869e-04
22	1.519e+01	3.415e-02	3.434e-02	1.904e-04
23	1.568e+01	3.152e-02	3.209e-02	5.684e-04
24	1.617e+01	2.928e-02	2.993e-02	6.493e-04
25	1.667e+01	2.691e-02	2.786e-02	9.452e-04
26	1.716e+01	2.486e-02	2.587e-02	1.004e-03
27	1.766e+01	2.336e-02	2.397e-02	6.051e-04
28	1.815e+01	2.133e-02	2.216e-02	8.360e-04
29	1.864e+01	1.925e-02	2.045e-02	1.193e-03
30	1.914e+01	1.786e-02	1.882e-02	9.660e-04
31	1.963e+01	1.654e-02	1.729e-02	7.513e-04
32	2.012e+01	1.507e-02	1.585e-02	7.769e-04
33	2.062e+01	1.367e-02	1.450e-02	8.327e-04

34	2.111e+01	1.250e-02	1.323e-02	7.345e-04
35	2.161e+01	1.179e-02	1.205e-02	2.646e-04
36	2.210e+01	1.021e-02	1.095e-02	7.432e-04
37	2.259e+01	9.349e-03	9.931e-03	5.818e-04
38	2.309e+01	8.350e-03	8.986e-03	6.359e-04
39	2.358e+01	7.434e-03	8.113e-03	6.789e-04
40	2.408e+01	6.844e-03	7.309e-03	4.648e-04

40 points for Integral 12, Integral Region from 3.459 to 3.367 ppm
Converged after 46 iterations!
Results Comp. 1
I[0] = 1.412e-01
Diff Con. = 1.100e-09 m2/s
Gamma = 4.258e+03 Hz/G
Little Delta = 3.400m
Big Delta = 49.900m
RSS = 3.316e-04
SD = 2.879e-03

Point	Gradient	Expt	Calc	Difference
1	0.000e+00	1.328e-01	1.412e-01	8.425e-03
2	0.000e+00	1.297e-01	1.412e-01	1.157e-02
3	5.803e+00	1.257e-01	1.216e-01	-4.091e-03
4	6.297e+00	1.231e-01	1.184e-01	-4.648e-03
5	6.790e+00	1.189e-01	1.151e-01	-3.836e-03
6	7.284e+00	1.152e-01	1.116e-01	-3.634e-03
7	7.778e+00	1.111e-01	1.080e-01	-3.109e-03
8	8.272e+00	1.070e-01	1.042e-01	-2.806e-03
9	8.766e+00	1.032e-01	1.004e-01	-2.832e-03
10	9.260e+00	9.853e-02	9.652e-02	-2.008e-03
11	9.753e+00	9.434e-02	9.259e-02	-1.758e-03
12	1.025e+01	9.006e-02	8.861e-02	-1.447e-03
13	1.074e+01	8.584e-02	8.463e-02	-1.215e-03
14	1.123e+01	8.110e-02	8.064e-02	-4.614e-04
15	1.173e+01	7.715e-02	7.668e-02	-4.640e-04
16	1.222e+01	7.275e-02	7.276e-02	9.036e-06
17	1.272e+01	6.916e-02	6.888e-02	-2.787e-04
18	1.321e+01	6.491e-02	6.508e-02	1.706e-04
19	1.370e+01	6.133e-02	6.135e-02	2.050e-05
20	1.420e+01	5.702e-02	5.771e-02	6.890e-04
21	1.469e+01	5.332e-02	5.417e-02	8.453e-04
22	1.519e+01	5.011e-02	5.073e-02	6.194e-04
23	1.568e+01	4.670e-02	4.741e-02	7.081e-04
24	1.617e+01	4.254e-02	4.422e-02	1.674e-03
25	1.667e+01	3.955e-02	4.114e-02	1.594e-03
26	1.716e+01	3.728e-02	3.820e-02	9.243e-04

27	1.766e+01	3.430e-02	3.539e-02	1.097e-03
28	1.815e+01	3.132e-02	3.272e-02	1.404e-03
29	1.864e+01	2.881e-02	3.018e-02	1.369e-03
30	1.914e+01	2.633e-02	2.778e-02	1.456e-03
31	1.963e+01	2.425e-02	2.552e-02	1.271e-03
32	2.012e+01	2.220e-02	2.339e-02	1.189e-03
33	2.062e+01	2.033e-02	2.139e-02	1.058e-03
34	2.111e+01	1.859e-02	1.952e-02	9.295e-04
35	2.161e+01	1.707e-02	1.778e-02	7.036e-04
36	2.210e+01	1.513e-02	1.615e-02	1.023e-03
37	2.259e+01	1.398e-02	1.465e-02	6.617e-04
38	2.309e+01	1.250e-02	1.325e-02	7.530e-04
39	2.358e+01	1.110e-02	1.196e-02	8.598e-04
40	2.408e+01	1.044e-02	1.077e-02	3.286e-04

40 points for Integral 15, Integral Region from 1.558 to 1.432 ppm
Converged after 33 iterations!
Results Comp. 1
I[0] = 7.972e-01
Diff Con. = 1.139e-09 m2/s
Gamma = 4.258e+03 Hz/G
Little Delta = 3.400m
Big Delta = 49.900m
RSS = 1.056e-02
SD = 1.624e-02

Point	Gradient	Expt	Calc	Difference
1	0.000e+00	7.512e-01	7.972e-01	4.601e-02
2	0.000e+00	7.318e-01	7.972e-01	6.533e-02
3	5.803e+00	7.120e-01	6.829e-01	-2.912e-02
4	6.297e+00	6.913e-01	6.643e-01	-2.697e-02
5	6.790e+00	6.689e-01	6.449e-01	-2.398e-02
6	7.284e+00	6.457e-01	6.246e-01	-2.108e-02
7	7.778e+00	6.210e-01	6.036e-01	-1.738e-02
8	8.272e+00	5.976e-01	5.820e-01	-1.558e-02
9	8.766e+00	5.732e-01	5.600e-01	-1.320e-02
10	9.260e+00	5.469e-01	5.375e-01	-9.365e-03
11	9.753e+00	5.239e-01	5.148e-01	-9.075e-03
12	1.025e+01	4.982e-01	4.920e-01	-6.271e-03
13	1.074e+01	4.740e-01	4.691e-01	-4.879e-03
14	1.123e+01	4.489e-01	4.462e-01	-2.690e-03
15	1.173e+01	4.251e-01	4.236e-01	-1.533e-03
16	1.222e+01	3.999e-01	4.012e-01	1.277e-03
17	1.272e+01	3.770e-01	3.791e-01	2.049e-03
18	1.321e+01	3.549e-01	3.574e-01	2.548e-03
19	1.370e+01	3.337e-01	3.362e-01	2.522e-03

20	1.420e+01	3.116e-01	3.156e-01	4.028e-03
21	1.469e+01	2.903e-01	2.956e-01	5.267e-03
22	1.519e+01	2.719e-01	2.762e-01	4.309e-03
23	1.568e+01	2.522e-01	2.575e-01	5.269e-03
24	1.617e+01	2.330e-01	2.396e-01	6.569e-03
25	1.667e+01	2.144e-01	2.223e-01	7.939e-03
26	1.716e+01	1.986e-01	2.059e-01	7.266e-03
27	1.766e+01	1.832e-01	1.903e-01	7.037e-03
28	1.815e+01	1.689e-01	1.754e-01	6.454e-03
29	1.864e+01	1.548e-01	1.613e-01	6.492e-03
30	1.914e+01	1.418e-01	1.481e-01	6.325e-03
31	1.963e+01	1.301e-01	1.356e-01	5.490e-03
32	2.012e+01	1.186e-01	1.239e-01	5.303e-03
33	2.062e+01	1.079e-01	1.130e-01	5.087e-03
34	2.111e+01	9.799e-02	1.028e-01	4.769e-03
35	2.161e+01	9.011e-02	9.326e-02	3.144e-03
36	2.210e+01	8.102e-02	8.445e-02	3.429e-03
37	2.259e+01	7.247e-02	7.631e-02	3.846e-03
38	2.309e+01	6.530e-02	6.879e-02	3.491e-03
39	2.358e+01	5.845e-02	6.188e-02	3.424e-03
40	2.408e+01	5.321e-02	5.553e-02	2.326e-03

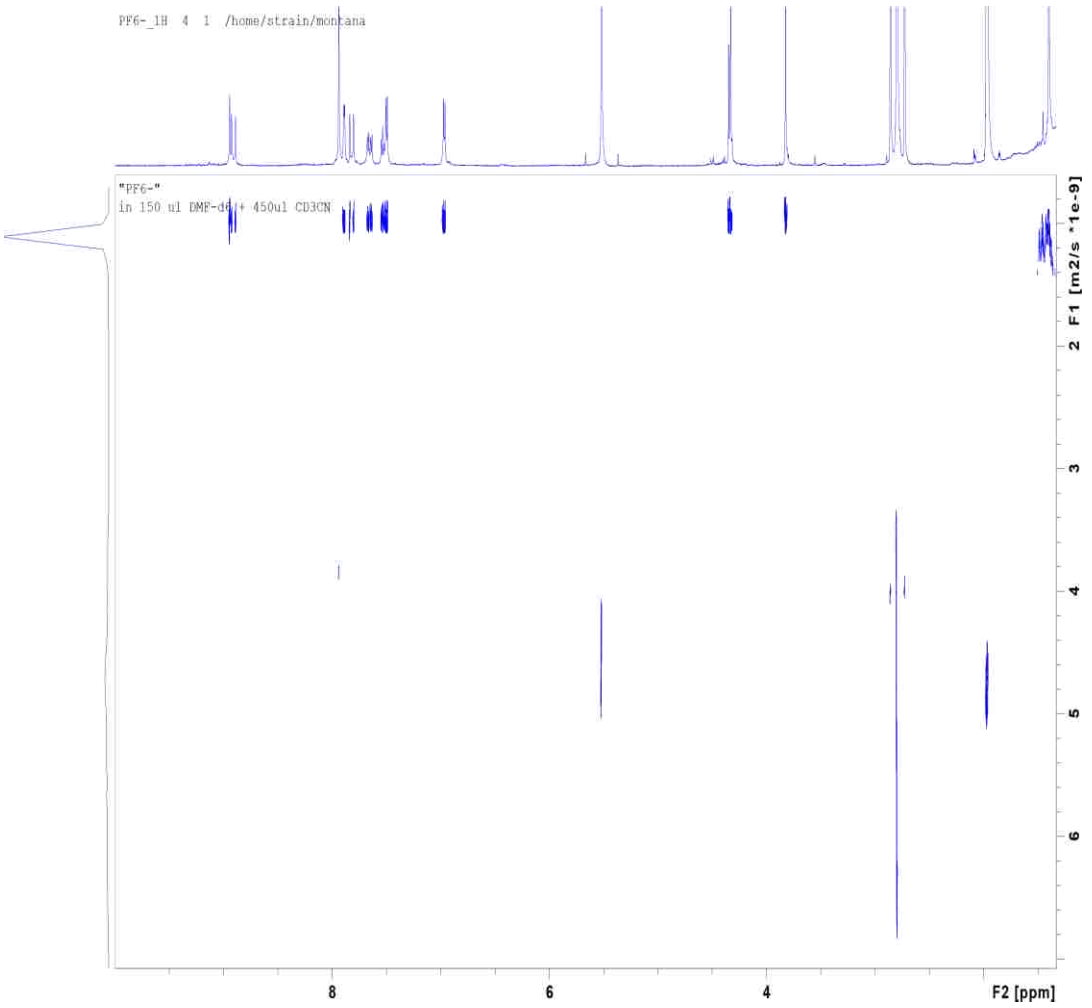

Figure 3.48 2D DOSY NMR spectrum of PF_6^- salt **8**. The average D_t is 8.56×10^{-10} m^2 s^{-1} (600 MHz, 1:3 *v*/*v* DMF-d_7-CD_3CN, 298 K).

SIMFIT RESULTS
Dataset : /home/strain/montana/PF6-_1H/4/pdata/1/ct1t2.txt
AREA fit : Diffusion : Variable Gradient :
I=I[0]*exp(-D*SQR(2*PI*gamma*Gi*LD)*(BD-LD/3)*1e4)
40 points for Integral 1, Integral Region from 8.995 to 8.865 ppm
Converged after 57 iterations!
Results Comp. 1
I[0] = 1.426e-01
Diff Con. = 8.521e-10 m2/s
Gamma = 4.258e+03 Hz/G
Little Delta = 3.400m
Big Delta = 49.900m

RSS = 2.876e-05
SD = 8.480e-04

Point	Gradient	Expt	Calc	Difference
1	0.000e+00	1.404e-01	1.426e-01	2.207e-03
2	0.000e+00	1.389e-01	1.426e-01	3.746e-03
3	3.519e+00	1.372e-01	1.367e-01	-5.195e-04
4	4.074e+00	1.351e-01	1.347e-01	-4.433e-04
5	4.630e+00	1.330e-01	1.325e-01	-5.079e-04
6	5.185e+00	1.303e-01	1.300e-01	-3.131e-04
7	5.741e+00	1.278e-01	1.273e-01	-4.257e-04
8	6.297e+00	1.253e-01	1.244e-01	-8.832e-04
9	6.852e+00	1.217e-01	1.214e-01	-3.581e-04
10	7.408e+00	1.182e-01	1.181e-01	-1.095e-04
11	7.963e+00	1.153e-01	1.147e-01	-6.024e-04
12	8.519e+00	1.114e-01	1.111e-01	-2.771e-04
13	9.074e+00	1.082e-01	1.075e-01	-7.459e-04
14	9.630e+00	1.043e-01	1.037e-01	-6.047e-04
15	1.019e+01	1.004e-01	9.983e-02	-5.696e-04
16	1.074e+01	9.647e-02	9.592e-02	-5.553e-04
17	1.130e+01	9.266e-02	9.196e-02	-6.938e-04
18	1.185e+01	8.834e-02	8.799e-02	-3.525e-04
19	1.241e+01	8.406e-02	8.400e-02	-6.189e-05
20	1.296e+01	8.018e-02	8.003e-02	-1.447e-04
21	1.352e+01	7.715e-02	7.608e-02	-1.070e-03
22	1.407e+01	7.225e-02	7.217e-02	-7.623e-05
23	1.463e+01	6.827e-02	6.833e-02	5.745e-05
24	1.519e+01	6.485e-02	6.454e-02	-3.053e-04
25	1.574e+01	6.091e-02	6.084e-02	-7.126e-05
26	1.630e+01	5.711e-02	5.723e-02	1.167e-04
27	1.685e+01	5.376e-02	5.372e-02	-4.325e-05
28	1.741e+01	5.027e-02	5.032e-02	4.610e-05
29	1.796e+01	4.678e-02	4.703e-02	2.419e-04
30	1.852e+01	4.345e-02	4.386e-02	4.166e-04
31	1.908e+01	4.063e-02	4.082e-02	1.908e-04
32	1.963e+01	3.775e-02	3.792e-02	1.630e-04
33	2.019e+01	3.452e-02	3.514e-02	6.214e-04
34	2.074e+01	3.215e-02	3.249e-02	3.438e-04
35	2.130e+01	2.970e-02	2.999e-02	2.869e-04
36	2.185e+01	2.660e-02	2.762e-02	1.015e-03
37	2.241e+01	2.508e-02	2.538e-02	2.951e-04
38	2.296e+01	2.227e-02	2.327e-02	9.983e-04
39	2.352e+01	2.047e-02	2.130e-02	8.283e-04
40	2.408e+01	1.884e-02	1.944e-02	6.003e-04

40 points for Integral 3, Integral Region from 7.856 to 7.784 ppm

Converged after 52 iterations!
Results Comp. 1
I[0] = 7.483e-02
Diff Con. = 8.470e-10 m2/s
Gamma = 4.258e+03 Hz/G
Little Delta = 3.400m
Big Delta = 49.900m
RSS = 1.325e-05
SD = 5.755e-04

Point	Gradient	Expt	Calc	Difference
1	0.000e+00	7.348e-02	7.483e-02	1.350e-03
2	0.000e+00	7.239e-02	7.483e-02	2.439e-03
3	3.519e+00	7.201e-02	7.173e-02	-2.775e-04
4	4.074e+00	7.078e-02	7.070e-02	-7.197e-05
5	4.630e+00	6.957e-02	6.954e-02	-2.601e-05
6	5.185e+00	6.850e-02	6.826e-02	-2.335e-04
7	5.741e+00	6.722e-02	6.686e-02	-3.575e-04
8	6.297e+00	6.548e-02	6.535e-02	-1.313e-04
9	6.852e+00	6.370e-02	6.374e-02	4.062e-05
10	7.408e+00	6.243e-02	6.203e-02	-3.976e-04
11	7.963e+00	6.064e-02	6.025e-02	-3.885e-04
12	8.519e+00	5.888e-02	5.839e-02	-4.827e-04
13	9.074e+00	5.701e-02	5.648e-02	-5.324e-04
14	9.630e+00	5.514e-02	5.451e-02	-6.342e-04
15	1.019e+01	5.274e-02	5.249e-02	-2.511e-04
16	1.074e+01	5.101e-02	5.045e-02	-5.621e-04
17	1.130e+01	4.901e-02	4.838e-02	-6.272e-04
18	1.185e+01	4.675e-02	4.630e-02	-4.444e-04
19	1.241e+01	4.462e-02	4.422e-02	-4.039e-04
20	1.296e+01	4.232e-02	4.214e-02	-1.820e-04
21	1.352e+01	4.081e-02	4.007e-02	-7.383e-04
22	1.407e+01	3.828e-02	3.802e-02	-2.592e-04
23	1.463e+01	3.609e-02	3.601e-02	-8.217e-05
24	1.519e+01	3.417e-02	3.403e-02	-1.405e-04
25	1.574e+01	3.155e-02	3.209e-02	5.334e-04
26	1.630e+01	3.003e-02	3.019e-02	1.632e-04
27	1.685e+01	2.831e-02	2.835e-02	4.003e-05
28	1.741e+01	2.640e-02	2.657e-02	1.665e-04
29	1.796e+01	2.459e-02	2.484e-02	2.518e-04
30	1.852e+01	2.297e-02	2.318e-02	2.082e-04
31	1.908e+01	2.114e-02	2.158e-02	4.414e-04
32	1.963e+01	1.988e-02	2.005e-02	1.688e-04
33	2.019e+01	1.819e-02	1.859e-02	4.061e-04
34	2.074e+01	1.692e-02	1.720e-02	2.761e-04

35	2.130e+01	1.562e-02	1.588e-02	2.612e-04
36	2.185e+01	1.435e-02	1.463e-02	2.853e-04
37	2.241e+01	1.329e-02	1.345e-02	1.660e-04
38	2.296e+01	1.161e-02	1.234e-02	7.321e-04
39	2.352e+01	1.080e-02	1.130e-02	4.996e-04
40	2.408e+01	9.789e-03	1.032e-02	5.356e-04

40 points for Integral 4, Integral Region from 7.704 to 7.610 ppm
Converged after 53 iterations!
Results Comp. 1
I[0] = 1.146e-01
Diff Con. = 8.531e-10 m2/s
Gamma = 4.258e+03 Hz/G
Little Delta = 3.400m
Big Delta = 49.900m
RSS = 2.073e-05
SD = 7.199e-04

Point	Gradient	Expt	Calc	Difference
1	0.000e+00	1.126e-01	1.146e-01	1.935e-03
2	0.000e+00	1.114e-01	1.146e-01	3.156e-03
3	3.519e+00	1.100e-01	1.098e-01	-1.812e-04
4	4.074e+00	1.083e-01	1.082e-01	-1.426e-04
5	4.630e+00	1.067e-01	1.064e-01	-3.184e-04
6	5.185e+00	1.048e-01	1.044e-01	-3.235e-04
7	5.741e+00	1.027e-01	1.023e-01	-4.055e-04
8	6.297e+00	1.006e-01	9.995e-02	-6.400e-04
9	6.852e+00	9.806e-02	9.747e-02	-5.916e-04
10	7.408e+00	9.514e-02	9.484e-02	-2.916e-04
11	7.963e+00	9.277e-02	9.210e-02	-6.670e-04
12	8.519e+00	8.988e-02	8.924e-02	-6.367e-04
13	9.074e+00	8.697e-02	8.629e-02	-6.823e-04
14	9.630e+00	8.404e-02	8.326e-02	-7.857e-04
15	1.019e+01	8.056e-02	8.016e-02	-3.991e-04
16	1.074e+01	7.738e-02	7.702e-02	-3.573e-04
17	1.130e+01	7.415e-02	7.384e-02	-3.119e-04
18	1.185e+01	7.106e-02	7.064e-02	-4.131e-04
19	1.241e+01	6.783e-02	6.744e-02	-3.871e-04
20	1.296e+01	6.455e-02	6.425e-02	-3.015e-04
21	1.352e+01	6.151e-02	6.107e-02	-4.390e-04
22	1.407e+01	5.820e-02	5.793e-02	-2.618e-04
23	1.463e+01	5.483e-02	5.484e-02	1.139e-05
24	1.519e+01	5.187e-02	5.180e-02	-7.211e-05
25	1.574e+01	4.833e-02	4.883e-02	4.995e-04
26	1.630e+01	4.576e-02	4.593e-02	1.637e-04
27	1.685e+01	4.259e-02	4.311e-02	5.190e-04

28	1.741e+01	4.050e-02	4.037e-02	-1.325e-04
29	1.796e+01	3.737e-02	3.773e-02	3.622e-04
30	1.852e+01	3.524e-02	3.519e-02	-4.500e-05
31	1.908e+01	3.217e-02	3.275e-02	5.775e-04
32	1.963e+01	3.041e-02	3.041e-02	6.517e-06
33	2.019e+01	2.780e-02	2.818e-02	3.799e-04
34	2.074e+01	2.570e-02	2.606e-02	3.624e-04
35	2.130e+01	2.348e-02	2.405e-02	5.713e-04
36	2.185e+01	2.144e-02	2.214e-02	7.075e-04
37	2.241e+01	2.009e-02	2.035e-02	2.613e-04
38	2.296e+01	1.845e-02	1.866e-02	2.016e-04
39	2.352e+01	1.638e-02	1.707e-02	6.954e-04
40	2.408e+01	1.540e-02	1.558e-02	1.875e-04

40 points for Integral 5, Integral Region from 7.581 to 7.479 ppm
Converged after 58 iterations!
Results Comp. 1
I[0] = 1.723e-01
Diff Con. = 8.480e-10 m2/s
Gamma = 4.258e+03 Hz/G
Little Delta = 3.400m
Big Delta = 49.900m
RSS = 3.978e-05
SD = 9.972e-04

Point	Gradient	Expt	Calc	Difference
1	0.000e+00	1.691e-01	1.723e-01	3.131e-03
2	0.000e+00	1.680e-01	1.723e-01	4.227e-03
3	3.519e+00	1.658e-01	1.651e-01	-6.603e-04
4	4.074e+00	1.635e-01	1.627e-01	-7.814e-04
5	4.630e+00	1.606e-01	1.601e-01	-4.915e-04
6	5.185e+00	1.583e-01	1.571e-01	-1.137e-03
7	5.741e+00	1.546e-01	1.539e-01	-7.035e-04
8	6.297e+00	1.509e-01	1.504e-01	-5.435e-04
9	6.852e+00	1.470e-01	1.467e-01	-3.350e-04
10	7.408e+00	1.432e-01	1.428e-01	-4.574e-04
11	7.963e+00	1.394e-01	1.387e-01	-7.165e-04
12	8.519e+00	1.346e-01	1.344e-01	-2.693e-04
13	9.074e+00	1.308e-01	1.300e-01	-8.229e-04
14	9.630e+00	1.260e-01	1.254e-01	-5.350e-04
15	1.019e+01	1.213e-01	1.208e-01	-5.294e-04
16	1.074e+01	1.167e-01	1.161e-01	-6.537e-04
17	1.130e+01	1.121e-01	1.113e-01	-7.405e-04
18	1.185e+01	1.066e-01	1.065e-01	-5.628e-05
19	1.241e+01	1.020e-01	1.017e-01	-2.708e-04
20	1.296e+01	9.701e-02	9.694e-02	-7.671e-05

21	1.352e+01	9.322e-02	9.217e-02	-1.049e-03
22	1.407e+01	8.782e-02	8.746e-02	-3.573e-04
23	1.463e+01	8.282e-02	8.282e-02	-6.546e-07
24	1.519e+01	7.852e-02	7.826e-02	-2.623e-04
25	1.574e+01	7.361e-02	7.379e-02	1.839e-04
26	1.630e+01	6.942e-02	6.943e-02	8.211e-06
27	1.685e+01	6.475e-02	6.519e-02	4.478e-04
28	1.741e+01	6.112e-02	6.108e-02	-3.502e-05
29	1.796e+01	5.685e-02	5.711e-02	2.541e-04
30	1.852e+01	5.330e-02	5.328e-02	-1.730e-05
31	1.908e+01	4.909e-02	4.961e-02	5.140e-04
32	1.963e+01	4.591e-02	4.609e-02	1.819e-04
33	2.019e+01	4.231e-02	4.273e-02	4.185e-04
34	2.074e+01	3.875e-02	3.953e-02	7.843e-04
35	2.130e+01	3.564e-02	3.650e-02	8.607e-04
36	2.185e+01	3.340e-02	3.362e-02	2.178e-04
37	2.241e+01	3.027e-02	3.091e-02	6.444e-04
38	2.296e+01	2.736e-02	2.836e-02	9.927e-04
39	2.352e+01	2.534e-02	2.596e-02	6.217e-04
40	2.408e+01	2.320e-02	2.371e-02	5.176e-04

40 points for Integral 6, Integral Region from 7.022 to 6.913 ppm
Converged after 59 iterations!
Results Comp. 1
I[0] = 1.280e-01
Diff Con. = 8.735e-10 m2/s
Gamma = 4.258e+03 Hz/G
Little Delta = 3.400m
Big Delta = 49.900m
RSS = 2.303e-05
SD = 7.588e-04

Point	Gradient	Expt	Calc	Difference
1	0.000e+00	1.261e-01	1.280e-01	1.867e-03
2	0.000e+00	1.244e-01	1.280e-01	3.608e-03
3	3.519e+00	1.232e-01	1.225e-01	-7.304e-04
4	4.074e+00	1.216e-01	1.207e-01	-8.525e-04
5	4.630e+00	1.190e-01	1.187e-01	-3.612e-04
6	5.185e+00	1.169e-01	1.164e-01	-5.019e-04
7	5.741e+00	1.148e-01	1.139e-01	-8.166e-04
8	6.297e+00	1.117e-01	1.113e-01	-4.433e-04
9	6.852e+00	1.086e-01	1.085e-01	-1.554e-04
10	7.408e+00	1.059e-01	1.055e-01	-3.802e-04
11	7.963e+00	1.028e-01	1.024e-01	-4.371e-04
12	8.519e+00	9.950e-02	9.910e-02	-4.027e-04
13	9.074e+00	9.628e-02	9.575e-02	-5.345e-04

14	9.630e+00	9.274e-02	9.230e-02	-4.345e-04
15	1.019e+01	8.918e-02	8.879e-02	-3.908e-04
16	1.074e+01	8.578e-02	8.522e-02	-5.584e-04
17	1.130e+01	8.176e-02	8.162e-02	-1.366e-04
18	1.185e+01	7.826e-02	7.801e-02	-2.483e-04
19	1.241e+01	7.462e-02	7.439e-02	-2.306e-04
20	1.296e+01	7.070e-02	7.079e-02	8.398e-05
21	1.352e+01	6.795e-02	6.721e-02	-7.415e-04
22	1.407e+01	6.352e-02	6.367e-02	1.525e-04
23	1.463e+01	5.972e-02	6.019e-02	4.739e-04
24	1.519e+01	5.717e-02	5.678e-02	-3.911e-04
25	1.574e+01	5.327e-02	5.344e-02	1.698e-04
26	1.630e+01	5.002e-02	5.019e-02	1.764e-04
27	1.685e+01	4.684e-02	4.704e-02	2.065e-04
28	1.741e+01	4.362e-02	4.399e-02	3.698e-04
29	1.796e+01	4.076e-02	4.104e-02	2.837e-04
30	1.852e+01	3.811e-02	3.822e-02	1.054e-04
31	1.908e+01	3.542e-02	3.550e-02	8.420e-05
32	1.963e+01	3.286e-02	3.291e-02	4.902e-05
33	2.019e+01	2.992e-02	3.044e-02	5.224e-04
34	2.074e+01	2.738e-02	2.810e-02	7.147e-04
35	2.130e+01	2.576e-02	2.588e-02	1.143e-04
36	2.185e+01	2.359e-02	2.378e-02	1.949e-04
37	2.241e+01	2.144e-02	2.181e-02	3.716e-04
38	2.296e+01	1.962e-02	1.995e-02	3.315e-04
39	2.352e+01	1.802e-02	1.822e-02	1.998e-04
40	2.408e+01	1.652e-02	1.660e-02	7.253e-05

40 points for Integral 8, Integral Region from 4.360 to 4.287 ppm
Converged after 46 iterations!
Results Comp. 1
I[0] = 2.876e-01
Diff Con. = 8.399e-10 m2/s
Gamma = 4.258e+03 Hz/G
Little Delta = 3.400m
Big Delta = 49.900m
RSS = 9.584e-05
SD = 1.548e-03

Point	Gradient	Expt	Calc	Difference
1	0.000e+00	2.832e-01	2.876e-01	4.366e-03
2	0.000e+00	2.805e-01	2.876e-01	7.124e-03
3	3.519e+00	2.764e-01	2.758e-01	-6.644e-04
4	4.074e+00	2.731e-01	2.719e-01	-1.253e-03
5	4.630e+00	2.684e-01	2.674e-01	-9.904e-04
6	5.185e+00	2.637e-01	2.625e-01	-1.134e-03

7	5.741e+00	2.585e-01	2.572e-01	-1.307e-03
8	6.297e+00	2.525e-01	2.514e-01	-1.096e-03
9	6.852e+00	2.463e-01	2.453e-01	-9.910e-04
10	7.408e+00	2.400e-01	2.388e-01	-1.184e-03
11	7.963e+00	2.330e-01	2.320e-01	-9.959e-04
12	8.519e+00	2.258e-01	2.249e-01	-9.070e-04
13	9.074e+00	2.185e-01	2.176e-01	-9.164e-04
14	9.630e+00	2.112e-01	2.100e-01	-1.169e-03
15	1.019e+01	2.031e-01	2.023e-01	-7.197e-04
16	1.074e+01	1.952e-01	1.945e-01	-6.796e-04
17	1.130e+01	1.871e-01	1.866e-01	-4.324e-04
18	1.185e+01	1.792e-01	1.787e-01	-5.761e-04
19	1.241e+01	1.714e-01	1.707e-01	-6.647e-04
20	1.296e+01	1.631e-01	1.627e-01	-3.919e-04
21	1.352e+01	1.566e-01	1.548e-01	-1.762e-03
22	1.407e+01	1.466e-01	1.470e-01	4.014e-04
23	1.463e+01	1.388e-01	1.392e-01	4.475e-04
24	1.519e+01	1.320e-01	1.316e-01	-3.516e-04
25	1.574e+01	1.239e-01	1.242e-01	2.681e-04
26	1.630e+01	1.167e-01	1.169e-01	2.213e-04
27	1.685e+01	1.097e-01	1.099e-01	1.537e-04
28	1.741e+01	1.024e-01	1.030e-01	6.027e-04
29	1.796e+01	9.604e-02	9.635e-02	3.138e-04
30	1.852e+01	8.974e-02	8.996e-02	2.222e-04
31	1.908e+01	8.302e-02	8.381e-02	7.862e-04
32	1.963e+01	7.745e-02	7.793e-02	4.808e-04
33	2.019e+01	7.178e-02	7.229e-02	5.151e-04
34	2.074e+01	6.609e-02	6.693e-02	8.397e-04
35	2.130e+01	6.105e-02	6.184e-02	7.865e-04
36	2.185e+01	5.667e-02	5.701e-02	3.473e-04
37	2.241e+01	5.141e-02	5.246e-02	1.045e-03
38	2.296e+01	4.733e-02	4.816e-02	8.345e-04
39	2.352e+01	4.329e-02	4.413e-02	8.351e-04
40	2.408e+01	3.932e-02	4.034e-02	1.024e-03

40 points for Integral 9, Integral Region from 3.859 to 3.780 ppm
Converged after 51 iterations!
Results Comp. 1
I[0] = 2.049e-01
Diff Con. = 8.391e-10 m2/s
Gamma = 4.258e+03 Hz/G
Little Delta = 3.400m
Big Delta = 49.900m
RSS = 4.794e-05
SD = 1.095e-03

Point	Gradient	Expt	Calc	Difference
1	0.000e+00	2.017e-01	2.049e-01	3.204e-03
2	0.000e+00	2.000e-01	2.049e-01	4.986e-03
3	3.519e+00	1.974e-01	1.965e-01	-8.736e-04
4	4.074e+00	1.950e-01	1.937e-01	-1.215e-03
5	4.630e+00	1.915e-01	1.906e-01	-8.788e-04
6	5.185e+00	1.879e-01	1.871e-01	-7.843e-04
7	5.741e+00	1.842e-01	1.833e-01	-9.091e-04
8	6.297e+00	1.801e-01	1.792e-01	-8.848e-04
9	6.852e+00	1.753e-01	1.748e-01	-4.595e-04
10	7.408e+00	1.707e-01	1.702e-01	-5.165e-04
11	7.963e+00	1.659e-01	1.653e-01	-5.414e-04
12	8.519e+00	1.610e-01	1.603e-01	-7.390e-04
13	9.074e+00	1.555e-01	1.551e-01	-4.330e-04
14	9.630e+00	1.504e-01	1.497e-01	-6.334e-04
15	1.019e+01	1.447e-01	1.442e-01	-4.313e-04
16	1.074e+01	1.391e-01	1.387e-01	-4.002e-04
17	1.130e+01	1.334e-01	1.330e-01	-3.917e-04
18	1.185e+01	1.277e-01	1.274e-01	-3.085e-04
19	1.241e+01	1.217e-01	1.217e-01	2.199e-05
20	1.296e+01	1.161e-01	1.160e-01	-9.973e-05
21	1.352e+01	1.116e-01	1.104e-01	-1.166e-03
22	1.407e+01	1.049e-01	1.048e-01	-1.172e-04
23	1.463e+01	9.909e-02	9.929e-02	2.058e-04
24	1.519e+01	9.365e-02	9.388e-02	2.230e-04
25	1.574e+01	8.858e-02	8.858e-02	-6.030e-06
26	1.630e+01	8.361e-02	8.339e-02	-2.159e-04
27	1.685e+01	7.826e-02	7.836e-02	9.323e-05
28	1.741e+01	7.351e-02	7.346e-02	-4.746e-05
29	1.796e+01	6.871e-02	6.873e-02	2.428e-05
30	1.852e+01	6.363e-02	6.418e-02	5.501e-04
31	1.908e+01	5.925e-02	5.979e-02	5.407e-04
32	1.963e+01	5.535e-02	5.560e-02	2.439e-04
33	2.019e+01	5.146e-02	5.158e-02	1.208e-04
34	2.074e+01	4.730e-02	4.776e-02	4.575e-04
35	2.130e+01	4.385e-02	4.413e-02	2.819e-04
36	2.185e+01	4.019e-02	4.069e-02	4.974e-04
37	2.241e+01	3.652e-02	3.744e-02	9.261e-04
38	2.296e+01	3.380e-02	3.438e-02	5.722e-04
39	2.352e+01	3.063e-02	3.150e-02	8.741e-04
40	2.408e+01	2.818e-02	2.880e-02	6.270e-04

40 points for Integral 12, Integral Region from 1.436 to 1.386 ppm
Converged after 37 iterations!
Results Comp. 1
I[0] = 7.228e-01

Diff Con. = 8.993e-10 m2/s
Gamma = 4.258e+03 Hz/G
Little Delta = 3.400m
Big Delta = 49.900m
RSS = 6.218e-04
SD = 3.943e-03

Point	Gradient	Expt	Calc	Difference
1	0.000e+00	7.171e-01	7.228e-01	5.712e-03
2	0.000e+00	7.099e-01	7.228e-01	1.295e-02
3	3.519e+00	6.999e-01	6.910e-01	-8.839e-03
4	4.074e+00	6.872e-01	6.806e-01	-6.599e-03
5	4.630e+00	6.754e-01	6.687e-01	-6.647e-03
6	5.185e+00	6.612e-01	6.556e-01	-5.537e-03
7	5.741e+00	6.455e-01	6.413e-01	-4.211e-03
8	6.297e+00	6.286e-01	6.259e-01	-2.702e-03
9	6.852e+00	6.106e-01	6.096e-01	-9.878e-04
10	7.408e+00	5.930e-01	5.923e-01	-6.898e-04
11	7.963e+00	5.750e-01	5.743e-01	-7.650e-04
12	8.519e+00	5.548e-01	5.555e-01	6.463e-04
13	9.074e+00	5.349e-01	5.361e-01	1.195e-03
14	9.630e+00	5.141e-01	5.163e-01	2.137e-03
15	1.019e+01	4.931e-01	4.961e-01	2.916e-03
16	1.074e+01	4.733e-01	4.756e-01	2.266e-03
17	1.130e+01	4.517e-01	4.549e-01	3.174e-03
18	1.185e+01	4.313e-01	4.342e-01	2.908e-03
19	1.241e+01	4.102e-01	4.134e-01	3.271e-03
20	1.296e+01	3.899e-01	3.929e-01	2.951e-03
21	1.352e+01	3.726e-01	3.724e-01	-1.880e-04
22	1.407e+01	3.486e-01	3.523e-01	3.607e-03
23	1.463e+01	3.287e-01	3.325e-01	3.773e-03
24	1.519e+01	3.106e-01	3.131e-01	2.447e-03
25	1.574e+01	2.920e-01	2.942e-01	2.156e-03
26	1.630e+01	2.739e-01	2.757e-01	1.825e-03
27	1.685e+01	2.569e-01	2.579e-01	1.006e-03
28	1.741e+01	2.401e-01	2.407e-01	6.317e-04
29	1.796e+01	2.241e-01	2.241e-01	5.887e-05
30	1.852e+01	2.088e-01	2.083e-01	-5.601e-04
31	1.908e+01	1.938e-01	1.931e-01	-7.303e-04
32	1.963e+01	1.799e-01	1.786e-01	-1.331e-03
33	2.019e+01	1.671e-01	1.648e-01	-2.321e-03
34	2.074e+01	1.539e-01	1.517e-01	-2.178e-03
35	2.130e+01	1.422e-01	1.394e-01	-2.806e-03
36	2.185e+01	1.308e-01	1.278e-01	-3.040e-03
37	2.241e+01	1.205e-01	1.169e-01	-3.646e-03
38	2.296e+01	1.108e-01	1.067e-01	-4.146e-03

39	2.352e+01	1.010e-01	9.714e-02	-3.858e-03
40	2.408e+01	9.295e-02	8.825e-02	-4.700e-03

DOSY Data and Refinement for the Internal Standard, CH_2Cl_2

40 points for Integral 8, Integral Region from 5.561 to 5.486 ppm
Converged after 52 iterations!
Results Comp. 1
I[0] = 2.797e-01
Diff Con. = 3.718e-09 m2/s
Gamma = 4.258e+03 Hz/G
Little Delta = 3.400m
Big Delta = 49.900m
RSS = 7.459e-03
SD = 1.366e-02

Point	Gradient	Expt	Calc	Difference
1	0.000e+00	2.711e-01	2.797e-01	8.564e-03
2	0.000e+00	2.429e-01	2.797e-01	3.680e-02
3	5.803e+00	2.152e-01	1.688e-01	-4.642e-02
4	6.297e+00	1.885e-01	1.543e-01	-3.417e-02
5	6.790e+00	1.635e-01	1.401e-01	-2.348e-02
6	7.284e+00	1.405e-01	1.262e-01	-1.427e-02
7	7.778e+00	1.188e-01	1.129e-01	-5.974e-03
8	8.272e+00	9.948e-02	1.002e-01	7.228e-04
9	8.766e+00	8.291e-02	8.832e-02	5.413e-03
10	9.260e+00	6.785e-02	7.728e-02	9.427e-03
11	9.753e+00	5.502e-02	6.714e-02	1.212e-02
12	1.025e+01	4.445e-02	5.789e-02	1.345e-02
13	1.074e+01	3.531e-02	4.956e-02	1.425e-02
14	1.123e+01	2.769e-02	4.211e-02	1.442e-02
15	1.173e+01	2.117e-02	3.552e-02	1.435e-02
16	1.222e+01	1.615e-02	2.974e-02	1.359e-02
17	1.272e+01	1.243e-02	2.472e-02	1.230e-02
18	1.321e+01	9.044e-03	2.041e-02	1.137e-02
19	1.370e+01	6.414e-03	1.672e-02	1.031e-02
20	1.420e+01	4.648e-03	1.360e-02	8.950e-03
21	1.469e+01	3.421e-03	1.098e-02	7.557e-03
22	1.519e+01	2.181e-03	8.797e-03	6.616e-03
23	1.568e+01	1.282e-03	6.999e-03	5.716e-03
24	1.617e+01	7.923e-04	5.530e-03	4.738e-03
25	1.667e+01	4.374e-04	4.335e-03	3.898e-03
26	1.716e+01	3.249e-05	3.374e-03	3.342e-03
27	1.766e+01	2.937e-05	2.607e-03	2.578e-03
28	1.815e+01	-2.249e-04	1.999e-03	2.224e-03
29	1.864e+01	-9.501e-05	1.522e-03	1.617e-03

30	1.914e+01	-3.932e-04	1.151e-03	1.544e-03
31	1.963e+01	-3.852e-04	8.638e-04	1.249e-03
32	2.012e+01	-4.265e-04	6.434e-04	1.070e-03
33	2.062e+01	-2.851e-04	4.757e-04	7.608e-04
34	2.111e+01	-4.428e-04	3.492e-04	7.920e-04
35	2.161e+01	-4.025e-04	2.545e-04	6.570e-04
36	2.210e+01	-3.278e-04	1.841e-04	5.118e-04
37	2.259e+01	-4.406e-04	1.323e-04	5.729e-04
38	2.309e+01	-1.505e-04	9.428e-05	2.448e-04
39	2.358e+01	-3.196e-04	6.672e-05	3.863e-04
40	2.408e+01	-3.161e-04	4.687e-05	3.630e-04

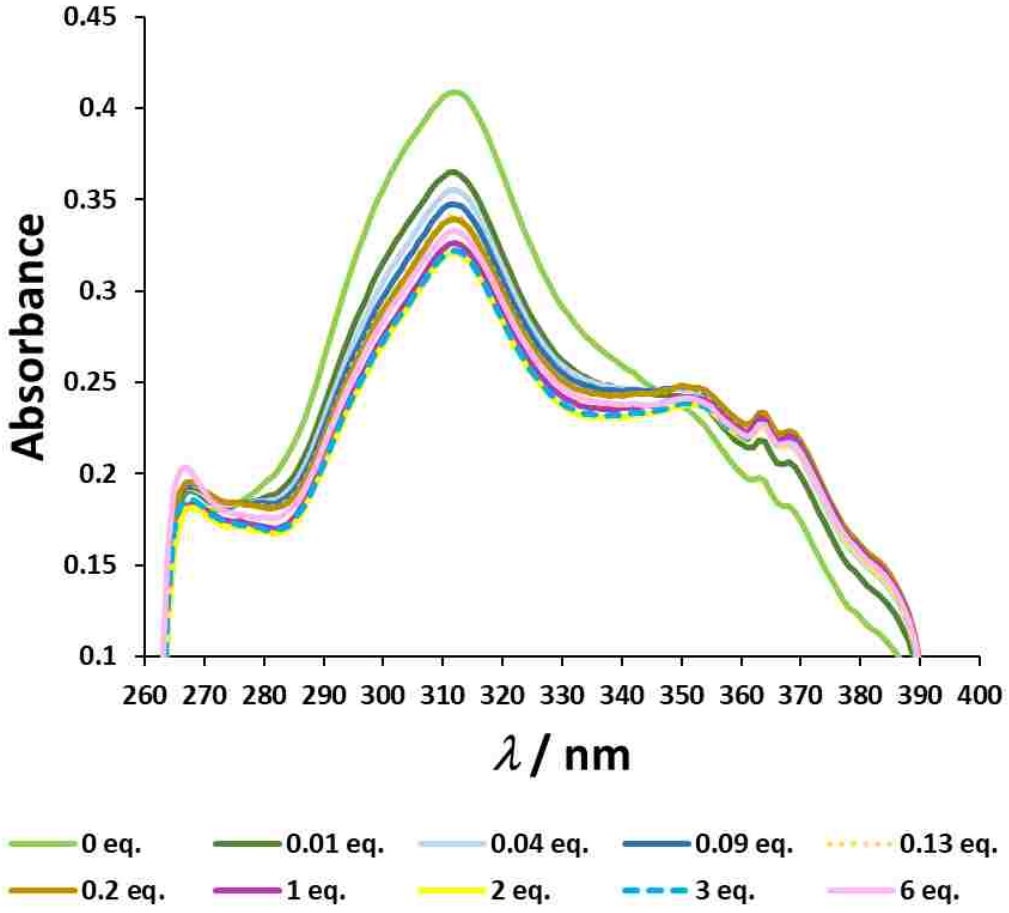

Figure 3.49 UV-Vis difference spectrum of **8** (5 μM) with additions of TBAI (colors represent equivalents of guest added; 1:3 *v*/*v* DMF-CH_3CN, 298 K).

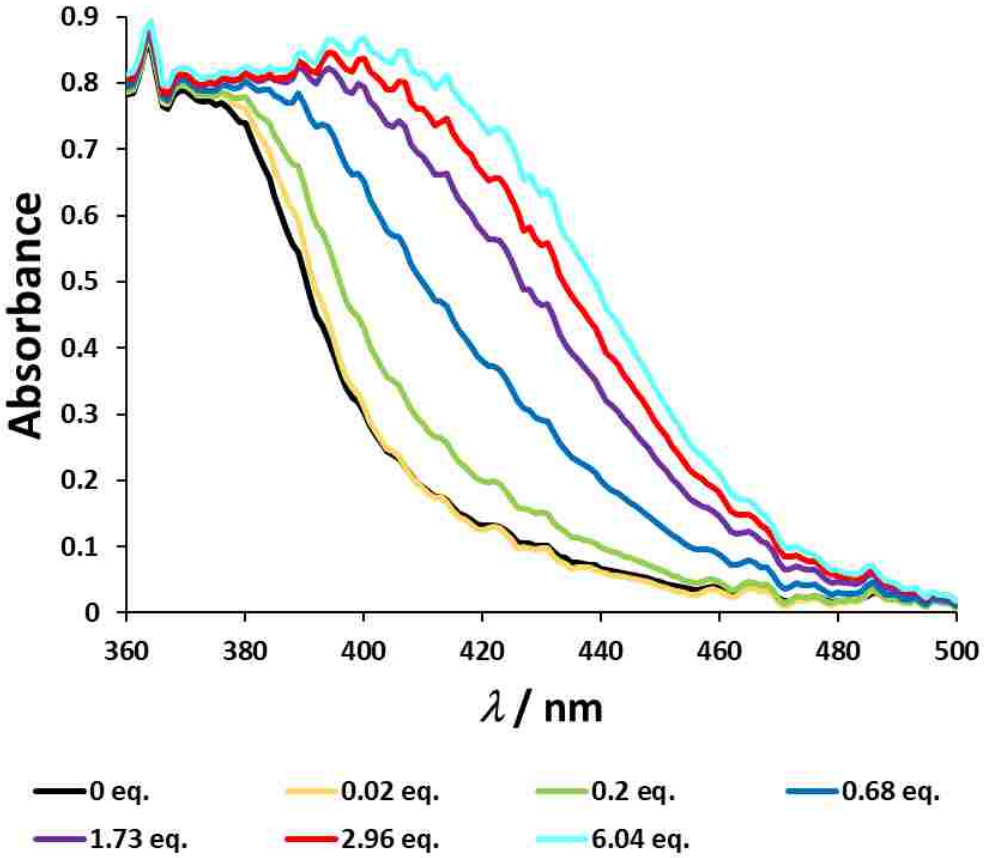

Figure 3.50 UV-Vis difference spectrum of **8** (0.3 mM) with additions of TBAI (colors represent equivalents of guest added; 1:3 *v*/*v* DMF-CH_3CN, 298 K).

3.5 Conclusion and Bridge to Chapter 4

In conclusion, we have described the first halogen-bond-induced triple helicate to bind I^- in solution and the solid state. The helicate is stabilized by multiple strong and linear halogen bonds and π-π stacking. Furthermore, we have demonstrated that the complex is shape-persistent at high temperatures and in aqueous phase. Given the competing speciation and myriad noncovalent interactions in solution, the thorough characterization of a self-assembling triple anion helicate is an important step towards the

rational design of large tubular containers with high affinity for complementary guests. We hypothesize that the combination of helical rise and halogen-bond linearity influences higher-order helication by destabilizing 1:1 complexes. Hence, the expedient self-assembly of a convergent, multidentate halogen-bonding microenvironment may be realized. These results have implications in anion sensing, nanomaterials, and synthetic ion channeling.

After discovering a new strategy to form I^- triple helicates, there were many options for future research including: backbone and active-site modification, anion binding in pure water, chiral induction, chain extension, light-switchable helication/anion binding, etc. Additionally, no kinetic studies of an anion helicate had been undertaken. Up to this point, only a few preliminary kinetic studies of anion foldamers were conducted by Maeda et al. (see Section 1.5). Whether the ligands of an anion helicate could maintain their shape for useful periods of time or whether the anions themselves were immobilized upon binding or exchanged rapidly was unknown. Hence, the first kinetic and mechanistic studies of an anion helicate were completed. In addition, the first Br^--encapsulating triple anion helicate was synthesized and characterized in solution and the solid state.

4 A Long-Lived Halogen-Bonding Anion Triple Helicate Accommodates Rapid Guest Exchange

4.1 Abstract and Artwork

Anion-templated helical structures are emerging as a dynamic and tractable class of supramolecules that exhibit anion-switchable self-assembly. We present the first kinetic studies of an anion helicate by utilizing halogen-bonding *m*-arylene-ethynylene oligomers. These ligands formed high-fidelity triple helicates in solution with surprisingly long lifetimes on the order of seconds even at elevated temperatures. We propose an associative ligand-exchange mechanism that proceeded slowly on the same timescale. In contrast, intrachannel anion exchange occurred rapidly within milliseconds or faster as determined by stopped-flow visible spectroscopy. Additionally, the helicate accommodated Br^- in solution and the solid state, while the thermodynamic stability of the triplex favored larger halide ions ($Br^- \approx I^- >> Cl^-$). Taken together, we elucidate a new class of kinetically stable helicates. These anion-switchable triplexes maintain their architectures while accommodating fast intrachannel guest exchange.

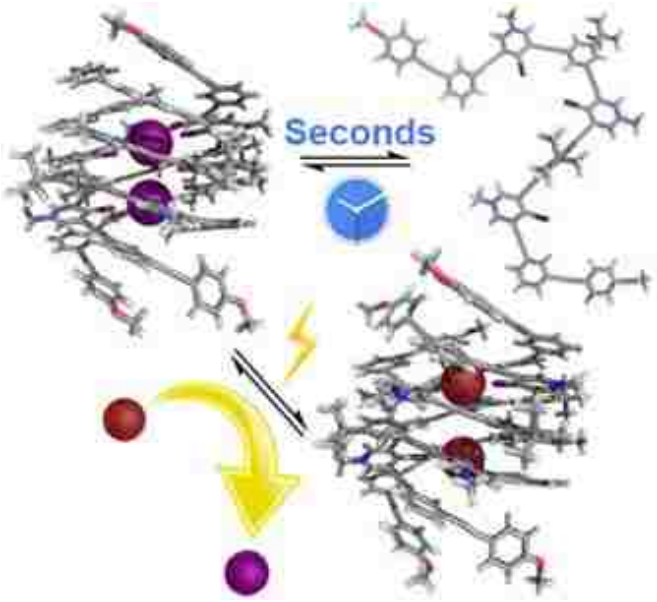

Figure 4.1 Table of contents artwork for *Angewandte Chemie International Edition* publication. Anion helicates are an emerging class of secondary structure that possess both anion-switchable and dynamic properties. The first kinetic studies of an anion helicate reveal that its ligands can hold their shape for seconds while anionic guests hop in and out on the order of milliseconds or faster.

4.2 Introduction

This chapter includes work that was published in *Angewandte Chemie International Edition* (**2018**, *published online*) and was co-authored by Daniel A. Decato and Dr. Orion B. Berryman. Decato collected and refined the X-ray crystallographic data. Dr. Berryman helped with data interpretation and edited all publication documents. Massena, the first author, conceived of the project, conducted all syntheses, conducted all solution-phase experiments, interpreted the data, and wrote all of the publication matierals.

Increasingly, chemists and biologists seek the underlying rules governing the structure and dynamics of organized matter, a task shared by physical scientists from diverse fields. To this end, supramolecular chemists have constructed and studied libraries of helical foldamers and metal-templated helicates—imitating and complementing one of the most pervasive structural elements of biomolecules (see Sections 1.2–1.4). In contrast, helicates that self-assemble around anions are underdeveloped, and there are only three other examples of kinetically stable higher-order anion helicates. De Mendoza's bicyclic guanidinium SO_4^{2-} duplexes and Wu's bis(biurea) triplexes chelated di- and trivalent oxoanions, respectively, while Maeda's pyrrole-based double helicates encapsulated Cl^- and Br^-. Elegant examples of the closely related mononuclear foldamers include Flood's aryl-triazole Cl^- duplex (for a review of anion helicates/foldamers, see Section 1.5). Thus, it has been established that anions instigate and maintain helical secondary structure, but how labile are the ligands, and are the anions dynamic? *Here, we present the first kinetic studies of an anion helicate to promote these supramolecular structures as useful and moving nanocomponents.*

Due to its stringent linearity, halogen bonding is a promising noncovalent interaction that has been successfully applied to many fields, including foldameric, capsular, and mechanical-bond-based self-assembly.[113–127] Recently, we assembled I^--binding triple helicates in solution utilizing halogen bonds. In the present study, we explore the ligand and guest dynamics of our triple-helicate system to better understand this nascent class of supramolecules. ^{1}H 2D EXSY NMR spectroscopy revealed surprisingly long ligand lifetimes—on the order of seconds even at elevated temperatures. Variable-temperature EXSY NMR and other kinetic studies suggested an associative

ligand-exchange mechanism that proceeded slowly on the same timescale. In contrast, stopped-flow visible spectroscopy established millisecond-or-faster anion exchange, demonstrating that the helicate holds its shape while Br^- and I^- flit in and out of its helical cavity. Furthermore, we characterize the first Br^- triple helicate in solution and the solid state. Through judicious use of the halogen bond, we offer a strategy to form Br^-- and I^--switchable triple helicates that, once assembled, accommodate seconds-long ligand transfers and rapid intrachannel guest exchange.

4.3 Results and Discussion

4.3.1 Optimized Synthesis of *m*-Arylene-Ethynylene Oligomers

Optimizing a previous route, we synthesized *m*-arylene ethynylene ligand **3** (Schemes 4.1–4.2) in higher yield (see Section 4.4.1). *tert*-Butyl and methoxy groups were appended to the oligomeric backbone to enhance solubility and serve as spectroscopic handles for ^{1}H NMR experiments.

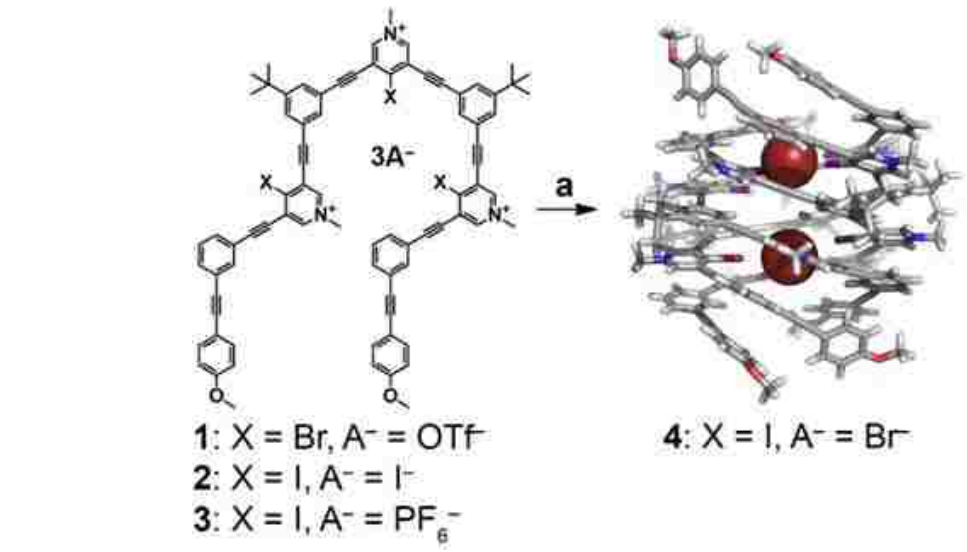

Scheme 4.1 *m*-Arylene-ethynylene ligands and synthesis of triple helicate **4**. Reagents and conditions: (a) TBABr, 1:3 *v*/*v* DMF-CH_3CN, RT. 4 is shown as its X-ray crystal structure (extrachannel Br^-s and intrachannel positional disorder not shown for clarity; for crystallographic data and structural refinement details; see Section 4.4.2).

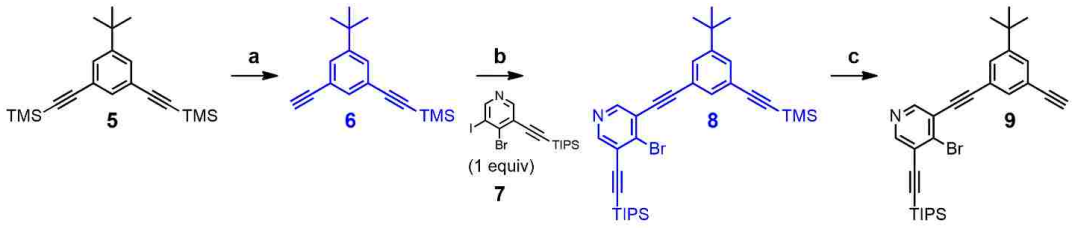

Scheme 4.2 Synthesis of *m*-arylene-ethynylene ligand precursors. Reagents and conditions: (a) MeLi•LiBr (1.3 equiv), THF, 0 °C, 20 min, 32 %; (b) $PdCl_2(PPh_3)_2$ (0.06 equiv), CuI (0.06 equiv), TEA, DMF, 50 °C, 12 h, 68 %; (c) K_2CO_3 (4.7 equiv), 1:4 *v*/*v* CH_3OH-THF, RT, 80 min, quantitative. New precursors shown in blue, previously characterized compounds in black.

4.3.2 Solid-State Characterization of the Br^- Triple Helicate

Yellow plates of Br^- helicate **4** suitable for single crystal X-ray diffraction were grown by slow vapor diffusion of Et_2O into a 1:1:2 *v*/*v*/*v* DMF-CH_3NO_2-CH_3CN solution of **2** with excess TBABr at 4 °C. As was the case with **2**, each triplex is composed of three intertwined tricationic ligands offset along a common screw axis as defined by the two intrachannel Br^-s (Scheme 4.1 and Figure 4.46). Each Br^- is bound by four strong and linear halogen bonds within the helical channel. The height and width of **4** are equivalent to that of **2** (13 and 19 Å, respectively). However, on average, **4** adopts shorter intrachannel CI···Br^- contacts and more linear CI···Br^- angles (3.3 Å, 84 % ΣvdW radii, and 173 °, respectively) as compared to the CI···I^- contacts and angles of **2** (Figure 4.47).

4.3.3 Summary of X-Ray Crystallographic Data

Crystallographic Data for **4** (UMT_OB12_sq) $C_{80}H_{61}Br_{2.83}I_3N_3O_2$, M = 1703.46, monoclinic, space group *C*2/*c* (no. 15), *a* = 54.427(4) Å, *b* = 36.427(3) Å, *c* = 35.844(3) Å, β = 128.989(2) °, *V* = 55236(7) $Å^3$, *Z* = 24, *T* = 100 K, μ(CuKα) = 9.728 mm^{-1}, $2\theta_{max}$ = 73.238 °, 96618 reflections collected, 13220 unique (R_{int} = 0.0939, R_{sigma} = 0.0831), R_1 = 0.0745 ($I > 2\sigma(I)$), wR_2 = 0.2298 (all data). See Section 4.4.2 for all crystallographic details. CCDC 1852577 contains the supplementary crystallographic data for this paper.

4.3.4 Solution-Phase Characterization of the Br^- Triple Helicate

Like its I^- counterpart, the Br^- triple helicate self-assembled with high fidelity in solution. Adding excess TBABr to **3** produced a ^1H NMR spectrum consistent with the molecular C_2 symmetry of **4** and **2** (Figures 4.2–4.5 and 4.7).

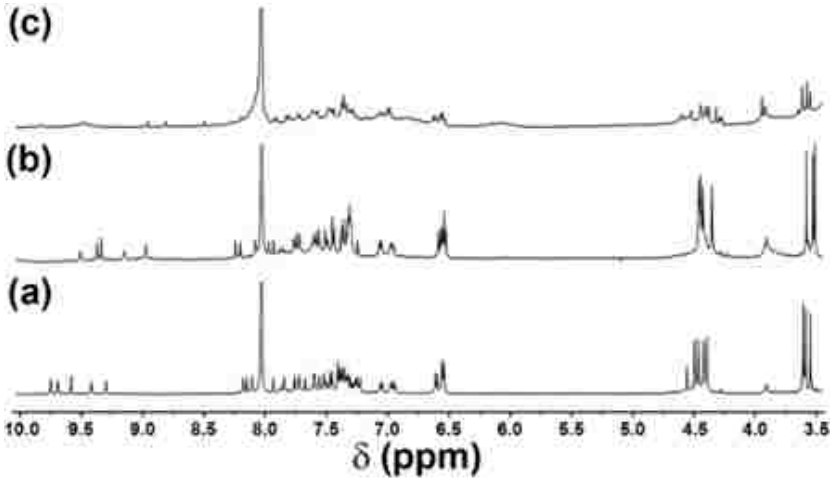

Figure 4.2 Partial ^1H NMR spectra of triple helicates and low-fidelity Cl^- species. (a) Br^- triple helicate **4**; (b) I^- triple helicate **2**; (c) low-fidelity Cl^- species. (a–b) 500 MHz; (c) 400 MHz; (a–c) 1:3 *v*/*v* DMF-d_7-CD_3CN.

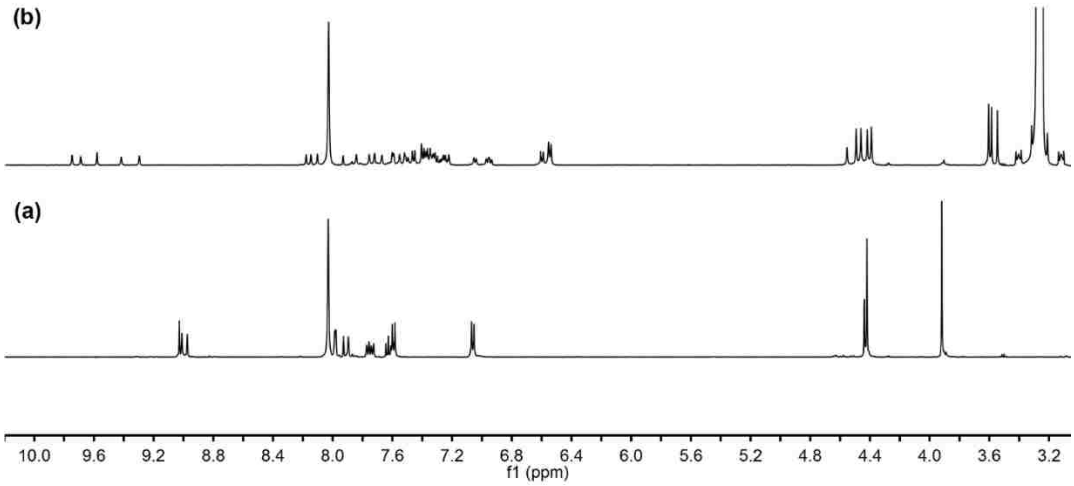

Figure 4.3 (a) Partial ^{1}H NMR spectrum of free ligand **3**; (b) partial ^{1}H NMR spectrum of **4**; (a–b) 500 MHz, 1:3 *v*/*v* DMF-d_7-CD_3CN.

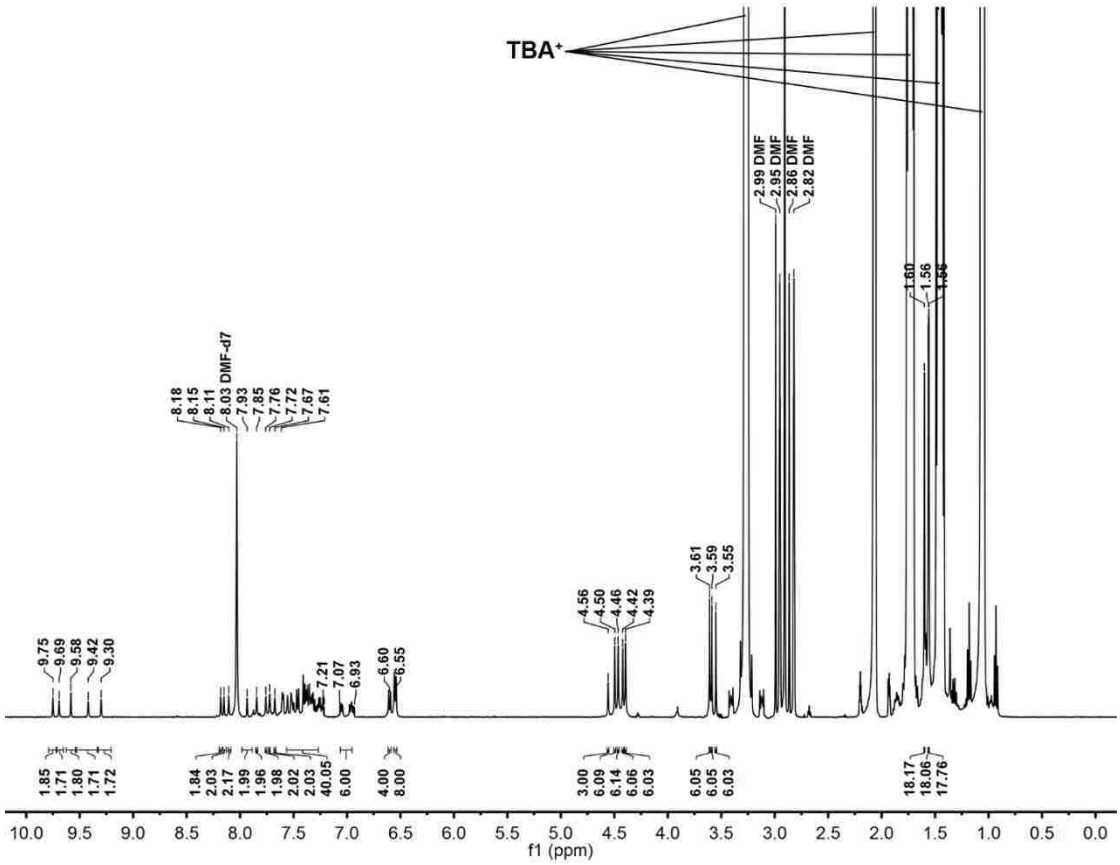

Figure 4.4 ^{1}H NMR spectrum of **4**. ^{1}H NMR (500 MHz, 1:3 *v*/*v* DMF-d_7-CD_3CN) δ 9.75 (s, 2H), 9.69 (s, 2H), 9.58 (s, 2H), 9.42 (s, 2H), 9.30 (s, 2H), 8.18 (s, 2H), 8.15 (s, 2H), 8.11 (s, 2H), 7.93 (s, 2H), 7.85 (s, 2H), 7.76 (s, 2H), 7.72 (s, 2H), 7.67 (s, 2H), 7.61–7.21 (m, 40H), 7.07–6.93 (m, 6H), 6.60 (d, *J* = 8.6 Hz, 4H), 6.55 (d, *J* = 7.5 Hz, 8H), 4.56 (s, 3H), 4.50 (s, 6H), 4.46 (s, 6H), 4.42 (s, 6H), 4.39 (s, 6H), 3.61 (s, 6H), 3.59 (s, 6H), 3.55 (s, 6H), 1.60 (s, 18H), 1.56 (s, 18H), 1.56 (s, 18H).

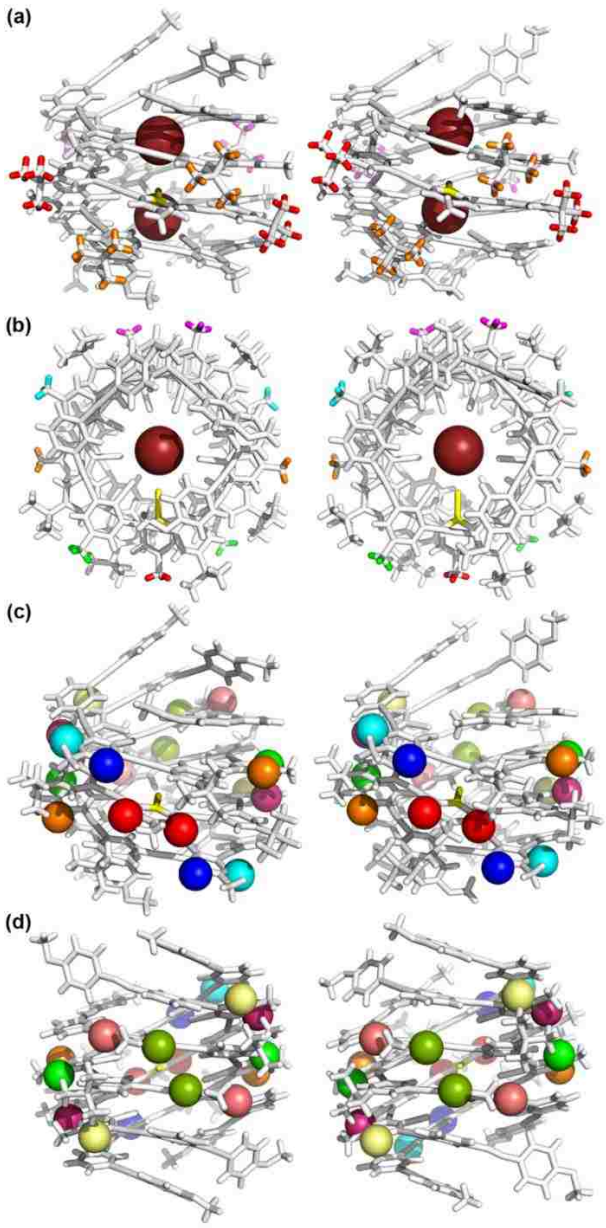

Figure 4.5 The molecular C_2 symmetry of **4** (scaffolding taken directly from the X-ray crystal structure). The left and right structures of each pair are related by a C_2 rotation along the CX bond of the non-bonding iodopyridinium (yellow sticks). Same-colored sticks/spheres of a given pair represent symmetrical hydrogens. (a) *tert*-Butyl hydrogens; (b) pyridinium-methyl hydrogens; (c–d) pyridinium hydrogens. **2** possesses the same molecular C_2 symmetry about the non-bonding iodopyridinium.

Addition of excess $AgPF_6$ resulted in complete recovery of **3** (Figure 4.6), demonstrating the switchability of the halogen-bond-induced self-assembly.

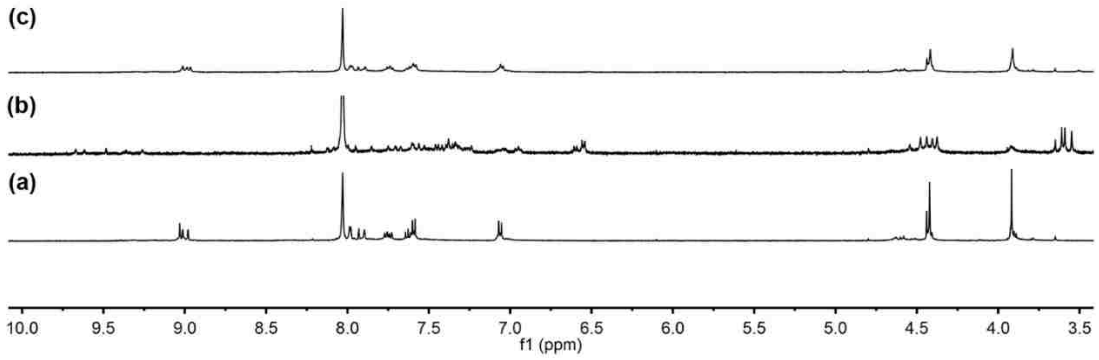

Figure 4.6 Partial ^{1}H NMR spectra of **3** and **4**. (a) Free ligand **3**; (b) same sample upon subsequently adding 10.4 ligand equiv of TBABr, resulting in the formation of **4** (intensity increased and DMF residual solvent peak cropped for clarity); (c) recovered free ligand **3** upon subsequently adding excess $AgPF_6$. (a–c) 500 MHz, 1:3 *v*/*v* DMF-d_7-CD_3CN.

A 1D selective transient nOe experiment (DPFGSE) corroborated the proximity of the pyridinium-methyl and *tert*-butyl extrachannel functionalities of **4** (Figure 4.7). The DPFGSE experiment—employed on account of the chemical instability of the iodopyridinium moieties of **4** (susceptible to slow S_NAr)—allowed for a shorter experiment time (6.5 h, 500 MHz, 1:3 *v*/*v* DMF-d_7-CD_3CN). The ^{1}H 1D NOESY acquisition parameters were the following: at = 2.045, d1 = 2.000, nt = 5000, sfrq = 499.803, pw = 9.600, mixN = 0.500. These NOE data were consistent with the solid-state structure of **4** but impossible for a single strand (over 7 Å apart, Figure 4.7g).

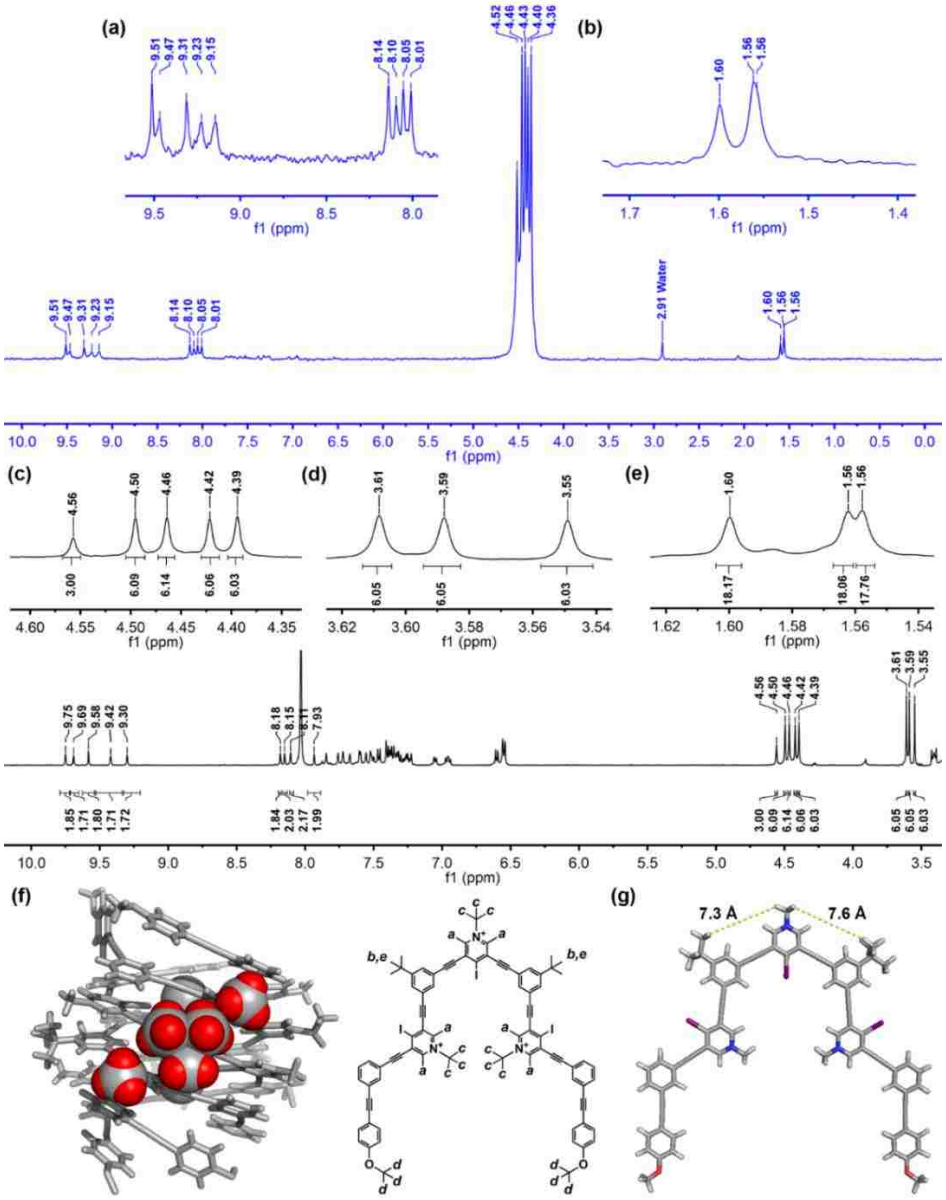

Figure 4.7 Partial ^{1}H 1D NOESY (blue, 500 ms mixing time, selective excitation of the pyridinium-methyl resonances) and ^{1}H NMR (black) spectra of **4**. (a) Nine pyridinium NOEs of equal intensity (see also ^{1}H NMR spectrum, bottom); (b) *tert*-butyl NOEs; (c) four pyridinium-methyl resonances of equal intensity and one of half intensity; (d) three methoxy-methyl resonances of equal intensity; (e) three *tert*-butyl resonances of equal intensity (two singlets are overlapping in 4.7b); (f) model of **4** illustrating the proximity of the *tert*-butyl and pyridinium-methyl protons (red); (g) model of a single ligand illustrating the long distances between the *tert*-butyl and pyridinium-methyl protons. (a–e) 500 MHz, 1:3 *v*/*v* DMF-d_7-CD_3CN. For comparison to **2**, see our previous report.

2D DOSY experiments were used to compare the r_Hs of both helicates in solution. First, a 2D DOSY experiment was conducted on **4** at 25 °C. The VnmrJ 4.2 software was used for acquisition (Gradient Compensated Stimulated Echo, DgcsteSL_cc, 400 MHz, 1:3 *v*/*v* DMF-d_7-CD_3CN) and data fitting. Due to its limited solubility, the maximum ligand concentration of **4** was roughly 1.0 mM ligand with three ligand equivalents of TBABr. Peaks of low amplitude generally did not fit well to the Stejskal-Tanner equation and were excluded from analysis. A standard error greater than 0.2 led to the rejection of a given fit. The same experiment was conducted on **2** (1.0 mM ligand with three ligand equivalents of I^-, 25 °C). The 2D DOSY acquisition parameters were the following: d1 = 6.500, nt = 32, sfrq = 399.760, pw = 6.600. The total experiment time was 3.1 h. Line broadening (3.0 Hz) was applied and the spectra were baseline corrected before full DOSY calculation. Each calculated D_t was normalized to that of the residual CH_3CN. Mean D_ts and normalized-mean D_ts were calculated for **4** and **2**. Ratios of D_ts afforded r_Hs ratios, which were used to compare the relative sizes of the triple helicates in solution. Unremarkably, this r_H ratio was 1.0(1), confirming the comparable size of **4** relative to **2** (Figures 4.51–4.52 and Tables 4.18–4.21).

As mentioned earlier, the iodopyridinium functional groups were not indefinitely stable; however, the helical conformation of the ligands afforded some protection as expected. To ascertain the approximate window of stability for the iodononameric *m*-arylene-ethynylene ligands in the presence of Br^-, we first prepared a solution of **1** (5.0 mM ligand, 1:3 *v*/*v* DMF-d_7-CD_3CN). 0.3 ligand equiv of TBAI were added, and the reaction mixture was allowed to sit for 18 h at RT. Subsequently, excess anhydrous $AgPF_6$ was added directly to the NMR tube, precipitating all halide ions from solution. A

^{1}H NMR spectrum was acquired to characterize the non-helical bromo- and iodopyridinium protons (Figure 4.8). With these data in hand, we prepared **4** (1.4 mM ligand with 4.1 ligand equiv of TBABr, 1:3 *v*/*v* DMF-d_7-CD_3CN). The Br^- triple helicate was allowed to sit for 3 h at RT. Subsequently, excess anhydrous $AgPF_6$ was added directly to the NMR tube, precipitating all halide ions from solution. A ^{1}H NMR spectrum was acquired, and the halopyridinium peaks of interest were integrated to assess the degree of bromination. After 3 h at RT, only 7 % bromination was observed, demonstrating the stabilizing effect of the triple-helical conformation (Figure 4.9).

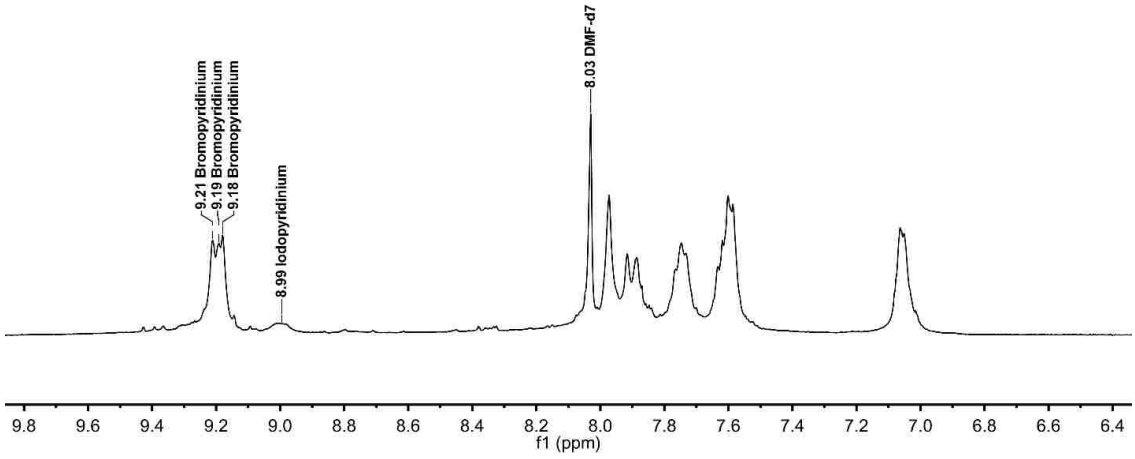

Figure 4.8 Partial ^{1}H NMR spectrum of **1** and some iodinated ligand (500 MHz, 1:3 *v*/*v* DMF-d_7-CD_3CN).

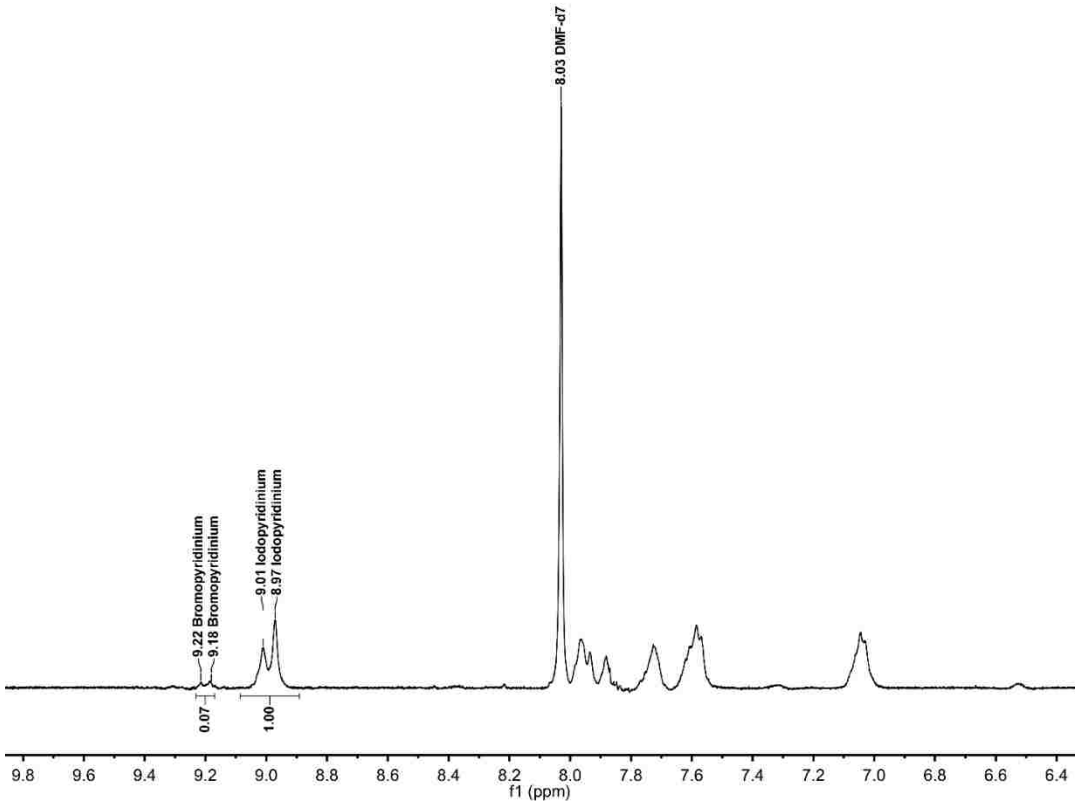

Figure 4.9 ^{1}H NMR spectrum of **3** and some brominated ligand (500 MHz, 1:3 *v*/*v* DMF-d_7-CD_3CN).

4.3.5 Thermodynamic Stability of the Triple Helicates

Quantification of ligands in the triple-helical vs. lower-order conformations was possible due to slow-exchanging and resolved sets of methoxy-methyl resonances (Figures 4.10–4.15). **2** with addition of TBAI/Br was used in all studies (400 MHz, 298 K, 1:3 *v*/*v* DMF-d_7-CD_3CN, 1.0 mM ligand). Triplicate ^{1}H qNMR spectra were acquired for the following solutions: (1) **2** with three ligand equivalents of TBAI (six overall ligand equivalents of I^-); (2) **2** with three ligand equivalents of TBABr (three ligand equivalents each of I^- and Br^-). The ^{1}H qNMR acquisition parameters were the following:

at = 5.000, nt = 500, pw = 6.625. The total relaxation delay (at + d1) was set to be greater than five times the largest methoxy-methyl T_1. Inversion recovery experiments (VnmrJ 4.2, T_1 Measurement) under the same conditions (400 MHz, 298 K, 1:3 *v*/*v* DMF-d_7-CD_3CN, 1.0 mM ligand with three ligand equivalents of TBAI/Br) were used to ascertain the T_1s of all methoxy-methyl resonances (in both helical and lower-order states). See Section 4.4.3 for all inversion-recovery data. These data were zero filled (fn = np × 2) and drift corrected, and line broadening was applied (0.2 Hz). The spectra were manually phased and baseline corrected. The methoxy-methyl signals in the triple-helical state were integrated and normalized to 100.00, and the lower-order methoxy-methyl resonances were also integrated. Mean values of the fractions of ligands in the helical state were calculated, and *P* values were calculated with a *t*-test. At RT, 65(1) % of the ligands formed triple helicates in the presence of only I^- (1.0 mM ligand with six ligand equivalents of I^-; see Figures 4.10–4.12).

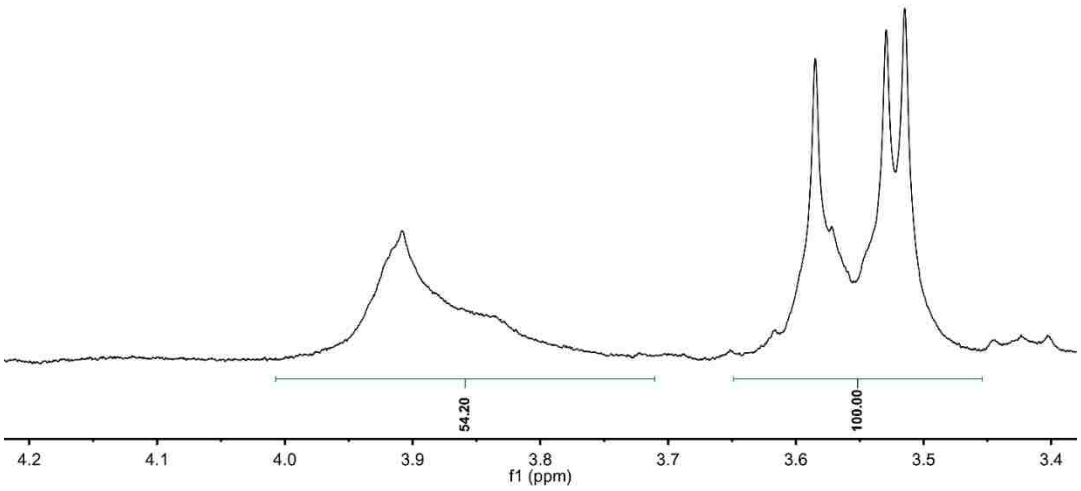

Figure 4.10 Partial ^{1}H NMR spectrum of **2** with three ligand equivalents of TBAI, replicate 1 (400 MHz, 298 K, 1:3 *v*/*v* DMF-d_7-CD_3CN).

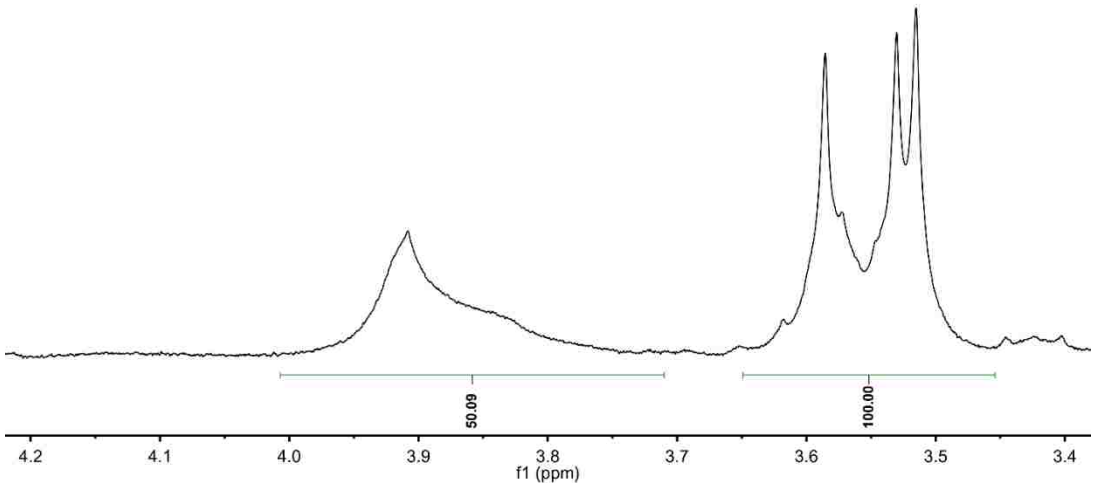

Figure 4.11 Partial ^{1}H NMR spectrum of **2** with three ligand equivalents of TBAI, replicate 2 (400 MHz, 298 K, 1:3 *v*/*v* DMF-d_7-CD_3CN).

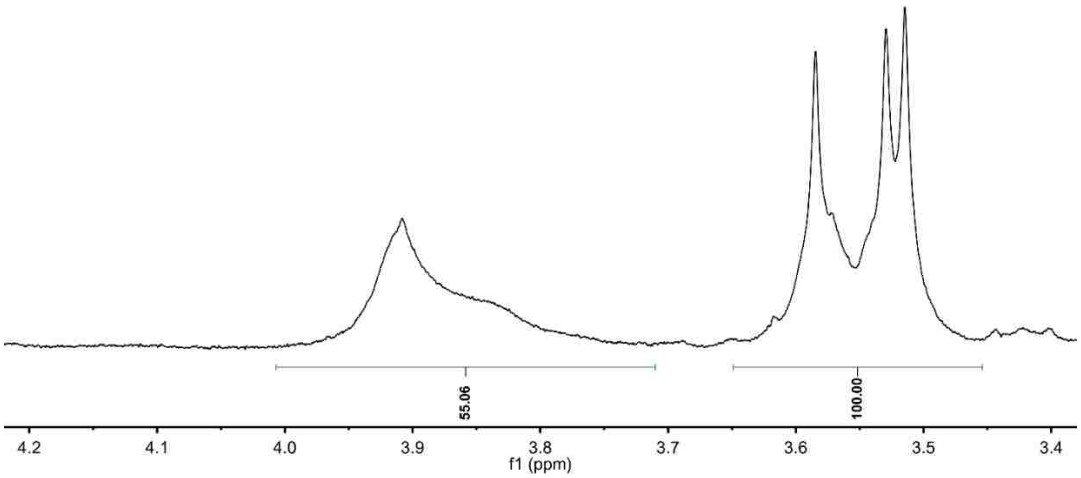

Figure 4.12 Partial ^{1}H NMR spectrum of **2** with three ligand equivalents of TBAI, replicate 3 (400 MHz, 298 K, 1:3 *v*/*v* DMF-d_7-CD_3CN).

We investigated the thermodynamic impact of adding TBABr to **2** (1.0 mM ligand with three ligand equivalents each of I^- and Br^-) due to the formation of fine precipitates

during the preparation of **4**. The resulting hybrid helicate that dynamically housed both halide ions (vide infra) was slightly more stable: 68(2) % of the ligands were triple helical (see Figures 4.13–4.15 and Table 4.1). In contrast, Cl^- failed to induce high-fidelity self-assembly (Figure 4.2c). The trend in thermodynamic stability—$Br^- \approx I^- >> Cl^-$—is unsurprising given the similar solid-state structures of **4** and **2**. Moreover, we have seen size selectivity for large halide ions in our previous work with iodopyridinium-ethynylene receptors.[142]

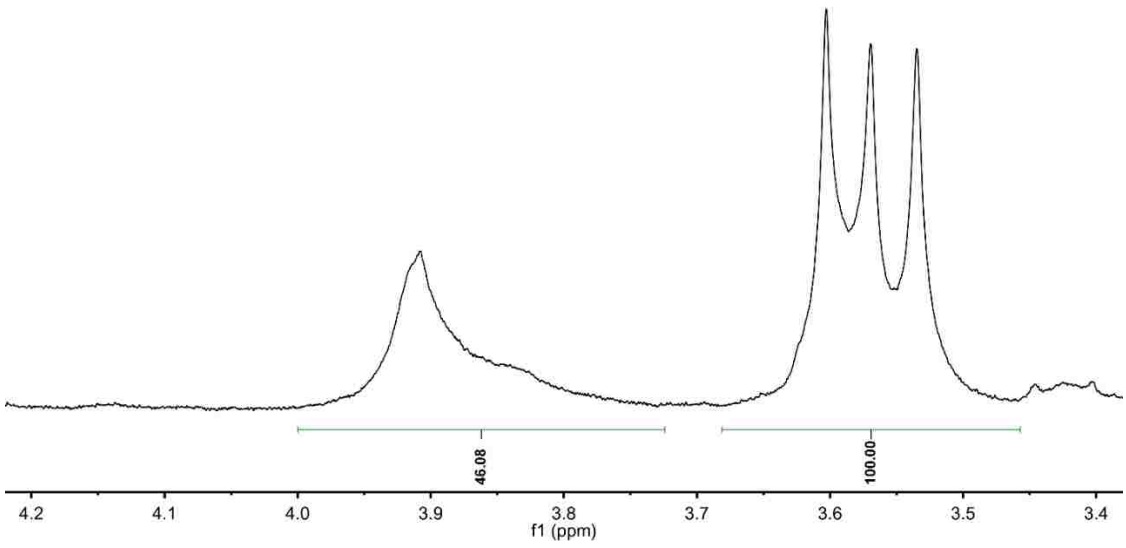

Figure 4.13 Partial ^{1}H NMR spectrum of **2** with three ligand equivalents of TBABr, replicate 1 (400 MHz, 298 K, 1:3 *v*/*v* DMF-d_7-CD_3CN).

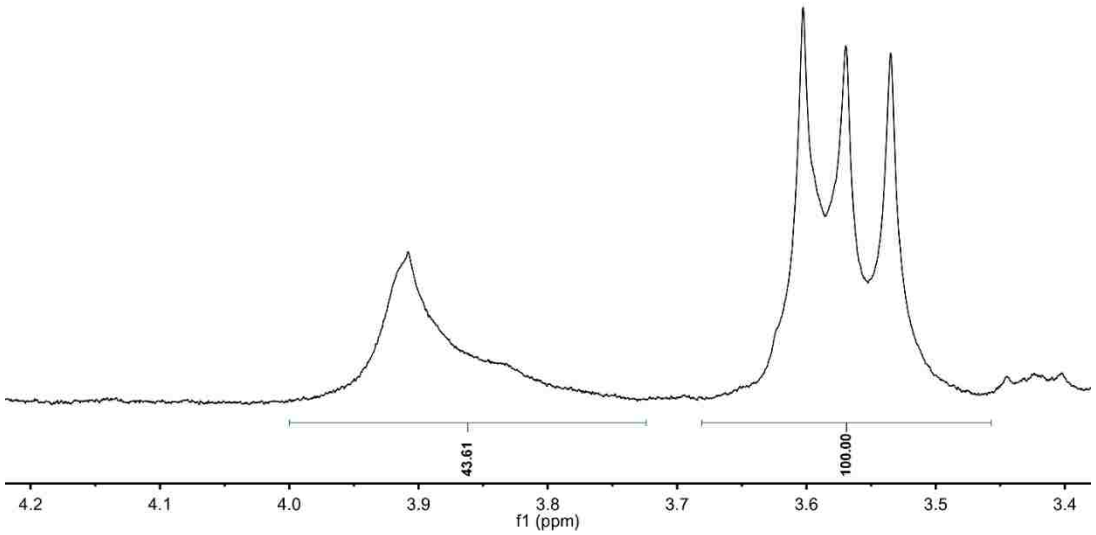

Figure 4.14 Partial ^{1}H NMR spectrum of **2** with three ligand equivalents of TBABr, replicate 2 (400 MHz, 298 K, 1:3 *v*/*v* DMF-d_7-CD_3CN).

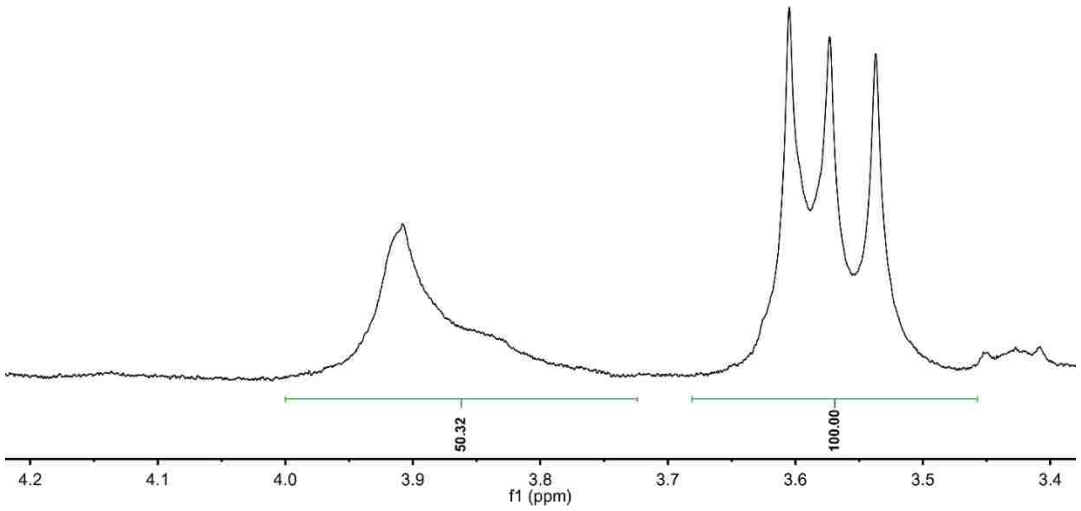

Figure 4.15 Partial ^{1}H NMR spectrum of **2** with three ligand equivalents of TBABr, replicate 3 (400 MHz, 298 K, 1:3 *v*/*v* DMF-d_7-CD_3CN).

Table 4.1 *t*-Test for two qNMR means of the fractions of triple-helical *m*-arylene-ethynylene ligands—**2** with three ligand equivalents of TBAI vs. **2** with three ligand equivalents of TBABr (400 MHz, 298 K, 1:3 *v*/*v* DMF-d_7-CD_3CN).

	2 + TBAI	**2 + TBABr**
Mean	0.65	0.68
Variance	0.0001	0.0002
Observations	3	3
Hypothesized Mean Difference	0	
P(T<=*t*) one-tail	0.012	
P(T<=*t*) two-tail	0.024	

4.3.6 Kinetic Analysis and Mechanism of Ligand Exchange

To probe the equilibrium dynamics of the *m*-arylene-ethynylene ligands, we subjected **2** to a series of variable-temperature ^{1}H 2D EXSY NMR experiments. An overall two-state equilibrium was evidenced by the two sets of methoxy-methyl resonances—corresponding to free ligand and/or lower-order speciation (Figure 4.16a, m_A; see Figures 4.51–4.52 and Tables 4.18–4.21 for 2D DOSY data) and the triple helicate (Figure 4.16a, m_B). The m_B singlets of **2** were shifted upfield as a result of ring shielding effects from the π-stacked *m*-arylene-ethynylene ligands.[50] Slow chemical exchange (confirmed by ^{1}H 2D ROESY NMR, Figures 4.17–4.19) allowed for the integration of cross peaks m_A–m_B and m_B–m_A along with their same-phase diagonal peaks (Figure 4.16a).

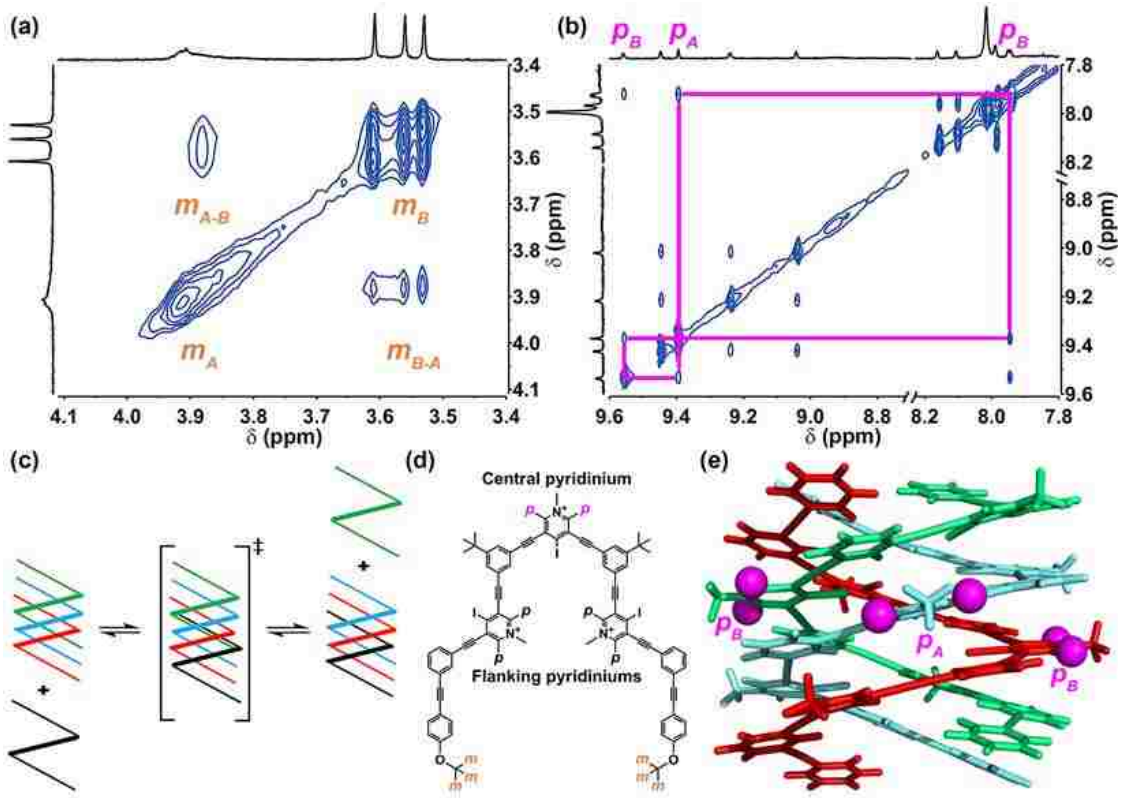

Figure 4.16 (a–b) Partial ^{1}H 2D NOESY NMR spectra of **2** (500 MHz, 333 K, 1:3 *v*/*v* DMF-d_7-CD_3CN, 300 ms mixing time); (c) proposed ligand-queuing exchange mechanism; (d) iodononameric *m*-arylene-ethynylene ligand with pyridinium (*p*) and methoxy-methyl (*m*) protons demarcated; (e) model of triple helicate with labeled central pyridiniums on the middle (p_A) and terminal (p_B) strands (anions and some functional groups not shown for clarity).

^{1}H 2D ROESY NMR experiments were conducted on **2** at 25 and 40 °C to confirm that the cross peaks of interest arose from chemical exchange (500 MHz, 1:3 *v*/*v* DMF-d_7-CD_3CN, 1.0 mM ligand; Figures 4.17–4.19). At RT, no appreciable pyridinium cross peaks were observed. At 60 °C, the intensity of the NOE cross peaks were low while EXSY cross peaks were amplified, eliminating the need for a ROESY experiment. The

^{1}H 2D ROESY acquisition parameters were the following: at = 0.406, np = 4096, nt = 16, ni = 256, sfrq = 499.803, pw = 9.950, mixR = 0.200.

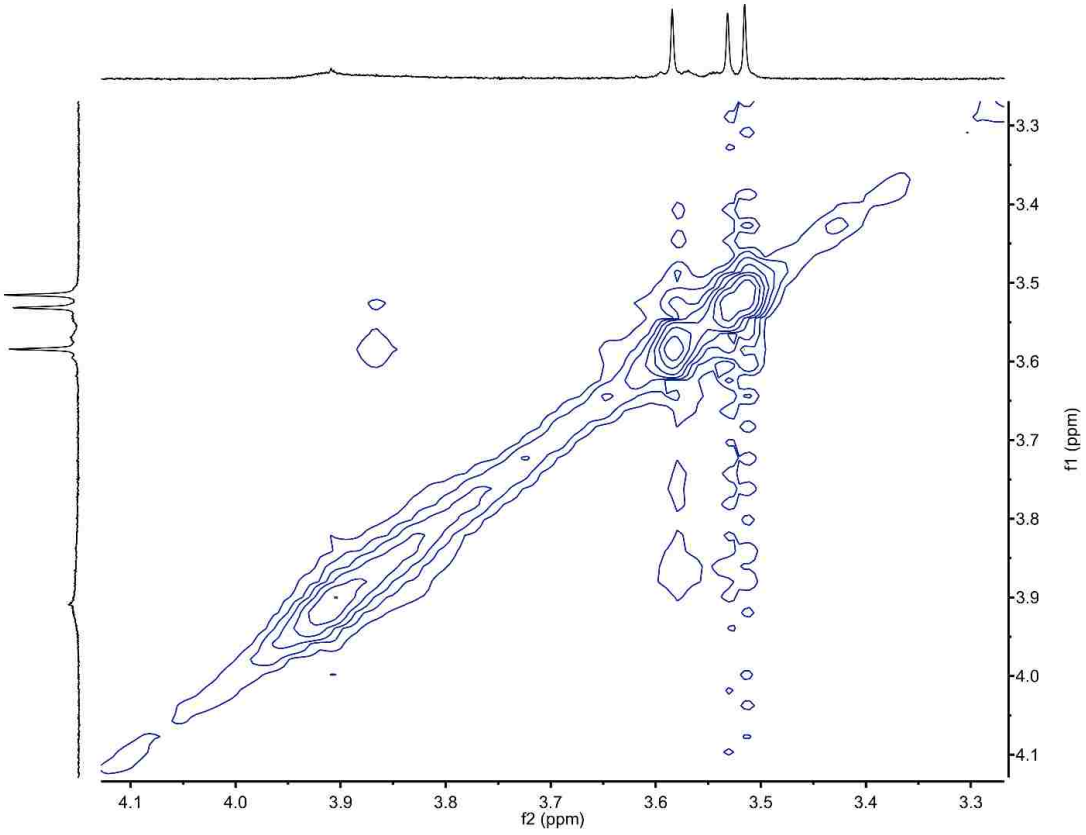

Figure 4.17 Partial ^{1}H 2D ROESY NMR spectrum of **2** (500 MHz, 298 K, 1:3 *v*/*v* DMF-d_7-CD_3CN, 1.0 mM ligand). Same-phase methoxy-methyl diagonal and cross peaks were observed.

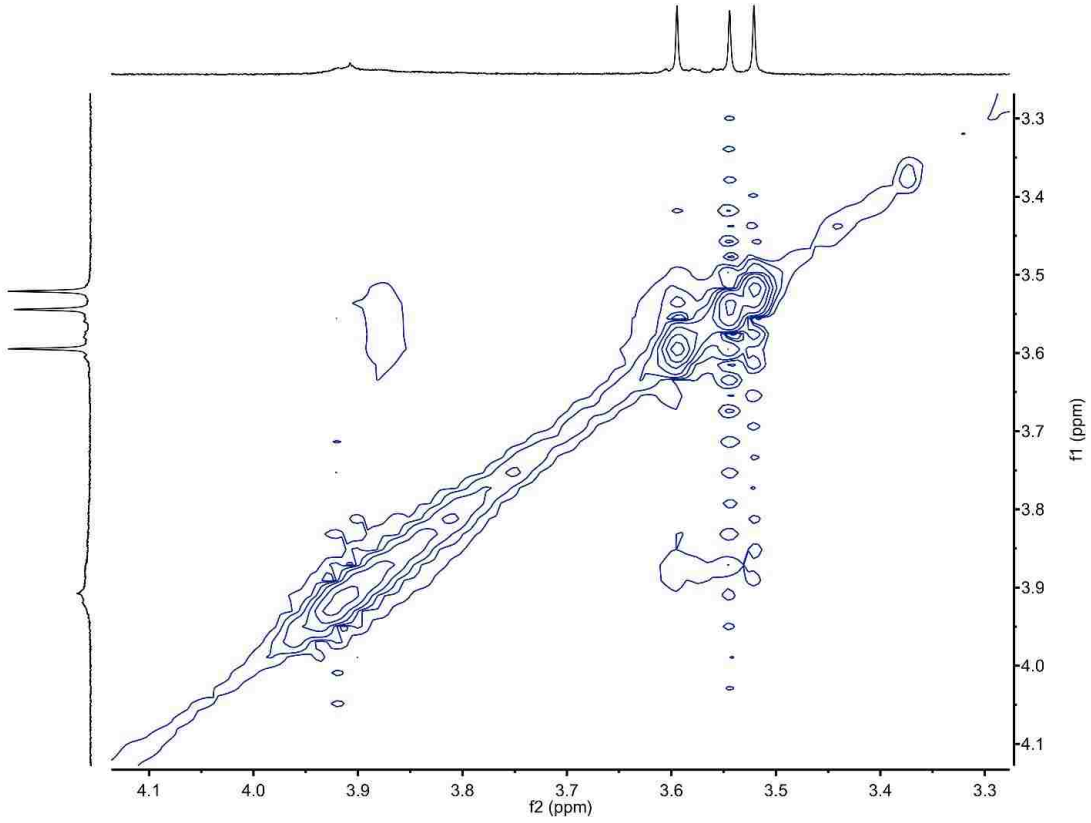

Figure 4.18 Partial ^{1}H 2D ROESY NMR spectrum of **2** (500 MHz, 313 K, 1:3 *v*/*v* DMF-d_7-CD_3CN, 1.0 mM ligand). Same-phase methoxy-methyl diagonal and cross peaks were observed.

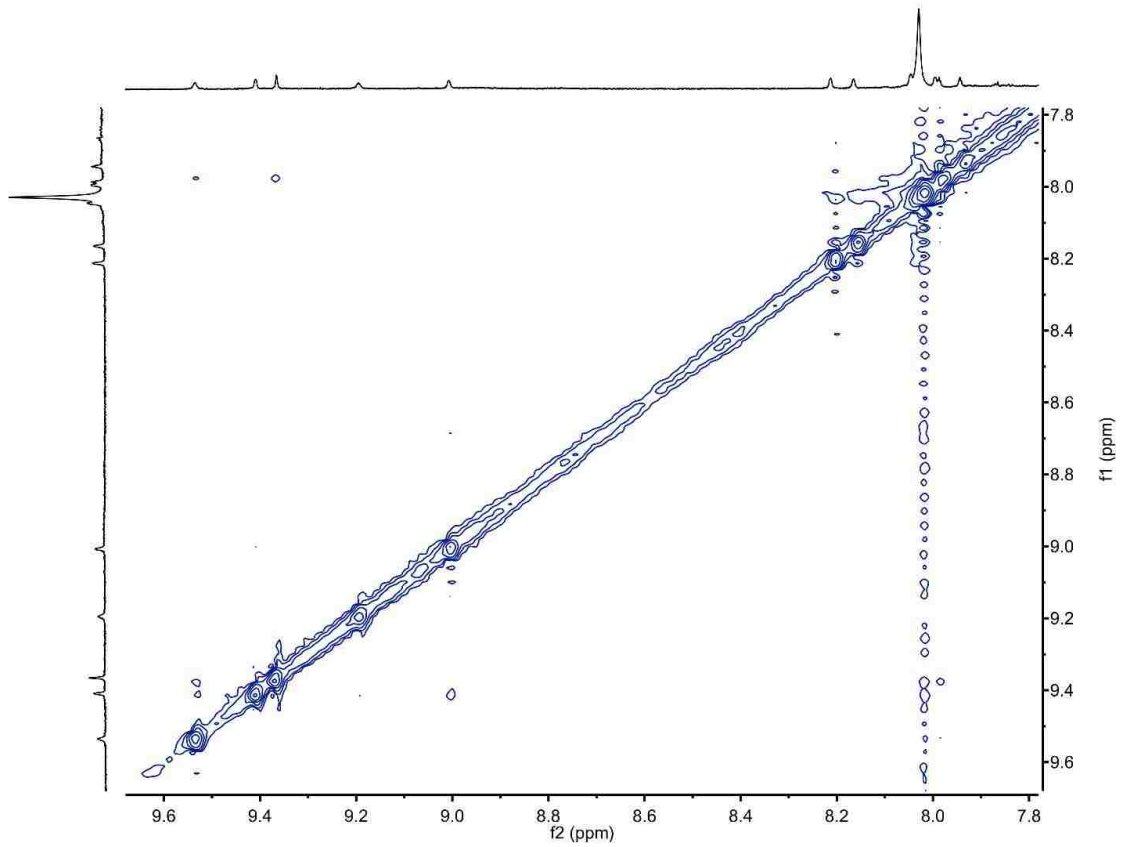

Figure 4.19 Partial ^{1}H 2D ROESY NMR spectrum of **2** (500 MHz, 313 K, 1:3 *v*/*v* DMF-d_7-CD_3CN, 1.0 mM ligand). Same-phase pyridinium diagonal and cross peaks were observed.

With the knowledge that the cross peaks in question arose from chemical exchange, ^{1}H 2D EXSY experiments were conducted. These EXSY experiment consisted of two 2D NOESY NMR experiments—one with a mixing time of 0 ms and the other 300 ms (unless otherwise specified)—performed on **2** at 25, 40, and 60 °C (500 MHz, 1:3 *v*/*v* DMF-d_7-CD_3CN, 1.0 mM ligand). The ^{1}H 2D NOESY acquisition parameters were the following: at = 0.410, np = 4096, nt = 16, ni = 256, sfrq = 499.803, pw = 10.100. The total relaxation delay for each experiment (at + d1 + mixN) was set to be comparable to three times the average methoxy-methyl T_1. Experiment times varied but ran up to 18 h

each. Using the VnmrJ 4.2 software, the data were zero filled (fn = np x 2, F2 dimension), drift corrected, and manually phased in both dimensions. Gaussian interactive weighting was used to remove sinc wiggles. The data were imported into MestReNova 8.1.2-11880, and a baseline correction was applied to both dimensions. The diagonal methoxy-methyl peaks in the helical state were normalized to 1000.00, and the remaining methoxy-methyl diagonal and cross peaks were also integrated. Peak volumes were used to calculate nucleus lifetimes. The 2D spectra were further phased in both dimensions in MestReNova 8.1.2-11880, and the most upfield integrated pyridinium diagonal peak was normalized to 1000.00. Non-overlapping pyridinium diagonal and cross peaks were integrated and used to calculate nucleus lifetimes. All peak volumes in question were inputted into EXSYCalc 1.0 (Mestrelab Research),[169] which calculates forward and reverse individual magnetization exchange rate constants (related to the reaction rate constants) of a two-state chemical exchange equilibrium:

$$A \underset{k_{-1}}{\overset{k_1}{\rightleftharpoons}} B \tag{4.1}$$

$$k_{ex} = k_1 + k_{-1} \tag{4.2}$$

Ligand lifetimes (averaged from the entire population) of a given state were calculated from the individual rate constants:

$$\tau_A = \frac{1}{k_1} \; and \; \tau_B = \frac{1}{k_{-1}} \tag{4.3}$$

For the m_A–m_B equilibrium (Figure 4.16a), τ_A is the average lifetime of a ligand as a lower-order species (m_A), while τ_B is the overall average lifetime of a ligand in the helical state (m_B). With regard to ligand positional exchange in Figure 4.16b–c,e, subscripts *A* and *B* were assigned to the middle- and terminal-strand central pyridinium protons, respectively. With regard to the other positional exchanges in this section, *A* and *B* were assigned arbitrarily. EXSYCalc 1.0 utilizes full relaxation matrix analysis with an estimated error of 10 %. Activation energies of ligand exchange ($\Delta G^{\ddagger}$) were calculated using the Eyring-Polanyi equation:

$$k = \frac{k_b T}{h} e^{-\frac{\Delta G^{\ddagger}}{RT}} \tag{4.4}$$

To maximize the accuracy of peak integrations during ^{1}H 2D EXSY NMR data processing, we performed inversion recovery experiments (VnmrJ 4.2, T_1 Measurement) on **2** at 25, 40, and 60 °C (500 MHz, 1:3 *v*/*v* DMF-d_7-CD_3CN, 1.0 mM ligand). T_1 values of all methoxy-methyl resonances (in both the helical and lower-order states) and for the downfield pyridinium resonances (when observable) were obtained. In the case of the methoxy-methyl protons, rates of spin-lattice relaxation decreased with increasing temperature—indicating that the complex was on the negative-slope side of the rotational correlation and spin lattice relaxation curve.

All EXSY data were inputted into EXSYCalc 1.0, and nuclear spin-state lifetimes were calculated. At RT, the helical-state lifetime was extremely long and outside the ideal range of 2D EXSY NMR (Figures 4.20–4.21; Table 4.2).[170] Additionally, no appreciable pyridinium exchange cross peaks were observed due to their low intensities and overall slow exchange at RT.

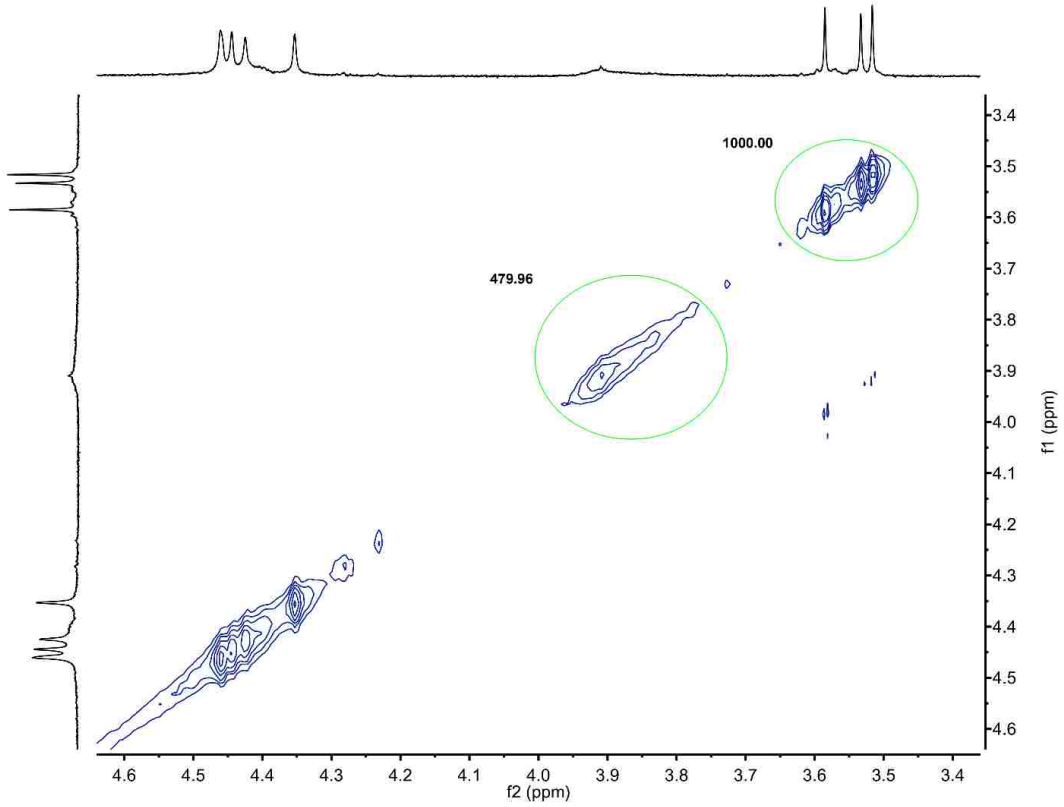

Figure 4.20 Partial ^{1}H 2D NOESY NMR spectrum of **2** (500 MHz, 298 K, 1:3 *v*/*v* DMF-d_7-CD_3CN, 0 ms mixing time, 1.0 mM ligand). Methoxy-methyl diagonal peaks were integrated.

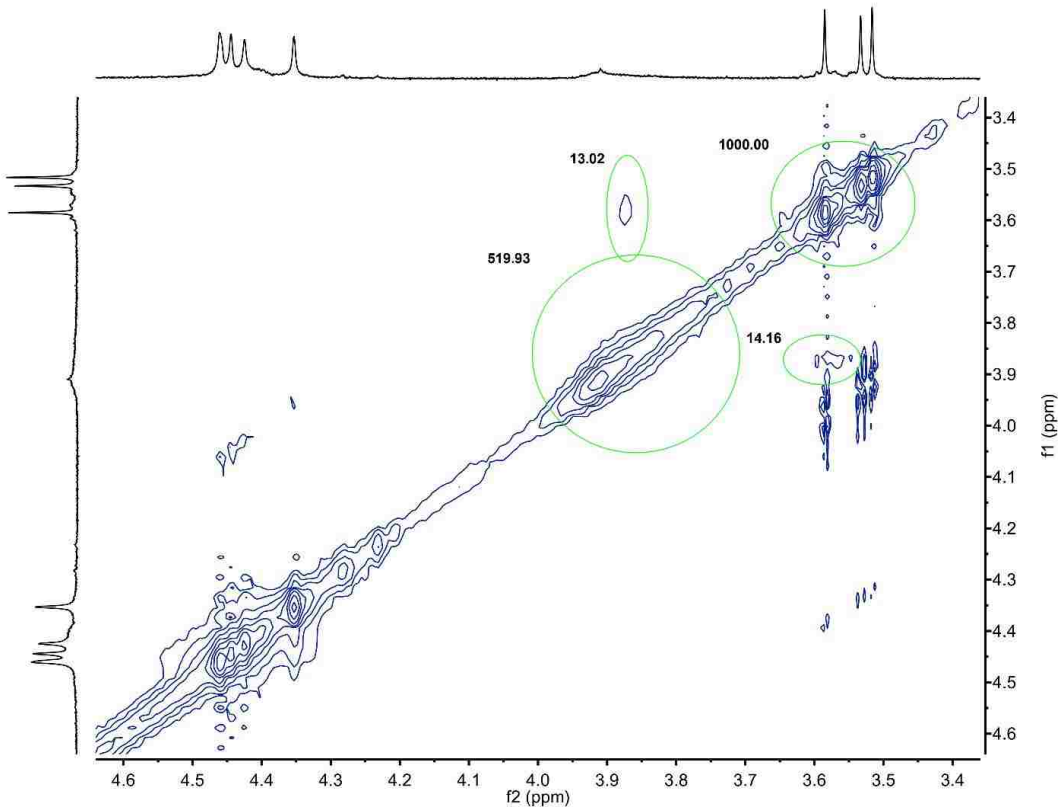

Figure 4.21 Partial ^{1}H 2D NOESY NMR spectrum of **2** (500 MHz, 298 K, 1:3 *v*/*v* DMF-d_7-CD_3CN, 300 ms mixing time, 1.0 mM ligand). Methoxy-methyl diagonal and cross peaks were integrated.

Table 4.2 Calculated rate constants and lifetime based on methoxy-methyl diagonal- and cross-peak integrations (**2**, 500 MHz, 298 K, 1:3 *v*/*v* DMF-d_7-CD_3CN, 1.0 mM ligand).

k_1 (s^{-1})	k_{-1} (s^{-1})	k_{ex} (s^{-1})	τ_B (s)	$1/T_1$	Ideal?
0.094	0.042	0.136	23.8	0.807	FALSE
$\Delta G^{\ddagger}_1$ (kcal•mol^{-1})	$\Delta G^{\ddagger}_{-1}$ (kcal•mol^{-1})	Temp (°C)			
18.9	19.3	25			

Repeating the experiment at 40 °C failed to shorten the lifetime sufficiently (Figures 4.22–4.23; Table 4.3).

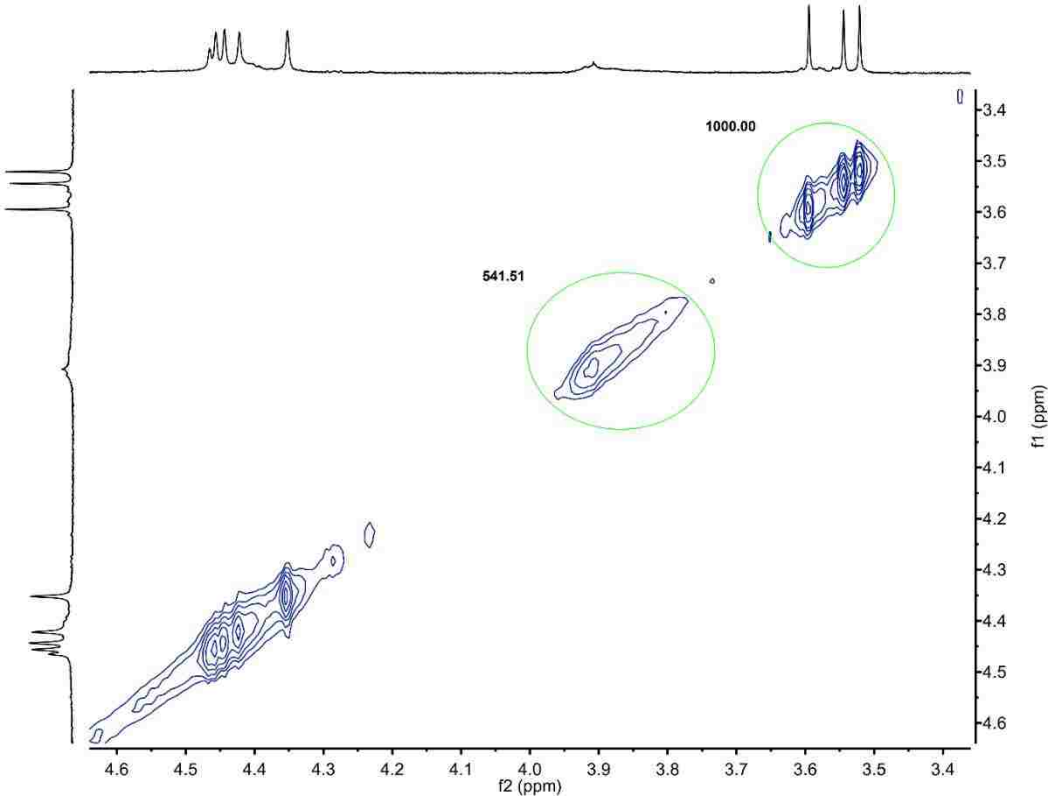

Figure 4.22 Partial ^{1}H 2D NOESY NMR spectrum of **2** (500 MHz, 313 K, 1:3 *v*/*v* DMF-d_7-CD_3CN, 0 ms mixing time, 1.0 mM ligand). Methoxy-methyl diagonal peaks were integrated.

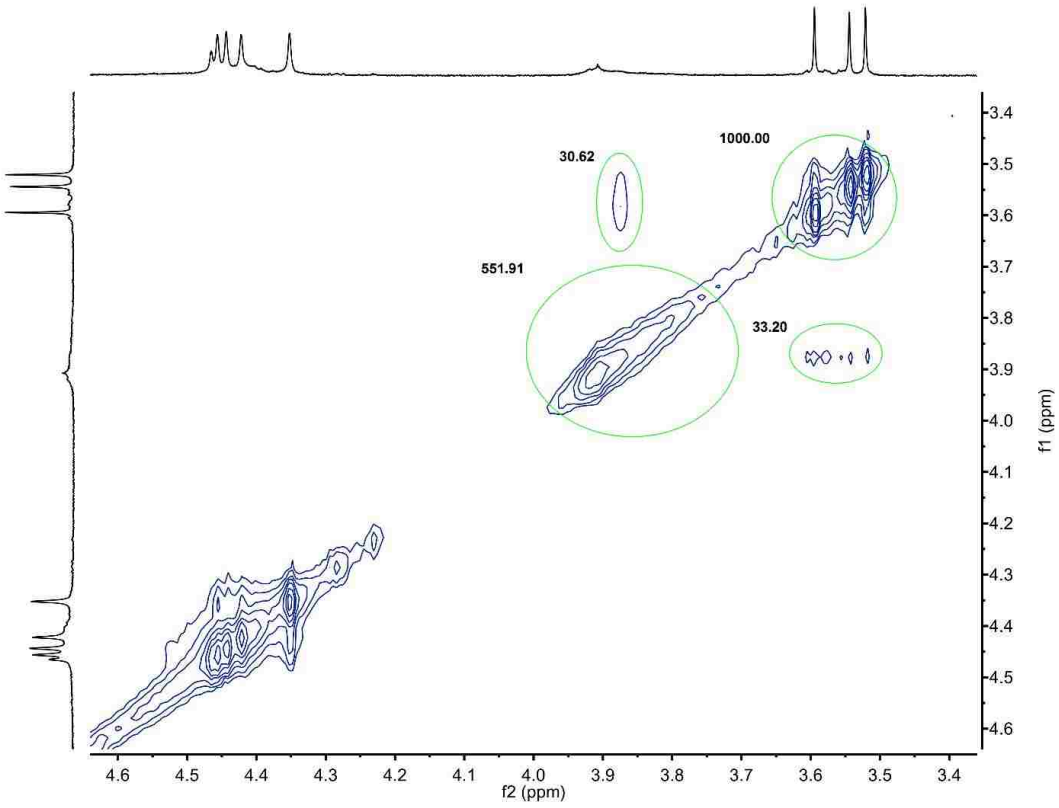

Figure 4.23 Partial ^{1}H 2D NOESY NMR spectrum of **2** (500 MHz, 313 K, 1:3 *v*/*v* DMF-d_7-CD_3CN, 300 ms mixing time, 1.0 mM ligand). Methoxy-methyl diagonal and cross peaks were integrated.

Table 4.3 Calculated rate constants and lifetime based on methoxy-methyl diagonal- and cross-peak integrations (**2**, 500 MHz, 313 K, 1:3 *v*/*v* DMF-d_7-CD_3CN, 1.0 mM ligand).

k_1 (s^{-1})	k_{-1} (s^{-1})	k_{ex} (s^{-1})	τ_B (s)	$1/T_1$	Ideal?
0.203	0.101	0.304	9.9	0.691	FALSE
$\Delta G^{\ddagger}_1$ (kcal•mol^{-1})	$\Delta G^{\ddagger}_{-1}$ (kcal•mol^{-1})	Temp (°C)			
19.4	19.8	40			

However, one set of pyridinium exchange cross peaks was observed, which allowed for the estimation of its corresponding nuclear spin-state lifetime (Figures 4.24–4.25; Table 4.5).

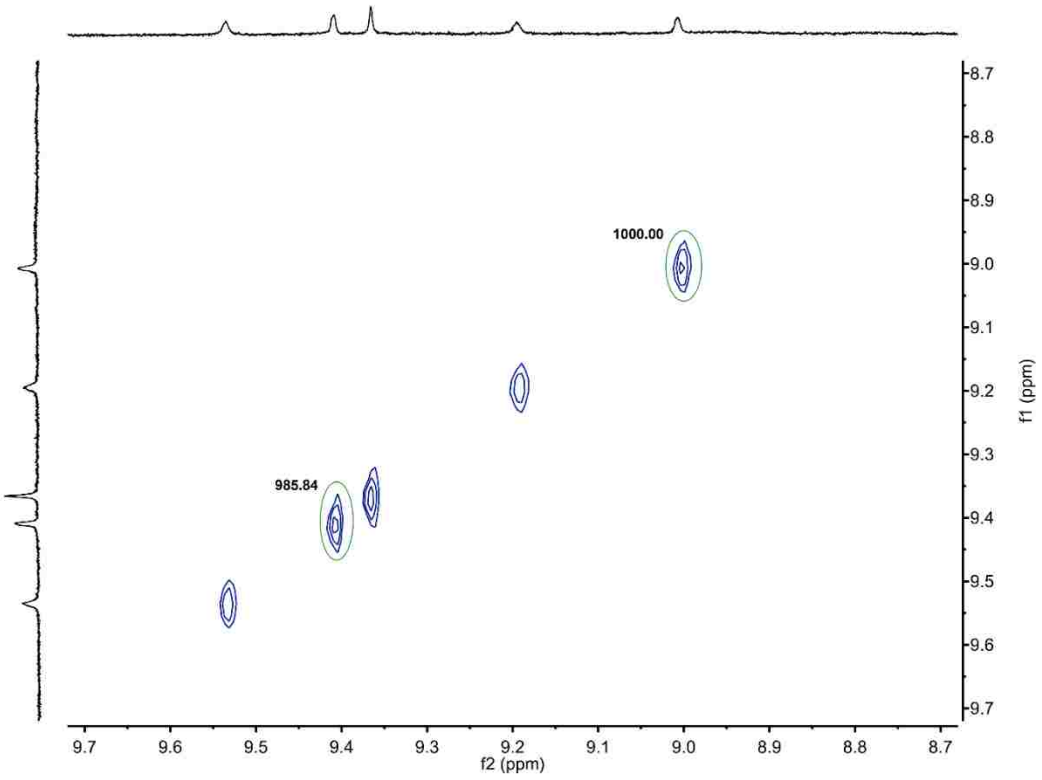

Figure 4.24 Partial ^{1}H 2D NOESY NMR spectrum of **2** (500 MHz, 313 K, 1:3 *v*/*v* DMF-d_7-CD_3CN, 0 ms mixing time, 1.0 mM ligand). Pyridinium diagonal peaks were integrated.

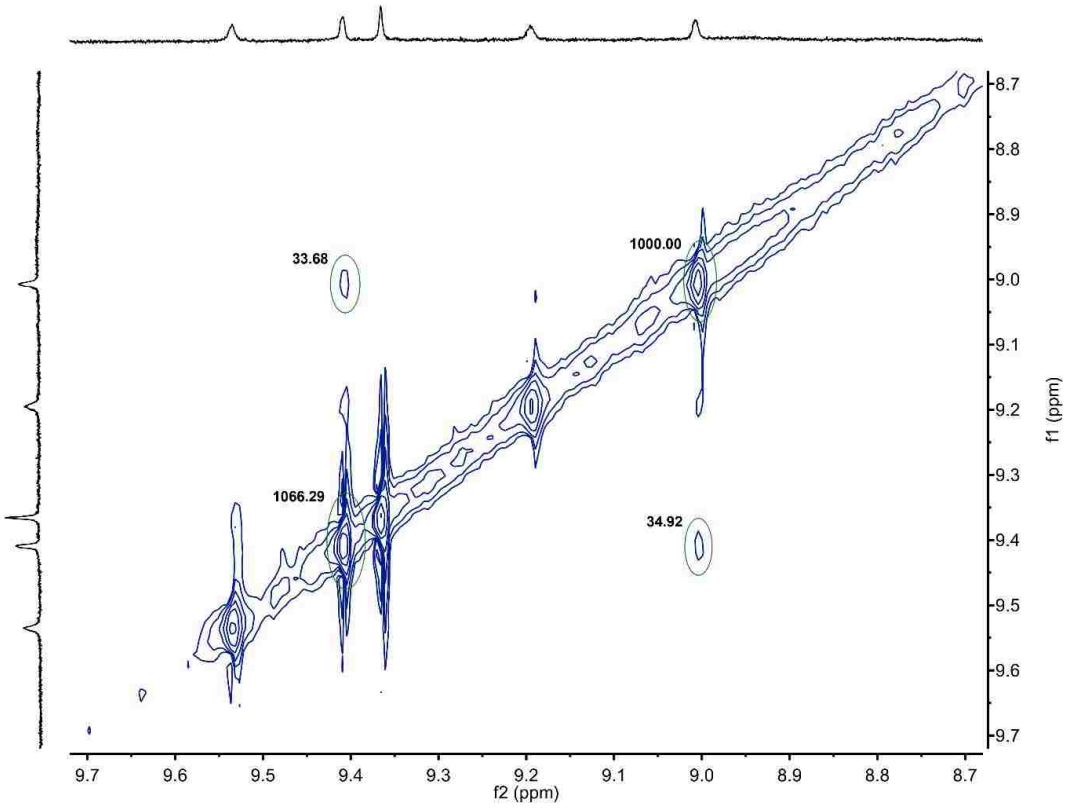

Figure 4.25 Partial ^{1}H 2D NOESY NMR spectrum of **2** (500 MHz, 313 K, 1:3 *v*/*v* DMF-d_7-CD_3CN, 300 ms mixing time, 1.0 mM ligand). Pyridinium diagonal and cross peaks were integrated.

Table 4.4 Calculated rate constants and lifetimes based on pyridinium diagonal- and cross-peak integrations (**2**, 500 MHz, 313 K, 1:3 *v*/*v* DMF-d_7-CD_3CN, 1.0 mM ligand).

k_1 (s^{-1})	k_{-1} (s^{-1})	k_{ex} (s^{-1})	τ_A (s)	τ_B (s)	$1/T_1$	Ideal?
0.114	0.108	0.222	8.8	9.3	0.500	FALSE
$\Delta G^{\ddagger}_1$ (kcal•mol^{-1})	$\Delta G^{\ddagger}_{-1}$ (kcal•mol^{-1})	Temp (°C)				
19.7	19.7	40				

Finally, at 60 °C, the lifetime of the ligands was still protracted and on the order of seconds (Figures 4.26–4.27; Table 4.5). For quantitative 2D EXSY, k_{ex} should ideally be greater than or equal to $1/T_1$, where T_1 is the smallest spin-lattice relaxation constant of interest.[12] Given this requirement, the most accurate lifetime estimates were extracted from the NOESY data acquired at 60 °C.

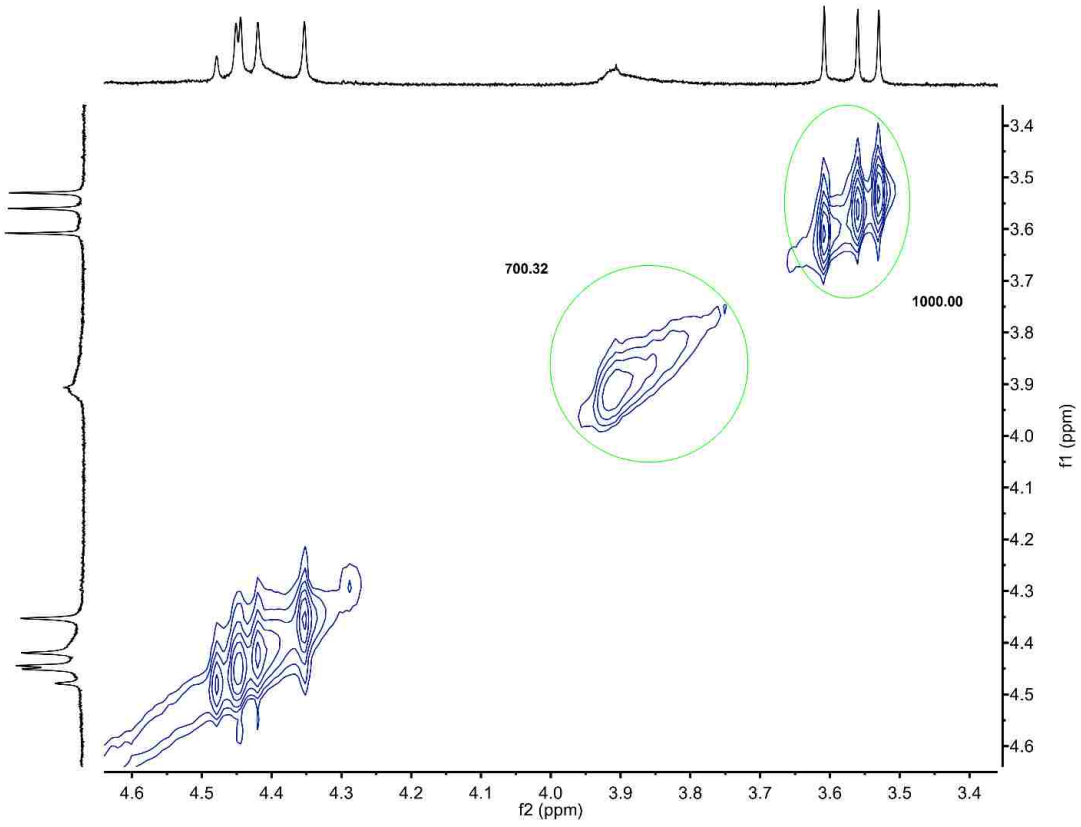

Figure 4.26 Partial ^{1}H 2D NOESY NMR spectrum of **2** (500 MHz, 333 K, 1:3 *v*/*v* DMF-d_7-CD_3CN, 0 ms mixing time, 1.0 mM ligand). Methoxy-methyl diagonal peaks were integrated.

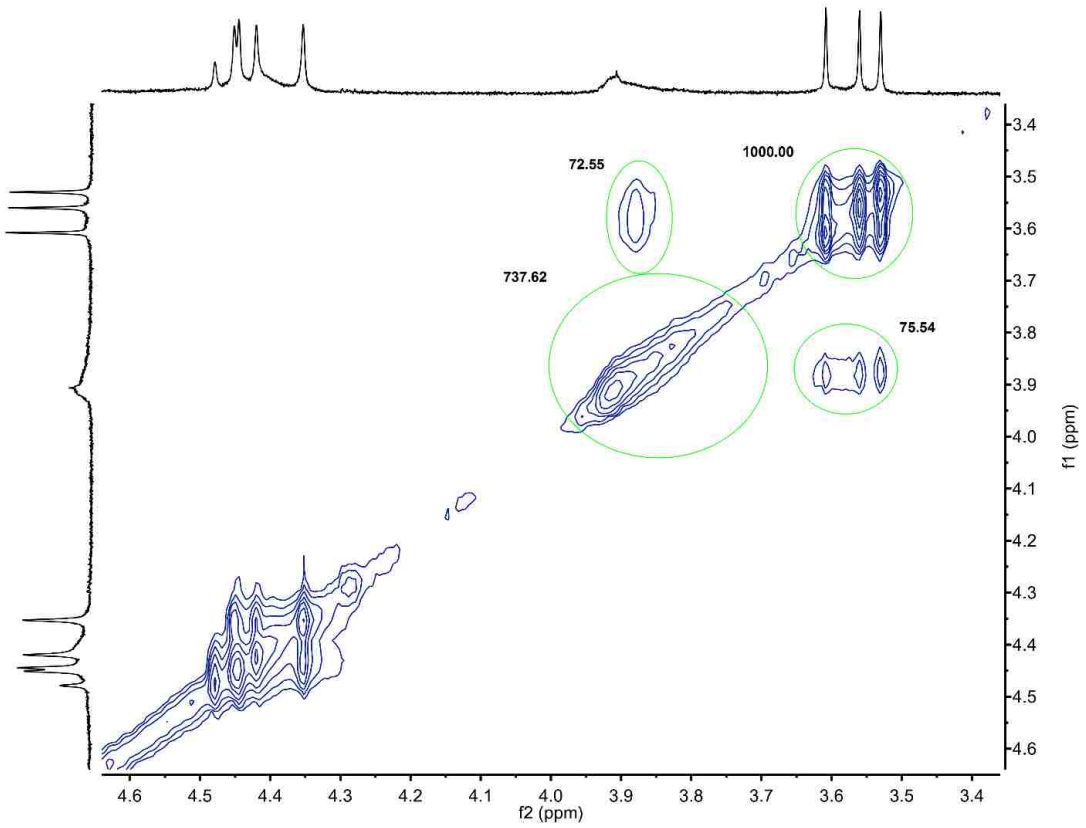

Figure 4.27 Partial ^{1}H 2D NOESY NMR spectrum of **2** (500 MHz, 333 K, 1:3 *v*/*v* DMF-d_7-CD_3CN, 300 ms mixing time, 1.0 mM ligand). Methoxy-methyl diagonal and cross peaks were integrated.

Table 4.5 Calculated rate constants and lifetime based on methoxy-methyl diagonal- and cross-peak integrations (**2**, 500 MHz, 333 K, 1:3 *v*/*v* DMF-d_7-CD_3CN, 1.0 mM ligand).

k_1 (s^{-1})	k_{-1} (s^{-1})	k_{ex} (s^{-1})	τ_B (s)	$1/T_1$	Ideal?
0.351	0.236	0.587	4.2	0.536	TRUE
$\Delta G^{\ddagger}_1$ (kcal•mol^{-1})	$\Delta G^{\ddagger}_{-1}$ (kcal•mol^{-1})	Temp (°C)			
20.3	20.5	60			

At 60 °C, examination of the pyridinium EXSY cross peaks of **2** (Figure 4.16b) resulted in comparable lifetimes to those extracted from the methoxy-methyl data at the same temperature (Figures 4.28–4.29; Table 4.6–4.10). These pyridinium exchange cross peaks arose on account of a ligand's transient position within a triplex (i.e. middle or terminal, Figure 4.16c,e). The slightly longer m_B lifetime vs. the lifetime of a single ligand position is sensible. Conceivably, a ligand could cycle through several positions (middle-to-terminal and vice-versa as well as terminal-to-terminal) before dissociating, lengthening the average lifetime of the m_B state.

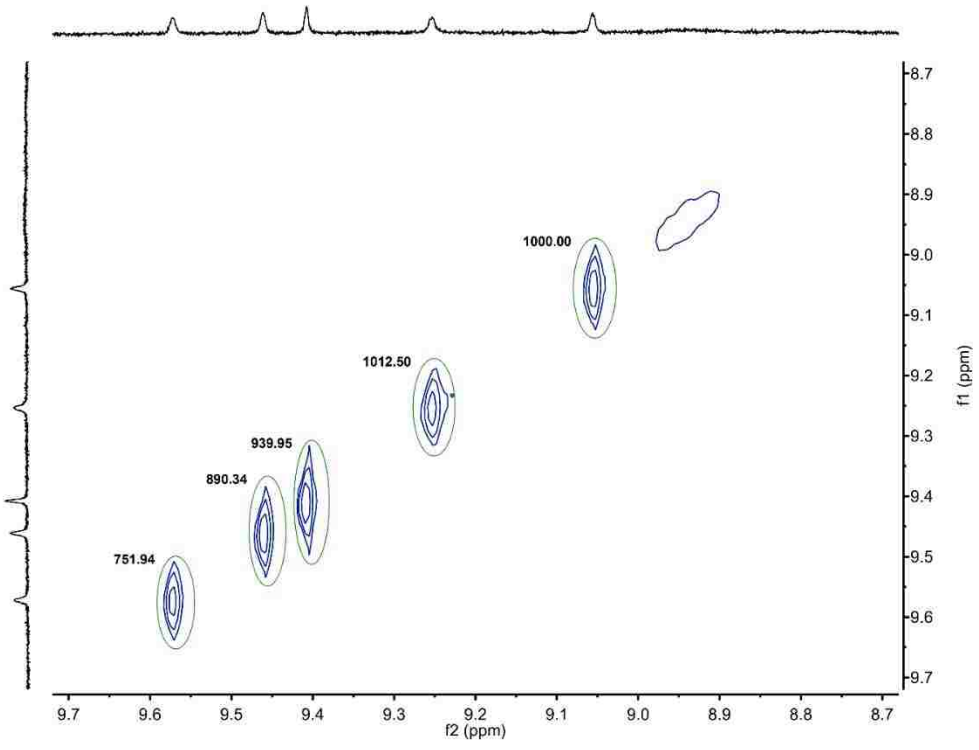

Figure 4.28 Partial ^{1}H 2D NOESY NMR spectrum of **2** (500 MHz, 333 K, 1:3 *v*/*v* DMF-d_7-CD_3CN, 0 ms mixing time, 1.0 mM ligand). Pyridinium diagonal peaks were integrated.

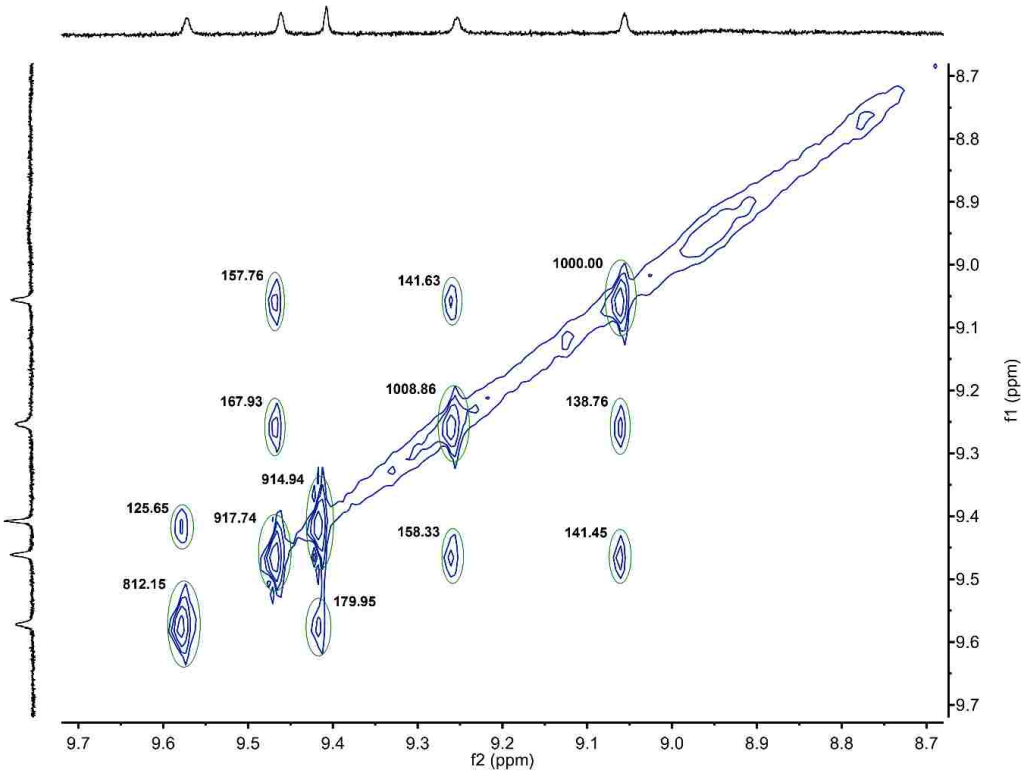

Figure 4.29 Partial ^{1}H 2D NOESY NMR spectrum of **2** (500 MHz, 333 K, 1:3 *v*/*v* DMF-d_7-CD_3CN, 300 ms mixing time, 1.0 mM ligand). Pyridinium diagonal and cross peaks were integrated.

Table 4.6 Calculated rate constants and lifetimes based on pyridinium (most-downfield and third-most-downfield) diagonal- and cross-peak integrations (**2**, 500 MHz, 333 K, 1:3 *v*/*v* DMF-d_7-CD_3CN, 1.0 mM ligand).

k_1 (s^{-1})	k_{-1} (s^{-1})	k_{ex} (s^{-1})	τ_A (s)	τ_B(s)	$1/T_1$	Ideal?
0.786	0.439	1.225	1.3	2.3	0.540	TRUE
$\Delta G^{\ddagger}_1$ (kcal•mol^{-1})	$\Delta G^{\ddagger}_{-1}$ (kcal•mol^{-1})	Temp (°C)				
19.7	20.1	60				

Table 4.7 Calculated rate constants and lifetimes based on pyridinium (second-most-downfield and fourth-most-downfield) diagonal- and cross-peak integrations (**2**, 500 MHz, 333 K, 1:3 *v*/*v* DMF-d_7-CD_3CN, 1.0 mM ligand).

k_1 (s^{-1})	k_{-1} (s^{-1})	k_{ex} (s^{-1})	τ_A (s)	τ_B (s)	$1/T_1$	Ideal?
0.591	0.551	1.142	1.7	1.8	0.540	TRUE
$\Delta G^{\ddagger}_1$ (kcal•mol^{-1})	$\Delta G^{\ddagger}_{-1}$ (kcal•mol^{-1})	Temp (°C)				
19.9	20.0	60				

Table 4.8 Calculated rate constants and lifetimes based on pyridinium (second-most-downfield and fifth-most-downfield) diagonal- and cross-peak integrations (**2**, 500 MHz, 333 K, 1:3 *v*/*v* DMF-d_7-CD_3CN, 1.0 mM ligand).

k_1 (s^{-1})	k_{-1} (s^{-1})	k_{ex} (s^{-1})	τ_A (s)	τ_B (s)	$1/T_1$	Ideal?
0.526	0.522	1.048	1.9	1.9	0.540	TRUE
$\Delta G^{\ddagger}_1$ (kcal•mol^{-1})	$\Delta G^{\ddagger}_{-1}$ (kcal•mol^{-1})	Temp (°C)				
20.0	20.0	60				

Table 4.9 Calculated rate constants and lifetimes based on pyridinium (fourth-most-downfield and fifth-most-downfield) diagonal- and cross-peak integrations (**2**, 500 MHz, 333 K, 1:3 *v*/*v* DMF-d_7-CD_3CN, 1.0 mM ligand).

k_1 (s^{-1})	k_{-1} (s^{-1})	k_{ex} (s^{-1})	τ_A (s)	τ_B (s)	$1/T_1$	Ideal?
0.461	0.476	0.937	2.2	2.1	0.540	TRUE

$\Delta G^{\ddagger}_1$ (kcal•mol^{-1})	$\Delta G^{\ddagger}_{-1}$ (kcal•mol^{-1})	Temp (°C)
20.1	20.1	60

Table 4.10 Mean kinetic values with σs based on all pyridinium diagonal- and cross-peak integrations (**2**, 500 MHz, 333 K, 1:3 *v*/*v* DMF-d_7-CD_3CN, 1.0 mM ligand).

Mean of All Individual $\Delta G^{\ddagger}$s (kcal•mol^{-1})
20.0(1)

Mean of All Individual ks (s^{-1})
0.5(1)

Mean of All Individual τs (s)
1.7(3)

Moreover, ^{1}H NOEs between pyridinium and pyridinium-methyl signals enabled the assignment of the single central iodopyridinium resonance (Figure 4.16d) of the middle strand (Figures 4.16b,e, p_A and 4.30). The two central iodopyridinium resonances arising from the terminal strands were deduced from EXSY cross peaks (Figure 4.16b,e, p_B). As evidenced by the magnetization transfer between protons p_A and p_B, dynamic ligand positional exchange (middle-to-terminal and vice versa) must occur. As the p_A resonance

becomes p_B, the pyridinium protons lose symmetry and become two singlets (Figures 4.16b,e and 4.30).

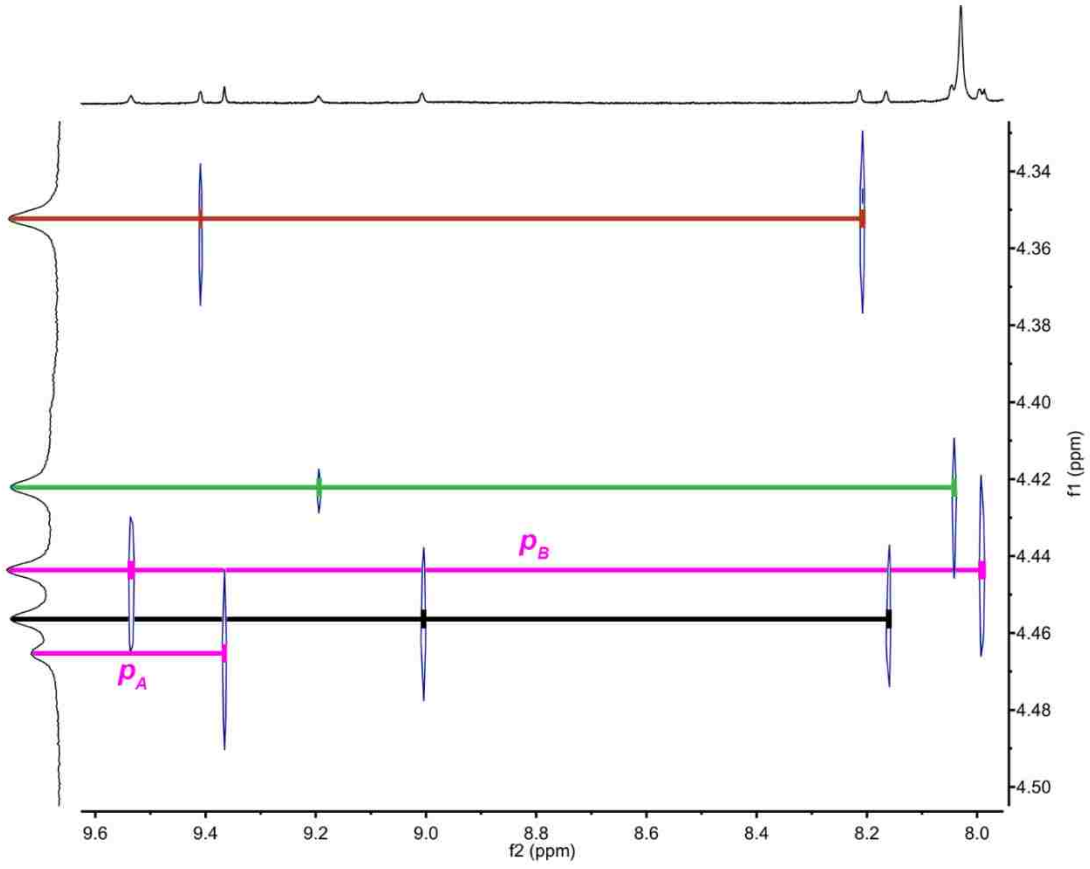

Figure 4.30 Partial ^{1}H 2D NOESY NMR spectrum of **2** (500 MHz, 313 K, 1:3 *v*/*v* DMF-d_7-CD_3CN, 300 ms mixing time, 1.0 mM ligand). Well-resolved pyridinium-methyl resonances allowed for the identification of same-ring pyridinium protons. The pyridinium-methyl peak of half intensity corresponds to the sole non-bonding halogen-bond donor (Figure 4.16b,e, p_A) of the middle-strand central pyridinium whose CX bond aligns with the C_2 axis of molecular symmetry. Additionally, the pyridinium chemical exchange data allowed us to identify the pyridinium-methyl and pyridinium resonances of the terminal-strand central pyridiniums (Figure 4.16b,e, p_B).

Flanking pyridinium resonances on the middle and terminal strands could not be assigned but their EXSY cross peaks validated the same mechanism along with terminal-to-terminal exchange (Table 4.11 and Figure 4.31).

Table 4.11 Pyridinium exchange processes of **2** (middle-to-terminal and vice-versa as well as terminal-to-terminal.

	Event	**Environment**	**Type**
1	p_A–p_{B1}	Bidentate–monodentate	Middle–terminal
2	p_A–p_{B2}	Bidentate–bidentate	Middle–terminal
3	p_C–p_D	Bidentate–bidentate	Middle–terminal
4	p_C–p_G	Bidentate–bidentate	Middle–terminal
5	p_E–p_F	Monodentate-monodentate	Middle–terminal
6	p_E–p_H	Monodentate-monodentate	Middle–terminal
7	p_D–p_G	Bidentate–bidentate	Terminal-terminal
8	p_F–p_H	Monodentate–monodentate	Terminal-terminal
9	p_{B1}–p_{B2}	Bidentate–monodentate	Terminal-terminal

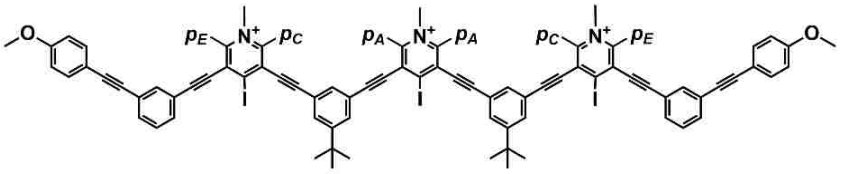

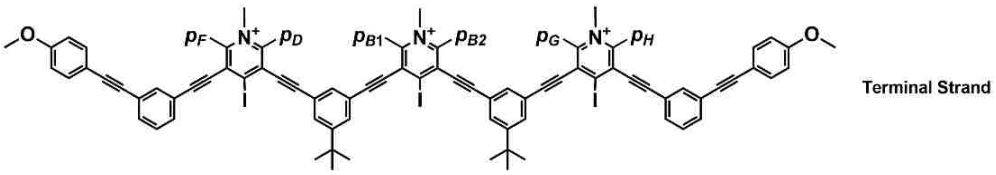

Based on an in-depth analysis, there are nine exchange processes that would give rise to a cross peak. Each event can be reversed (e.g. p_A–p_{B1} = p_{B1}–p_A). From the ^{1}H 2D NOESY NMR data (500 MHz, 333 K, 1:3 *v*/*v* DMF-d_7-CD_3CN, 300 ms mixing time, 1.0 mM ligand), eight out of the nine positional exchanges can be clearly distinguished. The monodentate-to-monodentate exchange between pyridinium protons at 8.16 and 8.12 ppm is obscured by resonance overlap. Close examination of the X-ray crystal structure of **2**/**4** reveals the underlying reason for the downfield shifts of five pyridiniums (at 9.56, 9.45, 9.39, 9.24, and 9.04 ppm) and upfield shifts of four pyridiniums (at 8.16, 8.12, 7.99 and 7.95 ppm). The downfield-shifted pyridinium protons are capable of forming bidentate hydrogen bonds with extrachannel I^-s/ Br^-s, whereas the upfield-shifted pyridinium protons are not (see the X-ray crystal structure of **2**/**4**). Moreover, the latter pyridinium protons are generally adjacent to sterically bulky *tert*-butyl groups, which would also impede favorable hydrogen-bonding interactions. Our structural analysis predicts two bidentate-to-monodentate, four bidentate-to-bidentate, and three monodentate-to-monodentate pyridinium exchanges. The ^{1}H 2D NOESY NMR data is in complete agreement with this prediction (Figures 4.31).

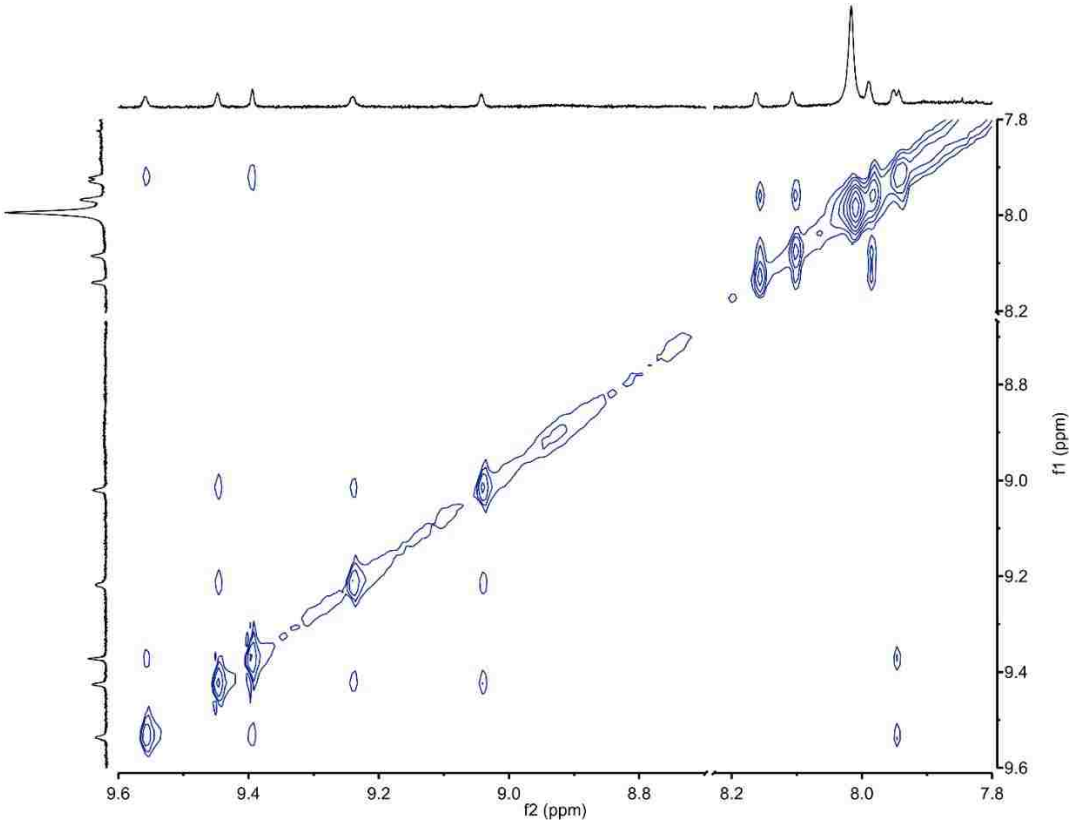

Figure 4.31 Partial ^{1}H 2D NOESY NMR spectrum of **2** (500 MHz, 333 K, 1:3 *v*/*v* DMF-d_7-CD_3CN, 300 ms mixing time, 1.0 mM ligand). Two bidentate-to-monodentate (downfield-to-upfield), four bidentate-to-bidentate (downfield-to-downfield), and two monodentate-to-monodentate (upfield-to-upfield) positional exchanges can be clearly distinguished. Only the third monodentate-to-monodentate exchange (between the protons at 8.16 and 8.12 ppm) is obscured by resonance overlap.

At 60 °C, the average lifetime of a given ligand position was 1.7(3) s. This value is the mean of eight calculated lifetimes extracted from four sets of pyridinium exchange cross peaks (see Tables 4.6–4.10). Due to their commensurate timescales, these helical movements were likely coupled with the m_A–m_B equilibrium. In support of a unified bimolecular process, all exchange rates were markedly accelerated upon increasing the

concentration of free ligand **3**. In this experiment, **3** (2.6 mM ligand) and TBAI (1.7 mM, 0.6 ligand equiv) were added to 630 μL of 1:3 *v*/*v* DMF-d_7-CD_3CN to assess the effect of a higher ligand concentration on ligand exchange kinetics (at 25 °C). The ligand-to-I^- ratio was 1.6, as compared to 0.3 for all prior ^{1}H 2D EXSY NMR experiments (1.0 mM ligand with three equivalents of I^-). The ^{1}H 2D NOESY NMR acquisition parameters were the following: at = 0.341, np = 4096, nt = 16, ni = 512, sfrq = 499.803, pw = 9.600. Methoxy-methyl diagonal and cross peaks were integrated (Figures 4.32–4.33), and a ligand lifetime value was calculated (Table 4.12).

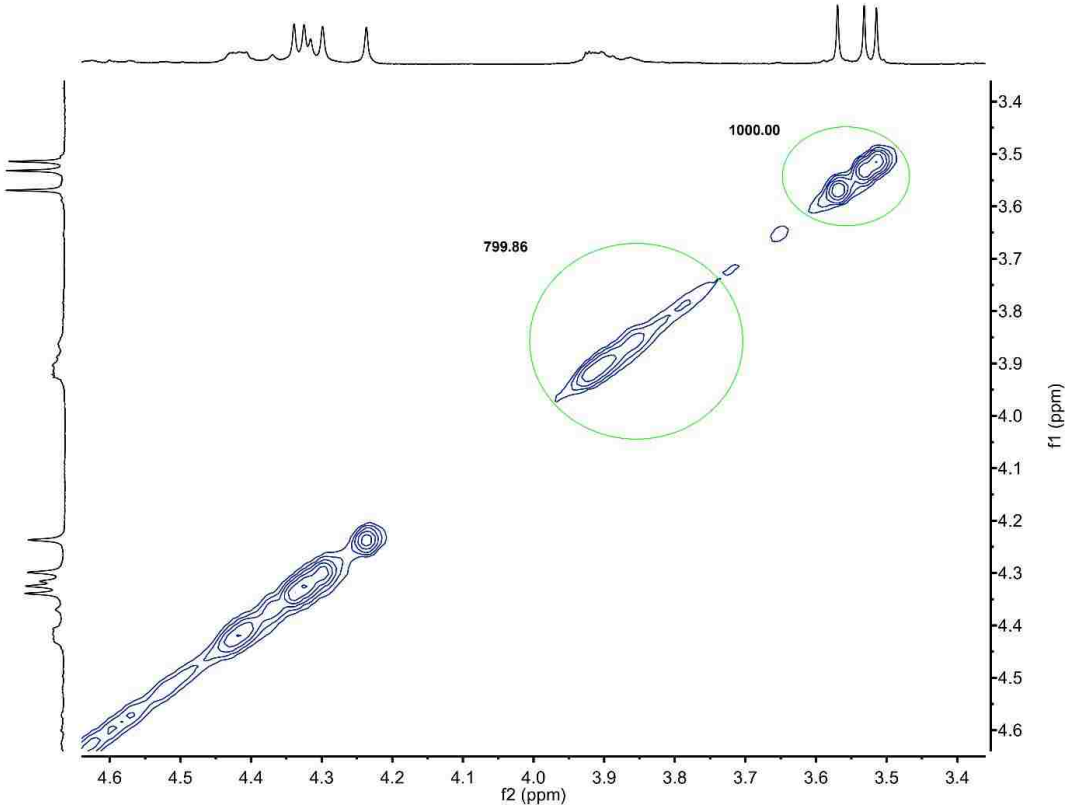

Figure 4.32 Partial ^{1}H 2D NOESY NMR spectrum of **3** with 0.6 ligand equiv of TBAI (500 MHz, 298 K, 1:3 *v*/*v* DMF-d_7-CD_3CN, 0 ms mixing time, 2.6 mM ligand). Methoxy-methyl diagonal peaks were integrated.

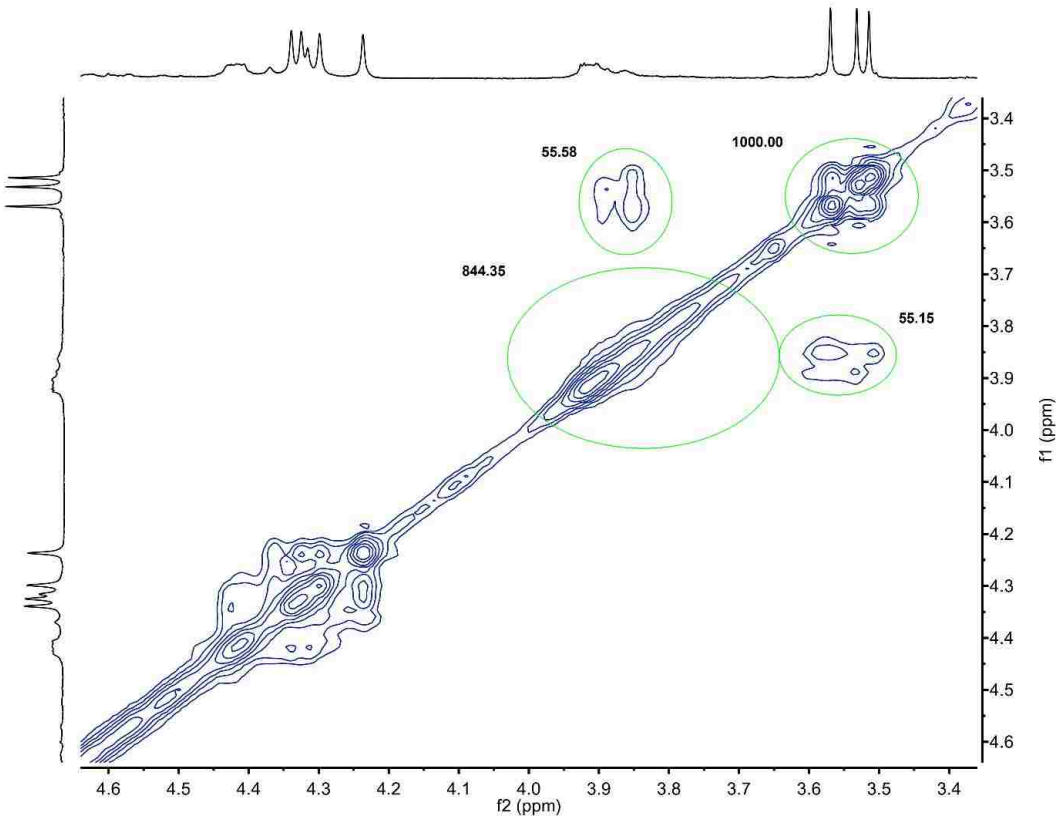

Figure 4.33 Partial ^{1}H 2D NOESY NMR spectrum of **3** with 0.6 ligand equiv of TBAI (500 MHz, 298 K, 1:3 *v*/*v* DMF-d_7-CD_3CN, 400 ms mixing time, 2.6 mM ligand). Methoxy-methyl diagonal and cross peaks were integrated.

Table 4.12 Calculated rate constants and lifetime based on methoxy-methyl diagonal- and cross-peak integrations (**3** with 0.6 ligand equiv of TBAI, 500 MHz, 298 K, 1:3 *v*/*v* DMF-d_7-CD_3CN, 2.6 mM ligand).

k_1 (s^{-1})	k_{-1} (s^{-1})	k_{ex} (s^{-1})	τ_B (s)	$1/T_1$	Ideal?
0.168	0.135	0.303	7.4	0.807	FALSE
$\Delta G^{\ddagger}_1$ (kcal•mol^{-1})	$\Delta G^{\ddagger}_{-1}$ (kcal•mol^{-1})	Temp (°C)			
18.5	18.6	25			

Moreover non-overlapping pyridinium diagonal and cross peaks were also integrated (Figures 4.34–4.35), and ligand lifetimes were calculated (Tables 4.13–4.14). The high degree of spectral overlap can be explained by the lower concentration of extrachannel I^- (i.e. fewer hydrogen-bonding interactions), resulting in the relative upfield shifts these resonances.

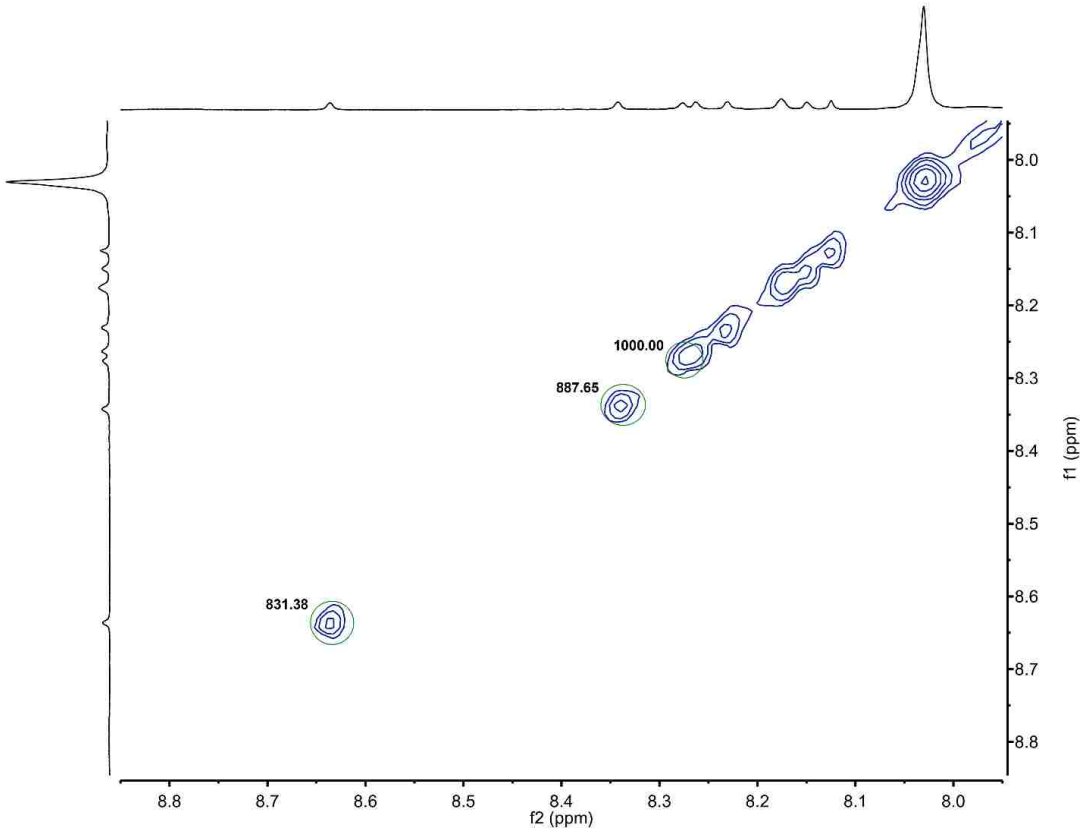

Figure 4.34 Partial ^{1}H 2D NOESY NMR spectrum of **3** with 0.6 ligand equiv of TBAI (500 MHz, 298 K, 1:3 *v*/*v* DMF-d_7-CD_3CN, 0 ms mixing time, 2.6 mM ligand). Pyridinium diagonal peaks were integrated.

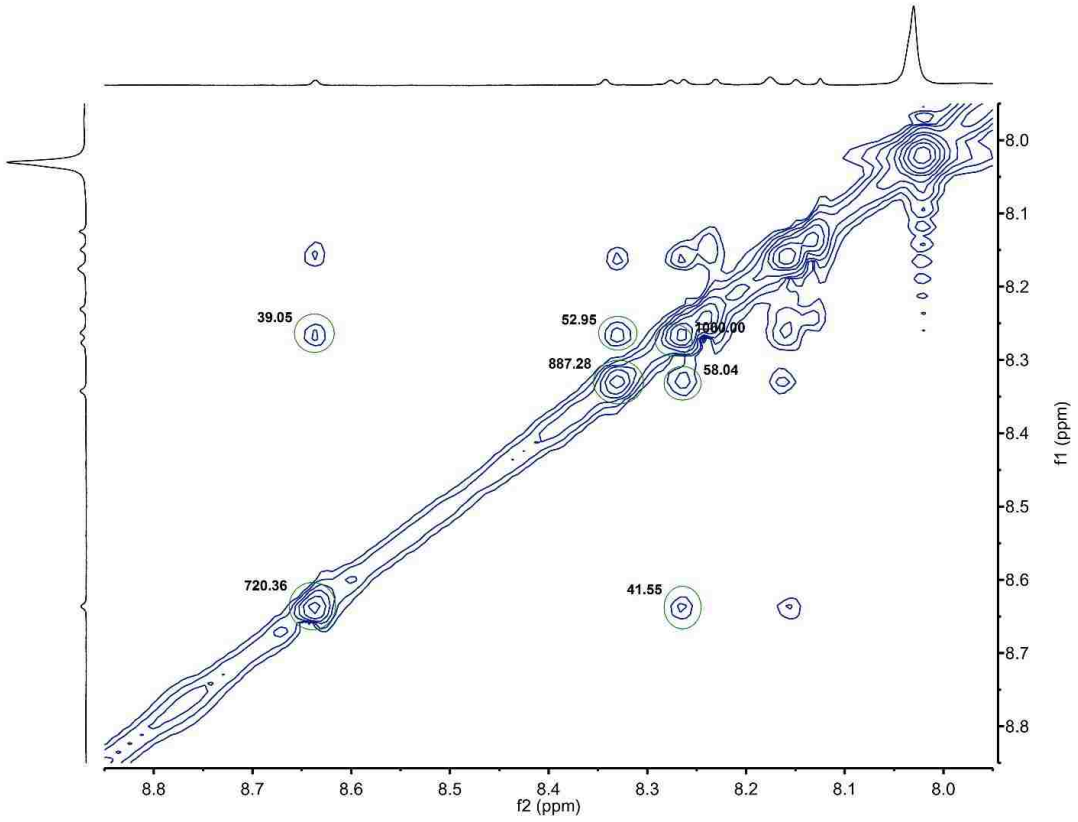

Figure 4.35 Partial ^{1}H 2D NOESY NMR spectrum of **3** with 0.6 ligand equiv of TBAI (500 MHz, 298 K, 1:3 *v*/*v* DMF-d_7-CD_3CN, 400 ms mixing time, 2.6 mM ligand). Pyridinium diagonal and cross peaks were integrated.

Table 4.13 Calculated rate constants and lifetimes based on pyridinium (most-downfield and third-most-downfield) diagonal- and cross-peak integrations (**3** with 0.6 ligand equiv of TBAI, 500 MHz, 298 K, 1:3 *v*/*v* DMF-d_7-CD_3CN, 2.6 mM ligand).

k_1 (s^{-1})	k_{-1} (s^{-1})	k_{ex} (s^{-1})	τ_A (s)	τ_B (s)	$1/T_1$	Valid?
0.134	0.105	0.239	7.5	9.5	0.536	FALSE
$\Delta G^{\ddagger}_1$ (kcal•mol^{-1})	$\Delta G^{\ddagger}_{-1}$ (kcal•mol^{-1})	Temp (°C)				
18.6	18.8	25				

Table 4.14 Calculated rate constants and lifetimes based on pyridinium (second-most-downfield and third-most-downfield) diagonal- and cross-peak integrations (**3** with 0.6 ligand equiv of TBAI, 500 MHz, 298 K, 1:3 *v*/*v* DMF-d_7-CD_3CN, 2.6 mM ligand).

k_1 (s^{-1})	k_{-1} (s^{-1})	k_{ex} (s^{-1})	τ_A (s)	τ_B (s)	$1/T_1$	Valid?
0.164	0.133	0.297	6.1	7.5	0.536	FALSE

$\Delta G^{\ddagger}_1$ (kcal•mol^{-1})	$\Delta G^{\ddagger}_{-1}$ (kcal•mol^{-1})	Temp (°C)
18.5	18.6	25

At the lower ligand concentration (1.0 mM ligand with three ligand equivalents of I^-, 25 °C), pyridinium cross peaks were nonexistent (Figure 4.36). Even the methoxy-methyl cross peaks were low in intensity under these conditions (Figure 4.21).

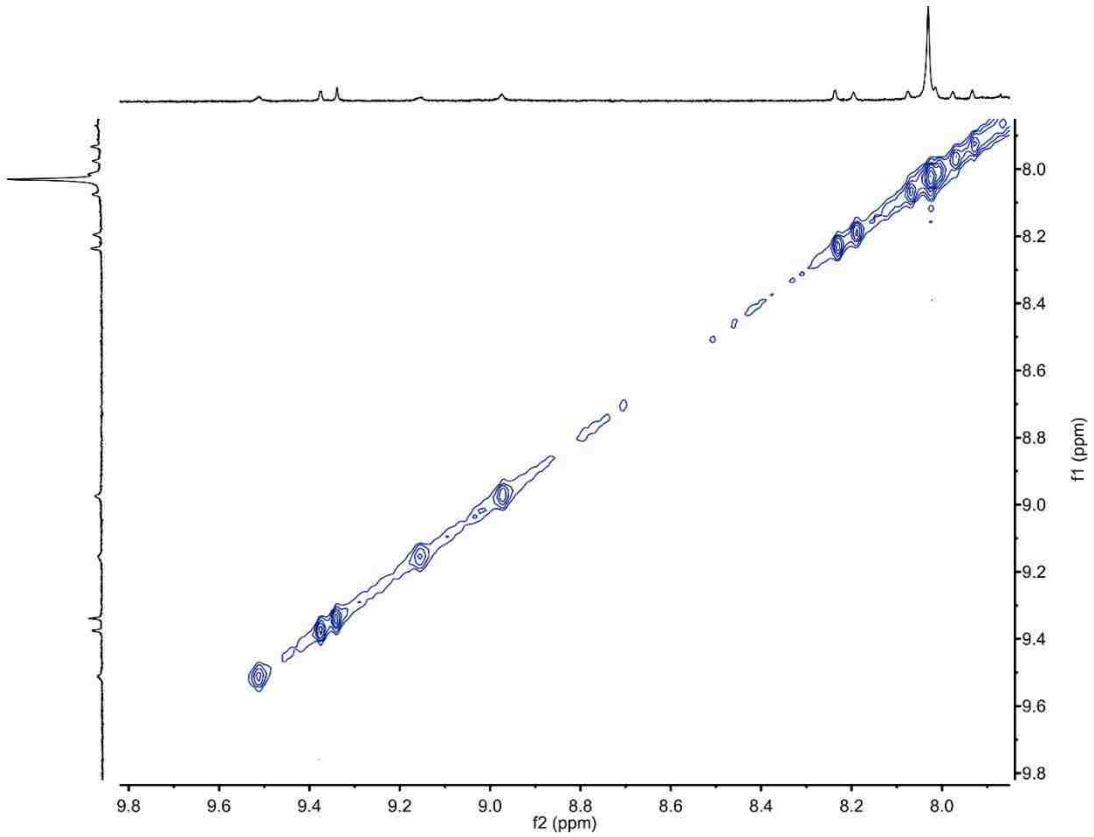

Figure 4.36 Partial ^{1}H 2D NOESY NMR spectrum of **2** with three ligand equivalents of I^- (500 MHz, 298 K, 1:3 *v*/*v* DMF-d_7-CD_3CN, 300 ms mixing time, 1.0 mM ligand). Only pyridinium diagonal peaks were observed.

The overall effect of ligand concentration on ligand exchange rates is summarized in Table 4.15.

Table 4.15 Rate enhancements of both the m_A–m_B (Figure 4.16a) and positional-exchange (Figure 4.16b) equilibria as a function of increasing free ligand concentration (500 MHz, 298 K, 1:3 *v*/*v* DMF-d_7-CD_3CN). These data suggest a unified bimolecular process (Figure 4.16c) rather than facile ligand corkscrewing, which likely occurs on a much faster timescale.

Ligand (mM)	**Nucleus**	k_1 **(s^{-1})**	k_{-1} **(s^{-1})**
1.0	Methoxy-Methyl	0.094	0.042
2.6	Methoxy-Methyl	0.168	0.135
1.0	Pyridinium	None observed	
2.6	Pyridinium	0.15(2)	0.12(2)

Finally, and without exception, activation energies ($\Delta G^{\ddagger}$) of all exchanges intensified with increasing temperature, indicating a negative entropy of activation ($\Delta S^{\ddagger}$; Table 4.16). Together, these data imply the formation of an activated complex that consists of a triplex and a queuing ligand (Figure 4.16c, black). We hypothesize that this incoming ligand competitively displaces a distal terminal strand (Figure 4.16, green) in an S_N2-like fashion.

Table 4.16 Increasing trends in $\Delta G^{\ddagger}$ implying a negative entropy of activation ($\Delta S^{\ddagger}$) for all ligand exchanges (500 MHz, 1:3 *v*/*v* DMF-d_7-CD_3CN, 1.0 mM ligand).

Temp (°C)	Nucleus	$\Delta G^{\ddagger}_{1}$ (kcal•mol^{-1})	$\Delta G^{\ddagger}_{-1}$ (kcal•mol^{-1})
25 °C	Methoxy-Methyl	18.9	19.3
40 °C	Methoxy-Methyl	19.4	19.8
40 °C	Pyridinium	19.7	19.7
60 °C	Methoxy-Methyl	20.3	20.5
60 °C	Pyridinium	19.9(2)	20.0(1)

4.3.7 Kinetic Analysis of Intrachannel Guest Exchange

Br^--for-I^- exchange at RT was monitored by visible absorption upon adding three ligand equivalents of TBABr to **2** at steady state (1.0 mM ligand). The absorption at 460 nm dropped by 38 %, concomitant with a lightening of the orange-yellow solution (Figure 4.37). This Br^--induced spectral change may have stemmed from $CI\cdots I^-/Br^-$ charge transfer effects.[160]

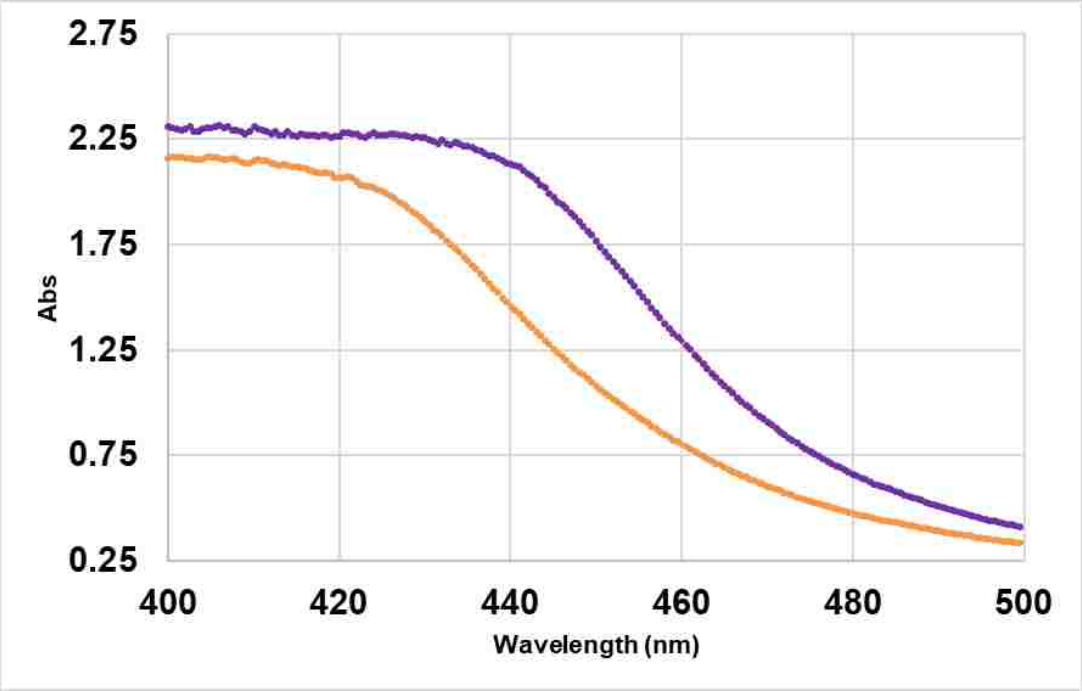

Figure 4.37 Steady-state visible spectrophotometric spectrum of **2** (purple, 1.0 mM ligand with three ligand equivalents of I^-) and the same sample with a subsequent addition of three ligand equivalents of TBABr (orange). Experimental conditions: RT, 1:3 *v*/*v* DMF-CH_3CN.

Under the same conditions, intrachannel guest exchange was monitored with stopped-flow visible spectroscopy at 460 nm. A stock solution of **2** (2.0 mM ligand with three ligand equivalents of I^-) and a separate stock solution of TBABr (6.0 mM) were prepared in 1:3 *v*/*v* DMF-CH_3CN. All stopped-flow visible kinetic experiments were conducted at 25 °C. After the rapid mixing of two given solutions in a 1:1 *v*/*v* ratio, each component was diluted to a post-mixing concentration of half its starting concentration. A flow cell with a 2 mm pathlength was used. The dead time of the stopped-flow was measured by reduction of dichlorophenolindophenol as a function of L-ascorbic acid concentration and was found to be 2 ms under the mixing conditions. Experiments were

conducted with five replications, and 10,000 data points were collected over the course of five seconds for each replicate. The following experiments were completed:

1) Blank after background subtraction
    a. Solution 1: plain solvent (1:3 *v*/*v* DMF-CH_3CN); solution 2: plain solvent."
2) **2** + Solvent
    a. Solution 1: **2** (1.0 mM ligand post-mixing with three ligand equivalents of I^-); solution 2: plain solvent."
3) **2** + TBABr
    a. Solution 1: **2** (1.0 mM ligand post-mixing with three ligand equivalents of I^-); solution 2: TBABr (3.0 mM post-mixing)."

σs of all data point are included in the PDFs as well as overall average σs (for the raw data, contact the authors). As alluded to previously, **2** was rapidly mixed with plain solvent, and the kinetic profile was monitored over the course of five seconds (Figure 4.38a, purple). A slight decay in absorption (0.003 AU) between 2–100 ms was noted—feasibly as a result of dilution-induced population shifts between **2** and lower-order species (Figure 4.39)—followed by a flat kinetic profile. However, rapidly mixing **2** with three ligand equivalents of TBABr produced a 35 % drop in absorption during the two-millisecond dead time (Figure 4.38a, orange). In contrast to the control trace, a more precipitous absorption decay between 2–4 ms was also evident, corresponding perhaps to the tail end of guest exchange (Figure 4.38b). Overall, the commensurate absorption

decrease monitored at steady state (38 %) and within the stopped-flow dead time upon perturbation (35 %) supports millisecond-or-faster intrachannel guest exchange.

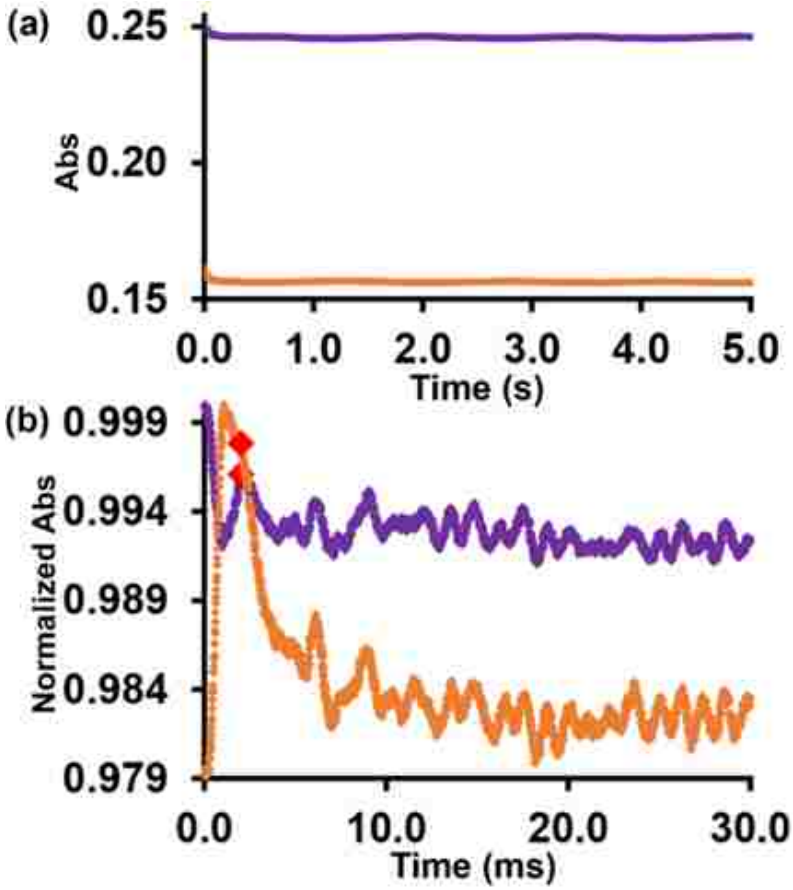

Figure 4.38 (a) Stopped-flow kinetic traces of **2** (purple) and **2** with three ligand equivalents of TBABr (orange); (b) same kinetic traces from 0–30 ms; (a–b) 298 K, 1:3 *v*/*v* DMF-CH_3CN, 1.0 mM ligand post-mixing, 2 ms deadtime (red diamonds), monitored at 460 nm, 2 mm pathlength; each kinetic trace is the mean of five independent experiments (average σ: 0.001 AU).

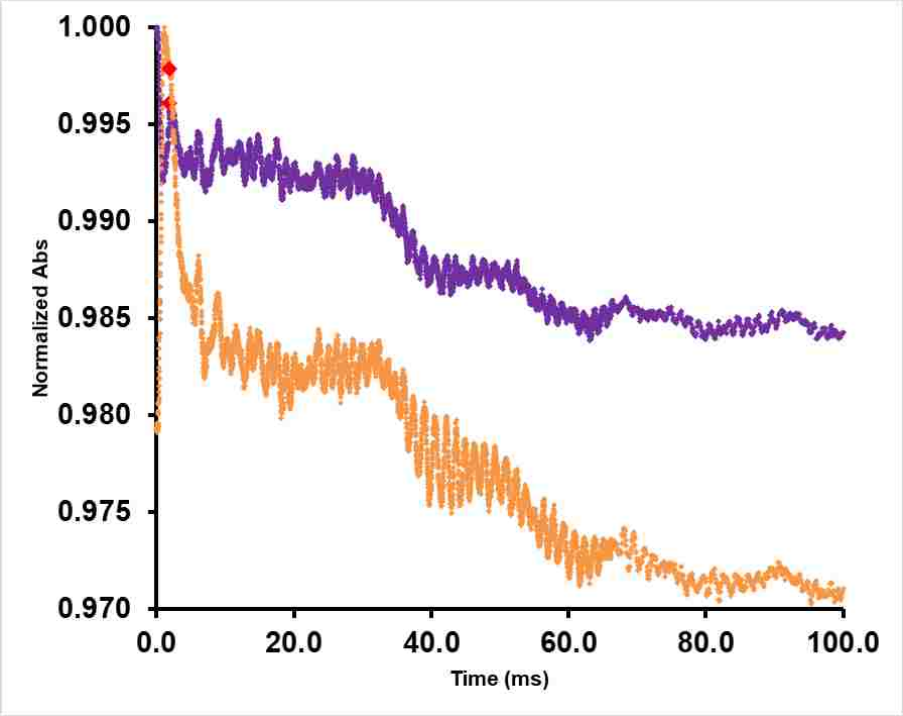

Figure 4.39 Stopped-flow kinetic traces of **2** (purple) and **2** with three ligand equivalents of TBABr (orange) from 0–100 ms. The subtle drop in absorption from 2–100 ms is common to both experiments and is feasibly due to dilution-induced population shifts between **2** and lower-order species. This spectrophotometric response is consistent with the observed concentration dependence of triple helicate self-assembly by ^{1}H NMR spectroscopy.

Additionally, we combined **2** with three ligand equivalents of TBABr and monitored the reaction at 460 nm for five minutes. Briefly, a stock solution of **2** (2.0 mM ligand with three ligand equivalents of I^{-}) and a separate stock solution of TBABr (6.0 mM) were prepared in 1:3 *v*/*v* DMF-CH_3CN. The visible spectrophotometric kinetic study was conducted at RT. Upon syringing then stirring both solutions (in a 1:1 *v*/*v* ratio) inside a 1-cm quartz cuvette for 4.8 s (0.08 min), each component was diluted to a post-

mixing concentration of half its starting concentration. Experimental details of the kinetic study were the following (for the raw data, contact the authors):

1) **2** + TBABr
    a. Solution 1: **2** (1.0 mM ligand post-mixing with three ligand equivalents of I^-); solution 2: TBABr (3.0 mM post-mixing).

Virtually no spectral changes were detected throughout the course of the experiment (Figure 4.40).

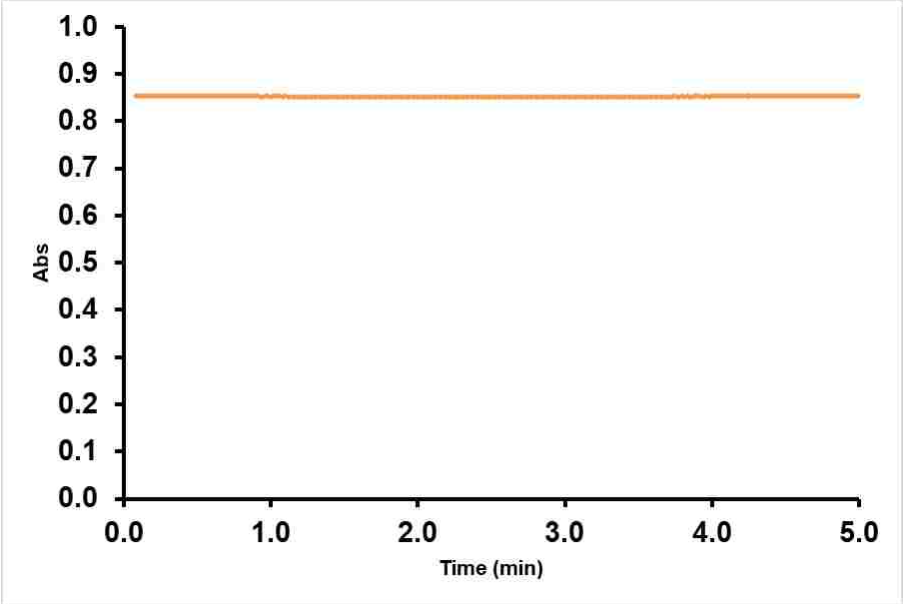

Figure 4.40 Visible spectrophotometric kinetic profile of **2** with three ligand equivalents of TBABr from 0.08–5 min. Experimental conditions: RT, 1:3 *v*/*v* DMF-CH_3CN, 1.0 mM ligand post-mixing, monitored at 460 nm, 1 cm pathlength.

To provide further evidence of fast exchange, we probed the structural features of **4**, **2**, **4** with addition of TBAI, and **2** with addition of TBABr using ^{1}H NMR

spectroscopy. Drawing from a stock solution of **3**, we formed both **4** and **2** in separate NMR tubes via inclusion of TBABr and TBAI, respectively (1:3 *v*/*v* DMF-d_7-CD_3CN, 1.0 mM ligand with three ligand equivalents of either halide ion as specified). The ^1H NMR spectrum of each triple helicate was acquired (500 MHz, 298 K; Figure 4.41a,b). Subsequently, 2.3 ligand equiv each of TBAI and TBABr were added to **4** and **2**, respectively. If no guest exchange ensued during the five-minute experiment, adding 2.3 ligand equiv of the substituting halide ion would have achieved equal extrachannel concentrations of both halide ions. For example, adding 2.3 ligand equiv of TBAI to **4** would have resulted in roughly 2.3 ligand equiv each of extrachannel I^- and Br^- as well as 0.7 ligand equiv of intrachannel Br^-. If intrachannel guest exchange were indeed this slow, we would have observed two very different ^1H NMR traces. Disparities would have been especially pronounced for non-hydrogen-bonding protons (i.e. methoxy-methyl and tert-butyl protons) as evidenced by the marked spectral discrepancies between **4** and **2** prior to halide ion addition (Figure 4.41a,b). However, upon adding the substituting halide ions, the aforementioned differences in chemical shifts were erased (Figure 4.41c,d). Nearly identical ^1H NMR traces corresponding to the formation of hybrid triple helicates were observed. Only subtle variations in chemical shifts were noted—also consistent with rapid exchange. For instance, adding 2.3 ligand equiv of TBAI to **4** resulted in three ligand equivalents of Br^- and 2.3 ligand equiv of I^- in rapid exchange between all environments. In contrast, adding 2.3 ligand equiv of TBABr to **2** resulted in three ligand equiv of I^- and 2.3 ligand equiv of Br^- in rapid exchange between all environments. Caused by fast guest exchange, these discrepancies in halide-ion concentrations resulted in subtle differences in chemical shifts. Lastly, significant

linewidth broadening of three downfield (Figure 4.41c,d) and likely one or more upfield (not shown) pyridinium signals was observed. All other resonances remained relatively sharp. As the pyridinium protons should be the most responsive spectroscopically to intrachannel halogen bonding, this linewidth broadening provides additional evidence for intrachannel exchange (intermediate on the ^{1}H NMR timescale). It is noteworthy that one of the signals that remained sharp likely belongs to the non-bonding iodopyridinium of the triple helicate. Collectively, these results are consistent with the stopped-flow and spectrophotometric kinetic data, which indicate millisecond-or-faster intrachannel exchange.

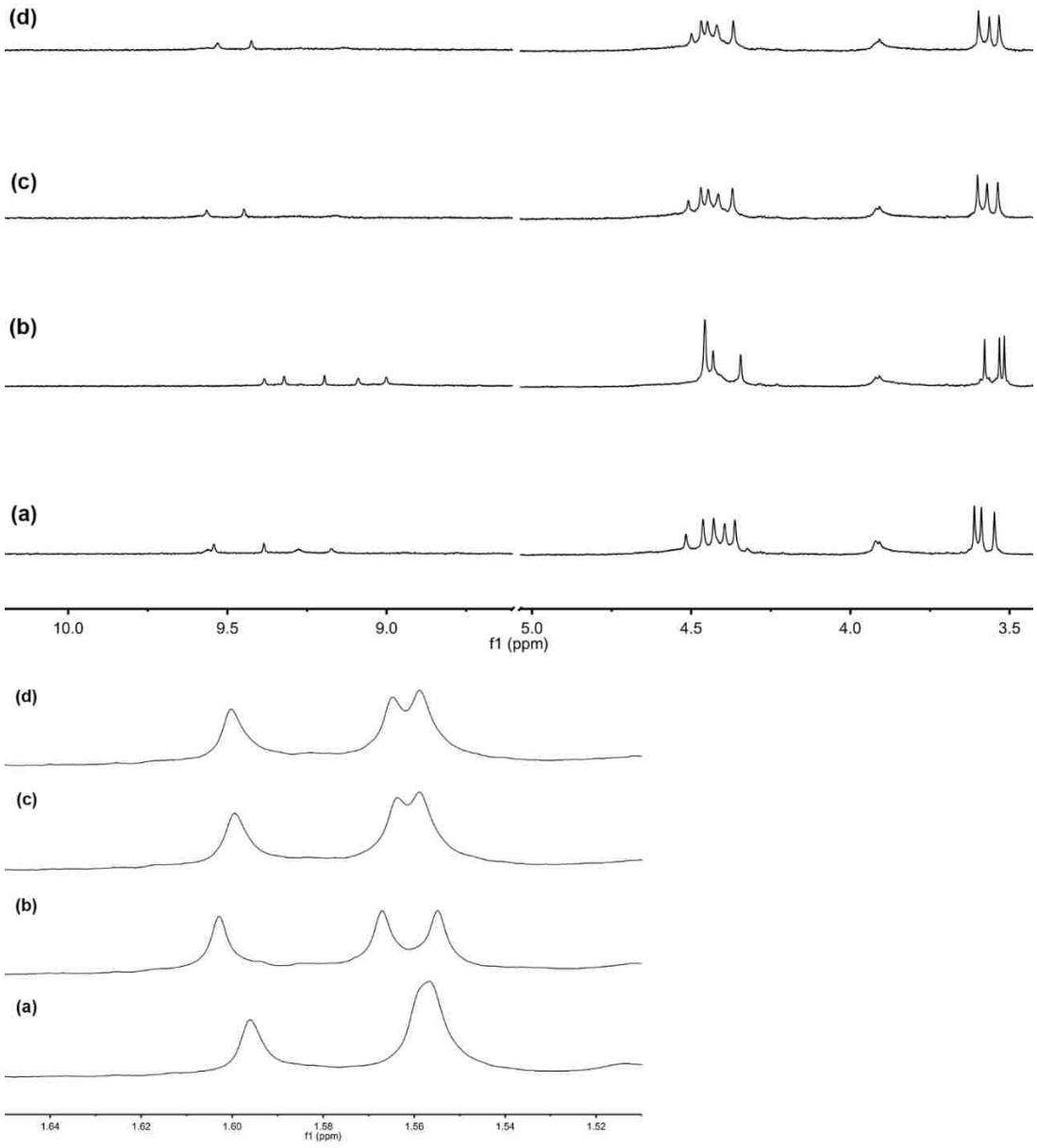

Figure 4.41 Partial ^{1}H NMR spectra of **4**, **2**, and a hybrid triple helicate. (a) Br^- triple helicate **4**; (b) I^- triple helicate **2**; (c) **4** with addition of 2.3 ligand equiv of TBAI; (d) **2** with addition of 2.3 ligand equiv of TBABr. Expansion of all spectra in the upfield region displaying the *tert*-butyl resonances (below). (a–d) 500 MHz, 298 K, 1:3 *v*/*v* DMF-d_7-CD_3CN, 1.0 mM ligand. See Figure 4.7 for proton assignments.

4.4 Experimental

All reagents were obtained from commercial sources and were used without further purification unless otherwise noted. Flash column chromatography was performed using normal-phase silica gel (230–400 mesh, SiliaFlash® P60, SiliCycle). TLC was performed using normal-phase silica gel glass-backed plates (0.25 mm, F-254, SiliCycle) and observed under UV light. Activated Fischer Grade 514 molecular sieves were used when anhydrous solvents were required. All compounds were dried in vacuo at RT as needed. For the synthesis of compound **8**, a modified Sonogashira procedure was utilized. Standard Schlenk line and air-free techniques were employed for these reactions. Preparatory HPLC separations were conducted with a Teledyne Isco CombiFlash RF+. A Teledyne Isco RediSep RF Gold Reversed-phase C18 column was utilized for these separations. High-resolution masses of new compounds were obtained using an Agilent 6520 Accurate-Mass Q-TOF LC/MS. Compound **4** was directly injected into a Bruker amaZon SL Ion Trap ESI-MS. X-ray crystallographic data were collected with a Bruker D8 Venture X-ray diffractometer. NMR spectra were obtained with a VNMRS Varian 500 MHz, Agilent DD2 400 MHz, or Bruker Avance 400 MHz spectrometer. The majority of the NMR data were acquired using the VnmrJ 4.2 acquisition software. Chemical shifts are reported in ppm from high to low frequency using the residual solvent peak as the internal reference ($CHCl_3$ = 7.26 ppm or DMF = 8.03 ppm). All ^{1}H resonances are reported to the nearest 0.01 ppm. The multiplicity of the signals is designated as: s = singlet, d = doublet, t = triplet, or m = multiplet. *J*s are reported to the nearest 0.1 Hz. All ^{13}C resonances are reported to the nearest 0.01 ppm and labeled relative to the center resonance of the residual solvent as the internal reference ($CDCl_3$ =

77.16 ppm). All NMR data were processed with VnmrJ 4.2 or MestReNova 8.1.2-11880. T_1 relaxation and 2D DOSY data were fitted with the VnmrJ 4.2 software. Nucleus lifetimes and rate constants were calculated using EXSYCalc 1.0 (Mestrelab Research). Visible spectrophotometric steady-state and kinetic experiments (0–5 min) were conducted using an Agilent Cary 60 UV-Vis Spectrophotometer. Fast intrachannel guest exchange kinetics (0–5 s) were measured with an Applied Photophysics SX20 stopped-flow apparatus. Spectrophotometric grade DMF and CH_3CN were used for all experiments involving spectrophotometry.

4.4.1 Synthesis and Characterization Data

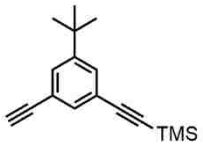

((3-(tert-butyl)-5-ethynylphenyl)ethynyl)trimethylsilane (**6**)

Pre-dried compound **5** (10.0 g, 30.6 mmol, 1.0 equiv) and anhydrous THF (500 mL) were added to a flame-dried 1000-mL round bottom flask. The solution was stirred, N_2-sparged, and cooled to 0 °C in an ice-water bath. Under N_2, 18 mL of MeLi•LiBr (2.2 M solution in Et_2O, 39.8 mmol, 1.3 equiv) were carefully added dropwise in 6-mL increments via an air-free syringe. The resulting dark solution was stirred for 20 min. During this time, a 1:3 *v*/*v* HCl-H_2O solution (200 mL) was prepared in a 1000-mL round bottom flask. The diluted HCl was stirred and allowed to reach 0 °C in an ice-water bath. When the deprotection reached equilibrium, the dark solution was slowly and carefully poured into the HCl-H_2O solution. The resulting mixture was stirred for 10 min. The reaction mixture along with brine (150 mL) were added to a large separatory funnel, and

the organics were extracted with DCM. After drying over $MgSO_4$ and gravity-filtering, the organic solvent was removed in vacuo, and the dark-yellow crude oil was adsorbed onto a small amount of silica. The product was semi-purified by flash column chromatography (0.5 % EtOAc-hexanes, 12 in of silica, 70-mm diameter glass column, dry loaded). A statistical mixture of poorly-resolved compounds eluted in the following order: bis-protected starting material **5**, mono-protected product **6**, and the bis-deprotected overshoot compound. Utilization of 3 % EtOAc-hexanes allowed for the visualization of all three compounds by TLC (R_fs: **5** = 0.67, **6** = 0.59, and overshoot = 0.5). Mixed fractions that contained both **5** and **6** were collected, as **5** did not affect the next reaction. The solvent was removed in vacuo, affording a yellow oil (**6**: 3.8 g, 32 % as assessed by ^{1}H qNMR spectroscopy). This semi-purified crude mixture was used directly in the next reaction. Product **6** was isolated for characterization using preparatory HPLC (30 % CH_3CN-H_2O → 100 % CH_3CN gradient over 15 min). ^{1}H NMR (400 MHz, $CDCl_3$) δ = 7.46 (d, *J* = 1.5 Hz, 2H), 7.43 (t, *J* = 1.5 Hz, 1H) 3.04 (s, 1H), 1.30 (s, 9 H), 0.25 (s, 9H). ^{13}C NMR (101 MHz, $CDCl_3$) δ = 151.55, 132.85, 129.60, 129.51, 123.21, 122.10, 104.74, 94.39, 83.42, 77.28, 34.74, 31.18, 0.10. HR-ESI-MS *m*/*z* = $[M\text{-}CH_3]^+$ 239.1255, calculated 239.1251.

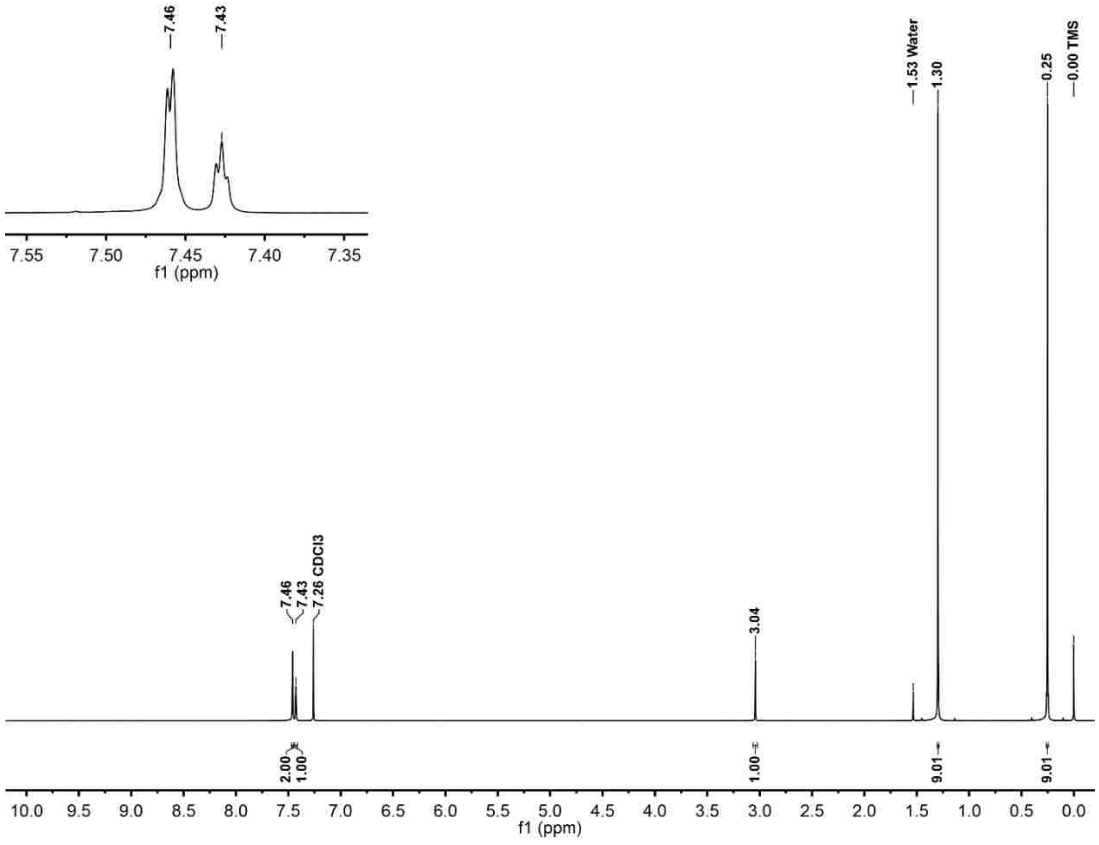

Figure 4.42 ^{1}H NMR spectrum of compound **6** (400 MHz, $CDCl_3$).

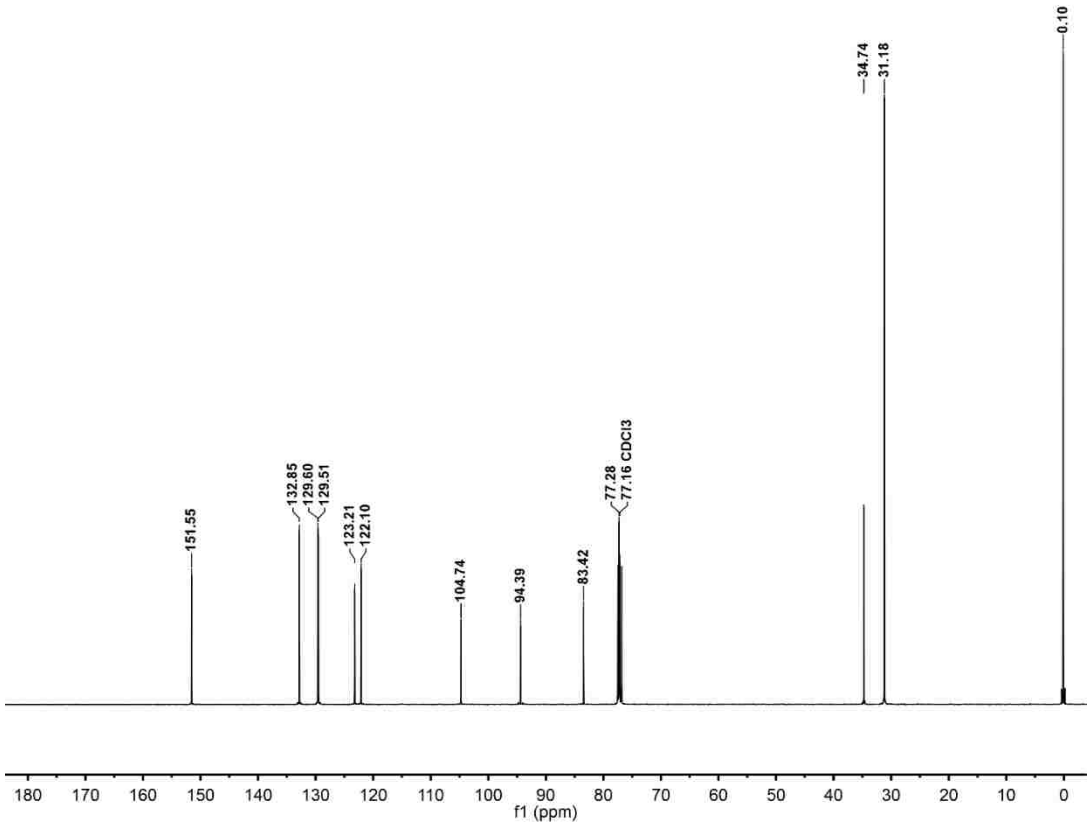

Figure 4.43 ^{13}C NMR spectrum of compound **6** (101 MHz, $CDCl_3$).

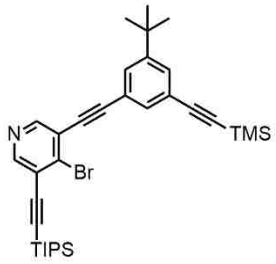

4-bromo-3-((3-(tert-butyl)-5-((trimethylsilyl)ethynyl)phenyl)ethynyl)-5-((triisopropylsilyl)ethynyl)pyridine (**8**)

Pre-dried compounds **6** (3.94 g, 15.5 mmol, 1.0 equiv) and **7** (7.2 g, 15.5 mmol, 1.0 equiv), Et_3N (50 mL), and anhydrous DMF (300 mL) were added to a flame-dried 500-mL round bottom flask and sparged with N_2 for 25 min. Meanwhile, $PdCl_2(PPh_3)_2$ (652 mg, 0.9 mmol, 0.06 equiv) and CuI (177 mg, 0.9 mmol, 0.06 equiv) were added to a flame-dried 500-mL Schlenk flask, which was evacuated and back-filled with N_2 four times. After sparging, the contents of the round bottom flask were transferred to the Schlenk flask via cannula. The orange-yellow solution was stirred for 12 h at 50 °C. The solvent was removed in vacuo, and the crude mixture was adsorbed onto a small amount of silica. The product was semi-purified with flash column chromatography (3 % EtOAc-hexanes, 12 in of silica, 70-mm diameter glass column, dry loaded). Compound **8** (Rf = 0.19) co-eluted with bromopyridine side products that originated from the synthesis of **7**. These side products did not affect the next reaction. All fractions that contained compound **8** were collected and consolidated, and the solvent was removed in vacuo affording a yellow oil (**8**: 6.2 g, 68 % as assessed by back calculation). A small amount of pure product **8** eluted during the aforementioned separation, which allowed for characterization. ^{1}H NMR (400 MHz, $CDCl_3$) δ 8.56 (s, 1H), 8.53 (s, 1H), 7.54–7.52 (m, 2H), 7.51 (t, J = 1.6 Hz, 1H), 1.33 (s, 9H), 1.19–1.13 (m, 21H) , 0.27 (s, 9H). ^{13}C NMR

(101 MHz, $CDCl_3$) δ 151.83, 151.75, 151.11, 137.97, 132.58, 130.13, 129.06, 123.51, 123.43, 123.20, 122.11, 104.55, 101.48, 100.97, 96.87, 94.73, 84.81, 34.87, 31.21, 18.78, 11.37, 0.09. HR-ESI-MS *m/z* = $[M+H]^+$ 590.2275, calculated 590.2268.

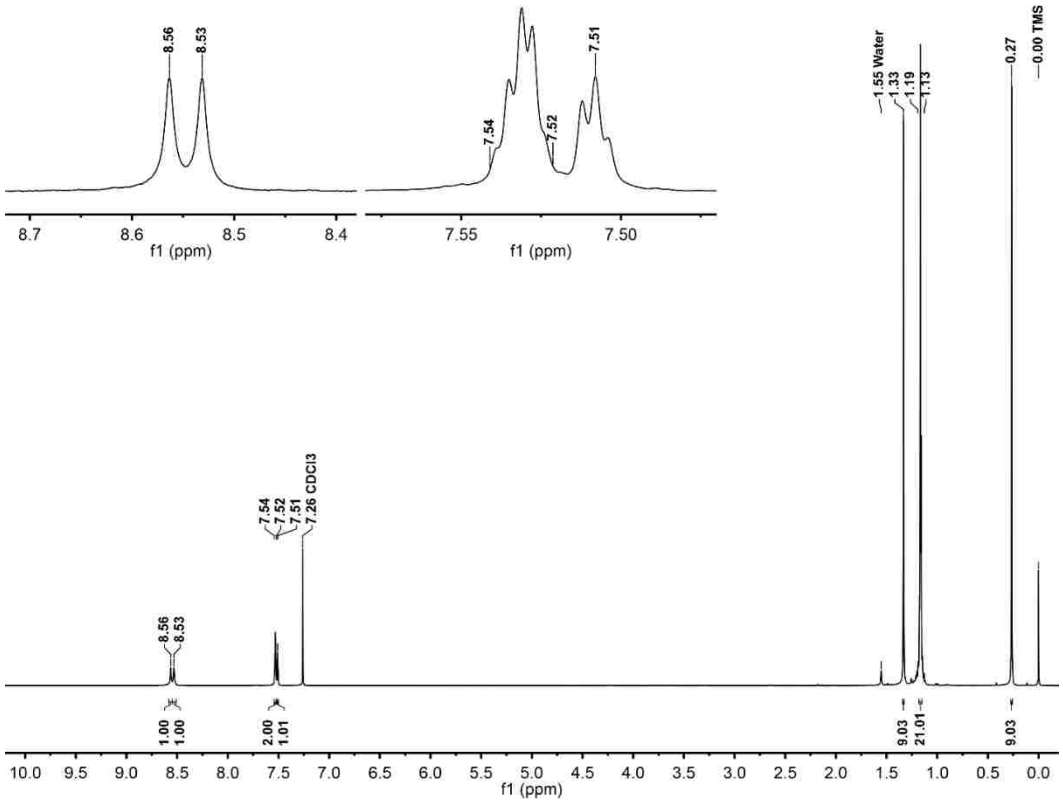

Figure 4.44 ^1H NMR spectrum of compound **8** (400 MHz, $CDCl_3$).

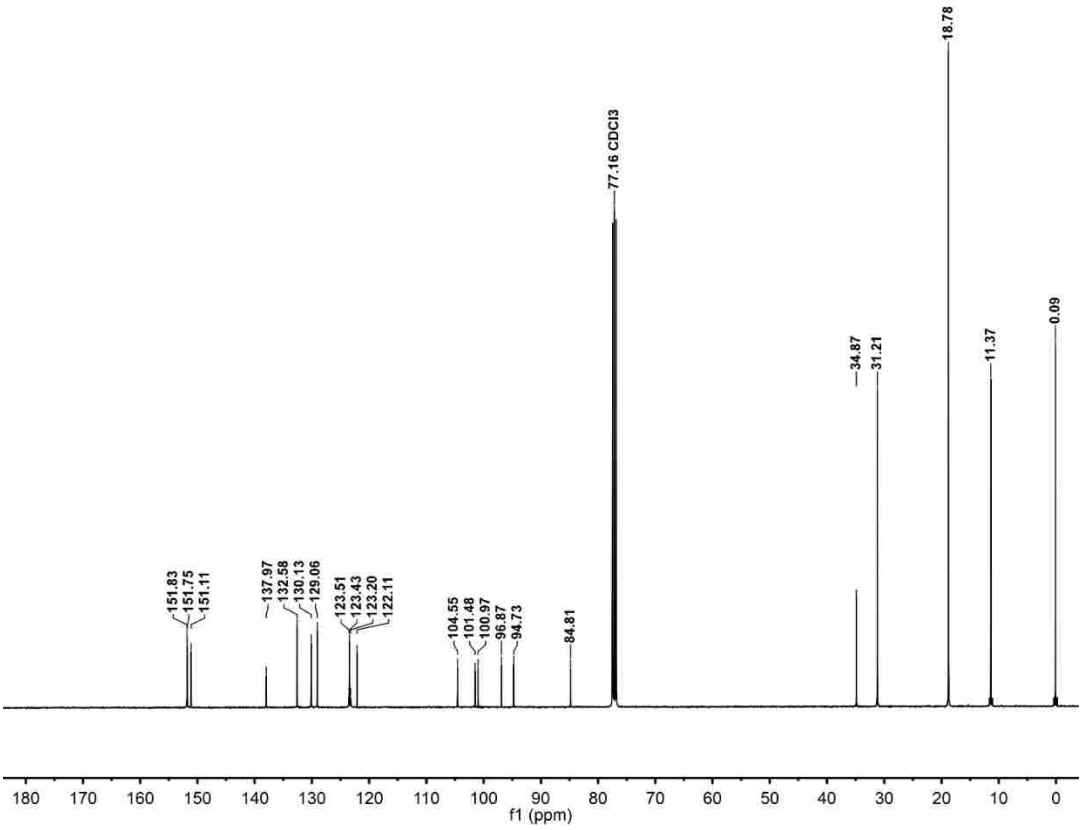

Figure 4.45 ^{13}C NMR spectrum of compound **8** (101 MHz, $CDCl_3$).

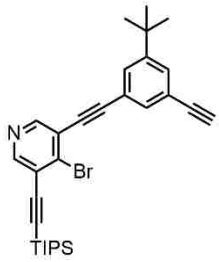

4-bromo-3-((3-(tert-butyl)-5-ethynylphenyl)ethynyl)-5-((triisopropylsilyl)ethynyl)pyridine (**9**)

The following procedure details a new strategy to create compound **9**, which was characterized previously. Pre-dried, semi-pure compound **8** (6.2 g, 10.5 mmol, 1.0 equiv), K_2CO_3 (6.8 g, 49.2 mmol, 4.7 equiv), and 1:4 *v*/*v* CH_3OH-THF (200 mL) were added to a 500-mL round bottom flask. The reaction was stirred for 80 min at RT. Subsequently, the reaction mixture was diluted with DCM (400 mL) and transferred to a separatory funnel. The organics were washed with H_2O and brine. The organic solvent was dried over $MgSO_4$ and removed in vacuo. The crude oil was adsorbed onto a small amount of silica. Compound **9** (R_f = 0.27) was purified with flash column chromatography (5 % EtOAc-hexanes, 12 in of silica, 70-mm diameter glass column, dry loaded). Clean fractions of the product were consolidated, and the solvent was removed in vacuo affording a yellow oil (5.4 g, quantitative). For characterization details of compound **9**, see Section 3.4.1 (in that section, it is compound **3**).

4.4.2 X-Ray Crystallographic Data

X-ray diffraction data for UMT_OB12_sq were collected at 100 K on a Bruker D8 Venture X-ray diffractometer using CuKα (λ = 1.54178) radiation. Data have been corrected for absorption using the SADABS area detector absorption correction program.

Utilizing Olex2,[157] the structure was solved with the ShelXT[158] structure solution program using Direct Methods and refined with the ShelXL refinement package using least squares minimization. Hydrogen atoms were placed in calculated positions using a ridged group model and refined with isotropic thermal parameters. The majority of non-hydrogen atoms were refined with anisotropic thermal displacement parameters (see below discussion for further details). The structure was found to contain indistinguishable solvent molecules within voids in the lattice. Attempts at modeling this solvent were not able to produce a suitable model. The SQUEEZE[167] routine within PLATON was utilized to account for the residual, diffuse electron density, and the model was refined against these data. A total of 4,293 electrons per unit cell were corrected for. All calculations and refinements were carried out using APEX3, SHELXTL, Olex2, and PLATON. The initial solution had a resemblance to the predicted iodononameric *m*-arylene-ethynylene ligands. After initial refinement, the main chains were fully established, and identification of the anisole rings and tert-butyl groups from the difference map were possible. The anisole rings required geometric restraints as refinement lacking these restraints led to chemically unreasonable rings. Displacement parameter restraints were employed, as the locations of the anisole rings lent themselves to multiple positions or thermal motion as illustrated by the elongated ellipsoidal shapes. The methoxy-methyl groups required bond length and angle restraints (1,3-distances) (DFIX 1.37(2) for O–C(sp^2) and O–C(sp^3) 1.42(2) and DANG 2.39(4)). A few methoxy-methyl groups were refined isotropically, as some of the anisotropic displacement parameters were rather unreasonable even with the use of displacement restraints. The difference map and the anisotropic displacement parameters of the *tert*-butyl carbons indicated possible positional disorder. Attempts at

modeling the disorder over several positions were unsuccessful. Given these results it was decided to leave the *tert*-butyl groups modeled in one position with enlarged thermal parameters. Distance and angle restraints have also been placed on the *tert*-butyl groups (DFIX 1.54(2) and DANG 2.68(4)). During refinement, the location of eight of the nine Br^- atoms were determined from the difference map. Two of the Br^-s were modeled as having disorder over two positions, and the third was modeled over three positions. The site occupancy factors of these Br^-s were refined using free variables. Unfortunately, the location of the last extrachannel Br^- was not determined and was likely disordered over many sites. There were several A and B level checkCIF alerts—all of which were attributed to the weakly diffracting data. Several crystals were screened over the course of a few days, and data were collected with the best possible sample using microfocus copper radiation at 100 K. Voids in the crystal packing were likely the largest contributor to the weakly diffracting samples. The large channels are best observed when viewing a packing diagram down the crystallographic *b* axis. The remaining alerts were also attributed to the weakly diffracting data and/or the use of SQUEEZE. Due to the chemical instability of iodopyridiniums in the presence of Br^-, we analyzed X-ray diffractable crystals of **4** by ESI-MS (direct infusion). The predominant ion was most likely $[M\text{-}Br_2]^{2+}$ (Figure 4.48). Given that naked iodononameric *m*-arylene-ethynylene ligands ($[M\text{-}Br_3]^{3+}$) were observed and not any appreciable amount of mono-brominated iodononamer (Figure 4.49), the $[M\text{-}Br_2]^{2+}$ ion was most likely an iodononameric ligand with one Br^- guest. Moreover, we confirmed that bromononamer **1** with even a gross excess of TBABr did not form helicates in solution (Figure 4.50). Therefore, the utilized crystal growth conditions were deemed suitable to form triplex **4** cleanly in the solid

state. CCDC 1852577: these data can be obtained free of charge via https://www.ccdc.cam.ac.uk/structures/.

Crystallographic Data for **UMT_OB12_sq** $C_{80}H_{61}Br_{2.83}I_3N_3O_2$, M = 1703.46, monoclinic, space group *C*2/*c* (no. 15), *a* = 54.427(4) Å, *b* = 36.427(3) Å, *c* = 35.844(3) Å, β = 128.989(2) °, *V* = 55236(7) Å^3, *Z* = 24, *T* = 100 K, μ(CuKα) = 9.728 mm^{-1}, $2\theta_{max}$=73.238 °, 96618 reflections collected, 13220 unique (R_{int} = 0.0939, R_{sigma} = 0.0831), R_1 = 0.0745 ($I > 2\sigma(I)$), wR_2 = 0.2298 (all data).

Table 4.17 Crystal data and structure refinement for Br^- triple helicate **4**.

Identification code	UMT_OB12_sq
Empirical formula	$C_{80}H_{61}Br_{2.83}I_3N_3O_2$
Formula weight	1703.46
Temperature/K	100
Crystal system	monoclinic
Space group	*C*2/*c*
a/Å	54.427(4)
b/Å	36.427(3)
c/Å	35.844(3)
α/°	90
β/°	128.989(2)

γ/°	90
Volume/Å^3	55236(7)
Z	24
ρ_{calc} *g*/cm^3	1.229
μ/mm^{-1}	9.728
F(000)	20068.0
Crystal size/mm^3	0.35 × 0.21 × 0.05
Radiation	CuKα (δ = 1.54178)
2θ range for data collection/°	4.178 to 73.238
Index ranges	$-42 \leq h \leq 42$, $-28 \leq k \leq 27$, $-27 \leq l \leq 27$
Reflections collected	96618
Independent reflections	13220 [R_{int} = 0.0939, R_{sigma} = 0.0831]
Data/restraints/parameters	13220/2178/2208
Goodness-of-fit on F^2	1.023
Final *R* indexes [*I*>=2σ (*I*)]	R_1 = 0.0745, wR_2 = 0.1977
Final *R* indexes [all data]	R_1 = 0.1259, wR_2 = 0.2298
Largest diff. peak/hole / e Å^{-3}	1.48/-0.50

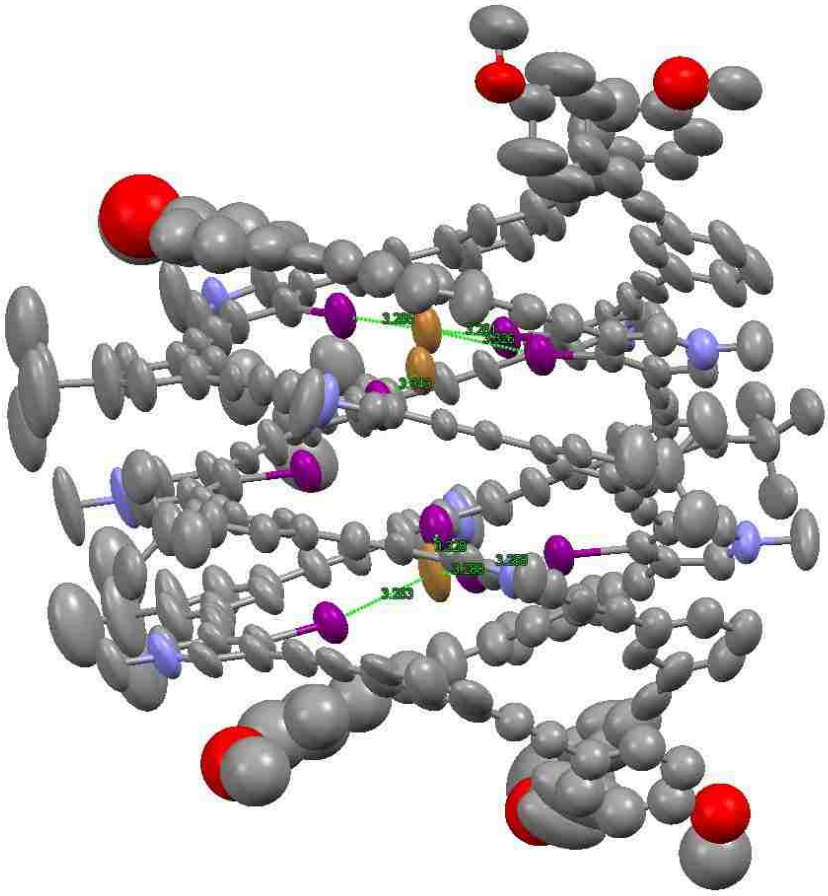

Figure 4.46 Side-view thermal ellipsoidal representation of **4** (at 50 % probability; hydrogen atoms not shown for clarity; positionally disordered intrachannel Br^{-}, 80:20, top). Overall, the intrachannel Br^{-}s favor closer and more linear contacts in comparison to the intrachannel I^{-}s of **2**—even at the expense of pseudo-square-planar coordination (see positionally disordered Br^{-}, top).

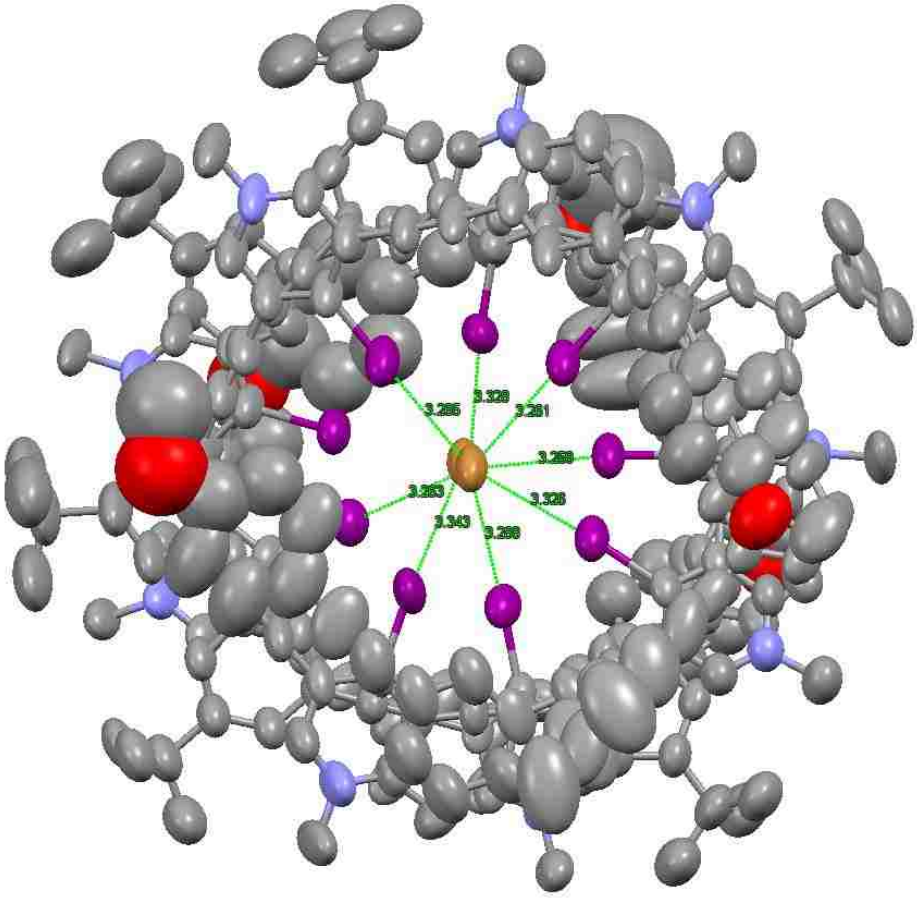

Figure 4.47 Top-view thermal ellipsoidal representation of **4** (at 50 % probability; hydrogen atoms not shown for clarity).

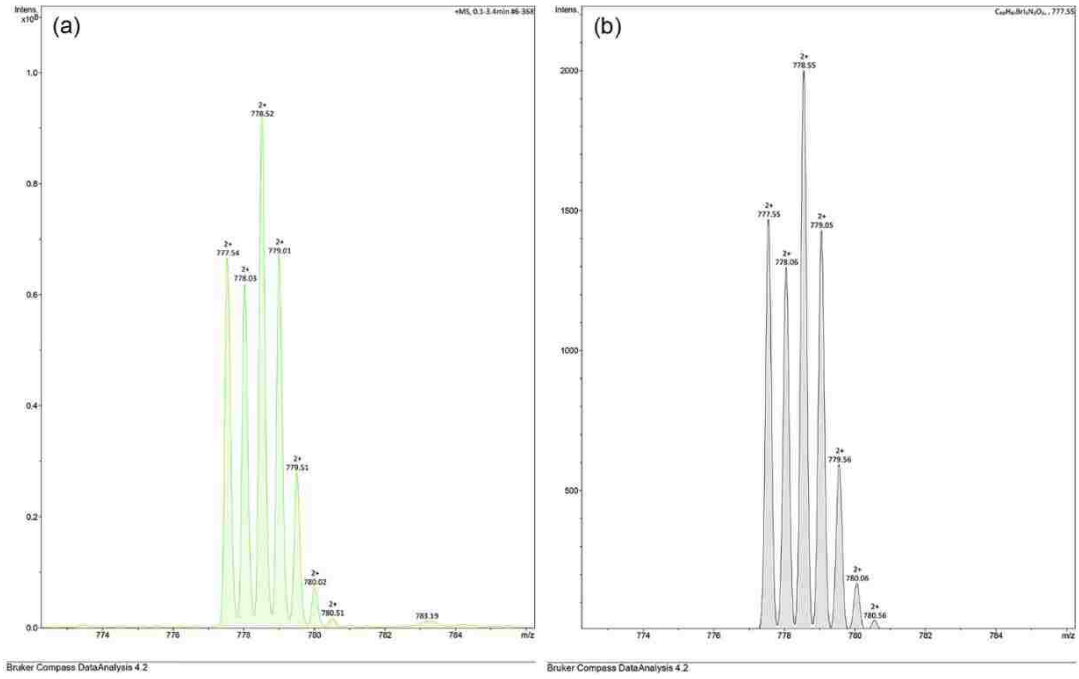

Figure 4.48 (a) ESI mass spectrum of **4** from the sample used for single crystal X-ray diffraction, $[M\text{-}Br_2]^{2+}$; (b) simulated isotopic distribution of $C_{80}H_{61}BrI_3N_3O_2^{2+}$.

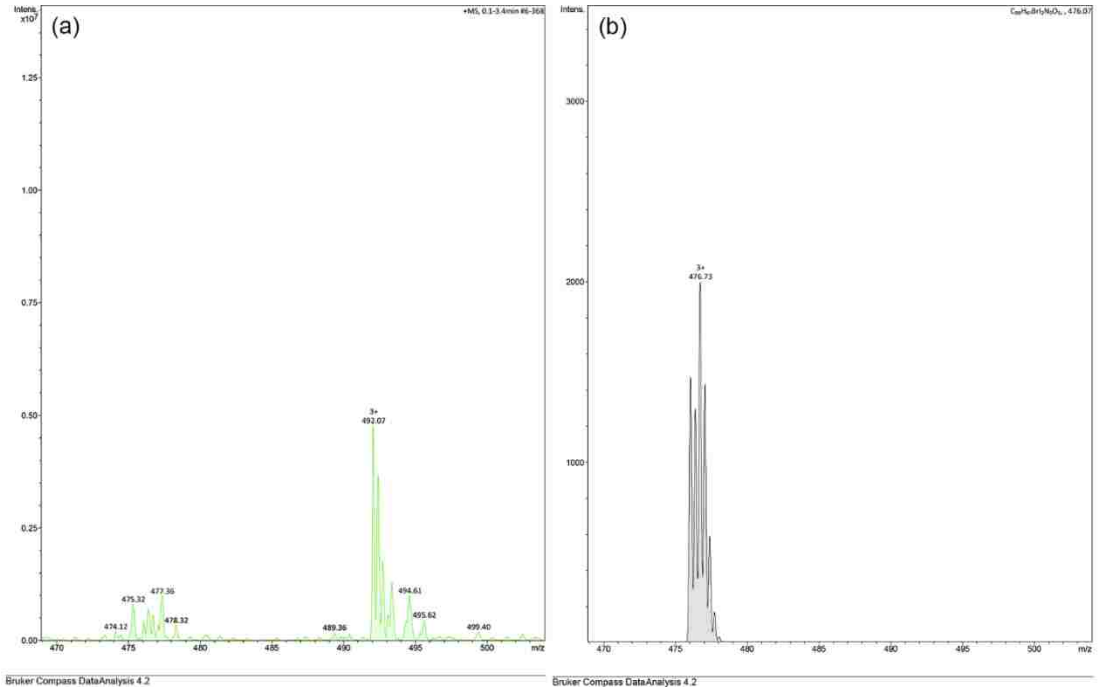

Figure 4.49 (a) ESI mass spectrum of **4** from the sample used for single crystal X-ray diffraction, $[M\text{-}Br_3]^{3+}$; (b) simulated isotopic distribution of $C_{80}H_{61}BrI_2N_3O_2^{3+}$ (mono-brominated iodononameric *m*-arylene-ethynylene ligand) demonstrating the chemical integrity of the solid-state iodononameric *m*-arylene-ethynylene ligands.

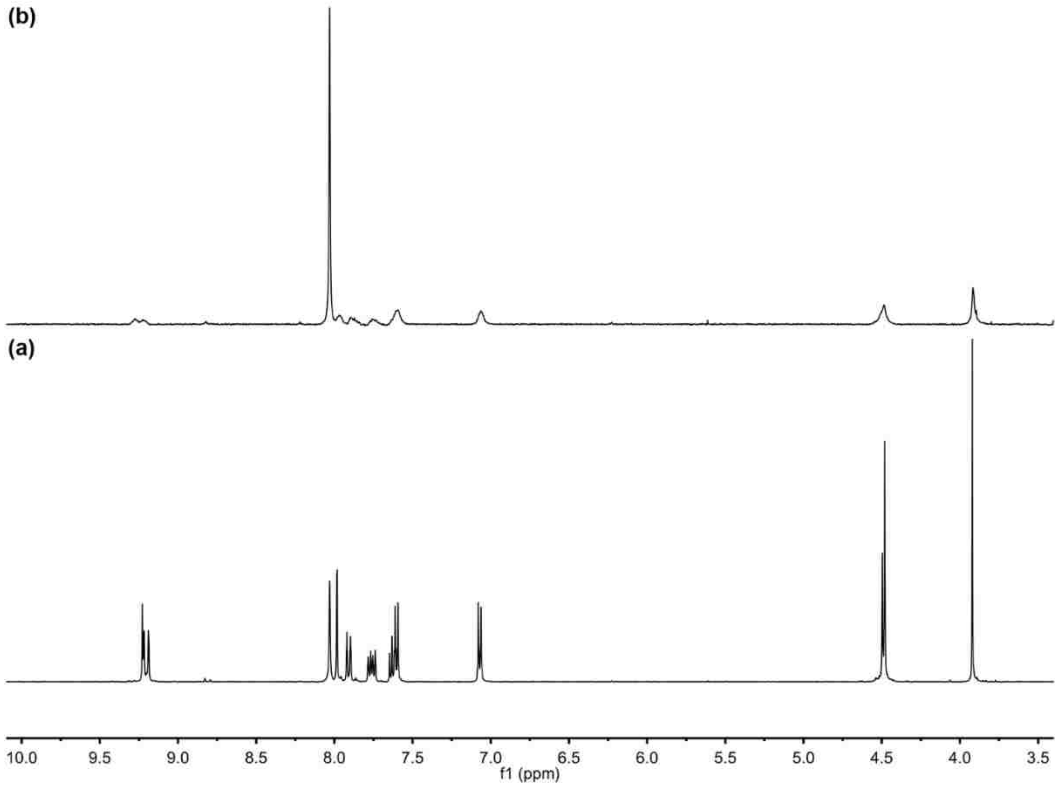

Figure 4.50 (a) Partial ^{1}H NMR spectrum of **1**; (b) partial ^{1}H NMR spectrum of the same sample upon adding excess TBABr. (a–b) 500 MHz, 1:3 *v*/*v* DMF-d_7-CD_3CN.

4.4.3 Solution-Phase Data

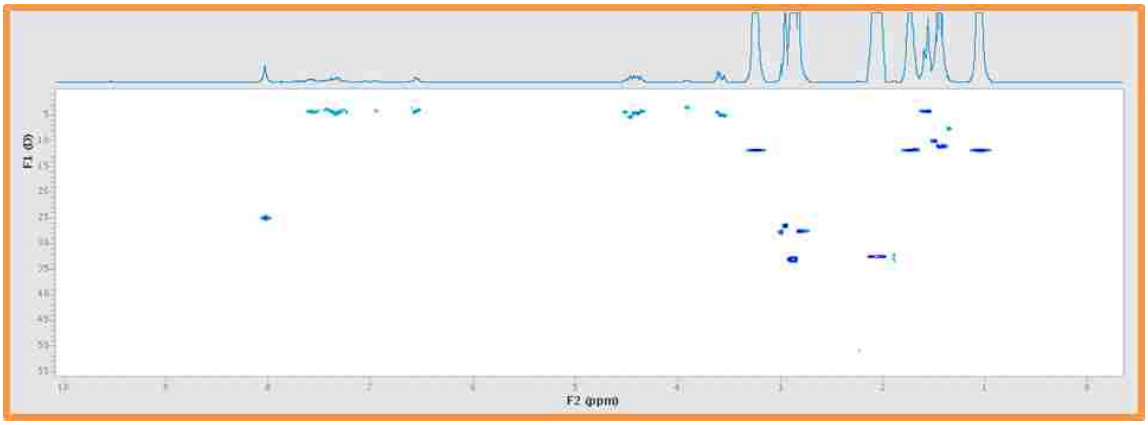

Figure 4.51 2D DOSY NMR spectrum of **4** (400 MHz, 298 K, 1:3 *v*/*v* DMF-d_7-CD_3CN, 1.0 mM ligand with three ligand equivalents of TBABr).

Table 4.18 Individual D_ts calculated for peaks of **4**, the lower-order species, and residual CH_3CN (400 MHz, 298 K, 1:3 *v*/*v* DMF-d_7-CD_3CN, 1.0 mM ligand with three ligand equivalents of TBABr).

Species	Frequency (ppm)	Amplitude	D_t x10E-10(m^2/s)	Standard Error	Mean D_t of 4 (m^2/s)
Helicate **4**	7.5916	5.7803	4.0	0.1771	4.1(4)
Helicate **4**	7.5649	4.4101	4.1	0.1679	
Helicate **4**	7.4217	4.0416	3.7	0.1984	
Helicate **4**	7.3886	4.6319	3.8	0.1786	
Helicate **4**	7.3753	5.4875	4.1	0.1480	
Helicate **4**	7.3448	5.9856	4.4	0.1811	

Helicate **4**	7.3244	7.0143	4.2	0.1420
Helicate **4**	7.3034	4.7616	3.9	0.1704
Helicate **4**	6.5584	5.9784	4.0	0.1271
Helicate **4**	6.5368	5.4056	3.7	0.1513
Helicate **4**	4.5145	4.6983	4.1	0.1937
Helicate **4**	4.4623	7.6367	5.1	0.1152
Helicate **4**	4.4267	8.5402	4.2	0.1044
Helicate **4**	4.3949	7.745	4.3	0.1210
Helicate **4**	4.3611	7.5811	3.9	0.1170
Helicate **4**	3.6085	9.9755	4.1	0.0762
Helicate **4**	3.5882	10.2	4.6	0.0749
Helicate **4**	3.5462	8.147	4.8	0.1122
Helicate **4**	1.5938	26.5427	3.9	0.0272
Helicate **4**	1.5557	50.5618	4.0	0.0202
Lower-order species	3.9171	4.374	3.1	0.2070
CH_3CN	2.0614	1900.1108	32.4	0.0163

Table 4.19 Normalized D_ts of **4** and the lower-order species (400 MHz, 298 K, 1:3 *v*/*v* DMF-d_7-CD_3CN, 1.0 mM ligand with three ligand equivalents of TBABr).

Species	Normalized D_t (m^2/s)	Mean Normalized D_t of 4 (m^2/s)
Helicate **4**	0.12	0.13(1)
Helicate **4**	0.13	
Helicate **4**	0.11	
Helicate **4**	0.12	
Helicate **4**	0.13	
Helicate **4**	0.14	
Helicate **4**	0.13	
Helicate **4**	0.12	
Helicate **4**	0.12	
Helicate **4**	0.11	
Helicate **4**	0.13	
Helicate **4**	0.16	
Helicate **4**	0.13	
Helicate **4**	0.13	
Helicate **4**	0.12	
Helicate **4**	0.13	
Helicate **4**	0.14	
Helicate **4**	0.15	

Helicate **4**	0.12
Helicate **4**	0.12
Lower-order species	0.10

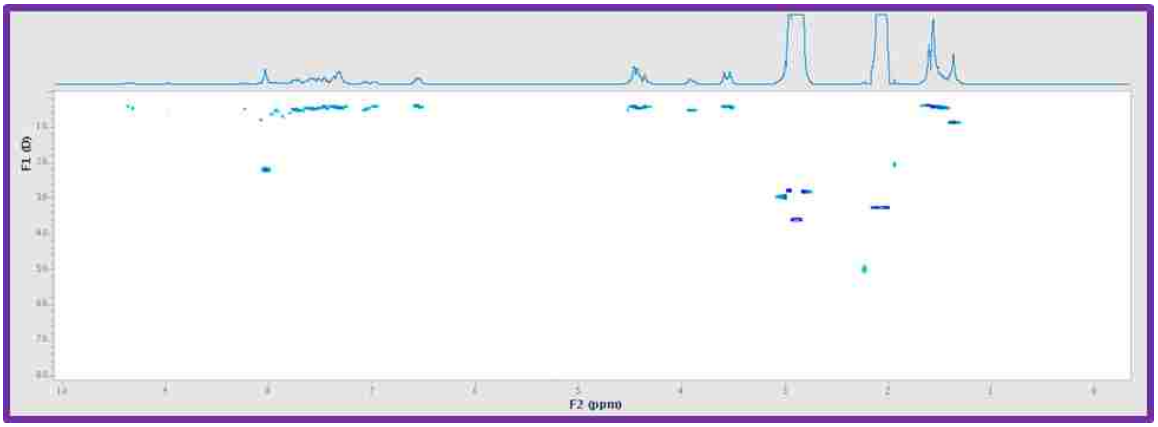

Figure 4.52 2D DOSY NMR spectrum of **2** (400 MHz, 298 K, 1:3 *v*/*v* DMF-d_7-CD_3CN, 1.0 mM ligand with three ligand equivalents I^-).

Table 4.20 Individual D_ts calculated for peaks of **2**, the lower-order species, and residual CH_3CN (400 MHz, 298 K, 1:3 v/v DMF-d7-CD3CN, 1.0 mM ligand with three ligand equivalents I^-).

Species	Frequency (ppm)	Amplitude	D_t x10E-10 (m^2/s)	Standard Error	Mean D_t of 2 (m^2/s)
Helicate **2**	7.7373	14.2316	4.5	0.1506	4.0(3)
Helicate **2**	7.7106	13.244	4.8	0.1548	
Helicate **2**	7.5859	17.2968	4.3	0.0674	
Helicate **2**	7.563	15.5081	4.4	0.1308	
Helicate **2**	7.5427	11.0482	4.5	0.1914	
Helicate **2**	7.5153	15.2783	4.2	0.1257	
Helicate **2**	7.4892	10.9362	3.8	0.1979	
Helicate **2**	7.4568	17.4579	3.9	0.1132	
Helicate **2**	7.4371	13.9197	4.3	0.1308	
Helicate **2**	7.3824	13.9395	3.7	0.1328	
Helicate **2**	7.3613	21.3233	3.9	0.1029	
Helicate **2**	7.3105	29.7513	4.0	0.0610	
Helicate **2**	7.2558	8.835	3.6	0.1705	
Helicate **2**	6.5865	10.1211	3.4	0.1707	
Helicate **2**	6.5636	16.1167	3.6	0.1059	
Helicate **2**	6.5439	17.1351	3.9	0.0997	
Helicate **2**	4.4585	37.5849	3.7	0.0543	
Helicate **2**	4.4464	36.4557	4.0	0.0370	

Helicate **2**	4.4255	31.5694	4.1	0.0652
Helicate **2**	4.3765	9.9482	4.0	0.1920
Helicate **2**	4.3529	22.1326	3.9	0.0904
Helicate **2**	3.5845	24.4818	3.8	0.0748
Helicate **2**	3.5323	27.9715	3.7	0.0671
Helicate **2**	3.517	28.395	4.0	0.0697
Helicate **2**	1.6028	78.1012	3.6	0.0307
Helicate **2**	1.5627	125.1848	3.7	0.0180
Helicate **2**	1.5105	35.7157	3.9	0.0449
Lower-order species	3.9095	13.4116	4.8	0.1382
CH_3CN	2.0634	4441.3753	32.3	0.0154

Table 4.21 Normalized D_ts of **2** and the lower-order species (400 MHz, 298 K, 1:3 *v*/*v* DMF-d_7-CD_3CN, 1.0 mM ligand with three ligand equivalents I^-).

Species	Normalized D_t (m^2/s)	Mean Normalized D_t of 2 (m^2/s)
Helicate **2**	0.14	0.12(1)
Helicate **2**	0.15	
Helicate **2**	0.13	
Helicate **2**	0.14	
Helicate **2**	0.14	
Helicate **2**	0.13	
Helicate **2**	0.12	
Helicate **2**	0.12	
Helicate **2**	0.13	
Helicate **2**	0.12	
Helicate **2**	0.12	
Helicate **2**	0.12	
Helicate **2**	0.11	
Helicate **2**	0.11	
Helicate **2**	0.11	
Helicate **2**	0.12	
Helicate **2**	0.12	
Helicate **2**	0.12	
Helicate **2**	0.13	

Helicate **2**	0.12
Helicate **2**	0.12
Helicate **2**	0.12
Helicate **2**	0.12
Helicate **2**	0.12
Helicate **2**	0.11
Helicate **2**	0.12
Helicate **2**	0.12
Lower-order species	0.15

T_1 Relaxation Studies

2 with Three Ligand Equivalents of TBAI

index	freq(ppm)	intensity
1	3.80675	30.1117
2	3.48475	64.4234
3	3.42896	70.6621
4	3.41526	70.3635

Exponential data analysis:

peak	T_1	error
1	1.633	0.0902
2	1.246	0.04579
3	1.331	0.05728
4	1.231	0.05894

peak number 1

T_1 = 1.63 error = 0.0902

time	observed	calculated	difference
0.0625	-28.8	-28.7	-0.1
0.125	-26.1	-26.5	0.388
0.25	-22.1	-22.3	0.202
0.5	-15.7	-14.8	-0.855
1	-3.34	-2.89	-0.451
2	14.4	12.4	2

4	23.4	25.1	-1.77
8	29	30	-0.921
16	32.3	30.4	1.89
32	30.1	30.4	-0.319

peak number 2

T_1 = 1.25 error = 0.0458

time	observed	calculated	difference
0.0625	-63	-62.6	-0.397
0.125	-55.6	-56.2	0.585
0.25	-45.4	-44.4	-1.04
0.5	-23.2	-23.9	0.739
1	7.11	6.43	0.677
2	39.9	40.4	-0.522
4	61.4	62.4	-1.04
8	70.4	67.8	2.64
16	70.1	68	2.07
32	64.4	68	-3.56

peak number 3

T_1 = 1.33 error = 0.0573

time	observed	calculated	difference
0.0625	-67.8	-66.9	-0.937
0.125	-61.3	-60.5	-0.886
0.25	-47.4	-48.5	1.04
0.5	-27	-27.6	0.571
1	5.55	4.06	1.49
2	40.1	40.7	-0.594
4	62.9	66.2	-3.31
8	74.5	73.1	1.41
16	77.7	73.5	4.2
32	70.7	73.5	-2.8

peak number 4

T_1 = 1.23 error = 0.0589

time	observed	calculated	difference
0.0625	-66.5	-67.3	0.841
0.125	-61	-60.2	-0.775
0.25	-47.6	-47	-0.558
0.5	-24.1	-24.4	0.287
1	9.51	9.21	0.301
2	46.4	46.5	-0.0842
4	70.1	70.4	-0.302
8	78.8	76	2.82
16	79.8	76.3	3.53
32	70.4	76.3	-5.9

2 with Three Ligand Equivalents of TBABr

index	freq(ppm)	intensity
1	3.80969	44.6667
2	3.50335	101.208
3	3.47203	91.9189
4	3.43581	94.8113

Exponential data analysis:

peak	T_1	error
1	1.549	0.07176
2	1.192	0.01978
3	1.234	0.04317
4	1.153	0.03089

peak number 1

T_1 = 1.55 error = 0.0718

time	observed	calculated	difference
0.0625	-41.3	-42.5	1.19
0.125	-39.8	-39	-0.795
0.25	-32.7	-32.4	-0.291
0.5	-20.7	-20.8	0.151
1	-4.33	-2.54	-1.79
2	23.2	20.3	2.9
4	36.5	38.5	-2.07
8	45.5	44.9	0.625
16	46.4	45.4	0.936
32	44.7	45.4	-0.767

peak number 2

T_1 = 1.19 error = 0.0198

time	observed	calculated	difference
0.0625	-96.3	-93.8	-2.51
0.125	-82.3	-83.8	1.52
0.25	-63.8	-65.3	1.52
0.5	-33.8	-33.7	-0.196
1	12.8	12.8	-0.0168
2	62.8	63.4	-0.597
4	94.7	94.8	-0.0632
8	102	102	0.375
16	103	102	0.864
32	101	102	-0.777

peak number 3

T_1 = 1.23 error = 0.0432

time	observed	calculated	difference

0.0625	-89.4	-87.2	-2.25
0.125	-79.5	-78.3	-1.26
0.25	-58.8	-61.8	2.93
0.5	-31.5	-33.4	1.87
1	8.39	8.68	-0.295
2	54.3	55.5	-1.13
4	83.8	85.6	-1.76
8	91.2	92.7	-1.47
16	97.6	93	4.63
32	91.9	93	-1.05

peak number 4

T_1 = 1.15 error = 0.0309

time	observed	calculated	difference
0.0625	-88.5	-88.3	-0.164
0.125	-80.3	-78.8	-1.55
0.25	-60	-61.2	1.15
0.5	-31.1	-31.2	0.0271
1	14.6	12.4	2.22
2	57.4	59	-1.55
4	83.5	86.7	-3.24
8	92.1	92.5	-0.388
16	94.1	92.7	1.45
32	94.8	92.7	2.14

2 at 25 °C (Methoxy-Methyl Protons)

index	freq(ppm)	intensity
1	3.81016	29.8061
2	3.48529	168.474
3	3.43343	146.527
4	3.4168	168.833

Exponential data analysis:

peak	T_1	error
1	1.239	0.1902
2	1.419	0.03052
3	1.382	0.03845
4	1.362	0.02482

peak number 1

T_1 = 1.24 error = 0.19

time	observed	calculated	difference
0.0625	-19.3	-20.9	1.56
0.125	-20.2	-18.5	-1.75
0.25	-13.1	-14	0.911
0.5	-7.51	-6.29	-1.22

1	3.78	5.13	-1.35
2	22.4	17.9	4.53
4	21	26.1	-5.1
8	26.4	28	-1.67
16	30.5	28.1	2.43
32	29.8	28.1	1.7

peak number 2

T_1 = 1.42 error = 0.0305

time	observed	calculated	difference
0.0625	-124	-124	-0.518
0.125	-111	-111	0.575
0.25	-90.4	-87.6	-2.77
0.5	-44.7	-46.3	1.53
1	21.9	17.5	4.38
2	90.1	93.9	-3.8
4	149	150	-1.03
8	168	167	0.252
16	170	168	1.54
32	168	168	-0.00436

peak number 3

T_1 = 1.38 error = 0.0384

time	observed	calculated	difference
0.0625	-108	-111	2.14
0.125	-100	-99.1	-1.17
0.25	-81.1	-77.6	-3.53
0.5	-37.8	-40.1	2.23
1	19.2	17.4	1.77
2	82.7	85.3	-2.57
4	136	134	1.29
8	153	148	4.31
16	148	149	-1.46
32	147	149	-2.74

peak number 4

T_1 = 1.36 error = 0.0248

time	observed	calculated	difference
0.0625	-121	-119	-1.88
0.125	-103	-106	3.16
0.25	-81.3	-81.7	0.375
0.5	-42.2	-39.3	-2.91
1	26.3	25.4	0.951
2	102	101	0.608
4	155	155	-0.274
8	172	170	2.2

16	171	171	0.283
32	169	171	-2.33

2 at 25 °C (Pyridinium Protons)

index	freq(ppm)	intensity
1	9.41218	15.6079
2	9.27519	25.2248
3	9.24192	33.7601
4	9.05502	13.0513
5	8.87497	18.6961

Exponential data analysis:

peak	T_1	error
1	1.865	0.5867
2	3.532	0.6433
3	2.535	0.2175
4	1.9	0.4703
5	2.451	0.3629

peak number 1

T_1 = 1.86 error = 0.587

time	observed	calculated	difference
0.0625	-11.4	-9.23	-2.17
0.125	-6.78	-8.55	1.77
0.25	-5.54	-7.25	1.71
0.5	-6.16	-4.89	-1.27
1	-2.46	-1.03	-1.43
2	7.02	4.18	2.84
4	7.3	9.01	-1.71
8	9.75	11.2	-1.48
16	9.2	11.5	-2.32
32	15.6	11.5	4.09

peak number 2

T_1 = 3.53 error = 0.643

time	observed	calculated	difference
0.0625	-9.97	-11.7	1.76
0.125	-10.5	-11.1	0.583
0.25	-9.79	-9.91	0.12
0.5	-10.3	-7.63	-2.65
1	-6.53	-3.52	-3.01
2	6.42	3.14	3.28
4	13.6	11.9	1.66
8	16.9	19.8	-2.82
16	22.4	23.1	-0.657
32	25.2	23.5	1.74

peak number 3

T_1 = 2.53 error = 0.217

time	observed	calculated	difference
0.0625	-26	-26.5	0.444
0.125	-25	-25.1	0.0933
0.25	-21.7	-22.3	0.576
0.5	-16.8	-17.1	0.277
1	-11.8	-8.21	-3.63
2	7.29	5.12	2.17
4	21.7	20.1	1.55
8	27.4	30.1	-2.72
16	32.9	32.5	0.345
32	33.8	32.7	1.11

peak number 4

T_1 = 1.9 error = 0.47

time	observed	calculated	difference
0.0625	-10.1	-8.01	-2.08
0.125	-6.48	-7.38	0.9
0.25	-2.96	-6.19	3.23
0.5	-5.59	-4.02	-1.57
1	-1.85	-0.462	-1.39
2	5.69	4.38	1.31
4	8.95	8.93	0.0233
8	10.7	11.1	-0.378
16	9.91	11.4	-1.45
32	13.1	11.4	1.68

peak number 5

T_1 = 2.45 error = 0.363

time	observed	calculated	difference
0.0625	-12.8	-11.2	-1.59
0.125	-9.77	-10.5	0.694
0.25	-9.65	-9.02	-0.626
0.5	-4.91	-6.36	1.45
1	-2.2	-1.77	-0.426
2	7.64	5.01	2.63
4	9.64	12.5	-2.88
8	16.9	17.3	-0.464
16	19.5	18.4	1.09
32	18.7	18.5	0.222

2 at 40 °C (Methoxy-Methyl Protons)

index	freq(ppm)	intensity
1	3.81799	45.8089

2	3.50584	180.791
3	3.45496	187.612
4	3.43147	194.451

Exponential data analysis:

peak	T_1	error
1	1.743	0.1394
2	1.538	0.02753
3	1.64	0.04206
4	1.447	0.04483

peak number 1

T_1 = 1.74 error = 0.139

time	observed	calculated	difference
0.0125	-43.2	-41.3	-1.91
0.025	-43.6	-40.6	-2.98
0.05	-39.8	-39.4	-0.378
0.1	-37.4	-36.9	-0.433
0.2	-26.9	-32.2	5.32
0.4	-20.4	-23.6	3.23
0.8	-11.1	-9.03	-2.03
1.6	10.3	11.8	-1.45
3.2	34.6	33.2	1.43
6.4	42	45.1	-3.15
12.8	52.7	47.4	5.32
25.6	46.4	47.4	-1.04
51.2	45.8	47.4	-1.6

peak number 2

T_1 = 1.54 error = 0.0275

time	observed	calculated	difference
0.0125	-164	-162	-2.24
0.025	-164	-159	-5.02
0.05	-152	-153	1.93
0.1	-142	-143	0.787
0.2	-119	-123	3.82
0.4	-83.8	-85.8	2
0.8	-24.9	-25.1	0.216
1.6	56.8	57.7	-0.947
3.2	135	136	-1.13
6.4	171	174	-3.24
12.8	182	179	2.7
25.6	179	179	-0.272
51.2	181	179	1.65

peak number 3

T_1 = 1.64 error = 0.0421

time	observed	calculated	difference
0.0125	-170	-165	-4.47
0.025	-169	-163	-6.7
0.05	-154	-157	3.82
0.1	-145	-147	1.99
0.2	-121	-128	6.22
0.4	-92.1	-91.8	-0.299
0.8	-30.7	-32.1	1.39
1.6	49.9	51.4	-1.47
3.2	134	134	-0.462
6.4	172	177	-4.81
12.8	184	184	0.164
25.6	186	184	1.42
51.2	188	184	3.46

peak number 4

T_1 = 1.45 error = 0.0448

time	observed	calculated	difference
0.0125	-177	-175	-2.23
0.025	-171	-172	0.534
0.05	-166	-166	-0.628
0.1	-161	-153	-7.8
0.2	-126	-130	4.78
0.4	-83.3	-88.5	5.18
0.8	-15.4	-20.3	4.96
1.6	67.6	70.5	-2.93
3.2	148	153	-4.5
6.4	182	189	-7.08
12.8	197	194	3.86
25.6	199	194	5.59
51.2	194	194	0.765

2 at 40 °C (Pyridinium Protons)

index	freq(ppm)	intensity
1	9.45915	8.93813
2	9.33488	14.1698
3	9.29378	19.1759
4	9.11569	8.13869
5	8.92488	11.3711

Exponential data analysis:

peak	T_1	error
1	2.026	0.3281
2	2.334	0.2134

3	2.923	0.5499
4	2.084	0.2743
5	1.999	0.1421

peak number 1

T_1 = 2.03 error = 0.328

time	observed	calculated	difference
0.0125	-3.39	-4.59	1.2
0.025	-4.31	-4.51	0.204
0.05	-4.46	-4.37	-0.0947
0.1	-5.12	-4.07	-1.05
0.2	-3.33	-3.51	0.179
0.4	-3.4	-2.46	-0.939
0.8	-0.96	-0.652	-0.308
1.6	3.08	2.05	1.03
3.2	5.11	5.1	0.00907
6.4	6.51	7.11	-0.603
12.8	6.6	7.61	-1.01
25.6	7.68	7.63	0.0451
51.2	8.94	7.63	1.31

peak number 2

T_1 = 2.33 error = 0.213

time	observed	calculated	difference
0.0125	-11.6	-11.5	-0.126
0.025	-10.7	-11.3	0.611
0.05	-9.94	-11.1	1.14
0.1	-10.1	-10.6	0.416
0.2	-11.1	-9.55	-1.59
0.4	-8.31	-7.66	-0.653
0.8	-5.08	-4.33	-0.752
1.6	1.76	0.84	0.92
3.2	7.68	7.11	0.568
6.4	11	11.9	-0.846
12.8	14.4	13.4	1.01
25.6	12.2	13.5	-1.24
51.2	14.2	13.5	0.687

peak number 3

T_1 = 2.92 error = 0.55

time	observed	calculated	difference
0.0125	-6.58	-10.2	3.58
0.025	-7.57	-10	2.47
0.05	-8.26	-9.78	1.52
0.1	-9.8	-9.29	-0.513

0.2	-12.5	-8.32	-4.16
0.4	-9.66	-6.47	-3.19
0.8	-5.03	-3.14	-1.89
1.6	2.21	2.29	-0.0837
3.2	11.9	9.57	2.36
6.4	16.7	16.2	0.448
12.8	20.1	19.2	0.929
25.6	18.4	19.6	-1.18
51.2	19.2	19.6	-0.385

peak number 4

T_1 = 2.08 error = 0.274

time	observed	calculated	difference
0.0125	-6.3	-7.24	0.939
0.025	-6.57	-7.14	0.572
0.05	-6.89	-6.95	0.0579
0.1	-6.43	-6.57	0.137
0.2	-6.5	-5.83	-0.668
0.4	-5.96	-4.46	-1.5
0.8	-2.23	-2.09	-0.137
1.6	1.47	1.48	-0.0101
3.2	6.5	5.57	0.927
6.4	8.57	8.35	0.216
12.8	8.03	9.08	-1.05
25.6	10.7	9.12	1.54
51.2	8.14	9.12	-0.978

peak number 5

T_1 = 2 error = 0.142

time	observed	calculated	difference
0.0125	-9.48	-10.5	0.986
0.025	-10.1	-10.3	0.197
0.05	-10.5	-10.1	-0.428
0.1	-9.17	-9.51	0.341
0.2	-9.22	-8.47	-0.752
0.4	-7.53	-6.53	-0.997
0.8	-2.6	-3.2	0.599
1.6	1.42	1.77	-0.345
3.2	8.15	7.32	0.828
6.4	10.3	10.9	-0.649
12.8	12.4	11.8	0.594
25.6	12	11.9	0.146
51.2	11.4	11.9	-0.484

2 at 60 °C (Methoxy-Methyl Protons)

index	freq(ppm)	intensity
1	3.82875	35.2539
2	3.53031	135.208
3	3.48236	127.124
4	3.45202	131.734

Exponential data analysis:

peak	T_1	error
1	2.513	0.265
2	1.865	0.05232
3	1.951	0.06811
4	1.937	0.04222

peak number 1

T_1 = 2.51 error = 0.265

time	observed	calculated	difference
0.0625	-29.4	-30.3	0.82
0.125	-26.3	-28.6	2.3
0.25	-25.4	-25.4	0.0189
0.5	-23.5	-19.4	-4.1
1	-11	-9.11	-1.86
2	10.3	6.24	4.06
4	22.6	23.5	-0.915
8	34	34.8	-0.721
16	40.6	37.5	3.08
32	35.2	37.6	-2.4

peak number 2

T_1 = 1.87 error = 0.0523

time	observed	calculated	difference
0.0625	-111	-112	0.756
0.125	-102	-104	1.27
0.25	-86.6	-88	1.4
0.5	-62	-59.6	-2.36
1	-17.2	-13.1	-4.07
2	51.8	49.7	2.1
4	110	108	2.27
8	138	135	3.43
16	137	138	-1.58
32	135	138	-2.94

peak number 3

T_1 = 1.95 error = 0.0681

time	observed	calculated	difference

0.0625	-103	-107	4.25
0.125	-102	-99.6	-2.45
0.25	-84.3	-85.2	0.944
0.5	-61.6	-59.1	-2.51
1	-18.1	-15.8	-2.31
2	44.4	43.6	0.857
4	103	100	2.21
8	132	128	3.75
16	133	132	0.642
32	127	132	-5.15

peak number 4

T_1 = 1.94 error = 0.0422

time	observed	calculated	difference
0.0625	-103	-104	0.87
0.125	-94.8	-96.1	1.26
0.25	-84.2	-81.6	-2.55
0.5	-54.3	-55.3	0.983
1	-13.2	-11.9	-1.3
2	47.9	47.5	0.38
4	105	104	0.578
8	133	131	1.86
16	137	135	1.78
32	132	135	-3.71

2 at 60 °C (pyridinium protons)

index	freq(ppm)	intensity
1	9.49927	26.7654
2	9.38772	35.903
3	9.33488	47.1783
4	9.17832	30.9242
5	8.97968	33.0298

Exponential data analysis:

peak	T_1	error
1	2.004	0.3596
2	2.345	0.3229
3	2.655	0.4444
4	1.925	0.2476
5	1.853	0.2234

peak number 1

T_1 = 2 error = 0.36

time	observed	calculated	difference
0.0625	-14.6	-17.3	2.65
0.125	-17.3	-15.9	-1.36

0.25	-15.4	-13.3	-2.13
0.5	-5.78	-8.47	2.69
1	-5.44	-0.489	-4.95
2	14.7	10.6	4.14
4	21	21.4	-0.4
8	24.4	26.8	-2.4
16	30.5	27.7	2.78
32	26.8	27.7	-0.917

peak number 2

T_1 = 2.35 error = 0.323

time	observed	calculated	difference
0.0625	-18.8	-21.9	3.13
0.125	-18.4	-20.4	1.99
0.25	-21.6	-17.5	-4.11
0.5	-15	-12	-2.92
1	-3.76	-2.79	-0.974
2	15.9	10.7	5.12
4	22.6	25.3	-2.7
8	34.2	34.2	0.00343
16	36.9	36.1	0.839
32	35.9	36.2	-0.256

peak number 3

T_1 = 2.66 error = 0.444

time	observed	calculated	difference
0.0625	-13.7	-21	7.29
0.125	-20.6	-19.4	-1.17
0.25	-19.5	-16.4	-3.12
0.5	-14.5	-10.8	-3.65
1	-5.73	-1.09	-4.64
2	18.9	13.7	5.25
4	32.5	30.7	1.78
8	39.2	42.5	-3.37
16	46	45.7	0.249
32	47.2	45.9	1.27

peak number 4

T_1 = 1.93 error = 0.248

time	observed	calculated	difference
0.0625	-21.1	-21.8	0.625
0.125	-20.1	-20.1	0.0218
0.25	-15.1	-17	1.89
0.5	-13.9	-11.3	-2.57
1	-4.95	-1.92	-3.03
2	15.8	10.9	4.95

4	20.9	23	-2.2
8	29.2	28.9	0.331
16	28.6	29.7	-1.05
32	30.9	29.7	1.22

peak number 5

T_1 = 1.85 error = 0.223

time	observed	calculated	difference
0.0625	-31.9	-28	-3.89
0.125	-22.9	-26	3.13
0.25	-20	-22.1	2.13
0.5	-15.9	-15.2	-0.686
1	-6.18	-3.79	-2.39
2	15.1	11.6	3.56
4	23.5	25.7	-2.23
8	30.1	32.2	-2.04
16	35.6	33	2.59
32	33	33	0.0226

4.4.4 Gas-Phase Data

Due to its chemical sensitivity at low concentrations, we directly infused a solution of 4 in 1:1 *v*/*v* EtOH-CH_3CN. Only the $[M\text{-}Br_2]^{2+}$ and $[M\text{-}Br_3]^{3+}$ species ionized, which is unsurprising due to the concentration dependence of triple helicate self-assembly.

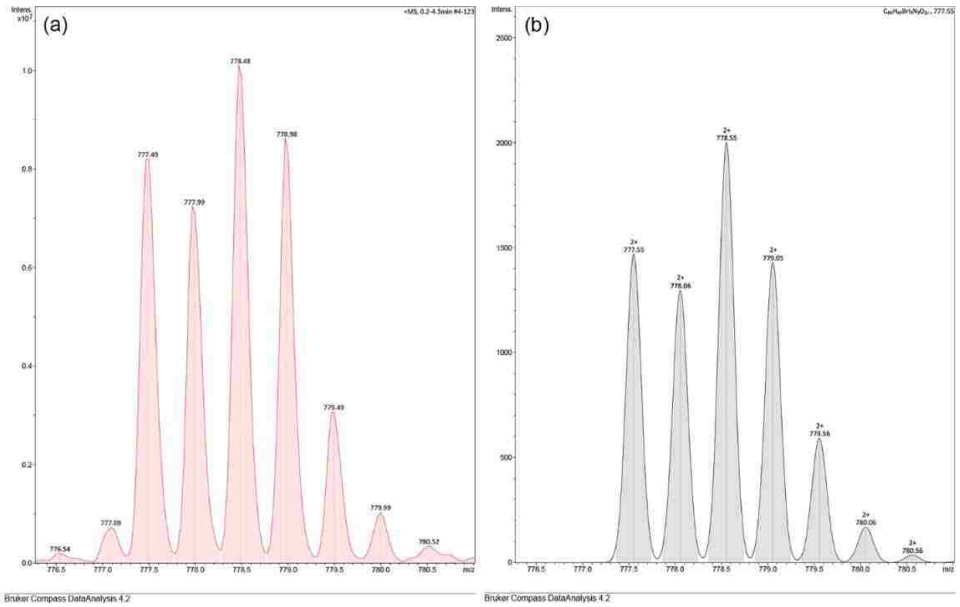

Figure 4.53 (a) ESI mass spectrum of **4**, $[M\text{-}Br_2]^{2+}$; (b) simulated isotopic distribution of $C_{80}H_{61}BrI_3N_3O_2^{2+}$.

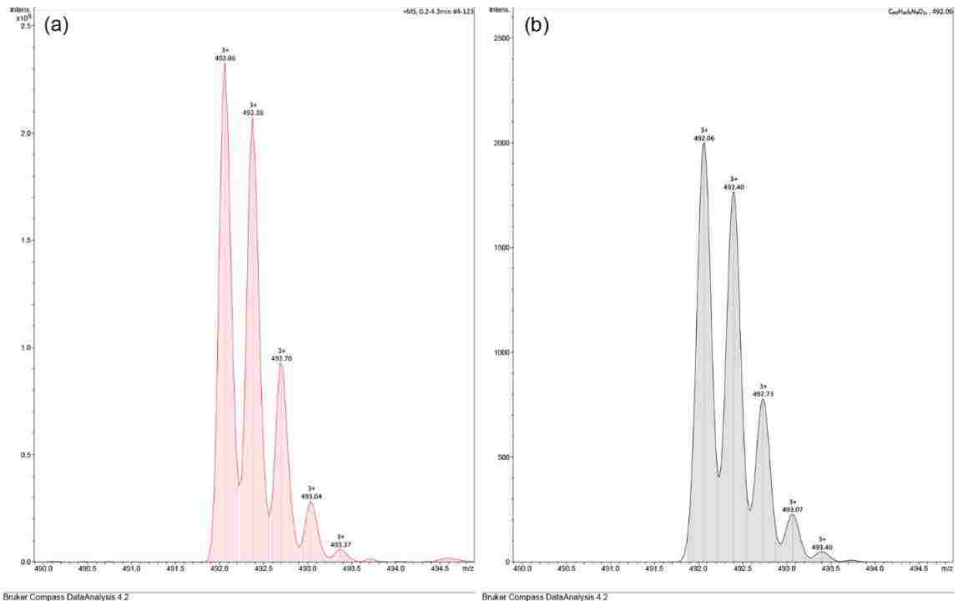

Figure 4.54 (a) ESI mass spectrum of **4**, $[M\text{-}Br_3]^{3+}$; (b) simulated isotopic distribution of $C_{80}H_{61}I_3N_3O_2^{3+}$.

4.5 Conclusion

In conclusion, we have elucidated the ligand and guest dynamics for a new class of halogen-bonding triple helicates. The triplex encapsulated both I^-, Br^-, and mixtures of both halide ions. Employing ^1H 2D EXSY NMR, we discovered the remarkably long lifetimes of the triplex ligands and found that they exchanged through an associative process. In contrast, stopped-flow visible spectroscopy evidenced millisecond-or-faster intrachannel anion exchange. With ^1H qNMR spectroscopy, we established that helicate stability favored larger halide ion ($Br^- \approx I^- >> Cl^-$). The biological and environmental relevance of anions and the previous lack of kinetic data on anion helicates underscores the importance of halogen bonding as a powerful strategy to create long-lived helical containers that facilitate rapid anion movement.

5 Concluding Remarks and Future Projects

The development of anion helicates is an exciting field with a bright future. Given the environmental and biological importance of anions as well as the myriad, life-enabling functions molecular helices provide, it seems highly likely that anion helicates/foldamers will become key players in future abiotic macromolecules. Through the imitation of natural biopolymers, supramolecular chemists have sought to introduce new building blocks, thereby creating structures with new functionality. This field is still in its infancy, and the challenges related to the long syntheses required to create new oligomers will need to be addressed. But as oligomer synthesis becomes increasingly automated in much the same way peptide synthesis has, the ability to create anion-, light-, solvent-, and chiral-responsive helices will have profound consequences. Moreover, the rate of assessing structure-function relationships will only increase with the eventual aim of precisely programming macromolecular form and function.

The Berryman Research Group has been working towards creating longer *m*-arylene-ethynylene oligomers that incorporate neutral halogen-bond donors and hydrogen-bond-enhancing moieties. We predict that chain extension of the nine-mer featured in this dissertation will result in the elongation of the parent triple helicate. However, the utilization of neutral halogen-bond donors may lead to the self-assembly of single-strand helicates. These lower-order complexes are expected to partition in lipid bilayers and may exhibit anion transport properties.

The nine-mers developed in this dissertation follow a simple A–B repeat (A = halogen-bond donor, B = *m*-arylene-ethynylene spacer). What would be the result of an A–B–B repeat? By increasing the number of *m*-arylene-ethynylene spacers, could a

quadruple-strand helicate be realized? Incorporating different arylene substitution patterns (involving mixtures of *m*-, *p*-, or even *o*-) could afford a larger binding cavity. Thereby, oxoanions and even chiral anions could be targeted. Additionally, Glaser couplings could introduce butadiynyl groups, accomplishing the same goal.

Currently, our research group is working towards creating membrane-spanning anion helicates. Once developed, we believe these artificial anion channels will exhibit anion selectivity and fast transport kinetics. Our ultimate goal is to create anion channels that can be turned on/off through various stimuli (i.e. light-, pH-, chemically-gated). This research will allow for the development of new biomedical research tools to elucidate anion transport across biological membranes at atomic scale. Additionally, potential anticancer and antibiotic small molecules will be created. On account of the anion switchability of these helicates, diffusion and dilution would lead to the unfolding and facile degradation of these potential therapeutics. Perhaps this anion switchability could help prevent unwanted side effects.

References

1 G. Guichard and I. Huc, *Chem. Commun.*, 2011, **47**, 5933–5941.

2 D. L. Caulder and K. N. Raymond, *J. Chem. Soc. - Dalt. Trans.*, 1999, 1185–1200.

3 W. S. Horne and S. H. Gellman, 2008, **41**, 1399–1408.

4 H. Juwarker and K.-S. Jeong, *Chem. Soc. Rev.*, 2010, **39**, 3664.

5 H. Juwarker, J. M. Suk and K. S. Jeong, *Chem. Soc. Rev.*, 2009, **38**, 3316–3325.

6 and J. S. Quing He, Peiyu Tu, 2012, **55**, 46–93.

7 J. Zhao, D. Yang, X. J. Yang and B. Wu, *Coord. Chem. Rev.*, , DOI:10.1016/j.ccr.2018.01.002.

8 D. Yang, J. Zhao, X. J. Yang and B. Wu, *Org. Chem. Front.*, 2018, **5**, 662–690.

9 C. R. Rice, *Coord. Chem. Rev.*, 2006, **250**, 3190–3199.

10 C. Jia, W. Zuo, D. Zhang, X. J. Yang and B. Wu, *Chem. Commun.*, 2016, **52**, 9614–9627.

11 E. Yashima, K. Maeda, H. Iida, Y. Furusho and K. Nagai, 2009, 6102–6211.

12 E. Yashima, N. Ousaka, D. Taura, K. Shimomura, T. Ikai and K. Maeda, *Chem. Rev.*, 2016, **116**, 13752–13990.

13 B. B. Ni, Q. Yan, Y. Ma and D. Zhao, *Coord. Chem. Rev.*, 2010, **254**, 954–971.

14 K. Lindorff-Larsen, S. Piana, R. O. Dror and D. E. Shaw, *Science (80-.).*, 2011, **334**, 517–520.

15 I. Saraogi and A. D. Hamilton, *Chem. Soc. Rev.*, 2009, **38**, 1726–1743.

16 B. Gong, *October*.

17 J.-M. Lehn, *Proc. Natl. Acad. Sci. U. S. A.*, 2002, **99**, 4763–4768.

18 B. Di Jeso and P. Arvan, *Endocr. Rev.*, 2016, **37**, 2–36.

19 A. S. McCall, C. F. Cummings, G. Bhave, R. Vanacore, A. Page-Mccaw and B. G. Hudson, *Cell*, 2014, **157**, 1380–1392.

20 D. C. Gadsby, P. Vergani and L. Csanády, *Nature*, 2006, **440**, 477–483.

21 V. Balzani, A. Credi, F. M. Raymo and J. F. Stoddart, *Angew. Chemie - Int. Ed.*, 2000, **39**, 104–116.

22 A. Giuliani and A. C. Rinaldi, *Cell. Mol. Life Sci.*, 2011, **68**, 2255–2266.

23 G. N. Tew, R. W. Scott, M. L. Klein and W. F. Degrado, *Acc. Chem. Res.*, 2010, **43**, 30–39.

24 A. D. Bautista, C. J. Craig, E. A. Harker and A. Schepartz, *Curr. Opin. Chem. Biol.*, 2007, **11**, 685–692.

25 J. A. Kritzer, O. M. Stephens, D. A. Guarracino, S. K. Reznik and A. Schepartz, *Bioorganic Med. Chem.*, 2005, **13**, 11–16.

26 R. Gopalakrishnan, A. I. Frolov, L. Knerr, W. J. Drury and E. Valeur, *J. Med. Chem.*, 2016, **59**, 9599–9621.

27 V. Azzarito, K. Long, N. S. Murphy and A. J. Wilson, *Nat. Chem.*, 2013, **5**, 161–173.

28 S. Fahs, Y. Patil-Sen and T. J. Snape, *ChemBioChem*, 2015, **16**, 1840–1853.

29 L. K. A. Pilsl and O. Reiser, *Amino Acids*, 2011, **41**, 709–718.

30 G. Licini, L. J. Prins and P. Scrimin, *European J. Org. Chem.*, 2005, 969–977.

31 D. J. Hill, M. J. Mio, R. B. Prince, T. S. Hughes and J. S. Moore, *Chem. Rev.*, 2001, **101**, 3893–4011.

32 T. A. Martinek and F. Fülöp, *Chem. Soc. Rev.*, 2012, **41**, 687–702.

33 M. S. Cubberley and B. L. Iverson, *Curr. Opin. Chem. Biol.*, 2001, **5**, 650–653.

34 T. A. Martinek and F. Fülöp, *Eur. J. Biochem.*, 2003, **270**, 3657–3666.

35 R. P. Cheng, *Curr. Opin. Struct. Biol.*, 2004, **14**, 512–520.

36 I. Huc, *European J. Org. Chem.*, 2004, 17–29.

37 D. W. Zhang, X. Zhao, J. L. Hou and Z. T. Li, *Chem. Rev.*, 2012, **112**, 5271–5316.

38 S. Mecozzi and J. Rebek, *Chem. - A Eur. J.*, 1998, **4**, 1016–1022.

39 Z. T. Li, J. L. Hou, C. Li and H. P. Yi, *Chem. - An Asian J.*, 2006, **1**, 766–778.

40 S. De, B. Chi, T. Granier, T. Qi, V. Maurizot and I. Huc, *Nat. Chem.*, 2018, **10**, 51–57.

41 Y. Ferrand and I. Huc, *Acc. Chem. Res.*, 2018, **51**, 970–977.

42 M. Albrecht and R. Fröhlich, *Bull. Chem. Soc. Jpn.*, 2007, **80**, 797–808.

43 C. Piguet, G. Bernardinelli and G. Hopfgartner, *Chem. Rev.*, 1997, **97**, 2005–2062.

44 D. L. White, R. C. Scarrow and K. N. Raymond, *J. Am. Chem. Soc.*, 1985, **107**, 6540–6546.

45 J. M. Lehn, A. Rigault, J. Siegel, J. Harrowfield, B. Chevrier and D. Moras, *Proc. Natl. Acad. Sci.*, 1987, **84**, 2565–2569.

46 M. J. Hannon and L. J. Childs, *Supramol. Chem.*, 2004, **16**, 7–22.

47 C. He, Y. Zhao, D. Guo, Z. Lin and C. Duan, *Eur. J. Inorg. Chem.*, 2007, 3451–3463.

48 M. Albrecht, *Chem. Rev.*, 2001, **101**, 3457–3497.

49 A. Orita, T. Nakano, D. L. An, K. Tanikawa, K. Wakamatsu and J. Otera, *J. Am. Chem. Soc.*, 2004, **126**, 10389–10396.

50 J. C. Nelson, J. G. Saven, J. S. Moore and P. G. Wolynes, *Science (80-.).*, 1997, **277**, 1793–1796.

51 R. B. Prince, J. G. Saven, P. G. Wolynes and J. S. Moore, *J. Am. Chem. Soc.*, 1999, **121**, 3114–3121.

52 R. B. Prince, S. A. Barnes and J. S. Moore, *J. Am. Chem. Soc.*, 2000, **122**, 2758–2762.

53 A. Tanatani, M. J. Mio and J. S. Moore, *J. Am. Chem. Soc.*, 2001, **123**, 1792–1793.

54 A. Tanatani, T. S. Hughes and J. S. Moore, *Angew. Chemie - Int. Ed.*, 2002, **41**, 325–328.

55 J. M. Cary and J. S. Moore, *Org. Lett.*, 2002, **4**, 4663–4666.

56 M. J. Leavens, M. M. Cherney, M. L. Finnegan and B. E. Bowler, *Biochemistry*, 2018, **57**, 1711–1721.

57 O. Keunchan, K. S. Jeong and J. S. Moore, *Nature*, 2001, **414**, 889–893.

58 T. Nishinaga, A. Tanatani, K. Oh and J. S. Moore, *J. Am. Chem. Soc.*, 2002, **124**, 5934–5935.

59 M. T. Stone and J. S. Moore, *Org. Lett.*, 2004, **6**, 469–472.

60 J. M. Heemstra and J. S. Moore, *J. Org. Chem.*, 2004, **69**, 9234–9237.

61 J. M. Heemstra and J. S. Moore, *J. Am. Chem. Soc.*, 2004, **126**, 1648–1649.

62 J. M. Heemstra and J. S. Moore, *Chem. Commun.*, 2004, 1480–1481.

63 J. M. Heemstra and J. S. Moore, *Org. Lett.*, 2004, **6**, 659–662.

64 H. Goto, J. M. Heemstra, D. J. Hill and J. S. Moore, *Org. Lett.*, 2004, **6**, 889–892.

65 K. Goto and J. S. Moore, *Org. Lett.*, 2005, **7**, 1683–1686.

66 R. A. Smaldone and J. S. Moore, *J. Am. Chem. Soc.*, 2007, **129**, 5444–5450.

67 R. A. Smaldone and J. S. Moore, *Chem. Commun.*, 2008, 1011–1013.

68 M. Inouye, M. Waki and H. Abe, *J. Am. Chem. Soc.*, 2004, **126**, 2022–2027.

69 H. Abe, D. Murayama, F. Kayamori and M. Inouye, *Macromolecules*, 2008, **41**, 6903–6909.

70 H. Abe, H. Machiguchi, S. Matsumoto and M. Inouye, *J. Org. Chem.*, 2008, **73**, 4650–4661.

71 Y. Ohishi, H. Abe and M. Inouye, *Chem. - A Eur. J.*, 2015, **21**, 16504–16511.

72 T. Hayashi, Y. Ohishi, S. Hee-Soo, H. Abe, S. Matsumoto and M. Inouye, *J. Org. Chem.*, 2018, **83**, 8724–8730.

73 Y. Ohishi, H. Abe and M. Inouye, *European J. Org. Chem.*, 2017, **2017**, 6975–6979.

74 A. Khan, C. Kaiser and S. Hecht, *Angew. Chemie - Int. Ed.*, 2006, **45**, 1878–1881.

75 A. Khan and S. Hecht, *Chem. - A Eur. J.*, 2006, **12**, 4764–4774.

76 K. Bowman-James, *Acc. Chem. Res.*, 2005, **38**, 671–678.

77 J. Keegan, P. E. Kruger, M. Nieuwenhuyzen, J. O'brien and N. Martin, *Chem. Commun.*, 2001, **1**, 2192–2193.

78 P. M. Selvakumar, P. Y. Jebaraj, J. Sahoo, E. Suresh, K. J. Prathap, R. I. Kureshy and P. S. Subramanian, *RSC Adv.*, 2012, **2**, 7689–7692.

79 K. J. Chang, B. N. Kang, M. H. Lee and K. S. Jeong, *J. Am. Chem. Soc.*, 2005, **127**, 12214–12215.

80 V. R. Naidu, M. C. Kim, J. M. Suk, H. J. Kim, M. Lee, E. Sim and K. S. Jeong, *Org. Lett.*, 2008, **10**, 5373–5376.

81 U. Il Kim, J. M. Suk, V. R. Naidu and K. S. Jeong, *Chem. - A Eur. J.*, 2008, **14**, 11406–11414.

82 J. M. Suk and K. S. Jeong, *J. Am. Chem. Soc.*, 2008, **130**, 11868–11869.

83 J. Il Kim, H. Juwarker, X. Liu, M. S. Lah and K. S. Jeong, *Chem. Commun.*, 2010, **46**, 764–766.

84 J. M. Suk, J. Il Kim and K. S. Jeong, *Chem. - An Asian J.*, 2011, **6**, 1992–1995.

85 J. M. Suk, V. R. Naidu, X. Liu, M. S. Lah and K. S. Jeong, *J. Am. Chem. Soc.*, 2011, **133**, 13938–13941.

86 J. M. Suk, D. A. Kim and K. S. Jeong, *Org. Lett.*, 2012, **14**, 5018–5021.

87 M. J. Kim, H. W. Lee, D. Moon and K. S. Jeong, *Org. Lett.*, 2012, **14**, 5042–5045.

88 D. A. Kim, P. Kang, M. G. Choi and K. S. Jeong, *Chem. Commun.*, 2013, **49**, 9743–9745.

89 H. G. Jeon, H. B. Jang, P. Kang, Y. R. Choi, J. Kim, J. H. Lee, M. G. Choi and K. S. Jeong, *Org. Lett.*, 2016, **18**, 4404–4407.

90 H. Juwarker, J. M. Lenhardt, D. M. Pham and S. L. Craig, *Angew. Chemie - Int. Ed.*, 2008, **47**, 3740–3743.

91 H. Juwarker, J. M. Lenhardt, J. C. Castillo, E. Zhao, S. Krishnamurthy, R. M. Jamiolkowski, K. H. Kim and S. L. Craig, *J. Org. Chem.*, 2009, **74**, 8924–8934.

92 Y. Wang, F. Li, Y. Han, F. Wang and H. Jiang, *Chem. - A Eur. J.*, 2009, **15**, 9424–9433.

93 Y. Wang, F. Bie and H. Jiang, *Org. Lett.*, 2010, **12**, 3630–3633.

94 W. Zhao, Y. Wang, J. Shang, Y. Che and H. Jiang, *Chem. - A Eur. J.*, 2015, **21**, 7731–7735.

95 J. Shang, W. Zhao, X. Li, Y. Wang and H. Jiang, *Chem. Commun.*, 2016, **52**, 4505–4508.

96 W. Zhao, F. Huang, Y. Wang, Q. Li, J. Shang, Y. Che and H. Jiang, *Tetrahedron*

Lett., 2016, **57**, 1691–1694.

97 L. Yang, Y. Wang, Y. Che and H. Jiang, *Org. Biomol. Chem.*, 2017, **15**, 7747–7752.

98 L. Yang, W. Zhao, Y. K. Che, Y. Wang and H. Jiang, *Chinese Chem. Lett.*, 2017, **28**, 1659–1662.

99 Y. X. Xu, G. T. Wang, X. Zhao, X. K. Jiang and Z. T. Li, *J. Org. Chem.*, 2009, **74**, 7267–7273.

100 Z. M. Shi, S. G. Chen, X. Zhao, X. K. Jiang and Z. T. Li, *Org. Biomol. Chem.*, 2011, **9**, 8122–8129.

101 Y. Hua and A. H. Flood, *J. Am. Chem. Soc.*, 2010, **132**, 12838–12840.

102 Y. Hua, R. O. Ramabhadran, J. A. Karty, K. Raghavachari and A. H. Flood, *Chem. Commun.*, 2011, **47**, 5979–5981.

103 S. Lee, Y. Hua and A. H. Flood, *J. Org. Chem.*, 2014, **79**, 8383–8396.

104 Y. Hua, Y. Liu, C. H. Chen and A. H. Flood, *J. Am. Chem. Soc.*, 2013, **135**, 14401–14412.

105 C. Jia, B. Wu, S. Li, X. Huang and X. J. Yang, *Org. Lett.*, 2010, **12**, 5612–5615.

106 Y. Haketa, Y. Bando, K. Takaishi, M. Uchiyama, A. Muranaka, M. Naito, H. Shibaguchi, T. Kawai and H. Maeda, *Angew. Chemie - Int. Ed.*, 2012, **51**, 7967–7971.

107 H. Maeda, T. Shirai, Y. Bando, K. Takaishi, M. Uchiyama, A. Muranaka, T. Kawai and M. Naito, *Org. Lett.*, 2013, **15**, 6006–6009.

108 Y. J. Li, L. Xu-, W. L. Yang-, H. B. Liu, S. W. Lai, C. M. Che and Y. L. Li, *Chem. - A Eur. J.*, 2012, **18**, 4782–4790.

109 L. Cao, R. Jiang, Y. Zhu, X. Wang, Y. Li and Y. Li, *European J. Org. Chem.*, 2014, **2014**, 2687–2693.

110 J. V. Gavette, C. J. Evoniuk, L. N. Zakharov, M. E. Carnes, M. M. Haley and D. W. Johnson, *Chem. Sci.*, 2014, **5**, 2899–2905.

111 J. V. Gavette, N. S. Mills, L. N. Zakharov, C. A. Johnson, D. W. Johnson and M. M. Haley, *Angew. Chemie - Int. Ed.*, 2013, **52**, 10270–10274.

112 M. Zurro, S. Asmus, S. Beckendorf, C. Mück-Lichtenfeld and O. G. Mancheño, *J. Am. Chem. Soc.*, 2014, **136**, 13999–14002.

113 R. Tepper and U. S. Schubert, *Angew. Chemie Int. Ed.*, 2018, **57**, 6004–6016.

114 J. Y. C. Lim and P. D. Beer, *Chem*, 2018, **4**, 731–783.

115 P. J. Costa, *Phys. Sci. Rev.*

116 D. Bulfield and S. M. Huber, *Chem. Eur. J.*, 2016, **22**, 14434–14450.

117 L. C. Gilday, S. W. Robinson, T. A. Barendt, M. J. Langton, B. R. Mullaney and P. D. Beer, *Chem. Rev.*, 2015, **115**, 7118–7195.

118 M. R. Scholfield, C. M. Vander Zanden, M. Carter and P. S. Ho, *Protein Sci.*, 2013, **22**, 139–152.

119 T. M. Beale, M. G. Chudzinski, M. G. Sarwar and M. S. Taylor, *Chem. Soc. Rev.*, 2013, **42**, 1667–1680.

120 M. Erdelyi, *Chem. Soc. Rev.*, 2012, **41**, 3547–3557.

121 G. Cavallo, P. Metrangolo, T. Pilati, G. Resnati, M. Sansotera and G. Terraneo, *Chem. Soc. Rev.*, 2010, **39**, 3772–3783.

122 P. Politzer, J. S. Murray and T. Clark, *Phys. Chem. Chem. Phys.*, 2010, **12**, 7748–7757.

123 A. C. Legon, *Phys. Chem. Chem. Phys.*, 2010, **12**, 7736–7747.

124 J. W. Lauher, F. W. Fowler and N. S. Goroff, *Acc. Chem. Res.*, 2008, **41**, 1215–1229.

125 P. Politzer, P. Lane, M. C. Concha, Y. Ma and J. S. Murray, *J. Mol. Model.*, 2007, **13**, 305–311.

126 P. Metrangolo, H. Neukirch, T. Pilati and G. Resnati, *Acc. Chem. Res.*, 2005, **38**, 386–395.

127 P. Metrangolo and G. Resnati, *Chem. Eur. J.*, 2001, **7**, 2511–2519.

128 F. Zapata, A. Caballero, P. Molina, I. Alkorta and J. Elguero, *J. Org. Chem.*, 2014, **79**, 6959–6969.

129 A. Borissov, J. Y. C. Lim, A. Brown, K. E. Christensen, A. L. Thompson, M. D. Smith and P. D. Beer, *Chem. Commun.*, 2017, **53**, 2483–2486.

130 B. Wu, C. Jia, X. Wang, S. Li, X. Huang and X. J. Yang, *Org. Lett.*, 2012, **14**, 684–687.

131 P. Yang, J. Wang, C. Jia, X.-J. Yang and B. Wu, *European J. Org. Chem.*, 2013, **2013**, 3446–3454.

132 F. Bie, Y. Wang, J. Shang, N. M. Gallagher and H. Jiang, *European J. Org. Chem.*, 2013, **1**, 8135–8144.

133 Y. Haketa and H. Maeda, *Chem. - A Eur. J.*, 2011, **17**, 1485–1492.

134 J. Sánchez-Quesada, C. Seel, P. Prados, J. De Mendoza, I. Dalcol and E. Giralt, *J. Am. Chem. Soc.*, 1996, **118**, 277–278.

135 S. Li, C. Jia, B. Wu, Q. Luo, X. Huang, Z. Yang, Q. S. Li and X. J. Yang, *Angew. Chemie - Int. Ed.*, 2011, **50**, 5721–5724.

136 M. Albrecht and S. Kotila, *Angew. Chemie Int. Ed.*, 2003, **34**, 2134–2137.

137 B. Wu, S. Li, Y. Lei, H. Hu, N. D. S. Amadeu, C. Janiak, J. S. Mathieson, D. L. Long, L. Cronin and X. J. Yang, *Chem. - A Eur. J.*, 2015, **21**, 2588–2593.

138 X. Bai, C. Jia, Y. Zhao, D. Yang, S.-C. Wang, A. Li, Y.-T. Chan, Y.-Y. Wang, X.-J. Yang and B. Wu, *Angew. Chemie*, 2018, **130**, 1869–1873.

139 C. Jia, W. Zuo, D. Yang, Y. Chen, L. Cao, R. Custelcean, J. Hostaš, P. Hobza, R. Glaser, Y.-Y. Wang, X.-J. Yang and B. Wu, *Nat. Commun.*, 2017, **8**, 938.

140 W. Zuo, Z. Huang, Y. Zhao, W. Xu, Z. Liu, X. J. Yang, C. Jia and B. Wu, *Chem. Commun.*, 2018, **54**, 7378–7381.

141 H. Maeda, K. Kitaguchi and Y. Haketa, *Chem. Commun.*, 2011, **47**, 9342–9344.

142 A. M. S. Riel, D. A. Decato, J. Sun, C. J. Massena, M. J. Jessop and O. B. Berryman, *Chem. Sci.*, 2018, **9**, 5828–5836.

143 E. A. Katayev, N. V Boev, V. N. Khrustalev, Y. A. Ustynyuk, I. G. Tananaev and J. L. Sessler, *J. Org. Chem.*, 2007, **72**, 2886–2896.

144 V. McKee, J. Nelson and R. M. Town, *Chem. Soc. Rev.*, 2003, **32**, 309–325.

145 B. M. Rambo and J. L. Sessler, *Chem. – A Eur. J.*, **17**, 4946–4959.

146 E. A. Katayev, G. V Kolesnikov and J. L. Sessler, *Chem. Soc. Rev.*, 2009, **38**, 1572–1586.

147 B. H. Kaae, K. Harpsøe, T. Kvist, J. M. Mathiesen, C. Mølck, D. Gloriam, H. N. Jimenez, M. A. Uberti, S. M. Nielsen and B. Nielsen, *ChemMedChem*, 2012, **7**, 440–451.

148 K. Sonogashira, Y. Tohda and N. Hagihara, *Tetrahedron Lett.*, 1975, **16**, 4467–4470.

149 A. R. Cowley, J. R. Dilworth and M. Salichou, *Dalt. Trans.*, 2007, 1621–1629.

150 A. Abate, J. Martí-Rujas, P. Metrangolo, T. Pilati, G. Resnati and G. Terraneo, *Cryst. Growth Des.*, 2011, **11**, 4220–4226.

151 S. H. Jungbauer, S. M. Walter, S. Schindler, L. Rout, F. Kniep and S. M. Huber, *Chem. Commun.*, 2014, **50**, 6281–6284.

152 C. Frassineti, S. Ghelli, P. Gans, A. Sabatini, M. S. Moruzzi and A. Vacca, *Anal. Biochem.*, 1995, **231**, 374–382.

153 P. Quagliotto, G. Viscardi, C. Barolo, E. Barni, S. Bellinvia, E. Fisicaro and C. Compari, *J. Org. Chem.*, 2003, **68**, 7651–7660.

154 S. Ladouceur, D. Fortin and E. Zysman-Colman, *Inorg. Chem.*, 2010, **49**, 5625–5641.

155 C. Uyeda and E. N. Jacobsen, *J. Am. Chem. Soc.*, 2008, **130**, 9228–9229.

156 D. L. Reger, T. D. Wright, C. A. Little, J. J. S. Lamba and M. D. Smith, *Inorg. Chem.*, 2001, **40**, 3810–3814.

157 O. V Dolomanov, L. J. Bourhis, R. J. Gildea, J. A. K. Howard and H. Puschmann, *J. Appl. Crystallogr.*, 2009, **42**, 339–341.

158 G. M. Sheldrick, *Acta Crystallogr. Sect. C Struct. Chem.*, 2015, **71**, 3–8.

159 G. R. Desiraju, P. S. Ho, L. Kloo, A. C. Legon, R. Marquardt, P. Metrangolo, P. Politzer, G. Resnati and K. Rissanen, *Pure Appl. Chem.*, 2013, **85**, 1711–1713.

160 S. V Rosokha, I. S. Neretin, T. Y. Rosokha, J. Hecht and J. K. Kochi, *Heteroat. Chem. An Int. J. Main Gr. Elem.*, 2006, **17**, 449–459.

161 W. B. Wan and M. M. Haley, *J. Org. Chem.*, 2001, **66**, 3893–3901.

162 S. Z. Vatsadze, I. D. Titanyuk, A. V Chernikov and N. V Zyk, *Russ. Chem. Bull.*,

2004, **53**, 471–473.

163 A. J. Martínez-Martínez, A. R. Kennedy, R. E. Mulvey and C. T. O'Hara, *Science (80-.).*, 2014, **346**, 834–837.

164 D. A. Shultz, H. Lee, R. K. Kumar and K. P. Gwaltney, *J. Org. Chem.*, 1999, **64**, 9124–9136.

165 Y. Tobe, J. Kishi, I. Ohki and M. Sonoda, *J. Org. Chem.*, 2003, **68**, 3330–3332.

166 T. Usuki, H. Yamada, T. Hayashi, H. Yanuma, Y. Koseki, N. Suzuki, Y. Masuyama and Y. Y. Lin, *Chem. Commun.*, 2012, **48**, 3233–3235.

167 A. L. Spek, *Acta Crystallogr. Sect. C Struct. Chem.*, 2015, **71**, 9–18.

168 K. L. Schuchardt, *J. Chem. Inf. Model.*, 2007, **47**, 1045.

169 J. Lu, D. Ma, J. Hu, W. Tang and D. Zhu, *J. Chem. Soc. Dalt. Trans.*, 1998, 2267–2274.

170 C. L. Perrin and T. J. Dwyer, *Chem. Rev.*, 1990, **90**, 935–967.